Physiopathologie de l'infection du système nerveux central par des virus respiratoires

Marion Ferren

N°d'ordre NNT : 2021LYSE1312

THESE de DOCTORAT DE L'UNIVERSITE DE LYON
opérée au sein de
l'Université Claude Bernard Lyon 1

Ecole Doctorale N° 340
Biologie Moléculaire, Intégrative et Cellulaire

Spécialité de doctorat : Virologie
Discipline : Sciences de la vie

Soutenue publiquement le 17/12/2021, par :
Marion Ferren

Physiopathologie de l'infection du système nerveux central par des virus respiratoires

Rôle de la machinerie de fusion

Devant le jury composé de :

Faure, Mathias	Professeur à l'Université de Lyon	Président du jury
Salinas, Sara	Chargée de recherche INSERM	Rapporteure
Plattet, Philippe	Professeur à l'Université de Berne	Rapporteur
Coulpier, Muriel	Directrice de recherche INRAE	Examinatrice
Lozach, Pierre-Yves	Directeur de recherche INRAE	Examinateur
Pain, Bertrand	Directeur de recherche INRAE	Examinateur
Muriaux, Delphine	Directrice de recherche IRIM	Examinatrice
Mathieu, Cyrille	Chargé de recherche CNRS	Directeur de thèse

A ma grand-mère,

A ma mère,

A mon père,

REMERCIEMENTS

Au Jury et au comité de suivi de thèse

Tout d'abord je remercie les membres du jury qui ont gentiment accepté d'évaluer mon travail de thèse. Sara Salinas et Philippe Plattet, merci d'avoir tout de suite accepté d'être rapporteurs de mon manuscrit. De par vos compétences respectives je n'aurais pas pu rêver mieux pour évaluer mon travail. Vos retours positifs et votre enthousiasme m'encouragent et signifient beaucoup pour moi. Merci également d'être venus de Montpellier et de Bern pour le jour de la soutenance.

Merci à tous les examinateurs. Mathias Faure, merci d'avoir pris le temps de participer à mon jury je sais que ton emploi du temps est particulièrement chargé. Merci à Muriel Coulpier, nous avons eu l'occasion d'interagir par visio-conférences et ça me fait particulièrement plaisir que tu aies pu faire le déplacement. Merci à Pierre-Yves Lozach, je me suis beaucoup appuyée sur vos travaux et je tiens une partie de ma thèse aux conseils de Colin ! Merci Bertrand Pain, grâce à vous nous avons pu réaliser un projet dont nous rêvions depuis des années ! Merci Delphine Muriaux d'avoir accepté de venir examiner mes travaux depuis Montpellier.

Je souhaite aussi remercier les membres de mon comité de suivi de thèse, Daniel Dunia et Hélène Dutartre. Vos conseils ont été d'or dès la première année. Je n'ai pas suivi tous vos conseils instantanément mais ils restent tous dans un coin de ma tête et me serviront tout au long de ma carrière. Vous avez toujours répondu présents lorsque j'avais des questions et je vous en suis reconnaissante.

Au labo

Evidemment, merci Cyrille. Le mot est faible pour exprimer ma gratitude ! Ton énergie débordante apporte de la bonne humeur au quotidien et tu es la preuve vivante que la rigueur et le travail sérieux ne sont pas incompatibles avec les plaisanteries, les paillardes et les bêtises en tout genre. Je te remercie particulièrement d'avoir toujours été présent quand j'en avais besoin, d'avoir été à l'écoute et d'avoir su me remotiver dans mes moments de doute. Ta réserve de secours inépuisable de kinders cachés dans ton tiroir a beaucoup aidé. Tu as été un directeur de thèse très exigeant et je t'en remercie car ça m'a poussé à relever le défi et le travail a payé. Tu m'as fait confiance en me permettant de présenter à plusieurs reprises mes résultats lors de congrès internationaux. Je mesure la chance que j'ai eue. Merci de m'avoir transmis tout ce que tu as pu avec passion et, au-delà de la thèse, de m'avoir fait découvrir tous les aspects du monde de la recherche. Merci d'avoir toujours cru en moi.

Je remercie Denis Gerlier, tu as été mon maitre de stage à deux reprises il y a 9 ans lorsque je n'étais qu'en licence et c'est à toi que je dois mon goût pour les Paramyxovirus. J'ai bien essayé d'autres virus par la suite mais dans mon cœur rien n'égalera jamais le bonheur de voir apparaitre un magnifique syncytium ! Tu prodigues toujours de précieux conseils, scientifiques mais également éthiques qui poussent à se poser les bonnes questions. Merci d'avoir corrigé mon manuscrit de thèse, de m'avoir remotivée lorsque même Cyrille n'y arrivait plus, d'avoir toujours été là pour répondre à toutes mes questions.

Merci Branka Horvat, tu m'as accueillie chaleureusement lorsque je suis revenue en 2018 et tu m'as permis de prendre part à des projets qui m'ont beaucoup apporté. J'ai adoré faire partie de l'équipe d'immunobiologie des infections virales dans laquelle je me suis sentie plus que jamais chez moi. Ta porte est toujours ouverte et tu t'es toujours intéressée à mes travaux. Tes conseils pertinents, particulièrement pour les présentations orales et les dossiers de candidatures m'ont beaucoup aidé.

Rodolphe, c'était génial de t'avoir comme coéquipier de thèse. Merci pour les milliers de cafés, les discussions sur le sens de la vie et les débats improbables, les après-midis jeux sociétés, ton aide informatique, etc. C'était rassurant de savoir que je n'étais pas seule dans cette ~~galère~~ merveilleuse aventure et je suis fière qu'on y soit arrivé tous les deux. Je sais que tu m'as confié la garde de Roule & Bille mais je te le prêterai de temps en temps, promis !

Mathieu, merci pour les véritables cours particuliers d'immunologie et de cytométrie. Tu m'as tellement aidé sans me juger tout au long de ma thèse. Tu vas t'ennuyer sans nos discussions sur le monde et le féminisme !

Merci à Didier, le MacGyver du labo, tu répares tout et tu es le roi des bons plans ! Merci pour tout ce que tu m'as appris et merci de m'avoir mis en relation avec Nadia sans qui notre papier aurait été beaucoup moins percutant. Merci aussi pour MiFoBio mais surtout merci pour ta gentillesse qui réchauffe le cœur tous les jours au labo.

Alexandre (Lalande), je te remercie par anticipation. Tu n'imagines pas à quel point ça m'enlève un poids de savoir que mes projets inachevés sont entre de bonnes mains. Je te confie mon bébé. Tu as toute ma confiance.

Merci aux stagiaires qui ont participé à mes projets et qui ont toutes apporté un vent de fraicheur : Victoire, Manon, Sophie, Elodie. A votre contact j'ai appris tout autant que vous !

Merci à tous les autres membres présents et passés du laboratoire : Valérie, Olivier, Claire, Géraldine, Lucia, Magalie, Saïd, Claudia, Alexandre, Maria, Aline, Florentine, Aude, Noémie, Andreas, Jonathan.

Merci à Sébastien du plateau de cytométrie en flux pour les centaines d'heures passées à s'arracher les cheveux sur ma problématique.

Merci à Jacques et à Elodie du PLATIM pour leur bonne humeur et pour m'avoir formé et aidé maintes fois sur les microscopes.

Je remercie tous les membres de l'équipe P4 : Christophe pour ta bonne humeur et pour avoir subi mes E63 très souvent faux ; Stéphane M, Stéphanie, Damien, Sabine et Elodie de la GDS et de l'équipe in-vitro pour avoir su vous adapter à mes protocoles imprévus ; et à tous les autres membres, Béatrice, Alban, Stéphane B, Audrey, Marie, Ophélie, Orianne, Hubert.

Je remercie également Christophe Gomez pour avoir pris soin de mes bébés hamsters, Elise pour sa bonne humeur qui a égayé mes journées et pour son efficacité, tous les membres du secrétariat de la tour pour votre réactivité, en particulier Carine qui m'a sauvé la vie un nombre de fois incalculable.

Je remercie les collègues de la tour CERVI, les membres des équipes VIRIMI et NOPAB avec qui j'ai vraiment apprécié interagir, notamment Pierre-Olivier, Laure, Clémence, Véronique B, Maxime et Xavier.

Je remercie les collègues du 3ème des équipes UBIV et BMPV, surtout ceux qui m'ont accompagné au P4 et gentiment aidé à chaque fois que j'ai eu besoin d'aide ; Valentina, Ronald, Emeric, Stéphanie R, Mathieu M, Xavier, Othman, Kodie, Virginie, Gustave, Jimmy, Clara, Alexandra et Caroline.

Je remercie aussi Joanna, tu resteras toujours ma formatrice et quelle chance j'ai eu ! Merci Justine pour ta spontanéité ! Enfin, je remercie toutes les personnes que je n'ai pas citées mais qui m'ont aidée ou encouragée, scientifiquement ou simplement par leurs sourires bienveillants, mention spéciale à Brenda.

A mes amis et ma famille

Je remercie mes amis qui m'ont soutenue, plus particulièrement Lucie et Julie qui m'ont écoutée attentivement pendant des heures lorsque j'avais envie de raconter mes déboires au labo et/ou mes incroyables découvertes. Vous m'avez toujours encouragée et vous avez toujours essayé de comprendre, à tous les niveaux. Merci Eléonore également d'avoir toujours été là quand j'ai eu besoin de toi, c'est précieux. Merci aux copines de l'ESTBB, Coralie C, Coralie R, Alice, Léa, Audrey et Blandine.

Enfin, un grand merci à ma famille. Je remercie surtout ma grand-mère, ma plus grande fan. Mamie, tu es la personne qui s'intéresse le plus à mon travail, toujours à me poser des questions improbables auxquelles je ne sais parfois pas répondre. Chaque semaine quand je viens manger chez toi tu prends soin de moi, tu ne perds pas une miette de ce que je raconte, tu prends des notes, et tu me donnes des leçons de vie ; je n'aurais pas pu rêver mieux comme soutien pendant ma thèse. Je remercie aussi ma mère, tu as tout mis en œuvre pour que je puisse réaliser cette thèse dans les meilleures conditions possibles. Merci Maman de t'être toujours intéressée à mes travaux, de m'avoir écoutée quand j'essayais tant bien que mal, tard le soir, de t'expliquer mes résultats avec des schémas gribouillés sur des post-it. Mais surtout, merci de m'avoir toujours fait confiance. Merci à Alain aussi, avec maman tu m'as supportée au quotidien et je sais que je peux compter sur toi en toute circonstance. Je remercie bien sur mon père pour avoir cru en moi et pour m'avoir ~~fait croire que faire deux thèses c'était facile~~ prouvé que le travail porte toujours ses fruits. Enfin, merci à tous les autres membres de ma famille sans exception, vous avez tous participé à me faire avancer, de près ou de loin, même sans le savoir.

TABLE DES MATIERES

RESUMÉ

Les virus respiratoires aéroportés sont particulièrement préoccupants du fait de la difficulté de contrôler leur transmission. Parmi ces virus, le virus du syndrome respiratoire aigu sévère 2 (SARS-CoV-2), le virus de la rougeole (VR) et les Henipavirus Nipah (NiV) et Hendra (HeV) peuvent infecter également le système nerveux central (SNC) chez l'homme et provoquent alors souvent des encéphalites létales. Par exemple, le SARS-CoV-2, responsable de la pandémie de COVID-19, entraine un syndrome respiratoire aigu sévère et des atteintes neurologiques. De son côté, et malgré un vaccin efficace, la rougeole connaît une réémergence inquiétante et cause la mort de plus de 200 000 personnes par an. Le VR peut entraîner des encéphalites rougeoleuses à corps d'inclusion (MIBE) dans un contexte d'immunodéficience ou une panencéphalite sclérosante subaiguë (PESS) parfois des décennies après l'exposition au virus chez des patients immunocompétents. NiV et HeV sont des Paramyxovirus zoonotiques hautement pathogènes du genre Henipavirus. Malgré le faible nombre de cas humains recensés depuis leur émergence à la fin des années 1990, les NiV et HeV sont classés parmi les huit pathogènes prioritaires pour la recherche par l'Organisation Mondiale de la Santé en raison de leur fort potentiel pandémique. Certaines souches sont mortelles dans plus de 70% des cas en moyenne.

À ce jour il n'existe pas de traitement efficace commercialisé pour traiter ces infections virales chez l'homme. De plus, les étapes précoces de l'infection du SNC par ces virus restent peu documentées car la majorité des données proviennent d'analyses réalisées *post mortem*. L'objectif global de cette thèse a été d'identifier des facteurs influençant l'invasion du SNC par ces virus. Le tropisme initial, la dissémination, ainsi que l'implication des glycoprotéines virales de surface et l'évolution génétique virale ont été analysées pour le SARS-CoV-2, le VR et plusieurs souches d'Henipavirus à l'échelle organique, cellulaire et moléculaire.

Deux nouveaux modèles de cultures organotypiques de poumons et de tronc cérébral chez le hamster ont été développés et caractérisés. Ces modèles *ex vivo* sont susceptibles à l'infection par le SARS-CoV-2 et par le NiV. En revanche, un mutant hyperfusogène du VR, pourtant capable de fusionner en l'absence de récepteur connu, n'infecte que les cultures de cerveau. Ces cultures organotypiques ont permis de valider le tropisme initial du SARS-CoV-2 dans les poumons et démontré la permissivité de certains neurones dans le cerveau. Ces modèles ont également permis d'établir que l'infection par le SARS-CoV-2 induit une réponse interféron spécifique et une réponse immunitaire innée, ainsi qu'une mort cellulaire par apoptose, nécroptose et pyroptose dans ces organes. Enfin, ces cultures organotypiques ont montré leur pertinence dans la validation d'antiviraux. L'étude de VR portant des mutations dans leur protéine de fusion observées lors d'encéphalites rougeoleuses a montré l'importance du caractère hyperfusogène de ces mutants pour se disséminer dans le SNC pourtant dépourvu de récepteurs connus. Des différences dans la machinerie de fusion de trois souches pathogènes d'Henipavirus ont aussi été identifiées et analysées.

Grace aux cultures organotypiques cérébrales de hamster et de souris transgéniques plusieurs candidats antiviraux ont été testés pour bloquer la dissémination du VR sauvage et de variants neuroinvasifs, mais aussi du NiV et du SARS-CoV-2. Ces résultats donnent des perspectives nouvelles d'utilisation de ces modèles *ex vivo* pour étudier l'infection par des virus émergents et pour évaluer l'efficacité de traitements en amont de validation *in vivo*. L'étude comparative de l'infection des cultures organotypiques par ces virus respiratoires à pathogénicité variable a illustré comment la machinerie de fusion peut influencer la dissémination virale dans le cerveau.

ABSTRACT

Airborne respiratory viruses are of particular concern because of the difficulty in controlling their transmission. Among these viruses, severe acute respiratory syndrome virus 2 (SARS-CoV-2), measles virus (MeV) and Henipavirus Nipah (NiV) and Hendra (HeV) can also infect the central nervous system (CNS) in humans and cause lethal encephalitis. For example, SARS-CoV-2, responsible for the COVID-19 pandemic, causes severe acute respiratory syndrome and neurological syndromes. Despite an effective vaccine, measles is reemerging and still responsible of more than 200 000 deaths per year. MeV can lead to measles inclusion-body encephalitis (MIBE) in immunocompromised patients or sub-acute sclerosing panencephalitis (SSPE) sometimes decades after exposure to the virus in immunocompetent patients. NiV and HeV are highly pathogenic zoonotic Paramyxoviruses that belong to the genus Henipavirus. Despite the low number of human cases recorded since their emergence in the late 1990s, NiV and HeV are classified among the top eight pathogens to prioritize for research and development in public health emergency contexts by the World Health Organization because of their high pandemic potential. Some strains are fatal in more than 70% of cases.

To date, there is no effective commercialized treatment to cure these viral infections in human. Moreover, the early stages of the CNS infection by these three viruses remain poorly documented because most of the data come from post-mortem analyzes. The overall objective of this thesis was to identify factors influencing the CNS invasion by these viruses. The initial tropism, the dissemination, as well as the involvement of viral surface glycoproteins and viral genetic evolution were analyzed for SARS-CoV-2, MeV and several Henipavirus strains at the organic, cellular, and molecular levels.

Two new models of organotypic cultures from hamster brainstem and lung have been developed and characterized. These *ex vivo* models are susceptible to the infection with SARS-CoV-2 and NiV. In contrast, a hyperfusogenic MeV mutant able to fuse in absence of known receptor, could only infect brain cultures. In these organotypic cultures the initial tropism of SARS-CoV-2 in the lungs was validated and the permissiveness of certain neurons in the brain was demonstrated. The results also showed that SARS-CoV-2 infection induces specific interferon and innate immune responses, along with cell death by apoptosis, necroptosis, and pyroptosis. Finally, these organotypic cultures have shown their relevance in validating the effect of antiviral treatments. The study of MeV carrying mutations in their fusion protein observed in measles encephalitis cases has shown the importance of the hyperfusogenic property to disseminate within the CNS, which lacks the expression of known receptors. Differences in the fusion machinery of three pathogenic Henipavirus strains were also identified and analyzed.

Several antiviral candidates have been tested in organotypic brain cultures from hamsters and transgenic mice to block the dissemination of wild-type MeV and neuroinvasive MeV variants, but also of NiV and SARS-CoV-2. These results pave the way for the use of these *ex vivo* models to study newly emerged viruses' pathogenesis and assess the efficacy of candidate antivirals before *in vivo* validation. The comparative study of the organotypic culture infections by these respiratory viruses with high pathogenicity differences illustrated how the fusion machinery can influence the viral dissemination in the brain.

TABLE DES FIGURES

TABLE DES TABLEAUX

LISTE DES ABREVIATIONS

17-DMAG	17-Dimethylaminoethylamino-17-demethoxygeldanamycin
3D	3 dimensions
3G	N-[3-cyanophenyl]-2-phenylacetamide
ACE2	Angiotensin converting enzyme 2
Ad26	Adénovirus humain de type 26
ADAR1	Adénosine désaminase agissant sur l'ARN 1
ADN	Acide désoxyribonucléique
ARN	Acide ribonucléique
ARNm	ARN messager
APME	Encéphalite aiguë post-infection
ATP	Adénosine-triphosphate
BHE	Barrière hémato-encéphalique
CADM1/CADM2	Molécules d'adhésion cellulaires 1 ou 2
CB-28k	Calbindin C28K
CDC	Centre pour le control des maladies
CDV	Canine distemper virus
CedV	Virus Cedar
COC	Cultures organotypiques de cervelet
COVID-19	Coronavirus disease 2019
CPA	Cellules présentatrices d'antigènes
DMV	Vésicules à double membranes induites par le virus
EFN B1	Ephrine B1
EFN B2	Ephrine B2
EFN B2	Ephrine B3
eGFP	Enhanced Green Fluorescent Protein
EPI	Programme étendu sur l'immunisation
F	Protéine de fusion
FIP	Peptide inhibiteur de fusion ; Carbobenzoxy-d-Phe-l-Phe-Gly
FP	Peptide de fusion
G	Glycoprotéine
GAG	Glyco-Amino-Glycanes
GFAP	Glial fibrillary acidic protein
Iba1	Ionized calcium-binding adapter molecule 1
IRA	Insuffisance rénale aiguë
ISG	Gènes stimulés par l'interféron
H	Hémagglutinine
HCoV	Coronavirus humains endémiques
HeV	Virus Hendra
hPIV3	Virus humain parainfluenza de type 3
HRN	Heptades répétées à l'extrémité N terminale
HRC	Heptades répétées à l'extrémité C terminale
HRC4	Peptide dimère dérivé de la séquence du HRC de la F du VR
HS	Héparanes sulfates
HSP90	Protéine de choc thermique Hsp90
IFN-1	Interféron de type 1
IFNAR	Récepteur de l'interféron de type 1
LCR	Liquide céphalo-rachidien
mAb	Anticorps monoclonal de souris
MBP	Protéine basique de myéline
MERS-CoV	Coronavirus relatif au syndrome respiratoire du Moyen-Orient

MIBE	Encéphalite rougeoleuse à corps d'inclusion
N	Nucléoprotéine
NECT	Transfert de cytoplasme induit par la nectine
NiV	Virus Nipah
NiV Mal	Souche Malaisienne du virus Nipah
NiV Ban	Souche du Bangladesh du virus Nipah
Nt	Nucléotides
Olig-2	Oligodendrocyte transcription factor 2
OMS	Organisation Mondiale de la Santé
PAHO	Organisation de santé pan américaines
PBMC	Cellules mononucléées du sang périphérique
PCR	Amplification en Chaîne par Polymérase
PEG	Polyéthylène glycol
PESS	Panencéphalite sclérosante subaiguë
PFU	Unité formant une plaque
PLR	Protéine de liaison au récepteur
PVLR4	Poliovirus receptor-related protein 4 ; nectine-4
RBD	Domaine de liaison au récepteur
RdRp	ARN polymérase ARN-dépendante
RIG-I	Retinoic acid-43 inducible gene I
RLR	RIG-I Like Receptors
RNP	Complexe ribonucléoprotéique
ROR	Vaccin combiné rougeole oreillons rubéole
RT-qPCR	Réverse transcription suivie d'une PCR quantitative
S	Protéine spike
SARS-CoV	Coronavirus du syndrome respiratoire aigu sévère
SARS-CoV-2	Coronavirus du syndrome respiratoire aigu sévère 2
scFv	Single-chain antibody fragment
sG	Glycoprotéine G soluble
siRNA	Petits ARN interférents
SLAMF1	Signaling lymphocytic activation molecule family 1 ; CD150
SNC	Système nerveux central
TMPRSS2	Protéase sérine transmembranaire 2
VIH	Virus de l'immunodéficience humaine
VLP	Pseudo-particules virales
VR	Virus de la rougeole
VSV	Virus de la stomatite vésiculaire
WT	Sauvage

Les virus respiratoires aéroportés sont particulièrement préoccupants de par leur fort pouvoir de transmission. Certains infectent également le SNC et provoquent des encéphalites.

Parmi ces virus, le virus de la rougeole (VR) reste un problème de santé publique malgré un vaccin efficace et le fait que l'Homme soit son unique réservoir et il connait ses dernières années une réémergence inquiétante. Les Henipavirus Nipah et Hendra sont des virus zoonotiques hautement pathogènes nécessitant d'être manipulés dans un laboratoire de niveau de confinement 4. Malgré le faible nombre de cas humains recensés depuis leur émergence à la fin des années 1990, les virus Nipah et Hendra sont classés prioritaires pour la recherche par l'Organisation Mondiale de la Santé de par leur fort potentiel pandémique.

L'objectif initial de ma thèse était d'étudier l'infection du SNC par les Paramyxovirus. L'émergence fin 2019 du virus du syndrome respiratoire aigu sévère 2 (SARS-CoV-2), lui aussi zoonotique, responsable du COVID-19, confirme l'importance d'étudier la pathogénèse des virus respiratoires provoquant des symptômes neurologiques. C'est donc en toute logique que le SARS-CoV-2 s'est imposé dans cette thèse.

L'infection du SNC par ces virus respiratoires est encore mal comprise. C'est pourquoi cette introduction essayera de donner tous les éléments nécessaires à la compréhension des résultats obtenus. L'introduction commence par décrire l'état de l'art des connaissances actuelles sur l'infection du SNC par le VR, virus ancestral qui sert de point de comparaison pour l'étude de l'infection du SNC par les Henipavirus et par le SARS-CoV-2 pour lesquels les connaissances sont moindres.

1) Virus respiratoires et encéphalites

Les principaux virus ciblant les voies respiratoires sont les *Pneumoviridae* (i.e. le virus respiratoire syncytial (RSV)) ; les *Paramyxoviridae* (majorirairement le virus humain parainfluenza de type 3 (hPIV3), le virus des oreillons, le virus de la rougeole et les Henipavirus) ; les *Picornaviridae* (Enterovirus et Rhinovirus) ; les Coronaviridae (notamment les Coronavirus humains endémiques mais aussi les virus SARS-CoV, MERS-CoV et SARS-CoV-2) ; les *Adenoviridae* (Adenovirus) ; les *Orthomyxoviridae* (avec le virus de la grippe) et les *Parvoviridae (B*ocavirus humain) [1].
Les virus les plus encéphalitogènes connus à ce jours appartiennent aux familles des Alphavirus, Bunyavirus, Bornavirus, Flavivirus, Herpesvirus, les virus Influenza, Picornavirus, Paramyxovirus et Rhabdovirus.
Cependant, d'après l'organisation mondiale de la santé (OMS, 2016) 50% des virus émergents pathogènes pour l'Homme sont capable d'infecter le SNC.

2) L’accès au système nerveux central

Malgré le rôle protecteur de la barrière hématoencéphalique (BHE) les virus parviennent tout de même à atteindre le SNC par différents moyens. Le virus de la rougeole et le virus des oreillons utilisent notamment la voie hématogène pour traverser la BHE et d’autres virus tels que les Enterovirus utilisent les voies digestives pour atteindre le SNC [2,3]. Les virus peuvent aussi atteindre le parenchyme cérébral en traversant la BHE directement via l’infection de cellules endothéliales cérébrales ou en empruntant les *plexi choroïdes.* De plus, certains virus peuvent envahir le SNC par le mécanisme du « cheval de Troie » qui consiste à infecter le SNC par biais de cellules immunitaires infectées ou portant le pathogène en surface. Enfin, l’accumulation de cytokines dans le sang en réponse à l’infection peut également perméabiliser de la BHE, particulièrement le TNF-α (ou « Tumor Necrosis Factor »), l’interleukine-6 (IL-6) et l’IL-1β entre autres. Ces lésions de la BHE permettent l’entrée directe du virus de l’herpès simplex 1 (HSV-1) et du VIH. L’entrée du SARS-CoV-2 dans le SNC à la suite de l’orage cytokinique est également très fortement suspecté [4,5]. Une autre stratégie consiste à infecter le système nerveux périphérique pour y migrer jusqu’au SNC, comme le virus de la rage par exemple. Enfin les bulbes olfactifs constituent également un accès directe au SNC. Le virus de la grippe illustre cette voie d’entrée en infectant les neurones olfactifs via leurs dendrites dans la muqueuse nasale. Les voies de propagation des virus dans le SNC sont plus détaillées dans la Figure 1 ci-dessous.

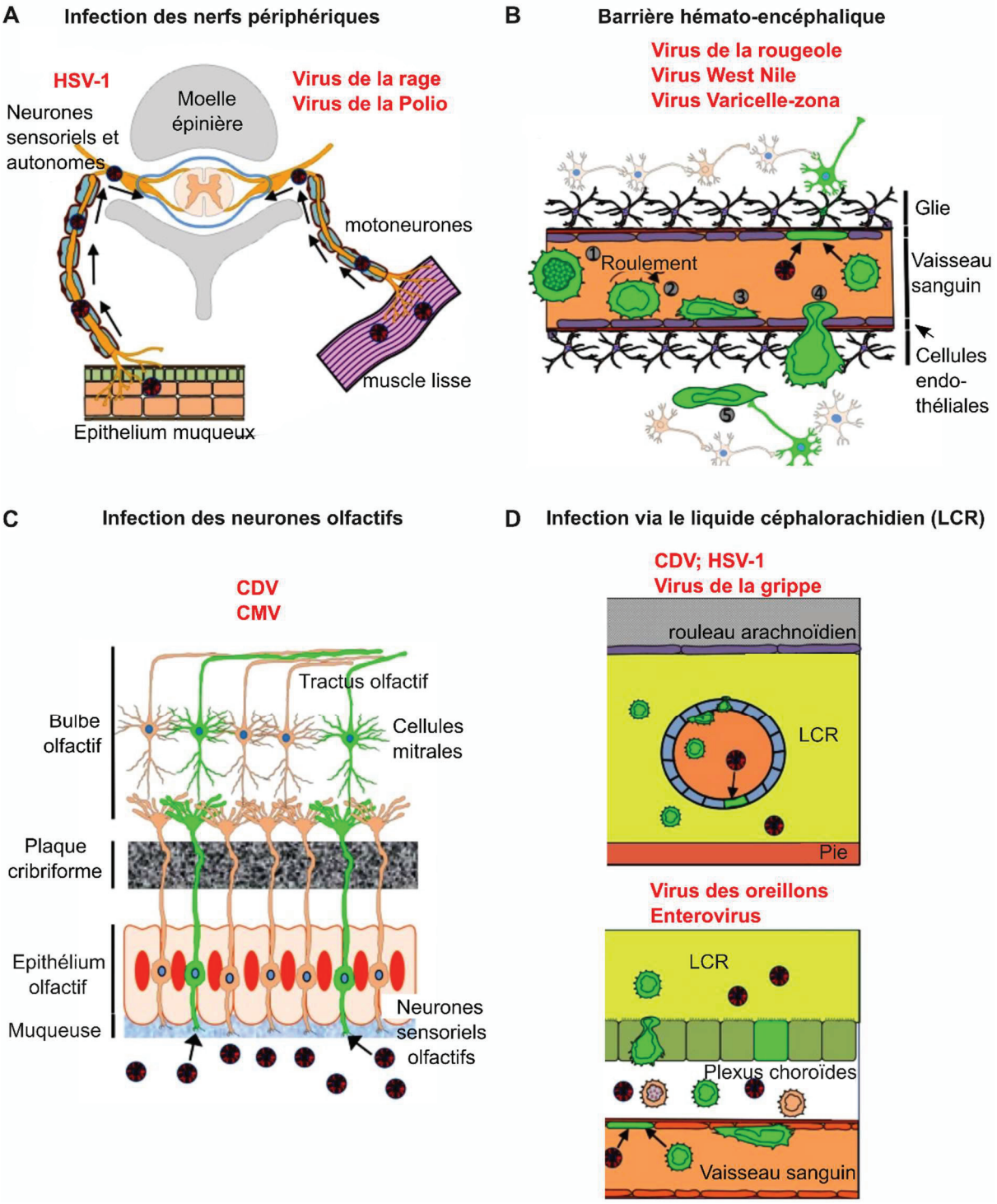

Figure 1 : Les voies de propagation des virus dans le système nerveux central.

A) Infection des nerfs périphériques. A gauche, le virus se propage de l'épithélium muqueux aux neurones sensoriels et autonomes à la suite d'une infection des terminaisons axonales. Le transport axonal rétrograde entraîne la propagation du virus à la moelle épinière. A droite, l'infection virale des motoneurones au niveau des jonctions neuromusculaires dans le muscle lisse entraîne un transport axonal rétrograde vers la moelle épinière et le cerveau.
B) Barrière hémato-encéphalique. Les lymphocytes infectés par le virus (en vert) dans les vaisseaux sanguins « roulent » le long de l'endothélium, se fixent aux cellules endothéliales et traversent la couche de cellules endothéliales et les limites

de la glie. Alternativement, une infection virale directe des cellules endothéliales peut se produire par une propagation ultérieure dans le parenchyme cérébral entraînant une infection neuronale.
C) Infection des neurones olfactifs. Le virus présent dans la muqueuse des voies respiratoires supérieures peut infecter directement les neurones sensoriels olfactifs présents dans l'épithélium olfactif. Le transport axonal antérograde conduit à la propagation du virus dans les faisceaux axonaux passant à travers la plaque cribriforme dans le bulbe olfactif. La propagation trans-synaptique aux cellules mitrales entraîne la propagation du virus le long du tractus olfactif vers d'autres régions du cerveau.
D) Barrière méningée et liquide céphalo-rachidien (LCR). Les leucocytes infectés par le virus dans les vaisseaux sanguins méningés présents dans l'espace sous-arachnoïdien entre la pie et le rouleau arachnoïdien, se fixent à l'endothélium et les cellules endothéliales transversales dans la barrière méningo-encéphalique. Les leucocytes infectés par le virus ou le virus acellulaire présents dans les vaisseaux sanguins traversent l'endothélium comme décrit précédemment. Cela peut conduire à l'infection des cellules épithéliales et à la libération apicale du virus ou à la propagation de leucocytes infectés par le virus à travers l'épithélium du plexus choroïde.
Figure adaptée de Ludlow et al., 2016 [6].

ETAT DE L’ART

I- Le COVID-19

1) Epidémiologie

Le SARS-CoV-2 a émergé fin 2019 dans la province de Wuhan en Chine et est responsable de la pandémie mondiale de COVID-19 (pour Coronavirus disease 2019) déclarée en mars 2020 par l'Organisation Mondiale de la Santé (OMS) [7]. En octobre 2021, plus de 244 millions de cas confirmés en laboratoire ont été signalés et plus de 5 millions de patients sont décédés du COVID-19 dans le monde [8].

Les coronavirus doivent leur nom à leur glycoprotéine de surface en forme de pointe (protéine Spike) qui confère un aspect de couronne aux particules virales. Il existe 4 genres de coronavirus : alpha, bêta, gamma et delta, qui sont génétiquement différents et peuvent infecter plusieurs espèces animales, notamment les chauves-souris, les porcs, les chats, les rongeurs et les humains [9]. Seuls les coronavirus alpha et bêta sont connus pour infecter les humains et entraînent une pathologie.

Quatre coronavirus humains endémiques (HCoV) ont été identifiés à ce jour : HCoV-229E, HCoV-NL63 [10,11], HCoV-OC43 et HCoV-HKU1 [12,13]. Ces HCoV infectent généralement les voies respiratoires supérieures et provoquent des épidémies saisonnières de rhumes chez l'Homme [14,15]. Ces 20 dernières années 3 coronavirus zoonotiques hautement pathogènes pour l'Homme ont émergé : le coronavirus du syndrome respiratoire aigu sévère (SARS-CoV) en 2002/2003[16,17], le coronavirus relatif au syndrome respiratoire du Moyen-Orient (MERS-CoV) en 2012 [18,19] , et le virus du syndrome respiratoire aigu sévère-2 (SARS-CoV-2) fin 2019 [20]. Le SARS-CoV a été rapidement stoppé, quelques cas de personnes infectées par le MERS-CoV sont encore rapportés de façon sporadique, mais la pandémie de COVID-19 causée par le SARS-CoV-2 est encore très loin d'être sous contrôle. Contrairement aux HCoV les coronavirus zoonotiques infectent également les voies respiratoires basses et provoquent un spectre de gravité de la maladie chez l'homme, allant d'infections asymptomatiques ou bénignes à une détresse respiratoire mortelle avec défaillance de plusieurs organes.

Les HCoV-OC43 et HCoV-HKU1 proviennent probablement de rongeurs tandis que les HCoV-229E, HCoV-NL63 ainsi que les trois coronavirus zoonotiques auraient pour origine la chauve-souris [20,21].
En effet, des coronavirus relatifs au SARS-CoV (SARSr-CoV) circulent chez les chauves-souris et ont une homologie de séquence génomique élevée avec le SARS-CoV et le SARS-CoV-2. Par exemple, le génome du SARS-CoV-2 partage 96,2 % d'identité avec le SARSr-CoV RaTG13 qui a été détecté chez des rhinolophes dans la province du Yunnan en 2013 [20,22]. L'hypothèse la plus robuste est donc que la chauve-souris serait le réservoir du SARS-CoV-2 qui aurait atteint l'Homme via des hôtes intermédiaires.

Tableau 1 : Les différents coronavirus

	Coronavirus endémiques humains	Coronavirus zoonotiques hautement pathogènes	Coronavirus relatifs au SARS
Pathogénicité chez l'Homme	Modérée, rhumes saisonniers	Variable allant d' asymptomatique à des arrêts respiratoires et cardiaques	-
Origine	Rongeurs ou chauves-souris	Chauves-souris ou chameaux	Chauves-souris
Genres et virus	*Betacoronavirus* • HCoV-OC43 • HCoV-HKU1 • HCoV-229E *Alphacoronavirus* • HCoV-NL63	*Betacoronavirus,* Sous-genre *Sarbecoronavirus* • SARS-CoV • MERS-CoV • SARS-CoV-2	*Betacoronavirus,* Sous-genre *Sarbecoronavirus* • SARSr-CoV RaTG13 (et d'autres)

2) Le virus du SARS-CoV-2

a. Classification

Le SARS-CoV-2 appartient au sous-genre Sarbecovirus, au sein du genre Betacoronavirus, de la sous-famille des Orthocoronavirinae et de la famille des Coronaviridae. La séquence génomique du SARS-CoV-2 partage 79,6% d'identité avec le SARS-CoV qui a émergé en 2002/2003 [16,17]. La taille des particules virales du SARS-CoV-2 varie entre 60 à 140 nm [20].

b. Le génome du SARS-CoV-2

Le SRAS-CoV-2 est un virus enveloppé à ARN simple brin de sens positif de 29 891 bases [23]. Le génome du SARS-CoV-2 code pour 16 protéines non structurales (nsp1 à nsp16), 8 protéines accessoires et 4 protéines structurales : la spike (S), la protéine de membrane (M), la protéine d'enveloppe (E) et la nucléocapside (N) [24]. Les protéines structurales sont codées par la région 3' du génome.

La S est une protéine homotrimérique transmembranaire de classe I. Pour permettre la fusion de la membrane de la particule virale avec celle de la cellule cible, la protéine S doit être clivée spécifiquement en deux sous-unités S1 et S2 par différentes protéases cellulaires. La première sous-unité (S1) est nécessaire pour se lier au récepteur cellulaire et initier l'infection grâce au domaine de liaison au récepteur (RBD)[25]. La sous-unité S2 contient le peptide de fusion (FP), et deux domaines complémentaires d'heptades répétées aux extrémités N terminale (HRN) et C terminale (HRC) permettant la fusion en tant que telle [26]. Le clivage de la S peut avoir lieu à la surface de la cellule par la protéase sérine transmembranaire 2 (TMPRSS2) ou au niveau de l'endosome par la Cathepsine B et la Cathepsine L [26,27] (Figure 2).

La S peut aussi être pré-clivée par la furine, une « proprotéine convertase ». Ce pré-clivage permet de réduire la dépendance du virus vis-à-vis de l'expression des protéases sur cellules cibles [26,28]. Le fragment S1 de la protéine Spike clivée par la

furine peut se lier à la Neuropiline-1, abondamment exprimée à la surface des cellules endothéliales et épithéliales. Cette liaison peut donc faciliter l'infection par le SRAS-CoV-2 en favorisant l'interaction virale avec l' « angiotensin converting enzyme 2 » (ACE2) [29,30]. Enfin, une interaction entre le récepteur CD147 à la surface des cellules hôtes et la S du SARS-CoV-2 pourrait également faciliter l'infection [31,32].

L'infection commence par la liaison de la glycoprotéine virale de surface, spike (S), à son récepteur ACE2 à la surface de la cellule cible [20]. L'expression et la distribution tissulaire de l'ACE2 influencent le tropisme viral et la pathogénicité [33].
La fusion des membranes entraine la libération du génome dans le cytoplasme de la cellule cible. Le génome positif du SARS-CoV-2 sert d'ARNm et est immédiatement traduit partiellement en protéines virales nécessaires pour la réplication et la transcription de l'ARN. La synthèse de l'ARN est réalisée par l'ARN polymérase virale dépendante de l'ARN codée par nsp12. La réplication virale a lieu dans des vésicules à double membranes induites par le virus (DMV) et dérivées du réticulum endoplasmique. Ceci permet de créer un microenvironnement pour la réplication virale induite par nsp4 [34]. Les ARN subgénomiques synthétisés via une transcription discontinue sont ensuite traduits en protéines non structurales et structurales. L'assemblage viral a lieu dans le réticulum endoplasmique. À la fin du cycle, les virions sont acheminés vers la membrane cellulaire pour ensuite bourgeonner par exocytose [33] ou par la voie lysosomale [35].

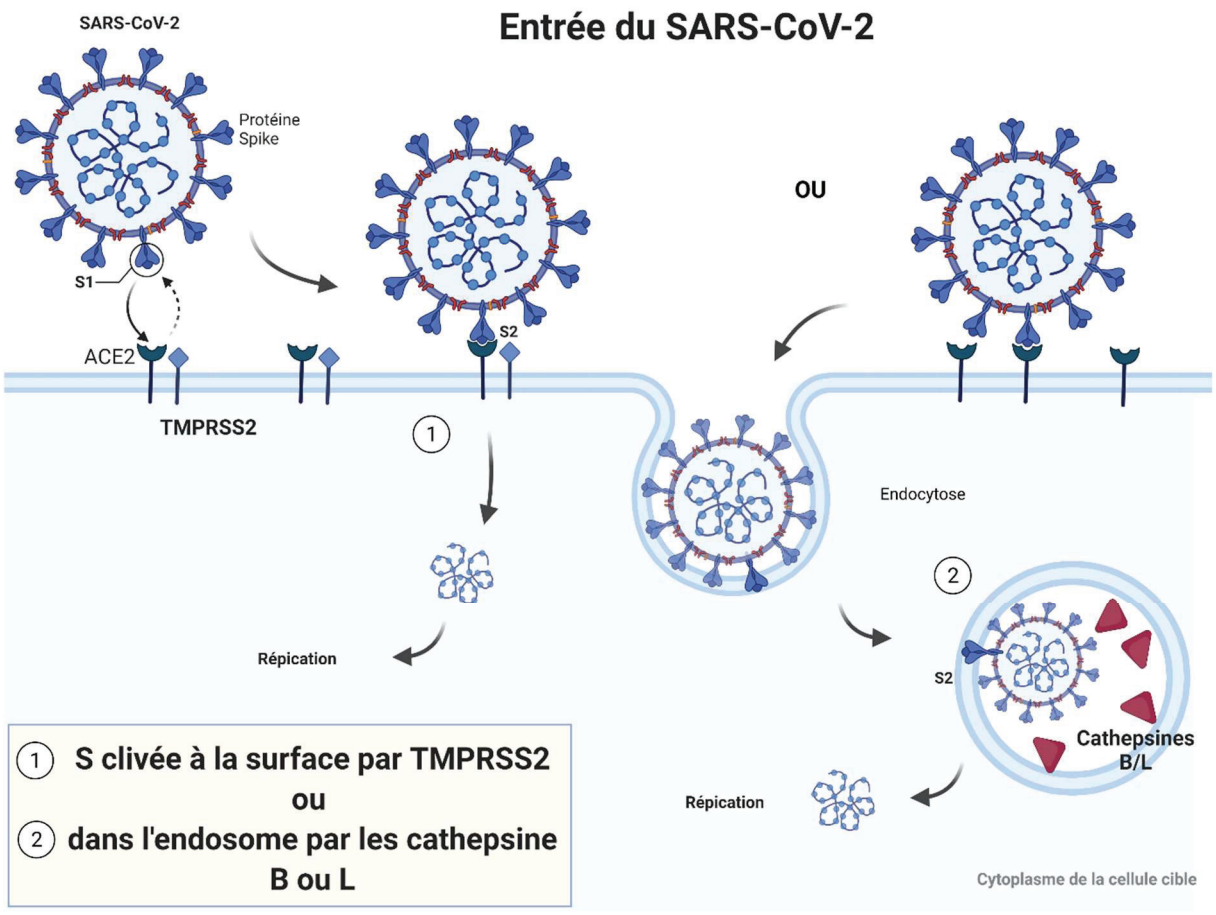

Figure 2 : Entrée de SARS-CoV-2 dans les cellules cibles.
Pour permettre la fusion la S doit d'abord être clivée à la surface par TMPRSS2 (1) ou dans l'endosome par les cathepsines B ou L (2). Figure réalisée sur BioRender.

3) Les variants

Le SARS-CoV-2 mute très rapidement et de nombreux variants ont émergé depuis le début de la pandémie. Ces variants sont caractérisés par l'apparition de mutations qui permettent l'acquisition d'avantages sélectifs vis-à-vis du virus avec menace d'échappement aux vaccins disponibles. A ce jour on compte 4 variants préoccupants et 7 variants d'intérêts. Sur décision de l'OMS les variants portent des noms de lettres grecques pour pouvoir les dénommer facilement, en plus de leur nom officiel et éviter leur assimilation à une origine géographique. Les variants préoccupants comportent tous des mutations dans la S et sont les variants alpha (B.1.1.7), bêta (B.1.351), gamma (B.1.1.28.1) et delta (B.1.617.2) initialement identifiés au Royaume-Uni, en Afrique du Sud au Brésil et Japon, et en Inde, respectivement. Les variants alpha et delta sont 50 à 75% plus contagieux que la souche initiale du SARS-CoV-2 [36].

Parmi les mutations les plus retrouvées dans les protéines S des variants préoccupants on retrouve les mutations D614G, N501Y et E484K. Les mutations D614G et N501Y confèrent aux virus une augmentation du pouvoir infectieux et une meilleure affinité de l'interaction entre la S et ACE2 [37–39]. Les variants portant la mutation E484K sont moins efficacement neutralisés par les anticorps conférés par une première exposition au virus ou par la vaccination [37].

4) Les vaccins

Les principales stratégies de vaccins et de traitements antiviraux ciblent la protéine S. Etant donné l'enjeu, le nombre de vaccins en cours de développement augmente continuellement. L'OMS a recensé 110 vaccins autorisés ou en phase d'étude clinique contre le SARS-CoV-2 [36].
En France quatre vaccins ont été administrés à ce jour : deux vaccins à ARN messager BNT162b2 (commercialisé par Pfizer) et Moderna-mRNA-1273 et deux vaccins à vecteur viral ; AstraZeneca AZD1222 (Univ. Oxford) basé sur un vecteur adénoviral de chimpanzé et Ad26COV2. S (Janssens, Johnson & Johnson) basé sur un adénovirus humain de type 26 (Ad26).
Il y a quelques années, des modifications bloquant la S du SARS-CoV et du MERS-CoV dans leur état de préfusion ont été identifiées [40,41]. Une substitution d'acides aminés aux codons K986P et V987P (insertion de 2 prolines) et la modification du site de clivage S1 RRAR682/5GSAS stabilisent la S dans son état de préfusion [42]. Ces modifications sont présentes partiellement dans certains vaccins tels que

BNT162b2 (commercialisé par Pfizer) et Moderna-mRNA-1273 (double substitution de proline) [43,44] et Ad26COV2. S (Janssens, Johnson & Johnson) (insertion de la double mutation de proline et modification du site de clivage polybasique) [45]. Les nouveaux vaccins sur le point d'être commercialisés, Zorecimeran (CureVac/Bayer) et MRT5500 (Sanofi Pasteur) comportent également la mutation des deux prolines. En revanche les vaccins AstraZeneca AZD1222 (Univ. Oxford), Spoutnik V, Spoutnik Light (Gamaleïa) et le vaccin Convidicea (CanSino) codent ou contiennent la S du virus d'origine sans aucune mutation [46].
L'efficacité de certains vaccins face à l'émergence de nouveaux variants peut être diminuée. Les anticorps neutralisants induits par les 4 vaccins administrés en France se sont avérés moins efficaces *in vitro* sur les variants beta (B.1.351) et delta (B.1.617.2) [47–50].

5) Le COVID-19

a. Pathogénèse

L'infection par le SARS-CoV-2 peut être asymptomatique chez certains patients. Dans les cas symptomatiques, il y a une atteinte des voies respiratoires avec apparition d'un syndrome respiratoire aigu qui peut être très sévère et laisser des séquelles irréparables. Dans les cas graves, on observe aussi des arrêts cardiaques et des arrêts respiratoires.
Le SARS-CoV-2 est aérosolisé dans la muqueuse des voies respiratoires supérieures où il commence à se répliquer probablement dans les cellules de l'épithélium cilié [51]. Les premiers symptômes peuvent être une rhinite, une glossite et une toux avec une possible intoxication systémique, se manifestant par de la fièvre et des douleurs articulaires [52]. Le virus atteint les poumons et pénètre ensuite dans la circulation systémique. Au cours de cette étape de la phase de virémie le virus infecte toujours les cellules qui expriment le récepteur ACE2 : les pneumocytes de type 2 de l'épithélium alvéolaire, le cœur, les reins, les cellules du tractus gastro-intestinal, les macrophages, et l'endothélium des vaisseaux artériels et veineux [53]. La deuxième étape de la maladie est la phase aiguë, et se caractérise par l'apparition de lésions dans les organes dues à l'infection. Chez l'Homme, le SARS-CoV-2 induit une faible réponse interféron de types I, II et III et une forte activation de la voie interleukine IL-1β/IL-6 [54]. Dans les poumons, l'infection entraine une tempête de cytokines. L'infection des cellules épithéliales alvéolaires de type II active l'inflammasome, ce qui induit la production d'IL-1β. L'IL-1β induit la sécrétion d'IL-6 par les cellules endothéliales et les cellules vasculaires musculaires lisses, ce qui renforce la réponse inflammatoire [55,56]. Dans les cas modérés de COVID-19, cette phase aiguë caractérisée par le développement d'une pneumonie est contrôlée par le système immunitaire qui permet une récupération des patients. Chez les patients à risques en raison de leur âge avancé, d'une immunodépression ou de maladies concomitantes, le système immunitaire ne peut généralement pas contrôler efficacement la maladie.

b. Tempête cytokinique

Les cytokines impliquées sont en particulier les cytokines pro-inflammatoires telles que l'IL-1β, l'IL-6, l'IL-15 et le TNF-α, qui sont produites sur les sites d'inflammation des tissus [57]. De nombreuses études relèvent aussi une augmentation significative des taux d'IL-6 et d'IL10 dans les sérums de patients critiques. En clinique, ces cytokines sont associées à la nécessité d'une ventilation mécanique et à la mort. Leur surexpression semble impliquée dans la sévérité des cas de COViD-19 [58]. A la suite de la tempête cytokinique le virus cible les organes qui expriment le plus ACE2 tels que les poumons, le cœur et les reins.

c. Complications neurologiques et COVID long

Le syndrome respiratoire aigu sévère peut également être associé à l'infection du SNC et à des symptômes neurologiques. Les symptômes neurologiques les plus fréquents sont une altération des niveaux de conscience, des maux de tête, une perte de l'odorat et du goût et des symptômes musculaires [5,59]. Cependant, les complications neurologiques peuvent aller jusqu'à une myopathie et, dans de rares cas, une myoclonie généralisée, un accident vasculaire cérébral ischémique et une encéphalomyélite périvasculaire disséminée aiguë [60–65]. Il a été suggéré que le SARS-CoV-2 atteint la moëlle « allongée » (*Medulla oblongata*) et que les arrêts respiratoires et cardiaques observés chez les patients pourraient être dus à l'infection du tronc cérébral [66–70].

Lorsque les symptômes durent plus de 12 semaines après la phase aiguë de l'infection on parle de COVID long. Les patients décrivent une fatigue, une difficulté à faire des activités physiques, une faible fièvre persistante, une perte de cheveux, une faiblesse musculaire, une dyspnée, une toux, des palpitations, une douleur thoracique, de l'anxiété et des troubles du sommeil. Cependant, le symptôme le plus préoccupant se caractérise par un état confusif incluant un manque de clarté intellectuelle, des difficultés de concentration et une fatigue mentale. 38% des patients hospitalisés atteints du COVID-19 montrent des signes d'altérations cognitives plus de 4 mois après leur hospitalisation. Cependant ce phénomène touche toutes les tranches d'âges (18% des cas totaux) [5,71,72].

d. L'infection du SNC par le SARS-CoV-2

Le potentiel neuro-invasif du SARS-CoV-2 chez l'homme est encore mal compris [73,74]. D'après la grande majorité des études, la plupart des symptômes liés à une atteinte du SNC sont associés à l'infection des vaisseaux sanguins du cerveau [75–82]. Cependant, la susceptibilité des neurones humains à l'infection par le SARS-CoV-2 et la permissivité d'organoïdes de cerveau humain générés à partir de cellules souches ont été observées *in vitro* [83–87]. Des particules virales ainsi que l'ARN du SARS-CoV-2 ont également déjà été retrouvées dans le liquide céphalo-rachidien (LCR) [88] et dans le cerveau de patients [70,89]. La présence du SARS-CoV-2 dans le LCR est toutefois très limitée et peut être liée à une faible capacité à bourgeonner dans ce tissu comme observé avec d'autres virus tels que le VR ou simplement due au fait que le virus n'a pas eu le temps d'envahir le cerveau dans les cas respiratoires les plus sévères qui représentent la grande majorité des échantillons.

Afin d'atteindre le SNC, le SARS-CoV-2 peut passer de la périphérie au SNC par les neurones olfactifs ou par le nerf vague, à partir des poumons ou de l'intestin[90]. De plus, l'infection par le SARS-CoV-2 endommage l'épithélium du plexus choroïde et entraine une tempête de cytokines et une inflammation systémique qui occasionnent une rupture de la barrière hémato-endothéliale[87,91–93] (Figure 3).

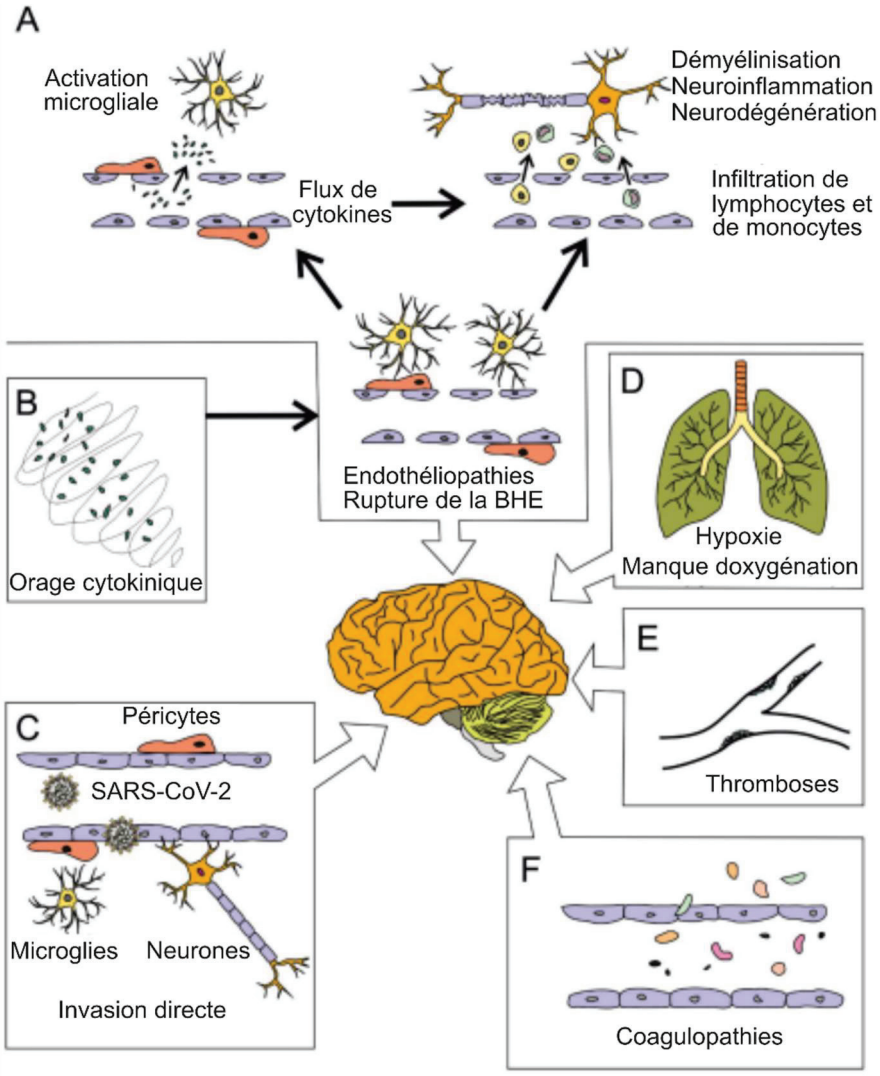

Figure 3 : Possibles mécanismes pouvant entrainer l'apparition de symptômes neurologiques à la suite de l'infection par le SARS-CoV-2.

A, B, La tempête de cytokines entraîne une perturbation de la barrière hémato-encéphalique (BHE) et un afflux de lymphocytes et de monocytes qui contribuent à une activation microgliale, à la démyélinisation, à la neuroinflammation et à la neurodégénération. C, L'infection des cellules endothéliales permet au SARS-CoV-2 d'envahir le cerveau et d'infecter à la fois les neurones et les cellules microgliales ; D, La dépression respiratoire déclenche une hypoxie cérébrale entraînant une anaérobie, une inflammation et la mort cellulaire ; E, La thrombose des vaisseaux sanguins du cerveau et l'hyper-viscosité sanguine induite par les cytokines pro-inflammatoires conduisent à un accident vasculaire cérébral ischémique ; F, La coagulopathie associée à l'endothéliopathie provoque un accident vasculaire cérébral hémorragique olfactif. Adapté de Bratosiewicz-Wąsik, 2021 [94].

6) Les modèles animaux

Les différents modèles animaux décrits pour étudier la pathogenèse et la transmission du SARS-CoV-2 et l'efficacité d'antiviraux sont majoritairement des souris exprimant le transgène ACE2 humain (de façon ubiquitaire ou en suivant la même répartition que chez l'Homme) associé ou non à d'autres modifications génétiques, des hamsters, des furets, et des primates non-humains (des macaques rhésus, des macaques cynomolgus et des singes verts africains) [95,96].
Le hamster doré Syrien (Mesocricetus auratus) est un petit modèle animal pertinent pour plusieurs virus[97] et plus particulièrement pour les virus respiratoires qui ciblent également le SNC [98,99]. Le hamster est naturellement susceptible à l'infection par tous les variants connus du SARS-CoV-2 et la pathogenèse du SARS-CoV [100,101] et du SARS-CoV-2 [102–105] chez cet animal est très proche de celle observée chez l'Homme[103,106,107].

7) Les traitements

a. Les traitements utilisés en clinique

Il n'existe pas de traitement efficace commercialisé pour traiter l'infection par les coronavirus. Les traitements administrés aujourd'hui visent surtout à traiter la symptomatologie de la maladie plutôt que le virus.

L'hydroxychloroquine a fait l'objet de nombreuses études et bloque l'entrée du SARS-CoV-2 *in vitro* en agissant au niveau de la voie endosomale [108–110]. Plus précisément, l'hydroxychloroquine empêche la fusion entre membrane virale et endosomale en augmentant le pH de l'endosome [111]. Mais, ni l'hydroxychloroquine ni la chloroquine n'ont d'effet thérapeutique *in vivo* chez l'animal et chez les patients atteints de COVID-19, même lorsque ces traitements ont été administrés au tout début de l'infection. Au contraire, une augmentation de la mortalité due au COVID-19 a même été associée à la prise de ces traitements [112].

Le Remdesivir (GS-5734) a une efficacité antivirale *in vitro* et *in vivo* et est utilisé dans certains cas cliniques pour traiter le COVID-19 [108,111,113–115]. Le Remdesivir est un analogue de nucléoside efficace sur un large spectre de virus, incluant le VR [116]. Pour être efficace, il doit être administré par voie intra-veineuse et à un stade précoce de la maladie, avant que le virus n'ait eu le temps d'entrainer des lésions alors irréparables. Dans les faits, le Remdesivir est malheureusement souvent administré trop tard, lorsque les patients sont déjà hospitalisés. Une formulation permettant l'administration du Remdesivir par voie orale rendrait le traitement plus accessible [117].
Beaucoup d'autres traitements ont été testés pour traiter le COVID-19 mais aucun ne se démarque vraiment aujourd'hui en dehors du Remdesivir.

b. Les traitements prometteurs

Parmi les traitements prometteurs en développement, des peptides dérivés du domaine HRC de la Spike et conjugués à un lipide sont en développement et ont prouvé leur efficacité *in vitro* et *in vivo*, notamment pour bloquer la transmission du SARS-CoV-2 chez le furet [118,119].

II- La rougeole

1) Epidémiologie

Le virus de la rougeole (VR), dont l'Homme est l'unique réservoir, est l'agent pathogène responsable de la rougeole. Malgré la disposition d'un vaccin très efficace [120] la rougeole est encore aujourd'hui responsable de plus de 140 000 morts par an dans le monde [121,122], principalement parmi les enfants de moins de 5 ans [123], cibles privilégiées du VR [124]. La rougeole reste à ce jour la maladie la plus contagieuse pour l'Homme avec un taux de reproduction R0 variant de 12 à 18 [125]. En d'autres termes, au sein d'un groupe de personnes non vaccinées, un patient infecté par le VR va contaminer en moyenne 12 à 18 individus. Ce taux de reproduction augmente encore parmi les personnes immunodéprimées [123]. Le VR se transmet généralement d'un patient à un autre par le biais des aérosols [123] y compris avant l'éruption cutanée caractéristique.
Pendant plusieurs décennies l'incidence de la rougeole a fortement décru et les cas de rougeole étaient principalement regroupés dans les pays en voie de développement où une ambitieuse campagne de vaccination généralisée est engagée par l'OMS.
La pandémie mondiale de COVID-19 en 2020 a fortement perturbé les campagnes de vaccination contre la rougeole chez les jeunes enfants. Plus de quarante pays ont même stoppé totalement la vaccination contre la rougeole; en conséquence, il faut s'attendre à une recrudescence de cas de rougeole dans les prochaines années [126].
Dans la plupart des pays industrialisés la rougeole était considérée comme éradiquée au début des années 2010. Mais, dans de nombreux pays comme la France ou les Etats-Unis, on constate environ 300% d'augmentation des cas de rougeole par an[127]. Cette réémergence de la rougeole s'explique par une baisse de la couverture vaccinale due principalement à des populations de plus en plus réticentes à la vaccination [128,129]. Ainsi, depuis 2016 le nombre de décès dus à la rougeole n'a cessé d'augmenter jusqu'à atteindre 207 500 personnes en 2019 [130].

2) Le virus de la rougeole

a. Classification

Le VR appartient au genre Morbillivirus, à la famille des *Paramyxoviridae* au sein de l'ordre des *Mononegavirales* (Figure 4). Ce virus enveloppé produit des particules virales pléiomorphes de 150 à 300 nm et pouvant aller jusqu'à 900 nm [131].

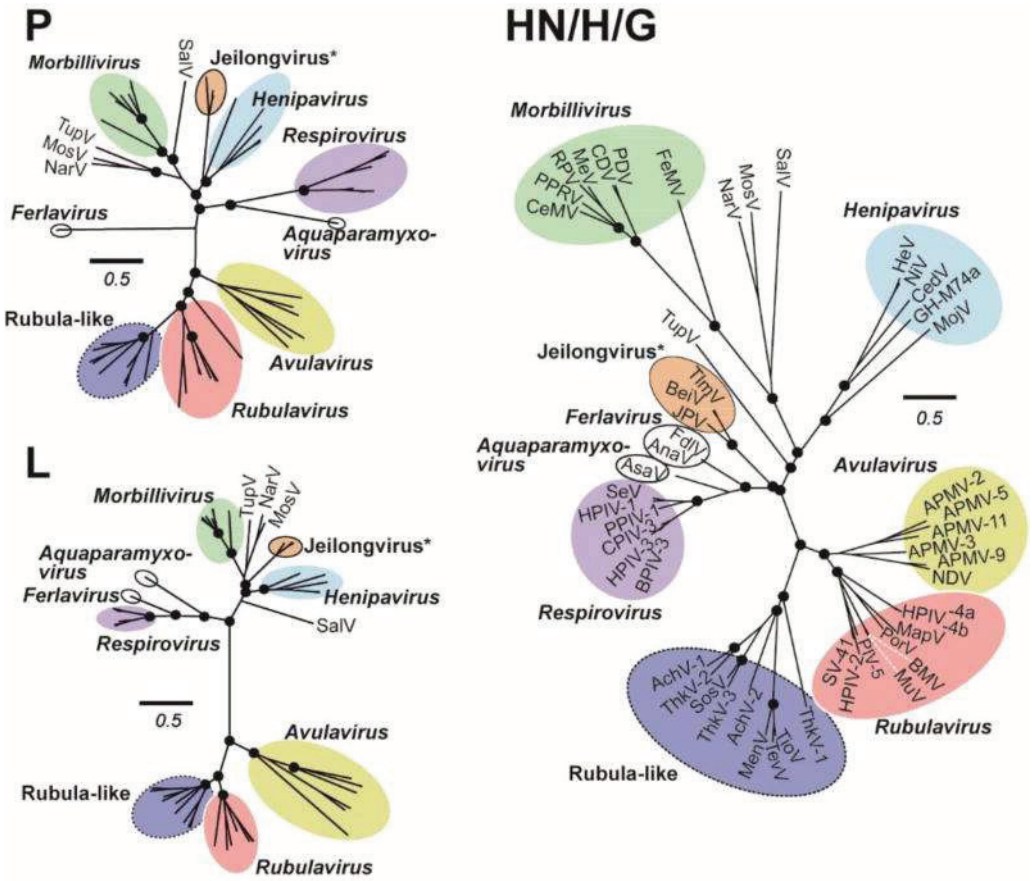

Figure 4 : Diversité des différents genres au sein des Paramyxoviridae

Arbres phylogénétiques à vraisemblance maximale des séquences de protéines P, L et d'attachement (HN/H/G) des Paramyxoviridae. Les cercles colorés englobent les groupements phylogénétiques mieux caractérisés en tant que genres. Les paramyxovirus non classés mais entièrement séquencés apparaissent individuellement dans chaque arbre. La barre d'échelle indique 0,5 substitution d'acides aminés par site, et les arbres sont mis à l'échelle de telle sorte que la barre d'échelle soit la même dans tous les arbres. Les cercles noirs aux nœuds représentent > 75 % de prise en charge à partir de 500 répliques d'amorçage. Toutes les analyses ont été effectuées dans MEGA 6 en utilisant une option de suppression complète et un modèle de substitution WAG. Figure adaptée de Thibault PA et al., 2016 [132].

b. Le génome du virus de la rougeole

Le génome du VR est un ARN simple brin de sens négatif de 15894 nucléotides qui code pour 6 protéines structurales : la protéine de nucléocapside (N), la phosphoprotéine (P), la protéine de matrice (M), la protéine de fusion (F), la protéine d'hémagglutinine (H) et la polymérase aussi appelée protéine large (L) (Figure 5). Deux protéines non-structurales, V et C, sont également produites par le gène P [133] et ont pour rôle principal d'altérer les voies de l'immunité innée [134–137].

Les souches sauvages du VR utilisent les récepteurs SLAM ou SLAMF1 (signaling lymphocytic activation molecule 1, aussi appelé CD150) et nectin-4 (aussi appelé PVLR4 pour poliovirus receptor-related protein 4) pour infecter les cellules cibles [138–

[140]. Les souches vaccinales du VR utilisent également la molécule CD46 exprimée de façon ubiquitaire [141,142].

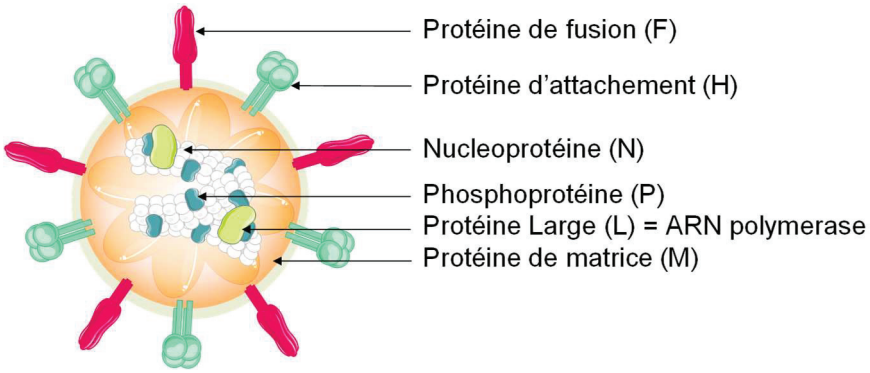

Figure 5 : Schéma de la particule virale du virus de la rougeole

c. Cycle viral et rôle des protéines virales

L'entrée du VR est indépendante du pH et a lieu directement à la surface des cellules cibles [143]. Le VR pourrait également entrer par endocytose via SLAM dans des cellules B lymphoblastiques ou en cellules A549 exprimant SLAM [144], et par macropinocytose via nectin-4 dans certaines lignées cellulaires de cancer du sein et de colon (MCF7, HTB-20, and DLD-1) [145].

Pour initier l'infection, la protéine H se lie au récepteur d'entrée à la surface de la cellule cible. Cet attachement déclenche la protéine F, ce qui permet d'exposer son peptide de fusion hydrophobe qui va ensuite pouvoir s'ancrer de façon irréversible dans la membrane de la cellule cible. La F suit ensuite plusieurs changements de conformation afin de créer un pore de fusion entre la membrane virale et la membrane de la cellule hotte. Cette fusion permet la libération du complexe ribonucléoprotéique (RNP) dans le cytoplasme de la cellule (Figure 6A,B) [146,147]. L'infection peut également se produire efficacement et de la même façon par simple contact cellule-cellule [148,149]. La fusion de plusieurs cellules infectées donne naissance à des cellules plurinucléées appelées syncytium.

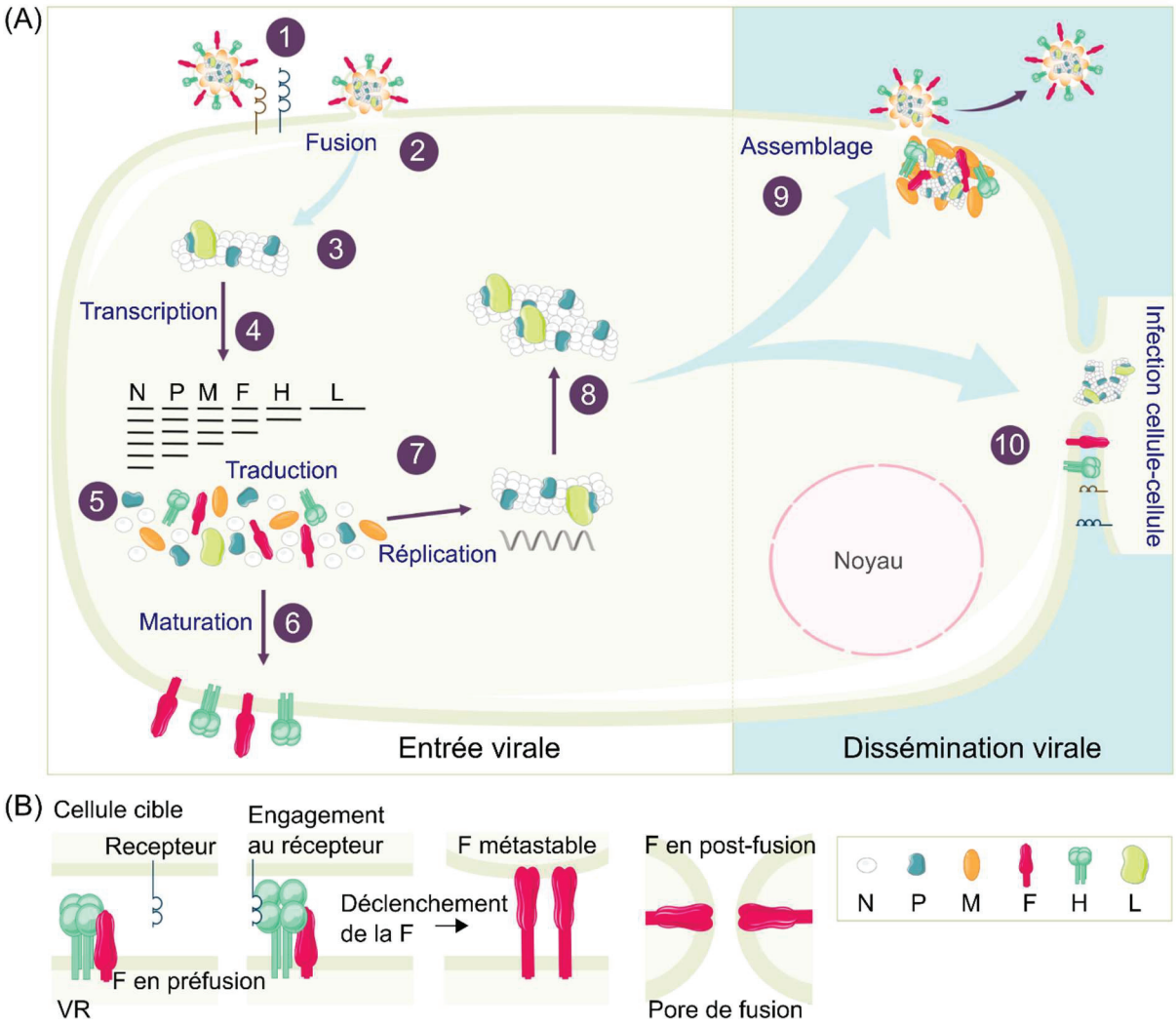

Figure 6 : Le cycle réplicatif du virus de la rougeole

(A) Pour infecter une cellule susceptible, le VR se lie à son récepteur d'entrée à la surface de la cellule (1) et initie la fusion des membranes virales et cellulaires, comme décrit plus en détail en (B). La fusion des membranes virales et cellulaires entraine la libération du génome viral dans le cytoplasme (3). L'ARN viral est transcrit en ARN messager (ARNm) (4) traduit ensuite en protéines virales (5). Les glycoprotéines virales maturent au cours de leur transport à la surface cellulaire (6). La réplication de l'ARN anti-génomique positif commence dans le cytoplasme (7) et sert de matrice pour la synthèse du nouveau brin d'ARN génomique négatif (8). L'assemblage des protéines virales a lieu à la surface cellulaire, entrainant soit le bourgeonnement des nouveaux virions (9) ou la fusion cellule-cellule (10). (B) La protéine H se lie au récepteur du VR à la surface de la cellule, permettant le déclenchement de la F qui va atteindre une conformation métastable. La F insert ensuite son peptide de fusion dans la membrane de la cellule cible. La F subit alors des changements de conformation qui vont mener au rapprochement des deux membranes et la formation d'un pore de fusion par lequel le complexe viral RNP sera libéré dans le cytoplasme.

La transcription par l'ARN polymérase ARN-dépendante (RdRp) commence à partir d'un simple promoteur et abouti à un gradient transcriptionnel allant de l'ARNm le plus abondant pour la N au moins abondant pour la L. Ces ARNm sont alors traduits en protéines virales. L'accumulation des protéines N et P sous forme du substrat d'encapsidation N^0P permet la réplication du génome viral en un brin d'ARN anti-génomique positif encapsidé. Celui-là sert de matrice pour la synthèse d'ARN négatif génomique qui seront immédiatement encapsidés par les protéines N [150]. La synthèse des ARN viraux et l'assemblage des particules virales est régulée par l'interaction entre la M et la N et la queue cytoplasmique de la F [151] . L'assemblage des protéines virales a lieu au niveau de la membrane plasmique et c'est alors que les nouveaux virions peuvent bourgeonner (Figure 6A). Alternativement, les glycoprotéines de surface sont également transportées à la membrane plasmique et permettent la dissémination virale de cellule à cellule par fusion de leurs membranes plasmiques avec formation d'un syncytia.

L'ARN viral est encapsidé par la protéine N et forme la nucléocapside hélicoïdale [152]. Chaque protéine N recouvre 6 nucléotides, par conséquent la longueur du génome doit impérativement suivre la « règle des 6 », c'est-à-dire compter un nombre de nucléotide qui soit un multiple de 6 pour être fonctionnel et complètement protégé [153,154]. Les protéines L et P s'associent pour former la RdRp. Cette polymérase virale interagit avec la nucléocapside pour progresser le long de l'ARN viral : l'ensemble de ces 2 protéines avec la nucléocapside forment le complexe ribonucléoprotéique (RNP).

La protéine M permet l'intégrité des particules virales. La M est le véritable chef d'orchestre de l'assemblage des nouveaux virions à la membrane et de leur bourgeonnement [143].

Les protéines H et F constituent le complexe de fusion viral nécessaire à l'entrée dans la cellule cible.
La protéine H est un tétramère organisé en un dimère de dimères et est responsable de l'attachement au récepteur d'entrée. Cette protéine de liaison au récepteur (PLR) est une glycoprotéine transmembranaire de type II. Chaque monomère de H est constitué d'une tige proximale membranaire et d'une tête globulaire en C-terminal.

La protéine F permet la fusion entre la membrane virale et la membrane de la cellule hôte. La F est une protéine transmembranaire de type I qui se présente sous forme de trimère. La F est synthétisée en précurseur F0 et est ensuite clivée dans le trans-Golgi par la protéase furine en deux sous-unités F1 et F2 reliées par un pont disulfure. Le domaine extracellulaire est constitué des sous-unités F1 et F2. F1, transmembranaire, contient le peptide de fusion à l'extrémité N terminale suivi par deux domaines complémentaires d'heptades répétés, respectivement aux extrémités N terminale (HRN) et C terminale (HRC). Le clivage est primordial pour permettre la fusion grâce à la libération du peptide de fusion de la F qui reste inaccessible dans une poche hydrophobe sous la forme de pré-fusion [155].

Bien que la structure cristallographique de la forme en pré-fusion de la F a été décrite [156], les délimitations exactes des sous-domaines de la F ne sont pas encore complètement définies [157–159]. D'après les outils bio-informatiques le domaine HRN inclut les résidus 116/138 au résidu 190 et le domaine HRC se situe entre les résidus 438 et 488/489. La structure montre en revanche une région désordonnée entre les résidus 438 et 458 et une heptade répétée canonique après le résidu 458 [160,161].
Dans son état de post-fusion, la F forme un complexe extrêmement stable naturellement irréversible.

d. Entrée virale

L'infection commence par la fixation de la protéine H sur le récepteur d'entrée. S'en suit le déclenchement de la protéine F. La sous unité F1 expose alors son peptide de fusion hautement hydrophobe qui s'insère dans la membrane plasmique de la cellule hôte. Cette étape intermédiaire est transitoire et très instable. En effet, la F subit une série de changements conformationnels conduisant par repliement à l'interaction entre les deux domaines HRN et HRC en heptades répétées. Cette forte interaction force le rapprochement des deux membranes au point de les fusionner pour former le pore de fusion à travers lequel la RNP entre dans le cytoplasme de la cellule hôte. Cette entrée virale a lieu indépendamment du pH.

Bien que la fusion des paramyxovirus ait été largement étudiée, le rôle exact de la H dans le déclenchement de la F est controversé et plusieurs modèles du processus de fusion sont proposés [162,163].

Dès leur biosynthèse, la protéine F est complexée à la protéine de liaison au récepteur qui exerce un rôle préventif du déclenchement de la F en maintenant cette dernière dans sa conformation de préfusion. Cette fonction permet de prévenir le déclenchement intempestif de la F [164–166]. Il a été proposé que c'est à la suite de l'interaction de la PLR à son récepteur que la F est alors libérée pour permettre la fusion[146]. La H subit en effet un changement conformationnel suite à la liaison au récepteur et va ensuite déclencher en continue la F par un « kick », entrainant ensuite la dissociation de H et F ; F assurant ensuite seule la fusion [158,167]. La tête globulaire de la PLR permet l'interaction avec le récepteur d'entrée tandis que le domaine de la tige interagit avec la F pour ensuite l'activer. Un grand nombre d'expériences ont montré que la F peut toutefois permettre la fusion en l'absence de la PLR ou de la tête globulaire de la PLR [168–172] à condition qu'un processus de rapprochement des membranes ait eu lieu.

Au cours de l'entrée, la protéine d'attachement met donc en œuvre 4 fonctions : (i) elle prévient le déclenchement aléatoire de F, (ii) assure l'attachement au récepteur et donc l'accolement des membranes virales et cellulaires, (iii) libère la F de son état métastable pour initier le processus de fusion et (iv) pousse la F à franchir son état métastable. Cet effet de « poussée » de la PLR stimule en effet la F par le biais de l'inclinaison répétée de la tête globulaire de la H qui engage son récepteur. La F est ainsi poussée pour atteindre le plus rapidement possible son état de post-fusion. Cette étape n'est pas nécessaire dans la nature car une fois le peptide de fusion

inséré dans la membrane de la cellule cible, la F est déjà très instable car cet état métastable consomme beaucoup d'énergie et le domaine HRN présente déjà une grande affinité pour le domaine HRC. L'effet de pushing est cependant visible en présence d'inhibiteurs de fusion et sera développé plus tard dans cette thèse.

e. Récepteurs d'entrée

Le récepteur du VR, SLAM, est exprimé à la surface des macrophages, des cellules dendritiques, des thymocytes, des cellules de Langerhans, des lymphocytes et des plaquettes [138,173,174]. Nectine-4 est exprimée sur la surface basale des cellules de l'épithélium, au niveau des jonctions adhérentes, et permet au VR de se propager des macrophages aux épithélium pour ensuite permettre la libération du virus et sa dissémination par les voies aériennes [139,140]. Ni SLAM ni nectine-4 ne sont exprimés dans le SNC.

3) Vaccin

Un vaccin vivant atténué très efficace est disponible pour prévenir les épidémies rougeoleuses. Compte tenu de la très forte contagiosité du VR, il est nécessaire que 95% de la population soit immunisée pour permettre l'éradication de la maladie [175]. En 1997, lors d'un congrès co-sponsorisé par l'organisation mondiale de la santé (OMS), l'organisation de santé pan américaine (Pan American Health Organization (PAHO)), et le centre pour le contrôle des maladies (Centers for Disease Control (CDC)), les experts se sont mis d'accord sur le fait que l'éradication de la rougeole serait techniquement possible aux alentours de 2005-2010. Aujourd'hui, l'éradication globale de la rougeole fait partie des priorités du programme étendu sur l'immunisation (Expanded Program on Immunization (EPI)) soutenu par l'OMS [129].

Plusieurs souches du VR ont été utilisées dans un but vaccinal. La souche Edmonston, isolée en 1954 s'est avérée réactogène. Cinq vaccins ont été dérivés par atténuation empirique à partir de la souche Edmonston: Edmonston-Zagreb, AIK-C, Moraten, Schwarz [176] utilisés depuis le milieu des années 60. Les souches Schwarz et Moraten partagent en fait un génome strictement identique [176]. D'autres vaccins dérivés d'autres souches ont aussi été développés. Les atténuations successives de la souche Leningrad (isolée en 1957) a conduit au vaccin Leningrad 4 et plus récemment au vaccin chinois Changchung-47. L'atténuation de l'isolat de Shanghai (1960) a permis la production du vaccin shanghai-191 et la souche Tanabe isolée au Japon en 1968 a mené au vaccin Cam-70 actuellement toujours produit et utilisé en Indonésie et au Japon.

Toutes ces souches vaccinales du VR ont en commun qu'elles appartiennent au génotype A [176] et toutes utilisent aussi CD46 comme autre récepteur cellulaire. Aujourd'hui le vaccin contre la rougeole est en général combiné avec les oreillons et la rubéole, connu sous le nom de vaccin ROR (MMR en anglaise pour measles, mumps and rubella), ou avec la varicelle [177]. La vaccination du ROR est administrée idéalement une première fois à partir de l'âge de 1 an et une deuxième fois 3 à 5 ans

après la première dose [129]. Comme le ROR est un virus vivant atténué son utilisation est proscrite chez les patients sévèrement immunodéprimés (avec peu de CD4+). En revanche, l'OMS recommande très fortement la vaccination pour les patients positifs au virus de l'immunodéficience humaine (VIH) qui ne souffrent pas d'immunosuppression sévère [178].
En général, les personnes vaccinées développent une forte immunité humorale et cellulaires. Deux à dix pour cent des personnes qui ont reçu deux doses de vaccin ne produisent toutefois pas d'anticorps protecteurs contre la rougeole. La plupart d'entre eux sont quand même protégés via l'immunité conférée par leurs cellules T mais certains redeviennent sensibles à la rougeole et dans ces cas-là il a été proposé de réitérer la vaccination tous les 10 ans par exemple [179,180].
En résumé, la couverture vaccinale reste trop faible et on compte de plus en plus de personnes immunodéprimées ou non-vaccinables. Le développement de traitements préventifs et curatifs semble donc incontournable.

4) La maladie

a. Symptômes et complications

Au cours de la phase aiguë de l'infection par le VR, les patients développent plusieurs symptômes, incluant de la fièvre, des congestions nasales, des éruptions maculopapuleuses érythémateuses caractéristiques, des conjonctivites et des taches de Koplik pathognomoniques sur la muqueuse buccale. Des diarrhées et des vomissements sont souvent observés chez les enfants infectés [181,182] ou apparaissent en tant que complications faisant suite à la maladie [121,183].
De plus, l'infection par le VR est associée à une forte immunosuppression pouvant durer plusieurs mois et jusqu'à deux ans [184,185]. Cette immunosuppression transitoire est consécutive à une amnésie immunitaire liée à la déplétion des lymphocytes T mémoires préexistants [181] et possiblement à une perturbation de l'homéostasie des cellules T régulatrices FoxP3 en augmentant leur fréquence et en atténuant leur hypersensibilité [186].
L'infection par le VR peut donc entrainer de sévères sur-infections comme des pneumonies, qui sont la cause majeure de mortalité dues à la rougeole [187]. D'autres pathologies moins fréquentes sont observées comme des complications du système nerveux central (SNC), une thrombocytopénie, une cécité ou perte auditive [188].

Des pneumonies interstitielles associées à une inflammation des muqueuses et à la formation de grands syncytia dans les poumons sont souvent observées chez les patients immunodéprimés (pneumonie de Hecht) [187,189]. Cependant, l'effet cytopathique généré par les syncytia conduit à une destruction broncho-épithéliale généralement résolue en quelques jours d'hospitalisation (Figure 7A).

Il existe plusieurs facteurs aggravants associés à une augmentation de la morbidité et de la mortalité due à la rougeole parmi lesquels la malnutrition et une déficience en vitamine A. En effet, indépendamment de la couverture vaccinale les personnes

infectées par le VR dans les pays les plus pauvres sont plus à risques de développer des complications amenant à une pathologie sévère [123,190–192].

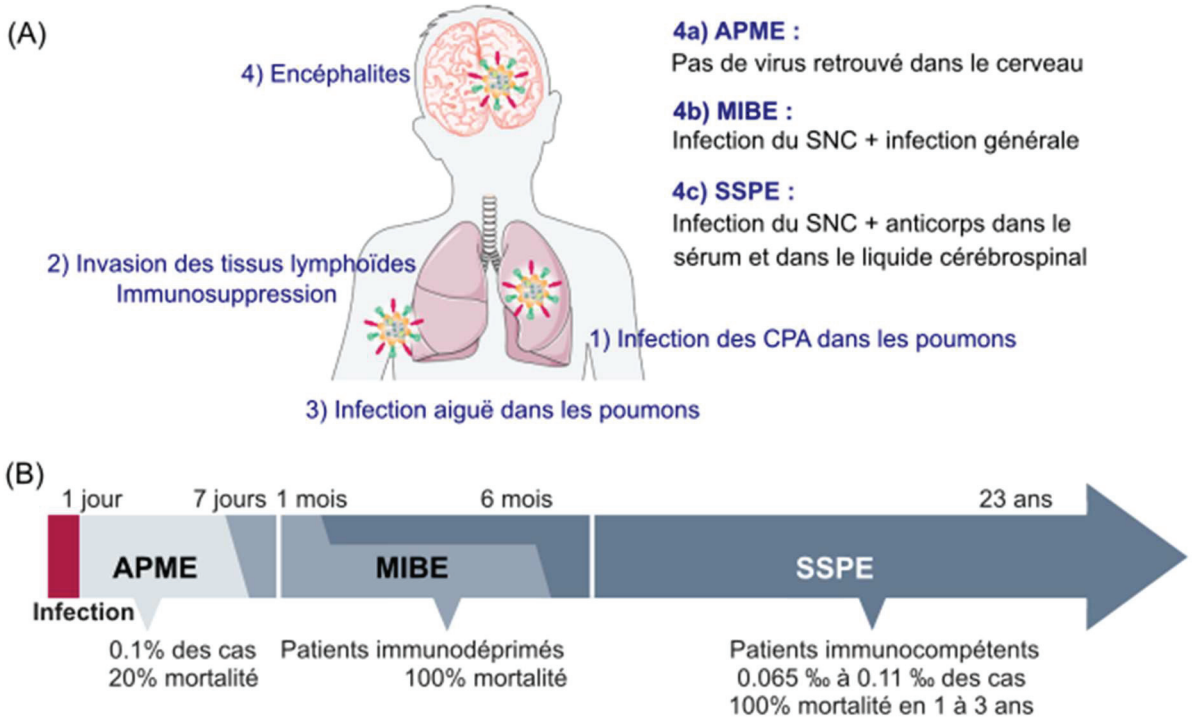

Figure 7 : Les différentes encéphalites rougeoleuses.
(A) Le VR infecte d'abord les cellules myéloïdes des voies respiratoires. Ensuite, les lymphocytes infectés disséminent l'infection par le biais des systèmes lymphatiques et vasculaires. (B) En conséquence de l'immunosuppression transitoire induite par l'infection ou de réactions auto-immunitaires les patients peuvent développer une encéphalite aiguë post-infection (acute post-infectious measles encephalitis (APME)) peu de temps après l'exposition au VR sans infection du SNC systématique. Plus tardivement peuvent survenir une encéphalite rougeoleuse à corps d'inclusion (Measles inclusion-body encephalitis (MIBE) dans un contexte d'immunodéficience ou une panencéphalite sclérosante subaiguë (PESS) associées à une persistance du VR dans le SNC.

b. Pathogénèse

La pathogénèse virale commence avec l'infection des cellules myéloïdes par le VR dans les voies respiratoires. Comme mentionné précédemment les deux récepteurs d'entrée connus du VR sauvage sont SLAM et nectin-4 [138,139]. Les souches sauvages ciblent les macrophages et/ou les cellules dendritiques résidentes des poumons qui expriment SLAM [193–195].

Ces cellules présentatrices d'antigènes (CPA) migrent vers les ganglions lymphatiques drainant, transmettent l'infection virale aux lymphocytes activés (mémoires) exprimant SLAM, entrainant la dissémination virale dans l'ensemble du système lymphatique via la lymphe et la circulation sanguine avec donc une virémie. Au cours de la phase tardive de l'infection, les cellules immunitaires circulantes

infectées qui atteignent les voies respiratoires et la peau transmettent l'infection aux cellules épithéliales exprimant nectine-4 sur leur pole basolatéral [140,196–198]. Les virions sont produits à la membrane apicale pour être libérés dans le mucus respiratoire ou sous forme d'aérosols et être expulsés lors de la respiration et amplifiés en cas de toux et éternuements [199].

5) Complications neurologiques

Le VR peut endommager le système nerveux et causer une perte de l'audition [200] ou une cécité.

Surdité :

Avant l'introduction de la vaccination, des pertes auditives liées à la rougeole étaient observées dans 5 à 10% des cas et restent fréquentes dans les pays sous-développés où la couverture vaccinale est encore trop faible [201]. Une explication possible est la surinfection de l'oreille entraînant une otite associée à la rougeole observée chez 25% des patients [202]. Des pertes auditives ont également été rapportées immédiatement après la phase aiguë de l'infection ou après une APME avec un surdité bilatérale modérée à profonde [200]. Cependant, les mécanismes associés aux pertes auditives induites par le VR sont encore peu compris et aucun antigène ni ARN viral n'a été détecté directement dans les échantillons d'oreille interne de patients [188].

Cécité :

Les symptômes oculaires tels que la conjonctivite ou l'inflammation de la cornée (kératite) sont couramment associés à la rougeole [188]. Ces complications sont souvent aggravées par les surinfections (bactériennes ou virales) qui surviennent à cause de l'immunosuppression induite par le VR. Il existe une corrélation entre la carence en vitamine A et la cécité induite par la rougeole. La carence en vitamine A est associée à des kératites sévères et augmente considérablement le risque de xérophtalmie, d'ulcération cornéenne et de cécité [203] et explique entre autres pourquoi la cécité liée à la rougeole est plus fréquente dans les régions où les enfants souffrent déjà de malnutrition.

L'ARN viral a été détecté dans les sécrétions lacrymales [204] et, *ex vivo,* le tissu cornéen humain est sensible à l'infection au VR sur son pôle basolatéral. Cependant, ni la formation de syncytium ni la libération de particules infectieuses n'ont été observées [205].

La relation entre l'infection des cellules épithéliales oculaires par le VR et l'infection potentielle des cellules neurales dans les cas de cécité reste donc hypothétique.

6) Les encéphalites rougeoleuses

Les récepteurs du VR ne sont pas exprimés dans le SNC et la façon dont le VR atteint et envahit le SNC reste inconnue.

Une expression apparemment seulement transitoire de nectin-4 dans le SNC, suggère un rôle de nectin-4 dans la neuro-invasion par le VR. En effet le tropisme neurologique d'un virus très proche du VR, le canine distemper virus (CDV), semblerait dépendre directement du modèle d'expression spécifique de nectin-4 [196,206–208]. Les cellules exprimant nectin-1 sont capables de capturer les membranes et cytoplasme de cellules adjacentes exprimant la nectin-4 à leur surface via un mécanisme de trans-endocytose [209]. Dans ce contexte, le complexe RNP pourrait transiter depuis les cellules exprimant nectin-4 dans les cornets nasaux ou les méninges vers les cellules neurales exprimant nectin-1 dans le bulbe olfactif ou le parenchyme cérébral, respectivement.
D'autres éléments clés impliqués dans la dissémination cellule-cellule dans le SNC restent à étudier (Figure 7A)
Trois principales complications du SNC sont associées à la rougeole : une forme aiguë et deux formes chroniques, la première sous forme d'encéphalite à corps d'inclusion (MIBE) chez les patients immunodéprimés et la seconde sous forme de panencéphalite sclérosante subaiguë (PESS) survenant chez des patients immunocompétents [210,211] (Figure 7B).

a. Encéphalite aiguë

L'encéphalite rougeoleuse aiguë post-infection (APME) touche 0,1% des patients infectés par le VR une semaine après l'apparition des premiers signes cliniques. Cette encéphalite est également connue sous le nom d'encéphalomyélite aiguë démyélinisante.
L'APME est associée à une mortalité de 20 % et à des séquelles neurologiques sévères, principalement chez l'adulte, avec de la fièvre, des maux de tête, des convulsions et des troubles de la conscience. L'APME semble liée à une réaction auto-immune contre la protéine basique de myéline (MBP) exprimée principalement par les oligodendrocytes [212–214]. Cette encéphalite provoque des lésions du SNC dans la matière blanche et la matière grise et se caractérise par une inflammation cérébrale et une démyélinisation péri-veineuse [6,199,215,216]. De plus, l'APME est souvent associée à d'autres anomalies immunologiques telles que des taux élevés d'anticorps IgE dans le sérum [217]. L'attachement de leucocytes infectés aux cellules endothéliales microvasculaires cérébrales, ou une infection directe des cellules endothéliales elles-mêmes dans le cerveau peuvent également contribuer en partie à cette réaction immunitaire inflammatoire [218].
Dans l'ensemble, l'encéphalite rougeoleuse aiguë est mal décrite dans la littérature. La présence du VR a été retrouvée dans la circulation sanguine mais jamais dans le parenchyme cérébral. De ce fait, plusieurs groupes ont suggéré que l'encéphalite pourrait être causée par une réponse de type auto-immune [219].

b. MIBE

Les MIBE surviennent chez des patients immunodéprimés, 3 semaines à 6 mois après une infection au VR sauvage ou dans de rares cas après une vaccination inappropriée avec une souche vaccinale [220–222]. La MIBE est caractérisée par la

présence de corps d'inclusions intracytoplasmiques ou intranucléaires composés de nucléocapsides, principalement dans les neurones, les oligodendrocytes et les astrocytes [223,224]. Les patients développent des convulsions focales fébriles et des troubles du comportement avant de sombrer dans le coma. Au niveau moléculaire, des mutations ont été observées dans certains cas dans le domaine intracytoplasmique de la protéine F et conduisent à l'expression de phénotypes viraux hyperfusogènes. L'hyperfusogénie se définit par la capacité de fusionner en l'absence de récepteur même à une faible température. Certaines mutations semblables à celles observées dans la PESS ont également été détectées dans le gène N, suggérant une similarité entre la MIBE et la PESS, indépendamment du développement plus rapide de la MIBE chez les sujets immunodéprimés [225]. Récemment, d'autres virus mutants associés à MIBE ont également été décrits et présentent un phénotype hyperfusogène [161,222]. Notamment, la mutation L454W dans le domaine HRC de la protéine F est apparue chez deux patients ayant contracté une MIBE en Afrique du Sud.
Des cas de MIBE sont également apparus suite à la vaccination de patients présentant une immunodépression qui n'était pas diagnostiquée au moment de la vaccination. Les séquences virales retrouvées dans le cerveau de ces patients confirment qu'il s'agissait bien d'une infection par la souche vaccinale. Ici aussi, les auteurs ont relevé la présence de mutations dans les séquences de la F, sans pour autant les nommer [224].

c. PESS

Les cas de PESS surviennent dans 6,5 à 11 cas pour 100 000 [226,227] chez des patients immunocompétents ayant contracté la rougeole dans leur enfance, avec un taux de mortalité proche de 100 %. Chez les enfants infectés par le VR avant l'âge de 12 mois, l'incidence de la PESS s'élève à 1/609, alors qu'elle atteint 1/1367 pour les enfants de moins de cinq ans [228]. Il y a une période de latence allant de un à 15 ans après la primo-infection et avant l'apparition des symptômes de la PESS [229,230]. A cause de la non-spécificité des premiers symptômes, le diagnostic de la PESS est souvent tardif [231]. Dans la plupart des cas, les patients ne survivent pas plus de 1 à 3 ans après l'apparition des symptômes neurologiques importants et de la démence. Les patients développent des déficiences physiques et mentales sévères mais aussi une perte de contrôle moteur qui tend à évoluer en contractions et spasmes myocloniques, des convulsions, jusqu'au coma. Ce serait le caractère immature du système immunitaire avant l'âge de deux ans qui pourrait contribuer à la propension accrue d'infection cérébrale persistante [214]. Alternativement, le développement de la PESS serait dû à une double exposition virale. En effet, lors d'une première exposition au VR, les patients immunocompétents ne développent pas d'encéphalite. Une première exposition (à un virus ou environnemental) conduisant à une immunosuppression même transitoire du patient, suivie d'une infection au VR favoriserait les maladies du SNC telles que la SSPE [232]. La plupart des études indiquent que les jeunes garçons sont plus souvent touchés par la PESS que les filles [137,233]. Dans une étude épidémiologique en Allemagne de 2003 à 2009, sur 31 cas de PESS les auteurs ont dénombré 21 individus masculins. La SSPE est

caractérisée par une synthèse intrathécale excessive d'anticorps spécifiques du VR. La plupart du temps, dans les échantillons provenant de cerveaux de patients SSPE, les gènes qui codent pour les M, F et H du VR sont mutées [146,234,235] (Figure 8 A).

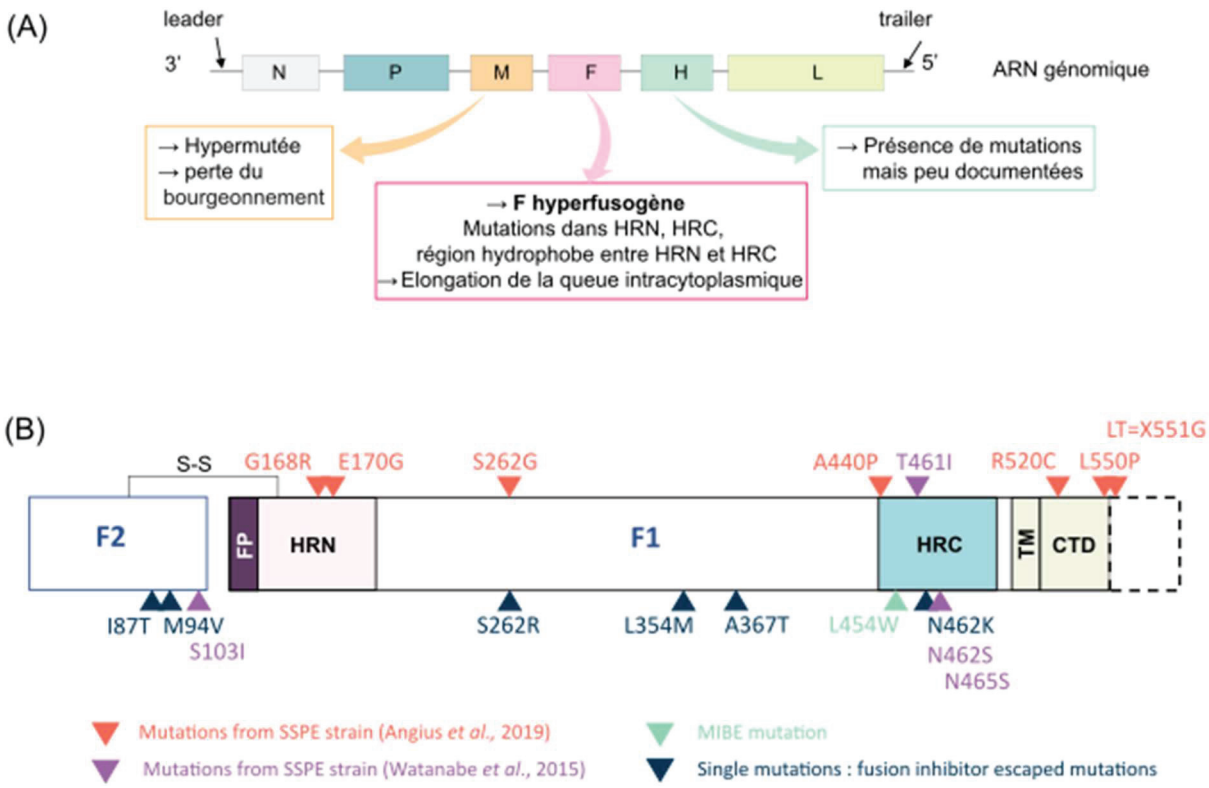

Figure 8 : Mutations du VR retrouvées dans les infections du SNC.
(A) Représentation schématique du génome du VR montrant les mutations retrouvées le plus couramment dans des cas de PESS. (B) Détails des mutations retrouvées dans le gène codant pour la F entrainant des phénotypes hyperfusogènes et/ou des infections du SNC.

7) Mutations associées aux infections du SNC

a. Protéine M

Dans les cas de PESS les hypermutations biaisées uridines à cystidines de la protéine M du VR sont caractéristiques [236]. Des études ont montré que le VR peut échapper au contrôle de l'immunité innée en tirant parti de l'adénosine désaminase agissant sur l'ARN 1 (ADAR1), un gène stimulé par l'interféron (IFN) qui lie l'ARN double brin et convertit l'adénosine en inosine par désamination [237]. L'étude suggère que les hypermutations biaisées du gène M (et des autres gènes) dans les cas de PESS (ou MIBE) pourraient être liées à l'activité d'ADAR1. ADAR1 ne peut cependant à priori pas accéder aux génomes ni aux antigénomes encapsidés. De ce fait ADAR1 ne pourrait donc modifier que les transcrits et ne permettrait pas le maintien et la transmission de l'hypermutation. L'hypermutation de la M conduit à une protéine M instable et défectueuse pour l'assemblage des particules virales [238]. Il en résulte un virus incapable de bourgeonner, rendant impossible la production de

nouvelles particules virales. Parmi le grand nombre de mutations dans l'ARNm, l'absence du codon d'initiation AUG conduit à une faible expression de la protéine M [239]. Néanmoins, dans le contexte de l'invasion cérébrale, le gène M hypermuté permet toujours au VR de se répliquer, de se propager et de provoquer la PESS [240,241]. En effet, la protéine M régule négativement l'activité de la polymérase virale et a donc un impact sur la transcription de l'ARNm et la réplication du génome [242]. L'un des rôles de la protéine M est l'adressage des glycoprotéines F et H à la surface apicale de la cellule [243]. De ce fait, les mutations de la protéine M pourraient impacter son association avec les queues glycoprotéiques de surface et conséquemment la stabilité de F et la fusion ; ainsi de telles mutations pourraient influencer la dissémination du virus dans le cerveau[244]. En effet, chez les souris transgéniques, l'infection par un VR codant pour une M hypermutée induit un phénotype plus fusogène malgré un bourgeonnement atténué, donnant naissance à un phénotype plus approprié pour l'infection cérébrale [240]. D'autres mutations impactent les interactions de la M avec la nucléocapside virale ou avec les glycoprotéines de surface [245,246]. Cette incapacité de bourgeonner explique l'absence de productions de particules virales dans le cerveau des patients souffrant de PESS et la non-contagiosité des patients [223]. De nombreuses études rapportent l'isolement de particules virales infectieuses à partir de cerveau de patients atteints de PESS. Cependant, aucun isolement physique de particules virales infectieuses ou des corps apoptotiques contenant des complexes RNP de virus exprimant des glycoprotéines de surface n'a été rapporté à partir du SNC [236,247–250].

b. Protéine F

Les protéines F observées dans les cas de PESS présentent plusieurs mutations conférant un phénotype hyperfusogène comme les mutations T461I, N462S, N465S, L454W localisées dans le domaine HRC.

La mutation du codon stop (X551G) dans les souches F-PESS a été fréquemment observée précédemment [236] et conduit à une queue cytoplasmique allongée (appelée LT pour Long Tail) qui peut améliorer l'incorporation de F et de protéines cellulaires non spécifiques dans le virion [251,252]. Une hypothèse serait que cette mutation pourrait être une réponse à des mutations de la M pour tenter de retrouver l'interaction entre la F et la M. D'autres mutations trouvées dans le domaine extracellulaire F à partir de séquences isolées de cerveau de patients souffrant de PESS (T461I et S103I/N462S/N465S) confèrent également une hyperfusogénicité et peuvent se propager dans des lignées cellulaires de neuroblastome humain et en cerveaux de jeunes hamsters en l'absence de récepteurs connus du VR [99,253].

D'autres mutations ayant un phénotype « fusion » altéré ont été isolées de virus ayant échappé aux inhibiteurs de fusion 3G ou le FIP (Fusion Inhibitory Peptide), repectivement N-[3-cyanophenyl]-2-phenylacetamide et Carbobenzoxy-d-Phe-l-Phe-Gly : I87T, M94V, S262R, L354M, A367T, N462K [254–256]. L'une des mutations localisée au niveau du résidu 262 (mutation d'échappement S262R) confère une hyperfusogénicité [99].

c. La protéine H

La protéine H des souches PESS est également souvent mutée et contribue à la neurovirulence [257].

Une souche Edmonston modifiée exprimant une protéine H adaptée aux souris provenant de la souche neurovirulente CAM/RB et porteuse des substitutions G195R et S200N perd complètement sa neurovirulence chez les souris C57BL/6 [214,258,259].

L'utilisation de souches très modifiées et le choix du modèle animal sont discutables ce qui rend les résultats difficiles à transposer aux cas humains de PESS. Néanmoins, ces données ont permis de mettre en évidence l'existence potentielle d'un site spécifique de la H qui serait impliqué dans la neurovirulence ou d'un site de reconnaissance par un récepteur neuronal putatif.

L'élongation de l'extrémité C-terminale de la protéine H due à une mutation ponctuelle au niveau du codon stop a également été rapportée à plusieurs reprises dans des cas de PESS [206,260]. Contrairement aux délétions dans la queue cytoplasmique de la H qui se sont avérées améliorer l'activité fusogénique [251], l'allongement du domaine extracellulaire de la H semble avoir un impact positif sur l'attachement et peut expliquer au moins partiellement le niveau élevé d'anticorps reportés dans les cas de PESS [206,260].

En opposition aux cas de PESS, les mutations du gène H des séquences virales issues de cas de MIBE semblent être moins fréquentes[222].

8) Modèles pour l'étude de la neuroinvasion

a. Les modèles animaux

L'homme est le seul réservoir naturel du VR. Ainsi, le choix du meilleur modèle animal reste un défi et dépend du type de question posée, à défaut d'être fidèlement représentatif de l'infection du SNC chez l'homme. Un résumé des petits modèles animaux les plus utilisés et de leurs applications associées est présenté dans le tableau 1. Plusieurs souris génétiquement modifiées ont été utilisées, principalement pour étudier le tropisme, la dissémination et pour développer de nouveaux traitements. Historiquement, le rat Lewis était couramment utilisé pour étudier le tropisme viral et sa dissémination à travers le SNC [261]. Plus récemment, on privilégie les hamsters dorés pour étudier la neurovirulence du VR en raison des similitudes des lésions cérébrales observées par le VR dans ce modèle par rapport aux cas humains de PESS. De plus, contrairement aux souris, les jeunes hamsters sont naturellement sensibles à l'infection au VR, en particulier dans le cerveau, malgré l'absence d'expression des récepteurs connus comme rapporté chez l'homme [99,262] (tableau 2).

Tableau 2 : Petits modèles animaux utilisés pour étudier l'infection par le virus de la rougeole.

Animal	Utilisation	Voie de l'infection
SOURIS		
NSE-CD46 : expression de l'isoforme BC1 de CD46 humain sous le control d'une enolase neurone-specifique (NSE) [263,264] **YAC-CD46 :** niveau d'expression et localisation similaire à l'Homme [263] **CD46** [265–267] **CD46-IFNAR-/-** [268]	Comportement du VR vaccinal dans le cerveau Capacité de dissemination dans le cerveau Pathogénèse de l'infection par le VR dans le SNC Permissivité Réponse immunitaire	Intranasale (i.n.) Intracraniale (i.c.)
SLAM : expression ubiquitaire [269] **SLAM :** expression restreinte aux cellules dendritiques [270,271] **CD46/CD150 inductible par TLR** [272] **CD46/CD150-IFNAR-/- inductible par TLR**	Réponse immunitaire innée Dissémination et pathogénèse des souches Edmonston et sauvage Ichinose (IC)	i.n. i.c.
SLAM IFNAR-/- [273] **IFNAR-/-** [161,274]	Tropisme Dissémination dans le SNC	Intrapéritonéale (i.p.) i.n.
SLAM(+/+)/Stat 1 (-/-) : Niveau d'expression similaire à l'Homme [275]	Réponse immunitaire innée	i.p. i.n.
CD46 IFN-α/βKO [268]	Induction d'encéphalite rougeoleuse avec la souche Edmonston	i.c.
CD46 RagKO [232,276]	Etude des PESS Rôle de l'immunosuppression dans la persistence du VR Test de traitements	Multiple
CD46 Neurokinin-1 KO [276]	Dissémination virale trans-synaptique	i.c.
C57BL/6 [277]	Persistance virale Tropism	i.c.
RAT		
Rat Lewis [261,278,279]	Tropisme	i.c.
Rat des cotonniers (Sigmodon hispidus) [131,280,281]	Développement de traitements Infection respiratoire Immunosuppression induite par le VR Infection du SNC	i.n.
Rat CD46 Sprague-Dawley rat [282]	Permissivité	Multiple
Rat surmulot brun [283]	Réponse immunitaire dans les maladies neurologiques associées au VR	i.c.
HAMSTER		

Hamster doré [99]	Tropisme Dissémination et invasion par des virus mutants	i.c.
Furet		
Furet [227,284–286]	Pour reproduire une PESS Transmission Pathogénèse de l'infection par CDV pour modéliser l'infection par le VR	i.c. i.n.

De nombreuses études ont été réalisées à partir de souches neurotropes obtenues par des passages multiples dans des cerveaux de hamster. Aujourd'hui, ces souches censées mimer une infection persistante du cerveau ne sont plus utilisées. En effet, les souches CAM/RB ou HNT étaient très virulentes chez la souris, le rat et le hamster mais l'infection induite n'était pas représentative d'une infection persistante du VR dans le cerveau. Ces souches neuro-adaptées hypermutées induisent une infection aiguë dans le cerveau qui n'est pas représentative de l'infection lente et progressive observée dans la PESS [261,278,287]. Un tel type d'infection n'est pas représentatif d'un APME ou d'un MIBE non plus.

Plusieurs modèles murins ont été développés pour répondre à des questions spécifiques sur la pathogenèse du VR, l'invasion du SNC, les traitements antiviraux et la persistance (tableau 2). La persistance du VR a été démontrée chez des souris infectées par la souche Edmonston ou un VR recombinant exprimant la H de la souche CAM/RB jusqu'à deux mois [288,289] et chez des souris immunodéprimées infectées par la souche Edmonston. Cette dernière étude a également permis de mettre en évidence l'émergence de mutations [290]. Les modèles de souris transgéniques (tg) sont toujours largement utilisés [266,269]. Ces modèles expriment en général les récepteurs SLAM ou CD46 humains de manière stable et ont été générés à partir de souris sauvages ou déjà transgéniques pour d'autres gènes. Lorsque ces récepteurs sont exprimés de manière ubiquitaire (notamment dans le SNC), ces modèles très artificiels facilitent grandement l'entrée du VR. De plus, de tels modèles animaux permettent non seulement d'étudier les facteurs clés de la permissivité des cellules indépendamment de l'étape d'entrée, mais aussi de valider l'efficacité des traitements antiviraux dans un contexte où la propagation du virus est la plus difficile à bloquer [147,276,291,292] (tableau 2).

Certains primates non humains représentent des modèles de choix de la rougeole car ils sont sensibles à l'infection par les souches sauvages du VR [293]. Ainsi, les macaques rhésus et cynomolgus ou les singes saïmiris, communément appelés singes écureuils sont souvent utilisés pour des études portant sur la pathogenèse aiguë [140,196,197,199,294–296]. Ces études ont mis en évidence de nombreuses similitudes de l'immunopathogenèse de la rougeole entre l'homme et ces primates. En particulier, le rôle essentiel de nectine-4 pour l'excrétion et la transmission interhumaine du VR a été confirmé, mais aucun symptôme lié à l'infection du SNC

n'a été rapporté à ce jour. Des transmissions accidentelles de souches circulantes du VR de l'homme au primate se sont déjà produites, causant notamment 5 décès sur 21 cas chez le singe rhésus [297].

Dans cette étude, l'infection du SNC n'a pas été étudiée et tous les décès étaient dus à une infection secondaire liée à l'immunosuppression induite par le VR. En 1999, une autre épidémie naturelle a entraîné la mort de 12 macaques japonais sur 53 cas. Une démyélinisation a été observée dans le cerveau d'un singe et deux singes ont montré des inclusions neuronales avec des antigènes de la rougeole [298] mais aucune particule virale infectieuse n'a été isolée. Afin de mieux caractériser l'infection du SNC, des singes rhésus ont été infectés par voie intracérébrale avec un virus dérivé de séquences connues de PESS mais les animaux n'ont pas développé de symptôme visible et plus aucun virus n'a été détecté trois semaines après l'infection, suggérant la résolution de l'infection [299]. Une autre étude a été réalisée sur des singes rhésus infectés par voie intracérébrale avec une souche adaptée au cerveau de hamster. Ces singes rhésus ont développé une encéphalite avec des caractéristiques morphologiques similaires à celles observées dans le cerveau des cas humains de PESS. Cependant, comme déjà observé chez le rongeur, ces infections cérébrales induites par une souche adaptée au cerveau de hamster ont évolué au cours de la phase aiguë de l'infection et ne reflètent pas la lente progression observée dans la PESS [300]. L'infection du SNC par le VR doit encore être caractérisée dans ce modèle.
Plus récemment, une analyse comparative de l'infection, du tropisme et de la propagation du VR chez l'homme et de l'infection par le virus CDV responsable de la maladie de Carré chez des espèces hôtes naturelles telles que le chien et le furet a été réalisée. Cette étude a mis en lumière l'intérêt d'étudier la pathogénèse du CDV pour mieux comprendre la pathogénèse du VR, ces deux morbillivirus étant très proches [286].
Le tamarin (Saguinus mystax), souvent appelé à tort ouistiti (marmoset en anglais) dans la littérature, s'est révélé sensible à l'infection par les souches Edmonston et JM [301,302]. La souche JM était hautement pathogène dans ce modèle, notamment après inoculation cérébrale [303].

b. Les modèles alternatifs pour étudier le tropisme

Le principal obstacle à l'étude du tropisme précoce du VR et d'autres Paramyxoviridae est le manque de modèles adéquats qui pourraient représenter fidèlement l'infection dans le cerveau humain. A ce jour, les modèles *ex vivo* semblent être un bon compromis [304]. Des cultures organotypiques de cerveaux de souris, de hamsters, de rats, de chiens, de furets et de primates non-humains ont déjà été générées avec plusieurs sous-structures cérébrales telles que le cervelet, le cortex cérébral, le bulbe olfactif ou l'hippocampe [278,304–306]. Les avantages de ces modèles sont la présence des quatre types cellulaires du SNC (neurones, astrocytes, oligodendrocytes et cellules microgliales), la possibilité de les produire à partir d'animaux transgéniques, et l'opportunité unique d'avoir une visibilité directe sur le SNC. De plus, plusieurs tranches peuvent être réalisées à partir de chaque sous-

structure. Par conséquent, un grand nombre de conditions peut être testé avec un nombre très limité d'animaux, ce qui rend ces modèles éthiquement préférables par rapport aux expériences *in vivo*. Les principales faiblesses des cultures organotypiques de cerveau sont l'absence d'un système vasculaire avec des leucocytes circulants et la diminution de la susceptibilité à l'infection au cours du temps concomitante au développement de l'astrogliose [274]. Les cultures organotypiques de cerveau de souris offrent de nombreuses possibilités, mais les souris sauvages ne sont pas sensibles à l'infection par le VR et les cultures organotypiques de cerveau de souris ne conviendraient donc pas pour étudier le tropisme précoce du VR dans le SNC. Par contre, les hamsters dorés sont sensibles à l'infection au VR. Ainsi, les cultures organotypiques de cerveau (COC) de hamsters pourraient offrir des modèles *ex vivo* plus pertinents mais le manque d'outils et d'anticorps disponibles pour cette espèce ralentissent encore fortement l'étude du tropisme précoce dans le SNC de hamster.

c. Les modèles alternatifs pour étudier la dissémination

Des lignées cellulaires neuronales telles que des cellules humaines NT2, des cellules d'astrocytome humain ou des cellules de neuroblastome de souris ont également été utilisées, mais leur pertinence reste difficile à apprécier compte tenu du changement de comportement des cellules en dehors de leur contexte tissulaire [149,227,307–310]. Des neurones primaires et des polycultures neurales ont également souvent été utilisés [227] mais sont peu représentatifs de la population neuronale dans le cerveau humain. Dans de nombreuses études, ces cultures ont été très utiles pour étudier la propagation intra et interneuronale du VR [276] car elles peuvent être établies à partir du cerveau de n'importe quelle souris transgénique.

Les organoïdes de cerveau humain en 3 dimensions (3D) récemment développés ont un potentiel élevé pour étudier la dissémination et l'évolution virale dans le cerveau. Les organoïdes cérébraux sont générés à partir de cellules souches pluripotentes humaines ou de cellules souches embryonnaires humaines. Ce modèle plus éthique offre une opportunité unique de générer des données pertinentes qui pourraient être transposées fidèlement à l'infection cérébrale chez l'homme [311]. Les organoïdes du cerveau humain nécessitent encore un développement supplémentaire afin de pallier le manque de microglie et de vascularisation, mais aussi le coût élevé et la variabilité du système [312]. Cependant, à ce jour, ce modèle peut être très utile en combinaison avec des modèles *ex vivo*, notamment pour tester l'efficacité d'inhibiteurs dans le cadre d'une infection cérébrale, suivre la dissémination virale et mettre en évidence l'émergence de mutations.

9) Le tropisme du VR dans le SNC

Le VR, bien que principalement lymphotrope, peut également infecter le SNC. Le virus pourrait entrer dans le SNC par la voie hématogène en traversant la barrière hémato-encéphalique (BHE) [137]. L'infection des cellules endothéliales, sensibles à l'infection in vitro et in vivo, au niveau de la BHE pourrait également permettre au VR

d'atteindre le SNC [218,313]. De plus, les lymphocytes sont aussi capables de traverser la BHE, signifiant que les lymphocytes infectés par le VR pourraient transporter le virus à travers la BHE [314,315].

Cependant, les mécanismes spécifiques permettant au virus d'entrer dans le SNC restent flous [218,234,316]. Le phénotype hyperfusogène semble être nécessaire pour permettre la dissémination virale à travers les neurones même en l'absence de récepteur connu. À ce jour, le tropisme précoce et la dissémination des Paramyxoviridae dans le SNC au cours des premiers stades de l'infection restent peu documentés. Il existe également très peu de données disponibles sur les mécanismes cellulaires et moléculaires régissant l'invasion du SNC. À ce jour, les investigations se limitent principalement aux symptômes cliniques, à la sérologie, au séquençage de l'ARN et aux immunomarquages tissulaires. Par ailleurs, la plupart des études ont été réalisées avec des souches vaccinales du VR telles que la souche Edmonston B ou des souches neuro-adaptées chez le hamster. Ces études utilisent généralement différentes espèces de rongeurs sauvages ou transgéniques, ou d'autres modèles in vitro tels que des cultures neurales primaires ou immortalisées. L'utilisation de ces souches virales et de ces modèles est toutefois discutable lorsqu'il s'agit de refléter ce qui se passe chez l'homme. En revanche, ces études permettent d'aborder des questions spécifiques pour obtenir des informations importantes concernant le tropisme de l'infection par le VR dans le cerveau.

a. Les études post mortem

Les analyses post-mortem de cerveaux humains infectés par le VR montrent des lésions dans presque toutes les zones (figure 9 A). Dans le même contexte tardif, des études d'infection cérébrale chez l'homme et dans des modèles animaux ont décrit les types cellulaires dans lesquels des antigènes viraux ont été retrouvés dans le SNC, néanmoins les premières cellules ciblées restent à déterminer.

Dans le SNC, l'infection au VR a été observée principalement dans les neurones mais aussi dans les oligodendrocytes, les astrocytes et les cellules microgliales [137,317,318] (Figure 9 B,C,D). Dans les cas de MIBE et de PESS, des antigènes viraux et de l'ARN viral ont été trouvés dans les neurones et les oligodendrocytes [316]. Dans les cas de PESS chez l'homme, les neurones sont la cible principale et la dissémination virale interneuronale a été démontrée au niveau des synapses via l'interaction de F avec la Neurokinine-1 [227]. Les oligodendrocytes infectés se situent souvent à proximité des neurones infectés, ce qui suggère une infection secondaire des oligodendrocytes par les axones. L'infection des oligodendrocytes par le VR est fortement liée à leur démyélinisation qui pourrait d'ailleurs être une caractéristique de la PESS (Figure 9 A, B).

Le génome du VR et les antigènes viraux ont également été retrouvés, dans une moindre mesure, dans le cytoplasme périnucléaire des astrocytes [316].

Dans une étude utilisant la souche Edmonston B, l'infection de cultures organotypiques d'hippocampes de rat *ex vivo* a montré que le virus peut infecter les neurones en l'absence du récepteur CD46 [278].

Une infection des méninges a également été observée suite à l'inoculation intracrânienne du VR chez des furets [319] et des hamsters [320], ainsi qu'après une infection intranasale de souris transgéniques SLAM [161]. Toutefois les souches du VR et les mutants utilisés dans ces études étaient tous connus comme hyperfusogènes et l'infection des méninges n'a pas encore été signalée chez l'homme.

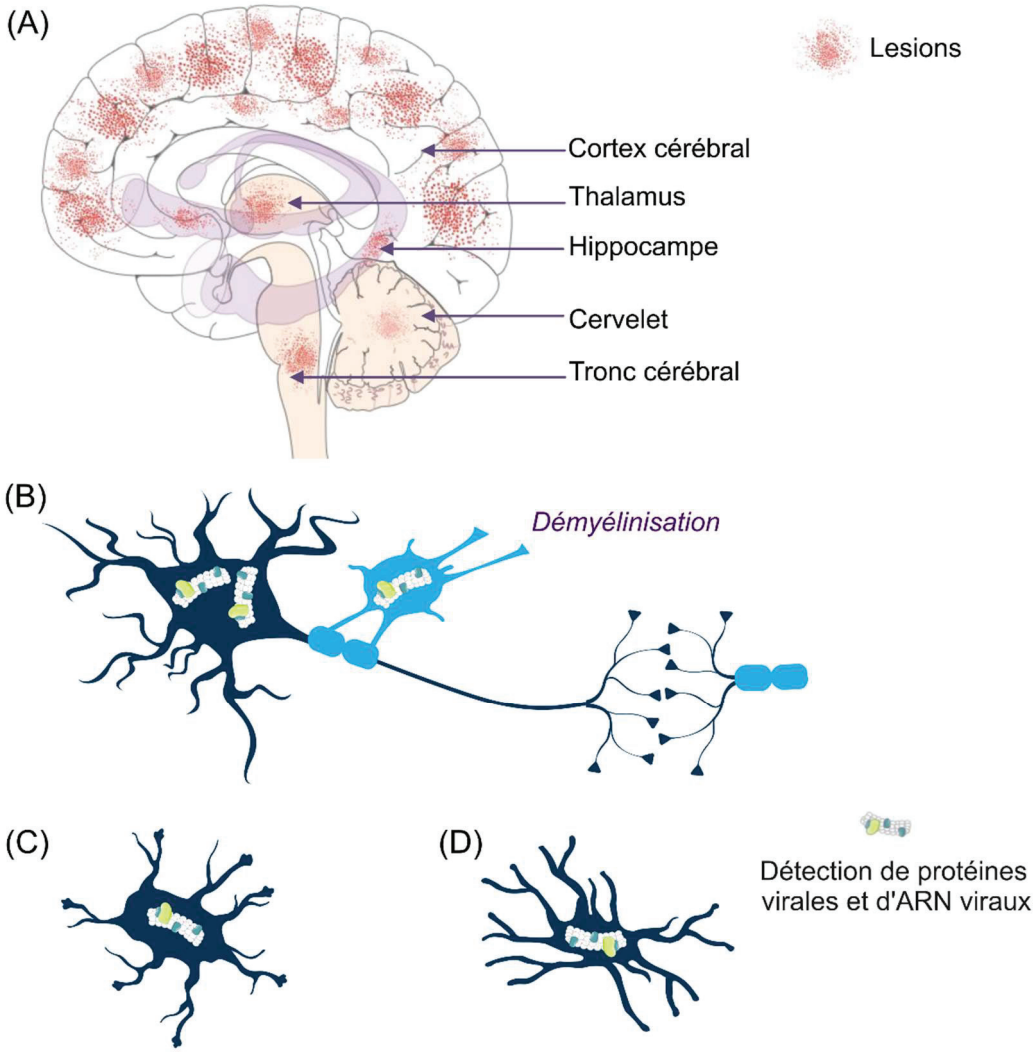

Figure 9 : Infection du système nerveux central par le virus de la rougeole (VR).

Des lésions sont retrouvées dans le cerveau de patients souffrant de PESS et de MIBE mais les zones spécifiques où de l'ARN viral a été retrouvé sont peu documentées (A). Dans les études post mortem chez l'Homme le VR a été retrouvé dans les neurones et les oligodendrocytes (B). Occasionnellement des ARN du VR sont retrouvés également dans les astrocytes (C) et les cellules microgliales (D).

b. Les évènements précoces de l'infection par le VR

Il est tout à fait envisageable que le VR puisse utiliser un troisième récepteur ou co-récepteur encore inconnu pour entrer dans le SNC. On pourrait d'ailleurs établir un parallèle avec les études d'invasion du SNC par le CDV, très proche du VR, montrant que dans les cerveaux de chiens les astrocytes qui n'expriment pourtant ni SLAM ni nectine-4 restent permissifs à l'infection [207]. Cependant, pour le VR, l'hypothèse selon laquelle une seule ou une combinaison de mutations serait suffisante pour conférer une adaptation dans les tissus cérébraux à l'invasion sans l'engagement d'aucun récepteur est également pertinente.

À ce jour, la toute première cible cellulaire de l'infection par le VR dans le SNC est inconnue. Une étude récente s'est concentrée sur la susceptibilité cellulaire lors d'une infection par le VR dans le SNC en utilisant des cultures organotypiques d'hippocampe de souris C57BL/6 génétiquement modifiées déficientes pour le récepteur à l'interféron et exprimant le récepteur SLAM humain (souris SLAM-IFNAR) [274]. Tous les types cellulaires se sont avérés susceptibles à l'infection en l'absence de réponse IFN-I, cependant dans les cultures organotypiques issues de souris immunocompétentes une astrogliose a été détectée et la permissivité des astrocytes et des cellules microgliales a de ce fait fortement diminué. L'astrogliose et la microgliose ont été observées dans les cas d'encéphalites rougeoleuses [269,321,322]. Ces données pourraient expliquer pourquoi les antigènes viraux sont à peine détectables dans les astrocytes et les microglies dans les analyses post mortem. Une autre étude récente réalisée à partir de cultures organotypiques de bulbe olfactif, d'hippocampe et de cortex chez le primate non-humain, le chien et le furet a identifié les cellules microgliales comme étant la cible principale du VR [306]. Les auteurs ont utilisé une souche de VR sauvage. L'infection de neurones et d'oligodendrocytes a également été observée. Les auteurs ont réalisé cette étude en parallèle avec le CDV et ils ne rapportent aucune infection des astrocytes, ni par le VR ni par le CDV. D'après les auteurs, les astrocytes ne seraient pas la cible initiale de ces virus. Toutefois l'étude ayant été réalisée 3 jours post infection et sur des cerveaux d'animaux adultes on pourrait envisager que l'absence d'infection des astrocytes serait plutôt consécutive à une forte astrogliose[274]. Concernant l'infection des cellules microgliales, on ne sait pas si ces cellules expriment CD150 comme les macrophages. Cependant l'expression de CD150 par les microglies serait inductible [323].

10) La dissémination du VR dans le SNC

Dans le tissu cérébral des cas de PESS on n'a pas détecté la présence extracellulaire du VR, ce qui suggère une dissémination virale de neurone à neurone possible sans libération de particules virales infectieuses [317]. La propagation du VR dans les neurones de souris et de rat est basée sur le contact de cellule à cellule [278,307,324]. L'analyse fonctionnelle de VR hyperfusogènes portant une protéine F mutée T461I a confirmé cette théorie. Ce virus mutant comportant cette mutation issue d'un patient souffrant de PESS est capable de se disséminer exclusivement de

cellule à cellule dans des neurones primaires humains [253,257]. La combinaison de mutations trouvées dans les souches issues de cas de PESS semble déterminante pour l'infection du cerveau et la neurovirulence [257]. Les virus porteurs de ces mutations peuvent se propager dans le cerveau de souris génétiquement modifiées [240].

Plusieurs hypothèses mentionnent l'implication d'un co-récepteur dans le SNC (Figure 10).
D'après certaines études, la dissémination du VR serait médiée par un mécanisme de microfusion au niveau des membranes synaptiques [227,257]. Selon cette théorie, la protéine F interagirait avec la Neurokinine-1, le récepteur de la substance P [276,278] (Figure 10). Cette interaction conduirait à la formation d'un micropore de fusion, permettant au complexe viral ribonucléique de se diffuser à travers le réseau neuronal sans avoir besoin de l'engagement d'un autre récepteur ni de bourgeonnement. Cela pourrait également expliquer l'absence de formation de syncytia dans les neurones primaires humains suite à une infection par des formes hyperfusogènes du VR.
Autre hypothèse, certaines cellules myélinisées du SNC pourraient bloquer le contact de cellule à cellule entre les neurones et la propagation trans-synaptique dans le cerveau serait le seul moyen de permettre la dissémination virale [157].
En 2019, Generous et ses collègues ont mis en évidence une autre façon possible et inédite de dissémination du VR dépendant de la nectine-4 dans les neurones[209]. Les cellules épithéliales infectées exprimant nectine-4 peuvent effectuer des transferts de leur matériel cytoplasmique (incluant le matériel infectieux) avec des neurones exprimant nectine-1 par un système de trans-endocytose. Ce procédé a été nommé « transfert de cytoplasme induit par la nectine », en anglais « nectin-elicited cytoplasm transfer » (NECT). L'utilisation du NECT par le VR pour se disséminer dans le SNC reste à être démontrée dans un contexte physiologique.

Dernière hypothèse alternative, d'après Shirogane et ses collègues, l'infection trans-synaptique de neurones est possible via les molécules d'adhésion cellulaires 1 et 2 (CADM1, aussi appelée IGSF4A, Necl-2, ou SynCAM1 ; et CADM2, aussi appelée IGSF4D, Necl-3 ou SynCAM2) [325]. Les résultats présentés dans cette étude sont incomplets et doivent être interprétés avec précaution, cependant, les auteurs ont identifié ici CADM1 et CADM2 comme agissant en tant que récepteurs en *cis* de basse affinité pour le VR. L'interaction entre ces molécules et la H, à condition qu'elles soient exprimées en *cis* sur la même cellule, est suffisante pour rapprocher les membranes de deux neurones et déclencher la F de mutants hyperfusogéniques du VR. Bien que non-formellement exploré par les auteurs, le rapprochement membranaire qui doit nécessairement avoir lieu pourrait être consécutif à la propriété d'homo- et/ou hétéro-philie démontrée des CADMs exprimées sur des membranes opposées. Les données montrent que l'inhibition de l'expression de CADM1 et CADM2 entraine une forte diminution de la fusion et de la dissémination des mutants hyperfusogéniques du VR, notamment le virus portant la mutation T461I dans la F [325]. CADM1 et CADM2 sont abondamment exprimés dans le cerveau humain et cette étude montre que leur faible interaction avec la H ne permet de déclencher la fusion

intercellulaire que par des virus déjà hyperfusogènes, connus pour être moins stables. A noter qu'aucun des CADM ne permet l'infection par une particule virale, ils sont seulement impliqués dans la dissémination entre cellules. Si les études approfondies à venir valident ces résultats ce procédé pourrait expliquer pourquoi les virus issus des cas de PESS sont capables d'envahir le cerveau en opposition aux souches sauvages.

Dissémination du virus de la rougeole cellule à cellule

dans le Système Nerveux Central?

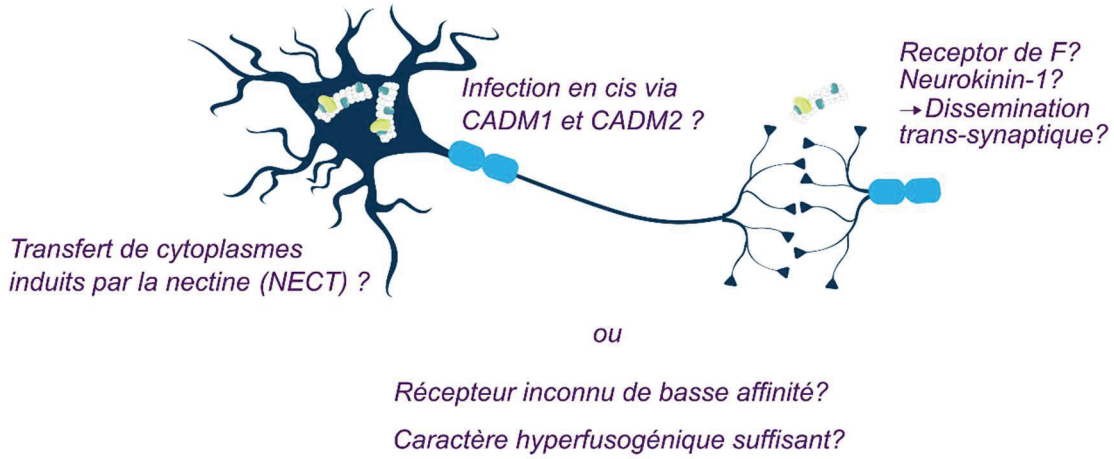

Figure 10 : Schéma des hypothèses pouvant expliquer la dissémination du virus de la rougeole dans le système nerveux central.

11) Les traitements

Aucun traitement ayant une efficacité démontrée n'est disponible pour traiter la rougeole ou a fortiori les encéphalites rougeoleuses.

a. Traitement des symptômes et prévention des surinfections

De manière courante, seuls sont utilisés des traitements symptomatiques et la prévention des surinfections par traitement antibiotique [326].

b. Traitements basés sur l'amélioration de la réponse immunitaire

Des traitements visant à stimuler la réponse immunitaire ont été utilisés pour traiter l'infection par le VR, incluant les immunoglobulines, la ribavirine et l'interféron alpha (IFN-α).

c. Immunoglobulines sériques

Historiquement, il a été estimé que l'injection intramusculaire d'immunoglobulines sériques en prophylaxie post-exposition protégeait jusqu'à 70% des patients [327]. Cependant cette méthode est controversée car les doses d'immunoglobulines injectées doivent être très élevée pour maintenir un niveau d'anticorps antirougeoleux suffisant [328]. D'autres données suggèrent que l'injection

d'immunoglobulines pourrait conduire à des cas de PESS [329] et favoriser la persistance du VR dans le cerveau [330–332].

d. Ribavirine, IFN-α, Isoprinosine

La ribavirine est un antiviral large spectre initialement utilisé pour le traitement du virus de l'hépatite C [333]. Il s'agit d'un analogue d'acides nucléiques dérivé de la guanosine qui agit sur l'ARN polymérase virale en incorporant des nucléosides mutagènes dans le génome [334]. La ribavirine semble diminuer les symptômes respiratoires chez les patients infectés par le VR [335] mais il n'y a pas de protocole standard ni de doses recommandées à ce jour. Il est critique de remarquer qu'in vitro, la concentration de ribavirine requise pour induire une mutagénèse catastrophique excède de beaucoup la dose tolérée chez l'homme [336–338].

L'IFN-α, la ribavirine et l'inosine pranobex ont été utilisées pour traiter des cas de PESS mais leur efficacité à long terme reste insuffisante [339]. De nombreux rapports cliniques montrent que la ribavirine induit une diminution des titres d'anticorps antirougeoleux dans le LCR des patients et améliore les symptômes neurologiques sans effets secondaires [340,341], en particulier lorsqu'elle est associée à l'IFN-α. Dans de rares cas, le traitement à long terme par l'IFN-α stabilise les symptômes cliniques des patients atteints de PESS pendant des années [342].

L'isoprinosine est un dérivé de l'inosine et vise à bloquer la réplication virale, probablement par une activité immunorégulatrice. Le traitement le plus couramment utilisé de nos jours pour limiter la progression des PESS est l'injection d'IFN-α intrathécale ou à l'aide d'une pompe à perfusion sous-cutanée associée à l'isoprinosine orale [343–345].

Ces traitements ne permettent pas de récupérer la perte de fonction mais ils peuvent stabiliser la maladie pendant plusieurs années [226,342,346]. Le traitement à l'IFN-α peut être associé à des effets secondaires et conduire à des interféronopathies [347].

e. Vitamine A

La carence en vitamine A est un facteur de risque pouvant entrainer des complications à la suite de l'infection par le VR. L'apport de vitamine A réduit la morbidité et la mortalité liées à la rougeole chez les enfants [190–192] et permet de prévenir la cécité [203,348]. Ainsi, l'OMS recommande l'administration immédiate de vitamine A aux enfants infectés par le VR et aux cas graves avec 2 doses répétées de 200 000 UI [123,349–352].

Au début de l'infection, la réponse immunitaire innée repose sur la détection des MAMPs (microbe-associated molecular pattern) par les récepteurs de reconnaissance de motifs (PRR) tels que les RIG-I Like Receptors (RLR) reconnaissant les motifs d'ARN double brin dans le cytoplasme [353]. Cette voie permet la synthèse et la sécrétion d'interféron de type I. Parmi les RLR, RIG-I (Retinoic acid-inducible gene I) est activé par plusieurs virus à ARN dont le VR [354–356]. Outre son effet sur la vision, l'efficacité d'un (pré)traitement à la vitamine A pourrait refléter aussi la capacité de son métabolite, l'acide rétinoïque, à inhiber *in vitro* la réplication du VR via une voie rétinoïde nucléaire d'activation de RIG-I [357,358] selon un mécanisme dépendant de l'interféron de type I (IFN) [359].

f. Gènes stimulés par l'interféron (ISG) et autres traitements

De nombreux autres traitements, tels que des immunomodulateurs, la carbamazépineamantadine, des stéroïdes, la cimétidine et la plasmaphérèse et d'autres inhibiteurs alternatifs ont été testés pour traiter la PESS mais sans efficacité prouvée [344,346,360].

Parmi les patients qui ont reçu deux doses de vaccin après l'infection initiale, certains ont quand même développé une PESS, suggérant que le vaccin post infection ne permet pas de prévenir l'encéphalite chez ces cas particuliers [361]. Le développement de PESS dans ce contexte pourrait possiblement être indicateur d'une persistance de l'infection virale dans le SNC, hors de portée de la réponse immunitaire spécifique du VR.

g. Inhibiteurs de transcription ou de réplication

Afin d'inhiber la prolifération du VR, une stratégie consiste à réprimer les ARNm codant pour l'un des complexes clés de la polymérase, la N, la P ou la L en utilisant de petits ARN interférents (siRNA) ou shRNA, sous forme d'oligonucléotides synthétiques, codés par des plasmides ou transduits à l'aide de vecteurs lentiviraux. Les siARN ciblant l'ARNm de la L[362], de la N[363], de la P[364], ou des trois en combinaison[365] sont efficaces pour prévenir la croissance virale sur quelques jours sans effet cytotoxique. Cependant, même dans les cellules qui expriment constitutivement le siRNA le VR finit toujours pas contourner l'action des siRNA sans pour autant acquérir de mutation[364].
Cela peut-être expliqué par la demi-vie remarquablement longue de la polymérase apportée par les particules virales entrantes qui dure plus de 24 heures [366,367] et la saturation des siRNA en opposition à la synthèse continue d'ARNm viral par les polymérases entrantes.

La protéine P du VR agit comme stabilisateur et cofacteur de la protéine L. La chaperone HSP90, en présence de P) est transitoirement nécessaire pour le bon repliement de la L conduisant à sa fonction de RdRp [367]. HSP90 constitue donc une cible potentielle pour l'inhibition de la transcription. En effet, la geldanamycine et ses dérivés tels que le 17-DMAG bloquent l'activité chaperonne de la HSP90 en entrant dans sa poche d'ATP. Ces composés sont très efficaces pour bloquer la transcription virale en prévention et post-infection *in vitro* et *ex vivo* dans des cultures organotypiques de cerveau [367]. De plus, il est peu probable qu'un inhibiteur de HSP90 conduise à l'émergence de virus mutants échappant au traitement[368]. Bien que proposés dans le traitement de cancers, les anti-HSP90 n'ont toujours pas été validés comme thérapeutique utilisable en application humaine.

Le Remdesivir et le R1479 présentent une activité à large spectre contre les infections aux paramyxovirus, y compris le VR [116]. En bref, dans les cellules, le Remdesivir est métaboliquement converti en nucléoside triphosphate actif. Le métabolite obtenu inhibe spécifiquement plusieurs polymérases de différents Mononegavirales tels que les Filovirus et les Henipavirus, mais pas les polymérases de l'hôte. Le Remdesivir inhibe l'activité de la polymérase du virus Nipah notamment

in vivo dans le modèle de singe vert africain [116,369]. Sur la base de la bonne conservation des polymérases parmi les Mononegavirales, il existe une forte probabilité que le Remdesivir puisse également inhiber l'activité de la polymérase du VR. Les études pharmacocinétiques réalisées chez les primates non humains ont montré des niveaux élevés et persistants du nucléoside actif ayant été converti à partir du Remdesivir dans les cellules mononucléées du sang périphérique (PBMC). Ces études sont intéressantes car les PBMC sont ciblées par la souche sauvage du VR au cours des premières étapes de la pathogenèse [370]. De plus, le Remdesivir et le nucléoside actif subséquent semblent être capable d'atteindre le cerveau et pourraient donc également inhiber les variants du VR adaptés au SNC que l'on observe dans les cas de MIBE et de PESS.

Enfin, le composé 16677 (acide 1-méthyl-3-trifluorométhyl-5-pyrazolecarboxylique) et son analogue AS-136A sont des inhibiteurs non-nucléosidiques de l'activité du complexe ARN polymérase ARN-dépendante [371]. L'AS-136A est capable de bloquer la synthèse d'ARN viral en ciblant la protéine L [372]. Comme les anciens candidats, cet antiviral reste assez cytotoxique et sa solubilité doit être améliorée mais il pourrait être particulièrement efficace en combinaison avec des inhibiteurs de fusion ou des activateurs de réponse immunitaire antivirale [373].

h. Inhibiteurs de fusion et d'entrée

Comme mentionné précédemment, la première étape de l'infection repose sur l'entrée du virus dans la cellule cible. Afin d'empêcher l'entrée virale, l'objectif principal est de bloquer la fusion du virus. Les deux possibilités principalement envisagées consistent à bloquer l'interaction de la H avec son récepteur ou les changements conformationnels de la F.
Le site de liaison au récepteur de la H est considéré comme une cible neutralisante potentielle. En effet, l'insertion de tout composé dans la poche de la H responsable de la liaison au récepteur pourrait soit empêcher l'attachement du virus à la cellule hôte, soit pré-déclencher la protéine F conduisant à la fusion des particules virales défectueuses pour la fusion et donc non infectieuses, en anglais « fusion dead particles».

Plusieurs anticorps neutralisants ciblant la protéine H se sont également avérés efficaces [374]. Plus récemment, les molécules neutralisantes dérivées d'anticorps telles que les fragments FV à chaîne unique ciblant la protéine H représentent une avancée majeure dans le domaine de la conception thérapeutique [375].

Comme décrit précédemment, la Neurokinin-1 est décrite comme un récepteur potentiel de la F du VR, et l'antagoniste de la Neurokinine-1, l'Aprépitant, a été décrit pour limiter la dissémination virale de la souche vaccinale dans le cerveau du modèle murins CD46+/RAG-2ko [276].

Le petit peptide hydrophobe appelé « peptide inhibiteur de fusion » (FIP), Z-D-Phe-L-Phe Gly, et d'autres petites molécules telles que AS-48 ou 3G (un analogue de AS-

48) peuvent bloquer la fusion des membranes *in vitro* [254,255,376]. Ces inhibiteurs sont connus pour stabiliser l'état de préfusion de la protéine F. Néanmoins après exposition prolongée à ces inhibiteurs, il émerge des virus avec des mutations dans le domaine HRC de la F, virus qui non seulement échappent à l'effet inhibiteur mais sont hyperfusogènes [377].

Des peptides dérivés du domaine HRC de la F visent à bloquer la fusion en capturant la protéine F dans son état métastable après avoir été déclenchée. Ces peptides permettent de stopper la fusion au début du processus (Figure 8 A, B, C, D). Les peptides dérivés des heptades répétées sont connus pour inhiber la fusion des protéines de classe I et l'un d'entre eux, le T20 (enfuvirtide) agit sur la protéine HIV-1 gp41 et est utilisé en clinique pour traiter le VIH-1 [378]. Cependant, des résistances au traitement ont été observées et des mutations ont émergé dans le domaine HRN de la gp41 [379,380].

Le peptide nommé HRC4 est un peptide dimère dérivé de la séquence du HRC de la F du VR qui interagit avec le domaine HRN pendant la transition structurelle de F [381]. Le dimère comporte le peptide dérivé du HRC lié à deux chaînes de PEG, qui agissent comme un espaceur, conjuguées chacune à une molécule de cholestérol. Le groupement cholestérol augmente la puissance antivirale du peptide de 2 log en lui permettant de s'ancrer dans la membrane de la cellule hôte et permet également une meilleure biodisponibilité dans le cerveau [382,383]. Les peptides dérivés du HRC conjugués au cholestérol ainsi qu'au tocophérol ont montré une efficacité élevée *in vitro, ex vivo* et *in vivo*, même dans le cadre de l'infection du SNC en traversant la barrière hémato-encéphalique [147,161,292]. La dissémination du virus portant la mutation L454W dans F peut être efficacement bloquée *in vitro* et *in vivo* par des inhibiteurs de fusion dérivés de F HRC, indépendamment de la présence de SLAM [161]. À ce jour, ces inhibiteurs de fusion sont le seul système déjà testé contre un virus sauvage et des variants hyperfusogènes observés dans l'infection du SNC, et figurent ainsi parmi les candidats prioritaires pour les études précliniques, à tester seuls et en association avec des traitements ciblant d'autres fonctions virales.

III- Les virus Nipah et Hendra

1) Epidémiologie

a. Hendra

Le premier cas de Hendra a été détecté en septembre 1994 chez l'Homme et chez des chevaux à Hendra, dans la banlieue de Brisbane en Australie [384]. Le virus responsable de ces syndromes respiratoires a d'abord été nommé « Morbillivirus de la pneumonie équine » [384] et a été classé dans le genre des Morbillivirus au sein des Paramyxovirus avant d'être renommé Hendra en 1998 et d'être classé dans le nouveau genre des Henipavirus [385].

On compte un nombre total de 105 cas de HeV chez les chevaux et sept chez l'Homme. 84 chevaux sont décédés à la suite d'une infection par HeV. Cependant tout animal testé positif à l'infection est euthanasié[386,387]. Ces chiffres ne permettent donc pas de calculer un pourcentage de mortalité chez les chevaux. Parmi les 7 cas humains, 4 sont décédés et 3 ont survécu mais ont gardé des séquelles de l'infection [388].

Le taux de létalité approximatif actuel chez les chevaux et les humains est respectivement de 80 % et 60 %. Cependant il est difficile de déterminer avec précision le taux de mortalité chez les chevaux car tous les animaux diagnostiqués positifs pour HeV sont désormais euthanasiés [389].

Les chauves-souris de la famille des *Pteropodidae* sont les réservoirs du HeV. Cependant, pour le HeV, la seule espèce de mammifère connue qui a été infectée directement par des chauves-souris sont les chevaux, considérés comme hôtes amplificateurs. En effet l'infection des hommes par HeV est très rare et semble donc accidentelle. Expérimentalement, de nombreux mammifères sont susceptibles à l'infection par le HeV ; les chiens[390], les porcs[391], les hamsters [392], les cobayes [393], les furets[394], les vervets[395], les chats[396], les chevaux[397] et les souris génétiquement modifiées déficientes pour le récepteur à l'interféron (souris IFNARKO) [398]. L'Homme semble être un hôte accidentel et 5 cas sur les 7 étaient vétérinaires ou en contact direct avec les chevaux contaminés au moment de l'autopsie.

b. Nipah

Les premiers cas d'infection par le NiV ont été identifiés en septembre 1998 dans le village de la rivière de Nipah (Sungai Nipah) dans la région de Perak, en Malaisie. Ce nouveau virus a alerté par son très fort pouvoir pathogène. En effet 40% des patients infectés sont décédés d'encéphalites aiguës létales. Deux flambées ont eu ensuite lieu dans l'état de Negri Sembilan. Les cas reportés survenaient principalement chez les adultes ayant été en contact avec des porcs [399–401]. En mars 1999 la même épidémie s'est propagée à Singapour où un groupe de 11 cas similaires a été identifié parmi des travailleurs d'abattoirs en contact avec des porcs importés des régions épidémiques de Malaisie [402]. On a retrouvé la présence du NiV à la fois chez les patients et chez les porcs contaminés. Le porc a été identifié

comme un hôte intermédiaire amplificateur, responsable de la transmission du virus à l'homme. Par la suite, les épidémies ont continué à se propager dans toute la Malaisie, entraînant des restrictions sur les importations de porcs. Cette épidémie a finalement abouti à l'abattage massif de plus d'un million de porcs dans les fermes de Malaisie avec au moins une infection confirmée. Ce désastre a été chiffré à plus de 100 millions de dollars US et a plongé la Malaisie dans une double crise économique et agricole. On parle alors pour la première fois de NiV comme un agent à risque pour le bioterrorisme [403].

Depuis cette catastrophe économique et humaine (265 cas d'encéphalites dues à NiV et 105 décès en 1999) des épidémies sporadiques de NiV ont continué à survenir dans plusieurs pays d'Asie du Sud et du Sud-Est. Cependant, ces flambées diffèrent des grandes épidémies précoces apparues en Malaisie, tant au niveau des signes cliniques que du taux de létalité et du mode de transmission.

Cette nouvelle souche distincte du NiV émergé en Malaisie est apparue au Bangladesh et en Inde en 2000-2001 et a été nommée NiV Bangladesh. Cette souche s'est avérée moins encéphalitogène et provoque principalement des symptômes respiratoires aigus sévères. La souche de NiV Bangladesh est encore plus léthal que la souche NiV Malaisie avec un taux de mortalité de 75% en moyenne pouvant atteindre 90 à 100% dans certaines flambées. De plus, des cas de transmission interhumaine ont été reportés avec NiV Bangladesh [404–406]. L'origine de ces nouvelles flambées restaient cependant à déterminer car les personnes contaminées n'avaient pas rapporté de contact avec des porcs.

Au moment où NiV a été identifié, le virus Hendra (HeV) étroitement apparenté était suspecté de persister chez les espèces de chauves-souris frugivores Pteropus. Cette nouvelle information a laissé supposer que ces chauves-souris pouvaient également servir de réservoir pour le NiV [407], hypothèse aujourd'hui largement confirmée[408]. Le virus a en effet été isolé dans des chauves-souris Pteropus en Malaisie, au Cambodge, en Thaïlande et au Bangladesh [409,410].

Les personnes infectées par NiV Bangladesh avaient toutes en commun la consommation de dattes ou de lait de palme frais, généralement à même l'arbre. Les chauves-souris Pteropus giganteus ont pour habitude de se nourrir de la sève des dattiers et de leurs fruits. les humains consommateurs ont donc été en contact direct avec la salive et l'urine des animaux contaminés [411–413]. On a par la suite retrouvé des anticorps neutralisant anti-NiV et de l'ARN viral de NiV dans l'urine, la salive, le sérum et d'autres organes chez plusieurs espèces de chauves-souris Pteropus en Asie (Cambodge[410] et Thailand[414]) mais également dans d'autres régions où aucun cas humain de NiV n'a été rapporté, à Madagascar et au Ghana [415–419].

En 2014, une épidémie de NiV causant des encéphalites aiguës et des méningites associées à des syndromes grippaux sévères a été détectée dans les Philippines [420]. 82 % des personnes atteintes d'encéphalite aiguë sont décédées. Cette flambée qui a touché 17 personnes se distingue des autres flambées par sa localisation et par le mode de transmission du virus qui semble avoir transité par le cheval en tant qu'hôte intermédiaire.

La dernière épidémie la plus récente a eu lieu en 2018 à Kerala, en Inde. Cette flambée a été particulièrement mortelle avec 21 morts sur 23 cas. Toutes les contaminations ont été nosocomiales. L'enquête effectuée sur les échantillons environnementaux du premier patient n'ont pas permis de retrouver la source de l'infection. La transmission s'est produite dans trois hôpitaux mais tous les cas primaires et secondaires ont été attribués directement à ce premier patient [421].

Bien que les flambées de NiV ne se soient pas reproduites en Malaisie ou à Singapour depuis la grande épidémie de 1998-1999 ou aux Philippines depuis la flambée unique de 2014, des flambées presque annuelles se sont produites au Bangladesh et en Inde [421–423]. Le nombre de cas est de plus en plus faible mais le virus circule toujours dans les chauves-souris. De plus, les changements climatiques associés aux déforestations massives par l'Homme entrainent des mouvements migratoires des chauves-souris qui se rapprochent alors des populations, facilitant ainsi l'apparition de nouvelles flambées de NiV chez les animaux et chez l'Homme ainsi que l'émergence de nouveaux virus [424–426] (Figure 11).

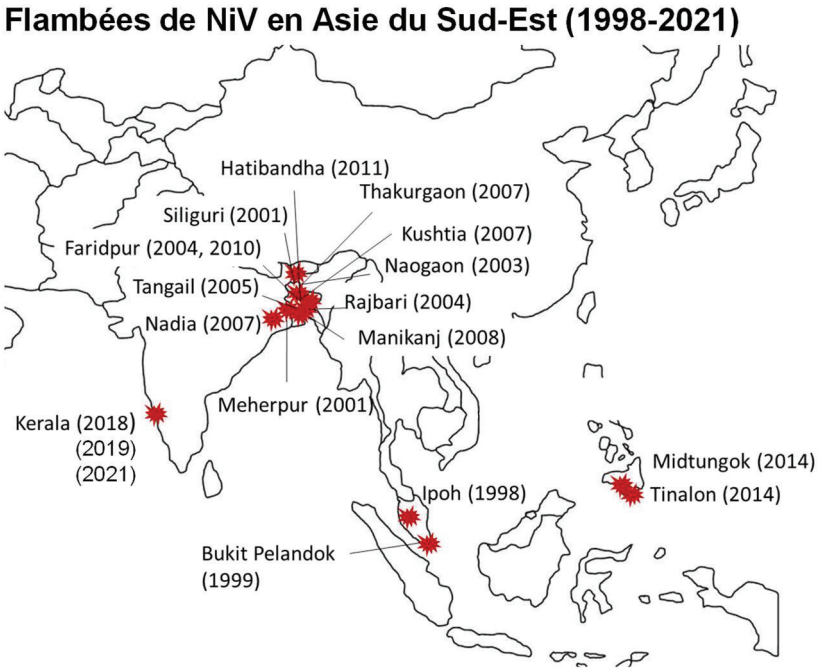

Figure 11 : Localisation des flambées épidémiques dues au virus Nipah en Asie du Sud-Est de 1998 à 2021.

c. Modèles animaux

NiV et HeV sont des virus zoonotiques et peuvent infecter un spectre d'espèces de mammifère exceptionnellement large. Les données d'infections naturelles ou expérimentales indiquent que ces Henipavirus peuvent infecter les porcs, les chevaux, les chats, les chiens, les cobayes, les souris, les hamsters, les furets, les singes écureuils, les singes verts africains et les humains. Ils peuvent théoriquement atteindre presque tous les mammifères en raison de leurs récepteurs d'entrée très conservés [427]. Cependant, la pathogénèse virale dans la plupart de ces modèles

n'est pas représentative de celle observée chez l'Homme[428]. Ainsi, les modèles retenus les plus pertinents pour l'étude de la physiopathologie du NiV sont le hamster doré [98] et le singe vert africain [429].

2) Les Henipavirus

a. Classification

Les virus Nipah et Hendra appartiennent, comme le VR, à l'ordre des Mononegavirales et à la famille des Paramyxoviridae. Ils font partie en revanche d'un genre à part, les Henipavirus, qui comprend également le virus Cedar.

b. Le génome des Hénipavirus

A l'image des autres Paramyxovirus les particules de NiV et de HeV sont pléiomorphes et ont une taille pouvant aller de 40 à 1900 nm [430,431]. L'organisation du virion est similaire à celle décrite pour le VR.

Ce sont des virus enveloppés à ARN simple brin négatif. Le génome de Nipah Malaisie est de 18 246 nucléotides (nt), le génome de Nipah Bangladesh est de 18 252 nt et le génome de HeV est de 18162 nt [430].

La taille du génome des Henipavirus correspond toujours à un multiple de 6, comme les autres paramyxovirus. Cette « règle des 6 » est primordiale pour permettre une encapsidation complète du génome par la nucléoprotéine qui est capable de couvrir 6 nt [154,432].

Le génome des Henipavirus est composé de 6 unités de transcription codant 6 protéines structurales : le gène N code la protéine de nucléocapside, le gène P code pour la phosphoprotéine, le gène M code pour la protéine de matrice, le gène G code pour la glycoprotéine d'attachement, le gène F code pour la protéine de fusion et le gène L code pour l'ARN polymérase ARN dépendante. Le gène P code en plus pour trois protéines non-structurales, les protéines C, V et W qui jouent un rôle dans le contrôle de l'immunité innée.

Tout comme le VR, le génome est flanqué de séquences promotrices appelés leader et trailer qui peuvent être transcrites. Le leader, long de 55 nucléotides, est synthétisé à partir de l'extrêmité 3' du génome et contient les promoteurs de transcription et de réplication génomique. Le trailer, de 33 nucléotides, est transcrit à partir de l'extrêmité 3' de l'antigénome qui englobe le promoteur de réplication antigénomique [433]. Ce trailer est l'unique transcrit antigénomique car l'antigénome ne possède pas de promoteur de transcription qui pourrait permettre l'expression de séquences plus en aval. Les ARN leader et trailer contiennent le signal d'encapsidation régulant l'attachement et la polymérisation de N autour du génome et de l'antigénome. Ils ne sont ni coiffés, ni polyadénylés. Les méthodes de séquençage haut débit ne permettent pas toujours de séquencer les extrémités des génomes, de ce fait, dans la littérature, les séquences publiées des leaders et des trailers des nouveaux Henipavirus sont souvent manquantes.

c. Les glycoprotéines de surface

La protéine de fusion est une protéine de type 1 qui s'organise en trimères à la surface des particules virales. Pour être active, sa forme de précurseur F0 doit être clivée par la cathepsine L (après Arg109 ou Lys109) en deux fragments F1 et F2 reliés par un pont disulfure [434].

La protéine d'attachement G est une glycoprotéine membranaire de type 2 qui s'organise en tétramères associés aux trimères de F à la surface des virions [434]. Elle n'a aucune fonction enzymatique connue. Cette protéine se compose d'une queue cytoplasmique de 50 aa, d'un domaine transmembranaire de 23 aa, suivi d'une tige de 100 aa terminée par une tête globulaire constituée des 419 aa restants. La G compte 8 sites de glycosylations, dont 5 utiles dans l'infection (positions 306, 378, 417, 481 et 529), et 7 ponts disulfures. L'interaction entre G et son récepteur a lieu au niveau de sa tête globulaire.

3) Les récepteurs

Les récepteurs d'entrée connus pour NiV et HeV sont les protéines éphrine B2 et éphrine B3 (appelées également EFN B2 et EFN B3). La famille des éphrines B se compose de 3 protéines nommées éphrine B1, éphrine B2 et éphrine B3. L'expression et la séquence de ces récepteurs sont très conservées chez les mammifères : cela explique le caractère zoonotique des Henipavirus. Ces éphrines se lient aux récepteurs de la famille EphB qui présentent une activité tyrosine-kinase.

a. Ephrine B2

Ephrine B2 est une protéine transmembranaire de 333 aa. Ephrine B2 est un ligand des récepteurs EphB4 et A3, exprimés notamment à la surface des monocytes. Ephrine B2 est exprimée dans les cellules endothéliales au niveau des artères et des capillaires, dans les cellules épithéliales alvéolaires bronchiques et pulmonaires de type II, dans les cellules musculaires lisses et dans les neurones [435–438]. Ephrine B2 est impliqué dans le développement embryonnaire et est indispensable dans les étapes de neurogenèse [439] et d'angiogenèse [440]. L'expression seule d'éphrine B2 dans des cellules non susceptibles est suffisante pour permettre l'entrée du NiV [441,442].

b. Ephrine B3

Ephrine B3 est une protéine transmembranaire de 340 aa. Son affinité avec la G du NiV est 10 fois inférieure à éphrine B2 mais est suffisante pour permettre l'entrée de NiV dans les cellules[443]. Ephrine B3 est exprimée dans le système vasculaire mais son expression est prédominante dans les cellules du SNC et particulièrement au niveau du tronc cérébral [436,444]. La forte expression des récepteurs des Henipavirus dans le SNC peut expliquer les cas d'encéphalites léthales lors de l'infection. L'affinité de la G de NiV avec éphrine B3 serait 30 fois supérieure à celle de la G du HeV et pourrait expliquer les différences au niveau de la neuropathogénèse des deux virus [445].

c. Ephrine B1

Malgré une forte homologie avec éphrine B2 et B3, éphrine B1 est présentée dans la littérature comme n'étant pas un récepteur d'entrée de NiV et HeV. En effet, les deux résidus en position 121 et 122 (leucine et tryptophane), communs à éphrine B2 et B3 diffèrent pour éphrine B1 (tyrosine et méthionine) et ont été montré comme étant critiques pour l'entrée du virus [443]. Le remplacement de ces aa LW par YM dans éphrine B3, aboli totalement la capacité d'éphrine B3 à lier la G de NiV tandis que l'expérience inverse permet la liaison entre la G et éphrine B1 mutée. Ephrine B1 est cependant un récepteur d'entrée pour le virus Cedar (CedV), un autre Henipavirus non pathogène qui a été isolé d'une chauve-souris en Australie en 2012 [446,447]. La G de CedV peut également se lier à éphrine B2 mais pas à éphrine B3 [448,449]. La structure cristalline de la tête globulaire de la G de CedV en complexe avec éphrine B2 révèle la présence de trois poches dans la cavité de liaison, tandis que la cavité de liaison de la G de HeV comporte quatre poches [449]. Cette altération structurelle dans la G de CedV permet d'accepter des résidus avec des chaînes latérales plus grandes [446,449].

d. Les Héparanes sulfates

Les Héparanes sulfates (HS) sont des récepteurs d'attachement pour NiV et HeV [450]. Ces Glyco-Amino-Glycanes (GAG) ubiquitaires sont présents à la membrane des cellules et ont la capacité de fixer un grand nombre de protéines à la surface des cellules [451]. NiV et HeV utilisent les HS dans le but de transiter dans l'organisme à la surface des leucocytes tout en étant protégés, permettant ensuite la *trans*-infection c'est-à-dire la transmission de l'infection à des cellules susceptibles par des cellules gardant le virus en surface et sans le produire[452].

4) Entrée des Henipavirus

L'entrée commence par l'attachement du récepteur à la tête globulaire de la glycoprotéine G, au niveau d'un sillon hydrophobe impliquant majoritairement les acides aminés W504 et E533 [453]. Cette liaison active un mécanisme d'endocytose, plus précisément de type macropinocytose mais n'exclut pas la fusion à la surface de la cellule [454].

La liaison de la G à son récepteur entraine un changement de conformation lui-même à l'origine du changement de conformation de la protéine de fusion F.

La majorité des protéines de fusion des Paramyxovirus sont clivées au cours de leur transport à travers le réseau trans golgien [455]. La F du VR est clivée par exemple par la furine après une séquence très conservée R-XK/R-R [455,456].

Ainsi, la protéine F exposée à la surface cellulaire et virale est déjà active. Les Henipavirus ne possèdent pas cette séquence. Leur protéine F reste donc sous la forme F0 jusqu'à l'arrivée de la particule à proximité de la cellule cible. La protéine de fusion est clivée en fragment F1 et F2 par la cathepsine L lorsque la particule virale arrive à proximité de la membrane plasmique des cellules ou même dans

l'endosome [457–459]. La suite de la fusion se produit de la même façon que décrit précédemment pour le VR [460].

5) Pathogénèse

Selon les connaissances disponibles, l'infection par le NiV et le HeV débute dans les cellules dendritiques de l'épithélium respiratoire ou digestif. Cependant aucun résultat ne démontre que les cellules épithéliales ne sont pas elles-mêmes infectées également et on ne peut pas exclure cette hypothèse. Le virus atteint ensuite les organes lymphoïdes via les cellules dendritiques, en infectant au passage les cellules endothéliales des vaisseaux lymphatiques. L'attachement des particules virales aux leucocytes par les HS permettrait au virus d'échapper à la reconnaissance du système immunitaire et d'envahir rapidement tout l'organisme par le système vasculaire. Dans les petits vaisseaux et les capillaires les lymphocytes interagissent avec l'endothélium vasculaire et provoquent un contact très étroit entre les virus présents à la surface des lymphocytes et Ephrine B2 et B3. Ce phénomène entraine une amplification de la dissémination virale qui s'étend alors aux cellules des muscles lisses à la paroi des vaisseaux. NiV et HeV pourraient utiliser le même mécanisme pour atteindre le SNC. Une fois dans les vaisseaux cérébraux, la formation de syncytia par le NiV entrainerait un effet cytopathique avec rupture de la barrière hémato-encéphalique, laissant libre accès au virus pour infecter les neurones, particulièrement permissifs [461]. Alternativement, d'autres voies d'infection par le nerf olfactif [462] ou par la transinfection de cellules neurales à partir des cellules immunitaires circulantes [452] ont été validées dans des études animales, sans pour autant induire de vascularite. Aucune de ces hypothèses n'a été confirmée chez l'homme qui développe toujours une vascularite généralisée.

La période d'incubation du NiV chez l'homme est généralement inférieure à deux semaines dans 90% des cas mais peut varier entre 4 jours à 2 mois [401]. Les patients infectés par la souche NiV Malaisie présentent de la fièvre, des maux de tête, des étourdissements et des vomissements, qui évoluent jusqu'à une encéphalite sévère. De nombreux patients manifestent un niveau de conscience réduit et des signes importants de dysfonctionnement du tronc cérébral, notamment un réflexe oculo-céphalique anormal, des réflexes pupillaires, des changements vasomoteurs et des convulsions [401].

Pour HeV, la période d'incubation varie de quelques jours à deux semaines chez l'homme et les signes cliniques bénins comprennent de la fièvre, des maux de tête, de la somnolence et des symptômes pseudo-grippaux [388]. Les infections sévères sont souvent fatales avec des signes respiratoires et/ou neurologiques.

Les atteintes neurologiques observées chez les patients infectés par NiV et HeV sont diverses : méningites aseptiques, encéphalites diffuses, atteinte focale du tronc cérébral, et des signes cérébelleux relativement fréquents.

L'infection par la souche de NiV Malaisie et HeV présente la caractéristique de développer des rechutes et des encéphalites tardives, parfois des mois ou des

années après la maladie aiguë [463]. Au cours de la première grande épidémie de Nipah en 1998 et 1999 7,5% des survivants apparemment guéris de l'encéphalite aiguë initiale ont subi des rechutes. À l'image des cas de SSPE observées avec le VR on a également relevé 3,4% de patients qui ont développé une encéphalite tardivement, jusqu'à 11 ans après le contact avec le NiV, alors que l'infection initiale n'avait pas provoqué de manifestation neurologique [464].

Des troubles psychiatriques, incluant une dépression, des changements de personnalité, une perte de l'attention, de la mémoire verbale ou visuelle [465] ont également été observés.

Cependant, les manifestations neurologiques diffèrent beaucoup suivant les souches de NiV.

La myoclonie segmentaire est prédominante dans les cas malaisiens, mais peu observée au Bangladesh et en Inde. En revanche, un tiers des survivants à NiV garde des séquelles neurologiques et un trouble cognitif persistant. Presque tous les patients souffrent de fatigue chronique invalidante et plus de la moitié présentent des changements comportementaux et neuropsychiatriques, similaires à ceux observés dans les cas de Malaisie et de Singapour[466].

Avec la souche malaisienne une atteinte respiratoire a été décrite dans 14 à 29% des cas [401,464]. Pour la souche NiV Bangladesh la grande majorité des patients présentait au contraire des symptômes respiratoires, incluant de la toux dans 62% des cas et des difficultés respiratoires dans 69% des cas, allant jusqu'à développer pour certains un syndrome de détresse respiratoire aiguë [467].

6) Différences entre les Henipaviruses

Plusieurs souches du NiV ont été isolées. La souche NiV Bangladesh partage 91,8% d'identité avec la souche NiV Malaisie et HeV partage 70% d'identité avec NiV Malaisie (Figure 12). Ces virus présentent de grandes différences, notamment dans leur façon de transmettre l'infection et dans leur pathogénicité. Par exemple, NiV Ban est le virus où la transmission interhumaine a le plus été observée. Les différences, déjà décrites dans cette introduction ont été résumées dans la Figure 13.

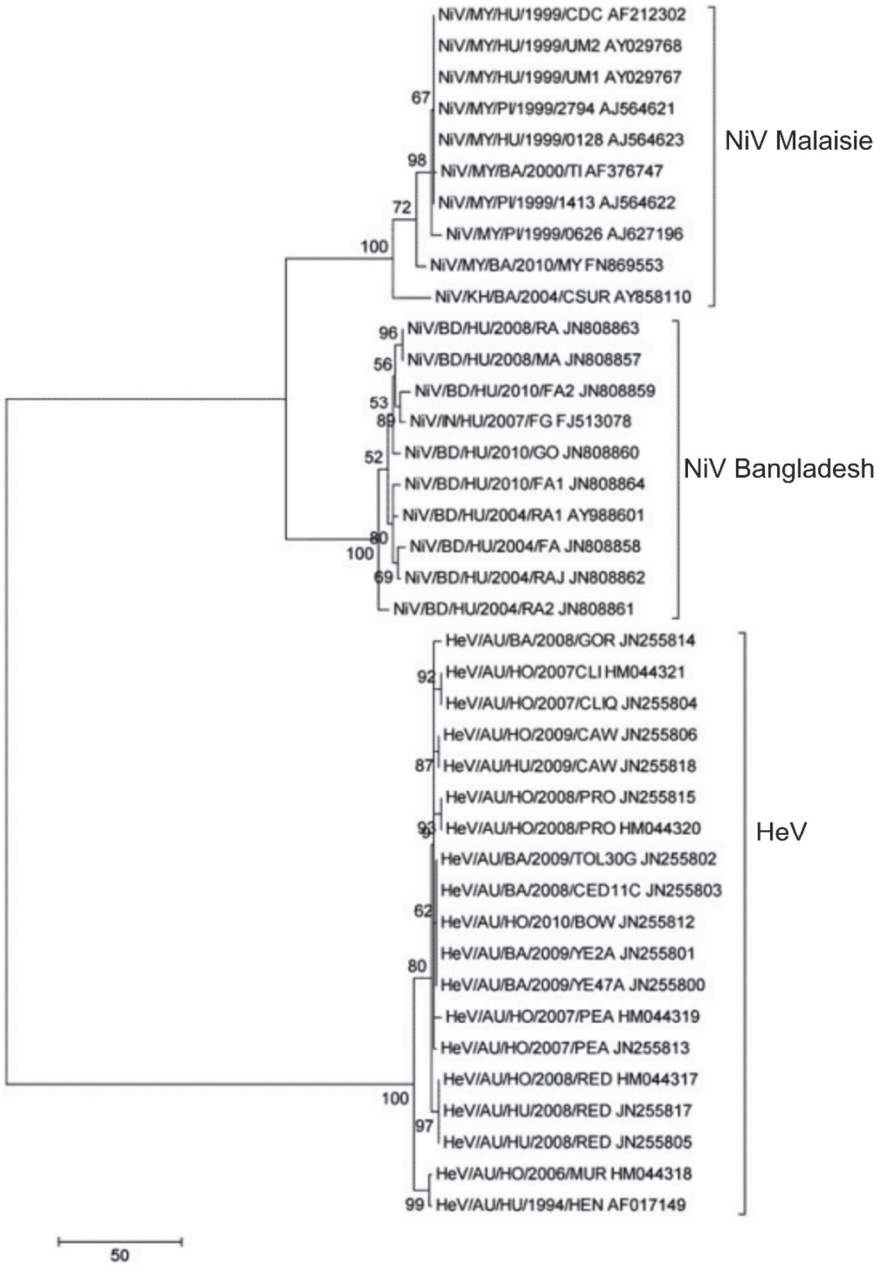

Figure 12 : : Analyses phylogénétiques des séquences du gène N des virus Nipah et Hendra

Arbre de parcimonie maximale, algorithme Close-NeighborInterchange, Les longueurs de branches sont exprimées en unités de nombre de changements sur l'ensemble de la séquence. Les numéros d'accession GenBank disponibles sont indiqués pour les séquences correspondantes. Les groupements de génotypes proposés sont indiqués par les parenthèses. Analyse réalisée à l'aide de MEGA 5. Figure adaptée de Tamura et al. 2011.

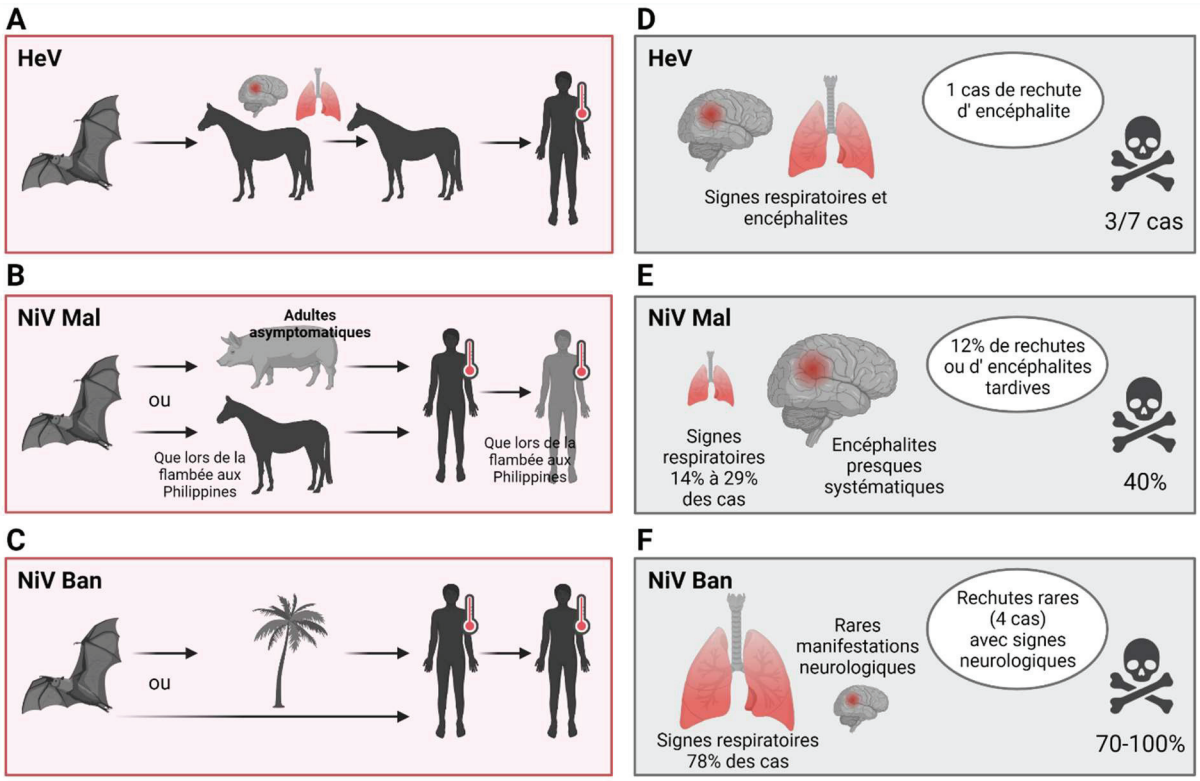

Figure 13 : Comparaison entre les souches d'Henipavirus pathogènes pour l'Homme.

A, B, C, Transmission de HeV, NiV Malaisie (NiV Mal) et NiV Bangladesh (NiV Ban), de la chauve-souris Pteropus Giganteus à l'Homme, via le cheval, le porc ou le lait de palme contaminé. D, E, F, Pathogénicité des différentes souches au niveau des voies respiratoires et du système nerveux central. Figure réalisée sur Biorender.

7) Encéphalites tardives et récidivantes dues aux Henipavirus

Environ 12% des patients infectés par NiV Mal ont ensuite développé une encéphalite décalée dans le temps ou récidivante [464]. Chez ces patients, les ARN et des antigènes viraux ont été retrouvés dans les neurones ainsi que dans les cellules gliales et épendymaires, sans marque évidente de démyélinisation, en opposition aux encéphalites aiguës [468] (Figure 13).

Dans le cas de NiV Ban, 4 cas de récidives d'encéphalites, ont été signalés au cours d'une seule épidémie [466]. Les patients présentaient notamment une paralysie des muscles oculomoteurs, un nystagmus ou affaissement du visage.

Dans le SNC, les principales lésions observables associées à l'infection sont une vascularite, une thrombose, de la nécrose cellulaire dans parenchyme et des « inclusions virales ». Les lésions induites par cette souche sont généralement plus grandes, parfois hémorragiques et associées à une perte neuronale sévère. Il est intéressant de noter que les rechutes et les encéphalites tardives ne s'accompagnent pas de vascularite qui est pourtant la caractéristique principale des infections aiguës [467].

Dans le cas de l'encéphalite récidivante à HeV, le patient présentait une méningite, une inflammation du cortex cérébral, une infiltration périvasculaire, une prolifération gliale dont le type cellulaire n'a pas été défini et une perte neuronale. Ces observations sont associées à la détection d'ARN viraux et d'antigènes dans les neurones et certaines cellules gliales [462].

8) Tropisme de NiV et HeV dans le SNC

À ce jour, le tropisme de l'infection à Henipavirus dans le SNC n'a été étudié qu'à partir d'analyses post mortem effectuées sur l'humain et des modèles animaux. Les résultats suggèrent que les neurones sont la cible principale de NiV Mal et de HeV [98,469]. Cependant, les connaissances sur le tropisme initial et la dissémination des Henipavirus dans le SNC sont embryonnaires.

9) Vaccins et traitements

a. Les vaccins

Aucun vaccin n'est à ce jour commercialisé pour prévenir l'infection contre Nipah. Cependant plusieurs stratégies vaccinales ont été développées et testées sur des modèles animaux. L'approche la plus étudiée a été un vaccin basé sur l'injection de glycoprotéine G soluble (sG) de NiV et HeV. HeV-sG provoque une réponse immunitaire qui confère une protection croisée contre HeV et NiV [470]. Depuis 2012 le vaccin Equivac (*Zoetis Australia Pty Ltd*) contre HeV a été commercialisé en Australie pour les chevaux. Il s'agit d'une HeV-sG qui induit chez les chevaux vaccinés des anticorps neutralisants contre HeV.

Des vaccins recombinants à base de vecteurs viraux : *virus de la Vaccine*[471]*, Canarypox* [472,473]*, adeno-associated virus (AAV)*[474]*, virus de la rougeole* [475]*, ou encore vesicular stomatitis virus (VSV)*[476,477] ont également été développés et testés respectivement chez le hamster, le porc, le singe et le furet (et le singe vert d'afrique également). Ces virus recombinants expriment les glycoprotéines F ou G à leur surface.

Un vaccin à particules virales dérivé de cellules de mammifères (Virus Like Particle, VLP) a également été produit et testé chez le hamster [478].

Récemment, un vaccin basé sur un ARN messager codant pour la G soluble du HeV a montré d'excellents résultats chez le hamster doré contre NiV et est en cours d'optimisation [479].

A part le dernier candidat qui a protégé 70% des animaux après une dose unique de vaccin, toutes ces approches ont conféré une protection complète contre NiV dans les modèles animaux testés indiquant que le développement d'un vaccin efficace est tout-à-fait envisageable.

b. Les traitements

À l'heure actuelle, il n'existe aucun médicament approuvé pour traiter ou prévenir l'infection par NiV ou par le HeV chez l'Homme. Cependant, divers traitements ont cependant conféré une protection *in vivo* chez l'animal [480].

L'administration quotidienne du Favipiravir, un analogue de purine, chez le Hamster a permis de protéger les animaux contre l'infection par NiV [481].
Le Remdesivir a largement été testé et son efficacité préventive a été confirmée sur les singes verts africains [482].
Des anticorps monoclonaux humains m102.4 (cible la G) et h5B3.1 (cible la F) montrent des résultats prometteurs chez le singe vert africain et le furet, même administrés après l'exposition à NiV et à HeV [483–486]. Le m102.4 a été administré à des humains lors de la flambée de NiV Ban à Kerala en Inde en 2018 comme traitement compassionnel expérimental. Les résultats ne sont pas encore publiés, cependant cet anticorps est actuellement en essai clinique de phase I [487].

Un peptide inhibiteur de fusion dérivé de la séquence du HRC du virus humain parainfluenza de type 3 (hPIV3) comportant les mutations VIKI, VIKI-PEG4-chol, s'est avéré très efficace contre l'infection par NiV et HeV, *in vitro* et *in vivo*. L'interaction entre le couple hétérologue HRN-HRC (NiV-HPIV3) est plus forte que le couple homologue (NiV-NiV), entrainant une meilleure avidité des deux heptades répétées [488]. De plus, l'ajout d'un groupement cholestérol a permisl'augmentation de l'efficacité du peptide[382] et son adressage au SNC avec traversée de la barrière hématoencéphalique[383]. Chez le hamster, ce peptide a protégé 100% des animaux en pré-traitement et 80% lorsque le traitement a commencé 48 heures après infection par le NiV [383,489]. Chez le singe vert africain le traitement par voie intratrachéale (comme par voie trachéale et sous-cutanée) a protégé un animal sur 3 malgré une quantité de virus administrée au moins 3 log supérieure à la dose létale (i.e. $>10^7$ PFU/animal) [489,490].

D'autres traitements ont été testés et abandonnés rapidement. L'analogue de nucléoside, la ribavirine [491], décrite pour son activité antivirale à large spectre sur les Paramyxovirus a été administrée chez l'Homme lors des épidémies de NiV mais n'a pas montré de résultats probants. La chloroquine a été envisagée pour bloquer le clivage de la F de par son action sur la cathépsine L mais sans efficacité comme dans le cas de toutes les infections virales, même en combinaison avec la Ribavirine [492,493].

Parmi les virus ciblant initialement les voies respiratoires certains sont capables d'infecter le SNC et d'induire des encéphalites dont la fréquence et la sévérité sont très variables. A ce jour très peu d'études permettent de déterminer les étapes précoces de l'infection du SNC par ces virus. L'infection du SNC est généralement étudiée dans le cadre d'analyses post-mortem chez l'Homme et chez l'animal ou dans des modèles in vitro spécifiques ne permettant pas de conclure sur les étapes précoces de l'infection du SNC à l'échelle organique.

Dans cette thèse mon intention a été de mieux comprendre les facteurs influençant l'infection du SNC par le SARS-CoV-2, le virus de la rougeole (VR) et les trois Henipavirus pathogènes pour l'Homme (virus Nipah Malaisie, virus Nipah Bangladesh et virus Hendra).

Pour répondre à cette question 3 objectifs se sont dessinés :

- Le premier objectif a été de mettre en place des nouveaux modèles *ex vivo* permettant d'étudier le tropisme précoce et la dissémination de ces virus. Pour mettre en parallèle l'infection des poumons avec l'infection du SNC j'ai développé et caractérisé des cultures organotypiques de poumon et de tronc cérébral de hamster.
- Le deuxième objectif a été d'étudier le tropisme et la dissémination du SARS-CoV-2, du VR et des Henipavirus grâce à une analyse comparative des différentes souches.
- Le dernier objectif a été de comprendre, à l'échelle moléculaire, les différences de tropisme et de dissémination identifiées selon le pouvoir fusogène des virus étudiés. Ce dernier axe vise également l'analyse d'évolution génétique des virus dans le SNC.

RESULTATS

Cette partie résultat est découpée en 3 grandes parties. Dans la première partie des nouveaux modèles permettant d'étudier la neuroinvasion par des virus respiratoires ont été développés et caractérisés. L'utilisation de ces modèles de cultures organotypiques peuvent être étendus pour l'étude de la pathogénèse virale à l'échelle organique et pour le développement de traitements. Cette partie s'appuie sur 3 articles scientifiques publiés ou en cours de publication ainsi que des résultats complémentaires, un article de vulgarisation scientifique en français et une revue sur l'infection du SNC par le VR. Ces résultats sont découpés de la façon suivante :

1) Pathogénèse de l'infection du SARS-CoV-2 dans des cultures organotypiques de poumons et de tronc cérébral de hamster
   a. *Article 1 : Modélisation organotypique de l'infection pulmonaire et du tronc cérébral du SARS-CoV-2 chez le hamster*

2) Caractérisation d'un nouveau modèle *ex vivo* : les cultures organotypiques de rein de hamsters
   a. *Article 2 : Développement de modèles organotypiques de hamster pour l'étude de l'infection rénale par le SARS-CoV-2 à un stade précoce*

3) Tropisme précoce et dissémination du virus de la rougeole dans le CNS
   a. Article de vulgarisation : Interféron de type I et sélectivité de l'infection des cellules du système nerveux central par le virus de la rougeole

   b. Revue : Les encéphalites rougeoleuses : vers de nouveaux traitements

4) Traitements antiviraux contre le virus de la rougeole
   a. Article 3 : Des fragments uniques des chaines variables d'anticorps neutralisent l'infection par le virus de la rougeole in vitro et in vivo

   b. Inhibition de l'infection par des virus de la rougeoles mutants neuropathogènes par un fragment unique des chaines variables d'anticorps

La deuxième partie porte sur le rôle du caractère hyperfusogène du virus de la rougeole pour l'infection du SNC. De nombreux VR mutants portant des mutations dans leur protéine de fusion ont été étudiés et comparés dans 4 publications scientifiques et une cinquième en préparation. Les résultats sont présentés comme ci-dessous :

1) Impacte de la déstabilisation de la F dans l'invasion du SNC
   a. Etude de l'impact des mutations dans la F et la H de souches du virus de la rougeole issus de cas SSPE dans la machinerie de fusion
   b. Article 4 : Caractéristiques moléculaires du complexe de fusion de virus de la rougeole favorisant l'infection et la propagation dans le cerveau

   c. Article 5 : Complexes de fusion du virus de la rougeole provenant d'isolats cliniques du système nerveux central : diminution de l'interaction entre l'hémagglutinine et les protéines de fusion

2) Pathogénicité des mutants hyperfosogènes du virus de la rougeole dans les voies respiratoires
   a. Article 6 : Le virus de la rougeole portant une protéine de fusion dérivée d'encéphalite rougeoleuse à corps d'inclusion est pathogène après une infection par voie respiratoire

   b. Tropisme initial de mutants hyperfusogènes du virus de la rougeole dans le système nerveux central

La troisième partie vise à transposer les compétences acquises avec le VR et le SARS-CoV-2 pour évaluer les différences d'encéphalitogenèse entre plusieurs souches d'Henipavirus. Les résultats présentés s'appuient sur des travaux publiés décrivant les différences génomiques entre les Henipavirus, un article en préparation et des résultats préliminaires de l'infection d'organoïdes de cerveau humain.

1) Différences génomiques entre les Henipavirus
2) Les facteurs influençant l'infection du système nerveux central par les Henipavirus
   a. *Article 7 : Comparaison de l'infection des Henipavirus dans le système nerveux central : tropisme précoce, entrée et machineries de fusion*
   b. *Comparaison de l'infection d'organoïdes de cerveau humain par les Henipavirus*

I. Développement de modèles au service de l'étude de la neuroinvasion par des virus respiratoires et du développement de traitements

1) Pathogénèse de l'infection du SARS-CoV-2 dans des cultures organotypiques de poumons et de tronc cérébral de hamster

a. Article 1 : Modélisation organotypique de l'infection pulmonaire et du tronc cérébral du SARS-CoV-2 chez le hamster

Marion Ferren, Valérie Favède, Didier Decimo, Mathieu Iampietro, Nicole A. P. Lieberman, Jean-Luc Weickert, Rodolphe Pelissier, Magalie Mazelier, Olivier Terrier, Anne Moscona, Matteo Porotto, Alexander L. Greninger, Nadia Messaddeq, Branka Horvat, Cyrille Mathieu

Nature Communications, 2021

Facteur d'impact : 14,919

Résumé de l'article :

Le SARS-CoV-2 est capable d'infecter le SNC chez l'Homme mais les premières étapes de l'infection restent à préciser car la plupart des résultats décrivant l'infection du SNC proviennent d'études *post-mortem*. A ce jour on manque de modèles reflétant la complexité organique et les modèles en 3D tels que les organoïdes de cerveau humain sont incomplets ou immatures (ne contiennent pas de cellules microgliales et contiennent beaucoup de cellules précurseurs pas encore différenciées). Ces modèles sont très utiles pour étudier l'évolution génétiques des virus et pour réaliser des analyses transcriptomiques dans le contexte du SNC chez l'Homme mais sont insuffisants lorsqu'il s'agit d'étudier les premières étapes d'une infection ou de tester des traitements.

Dans cet article nous avons ainsi caractérisé deux nouveaux modèles de cultures organotypiques de poumons et de tronc cérébral de hamster. Ces modèles *ex vivo* offrent une opportunité unique pour l'étude des étapes précoces d'une infection et pour cribler des traitements antiviraux.

Ici les deux systèmes organotypiques semblent conserver leurs propriétés physiologiques pendant toute la durée de l'expérience (4 jours). Les cultures sont susceptibles à l'infection par le SARS-CoV-2 et par le NiV alors qu'un mutant hyperfusogène du VR n'infecte que les cultures de cerveau, suggérant que des mécanismes supplémentaires sont requis pour accéder au récepteur Nectin-4 dans les cultures de poumons.

Nous avons validé le tropisme initial du SARS-CoV-2 observé chez l'Homme dans les poumons, en montrant l'infection des pneumocytes de type 1 et de type 2, ainsi

que les cellules ciliées dans les cultures organotypiques de poumon de hamster et démontré l'infection des neurones granulaires et des neurones de golgi dans le cerveau. Nous avons également démontré que l'infection par le SARS-CoV-2 induit une réponse interféron spécifique et une réponse immunitaire innée, ainsi qu'une mort cellulaire par apoptose, nécroptose et pyroptose.

En plus de permettre une meilleure caractérisation de l'infection par le SARS-CoV-2 dans les tissus, nos cultures organotypiques se sont avérées particulièrement utiles pour cribler des traitements antiviraux. Nos résultats obtenus avec le remdesivir, l'hydroxychloroquine et le 17-DMAG ont démontré que les cultures organotypiques de poumon et de tronc cérébral de hamster permettent de prédire de manière pertinente non seulement l'efficacité mais aussi la toxicité de traitements *in vivo*. Par exemple, dans les poumons la spike peut être clivée par TMPRSS2 comme par des cathepsines suggérant que le virus peut entrer en fusionnant à la membrane plasmique ou par voie endosomale. En revanche TMPRSS2 n'est pas exprimée dans le tronc cérébral contrairement aux Cathepsines ce qui suggère que le virus entrera principalement par voie endosomale dans le cerveau. L'hydroxychloroquine agit au niveau des endosomes mais pas sur la fusion à la surface des cellules. Comme attendu, l'hydroxychloroquine a montré une efficacité dans le tronc cérébral mais pas dans les poumons aux doses subtoxiques.

Ces données illustrent le potentiel d'une modélisation rapide des interactions complexes au niveau des tissus au cours d'une infection et ouvrent la voie pour l'utilisation de ces modèles *ex vivo* pour étudier la pathogénèse de virus émergents et pour évaluer l'efficacité de candidats antiviraux en amont de validation *in vivo*.

nature COMMUNICATIONS

ARTICLE

https://doi.org/10.1038/s41467-021-26096-z OPEN

Hamster organotypic modeling of SARS-CoV-2 lung and brainstem infection

Marion Ferren[1✉], Valérie Favède[1,2], Didier Decimo[1], Mathieu Iampietro[1], Nicole A. P. Lieberman[3], Jean-Luc Weickert[4], Rodolphe Pelissier[1], Magalie Mazelier[1], Olivier Terrier[5], Anne Moscona[6,7,8,9], Matteo Porotto[6,7,10], Alexander L. Greninger[3], Nadia Messaddeq[4], Branka Horvat[1] & Cyrille Mathieu[1✉]

SARS-CoV-2 has caused a global pandemic of COVID-19 since its emergence in December 2019. The infection causes a severe acute respiratory syndrome and may also spread to central nervous system leading to neurological sequelae. We have developed and characterized two new organotypic cultures from hamster brainstem and lung tissues that offer a unique opportunity to study the early steps of viral infection and screening antivirals. These models are not dedicated to investigate how the virus reaches the brain. However, they allow validating the early tropism of the virus in the lungs and demonstrating that SARS-CoV-2 could infect the brainstem and the cerebellum, mainly by targeting granular neurons. Viral infection induces specific interferon and innate immune responses with patterns specific to each organ, along with cell death by apoptosis, necroptosis, and pyroptosis. Overall, our data illustrate the potential of rapid modeling of complex tissue-level interactions during infection by a newly emerged virus.

[1] CIRI, Centre International de Recherche en Infectiologie, Team Immunobiology of the Viral infections, Univ Lyon, Inserm, U1111, CNRS, UMR5308, Université Claude Bernard Lyon 1, Ecole Normale Supérieure de Lyon, LYON, France. [2] Département du Rhône, Lyon, France. [3] Department of Laboratory Medicine, University of Washington Medical Center, Seattle, WA, USA. [4] Institut de Génétique et Biologie Moléculaire et Cellulaire (IGBMC), INSERM U1258, CNRS UMR 7104, Université de Strasbourg, Illkirch, France. [5] CIRI, Centre International de Recherche en Infectiologie, Team VirPath, Univ Lyon, Inserm, U1111, CNRS, UMR5308, Université Claude Bernard Lyon 1, Ecole Normale Supérieure de Lyon, LYON, France. [6] Center for Host-Pathogen Interaction, Columbia University Medical Center, New York, USA. [7] Department of Pediatrics, Columbia University Medical Center, New York, USA. [8] Department of Microbiology & Immunology, Columbia University Medical Center, New York, USA. [9] Department of Physiology & Cellular Biophysics, Columbia University Medical Center, New York, USA. [10] Department of Experimental Medicine, University of Study of Campania 'Luigi Vanvitelli', Naples, Italy. ✉email: marion.ferren@inserm.fr; cyrille.mathieu@inserm.fr

In late 2019, the emergence of the severe acute respiratory syndrome coronavirus 2 (SARS-CoV-2) led to a global pandemic of COVID-19. As of August 2021, >215 million laboratory-confirmed cases were reported, and >4.5 million patients died worldwide from this disease[1]. SARS-CoV-2 infection induces severe acute respiratory syndrome, which can also be associated with central nervous system (CNS) infection and neurological symptoms including smell dysfunction, headache, muscle pain, myopathy, and in rare cases, generalized myoclonus, ischemic stroke, and perivascular acute disseminated encephalomyelitis[2–7]. It has been suggested that SARS-CoV-2 reaches the medulla oblongata and that brainstem infection may be involved in both respiratory and heart failure in patients[8–12]. To date, the neuro-invasive potential of SARS-CoV-2 in humans remains poorly understood[13,14]. The great majority of studies show that most of the symptoms reflecting CNS affection are related to brain blood vessel infections[15–22]. Although less common, the susceptibility of human neurons to the infection and the permissiveness of human brain organoids was observed in vitro[23–27] and SARS-CoV-2 viral particles or RNA have already been found in the cerebrospinal fluid[28] and in the brain of a subset of patients[12,29]. The low representation of SARS-CoV-2 in CSF may be related to a poor ability to bud in this tissue as observed for measles virus (MeV) or to any limitation to invade the brain in the most severe respiratory cases which represent the large majority of the samples. In order to reach the CNS, SARS-CoV-2 may travel from the periphery into the CNS through the olfactory neurons or through the vagus nerve from the lungs or gut. In addition, SARS-CoV-2 infection has been shown to disrupt the blood-endothelial barrier by damaging the choroid plexus epithelium and as a consequence of cytokine storm and systemic inflammation[27,30,31].

SARS-CoV-2 is an enveloped, positive-sense, single-stranded RNA virus that belongs to the *Betacoronavirus* genus within the *Coronaviridae* family. The infection starts with the attachment of the viral surface glycoprotein, Spike (S), to the human angiotensin-converting enzyme 2 (ACE2) at the surface of the target cell[32]. To execute its functions, the S must be in its protease-cleaved form composed of the S1 and S2 subunits. The activity of the cellular transmembrane serine protease TMPRSS2 highly correlates with viral dissemination, suggesting that it may participate in the processing of S, but S can also be cleaved by the endosomal proteases Cathepsin B and Cathepsin L[33]. In addition, cell entry of SARS-CoV-2 can be pre-activated by the proprotein convertase furin, reducing the virus's dependence on target cell proteases for entry[34,35]. The S1 fragment of the Spike protein cleaved by furin can also bind to Neuropilin-1, which is abundantly expressed at the surface of endothelial and epithelial cells. This binding may also facilitate SARS-CoV-2 infection by promoting the viral interaction with ACE2[36,37].

Most observations of the pathogenesis of SARS-CoV-2 arise either from in vitro studies or post mortem analysis of infected patients, and there is a need for models that can help decipher the initial steps of infection in real time. To date, different animal models have been described to study SARS-CoV-2 pathogenesis, transmission, or antiviral efficacy, including transgenic mice expressing human ACE2, hamsters, ferrets, rhesus macaques, cynomolgus macaques, and African green monkeys[38].

Golden Syrian hamsters have been shown to be a relevant small animal model for several viruses[39] and more specifically for respiratory viruses that also target the CNS, such as the paramyxoviruses Nipah virus (NiV)[40] and MeV[41]. The pathogenesis of SARS-CoV[42,43] and SARS-CoV-2[44–47] in Syrian hamsters is similar to that observed in humans, supporting the use of hamsters as models for studying these infection[45,48,49]. Cerebellar and hippocampal organotypic cultures from small rodent models have been characterized in the laboratory and shown to be relevant for studying CNS infection by neurotropic viruses and screening antiviral drugs[50]. These ex vivo cultures offer a unique opportunity to access the infected organ directly in order to observe early viral tropism. In this study, we characterize two new three-dimensional (3D) organotypic culture models obtained from suckling hamster brainstems and lungs and compare SARS-CoV-2 infection with that of two neuro-invasive respiratory viruses (NiV and MeV) in lung and brainstem ex vivo models.

Here, we show that both organotypic systems retain their relevant physiological properties for the duration of the experiment (4 days) and are susceptible to NiV and SARS-CoV-2 infection, whereas a hyperfusogenic encephalitic MeV strain infects only the brain organotypic cultures. Type 1 and type 2 pneumocytes, as well as ciliated cells, are susceptible to infection in hamster lung explant cultures, reflecting what has been shown in humans[51]. As for the hamster brainstem, we show that SARS-CoV-2 targets granular neurons. Real-time characterization also highlights the induction of type I and III innate immune responses and an inflammatory response to infection at the organ level, as well as the caspase-3-independent apoptosis, necroptosis, and pyroptosis cell death signatures, during the first days of SARS-CoV-2 infection in both organs. Taken together, our results pave the way for the use of these models to study SARS-CoV-2 infection in organs and assess the efficacy of candidate antivirals before in vivo validation.

Results

Hamster lung and brainstem ex vivo cultures are viable and susceptible to SARS-CoV-2 infection. Since SARS-CoV-2 notably targets the upper respiratory tract and lungs and may also infect the brainstem, we have developed new ex vivo models of these organs from naive suckling hamsters, based on our previous experience using organotypic cerebellum cultures[50]. Lungs and brainstems were isolated and sliced, at 500 µm and 350 µm thicknesses, respectively, based on the stability of each structure in the slicing process. The 3D cultures were then maintained on a polytetrafluoroethylene (PTFE) membrane in order to keep an air–liquid interface for up to 4 days (Fig. 1a). In opposition with primary cultures, organotypic cultures are usually not fully soaked in the medium in order to allow oxygenation[52]. The 0.4 µm semipermeable pores of the insert permit the diffusion of the medium into the cultures. Metabolic activity, the main parameter reflecting the viability of the cultures, did not decrease over time as quantified by Alamar blue assay (Fig. 1b). To evaluate the susceptibility of ex vivo cultures to SARS-CoV2 infection, we first quantified the activity of its entry receptor ACE2. Then, we quantified the expression level of the proteases known to cleave and mature the viral surface Spike glycoprotein (S) and the viral receptors ACE2 and Neuropilin-1. The ACE2 activity/µg of total protein lysate from hamster organs on the day of slice preparation was assessed in the lung and brainstem cultures and compared with cerebellum cultures used as a reference. An ACE2 inhibitor was used to confirm that the quantified activity was real. The three cultures were found to exhibit a similar ACE2 activity, with the lung displaying a slightly higher activity (Fig. 1c). The transcription level of *ACE2* and *Neuropilin-1* were quantified in non-infected cultures by RT-qPCR (Fig. 1d). This confirmed the mRNA expression of *ACE2* in both cultures and the higher *Neuropilin-1* mRNA expression in the lung cultures compared to brain cultures. The mRNA of *TMPRSS2*, *Cathepsin* B, and *Cathepsin* L, the three proteases that are known to cleave and activate SARS-CoV-2 S, was also quantified by RT-qPCR. As in human tissues, *TMPRSS2* was highly expressed in hamster lungs but below the quantification limit in the brainstem and

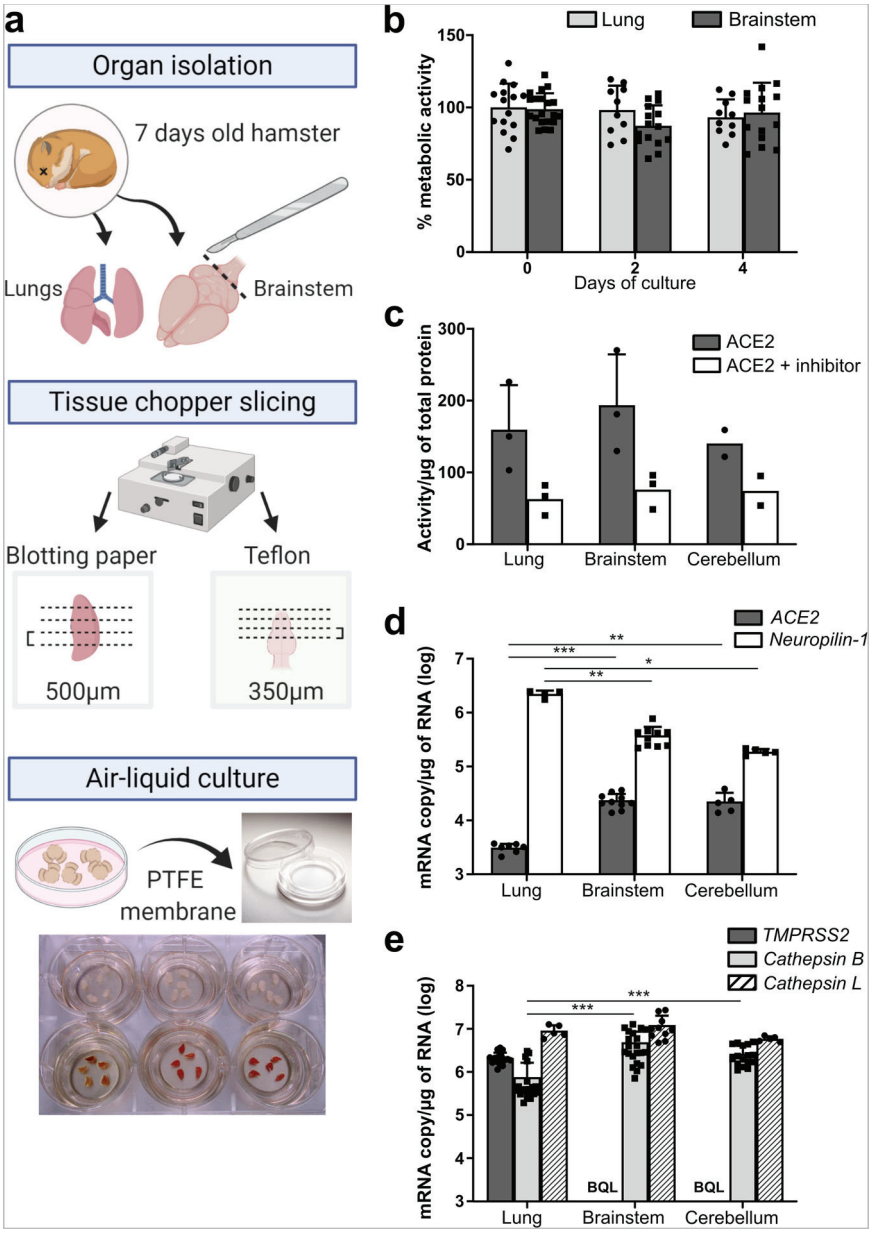

Fig. 1 Characterization of the lung and brainstem organotypic cultures. a Schematic representation of the generation of hamster organotypic cultures. **b** Cellular metabolism activity over time in % of day 0 of culture, quantified by the Alamar blue assay. ($n =$ minimum 10 biologically independent animals). **c** ACE2 activity quantified with the fluorometric ACE2 Activity Assay Kit. ($n = 3$ biologically independent animals). **d** *ACE2* and Neuropilin-1 basal mRNA expression ($n =$ minimum five biologically independent animals) and **e***TMPRSS2*, *Cathepsin* B, and *Cathepsin* L basal mRNA expression in the models quantified by RT-qPCR (day 0 of culture). ($n =$ minimum 12 biologically independent animals). *BQL* below the quantification limit, *ACE2* angiotensin-converting enzyme 2, *PTFE* polytetrafluoroethylene. Error bars represent SD. Statistical analyses were performed using the Kruskal–Wallis test. $^{*}P < 0.05$; $^{**}P < 0.01$; $^{***}P < 0.001$ Source data are provided as a Source Data file.

cerebellum[26,53]. On the contrary, *Cathepsin B* mRNA expression levels were significantly higher (≈$2^{*}10^{6}$ mRNA copies/µg of RNA) in the brain cultures compared with the lung (3.6×10^{5} mRNA copies/µg of RNA) (Fig. 1e). Resources available to work with hamsters remain very limited, notably the antibodies for immunostainings. However, in order to look deeper into the expression level of *ACE2*, *Neuropilin-1*, and the serine proteases in the brain, all four cell populations from suckling hamster cerebella were sorted by flow cytometry (Supplementary Fig. 1f). Apart from *TMPRSS2* that remained undetected, mRNA from *ACE2*, *Neuropilin-1*, and *Cathepsin* B and L were all expressed in neurons, oligodendrocytes, astrocytes, and microglia. mRNA expression of *ACE2* was still below 1 copy per cell in all cell types, even in neurons (3.56×10^{2} mRNA copies/10,000 cells), suggesting that few neural cells or their subsets express the receptor.

These results suggest that the lung organotypic models harbor all the main components required for SARS-CoV-2 infection and virus fusion at the membrane or in the endosome, whereas the brain slices might allow SARS-CoV-2 infection only via the endosomal pathway in a small subset of cells as implied by the lack of *TMPRSS2* mRNA expression.

Organotypic cultures are susceptible and permissive to SARS-CoV-2 infection. In order to evaluate the infectability of our new models, hamster lung, brainstem, and cerebellum organotypic cultures were infected with recombinant SARS-CoV-2_neon

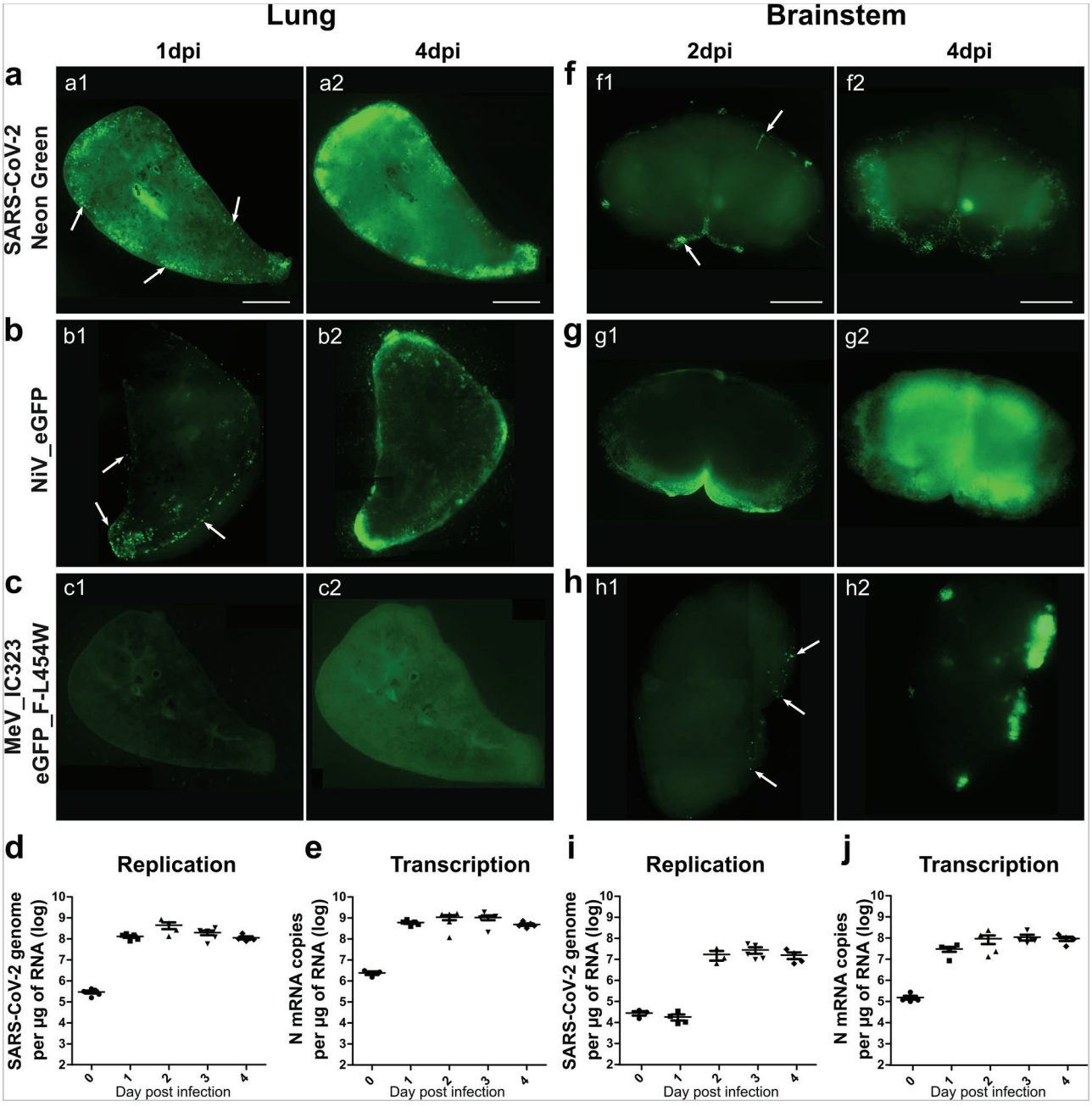

Fig. 2 Hamster organotypic culture infection by three respiratory viruses and the dissemination of SARS-CoV-2. a–c, **f–h** The entry of three different encephalitogenic respiratory viruses, icSARS-CoV-2-mNG (infection: 10,000 plaque-forming unit (pfu)), NiV-EGFP (infection: 5000 pfu) and the hyperfusogenic variant MeV IC323-EGFP-F L454W (infection: 1000 pfu) was monitored by following the fluorescence at 1 dpi (**a1**; **b1**; **c1**), or 2 dpi (**f1**; **g1**; **h1**) and 4 dpi (**a2**; **b2**; **c2**; **f2**; **g2**; **h2**). Pictures were taken using a Nikon Eclipse Ts2R microscope (500 ms of exposure), reconstituted using the Stitching plug-in with ImageJ software[119] and are representative of three independent experiments. Scale bar = 1 mm. **d**, **i** SARS-CoV-2 genomes per µg of total RNA and **e**, **j** SARS-CoV-2 N mRNA copies per µg of total RNA were quantified by RT-qPCR in the lung, and brainstem organotypic cultures at 90 min post infection and 1–4 days post infection (dpi) with 5000 pfu and normalized to the standard deviation for *GAPDH* mRNA. ($n = 5$ biologically independent animals). Source data are provided as a Source Data file.

green (icSARS-CoV-2-mNG)[54]. To compare the permissiveness of the organotypic cultures to other encephalitic respiratory viruses, they were infected in parallel with recombinant NiV and MeV, both expressing enhanced green fluorescent protein (EGFP) (referred to as rNiV-EGFP and MeV IC323-EGFP-F L454W, a CNS-adapted MeV that can infect in the absence of known receptors[55], respectively). Viral entry and dissemination were tracked by microscopy at 1 or 2 and 4 days post infection (dpi) (Fig. 2; Supplementary Fig. 2). Interestingly, icSARS-CoV-2-mNG and NiV-EGFP entered and disseminated in both lung and brain cultures (Fig. 2a, b and Supplementary Fig. 2a, b), whereas MeV IC323-EGFP-F L454W only infected the brainstem and the cerebellum (Fig. 2c and Supplementary Fig. 2c). Even at 4 dpi the hyperfusogenic MeV did not infect any cells in the lung cultures, suggesting that MeV entry in lung epithelial cells may require additional factors in this model (Fig. 2c). The pictures taken 2 h following infection of the hamster organotypic cultures with 10,000 PFU do not show more fluorescence than the basal

autofluorescence observed in non-infected cultures (Supplementary Fig. 3a, b). On the contrary, neon green specific fluorescent cells are clearly detected at 4 dpi in hamster cultures infected with only 100 plaque-forming unit (PFU) of icSARS-CoV-2-mNG, confirming that the susceptibility of the brain cultures is not related to the high viral charge used for infection (i.e., 100 PFU/10^7 cells at least) (Supplementary Fig. 3c). All positive cells for neon green fluorescence were also positive for the immunofluorescent staining of SARS-CoV-2 nucleoprotein, confirming that the neon green fluorescence provides evidence of infection (Supplementary Fig. 3d). In order to test the relevance of our models and confirm that SARS-CoV-2 entry is specific regardless of the dose of virus, organotypic cultures from wild-type C57BL/6-suckling mice, which are supposed to be resistant to SARS-CoV-2 infection, were infected with 10,000 PFU of icSARS-CoV-2-mNG. The absence of fluorescence even at 4 dpi confirms that the dose of 10,000 PFU does not force viral entry in a non-susceptible model (Supplementary Fig. 3e, f). SARS-CoV-2 replication and transcription were then followed, respectively, by specific genome and nucleoprotein mRNA copy number quantification by RT-qPCR (Supplementary Fig. 6). The viral genomes and nucleoprotein transcripts were higher in the lungs than in the brainstems and cerebella (Fig. 2d, e, i, j; Supplementary Fig. 2d). These differences were already observed on the day of infection (Fig. 2d, e). The greater susceptibility of lung cultures might emerge either from the greater thickness of lung slices compared with that of brainstem and cerebellum cultures, or perhaps from a greater number of *Neuropilin-1*-expressing cells (Fig. 1d). In the lung, viral replication was very fast and the number of SARS-CoV-2 genomes/µg of RNA almost reached the plateau after 1 dpi (1.2×10^8 genomes/µg of RNA) (Fig. 2d, e). In the brainstem and the cerebellum, transcription was initiated at 1 dpi. However, replication was delayed, with an increase in genome copies being observed only after 2 days, and by the end of the experiment reached lower values than detected in the lungs (Fig. 2i, j). The mRNA expression level of SARS-CoV-2 entry receptors and the proteases involved in the cleavage of the S was followed in the context of infection (Supplementary Fig. 1a–e). *ACE2* mRNA expression increased from days 3 and 4 post infection, but the *Neuropilin-1* mRNA expression did not vary over time (Supplementary Fig. 1a, b). Expression of *Cathepsin* B and L mRNA increased through time in both organs while *TMPRSS2* mRNA expression remained below the quantification limit in brainstem cultures (Supplementary Fig. 1c–e).

Altogether, these results show that all analyzed ex vivo cultures are susceptible to SARS-CoV-2 infection, although with slightly different kinetics.

SARS-CoV-2 infection is blocked by remdesivir in organotypic lung and brainstem cultures. Remdesivir showed antiviral efficacy in vitro and in vivo, and is in clinical use for COVID-19 treatment in certain countries[56–60]. We used it to validate our models for drug evaluation. The slices were treated daily at two different concentrations of remdesivir, one right over the IC90 in cell culture and one five times higher, as our organotypic cultures are more complex than regular monolayer cultures. The treatment started two hours after infection (Fig. 3a) and continued for up to 4 dpi to make sure that the treatment not only delays the infection but also blocks viral dissemination. Mock organotypic cultures were maintained under similar conditions and treated using a vehicle. After 4 days of treatment, the total amount of RNA extracted remained unchanged and the metabolic activity of both lung and brainstem slices remained very close to 100% and to that of non-treated slices, suggesting the very low, not to say null, effect of the drug on the metabolic activity at these doses (Fig. 3b, c). The lower dose (2 µM) of remdesivir did not have a significant inhibitory effect on infection as assessed by RT-qPCR. However, after treatment with 10 µM of remdesivir, infection was reduced by almost 100% at 4 dpi in both lungs and brainstems.

Hydroxychloroquine has been shown to inhibit SARS-CoV-2 entry in vitro by acting on the endosomal pathway[56,61,62]. In order to evaluate how drug screening in organotypic cultures is predictive of in vivo results, we included hydroxychloroquine in our study. Based on the absence of *TMPRSS2* in brainstem cultures, we first speculated that viral entry in these cultures should occur through the endosomal pathway, where hydroxychloroquine should be effective. At the dose of 10 µM, hydroxychloroquine blocked >90% of the infection in our brainstem cultures (Fig. 3d). At 20 µM, the efficacy decreased concomitantly to the appearance of signs of toxicity highlighted by a 20% reduction of the total RNA extracted per culture compared with the non-treated samples (Fig. 3e). In the lung cultures, where both *TMPRSS2* and *Cathepsin* B/L are expressed, providing the virus with the ability to fuse both at the cell surface and in endosomes, hydroxychloroquine did not inhibit the infection significantly (Fig. 3d, e). Taken together, these data confirm that our model can be used to predict the in vivo efficacy of a drug.

To go further, we have tested totally different antiviral compounds such as Hsp90 inhibitors that also hold promise as modulators of SARS-CoV-2 infection. Derivatives of geldanamycin such as 17-DMAG have been developed to limit hepatotoxicity and are very promising in vitro studies but toxic in vivo[63–65]. Here, 17-DMAG treatment inhibits 28% of the infection in the lung and 90% in brainstem cultures (Fig. 3f). However, four times less of total RNA has been extracted from the treated cultures compared to the non-treated ones in both lung and brainstem (Fig. 3g). Our results confirm that organotypic culture models mimic precisely the patterns observed in vivo, and therefore, can be used for assessing drugs prior to in vivo experiments.

SARS-CoV-2 preferentially targets neurons in the brain, and ciliated cells, type 1 and type 2 pneumocytes in the lungs. To determine which cells are the main targets of SARS-CoV-2, viral tropism was evaluated by transmission electron microscopy (TEM) in lung and brainstem organotypic cultures, followed by immunofluorescent staining analyzed by confocal microscopy (Fig. 4). Based on the kinetics of viral replication, all the organotypic cultures shown in Figs. 4–6 were collected at 1 dpi for the lung and at 2 dpi for the brainstem and cerebellum. In lung cultures, infection was observed in type 1 and type 2 pneumocytes, as well as in the ciliated cells from the general area of the bronchioles (Fig. 4a–c). Immunofluorescence analysis confirmed these observations by showing the presence of SARS-CoV-2_S staining in cells positive for surfactant protein C (SP-C), Aquaporin 5 (AQP5), and α acetylated Tubulin (Tub) staining that are specific for type 2, type 1 pneumocytes, and ciliated cells, respectively (Fig. 4d–f). Most of the cells display microvilli as expected in young animals (Fig. 4c and Supplementary Fig. 4a). Infected cells harbored a large number of vacuoles and showed multiple signs of cell degradation: cytoplasmic material degradation, membrane coiling (blue star), large empty vacuoles (green arrow) (Fig. 4b1, b2). We observed autophagosomal vacuoles containing virions or degraded viral particles in all types of infected cells (Fig. 4a–c; Fig. 5a and Supplementary Fig. 4c). Virions were also found attached to the microvilli outside the cells (Supplementary Fig. 4a), and several cells showed disorganization of the smooth endoplasmic reticulum (SER), as well as accumulation of lipids and mitochondria that were undergoing degradation (Supplementary Fig. 4b).

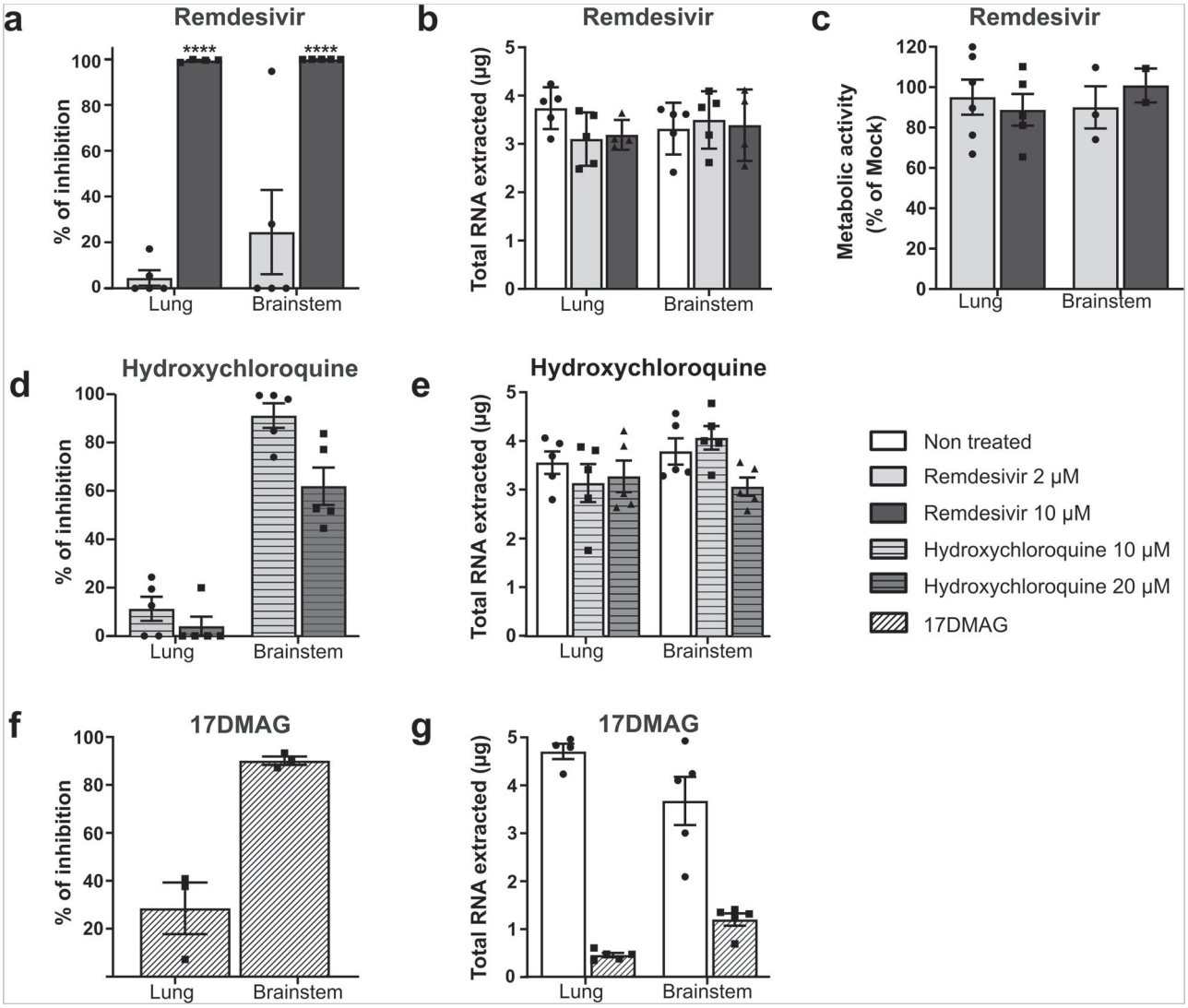

Fig. 3 Antiviral activity of remdesivir, hydroxychloroquine, and 17-DMAG in hamster organotypic cultures infected by SARS-CoV-2. a, **d**, **f** Organotypic cultures from hamsters were infected with SARS-CoV-2 at 1000 pfu/slice and treated at the indicated concentrations of remdesivir, hydroxychloroquine, and 17-DMAG at 90 min, 24, 48, and 72 h after infection ($n = 5$ biologically independent animals). Total RNA was harvested at 4 days post infection and the number of SARS-CoV-2 genomes was quantified by RT-qPCR. Results are expressed in % of inhibition of the infection compared with non-treated cultures. Statistical analyses were performed using the Kruskal–Wallis test. $^{*}P < 0.05$; $^{**}P < 0.01$; $^{***}P < 0.001$. **b**, **e**, **g** Total RNA extracted per organotypic culture was quantified. **c** The toxicity of remdesivir on uninfected cultures that were treated in the same way was assessed via the Alamar blue assay. Results are expressed as the percentage of metabolic activity after 4 days compared with the non-treated samples. All error bars represent SD. Source data are provided as a Source Data file.

In the brainstem and in the cerebellum, TEM analysis revealed viruses in granular neurons (Fig. 5a and Supplementary Fig. 4d) with a developed Golgi apparatus. Moreover, the viral particles were often localized in double-membraned vacuoles (red arrows) inside the cells where other Coronaviruses are generally observed during their cell cycle (Fig. 5a1, a2)[66,67]. In the immunofluorescence analysis, SARS-CoV-2_S staining colocalized with NeuN-positive cells (Fig. 5b), confirming the infection of granular neurons. Myelin Basic Protein (MBP) staining surrounded the SARS-CoV-2_S without colocalization, suggesting that the cells positive for the infection could also be myelinated neurons and not oligodendrocytes (Fig. 5c). The cultures were also stained for microglia marker (Iba1), astrocytes (GFAP), and Olig2 (used as a second marker for oligodendrocytes), and SARS-CoV-2_S staining was not found in these cells (Fig. 5c–e). In the cerebellum, TEM analysis showed the infection of Golgi neurons with viral particles in autophagosomes. We did not observe infection of Purkinje neurons (Supplementary Fig. 4d1, d2), suggesting that under the given conditions a selective infection of specific neuronal subtypes has occurred.

In these models, SARS-CoV-2 infects almost all epithelial lung cells but is selective for neuronal subtypes in the CNS. In both lung and brain organotypic cultures, the infection led to a marked cell degeneration that could conceivably affect organ functions.

Apoptotic, necroptotic, and pyroptotic signatures are detected in both organotypic cultures. Since unbalanced inflammatory responses can provoke organ failure, we evaluated cell death signatures in SARS-CoV-2-infected organotypic cultures. First, we performed TEM analysis, which highlighted the presence of apoptotic and necrotic cellular disorders in both infected lungs and brainstems as opposed to the non-infected cultures (Fig. 6a, b; Supplementary Fig. 5). The involvement of apoptosis was verified by transferase dUTP nick end labeling (TUNEL)

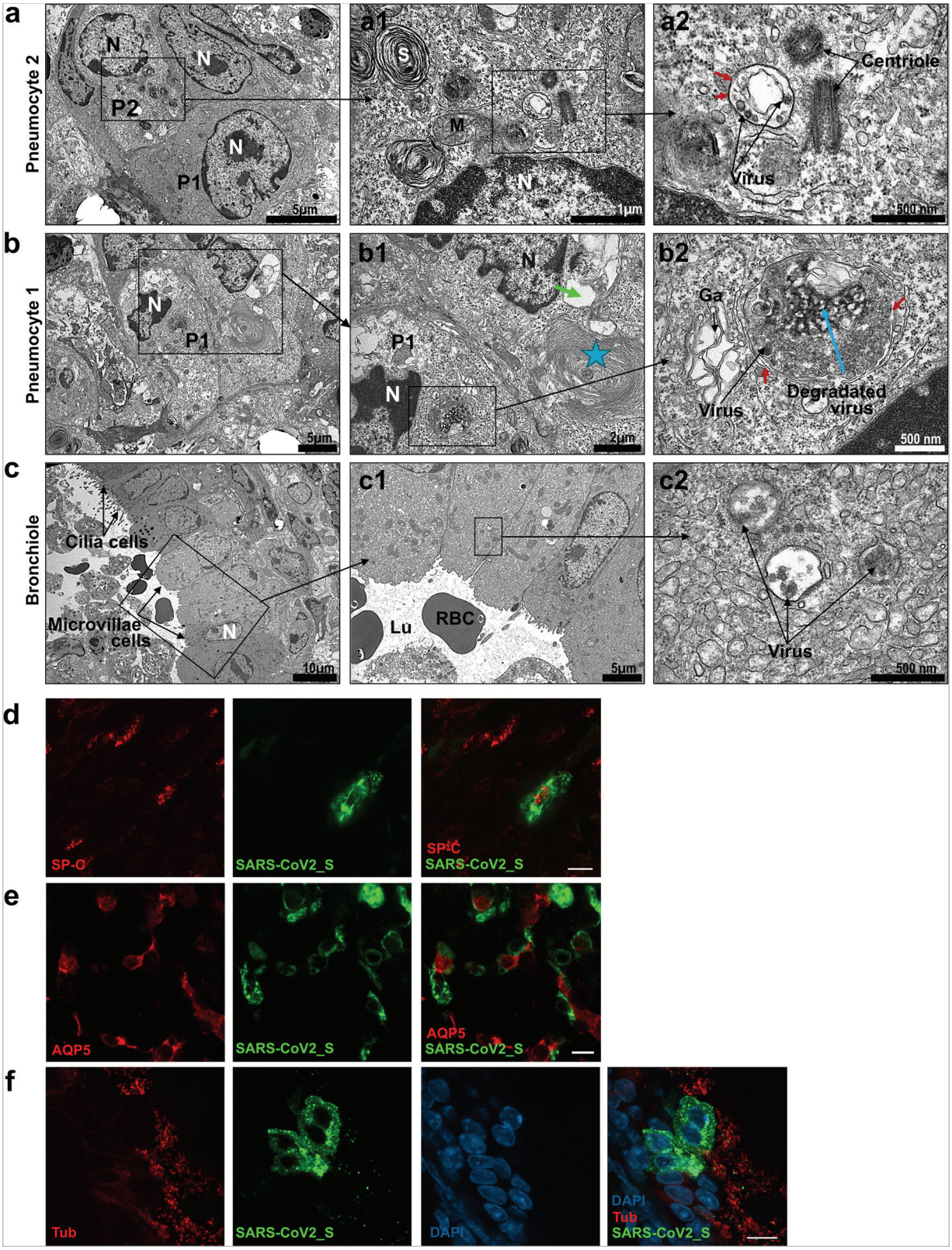

assays in both organotypic cultures (Fig. 6c, d). TUNEL staining was observed similarly in both non-infected and infected cultures, potentially as an artifact of the experimental procedure. However, most of the cells positive for SARS-CoV-2 staining were not positive for TUNEL, confirming that apoptotic cell death observed by TEM might not be a direct consequence of viral infection. Alternatively, cell death related to viral infection may have been caspase-independent (Fig. 6c, d). Using RT-qPCR, we corroborated necroptotic events in line with microscopic observations despite an erratic expression of Tumor Necrosis Factor α (*TNFα*) throughout the four days of infection (Fig. 6f). As described in the former experiment (Fig. 6a, b), mRNA levels of the infected cultures were compared with uninfected cultures maintained under similar conditions ($n = 5$). Indeed, in both

Fig. 4 SARS-CoV-2 tropism in hamster lung organotypic cultures during the first day of infection. Cultures were infected with 1000 pfu of SARS-CoV-2 and fixed at day 1 post infection. **a**–**c** Ultrastructure of infected lung cells by transmission electron microscopy (TEM), scale bar is represented bottom right on each picture, representative of two independent experiments. **a** Low magnification of lung cells; P1 = type 1 pneumocyte, P2 = type 2 pneumocyte, *N* = nucleus. **a1** Enlargement of an infected type 2 pneumocyte with dense lamellar bodies in the cytoplasm (S = surfactant synthesis), a part of the nucleus, the centriole, mitochondria, and autophagosomal vacuoles containing virions. **a2** High magnification showing the centriole and the autophagosomal vacuole containing virions. Black arrows point to the double membrane. **b** Lung cells undergoing degeneration, displaying vacuoles and degraded cytoplasmic material. *N* = nucleus, P1 = type 1 pneumocyte. **b1** Enlargement of cells from the **b**, P1 cell contains an autophagosome containing virions, several vacuoles, and heterochromatin in the nucleus. The second cell exhibits membrane coiling (star) and large empty vacuoles (green arrow), indicating degradation. **b2** High magnification showing the double membrane of the autophagosome (red arrows) containing an accumulation of viral material (blue arrow). The black arrow show viruses surrounding the vacuole. Ga = swelled Golgi apparatus. **c** Respiratory bronchiole showing ciliated cells and microvillous cells. *N* = nucleus. **c1** Enlargement of the cells from **c**, showing microvillous cells and red blood cells (RBC) in the lumen of the bronchia (Lu). C2: high magnification showing three autophagosomes containing virions (arrows). **d**–**f** Lung cultures were stained with antibodies: anti-SARS-CoV-2_S, **d** anti-surfactant protein c (SP-C), **e** anti-Aquaporin 5 (AQP5), and **f** anti-α acetylated Tubulin (Tub). The immunofluorescence staining analysis was performed by confocal microscopy and is representative of three independent experiments. Scale bar 10 μm.

cultures, we observed a sharp increase in Mixed Lineage Kinase Domain Like Pseudokinase (*MLKL*) mRNA levels (Fig. 6e), which is known to be associated with Caspase 8 deficiency and Inflammatory Bowel Disease commonly observed in patients. Moreover, we showed that pyroptosis also occurs during viral infection, as inferred from the increase in *Gasdermin D* mRNA levels in both infected lung and brainstem cultures (Fig. 6g). Gasdermin D is also known to be a substrate of inflammation-related caspases, thus triggering an unbalanced inflammatory response potentially leading to organ failure[68,69]. Interestingly, although *Gasdermin D* levels decreased at day 4 post infection in the lungs, its expression kept increasing in the brainstem, possibly due to a difference in infection kinetics between the tissues. Furthermore, while the levels of Interleukin 18 (*IL-18*) mRNA remained low in both organotypic cultures (Fig. 6h), we documented a difference in the expression of Interleukin 1 β (*IL-1β*) mRNA that increased in the brainstem but remained low in the lungs (Fig. 6i). These data reveal that distinct cellular mechanisms leading to pyroptosis in the two organs.

Innate and inflammatory responses are increased in both organotypic cultures. To characterize the recapitulation of the responses of these models to SARS-CoV-2 infection, we transcriptomically profiled infected and uninfected organotypic cultures of both hamster brainstem and lungs (Fig. 7a–d). All results are presented here as the fold change of the infected condition compared to the non-infected one ($n = 5$). The transcriptomic first level of analysis pointed out the strong stimulation of the immune response with 19 and 20 out of 20 mainly altered Gene Ontology (GO) categories related to immunity in lung and brainstem, respectively (Fig. 7a, b). Alternatively, eight GO categories related to lymphocyte responses were altered in the brainstem versus two in the lung. To go further, the dichotomy in cellular responses occurring in both tissues at day 4 post infection was confirmed by the gene expression patterns, highlighting organ-dependent specificities in the host response to the infection (Fig. 7c, d). Indeed, the most significantly differentially expressed genes (DEG) in the lung include a plethora of upregulated interferon-stimulated genes (ISGs, Fig. 7c). Conversely, in the brainstem, these significant DEG contained many downregulated neuronal markers (Fig. 5d). This is consistent with the observation that the percentage of polyadenylated transcripts aligning to the SARS-CoV-2 genome is 6.74-fold higher in the lung than in the brainstem (2.90% vs 0.43%) (Fig. 7c, d).

In parallel, specific immunological markers including Myxovirus Resistance 1 (*MX1*), Interferon Stimulated Exonuclease Gene 20 (*ISG20*), C-X-C Motif Chemokine Ligand 10 (*CXCL10*), and C-C Motif Chemokine Ligand 5 (*CCL5*) mRNA were quantified by RT-qPCR and presented in terms of the fold change between the infected and uninfected conditions (Fig. 7e–h). However, specific genes encoding ISG or chemokines were similarly upregulated in both organotypic cultures, pointing to these as potentially relevant to the innate immune response. Indeed, RT-qPCR profiles showed that the expression of *MX1* and *ISG20* ISGs and of *CCL5* and *CXCL10* chemokines were increased within the 4 days kinetics following SARS-CoV-2 infection in both cultures compared with the respective uninfected conditions. Interestingly, *ISG20* mRNA amounts decreased rapidly to lower levels, suggesting that its reduced antiviral exonuclease activity may be compensated at later times (Fig. 7f). Moreover, we noticed that, while exhibiting a similar trend, all these responses were delayed in brain cultures compared with the lungs (Fig. 7e–h).

Discussion

SARS-CoV-2 infection starts in the lungs, inducing the severe acute respiratory syndrome regularly associated with neurological symptoms. Although CNS involvement has been a topic of extensive study, little attention has been paid to the possible role of brainstem infection in organ failure. In the ventral medulla oblongata, the preBötzinger complex is a defined neural network that is critical for generating the respiratory rhythm[70]. It is plausible that brainstem infection during its acute phase could affect both respiratory and cardiac function[8–12].

Organotypic cultures offer an opportunity to follow early steps of infection in real-time in a native 3D multicellular context[71]. Non-standardized lung ex vivo slices have been used for studying respiratory virus pathogenesis in multiple host species (from mice to monkeys)[72,73]. The highly standardized lung organotypic cultures we describe can be extended to several small animal models. Organotypic brainstem cultures have been previously characterized using 3–18-day-old mice or rats, with a focus on brain development, neuronal respiratory networks, and neurodegenerative diseases[74–77]. Our study provides a characterization of these models for investigating the initial 4 days of infection for the first time. From a single animal, we can prepare a large number of organotypic cultures (e.g., ≈8 from the brainstem, ≈20 from the lungs, and up to ≈10 from the cerebellum), allowing for numerous comparisons to be carried out in real time and simultaneously on several organs. In terms of assessing antiviral drugs prior to in vivo work, organotypic cultures are complementary to human airway epithelia (HAE) that are used for preliminary screening[56,78], since they are a more complex organ-like system. As such, they complement the HAE system, also a 3D lung model grown at an air–liquid interface, that has been recently used to evaluate SARS-CoV-2 antiviral molecules[79].

The use of viruses encoding a fluorescent protein allows the monitoring of the infection in real-time within tissues. The lung

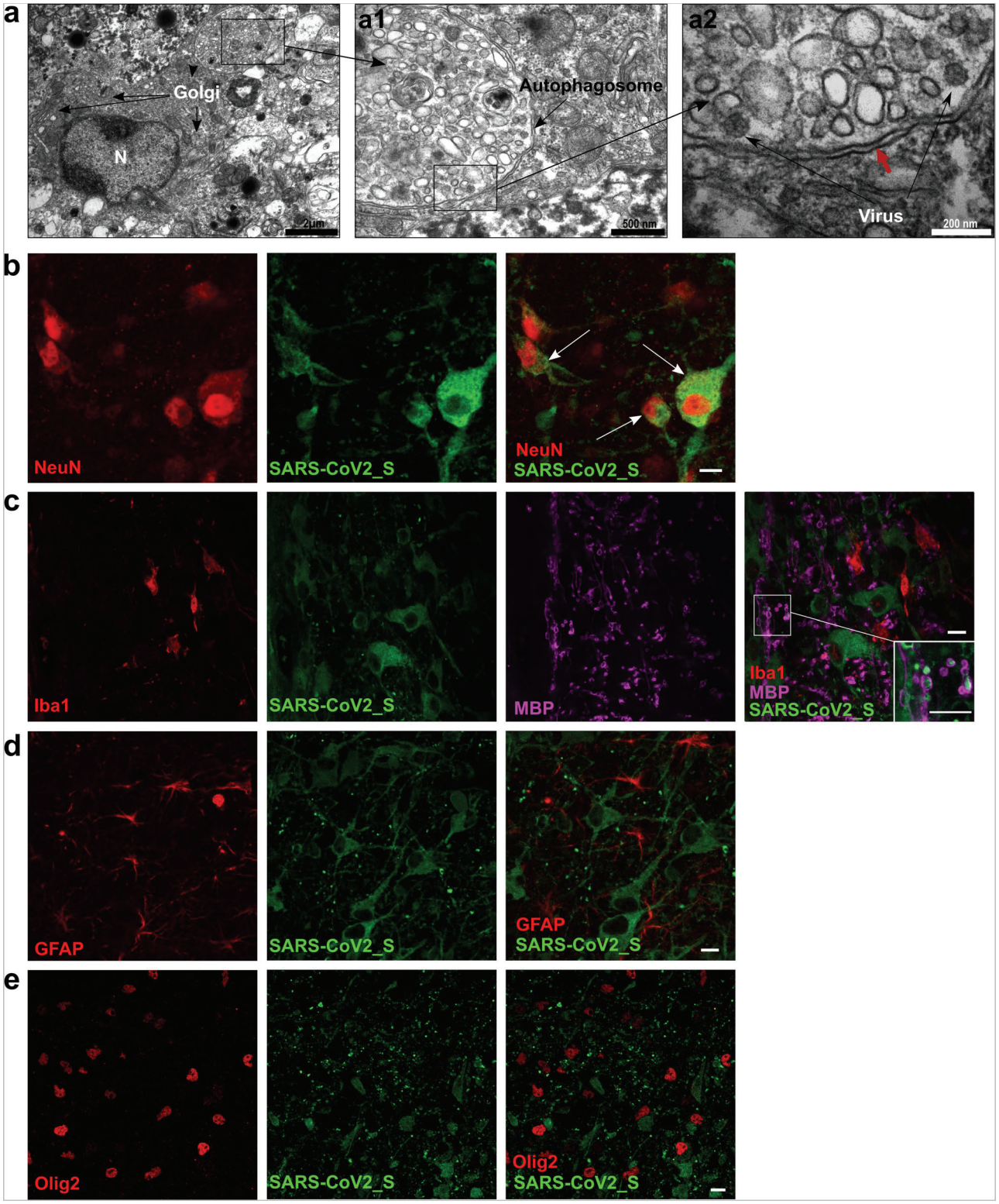

Fig. 5 SARS-CoV-2 tropism in hamster brainstem organotypic cultures during the first 2 days of infection. Cultures were infected with 1000 pfu of SARS-CoV-2 and fixed at day 2 days post infection. **a** Transmission electron microscopy (TEM) analysis of a brainstem slice showing an infected neuron with a large Golgi apparatus. **a1**, **2** Enlargement of the autophagosome containing viral particles (white arrows). The double membrane of the autophagosome is indicated with the red arrow. The results are representative of two independent experiments. **b**–**e** Brainstem slices stained with antibodies anti-SARS-CoV-2_S, **b** anti-NeuN, **c** anti-Myelin Basic Protein (MBP), and ionized calcium-binding adaptor molecule 1 (Iba1), **d** anti-glial fibrillary acidic protein (GFAP), and **e** anti-Olig2. The immunofluorescence staining analysis was performed by confocal microscopy and is representative of three independent experiments. Scale bar 10 µm.

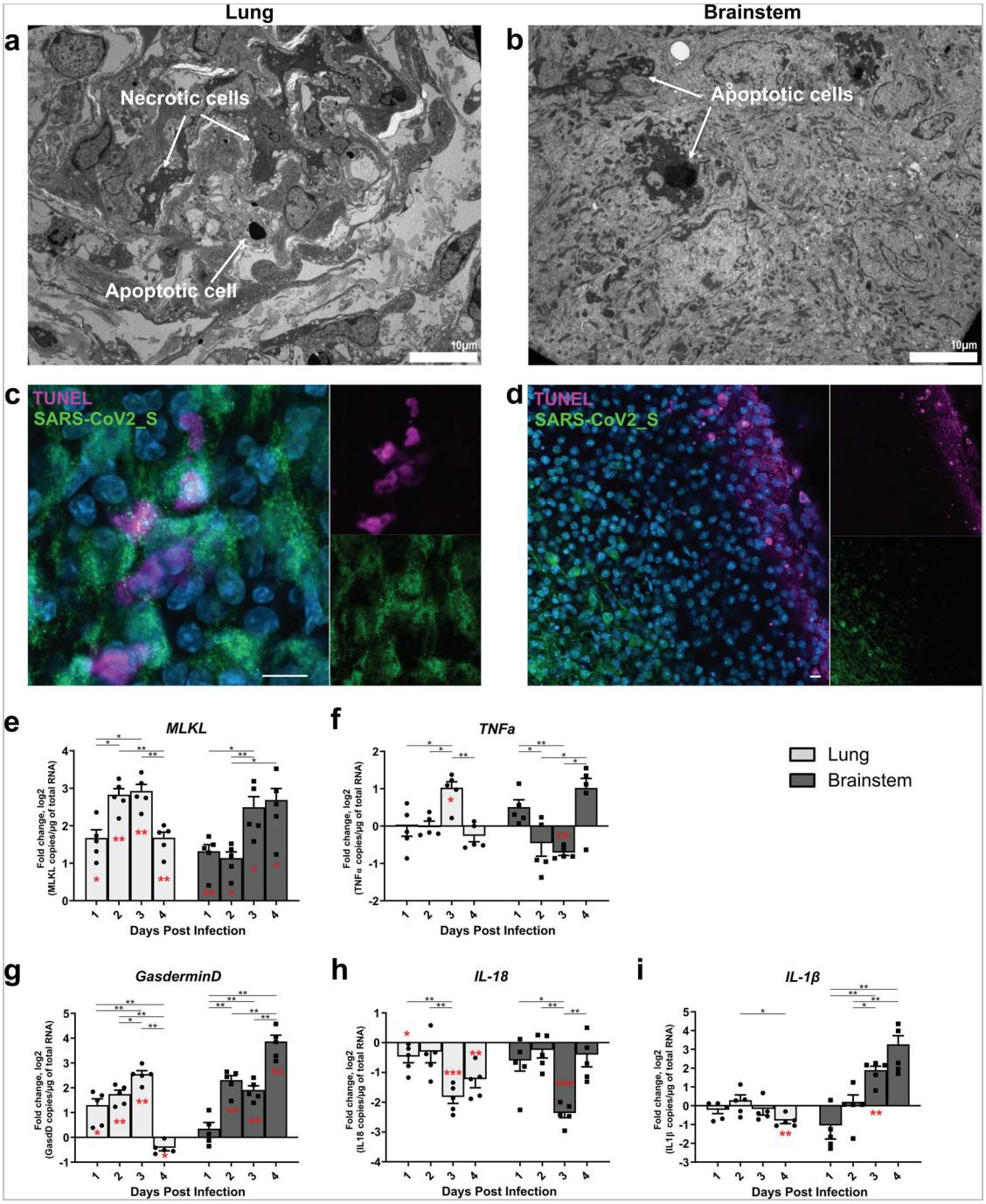

Fig. 6 Cell death in the ex vivo cultures. Hamster ex vivo cultures were infected with 1000 pfu of SARS-CoV-2 ($n = 5$ biologically independent animals). **a**–**c** Lung and brainstem slices were fixed at 1 day post infection (dpi) or 2 dpi, respectively. **a**, **b** Transmission electron microscopy analysis showing necrotic cells and apoptotic cells, scale bar is represented bottom right on each picture. **c**, **d** SARS-CoV-2_S protein immunostaining, and terminal deoxynucleotidyl transferase dUTP nick end labeling (TUNEL) labeling in the lung and brainstem. Nuclei were counterstained with DAPI. **e**–**i** mRNA expression level of **e** *MLKL*, **f** *TNF-α*, **g** *Gasdermin D*, **h***IL1β*, and **i** *IL-18* over time. mRNA copies per µg of total RNA were quantified by RT-qPCR and normalized to the variation of the amounts of *GAPDH* mRNA. Fold changes are relative to the number of copies of mRNAs in infected organotypic cultures compared to the uninfected ones. Error bars represent SD. Statistical analyses were performed using the Mann–Whitney test two-sided to compare the fold changes between days of culture (black stars). mRNA expression levels in infected samples were also compared with non-infected samples at the corresponding time point (red stars) using the one-sample T-test. $^{*}P < 0.05$; $^{**}P < 0.01$; $^{***}P < 0.001$. Scale bar 10 µm. Source data are provided as a Source Data file.

organotypic cultures were found to be highly suited for studying viruses able to directly infect the respiratory tract. In line with our previous studies showing that hyperfusogenic neurotropic variants are generally found in the brain[80], the neuro-adapted MeV IC323-EGFP-F L454W did not directly infect lung cultures, suggesting that additional mechanisms are required to access the Nectin-4 viral entry receptor. We found that ACE2 activity per µg of total protein was similar in the lung and the brain, with the caveats that the assay does not specify which cells express the receptor and to what extent (Fig. 1 and Supplementary Fig. 1) and

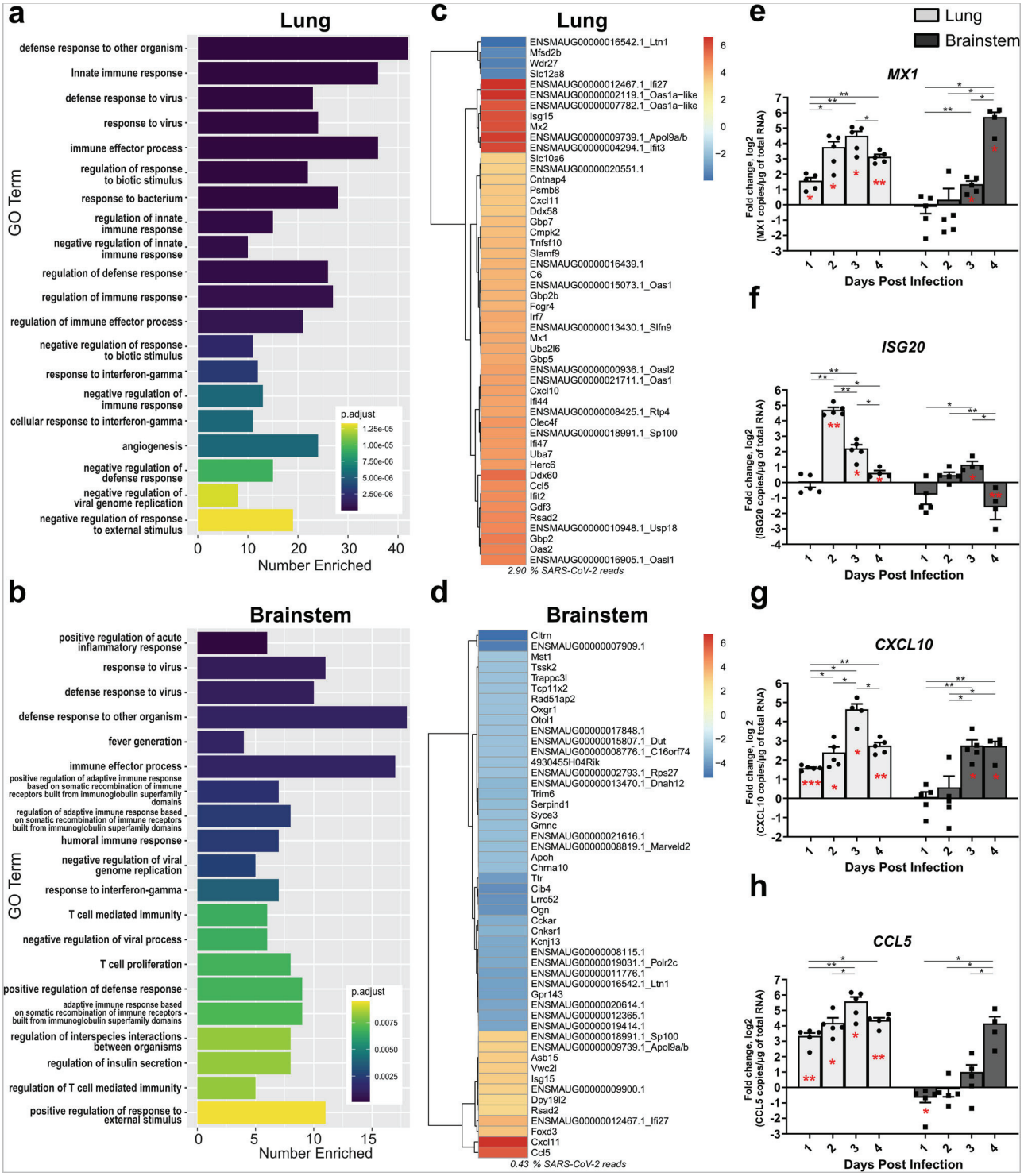

Fig. 7 Innate immune transcriptional signature in lung and brainstem organotypic cultures during SARS-CoV-2 infection. Hamster ex vivo cultures were infected with 1000 pfu of SARS-CoV-2 ($n = 5$ biologically independent animals). **a**–**d** Transcriptomic analysis of the organotypic lung cultures and brainstem cultures 4 days post infection. **a**, **b** Gene Ontology (GO) analysis. For each tissue, the 20 non-redundant GO categories with the lowest adjusted *p* value for Fisher exact test of enrichment were displayed using ggplot. **c**, **d** Heatmaps generated by calculating the log2-fold change for infected samples relative to uninfected samples and taking the 50 with the largest absolute value. **e**–**h** mRNA expression level of **e** *MX1*, **f** *ISG20*, **g** *CXCL10*, and **h** *CCL5* over time. mRNA copies per µg of total RNA were quantified by RT-qPCR and normalized to the variation of the amounts of *GAPDH* mRNA. Fold changes are relative to the number of copies of mRNA in infected organotypic cultures compared to the uninfected ones. Error bars represent SD. Statistical analyses were performed using the Mann–Whitney test two-sided to compare the fold changes between days of culture (black stars). mRNA expression level in infected samples was also compared with non-infected samples at the corresponding time point (red stars) using the one sample *t* test. $^{*}P < 0.05$; $^{**}P < 0.01$; $^{***}P < 0.001$. *MX1* Myxovirus Resistance 1, *ISG20* Interferon Stimulated Exonuclease Gene 20, *CXCL10* C-X-C Motif Chemokine Ligand 10, CCL5: C-C Motif Chemokine Ligand 5. Source data are provided as a Source Data file.

that ACE2 mRNA levels were quite low in both organs. RT-qPCR analysis showed that all receptors and enzymes required for viral entry are expressed in the lungs, suggesting that SARS-CoV-2 could infect the organ either by fusing at the cell surface or through the endosomal pathways. In hamster lungs, a recent study described that both ACE2 and TMPRSS2 expression are required for efficient SARS-CoV-2 infection[81].

In the human lung, ACE2 expression concentrates at the surface of lung alveolar epithelial cells, mainly on type 1 and type 2 pneumocytes but also in bronchial epithelial cells[82]. In the hamster organotypic lung culture model, ciliated cells, type 1 and type 2 pneumocytes are infected (Fig. 4). Our findings are consistent with other in vivo SARS-CoV-2 studies in hamsters that reveal inflammation and severe lesions in the lung with infection of the bronchiolar epithelial cells, type 1 and 2 pneumocytes[45,47]. We also found viral clusters in autophagosomes, confirming that this observation is conserved between infected species (Fig. 4, Fig. 5). In bronchial HAE apically infected with SARS-CoV-2, TEM analysis also highlighted double-membrane vesicles and spherule-containing virions[83].

In distinction to SARS-CoV, it remains unclear whether SARS-CoV-2 targets the brain, and the organotypic models do not allow investigating how the virus spread to CNS. The most commonly observed affection of the CNS seems to be related to immune (/inflammation) response to the infection of choroid plexi or brain vasculature[27]. Multiple alternative routes of entry in the CNS are regularly proposed such as direct entry through the sensorial neurons of the olfactory bulb or cranial nerves (CN)[12,14,46,53]. Secondary infections of the CNS through retrograde transport from sensory neurons (notably the vagus nerve) from initially infected lungs or gut via the enteric nervous system are also commonly suspected[84]. As for other viruses, it remains very difficult to appreciate the real ability of SARS-CoV-2 to infect CNS cells in humans since most of the data are coming post mortem analyses performed mainly on patients who died from acute respiratory syndrome associated with cytokine storm which may strongly affect viral spread to the brain parenchyma. Our data show that, provided that SARS-CoV-2 reaches the brain parenchyma, it can infect CNS cells, initiate transcription (confirmed by neon green expression), and spread in at least two brain substructures (as shown by cell-to-cell dissemination of neon green fluorescent protein) (Fig. 2 and Supplementary Fig. 2). Viral replication is confirmed by the over three logs increase in the number of viral genome copies in a culture in which cell division is very limited (as confirmed by Alarmar blue measurements over time) compared with cell cultures.

Our brainstem cultures derive mainly from the medulla and the pons for the top-central part[85]. SARS-CoV-2 seems to target specific locations in the pons and in the medulla: the motor and sensory areas, respectively. We observed green fluorescence in the zone of X and XII CN fibers, which are responsible for motor (CN X and CN XII) and sensory functions (CN X). In the cerebellar cultures, the infection starts from the deep nucleus and the thin layer of granular cells (Fig. 2 and Supplementary Fig. 2). Interestingly, NiV and MeV infections target quite different areas and propagate more extensively, possibly due to their broader tropism in the CNS. This underlines the interest of organotypic cultures to reveal cell specificity of different viral infections not previously observed in vivo.

At the molecular level, *TMPRSS2* expression in the brain tissues was below the quantification limit, which is aligned with the literature that describes a very low expression of *TMPRSS2*, as well as *ACE2*, in the brain and neural tissue[53,86,87]. Several studies highlighted the high variation of *ACE2* mRNA and protein expression depending on the brain region and established a link with viral tropism[24,88–90]. In the hamster brainstem and cerebellum, we quantified less than one *ACE2* mRNA copy per cell, for all cell types, suggesting that either brain cells expressing ACE2 are very few or that SARS-CoV-2 may not use ACE2 to enter the few CNS target cells when it infects neural tissue.

As expected, *Neuropilin-1* transcription in both lung and brain cultures was confirmed[86], with significantly higher mRNA expression levels in the lung than in brain cultures. *Cathepsin* B and L expressions were similar in both organs. In addition, while cathepsin B and L can replace TMPRSS2 for S cleavage[91], their endosomal distribution may not allow the virus to enter as efficiently as TMPRSS2. We suggest that a lower level of host protease activity in the brain may contribute to the delayed infection by constraining the virus to the alternative endosomal-lysosomal pathway for entry[92]. Another more technical explanation for the faster replication of SARS-CoV-2 in lung cultures is that these organotypic cultures are larger and thicker than brainstem cultures and may contain a broader range and a higher quantity of susceptible cells, accounting for the higher concentration of viral RNA after 2 hours (Fig. 2).

Several studies have shown that SARS-CoV-2 can infect neurons from human induced pluripotent stem cells-derived brain organoids[25,27,29,93]. In hamsters, viral antigens are commonly observed in olfactory neurons, but very few or none in the brain parenchyma, while the virus can be recovered from the brain of a one-month-old infected animal[46,47]. These data suggest that the virus may have limited capacity to cross the blood-brain barrier. Here, we show that neurons from hamster brainstems and cerebella can be infected by SARS-CoV-2 (Fig. 5). As observed by TEM analysis, NeuN staining revealed infection of granular neurons, which are likely to be Golgi II neurons (Fig. 5a,b). Interestingly, we came to the same conclusion with regards to cerebellum cultures in which we did not detect any infection of Purkinje neurons (Supplementary Fig. 4). Although ACE2 expression has been described in neurons and glial cells, we detected fewer than one mRNA copy of *ACE2* per cell, and in the conditions tested we did not detect any infection in oligodendrocytes, neither in their cell bodies, nor in myelin fibers. However, myelinated neurons were infected[94]. Neurons are largely nonrenewable and are known to respond moderately to inflammatory and antiviral cytokine stimuli in order to maintain their essential activity[71,95,96]. This may explain at least partially their higher susceptibility to numerous viruses, including SARS-CoV-2. Overall, our results in hamsters but not in wild-type mice suggest an early tropism for specific subtypes of neurons in the CNS, in distinction to the broader range of cells targeted in the lungs.

At the intracellular level, infected lung and brain cultures displayed numerous vacuoles, cytoplasm material degradation, marks of stress, membrane coiling, and disorganized Golgi apparatuses as evidence of cell degeneration or death. Cell death has been evaluated in SARS-CoV-2-infected organs in vivo (i.e., in hamster lungs) and in neurons from human brain organoids[45,93]. Our experiments revealed that apoptosis, necroptosis, and pyroptosis occurred during SARS-CoV-2 infection in both lungs and the brainstem (Fig. 6). Apoptosis was directly observed in both lung and brainstem cells via TEM analysis (Fig. 6), and TUNEL assays showed that very few cells undergoing apoptosis were infected, suggesting that apoptosis may occur through indirect stimuli. Necroptosis, a cell death mechanism involving TNFα stimuli[97,98], appeared in both organotypic cultures, consistent with the uncontrolled expression of TNFα and high levels of MLKL mRNA we found over the 4 days of infection in both the lungs and brainstem, compared to non-infected cultures. A signature of pyroptosis emerged in both ex vivo systems, as indicated by the high levels of Gasdermin D mRNA. However, it has been reported that pyroptosis can be triggered through two distinct pathways, either

through direct pathogen recognition and IL-1β[99] or the activation of ST2 receptors by IL-33[100]. The discordant results we obtained for IL-1β mRNA between the brainstem and the lungs demonstrate tissue-dependent pyroptosis. Although IL-18 mRNA copy number remained low in both organs, the brainstem showed a large increase in IL-1β mRNA levels that are known to be associated with Gasdermin D involvement[101]. In contrast, the levels of IL-1β mRNA remained low despite the upregulation of IL-1β, demonstrating that pyroptosis operates differently in the lungs and the brainstem.

In support of this hypothesis, a previous study demonstrated that high levels of IL-33 were released and ST2 receptors signaling pathways were highly triggered during infection of epithelial airway tissues, provoking further pyroptosis[102]. Altogether, our observations suggest that tissue-associated cell death induced by SARS-CoV-2 infection in both organs could be the result of distinct dysregulated inflammatory responses. Such distinct cytotoxicity may also partially explain the lower representation of SARS-CoV-2 in the human CNS. In this case, the virus may kill neurons it infects at the periphery faster than it spreads. Thus, even a very low level of neuron infection may have important side effects leading to vagus nerve dysfunction or to the initiation of encephalitis[84].

The IFN-I and IFN-III responses were triggered in various in vitro and in vivo models during SARS-CoV-2 infection[103,104]. We confirmed these results in our ex vivo organotypic cultures, showing an increase of both IFN-I and IFN-III-triggered ISGs ISG20 and MX1 mRNA levels mainly involved in establishing optimal antiviral and inflammatory environments when their expressions are correctly balanced (Fig. 7).

In parallel, we demonstrated increased mRNA levels for CXCL10 and CCL5, attractant chemokines that recruit inflammatory mediators. As expected from the delay in the start of viral replication, CXCL10, and CCL5 responses were delayed in the brainstem compared with the lungs, reflecting the discrepancies in cell susceptibility to viral infection in the two tissues.

Apart from allowing better characterizing SARS-CoV-2 infection in the tissue, our organotypic cultures have proved applicable for drug testing. Our data with remdesivir, hydroxychloroquine, and 17-DMAG demonstrated that both hamster lung and brainstem organotypic cultures can serve as efficient tools for screening antiviral drugs and predicting their efficacy and toxicity in vivo. More specifically, the lack of expression of *TMPRSS2* in the brainstem suggests that, unlike in the lungs, the S in it is cleaved predominantly by endosomal cathepsins as opposed to cell-surface proteases. As hydroxychloroquine blocks virus-endosome fusion by increasing the endosomal pH[59], our data showing its efficacy in the brainstem but not in the lungs confirm that our model can predict the lack of in vivo effectiveness of a drug. Even in the context of infection with respiratory viruses such as SARS-CoV-2, which do not use the CNS as their main target, brainstem and cerebellum cultures are highly relevant tools for testing drugs that may target the endosomal pathway. The use of both lung and brain cultures to assess the efficacy of antivirals creates an ideal combination for extrapolating their activity in vivo. This could be applied not only against SARS-CoV-2 but also against other respiratory viruses known to be capable of invading the CNS.

In this study, we characterize two ex vivo models to establish their utility for investigating infectious pathogens. We demonstrate that organotypic lung and brainstem cultures are relevant 3D physiological models for several human viral infections, including that by SARS-CoV-2, which are useful for assessing antiviral drugs potentially efficient during the early stages of the infection. These models can also lend themselves to real-time evaluation of emerging mutants. SARS-CoV-2-infected type 1 and type 2 pneumocytes and ciliated cells in the lungs, and granular and Golgi neurons in cerebral structures.

Expression of *ACE2*, *TMPRSS2,* and *Cathepsin* B in organotypic cultures was consistent with the in vivo distribution of SARS-CoV-2 during the first 4 days of infection. We highlight a correlation between *TMPRSS2* expression levels and a delay in CNS infection at the organ level, which could offer the innate immune system a window of opportunity for preventing CNS infection. Once SARS-CoV-2 reaches the brain parenchyma, the virus could infect specific neurons potentially involved in respiratory and cardiac function in the brainstem and cerebellum. We describe the induction of type I and III innate immune responses and an inflammatory response to infection at the organ level. Finally, in both organotypic cultures, we observe cell death caused by the infection via caspase-3-independent apoptosis, necroptosis, and pyroptosis.

Methods

Viruses. BetaCoV/France/IDF0571/2020 virus (GISAID Accession ID = EPI_ISL_411218) was isolated in Vero E6 from a nasal swab of one of the first COVID-19-positive patients in France[105] and was kindly provided by the Virpath lab.

2019-nCoV/USA_WA1/2020 virus was isolated by the CDC in the United States, from the first patient diagnosed in the US.

The recombinant NeonGreen SARS-CoV-2 virus (icSARS-CoV-2-mNG) has been generated by introducing the neon green reporter gene into the ORF7 of the viral genome as described elsewhere[54].

The recombinant Measles virus (MeV IC323-EGFP-F L454W) is a hyperfusogenic MeV variant able to disseminate in the absence of known receptors[106]. This variant is expressing the gene encoding EGFP and was generated using reverse genetics in 293-3-46 cells as previously described[107] after modification of the plasmid encoding MeV IC323-EGFP (kindly provided by Yanagi, Kyushu University, Fukyoka, Japan). The recombinant Nipah virus (rNiV-EGFP) is expressing the gene encoding the EGFP and was generated using reverse genetics in 293 cells and prepared as previously described[108]. NiV infections were carried out at the INSERM Jean Mérieux BSL4 laboratory in Lyon, France.

All viruses have been produced and titrated at 37 °C in Vero E6 cells (SARS-CoV-2 and rNiV-EGFP viruses) or in Vero E6-expressing human SLAM receptor (MeV IC323-EGFP-F L454W) (Supplementary Table 1). Briefly, for stock production, cells were infected with MOI = 0.01 in DMEM. After 90 min of incubation at 37 °C, the medium was replaced with DMEM-2% FBS (SARS-CoV-2) or added in order to obtain DMEM-5% FBS (rNiV-EGFP and MeV IC323-EGFP-F L454W), and the cells were incubated at 37 °C in 5% CO_2 atmosphere for two days. Viral supernatants were collected and centrifuged (400 × *g*, 5 min), aliquoted, and titrated as plaque-forming units using a classic dilution limit assay.

Alamar blue assay. The organotypic cultures ($n = 6$) were immersed in 200 µl of 1× Alamarblue® (Invitrogen; DAL1025) solution in a culture medium for 2 h at 37 °C in a humidified atmosphere in 5% CO_2. The fluorescence was read in a 96-well white plate using 560/590 nm (ex/em) filter settings according to the manufacturer's protocol.

ACE2 activity assay. The ACE2 enzymatic activity was quantified using 100 µg of organotypic cultures ($n = 3$) using the ACE2 Activity Assay Kit (Fluorometric) (CliniSciences; K897-100) and following the manufacturer recommendations. Total protein was quantified using the Micro BCA Protein Assay Kit (Thermo Fisher Scientific).

Animals. Suckling Syrian golden hamsters (Mesocricetus auratus) used in our study were obtained from Janvier Labs (53940 Le Genest-Saint-Isle, France) with clean health monitoring report. C57BL/6 suckling mice are coming from the animal facility "Plateau de Biologie Expérimentale de la Souris" (PBES) in Lyon.

All animals were used at seven days old. The sex of the animals was random and dependent on the litter threw by the mother.

This study was performed according to French ethical committee (CECCAPP) regulations (accreditation CECCAPP_ENS_2014_034).

Organotypic culture preparation and treatment. Organotypic cultures were prepared from suckling hamsters (*Mesocricetus auratus*, Janvier lab) or C57BL/6 mice (Supplementary Fig. 3) and maintained in culture as detailed elsewhere[50]. In brief, organ substructures (i.e., cerebellum, brainstem, left lung) were isolated from 7-day-old animals ($n = 5$; sex non-discriminated) and cut with a McIlwain tissue chopper (WPI-Europe): 350-µm-thick progressive slices were prepared for brainstems and cerebella, and 500-µm-thick slices for the lungs. The cultures were then separated from each other in cold Hibernate®-A/5 g/L D-Glucose/1× Kynurenic acid buffer and laid out on hydrophilic PTFE cell culture insert membranes (PICM0RG50, Millipore). Slices were subsequently cultured in Minimal Essential

Medium GlutaMAX supplemented with 25% horse serum, 5 g/L glucose, 1% HEPES (all Thermo Fisher Scientific), and 0.1 mg/L human recombinant insulin (Sigma-Aldrich) at 37 °C in 5% CO_2. The medium was changed every other day after the slicing procedure. Slices from 5 hamsters were infected on the day of slicing with SARS-CoV-2 (BetaCoV/France/IDF0571/2020), icSARS-CoV-2-mNG[54], MeV IC323-EGFP-F L454W and rNiV-eGFP. For the treatment, cultures were then treated from 90 min post infection to day 4 post infection either with remdesivir (GS-5734; Clinisciences) diluted in Neurobasal medium or with vehicle (untreated condition) once a day for the 10 µM dose and twice a day for the 2 µM condition. In all, 2 µl of 100 µM or 20 µM of remdesivir were added on top of each of the 5 slices in each well and the remdesivir concentration in the feeding medium was also adjusted in order to reach a final concentration of 10 µM or 2 µM in the insert. The cultures were also treated daily under the same condition with the 17-DMAG (17-Dimethylaminoethylamino-17-demethoxygeldanamycin, Sigma; D5193) at 3 µM and with Hydroxychloroquine sulfate (Sigma; H0915-5MG) at 10 µM and 20 µM. At each time point, slices were collected, and the RNA was extracted in order to perform RT-qPCR.

RNA extraction and quantitative RT-PCR. Total RNA from organotypic cultures was extracted using the NucleoSpin RNA Kit (Macherey-Nagel) and quantified with a spectrophotometer (DS-11-FX, DeNovix). For an upcoming SARS-CoV-2 genome quantification, reflecting the viral replication, 100 ng of total RNA were reverse-transcribed using the SuperScript™ III Reverse Transcriptase (Invitrogen) with the SARS-CoV2_tagged primer: 5′-gcagggcaatctca-caatcaggGGTCTGCATGAGTTTAGG-3′ that binds in the intergenic sequence between the N gene and the ORF10. To improve the specificity of the RT-qPCR we have opted for this specific reverse transcription using a primer specific to SARS-CoV-2 genome tagged with a Nipah virus (NiV) derived sequence. The qPCR step uses then a reverse primer against SARS-CoV-2 and a forward primer against NiV extension. To quantify the viral transcription, 100 ng of total RNA were reverse-transcribed using the SuperScript™ III Reverse Transcriptase (Invitrogen) with oligo-dT primers. qPCR was performed using the primers for SARS-CoV-2 Nucleoprotein (Supplementary Table 2).

For the *GAPDH* (Glyceraldehyde 3-phosphate dehydrogenase) and all other genes, 100 ng of total RNA were reverse-transcribed using the iScript cDNA Synthesis Kit (Bio-Rad), based on oligo-dT and random hexamer primers. Obtained cDNAs were diluted 1 : 10. Quantitative PCR was performed using Platinum SYBR Green qPCR SuperMix-UDG (Invitrogen) on a StepOnePlus Real-Time PCR System (Applied Biosystems). Primers were either designed using the Beacon Designer (version 8) software or chosen after validation that their efficacy was close to 100% according to the MIQE checklist[109]. All samples were run in duplicates and results were analyzed using StepOne version 2.3 (Applied Biosystems). All results were normalized to the standard deviation (SD) for *GAPDH* mRNA, and the calculations were performed using the 2ΔΔCT model[110]. For each time point, fold changes are relative to the number of copies of mRNAs in infected organotypic cultures compared to the uninfected ones.

Organotypic culture RNA-Seq and analysis. RNA from uninfected and infected hamster organotypic cultures (a pool of five slices) was collected and extracted as described above and submitted to the JP Sulzberger Columbia Genome Center for library preparation and sequencing. Strand-specific RNA-Seq libraries were prepared using a poly-A enrichment and were sequenced on an Illumina NovaSeq 6000 with paired-end 2 × 100 reads (Nextera xt kit; Illumina). After quality and adapter trimming with Trimmomatic v0.39[111], transcript abundance quantification was performed using Kallisto version 0.46.0[112] with the Ensembl *Mesocricetus auratus* v1.0 as the reference genome.

Differential gene expression analysis was performed using the Kallisto transcript abundances and the R Bioconductor package DESeq2[113]. In lung cultures, 262 genes out of 15,870 expressed genes were differentially expressed (DE) at a threshold of the absolute value of log2-fold change >2. In brainstem cultures, 170/16041 expressed genes were DE. Code for analysis is available at https://github.com/greninger-lab/SARS-CoV-2_hamster_RNAseq.

Since the hamster genome remains relatively poorly annotated, GO analysis was performed using mouse annotations to test for statistical enrichment of DE genes in GO categories. After the exclusion of genes that did not have a mouse ortholog, 195 DE genes out of 11,726 were analyzed for the lung, and 125/12,698 for the brainstem, using the R package clusterProfiler[114]. For each tissue, the 20 non-redundant GO categories with the lowest adjusted p value for Fisher exact test of enrichment were displayed using ggplot, version 3.3.5[115].

To calculate % reads on target for SARS-CoV-2 reads, each sample was aligned against the EPI_ISL_411218 SARS-CoV-2 reference sequence using Bowtie2 with default parameters[116]. SARS-CoV-2 on target percentages were calculated using the number of mapped reads in the resulting BAM file.

Heatmaps were generated using the R package pheatmap by calculating the log2-fold change for infected samples relative to uninfected ones and taking the 50 with the largest absolute value, after eliminating those in which there were fewer than five normalized counts in the uninfected sample for the lungs, or one for the brain. Genes for which the annotation did not include a formal gene symbol were manually searched in the Ensembl database for highly conserved rodent orthologs, which are included next to the Ensembl gene name in the heatmaps.

Immunofluorescent staining. Organotypic cultures from 7-day-old hamsters were infected with 1000 PFU of BetaCoV/France/IDF0571/2020 virus. In all, 24 h post infection, the slices were fixed during 1 h in 4% paraformaldehyde (PFA), washed in 1× Dulbecco's phosphate-buffered saline (DPBS), and permeabilized and blocked in 1× DPBS-3% BSA- Triton X-100 (perm and block solution) overnight at 4 °C. Slices were incubated in the perm and block solution containing the primary antibodies overnight at 4 °C. After three washes (5 min each) in 1× DPBS, slices were incubated in the perm and block solution containing the secondary antibodies for 1 h at RT; donkey anti-rabbit conjugated with Alexa 488 or 555, donkey anti-mouse conjugated with Alexa 488 or 555, and donkey anti-goat conjugated with Alexa 555 or 647 antibodies (1:500 each) (Supplementary Table 3). After 3 washes in 1× DPBS, slices were mounted with Fluoromount-G® aqueous mounting medium (SouthernBiotech, catalog no. 0100-01) on epoxy slides (CEL-LINE, catalog no. 30-12A-BLACK-CE24) and coverslipped. Images were taken using an inverted microscope Zeiss Axio Observer. Z1 with confocal unit LSM 800 and analyzed using ImageJ software. All primary antibodies used in this study were validated previously for use in hamster tissue or the sequence homology of the epitopes was more than 85%.

TUNEL assay. TUNEL assay (Click-iT™ Plus TUNEL Assay for In Situ Apoptosis Detection, Alexa Fluor™ 647 dye, Thermo Fisher Scientific) was performed following the manufacturer's recommendations.

Transmission electron microscopy. Infected organotypic cultures were fixed by immersion in 2.5% glutaraldehyde (Sigma) and 2.5% PFA in cacodylate buffer (0.1 M, pH 7.2) at 4 °C for several days. The samples were post fixed in 1% osmium tetroxide in 0.1 M cacodylate buffer for 1 h at 4 °C, and rinsed with Cacodylate buffer 0.1 M (2 × 10 min) and with water (2 × 10 min) and immersed in uranyl acetate at 4% for 2 h at 4 °C. Samples were dehydrated through graded alcohol (50, 70, 90, and 100%) and propylene oxide for 30 min each and embedded in Epon™ 812 (Sigma-Aldrich, Saint-Louis, Missouri, USA). Semi-thin sections were cut at 2 µm with an ultra-microtome (Leica Ultracut UCT) and stained with 1% Toluidine blue in 1% sodium borate, examined by Leica optical microscope (LEICA DMLB, Leica Microsystems GmbH; Germany). Ultrathin sections were cut at 70 nm and contrasted with uranyl acetate and lead citrate and examined at 70 kv with a Morgagni 268D electron microscope (FEI Electron Optics, Eindhoven, and the Netherlands). Images were captured digitally by Mega View III camera (Soft Imaging System).

Fluorescence-activated single-cell sorting (FACS). Five cerebella from suckling hamster (10 organotypic cultures per cerebellum) were dissociated in a solution of 10 mg/ml of pre-activated papaïn diluted in DMEM containing 10% kynurenic acid. After a 30 min incubation at 37 °C the reaction was stopped by adding FBS. The cells were then split into five separate tubes, washed with Neurobasal medium (Gibco; 12348017), and centrifuged at 400 × g for 5 min. Each cell population was stained for 30 min at 4 °C using the following antibodies (Supplementary Table 4). Cells were washed with Neurobasal medium, centrifuged at 400 × g for 5 min, and resuspended in 1 ml of Neurobasal medium. The cell was sorted using BD FACSAria™ II and collected in 600 µl of RLT with beta-mercaptoethanol. The RNA was then extracted as described above, Reverse transcription was performed using the iScript kit (Biorad) and the mRNA copies of the gene of interest were quantified by RT-qPCR as described above.

Statistical analysis. Statistical analyses for figs. 1 and 2 were performed using the Kruskal–Wallis test. ***$P < 0.001$. For Figs. 4 and 5, statistical analyses were performed using the Mann–Whitney test and the one-sample t test. *$P < 0.05$; **$P < 0.01$; ***$P < 0.001$. All statistical analyses were performed in GraphPad Prism5 software.

Reporting summary. Further information on research design is available in the Nature Research Reporting Summary linked to this article.

Data availability

The data generated in this study have been deposited in the Figshare database under accession code https://doi.org/10.6084/m9.figshare.15112443.v1[117]. Source data are provided with this paper.

Code availability

For the RNA-seq data, code for analysis is available at https://github.com/greninger-lab/SARS-CoV-2_hamster_RNAseq[118].

Received: 27 November 2020; Accepted: 9 September 2021;
Published online: 04 October 2021

References

1. Worldometer. Coronavirus Cases. *Worldometer* (2021). Available at: https://www.worldometers.info/coronavirus/. (Accessed: 20th April 2021).
2. Orsucci, D., Ienco, E. C., Nocita, G., Napolitano, A. & Vista, M. Neurological features of COVID-19 and their treatment: a review. *Drugs Context* **9**, 2020-5-1 (2020).
3. Khoo, A. et al. Postinfectious brainstem encephalitis associated with SARS-CoV-2. *J. Neurol. Neurosurg. Psychiatry* **91**, jnnp-2020–323816 (2020).
4. Rábano-Suárez, P. et al. Generalized myoclonus in COVID-19. *Neurology* **95**, e767–e772 (2020).
5. Solomon, I. H. et al. Neuropathological features of covid-19. *N. Engl. J. Med.* **383**, 989–992 (2020).
6. Bougakov, D., Podell, K. & Goldberg, E. Multiple Neuroinvasive Pathways in COVID-19. *Mol. Neurobiol.* https://doi.org/10.1007/s12035-020-02152-5 (2020).
7. Jafari Khaljiri, H. et al. Comprehensive review on neuro-COVID-19 pathophysiology and clinical consequences. *Neurotox. Res.* **39**, 1613–1629 (2021).
8. Chigr, F., Merzouki, M. & Najimi, M. Comment on "The neuroinvasive potential of SARS-CoV-2 may play a role in the respiratory failure of COVID-19 patients". *J. Med. Virol.* **92**, 703–704 (2020).
9. Li, Y. C., Bai, W. Z. & Hashikawa, T. The neuroinvasive potential of SARS-CoV2 may play a role in the respiratory failure of COVID-19 patients. *J. Med. Virol.* **92**, 552–555 (2020).
10. Smith, J. C., Ellenberger, H. H., Ballanyi, K., Richter, D. W. & Feldman, J. L. Pre-Bötzinger complex: a brainstem region that may generate respiratory rhythm in mammals. *Science* **254**, 726–729 (1991).
11. Netland, J., Meyerholz, D. K., Moore, S., Cassell, M. & Perlman, S. Severe acute respiratory syndrome coronavirus infection causes neuronal death in the absence of encephalitis in mice transgenic for human ACE2. *J. Virol.* **82**, 7264–7275 (2008).
12. Meinhardt, J. et al. Olfactory transmucosal SARS-CoV-2 invasion as a port of central nervous system entry in individuals with COVID-19. *Nat. Neurosci.* **24**, 168–175 (2021).
13. Liu, K., Pan, M., Xiao, Z. & Xu, X. Neurological manifestations of the coronavirus (SARS-CoV-2) pandemic 2019-2020. *J. Neurol. Neurosurg. Psychiatry* **91**, 669–670 (2020).
14. Bulfamante, G. et al. First ultrastructural autoptic findings of sars-cov-2 in olfactory pathways and brainstem. *Minerva Anestesiologica* **86**, 678–679 (2020).
15. Xiang, P. et al. Case report: identification of SARS-CoV-2 in cerebrospinal fluid by ultrahigh-depth sequencing in a patient with coronavirus disease 2019 and neurological dysfunction. *Front. Med.* **8**, 629828 (2021).
16. Domingues, R. B. et al. First case of SARS-COV-2 sequencing in cerebrospinal fluid of a patient with suspected demyelinating disease. *J. Neurol.* **267**, 3154–3156 (2020).
17. Huang, Y. H., Jiang, D. & Huang, J. T. SARS-CoV-2 detected in cerebrospinal fluid by PCR in a case of COVID-19 encephalitis. *Brain Behav. Immun.* **87**, 149 (2020).
18. Färber, K., Stäbler, P., Getzinger, T. & Uhlig, T. Suspected sepsis in a 10-week-old infant and SARS-CoV-2 detection in cerebrospinal fluid and pharynx. *Monatsschr. Kinderheilkd.* **169**, 312–316 (2021).
19. Fadakar, N. et al. A first case of acute cerebellitis associated with coronavirus disease (COVID-19): a case report and literature review. *Cerebellum* **19**, 911–914 (2020).
20. Khodamoradi, Z. et al. COVID-19 meningitis without pulmonary involvement with positive cerebrospinal fluid PCR. *Eur. J. Neurol.* **27**, 2668–2669 (2020).
21. Destras, G. et al. Systematic SARS-CoV-2 screening in cerebrospinal fluid during the COVID-19 pandemic. *Lancet Microbe* **1**, e149 (2020).
22. Westhoff, T. H. et al. Allograft infiltration and meningoencephalitis by SARS-CoV-2 in a pancreas-kidney transplant recipient. *Am. J. Transplant.* **20**, 3216–3220 (2020).
23. Yachou, Y., El Idrissi, A., Belapasov, V. & Ait Benali, S. Neuroinvasion, neurotropic, and neuroinflammatory events of SARS-CoV-2: understanding the neurological manifestations in COVID-19 patients. *Neurol. Sci.* **41**, 2657–2669 (2020).
24. Yi, S. A. et al. Infection of brain organoids and 2D cortical neurons with SARS-CoV-2 pseudovirus. *Viruses* **12**, 10004 (2020).
25. Zhang, B. Z. et al. SARS-CoV-2 infects human neural progenitor cells and brain organoids. *Cell Res.* **30**, 928–931 (2020).
26. Bullen, C. K. et al. Infectability of human BrainSphere neurons suggests neurotropism of SARS-CoV-2. *ALTEX* **37**, 665–671 (2020).
27. Pellegrini, L. et al. SARS-CoV-2 infects the brain choroid plexus and disrupts the blood-CSF barrier in human brain organoids. *Cell Stem Cell* **27**, 951–961.e5 (2020).
28. Moriguchi, T. et al. A first case of meningitis/encephalitis associated with SARS-coronavirus-2. *Int. J. Infect. Dis.* **94**, 55–58 (2020).
29. Song, E. et al. Neuroinvasion of SARS-CoV-2 in human and mouse brain. *J Exp Med.* **218**, e20202135. https://doi.org/10.1084/jem.20202135 (2021).
30. Buzhdygan, T. P. et al. The SARS-CoV-2 spike protein alters barrier function in 2D static and 3D microfluidic in-vitro models of the human blood–brain barrier. *Neurobiol. Dis.* **146**, 105131 (2020).
31. Uversky, V. N. et al. Severe acute respiratory syndrome coronavirus 2 infection reaches the human nervous system: how? *J. Neurosci. Res.* **99**, 750–777 (2021).
32. Zhou, P. et al. A pneumonia outbreak associated with a new coronavirus of probable bat origin. *Nature* **579**, 270–273 (2020).
33. Hoffmann, M. et al. SARS-CoV-2 cell entry depends ACE2 TMPRSS2 and is blocked a clinically proven protease inhibitor. *Cell* **181**, 271–280.e8 (2020).
34. Coutard, B. et al. The spike glycoprotein of the new coronavirus 2019-nCoV contains a furin-like cleavage site absent in CoV of the same clade. *Antiviral Res.* **176**, 104742 (2020).
35. Shang, J. et al. Cell entry mechanisms of SARS-CoV-2. *Proc. Natl. Acad. Sci. USA* **117**, 104742 (2020).
36. Cantuti-Castelvetri, L. et al. Neuropilin-1 facilitates SARS-CoV-2 cell entry and infectivity. *Science* **370**, 856–860 (2020).
37. Daly, J. L. et al. Neuropilin-1 is a host factor for SARS-CoV-2 infection. *Science* **370**, 861–865 (2020).
38. Lee, C.-Y. & Lowen, A. C. Animal models for SARS-CoV-2. *Curr. Opin. Virol.* **68**, 1868–1885 (2021).
39. Miao, J., Chard, L. S., Wang, Z. & Wang, Y. Syrian hamster as an animal model for the study on infectious diseases. *Front. Immunol.* **10** (2019).
40. Wong, K. T. et al. A golden hamster model for human acute Nipah virus infection. *Am. J. Pathol.* **163**, 2127–2137 (2003).
41. Watanabe, S. et al. Mutant fusion proteins with enhanced fusion activity promote measles virus spread in human neuronal cells and brains of suckling hamsters. *J. Virol.* **87**, 2648–2659 (2013).
42. Roberts, A. et al. Severe acute respiratory syndrome coronavirus infection of golden syrian hamsters. *J. Virol.* **79**, 503–511 (2005).
43. Roberts, A. et al. Animal models and vaccines for SARS-CoV infection. *Virus Res.* **133**, 20–32 (2008).
44. Imai, M. et al. Syrian hamsters as a small animal model for SARS-CoV-2 infection and countermeasure development. *Proc. Natl. Acad. Sci. USA* **117**, 16587–16595 (2020).
45. Chan, J. F. W. et al. Simulation of the clinical and pathological manifestations of Coronavirus Disease 2019 (COVID-19) in golden Syrian hamster model: implications for disease pathogenesis and transmissibility. *Clin. Infect. Dis.* **71**, 2428–2446 (2020).
46. Bryche, B. et al. Massive transient damage of the olfactory epithelium associated with infection of sustentacular cells by SARS-CoV-2 in golden Syrian hamsters. *Brain. Behav. Immun.* **89**, 579–586 (2020).
47. Sia, S. F. et al. Pathogenesis and transmission of SARS-CoV-2 in golden hamsters. *Nature* **583**, 834–838 (2020).
48. Abbas Rizvi, Z. et al. Immunological and cardio-vascular pathologies associated with SARS-CoV-2 infection 1 in golden syrian hamster. *Transl. Heal. Sci. Technol. Inst.* https://doi.org/10.1101/2021.01.11.426080 (2021).
49. Nouailles, G. et al. Longitudinal omics in Syrian hamsters integrated with human data unravel 1 cellular effector responses to moderate COVID-19 2 3. *bioRxiv* https://doi.org/10.1101/2020.12.18.423524 (2021).
50. Welsch, J. et al. Organotypic brain cultures: a framework for studying CNS infection by neurotropic viruses and screening antiviral drugs. *Bio-protocol* **7**, https://doi.org/10.21769/BioProtoc.2605 (2017).
51. Gkogkou, E., Barnasas, G., Vougas, K. & Trougakos, I. P. Expression profiling meta-analysis of ACE2 and TMPRSS2, the putative anti-inflammatory receptor and priming protease of SARS-CoV-2 in human cells, and identification of putative modulators. *Redox Biol.* **36**, 101615 (2020).
52. Humpel, C. Organotypic brain slice cultures: a review. *Neuroscience* **305**, 86–98 (2015).
53. Brann, D. H. et al. Non-neuronal expression of SARS-CoV-2 entry genes in the olfactory system suggests mechanisms underlying COVID-19-associated anosmia. *Sci. Adv.* **6**, eabc5801 (2020).
54. Xie, X. et al. An Infectious cDNA Clone of SARS-CoV-2. *Cell Host Microbe* **27**, 841–848.e3 (2020).
55. Jurgens, E. M. et al. Measles fusion machinery is dysregulated in neuropathogenic variants. *MBio* **6**, 1–12 (2015).
56. Pizzorno, A. et al. In vitro evaluation of antiviral activity of single and combined repurposable drugs against SARS-CoV-2. *Antiviral Res.* **181**, 104878 (2020).
57. Wang, Y. et al. Remdesivir in adults with severe COVID-19: a randomised, double-blind, placebo-controlled, multicentre trial. *Lancet* **395**, 1569–1578 (2020).
58. Beigel, J. H. et al. Remdesivir for the treatment of Covid-19 — final report. *N. Engl. J. Med.* **383**, 1813–1826 (2020).
59. Kivrak, A., Ulaş, B. & Kivrak, H. A comparative analysis for anti-viral drugs: their efficiency against SARS-CoV-2. *Int. Immunopharmacol.* **90**, 107232 (2021).

60. NIH Clinical Trial Shows Remdesivir Accelerates Recovery from Advanced COVID-19 | NIH: National Institute of Allergy and Infectious Diseases. Available at: https://www.niaid.nih.gov/news-events/nih-clinical-trial-shows-remdesivir-accelerates-recovery-advanced-covid-19. (Accessed: 18th April 2021).
61. Wang, M. et al. Remdesivir and chloroquine effectively inhibit the recently emerged novel coronavirus (2019-nCoV) in vitro. *Cell Res.* **30**, 269–271 (2020).
62. Yao, X. et al. In vitro antiviral activity and projection of optimized dosing design of hydroxychloroquine for the treatment of severe acute respiratory syndrome coronavirus 2 (SARS-CoV-2). *Clin. Infect. Dis.* **71**, 732–739 (2020).
63. Sultan, I., Howard, S. & Tbakhi, A. Drug repositioning suggests a role for the heat shock protein 90 inhibitor geldanamycin in treating COVID-19 infection. https://doi.org/10.21203/rs.3.rs-18714/v1 (2020).
64. Kim, W. et al. Rational biosynthetic engineering for optimization of geldanamycin analogues. *ChemBioChem* **10**, 1243–1251 (2009).
65. Bloyet, L.-M. et al. HSP90 chaperoning in addition to phosphoprotein required for folding but not for supporting enzymatic activities of measles and nipah virus L polymerases. *J. Virol.* **90**, 15 (2016).
66. Miller, S. & Krijnse-Locker, J. Modification of intracellular membrane structures for virus replication. *Nat. Rev. Microbiol.* **6**, 363–374 (2008).
67. Snijder, E. J. et al. Ultrastructure and origin of membrane vesicles associated with the severe acute respiratory syndrome coronavirus replication complex. *J. Virol.* **80**, 5927–5940 (2006).
68. Lieberman, J., Wu, H. & Kagan, J. C. Gasdermin D activity in inflammation and host defense. *Sci. Immunol.* **4**, eaav1447 (2019).
69. de Vasconcelos, N. M., Van Opdenbosch, N., Van Gorp, H., Parthoens, E. & Lamkanfi, M. Single-cell analysis of pyroptosis dynamics reveals conserved GSDMD-mediated subcellular events that precede plasma membrane rupture. *Cell Death Differ.* **26**, 146–161 (2019).
70. Viemari, J. C., Menuet, C. & Hilaire, G. Complexe de pré-Bötzinger et automatisme respiratoire Identification lectrophysiologique, molculaire et gntique dune structure cruciale pour la respiration. *Med. Sci.* **29**, 875–882 (2013).
71. Welsch, J. C. et al. Type I interferon receptor signaling drives selective permissiveness of astrocytes and microglia to measles virus during brain infection. *J. Virol.* **93**, e00618-19 (2019).
72. de Vries, R., Rennick, L., Duprex, W. & de Swart, R. Paramyxovirus infections in ex vivo lung slice cultures of different host species. *Methods Protoc.* **1**, 12 (2018).
73. Nguyen, D. T. et al. Paramyxovirus infections in ex vivo lung slice cultures of different host species. *J. Virol. Methods* **193**, 159–165 (2013).
74. Forsberg, D. et al. CO2-evoked release of PGE2 modulates sighs and inspiration as demonstrated in brainstem organotypic culture. *Elife* **5**, e14170 (2016).
75. Phillips, W. S., Herly, M., Del Negro, C. A. & Rekling, J. C. Organotypic slice cultures containing the preBötzinger complex generate respiratory-like rhythms. *J. Neurophysiol.* **115**, 1063–1070 (2016).
76. Cavaliere, F., Vicente, E. S. & Matute, C. An organotypic culture model to study nigro-striatal degeneration. *J. Neurosci. Methods* **188**, 205–212 (2010).
77. Busceti, C. L. et al. Corticosterone upregulates gene and protein expression of catecholamine markers in organotypic brainstem cultures. *Int. J. Mol. Sci.* **20**, 2901 (2019).
78. Han, Y. et al. Identification of candidate COVID-19 therapeutics using hPSC-derived lung organoids. *bioRxiv* https://doi.org/10.1101/2020.05.05.079095 (2020).
79. Outlaw, V. K. et al. Inhibition of Coronavirus entry in vitro and ex vivo by a lipid-conjugated peptide derived from the SARS-CoV-2 spike glycoprotein HRC domain. *MBio* **11**, e01935-20 (2020).
80. Ferren, M., Horvat, B. & Mathieu, C. Measles encephalitis: towards new therapeutics. *Viruses* **11**, 1017 (2019).
81. Tomris, I. et al. 3D visualization of SARS-CoV-2 infection and receptor distribution in Syrian hamster lung lobes display distinct spatial arrangements. *bioRxiv* https://doi.org/10.1101/2021.03.24.435771 (2021).
82. Hamming, I. et al. Tissue distribution of ACE2 protein, the functional receptor for SARS coronavirus. A first step in understanding SARS pathogenesis. *J. Pathol.* **203**, 631–637 (2004).
83. Pizzorno, A. et al. Characterization and treatment of SARS-CoV-2 in nasal and bronchial human airway epithelia. *Cell Rep. Med.* **1**, 100059 (2020).
84. Yavarpour-Bali, H. & Ghasemi-Kasman, M. Update on neurological manifestations of COVID-19. *Life Sci.* **257**, 118063 (2020).
85. atlas.brain-map.org. Interactive Atlas Viewer: Atlas Viewer. Available at: http://atlas.brain-map.org/atlas?atlas=1#atlas=1&plate=100960184&structure=987&x=4526&y=4727.25&zoom=-4&resolution=16.75&z=6. (Accessed: 26th August 2020).
86. Kumar, A. et al. Possible routes of SARS-CoV-2 invasion in brain: in context of neurological symptoms in COVID-19 patients. *J. Neurosci. Res.* **98**, 2376–2383 (2020).
87. Iadecola, C., Anrather, J. & Kamel, H. Effects of COVID-19 on the nervous system. *Cell* **183**, 16–27.e1 (2020).
88. Muus, C. et al. Integrated analyses of single-cell atlases reveal age, gender, and smoking status associations with cell type-specific expression of mediators of SARS-CoV-2 viral entry and highlights inflammatory programs in putative target cells. *bioRxiv* https://doi.org/10.1101/2020.04.19.049254 (2020).
89. Puelles, V. G. et al. Multiorgan and renal tropism of SARS-CoV-2. *N. Engl. J. Med.* **383**, 590–592 (2020).
90. Liu, J. et al. SARS-CoV-2 cell tropism and multiorgan infection. *Cell Discov.* **7**, 17 (2021).
91. Heurich, A. et al. TMPRSS2 and ADAM17 cleave ACE2 differentially and only proteolysis by TMPRSS2 augments entry driven by the severe acute respiratory syndrome coronavirus spike protein. *J. Virol.* **88**, 1293–1307 (2014).
92. Murgolo, N. et al. SARS-CoV-2 tropism, entry, replication, and propagation: considerations for drug discovery and development. *PLoS Pathogens* **17**, e1009225 (2021).
93. Ramani, A. et al. SARS-CoV-2 targets neurons of 3D human brain organoids. *EMBO J.* **39**, e106230 (2020).
94. Baig, A. M., Khaleeq, A., Ali, U. & Syeda, H. Evidence of the COVID-19 virus targeting the CNS: tissue distribution, host-virus interaction, and proposed neurotropic mechanisms. *ACS Chem. Neurosci.* **11**, 995–998 (2020).
95. Cavanaugh, S. E., Holmgren, A. M. & Rall, G. F. Homeostatic interferon expression in neurons is sufficient for early control of viral infection. *J. Neuroimmunol.* **279**, 11–19 (2015).
96. Patterson, C. E., Daley, J. K., Echols, L. A., Lane, T. E. & Rall, G. F. Measles virus infection induces chemokine synthesis by neurons. *J. Immunol.* **171**, 3102–3109 (2003).
97. Christofferson, D. E. & Yuan, J. Necroptosis as an alternative form of programmed cell death. *Curr. Opin. Cell Biol.* **22**, 263–268 (2010).
98. Vandenabeele, P., Galluzzi, L., Vanden Berghe, T. & Kroemer, G. Molecular mechanisms of necroptosis: an ordered cellular explosion. *Nat. Rev. Mol. Cell Biol.* **11**, 700–714 (2010).
99. Fink, S. L. & Cookson, B. T. Caspase-1-dependent pore formation during pyroptosis leads to osmotic lysis of infected host macrophages. *J. Immunol.* **202**, 1913–1926 (2006).
100. Cohen, E. S. et al. Oxidation of the alarmin IL-33 regulates ST2-dependent inflammation. *Nat. Commun.* **6**, 8327 (2015).
101. Liu, X. et al. Inflammasome-activated gasdermin D causes pyroptosis by forming membrane pores. *Nature* **535**, 153–158 (2016).
102. Yagami, A. et al. IL-33 mediates inflammatory responses in human lung tissue cells. *J. Immunol.* **185**, 5743–5750 (2010).
103. Lokugamage, K. et al. Type I interferon susceptibility distinguishes SARS-CoV-2 from SARS-CoV. *bioRxiv Prepr. Serv. Biol.*, https://doi.org/10.1101/2020.03.07.982264 (2020).
104. Stanifer, M. L. et al. Critical role of type iii interferon in controlling SARS-CoV-2 infection in human intestinal epithelial cells. *Cell Rep.* **32**, 107863 (2020).
105. Lescure, F. X. et al. Clinical and virological data of the first cases of COVID-19 in Europe: a case series. *Lancet Infect. Dis.* **20**, 697–706 (2020).
106. Mathieu, C. et al. Measles virus bearing measles inclusion body encephalitis-derived fusion protein is pathogenic after infection via the respiratory route. *J. Virol.* **93**, e01862-18 (2019).
107. Radecke, F. et al. Rescue of measles viruses from cloned DNA. *EMBO J.* **14**, 5773–5784 (1995).
108. Yoneda, M. et al. Establishment of a Nipah virus rescue system. *Proc. Natl Acad. Sci. USA* **103**, 16508–16513 (2006).
109. Bustin, S. A. et al. The MIQE guidelines: minimum information for publication of quantitative real-time PCR experiments. *Clin. Chem.* **55**, 611–622 (2009).
110. Pfaffl, M. W. A new mathematical model for relative quantification in real-time RT-PCR. *Nucleic Acids Res.* **29**, e45 (2001).
111. Bolger, A. M., Lohse, M. & Usadel, B. Trimmomatic: a flexible trimmer for Illumina sequence data. *Bioinformatics* **30**, 2114–2120 (2014).
112. Bray, N. L., Pimentel, H., Melsted, P. & Pachter, L. Near-optimal probabilistic RNA-seq quantification. *Nat. Biotechnol.* **34**, 525–527 (2016).
113. Love, M. I., Huber, W. & Anders, S. Moderated estimation of fold change and dispersion for RNA-seq data with DESeq2. *Genome Biol.* **15**, 550 (2014).
114. Yu, G., Wang, L. G., Han, Y. & He, Q. Y. ClusterProfiler: an R package for comparing biological themes among gene clusters. *Omi. A J. Integr. Biol.* **16**, 284–287 (2012).
115. Wickham, H. Create Elegant Data Visualisations Using the Grammar of Graphics • ggplot2. (2016). Available at: https://ggplot2.tidyverse.org/.
116. Langmead, B. & Salzberg, S. L. Fast gapped-read alignment with Bowtie 2. *Nat. Methods* **9**, 357–359 (2012).
117. Ferren, M. Data availability_Ferren et al 2021_Hamster organotypic modeling of SARS-CoV-2 lung and brainstem infection.xlsx. *Figshare*, https://doi.org/10.6084/m9.figshare.15112443.v1 (2021).

118. Lieberman, N. A. P. GitHub - greninger-lab/SARS-CoV-2_hamster_RNAseq. *GitHub* (2021). Available at: https://github.com/greninger-lab/SARS-CoV-2_hamster_RNAseq. (Accessed: 6th August 2021).
119. Preibisch, S., Saalfeld, S. & Tomancak, P. Globally optimal stitching of tiled 3D microscopic image acquisitions. *Bioinformatics* **25**, 1463–1465 (2009).

Acknowledgements

Figure 1a has been created with BioRender.com. We thank Bruno Lina, Andres Pizzorno, and Manuel Rosa-Calatrava from the CIRI, Centre International de Recherche en Infectiologie, LYON, France, for providing us with the BetaCoV/France/IDF0571/2020 virus. We acknowledge World Reference Center for Emerging Viruses and Arboviruses (WRCEVA) and UTMB investigator, Dr. Pei Yong Shi for kindly providing recombinant icSARS-CoV-2-mNG virus based on 2019-nCoV/USA_WA1/2020 isolate. We thank Sonia Longhi from AFMB UMR 7257, CNRS and Aix-Marseille University, France, and Frédéric Carrière from BIP UMR 7281, CNRS and Aix-Marseille University, France, for their advice and help with proofreading of the manuscript. We thank Denis Gerlier for his helpful advice and critical reading of the manuscript. We thank Fabienne Archer for providing us with anti-SP-C and anti-αTubulin antibodies and for her precious advice. We thank Sophie Shyfrin for technical assistance and English language revision, and Géraldine Gourru-Lesimple for assistance in laboratory management. This work was supported by ANR-CoronaPepStop (ANR-20-COVI-000) and Fondation de France to BH and ANRS-COV8-SARSRhinCell to CM.

Author contributions

Conceptualization, M.F., C.M., D.D. and M.I.; methodology, M.F. and C.M.; formal analysis, M.F., N.A.P.L. and N.M.; investigation, M.F., D.D., V.F., M.M., J.L.W. and R.P.; resources, O.T.; writing—original draft, M.F., C.M. and M.I.; writing—review & editing, A.M., A.L.G., M.P., N.M., O.T. and B.H.; supervision, C.M.

Competing interests

The authors declare no competing interests.

Additional information

Supplementary information The online version contains supplementary material available at https://doi.org/10.1038/s41467-021-26096-z.

Correspondence and requests for materials should be addressed to Marion Ferren or Cyrille Mathieu.

Peer review information *Nature Communications* thanks Tracy Fischer and the other, anonymous, reviewer(s) for their contribution to the peer review of this work. Peer reviewer reports are available.

Reprints and permission information is available at http://www.nature.com/reprints

Publisher's note Springer Nature remains neutral with regard to jurisdictional claims in published maps and institutional affiliations.

2) Caractérisation d'un nouveau modèle *ex vivo* : les cultures organotypiques de reins de hamsters

a. Article 2 : Développement de modèles organotypiques de hamster pour l'étude de l'infection rénale par le SARS-CoV-2 à un stade précoce

Sophie Shyfrin, Marion Ferren, Didier Decimo, Laure Perrin-Cocon, Maxime Espi, Xavier Charmetant, Manon Brailly, Branka Horvat, Olivier Thauna, Cyrille Mathieu

Prêt pour soumission, 2021

Résumé de l'article :

Chez les patients souffrant du COVID-19 des atteintes rénales allant de la protéinurie à l'insuffisance rénale aiguë (IRA) ont fréquemment été rapportées. En effet, on retrouve une IRA chez 20 % des patients hospitalisés et chez 50 % des patients admis dans les unités de soins intensifs. Malgré les échantillons d'autopsie de patients l'infection du rein par le SARS-CoV-2 reste peu documentée. Dans cet article nous présentons un système de cultures organotypiques de reins de hamsters pour étudier l'infection précoce par le SARS-CoV-2 dans le rein.

La caractérisation de ces nouvelles cultures *ex vivo*, a d'abord confirmé la conservation de la structure avec la présence des néphrons, des tubules proximaux, des podocytes et des cellules endothéliales CD34+ du système vasculaire rénal.

L'évaluation de l'activité respiratoire mitochondriale des cultures a été réalisée par une analyse avec le Seahorse XF Analyzer et a montré que malgré une diminution de l'oxido-réduction mesurée par un test Alamar blue les fonctions mitochondriales (respiration basale, et maximale, consommation d'ATP) n'étaient réduites d'environ 25% qu'après 4 jours de culture. Ce résultat suggère une bonne viabilité des cultures sur cette période. De plus, comme décrit dans la littérature, les récepteurs d'entrée ACE2 et neuropiline-1, ainsi que les protéases TMPRSS2 et les cathepsines B et L sont fortement exprimées dans les cultures. Les cultures organotypiques de rein se sont avérées hautement susceptibles à l'infection par le SARS-CoV-2. Le SARS-CoV-2 cible d'abord les cellules endothéliales puis les tubules proximaux après quelques jours mais très peu de podocytes ont été retrouvés positifs à l'infection après immunomarquage fluorescent. Cela suggère une invasion de l'organe en deux temps avec une évolution permissive des cellules tubulaires suite à l'infection des cellules endothéliales

L'analyse transcriptomique a révélé une répression initiale des cytokines pro-inflammatoires suivie d'une forte régulation positive 3 jours post-infection. L'expression des gènes de réponse à l'interféron est également faible dans les cultures de rein, en accord avec la littérature, et augmente seulement 2 ou 3 jours après le début de l'infection. A moindre niveau que dans les cultures organotypiques de poumons et de tronc cérébral la mort cellulaire par nécroptose et pyroptose

associées à l'infection ont également été observées comme dans les modèles pulmonaires et cérébraux précédemment développés.

Ces résultats montrent que ce nouveau modèle de cultures organotypiques de rein de hamster fournit de nouvelles informations sur la cinétique de l'infection et de la propagation du SARS-CoV-2 dans les reins.

Comme les cultures organotypiques de poumon, de cervelet, d'hippocampe et de tronc cérébrale ces cultures de reins peuvent être réalisées à partir de souris sauvages ou génétiquement modifiées ou à partir d'autres rongeurs, offrant de nombreuses possibilités. De plus, on peut envisager à l'avenir d'étendre cette étude sur des cultures organotypiques de reins humains. On pourrait en effet se procurer des échantillons de reins de patients prélevés au cours d'interventions chirurgicales. L'utilisation de ce modèle peut également être élargie à l'étude de l'infection du rein par d'autres virus et pour évaluer la toxicité rénale de traitements antiviraux. C'est pour compléter mon arsenal d'évaluation de la toxicité organique des antiviraux contre les virus encéphalitogènes que je me suis impliquée dans le développement de ce nouvel outil.

Hamster Organotypic Kidney Culture Modelling of Early-Stage SARS-CoV-2 Infection Highlights a Two-Step Renal Susceptibility

Shyfrin SR[1,2], Ferren M[1,2], Perrin-Cocon L[3], Espi M[4], Charmetant X[4], Brailly M[2], Decimo D[1,2], Horvat B[2], Lotteau V[3], Vidalain P-O[3], Thaunat O[4] and Mathieu C[1,2*].

1- CIRI, Centre International de Recherche en Infectiologie, Team Neuro-Invasion, TROpism and VIRal Encephalitis, Univ Lyon, Inserm, U1111, CNRS, UMR5308, Université Claude Bernard Lyon 1, Ecole Normale Supérieure de Lyon, LYON, France
2-CIRI, Centre International de Recherche en Infectiologie, Team Immunobiology of the Viral infections, Univ Lyon, Inserm, U1111, CNRS, UMR5308, Université Claude Bernard Lyon 1, Ecole Normale Supérieure de Lyon, LYON, France
3-CIRI, Centre International de Recherche en Infectiologie, Team Viral Infection, Metabolism and Immunity, Univ Lyon, Inserm, U1111, CNRS, UMR5308, Université Claude Bernard Lyon 1, Ecole Normale Supérieure de Lyon, LYON, France
4-CIRI, Centre International de Recherche en Infectiologie, Team Normal and pathogenic B cell responses, Univ Lyon, Inserm, U1111, CNRS, UMR5308, Université Claude Bernard Lyon 1, Ecole Normale Supérieure de Lyon, LYON, France
*Correspondence To Cyrille Mathieu at : cyrille.mathieu@inserm.fr

Abstract

The Severe acute respiratory syndrome related coronavirus 2 (SARS-CoV-2) is the etiologic pathogen responsible for Coronavirus disease 2019 (COVID-19). Initially infecting cells in the respiratory tract, it can adversely affect organs outside the respiratory system either via direct infection or its systemic effects such as thrombosis or a deregulated inflammatory response. Kidney pathology is frequently reported in patients hospitalized with COVID-19. Although autopsy samples have provided valuable insights into the renal effects of severe COVID-19 infection, it remains unknown what occurs in the kidney during its initial stages due to the lack of suitable study models. We present a hamster organotypic kidney system as a window onto early SARS-CoV-2 renal infection and a model extendable to other pathogens. We have successfully prepared, maintained and characterized hamster organotypic kidney cultures (OKCs). OKCs maintained key renal structures in their native three-dimensional arrangement. Here, SARS-CoV-2 infected hamster OKCs and replicated

in them, initially targeting endothelial cells and later disseminating into proximal tubules, which are commonly found to be antigen-positive post-mortem. Concomitantly, transcriptomic analysis revealed an initial repression of pro-inflammatory cytokines followed by a strong upregulation. The interferon response was delayed, and indicators of cell death by necroptosis and pyroptosis associated with the infection were observed as well. Our model thus provides new insights into the kinetics of SARS-CoV-2 infection and propagation in the kidneys. They can further serve as a powerful tool for testing the renal toxicity of efficient antivirals in detail prior to *in vivo* validation.

Introduction

Severe acute respiratory syndrome coronavirus 2 (SARS-CoV-2) is the causative agent of Coronavirus Disease 2019 (COVID-19) (P. Zhou et al., 2020), a pandemic disease that has affected 259 million patients and claimed 5.18 million lives worldwide (*Worldometer*, 2021), leading to devastating personal, social, and economic consequences.

Severe clinical manifestations of COVID-19 include but are not limited to acute respiratory distress syndrome (ARDS), thrombosis and cytokine storm. SARS-CoV-2 displays a broad tissue tropism and can cause multiorgan dysfunction (Y. Wang et al., 2020; WHO, 2020). In particular, renal involvement ranging from proteinuria to acute kidney injury (AKI) has been reported. AKI occurs on average in 20% of hospitalized COVID-19 patients and in 50% of those in intensive care units (Nadim et al., 2020). It has been linked to poor prognosis (Pei et al., 2020) and can occur even in the absence of pronounced respiratory symptoms (Peleg et al., 2020). Risk factors associated with developing AKI following SARS-CoV-2 infection include old age (>60 years), hypertension and coronary heart disease (Diao et al., 2021a). In patients infected by the closely related SARS-CoV and Middle Eastern respiratory coronavirus (MERS-CoV), renal involvement has also been reported (Chen et al., 2020; S. Zhou et al., 2020).

Overall, renal symptoms associated with COVID-19 can be caused either by direct infection of renal tissue or its systemic effects such as microangiopathy, thrombosis, complement activation and cytokine storm (Khan et al., 2020; Nadim et al., 2020). While it does not shed light on the quantitative contribution of kidney infection to the global pathogenesis, accumulating evidence suggests that SARS-CoV-2 may directly infect renal tissue with potential long term side effects. Further investigation is now required to identify the initial targets of the virus in the kidney, as well as to elucidate the pattern of its dissemination and the organ's response to infection. Indeed, as for numerous other pathogens, no virological information regarding the early stages of renal infection is available. To date, the vast majority of samples used to study renal involvement in COVID-19 were obtained via autopsy or biopsy from patients with advanced disease (Nadim et al., 2020). Thus, in order to gain insight into the early stages of SARS-CoV-2 infection in the kidney, we have turned to organotypic systems.

Organotypic cultures are 350-500 nm thick slices of organs collected from small animals such as suckling hamsters or mice. Currently they represent the only model

containing all cell types present in the organ in their native three-dimensional arrangement (Ferren et al., 2021; Welsch et al., 2019). Organotypic brain cultures have been successfully used to study the central nervous system infection by Measles virus (Welsch et al., 2019) and Nipah virus (Bloyet et al., 2016).

Golden Syrian hamsters (*Mesocricetus auratus*) are a representative and economical model for SARS-CoV-2 infection. When challenged with SARS-CoV-2, they develop symptoms mimicking mild disease in humans and accumulate a viral load in a range of organs including the kidney (Chan et al., 2020). Recently, our group has developed and characterized hamster organotypic lung, brainstem and cerebellum cultures as models for studying SARS-CoV-2 infection and platforms for testing antiviral drugs (Ferren et al., 2021). For the first time we present organotypic kidney cultures (OKCs) as a means to decipher the initial stages of SARS-CoV-2 renal infection. Here we investigate the tropism and dissemination of SARS-CoV-2 in hamster OKCs and their innate immune response to infection. However, the use of our model can be extended to studying other nephrotropic pathogens and their hosts.

MATERIALS AND METHODS

Ethical authorization. Animals were euthanized directly. Direct euthanasia is not regarded as animal experimentation in France and does not require specific ethical authorization.

Preparation of organotypic kidney cultures. The procedure for preparing organotypic kidney cultures was adapted from the protocol for producing organotypic brain cultures as described previously (Welsch et al., 2017). A day before the dissection, Millicell® cell culture inserts with PTFE membranes (Merck) were pre-activated with organotypic kidney culture (OKC) medium. The recipe of the OKC medium (375 mL Minimal Essential Medium GlutaMAX (ThermoFisher Scientific), 125 mL of heat-inactivated horse serum (Gibco), 2.5 g of D- glucose (Sigma-Aldrich), 1 mL human recombinant insulin (Sigma-Aldrich), sterilized with a 0.22 µm filter) is identical to that of the organotypic brain culture (OBC) medium described by Welsch et al. (2017) and applied by Ferren et al. (2021) to organotypic lung, brainstem and cerebellum cultures. Seven-day suckling hamsters were sacrificed. Their abdominal cavity was opened and the kidneys collected and placed into a solution of Hibernate®-

A medium (Sigma-Aldrich), 1X kynurenic acid solution (for a 10X solution: 378 mg of kynurenic acid (Sigma-Aldrich) in 170 mL of H2O, 20 mL of 1M $MgCl_2$ (Sigma-Aldrich) adjusted to pH 7.4 with 0.1M NaOH (Sigma-Aldrich), 1 mL HEPES (Sigma-Aldrich), adjusted to a final volume of 200 mL) and 1X penicillin/streptomycin solution (Corning). Kidneys were placed on 6 layers of Whatman paper with their longitudinal axis perpendicular to the tissue chopper blade and sliced transversely using the McIlwain® tissue chopper (Campden Instruments) at 500 µm thickness for all experiments except the Seahorse XF Analyzer Respiratory Assay, where they were prepared to be 400 nm thick. The slices were dissociated under a dissection microscope. Undamaged and homogenous slices were selected and maintained on an air-liquid interface provided by PTFE membranes pre-activated with OBC medium.

Infection of organotypic kidney cultures. A 2 µL drop containing the required amount of viral plaque-forming units (pfu) was placed on each organotypic kidney slice. Infected slices were incubated at 37℃ until collection. Slices were infected with wild-type SARS-CoV-2 (2019-nCoV/USA_WA1/2020) or a recombinant strain icSARS-CoV-2-mNG expressing the mNeonGreen reporter gene inserted into its ORF7 (Xie et al., 2020).

Seahorse XF Analyzer Respiratory Assay. Seahorse XF Sensor Cartridges were hydrated with the Neurobasal®-A Medium 1X (Gibco) 24 hours prior to the assay. Organotypic kidney slices were prepared and sliced at 400 nm and assayed on the day of preparation (day 0) or following 1 or 4 days of incubation in OKC medium at 37 ˚C. OKCs were washed in 1X phosphate buffer saline (Gibco). 1 mm punches were prepared from the renal cortex and centered in the middle of the Seahorse Analyzer (Agilent) microplate wells. 500 µL of Seahorse XF DMEM medium (pH 7.4) supplemented with glucose (10 mM), pyruvate (1 mM0) and L-glutamine (2 mM) were added to each well. The injection solutions with drugs (oligomycin, carbonyl cyanide-p-trifluoromethoxyphenylhydrazine (FCCP), rotenone + antimycin A) were prepared, preloaded into the delivery chamber of the Seahorse XF Analyzer and calibrated for 30 min. Oxygen consumption rate (OCR) was measured and results were viewed using the Seahorse Wave software.

Quantitative RT-PCR. Each organotypic kidney slice was collected in 350 µL of RA1 buffer (NucleoSpin RNA, Macherey-Nagel) and 3.5 µL of 2-Mercaptoethanol (Sigma-Aldrich), and lysed using a pestle mixer (Argos Technologies). RNA was extracted from the lysates with the NucleoSpin RNA kit (Macherey-Nagel). 200 ng of RNA was reverse transcribed with the iScript cDNA Synthesis Kit (Bio-Rad) according to the manufacturers' protocols. cDNA was diluted 1:10 to avoid inhibition between mix with the following step. Gene transcription was quantified via qPCR using the Platinum SYBR Green qPCR SuperMix-UDG (Invitrogen), according to the manufacturer's protocol. Readings were made with the StepOnePlus Quantitative PCR System (Applied Biosystems) and viewed in the StepOne version 2.3 software (Applied Biosystems). The efficacy (*E)* of the primers was calculated as $10^{-1/slope}$ based on the slope of the standard curve. The copy number of mRNA per µg of total RNA was calculated using the $E^{-\Delta\Delta CT}$ model (Pfaffl, 2001) for each gene and normalized by the standard deviation in the expression of glyceraldehyde-3-phosphate dehydrogenase (GAPDH), a housekeeping gene (UniProtKB P04406), from the mean of its expression level across all days (Mathieu et al., 2011).

Immunofluorescence staining. Organotypic kidney slices were fixed in 4% paraformaldehyde (16% paraformaldehyde (methanol-free) (ThermoFisher Scientific) diluted by 4 in 1X phosphate buffer saline (PBS 1X) (Gibco)) for 4 hours or overnight at 4℃, washed with PBS 1X (here and later: 4 times, 5 mins each wash) and placed into a sucrose (Sigma-Aldrich) gradient (5%, 15%, 20%) solution overnight at 4 ˚C. Slices were embedded in the Optimal Cutting Temperature (OCT) solution (ThermoFisher Scientific) and sectioned along the horizontal plane with the Leica CM3050 S cryostat-microtome (Leica Biosystems). 10 µm sections were placed on Superfrost Gold Plus adhesion slides (Fisher Scientific), washed in PBS 1X, permeabilized and blocked in permeabilization and blocking solution (perm and block) (1X DPBS (ThermoFisher Scientific), 3% BSA (Sigma-Aldrich), 0.3% Triton-X100 (Sigma-Aldrich)) for 30 mins at 4 ˚C. Slices were incubated overnight with primary antibodies diluted in permeabilization and blocking solution, washed in PBS 1X, stained for 1 hour with secondary antibodies diluted in permeabilization and blocking solution, washed with PBS 1 X and mounted in Fluoromount-G® aqueous mounting medium (SouthernBiotech). Anti-SARS-CoV-2 nucleoprotein (NP) antibodies (SinoBiological, Cat# 40143-MM05 mouse, 1:200 dilution) were used to detect the

presence of virus. Endothelial cells were stained with anti-CD34 antibodies (abcam, Cat# ab81289 rabbit, 1:100 dilution), proximal tubular epithelial cells with anti-aquaporin-1 (ThermoFisher Scientific, Cat# PA5-53954 rabbit, 1:100 dilution), and podocytes with anti-nephrin (abcam, Cat# ab216341, rabbit, 1:100 dilution). Alexa FluorTM 488 donkey anti-rabbit (ThermoFisher Scientific, Cat# A21206, 1:500 dilution) and Alexa FluorTM 555 donkey anti-mouse (ThermoFisher Scientific, Cat# A31570, 1:500 dilution) secondary antibodies were used.

Imaging. OKCs infected with icSARS-CoV-2-mNG were photographed using the Nikon Eclipse Ts2R optical microscope and stitched using the Stitching plugin in ImageJ (Preibisch et al., 2009). Immunostained OKCs were examined and photographed using the Zeiss Axio Observer.Z1 microscope with confocal unit LSM 980 (Zeiss). Images were edited and analyzed using the ImageJ software (Schneider et al., 2012) and assembled in Inkscape.

Statistical analysis. Statistical analysis was performed in GraphPad Prism version 9. For the Seahorse XF metabolic activity assay, day 1 and day 4 OCRs of punches were compared to the day 0 OCR using ordinary one-way ANOVA. For the transcriptomic analysis, differences between normalized mRNA copy numbers per µg RNA in infected and non-infected samples were compared using a Mann-Whitney U-test. * = $p < 0.05$; ** = $p < 0.01$; *** = $p < 0.001$.

RESULTS

Organotypic kidney cultures contain key renal structures in their native arrangement

Kidneys were collected from 7-day-old suckling hamsters, sliced on a tissue chopper into 500 nm thick slices and maintained on an air-liquid interface provided by polytetrafluoroethylene membranes. The renal capsule, cortex and medulla were clearly identifiable in hamster OKCs (Fig. 1A). A nephron (Fig. 2B) is a functional unit of the kidney and the site of filtrate formation. Blood is filtered in the renal corpuscle (Fig. 2C). Through the afferent arteriole, it enters under high pressure a capillary bundle known as the glomerulus and passes the filtration barrier consisting of the glomerular endothelium, basement membrane and podocytes. The filtration barrier retains blood cells, large particles and proteins but not nutrients or ions. Glucose,

amino acids, water and salts are re-absorbed into capillaries from the filtrate in the proximal convoluted tubule, loop of Henle and distal convoluted tubule. Following reabsorption, the filtrate becomes urine and flows into the collecting duct leading to the renal pelvis and, eventually, the ureter (Kurts et al., 2013). We confirmed the presence of essential functional elements of nephrons in our OKCs via immunofluorescence staining of proximal tubules (Fig. 1D1), podocytes (Fig. 1D2) and $CD34^{+}$ endothelial cells (Fig. 1D3) of the renal vasculature. Reflecting their native arrangement, proximal tubules and renal corpuscles were localized in the cortex.

Organotypic kidney culture remain viable for at least 4 days of culture

We characterized whether organotypic kidney slices are tenable in culture and maintain a healthy metabolic activity for up to 4 days after preparation. To obtain a specific measure of the mitochondrial respiratory activity of OKCs, a Seahorse XF Analyzer respiratory assay was performed on 1 mm large punches prepared from the cortical zone of 400 nm-thick slices. Oxygen consumption rate (OCR) was quantified as a measure of mitochondrial respiratory activity.

Fig. 1A illustrates the workflow of the experiment and the evolution of the punches' OCR over all timepoints. The basal metabolic rate of punches from OKC cortices was maintained after 1 day of culture and remained at more than 60% of its initial level on day 4 (Fig. 2A and 2B). To determine the extent of cell death occurring in the slices, the maximal metabolic rate of punches was measured following the disruption of the proton gradient by FCCP and the complete inhibition of mitochondrial respiration by rotenone and antimycin A. It remained stable after 1 day of culture and decreased by 20% by day 4 (Fig. 2A and 2C).

RNA was extracted from non-infected slices and quantified as another measure of their viability. Over the duration of the experiment, its amount did not decrease (Fig. 2D). The expression of glyceraldehyde-3-phosphate dehydrogenase (GAPDH), a key enzyme in the glycolysis pathway and a household gene (UniProtKB P04406), has also remained stable (Fig. 2E), reflecting the ability of non-infected OKCs to maintain steady glycolytic activity in culture. Such results indicate that, despite a reduction in mitochondrial respiration, organotypic kidney cultures can remain viable on an air-liquid interface for at least 4 days.

Organotypic kidney cultures are highly permissive to SARS-CoV-2 infection

SARS-CoV-2 mainly enters cells via the binding of the Spike glycoprotein to one of its target receptors such as angiotensin converting enzyme 2 (ACE2) or Neuropilin-1. The fusion of the viral envelope and the cell membrane is enhanced by the cleavage of the Spike by host proteases such as TMPRSS2 on the cell surface or cathepsins B and L in endosomes among others (Hoffmann et al., 2020; Ou et al., 2020). All of these proteins are expressed in the kidney (Uhlén et al., 2015). Notably, the kidney is a prominent site of ACE2 expression (Gkogkou et al., 2020). ACE2 comprises a part of the renin–angiotensin system, which is responsible for controlling blood pressure and vascular resistance (Paul et al., 2006). In the kidney, it is expressed by tubular and glomerular epithelial cells (including podocytes), vascular smooth muscle cells, arterial endothelium and the tunica media of arterioles. Renal disease and transplantation can also induce neo-expression of ACE2 in the endothelia of the glomeruli and peritubular capillaries (Lely et al., 2004; Soler et al., 2009).

In order to probe the susceptibility of hamster OKCs to SARS-CoV-2, a subset (n = 5) of them was infected with wild-type SARS-CoV-2 (2019-nCoV/USA_WA1/2020) while maintained in culture on an air-liquid interface. The number of copies of mRNA encoding the viral nucleocapsid protein (NP) was quantified via RT-qPCR in slices collected every day post-infection, starting 90 min post-infection to evaluate how much virus was retained by each slice at this timepoint. Akin to the pattern observed in hamster organotypic lung cultures by Ferren et al. (2021), in organotypic kidney cultures infection increased by 4 logs and approached a plateau at 1 day post-infection (Fig. 3A). Mirroring our RT-qPCR results, in slices infected with a recombinant SARS-CoV-2 strain encoding a mNeonGreen reporter (icSARS-CoV-2-mNG), infected cells were observed from day 1 post-infection. Infection started in the capsular zone and propagated towards the center of the slice (Fig. 3B).

The global expression of SARS-CoV-2 entry factors in hamster OKCs was quantified via RT-qPCR. The entry receptors ACE2 and neuropilin-1, as well as the proteases TMPRSS2 and cathepsins B and L were highly expressed in the slices (Fig. 3C), with all proteins except for neuropilin-1 being significantly enriched compared to lung organotypic cultures (Fig. 3D).

In hamster organotypic kidney cultures SARS-CoV-2 targets endothelial cells and proximal tubules but not podocytes

To investigate the early tropism and subsequent propagation of SARS-CoV-2 in hamster OKCs more deeply, we assessed which cells serve as its targets by immunofluorescence double-staining. 10 µm thick cryosections of OKCs were stained with antibodies against the SARS-CoV-2 nucleoprotein (NP) and markers of endothelial cells (CD34+), proximal tubular epithelial cells (Aquaporin 1+) and podocytes (Nephrin +).

Reflecting what we had observed by photographing live 500-nm slices infected with icSARS-CoV-2-mNG, infection initiated in the subcapsular zone (Fig. 4A1) and propagated towards the center of the cryosection (Fig. 4A2). Colocalization of CD34 and SARS-CoV-2 NP was observed on day 1 (Fig. 4A1) and day 2 (Fig. S1A1) post-infection. At later timepoints it remained restricted to peripheral blood vessels (Fig. S1A2; Fig. 4A2) and appeared less prominent than on day 1 (Fig. 4A1). Infection of podocytes was not detected over the 4 days of the experiment (Fig. 4B; Fig. S1B). Proximal tubular epithelial cells positive for viral nucleoprotein were very rare on the first 3 days post-infection (Fig. 4C1 and Fig. S1D1). However, the virus disseminated into them on day 4 (Fig. 4C2 and Fig. S1D2). These results suggest that early targets of SARS-CoV-2 in hamster OKCs include $CD34^{+}$ endothelial cells and other subcapsular parietal cells, while the highly susceptible proximal tubular epithelial cells serve as later sites of viral dissemination. Fig. S1D highlights the difference in the proportion of infected proximal tubular epithelial cells on day 1 and day 4 post-infection.

Transcriptomic analysis of organotypic kidney cultures challenged with SARS-CoV-2

In order to evaluate how organotypic kidney cultures respond to infection over the first 4 days after its onset, we have challenged them with wild-type SARS-CoV-2 and compared gene expression in infected and non-infected slices maintained in culture for equal periods of time.

SARS-CoV-2 infection has been shown to provoke upregulation of inflammatory cytokines known as cytokine storm in critically ill patients. Cytokine storm usually occurs at least a week after the onset of symptoms and can be responsible for some of the lethal symptoms of COVID-19, including ARDS and acute kidney injury (Song et al., 2020). IL-6, IL-1β, IL-18 from the interleukin (IL) family and tumor necrosis factor alpha (TNFα) are pro-inflammatory cytokines known to play an important role in

antiviral defense and to be upregulated in severe cases of COVID-19 (Colafrancesco et al., 2012; Huang et al., 2020; Tisoncik et al., 2012). Infected OKCs display a repression of IL-1β (Fig. 5A), IL-18 (Fig. 5B) and IL-6 (Fig. 5C) on day 1 and 2 post-infection, followed by strong induction from day 3 onwards, suggesting that an important event may be occurring during infection at this timepoint. This effect is particularly pronounced for IL-1β (Fig. 5A), which becomes upregulated more than 100-fold. Although TNFα (Fig. 5D) is not repressed initially, it only displays a statistically significant upregulation on day 4. The expression of IL-1β drops dramatically on day 4, while the expression of IL-18 and IL-6 is maintained.

Interferons (IFNs) are another family of cytokines essential for the innate immune response against viruses. Activated upon the detection of pathogen-associated molecular patterns (PAMPs) by pattern-recognition receptors (PRR), interferons induce the expression of interferon-stimulated genes (ISG) and thus convert cells into an antiviral state (Randall & Goodbourn, 2008). Studies performed in COVID-19 patients suggest that an efficient early type I IFN response could play an important role in resolving infection, while a strong late response may exacerbate the cytokine storm symptoms (J. S. Lee & Shin, 2020). Due to the poor annotation of hamster genomes, we were unable to design oligonucleotides to measure the expression of IFNs directly. Instead, the expression of ISGs such as CXCL10 (Fig. 4E) of the chemokine family and myxovirus resistance 1 (MX1) (Fig. 4F) were measured as a proxy for establishing whether hamster OKCs mount an efficient IFN response when challenged with SARS-CoV-2. CXCL10 expression was only induced on day 4, whereas MX1 expression increased 13-fold at day 2 post-infection and continued to rise up to day 4, reaching a 24-fold level compared to non-infected cultures. Thus, it mirrors the infection kinetics observed (Fig. 3A) with a 24-hour delay.

Studies in primary and immortalized human cell lines indicate that the expression of ACE2, one of the main candidate SARS-CoV-2 entry receptors, may be inducible by interferons (Busnadiego et al., 2020; Ziegler et al., 2020). We extended our transcriptomic analysis to observe how infection may impact the transcription of ACE2 and other putative viral entry factors such as the neuropilin-1 receptors and the proteases TMPRSS2 and cathepsin B. A slight tendency towards the upregulation over the course of infection was detected for ACE2 (Fig. 5G). Neuropilin-1 (Fig. S2A), TMPRSS2 (Fig. S2B) and cathepsin B (Fig. S2C) have also tended towards overexpression in infected slices.

Necroptosis and pyroptosis are highly inflammatory types of programmed cell death which play a role in the innate antiviral response (Bertheloot et al., 2021). An upregulation of mixed lineage kinase domain-like pseudokinase (MLKL), a marker of necroptosis, was observed at 4 days post-infection in OKCs, suggesting that necroptosis had likely been induced at this stage of infection (Fig. 5H). The expression of gasdermin D, a key mediator of pyroptosis, was elevated throughout the experiment, peaking at day 2 post-infection (Fig. 5I).

Discussion

It remains controversial whether active replication of SARS-CoV-2 takes place in the kidneys of COVID-19 patients with AKI. Several groups have failed to find viral particles or RNA in autopsy samples (Gaillard et al., 2020; Peleg et al., 2020; Santoriello et al., 2020), which provide information only about the terminal stage of infection. Others have detected the presence of a viral load in the kidney via methods such as RT-qPCR, *in situ* hybridization, immunohistochemistry, transmission electron microscopy and isolation of live virus (Braun et al., 2020; Diao et al., 2021a; Farkash et al., 2020; Hanley et al., 2020; Liu et al., 2021; Puelles et al., 2020; Su et al., 2020).

The absence of an appropriate model is the principal reason for the lack of knowledge on the early renal effects of COVID-19 (Nadim et al., 2020). In humans, SARS-CoV-2 infection tends to progress asymptomatically or with mild symptoms before deteriorating into a severe form (Y. Wang et al., 2020). Therefore, only late samples are available, without the possibility to pinpoint the starting point of renal infection. We present a model for elucidating the nature of early infection of the kidney that has the potential to overcome these limitations.

Hamster organotypic kidney cultures reflected the native structure of the kidney (Fig. 1) and could be maintained in culture for at least 4 days (Fig. 2). While their mitochondrial metabolic activity has decreased by day 4 (Fig. 2A, 2B and 2C), even at this timepoint good viability was maintained as suggested by the stable quantity of RNA extracted from OKCs and their GAPDH expression pattern (Fig. 2D and 2E). These indicators could potentially be improved via the optimization of the culture medium. Moreover, additional experiments are necessary to confirm the maintenance of the metabolic activity of OKCs at later timepoints.*In vivo* experiments have shown that hamster kidneys accumulate a viral load during SARS-CoV-2 infection (Chan et al., 2020). In line with these observations, we have shown that hamster OKCs are

highly permissive and susceptible to SARS-CoV-2 infection and approach a peak viral load on day 1 post-infection, similarly to the dynamics observed in organotypic lung cultures but distinctly from those observed in organotypic cerebellum and brainstem cultures, where infection peaks at day 2 (Ferren et al., 2021).

Our immunofluorescence staining results reveal the predominant infection of $CD34^+$ endothelial cells already on day 1 post-infection (Fig. 5A1). SARS-CoV-2 infection is able to provoke endothelitis in a range of organs, including the kidney. The presence of viral particles in glomerular endothelial cells in a kidney autopsy sample has also been confirmed via transmission electron microscopy (Varga et al., 2020). Thus, in hamster OKCs, SARS-CoV-2 could first target endothelial cells and later disseminate to other sites, including proximal tubules. In contrast, we did not observe any infection in podocytes (Fig. 4B and Fig. S1B). Endothelial cells would be the first renal cells to encounter viral particles in case of viremia in a living organism. Unexpectedly, this logical order of susceptibility is maintained in organotypic cultures.

The early tropism of SARS-CoV-2 may also be influenced by the expression of viral entry factors (Khan et al., 2020), especially in an organotypic model. For a more robust explanation, measuring the expression of these factors at the cell surface (or in endosomes) as functional mature proteins in distinct hamster kidney cell types would be required. Possibly, infection of endothelial and other cells triggers an event allowing the propagation of SARS-CoV-2 to proximal tubular cells.

Acute tubular injury is the most common renal pathology observed in kidney autopsy samples of COVID-19 patients (Bouquegneau et al., 2021; Diao et al., 2021a; Farkash et al., 2020; Su et al., 2020). Although organotypic cultures are inoculated via placing a virus-containing droplet on top of the entire slice, infection of proximal tubular epithelial cells before day 4 post-infection appeared very rare (Fig. 4C and Fig. S1D). In contrast, after 4 days they have become the main infected cell population (Fig. 4 C). This suggests that the susceptibility and permissiveness of tubular epithelia is enhanced by additional factors expressed after the infection of other cell populations. All studies reporting proximal tubular injury in COVID-19 patients were based on samples obtained at advanced or terminal stages of infection. Our results may reflect the fact that tubular damage is a late event in pathogenesis, explaining why it may be difficult to predict it in patients.

Despite the viral load peaking at day 1 post-infection, pro-inflammatory cytokine upregulation was not observed in hamster OKCs until day 3 for IL-1β (Fig. 4A), IL-18

(Fig. 4B), IL-6 (Fig. 4C), and day 4 for CXCL10 and TNFα (Fig. 4D) (Fig. 4E). Moreover, a strong repression of IL-1β, IL-18 and IL-6 was observed on day 1 and 2 post-infection. Interleukins from the IL-1 family, which include IL-1β and IL-18, can positively regulate IL-6 (J.-K. Lee et al., 2004; Tanaka et al., 2014). This may explain the synchronous upregulation of these three cytokines. In addition, the upregulation of pro-inflammatory cytokine expression on day 4 post-infection may be reflecting the dissemination of the virus into the proximal tubular epithelial cells revealed by immunofluorescence staining.

MX1 and CXCL10 are interferon-stimulated genes (Haller et al., 2007; Majumder et al., 1998). CXCL10 can also be induced directly upon the sensing of PAMPs by Toll-like receptors (TLR) (C. Wong et al., 2009), as well as upon stimulation by IL-6. Indeed, in lungs, SARS-CoV-2 infection leads to the overexpression of IL-6, which then stimulates CXCL10 production (Coperchini et al., 2021). Here, while MX1 becomes upregulated strongly on day 2 post-infection (Fig. 4F), CXCL10 expression does not increase markedly until day 4 (Fig. 4E), suggesting its independence from the interferon pathway in this specific context. However, it may simply reflect the two-step susceptibility of the model, where induction of IL-6 only occurs when enough virus infects proximal tubular cells, eventually leading to the late overexpression of CXCL10 mRNA. In addition, IL-6 and CXCL10 expression may be further stimulated by type I IFN signalling (Anders et al., 2010).

The delayed upregulation of MX1 (Fig. 4F), in turn, indicates a delayed IFN response. SARS-CoV non-structural protein 1 (nsp1) and structural proteins M and N have been reported to target the IFN signalling pathway by inhibiting STAT1 phosphorylation (nsp1) and the formation of the TRAF3-containing complex (M and N proteins) (Narayanan et al., 2008; Siu et al., 2014). As a result, SARS-CoV infection causes a delayed type-I IFN response in mice that, together with the resulting accumulation of PAMPs, enhances pro-inflammatory cytokine expression (Channappanavar et al., 2016; Song et al., 2020). The N protein of SARS-CoV-2 has been shown to inhibit IFN signalling by interacting with STAT1/STAT2 (Mu et al., 2020). SARS-CoV-2 may also interfere with the expression of IFN and pro-inflammatory cytokines at the levels of translation and nuclear export of mRNA (Finkel et al., 2021). Interestingly, the peak IFN response mounted by OKCs challenged with SARS-CoV-2 was significantly less pronounced in comparison to that observed in organotypic lung and brainstem cultures (Ferren et al., 2021). Whether this potential

weaker capacity of the kidney to mount an interferon response contributes or not to any virus associated pathogenesis remains to be further investigated.

As subcapsular parietal initially infected cells die, they may relay the infection to proximal tubular epithelial cells, where repression of cytokine expression and IFN signalling no longer occurs. Such cyclical tropism would be expected *in vivo* since endothelial cells would be the first to encounter the virus. From capillaries, SARS-CoV-2 could then propagate to the proximal tubules, as suggested by the high incidence of proximal tubular injury at the terminal stage COVID-19 (Khan et al., 2020; Nadim et al., 2020). The sustained IFN response at later timepoints might also induce the upregulation of ACE2 (Fig. 5G) (Busnadiego et al., 2020; Ziegler et al., 2020).

In our model, the upregulation of MLKL (Fig. 5H) indicative of cell death via necroptosis occurs concomitantly with the increase in TNFα expression on day 4 post-infection (Fig. 5D). TNFα binding to tumour necrosis factor receptors (TNFR) is known to trigger necroptosis (Holler et al., 2000). In addition, necroptosis can be activated via direct sensing of PAMPs by TLRs (He et al., 2011) and cytosolic nucleic acid sensors (Schock et al., 2017). Day 4 post-infection is also the point where immunofluorescence staining reveals significant virus propagation into proximal tubules (Fig. 4C2 and Fig. S1D2). Possibly, proximal tubular epithelia are more susceptible to necroptosis than the initial targets of SARS-CoV-2 in hamster OKCs.

Pyroptosis is induced by inflammasome sensors responsive to activation by nuclear factor kappa B (NF-κB) following TLR, TNFR and interleukin-1 receptor (IL-1R) sensing. While the expression of the pyroptosis mediator gasdermin D in OKCs precedes the upregulation of cytokines from the IL-1 family (Fig. 5A–B, 5I), pyroptosis itself results in the cleavage of cytosolic pro-IL-1β and pro-IL-18 into their active forms and their release from the cell (Baroja-Mazo et al., 2014; Kanneganti et al., 2006; K. Wang et al., 2020). This amplifies inflammation and may account for a positive feedback loop leading to IL-1β (Fig. 5A) and IL-18 (Fig. 5B) upregulation on day 3 post-infection.

To which extent observations made in hamster correspond to the pathogenesis of SARS-CoV-2 infection in human remains to be investigated. However, OKCs offer for the first time a window on the events of early infection at the organ level. Thanks to the current pandemic, the poor annotation of hamster genomes and the lack of molecular biology tools adapted to hamsters begin to be inverted, allowing for better and deeper characterization of host-pathogen interactions. The applications of OKCs

could be extended to studying other human nephrotropic pathogens such as the Nipah virus, for which golden Syrian hamsters are an established model (K. T. Wong et al., 2003) as well as other emergent viruses including Feline Morbillivirus (FeMV) (Choi et al., 2020; Luca et al., 2021) and bat nephrotropic Paramyxoviruses (de Souza et al., 2021). Other human viruses capable of replicating in the kidney include cytomegalovirus, Epstein-Barr virus, adenovirus, and polyomavirus. Such infections are especially common in immunocompromised patients.

Organotypic models have not been previously used to study kidney infection. The hamster OKCs described here are still at the initial stages of their development. Performing a detailed analysis of their metabolic activity beyond 4 days would permit optimizing the protocol for maintaining them in culture. With regards to SARS-CoV-2 pathogenesis, the localization of virus entry factors and the full range of target cell populations in OKCs remain to be investigated. Monitoring infection progression and the innate immune response beyond 4 days post-infection could reveal the consequences of viral dissemination into the tubules.

Numerous viral, bacterial, and fungal pathogens target the kidney. However, early stages of renal infections remain poorly characterized due to the impossibility to follow them in a non-invasive way. Organotypic kidney cultures are a viable and representative model for deciphering early events in pathogenesis. Their use could provide insights into issues that cannot be addressed with post-mortem or late biopsy samples while reducing the number of animals sacrificed per question. They could also be applied for early screening of drug candidates. It would therefore be of interest to examine their potential for early drug screening, and to extend their use to other hosts and infections.

Acknowledgements

We acknowledge World Reference Center for Emerging Viruses and Arboviruses (WRCEVA) and UTMB investigator, Dr. Pei Yong Shi for kindly providing recombinant icSARS-CoV-2-mNG virus based on 2019-nCoV/USA_WA1/2020 isolate. This work was supported by ANR-CoronaPepStop (ANR-20-COVI-000) and Fondation de France to BH, ANRS-COV8-SARSRhinCell to CM and CIRI-Intramural grant to LPC and CM.

References

Anders, H. J., Lichtnekert, J., & Allam, R. (2010). Interferon-α and -β in kidney inflammation. *Kidney International*, *77*(10), 848–854. https://doi.org/10.1038/KI.2010.71

Baroja-Mazo, A., Martín-Sánchez, F., Gomez, A. I., Martínez, C. M., Amores-Iniesta, J., Compan, V., Barberà-Cremades, M., Yagüe, J., Ruiz-Ortiz, E., Antón, J., Buján, S., Couillin, I., Brough, D., Arostegui, J. I., & Pelegrín, P. (2014). The NLRP3 inflammasome is released as a particulate danger signal that amplifies the inflammatory response. *Nature Immunology*, *15*(8), 738–748. https://doi.org/10.1038/ni.2919

Bertheloot, D., Latz, E., & Franklin, B. S. (2021). Necroptosis, pyroptosis and apoptosis: an intricate game of cell death. In *Cellular and Molecular Immunology* (Vol. 18, Issue 5, pp. 1106–1121). Springer Nature. https://doi.org/10.1038/s41423-020-00630-3

Bloyet, L.-M., Welsch, J., Enchery, F., Mathieu, C., de Breyne, S., Horvat, B., Grigorov, B., & Gerlier, D. (2016). HSP90 Chaperoning in Addition to Phosphoprotein Required for Folding but Not for Supporting Enzymatic Activities of Measles and Nipah Virus L Polymerases. *Journal of Virology*, *90*(15), 6642–6656. https://doi.org/10.1128/jvi.00602-16

Bouquegneau, A., Erpicum, P., Grosch, S., Habran, L., Hougrand, O., Huart, J., Krzesinski, J.-M., Misset, B., Hayette, M.-P., Delvenne, P., Bovy, C., Kylies, D., Huber, T. B., Puelles, V. G., Delanaye, P., & Jouret, F. (2021). COVID-19–associated Nephropathy Includes Tubular Necrosis and Capillary Congestion, with Evidence of SARS-CoV-2 in the Nephron. *Kidney360*, *2*(4), 639–652. https://doi.org/10.34067/kid.0006992020

Braun, F., Lütgehetmann, M., Pfefferle, S., Wong, M. N., Carsten, A., Lindenmeyer, M. T., Nörz, D., Heinrich, F., Meißner, K., Wichmann, D., Kluge, S., Gross, O., Pueschel, K., Schröder, A. S., Edler, C., Aepfelbacher, M., Puelles, V. G., & Huber, T. B. (2020). SARS-CoV-2 renal tropism associates with acute kidney injury. In *The Lancet* (Vol. 396, Issue 10251, pp. 597–598). Lancet Publishing Group. https://doi.org/10.1016/S0140-6736(20)31759-1

Busnadiego, I., Fernbach, S., Pohl, M. O., Karakus, U., Huber, M., Trkola, A., Stertz, S., & Hale, B. G. (2020). Antiviral activity of type i, ii, and iii interferons counterbalances ace2 inducibility and restricts sars-cov-2. *MBio*, *11*(5), 1–10. https://doi.org/10.1128/mBio.01928-20

Chan, J. F. W., Zhang, A. J., Yuan, S., Poon, V. K. M., Chan, C. C. S., Lee, A. C. Y., Chan, W. M., Fan, Z., Tsoi, H. W., Wen, L., Liang, R., Cao, J., Chen, Y., Tang, K., Luo, C., Cai, J. P., Kok, K. H., Chu, H., Chan, K. H., … Yuen, K. Y. (2020). Simulation of the Clinical and Pathological Manifestations of Coronavirus Disease 2019 (COVID-19) in a Golden Syrian Hamster Model: Implications for Disease Pathogenesis and Transmissibility. *Clinical Infectious Diseases*, *71*(9), 2428–2446. https://doi.org/10.1093/cid/ciaa325

Channappanavar, R., Fehr, A. R., Vijay, R., Mack, M., Zhao, J., Meyerholz, D. K., & Perlman, S. (2016). Dysregulated Type I Interferon and Inflammatory Monocyte-Macrophage Responses Cause Lethal Pneumonia in SARS-CoV-Infected Mice. *Cell Host & Microbe*, *19*(2), 181–193. https://doi.org/https://doi.org/10.1016/j.chom.2016.01.007

Chen, Y. T., Shao, S. C., Lai, E. C. C., Hung, M. J., & Chen, Y. C. (2020). Mortality rate of acute kidney injury in SARS, MERS, and COVID-19 infection: A systematic review and meta-analysis. *Critical Care*, *24*(1). https://doi.org/10.1186/s13054-020-03134-8

Choi, E. J., Ortega, V., & Aguilar, H. C. (2020). Feline Morbillivirus, a New Paramyxovirus Possibly Associated with Feline Kidney Disease. *Viruses*, *12*(5). https://doi.org/10.3390/V12050501

Colafrancesco, S., Priori, R., Alessandri, C., Perricone, C., Pendolino, M., Picarelli, G., & Valesini, G. (2012). IL-18 Serum Level in Adult Onset Still's Disease: A Marker of Disease Activity. *International Journal of Inflammation*, *2012*, 156890. https://doi.org/10.1155/2012/156890

Coperchini, F., Chiovato, L., & Rotondi, M. (2021). Interleukin-6, CXCL10 and Infiltrating Macrophages in COVID-19-Related Cytokine Storm: Not One for All But All for One! *Frontiers in Immunology*, *12*, 1347. https://doi.org/10.3389/FIMMU.2021.668507/BIBTEX

de Souza, W. M., Fumagalli, M. J., Carrera, J. P., de Araujo, J., Cardoso, J. F., de Carvalho, C., Durigon, E. L., Queiroz, L. H., Faria, N. R., Murcia, P. R., & Figueiredo, L. T. M. (2021). Paramyxoviruses from neotropical bats suggest a novel genus and nephrotropism. *Infection, Genetics and Evolution*, *95*, 105041. https://doi.org/10.1016/J.MEEGID.2021.105041

Diao, B., Wang, C., Wang, R., Feng, Z., Zhang, J., Yang, H., Tan, Y., Wang, H., Wang, C., Liu, L., Liu, Y., Liu, Y., Wang, G., Yuan, Z., Hou, X., Ren, L., Wu, Y., & Chen, Y. (2021a). Human kidney is a target for novel severe acute respiratory syndrome coronavirus 2 infection. *Nature Communications*, *12*(1), 2506. https://doi.org/10.1038/s41467-021-22781-1

Diao, B., Wang, C., Wang, R., Feng, Z., Zhang, J., Yang, H., Tan, Y., Wang, H., Wang, C., Liu, L., Liu, Y., Liu, Y., Wang, G., Yuan, Z., Hou, X., Ren, L., Wu, Y., & Chen, Y. (2021b). Human kidney is a target for novel severe acute respiratory syndrome coronavirus 2 infection. *Nature*

Communications, *12*(1), 1–9. https://doi.org/10.1038/s41467-021-22781-1
Divakaruni, A. S., Paradyse, A., Ferrick, D. A., Murphy, A. N., & Jastroch, M. (2014). Analysis and interpretation of microplate-based oxygen consumption and pH data. *Methods in Enzymology*, *547*(C), 309–354. https://doi.org/10.1016/B978-0-12-801415-8.00016-3
Farkash, E. A., Wilson, A. M., & Jentzen, J. M. (2020). Ultrastructural Evidence for Direct Renal Infection with SARS-CoV-2. *Journal of the American Society of Nephrology*, *31*(8), 1683 LP – 1687. https://doi.org/10.1681/ASN.2020040432
Ferren, M., Favède, V., Decimo, D., Iampietro, M., Lieberman, N. A. P., Weickert, J. L., Pelissier, R., Mazelier, M., Terrier, O., Moscona, A., Porotto, M., Greninger, A. L., Messaddeq, N., Horvat, B., & Mathieu, C. (2021). Hamster organotypic modeling of SARS-CoV-2 lung and brainstem infection. *Nature Communications 2021 12:1*, *12*(1), 1–17. https://doi.org/10.1038/s41467-021-26096-z
Finkel, Y., Gluck, A., Nachshon, A., Winkler, R., Fisher, T., Rozman, B., Mizrahi, O., Lubelsky, Y., Zuckerman, B., Slobodin, B., Yahalom-Ronen, Y., Tamir, H., Ulitsky, I., Israely, T., Paran, N., Schwartz, M., & Stern-Ginossar, N. (2021). SARS-CoV-2 uses a multipronged strategy to impede host protein synthesis. *Nature*, *594*(7862), 240–245. https://doi.org/10.1038/s41586-021-03610-3
Gaillard, F., Ismael, S., Sannier, A., Tarhini, H., Volpe, T., Greze, C., Verpont, M. C., Zouhry, I., Rioux, C., Lescure, F. X., Buob, D., & Daugas, E. (2020). Tubuloreticular inclusions in COVID-19–related collapsing glomerulopathy. *Kidney International*, *98*(1), 241. https://doi.org/10.1016/j.kint.2020.04.022
Gkogkou, E., Barnasas, G., Vougas, K., & Trougakos, I. P. (2020). Expression profiling meta-analysis of ACE2 and TMPRSS2, the putative anti-inflammatory receptor and priming protease of SARS-CoV-2 in human cells, and identification of putative modulators. *Redox Biology*, *36*. https://doi.org/10.1016/j.redox.2020.101615
Haller, O., Staeheli, P., & Kochs, G. (2007). Interferon-induced Mx proteins in antiviral host defense. *Biochimie*, *89*(6), 812–818. https://doi.org/https://doi.org/10.1016/j.biochi.2007.04.015
Hanley, B., Naresh, K., Roufosse, C., Nicholson, A., Weir, J., Cooke, G., Thursz, M., Manousou, P., Corbett, R., Goldin, R., Al-Sarraj, S., Abdolrasouli, A., Swann, O., Baillon, L., Penn, R., Barclay, W., Viola, P., & Osborn, M. (2020). Histopathological findings and viral tropism in UK patients with severe fatal COVID-19: a post-mortem study. *The Lancet Microbe*, *1*. https://doi.org/10.1016/S2666-5247(20)30115-4
He, S., Liang, Y., Shao, F., & Wang, X. (2011). Toll-like receptors activate programmed necrosis in macrophages through a receptor-interacting kinase-3-mediated pathway. *Proceedings of the National Academy of Sciences of the United States of America*, *108*(50), 20054–20059. https://doi.org/10.1073/pnas.1116302108
Hoffmann, M., Kleine-Weber, H., Schroeder, S., Krüger, N., Herrler, T., Erichsen, S., Schiergens, T. S., Herrler, G., Wu, N. H., Nitsche, A., Müller, M. A., Drosten, C., & Pöhlmann, S. (2020). SARS-CoV-2 Cell Entry Depends on ACE2 and TMPRSS2 and Is Blocked by a Clinically Proven Protease Inhibitor. *Cell*, *181*(2), 271-280.e8. https://doi.org/10.1016/j.cell.2020.02.052
Holler, N., Zaru, R., Micheau, O., Thome, M., Attinger, A., Valitutti, S., Bodmer, J. L., Schneider, P., Seed, B., & Tschopp, J. (2000). Fas triggers an alternative, caspase-8-independent cell death pathway using the kinase RIP as effector molecule. *Nature Immunology*, *1*(6), 489–495. https://doi.org/10.1038/82732
Huang, C., Wang, Y., Li, X., Ren, L., Zhao, J., Hu, Y., Zhang, L., Fan, G., Xu, J., Gu, X., Cheng, Z., Yu, T., Xia, J., Wei, Y., Wu, W., Xie, X., Yin, W., Li, H., Liu, M., … Cao, B. (2020). Clinical features of patients infected with 2019 novel coronavirus in Wuhan, China. *Lancet (London, England)*, *395*(10223), 497–506. https://doi.org/10.1016/S0140-6736(20)30183-5
Kanneganti, T. D., Body-Malapel, M., Amer, A., Park, J. H., Whitfield, J., Franchi, L., Taraporewala, Z. F., Miller, D., Patton, J. T., Inohara, N., & Núñez, G. (2006). Critical role for Cryopyrin/Nalp3 in activation of caspase-1 in response to viral infection and double-stranded RNA. *Journal of Biological Chemistry*, *281*(48), 36560–36568. https://doi.org/10.1074/jbc.M607594200
Khan, S., Chen, L., Yang, C. R., Raghuram, V., Khundmiri, S. J., & Knepper, M. A. (2020). Does SARS-cov-2 infect the kidney? In *Journal of the American Society of Nephrology* (Vol. 31, Issue 12, pp. 2746–2748). American Society of Nephrology. https://doi.org/10.1681/ASN.2020081229
Kurts, C., Panzer, U., Anders, H. J., & Rees, A. J. (2013). The immune system and kidney disease: Basic concepts and clinical implications. In *Nature Reviews Immunology* (Vol. 13, Issue 10, pp. 738–753). Nat Rev Immunol. https://doi.org/10.1038/nri3523
Lee, J.-K., Kim, S.-H., Lewis, E. C., Azam, T., Reznikov, L. L., & Dinarello, C. A. (2004). Differences in signaling pathways by IL-1β and IL-18. *Proceedings of the National Academy of Sciences of the United States of America*, *101*(23), 8815 LP – 8820. https://doi.org/10.1073/pnas.0402800101
Lee, J. S., & Shin, E. C. (2020). The type I interferon response in COVID-19: implications for treatment. In *Nature Reviews Immunology* (Vol. 20, Issue 10, pp. 585–586). Nature Research. https://doi.org/10.1038/s41577-020-00429-3

Lely, A. T., Hamming, I., van Goor, H., & Navis, G. J. (2004). Renal ACE2 expression in human kidney disease. *Journal of Pathology*, *204*(5), 587–593. https://doi.org/10.1002/path.1670

Liu, J., Li, Y., Liu, Q., Yao, Q., Wang, X., Zhang, H., Chen, R., Ren, L., Min, J., Deng, F., Yan, B., Liu, L., Hu, Z., Wang, M., & Zhou, Y. (2021). SARS-CoV-2 cell tropism and multiorgan infection. *Cell Discovery*, *7*(1), 17. https://doi.org/10.1038/s41421-021-00249-2

Luca, E. De, Sautto, G. A., Crisi, P. E., & Lorusso, A. (2021). Feline Morbillivirus Infection in Domestic Cats: What Have We Learned So Far? *Viruses*, *13*(4). https://doi.org/10.3390/V13040683

Majumder, S., Zhou, L. Z., Chaturvedi, P., Babcock, G., Aras, S., & Ransohoff, R. M. (1998). p48/STAT-1alpha-containing complexes play a predominant role in induction of IFN-gamma-inducible protein, 10 kDa (IP-10) by IFN-gamma alone or in synergy with TNF-alpha. *Journal of Immunology (Baltimore, Md. : 1950)*, *161*(9), 4736–4744.

Mathieu, C., Pohl, C., Szecsi, J., Trajkovic-Bodennec, S., Devergnas, S., Raoul, H., Cosset, F.-L., Gerlier, D., Wild, T. F., & Horvat, B. (2011). Nipah Virus Uses Leukocytes for Efficient Dissemination within a Host. *Journal of Virology*, *85*(15), 7863. https://doi.org/10.1128/JVI.00549-11

Mu, J., Fang, Y., Yang, Q., Shu, T., Wang, A., Huang, M., Jin, L., Deng, F., Qiu, Y., & Zhou, X. (2020). SARS-CoV-2 N protein antagonizes type I interferon signaling by suppressing phosphorylation and nuclear translocation of STAT1 and STAT2. *Cell Discovery 2020 6:1*, *6*(1), 1–4. https://doi.org/10.1038/s41421-020-00208-3

Nadim, M. K., Forni, L. G., Mehta, R. L., Connor, M. J., Liu, K. D., Ostermann, M., Rimmelé, T., Zarbock, A., Bell, S., Bihorac, A., Cantaluppi, V., Hoste, E., Husain-Syed, F., Germain, M. J., Goldstein, S. L., Gupta, S., Joannidis, M., Kashani, K., Koyner, J. L., … Kellum, J. A. (2020). COVID-19-associated acute kidney injury: consensus report of the 25th Acute Disease Quality Initiative (ADQI) Workgroup. In *Nature Reviews Nephrology* (Vol. 16, Issue 12, pp. 747–764). Nature Research. https://doi.org/10.1038/s41581-020-00356-5

Narayanan, K., Huang, C., Lokugamage, K., Kamitani, W., Ikegami, T., Tseng, C.-T. K., & Makino, S. (2008). Severe Acute Respiratory Syndrome Coronavirus nsp1 Suppresses Host Gene Expression, Including That of Type I Interferon, in Infected Cells. *Journal of Virology*, *82*(9), 4471–4479. https://doi.org/10.1128/jvi.02472-07

Ou, X., Liu, Y., Lei, X., Li, P., Mi, D., Ren, L., Guo, L., Guo, R., Chen, T., Hu, J., Xiang, Z., Mu, Z., Chen, X., Chen, J., Hu, K., Jin, Q., Wang, J., & Qian, Z. (2020). Characterization of spike glycoprotein of SARS-CoV-2 on virus entry and its immune cross-reactivity with SARS-CoV. *Nature Communications*, *11*(1). https://doi.org/10.1038/s41467-020-15562-9

Paul, M., Poyan Mehr, A., & Kreutz, R. (2006). Physiology of Local Renin-Angiotensin Systems. *Physiological Reviews*, *86*(3), 747–803. https://doi.org/10.1152/physrev.00036.2005

Pei, G., Zhang, Z., Peng, J., Liu, L., Zhang, C., Yu, C., Ma, Z., Huang, Y., Liu, W., Yao, Y., Zeng, R., & Xu, G. (2020). Renal involvement and early prognosis in patients with COVID-19 pneumonia. In *Journal of the American Society of Nephrology* (Vol. 31, Issue 6, pp. 1157–1165). American Society of Nephrology. https://doi.org/10.1681/ASN.2020030276

Peleg, Y., Kudose, S., D'Agati, V., Siddall, E., Ahmad, S., Nickolas, T., Kisselev, S., Gharavi, A., & Canetta, P. (2020). Acute Kidney Injury Due to Collapsing Glomerulopathy Following COVID-19 Infection. *Kidney International Reports*, *5*(6), 940–945. https://doi.org/10.1016/j.ekir.2020.04.017

Pfaffl, M. W. (2001). A new mathematical model for relative quantification in real-time RT-PCR. *Nucleic Acids Research*, *29*(9), e45. https://doi.org/10.1093/nar/29.9.e45

Preibisch, S., Saalfeld, S., & Tomancak, P. (2009). Globally optimal stitching of tiled 3D microscopic image acquisitions. *BIOINFORMATICS APPLICATIONS NOTE*, *25*(11), 1463–1465. https://doi.org/10.1093/bioinformatics/btp184

Puelles, V. G., Lütgehetmann, M., Lindenmeyer, M. T., Sperhake, J. P., Wong, M. N., Allweiss, L., Chilla, S., Heinemann, A., Wanner, N., Liu, S., Braun, F., Lu, S., Pfefferle, S., Schröder, A. S., Edler, C., Gross, O., Glatzel, M., Wichmann, D., Wiech, T., … Huber, T. B. (2020). Multiorgan and Renal Tropism of SARS-CoV-2. *New England Journal of Medicine*, *383*(6), 590–592. https://doi.org/10.1056/nejmc2011400

Randall, R. E., & Goodbourn, S. (2008). Interferons and viruses: an interplay between induction, signalling, antiviral responses and virus countermeasures. *The Journal of General Virology*, *89*(Pt 1), 1–47. https://doi.org/10.1099/vir.0.83391-0

Santoriello, D., Khairallah, P., Bomback, A. S., Xu, K., Kudose, S., Batal, I., Barasch, J., Radhakrishnan, J., D'Agati, V., & Markowitz, G. (2020). Postmortem Kidney Pathology Findings in Patients with COVID-19. *Journal of the American Society of Nephrology*, *31*(9), 2158–2167. https://doi.org/10.1681/ASN.2020050744

Schneider, C. A., Rasband, W. S., & Eliceiri, K. W. (2012). NIH Image to ImageJ: 25 years of image analysis. *Nature Methods*, *9*(7), 671–675. https://doi.org/10.1038/nmeth.2089

Schock, S. N., Chandra, N. V., Sun, Y., Irie, T., Kitagawa, Y., Gotoh, B., Coscoy, L., & Winoto, A.

(2017). Induction of necroptotic cell death by viral activation of the RIG-I or STING pathway. *Cell Death and Differentiation*, *24*(4), 615–625. https://doi.org/10.1038/cdd.2016.153

Siu, K.-L., Chan, C.-P., Kok, K.-H., Chiu-Yat Woo, P., & Jin, D.-Y. (2014). Suppression of innate antiviral response by severe acute respiratory syndrome coronavirus M protein is mediated through the first transmembrane domain. *Cellular & Molecular Immunology*, *11*(2), 141–149. https://doi.org/10.1038/cmi.2013.61

Soler, M. J., Ye, M., Wysocki, J., William, J., Lloveras, J., & Batlle, D. (2009). Localization of ACE2 in the renal vasculature: Amplification by angiotensin II type 1 receptor blockade using telmisartan. *American Journal of Physiology - Renal Physiology*, *296*(2), 398–405. https://doi.org/10.1152/ajprenal.90488.2008

Song, P., Li, W., Xie, J., Hou, Y., & You, C. (2020). Cytokine storm induced by SARS-CoV-2. *Clinica Chimica Acta*, *509*, 280–287. https://doi.org/https://doi.org/10.1016/j.cca.2020.06.017

Su, H., Yang, M., Wan, C., Yi, L. X., Tang, F., Zhu, H. Y., Yi, F., Yang, H. C., Fogo, A. B., Nie, X., & Zhang, C. (2020). Renal histopathological analysis of 26 postmortem findings of patients with COVID-19 in China. *Kidney International*, *98*(1), 219–227. https://doi.org/10.1016/j.kint.2020.04.003

Tanaka, T., Narazaki, M., & Kishimoto, T. (2014). IL-6 in inflammation, immunity, and disease. *Cold Spring Harbor Perspectives in Biology*, *6*(10), a016295. https://doi.org/10.1101/cshperspect.a016295

Tisoncik, J. R., Korth, M. J., Simmons, C. P., Farrar, J., Martin, T. R., & Katze, M. G. (2012). Into the Eye of the Cytokine Storm. *Microbiology and Molecular Biology Reviews*, *76*(1), 16 LP – 32. https://doi.org/10.1128/MMBR.05015-11

Uhlén, M., Fagerberg, L., Hallström, B. M., Lindskog, C., Oksvold, P., Mardinoglu, A., Sivertsson, Å., Kampf, C., Sjöstedt, E., Asplund, A., Olsson, I., Edlund, K., Lundberg, E., Navani, S., Szigyarto, C. A.-K., Odeberg, J., Djureinovic, D., Takanen, J. O., Hober, S., … Pontén, F. (2015). Tissue-based map of the human proteome. *Science*, *347*(6220), 1260419. https://doi.org/10.1126/science.1260419

Varga, Z., Flammer, A. J., Steiger, P., Haberecker, M., Andermatt, R., Zinkernagel, A. S., Mehra, M. R., Schuepbach, R. A., Ruschitzka, F., & Moch, H. (2020). Endothelial cell infection and endotheliitis in COVID-19. In *The Lancet* (Vol. 395, Issue 10234, pp. 1417–1418). Lancet Publishing Group. https://doi.org/10.1016/S0140-6736(20)30937-5

Wang, K., Sun, Q., Zhong, X., Zeng, M., Zeng, H., Shi, X., Li, Z., Wang, Y., Zhao, Q., Shao, F., & Ding, J. (2020). Structural Mechanism for GSDMD Targeting by Autoprocessed Caspases in Pyroptosis. *Cell*, *180*(5), 941-955.e20. https://doi.org/10.1016/j.cell.2020.02.002

Wang, Y., Wang, Y., Chen, Y., & Qin, Q. (2020). Unique epidemiological and clinical features of the emerging 2019 novel coronavirus pneumonia (COVID-19) implicate special control measures. *Journal of Medical Virology*, *92*(6), 568–576. https://doi.org/https://doi.org/10.1002/jmv.25748

Welsch, J. C., Charvet, B., Dussurgey, S., Allatif, O., Aurine, N., Horvat, B., Gerlier, D., & Mathieu, C. (2019). Type I Interferon Receptor Signaling Drives Selective Permissiveness of Astrocytes and Microglia to Measles Virus during Brain Infection. *Journal of Virology*, *93*(13). https://doi.org/10.1128/JVI.00618-19/ASSET/A08B1FA3-E64B-4C56-AEC6-540E338079CB/ASSETS/GRAPHIC/JVI.00618-19-F0008.JPEG

Welsch, J., Lionnet, C., Terzian, C., Horvat, B., Gerlier, D., & Mathieu, C. (2017). Organotypic Brain Cultures: A Framework for Studying CNS Infection by Neurotropic Viruses and Screening Antiviral Drugs. *BIO-PROTOCOL*, *7*(22). https://doi.org/10.21769/bioprotoc.2605

WHO. (2020). *Coronavirus disease (COVID-19)*. https://www.who.int/emergencies/diseases/novel-coronavirus-2019/question-and-answers-hub/q-a-detail/coronavirus-disease-covid-19

Wong, C., Wong, P., Tam, L.-S., Li, E., Chen, D., & Lam, C. (2009). Activation profile of Toll-like receptors of peripheral blood lymphocytes in patients with systemic lupus erythematosus. *Clinical and Experimental Immunology*, *159*, 11–22. https://doi.org/10.1111/j.1365-2249.2009.04036.x

Wong, K. T., Grosjean, I., Brisson, C., Blanquier, B., Fevre-Montange, M., Bernard, A., Loth, P., Georges-Courbot, M. C., Chevallier, M., Akaoka, H., Marianneau, P., Lam, S. K., Wild, T. F., & Deubel, V. (2003). A Golden Hamster Model for Human Acute Nipah Virus Infection. *American Journal of Pathology*, *163*(5), 2127–2137. https://doi.org/10.1016/S0002-9440(10)63569-9

Worldometer. Coronavirus Cases. (2021). https://www.worldometers.info/coronavirus/

Xie, X., Muruato, A., Lokugamage, K. G., Narayanan, K., Zhang, X., Zou, J., Liu, J., Schindewolf, C., Bopp, N. E., Aguilar, P. V, Plante, K. S., Weaver, S. C., Makino, S., LeDuc, J. W., Menachery, V. D., & Shi, P.-Y. (2020). An Infectious cDNA Clone of SARS-CoV-2. *Cell Host & Microbe*, *27*(5), 841-848.e3. https://doi.org/10.1016/j.chom.2020.04.004

Zhou, P., Yang, X. Lou, Wang, X. G., Hu, B., Zhang, L., Zhang, W., Si, H. R., Zhu, Y., Li, B., Huang, C. L., Chen, H. D., Chen, J., Luo, Y., Guo, H., Jiang, R. Di, Liu, M. Q., Chen, Y., Shen, X. R., Wang, X., … Shi, Z. L. (2020). A pneumonia outbreak associated with a new coronavirus of probable bat

origin. *Nature*, *579*(7798), 270–273. https://doi.org/10.1038/s41586-020-2012-7
Zhou, S., Xu, J., Xue, C., Yang, B., Mao, Z., & Ong, A. C. M. (2020). Coronavirus-associated kidney outcomes in COVID-19, SARS, and MERS: a meta-analysis and systematic review. In *Renal Failure* (Vol. 43, Issue 1, pp. 1–15). Taylor and Francis Ltd. https://doi.org/10.1080/0886022X.2020.1847724
Ziegler, C. G. K., Allon, S. J., Nyquist, S. K., Mbano, I. M., Miao, V. N., Tzouanas, C. N., Cao, Y., Yousif, A. S., Bals, J., Hauser, B. M., Feldman, J., Muus, C., Wadsworth, M. H., Kazer, S. W., Hughes, T. K., Doran, B., Gatter, G. J., Vukovic, M., Taliaferro, F., … Zhang, K. (2020). SARS-CoV-2 Receptor ACE2 Is an Interferon-Stimulated Gene in Human Airway Epithelial Cells and Is Detected in Specific Cell Subsets across Tissues. *Cell*, *181*(5), 1016-1035.e19. https://doi.org/10.1016/j.cell.2020.04.035

Figure 1. Schematic representation of the anatomy of hamster organotypic kidney cultures.

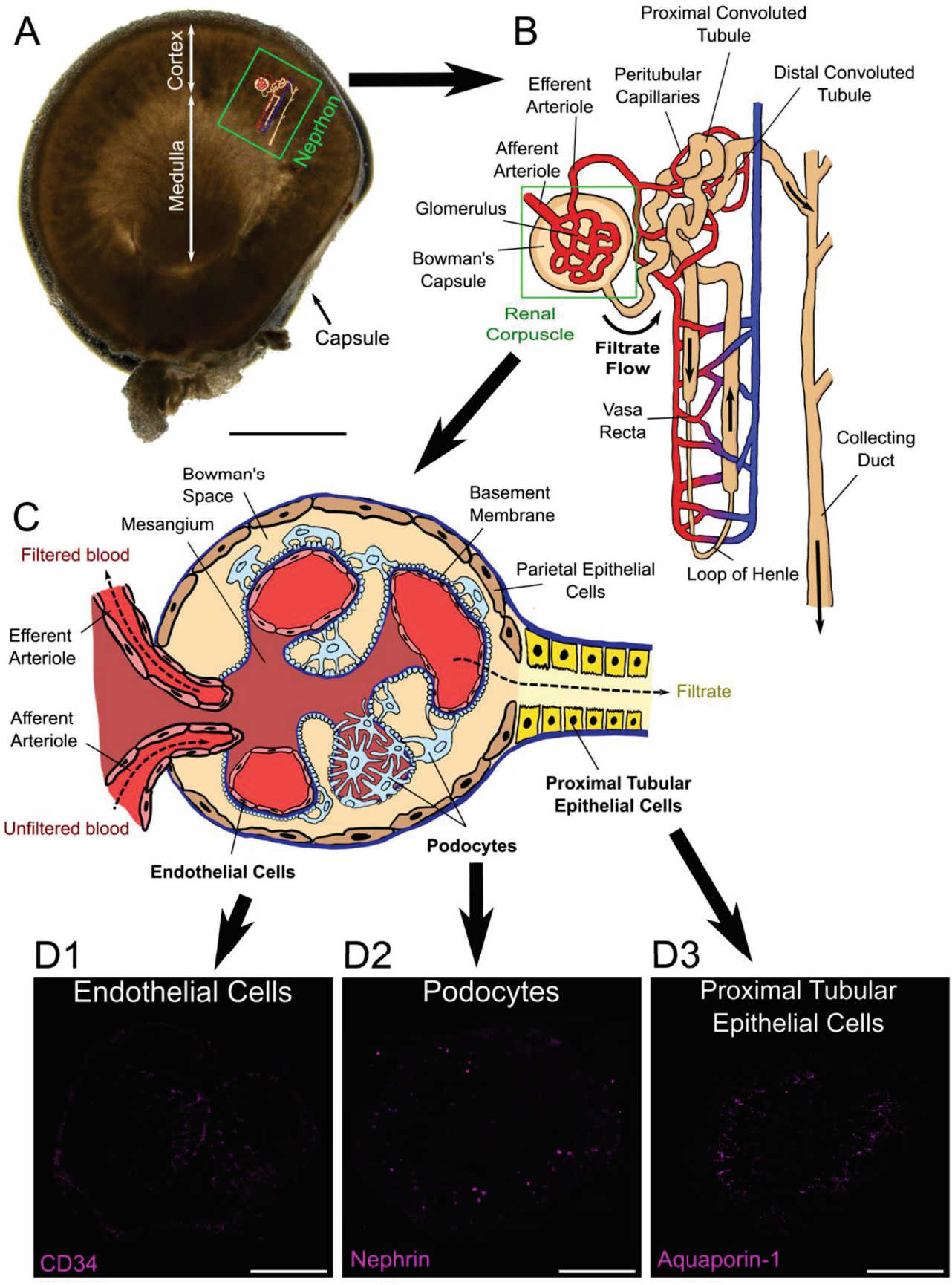
A
Cortex
Medulla
Nephron
Capsule
B
Proximal Convoluted Tubule
Peritubular Capillaries
Distal Convoluted Tubule
Efferent Arteriole
Afferent Arteriole
Glomerulus
Bowman's Capsule
Renal Corpuscle
Filtrate Flow
Vasa Recta
Collecting Duct
Loop of Henle
C
Bowman's Space
Mesangium
Basement Membrane
Filtered blood
Parietal Epithelial Cells
Efferent Arteriole
Filtrate
Afferent Arteriole
Proximal Tubular Epithelial Cells
Unfiltered blood
Podocytes
Endothelial Cells
D1
Endothelial Cells
CD34
D2
Podocytes
Nephrin
D3
Proximal Tubular Epithelial Cells
Aquaporin-1

(A) A 500-nm thick organotypic kidney slice maintained on an air-liquid interface provided by a PTFE membrane was photographed in brightfield using a Nikon Eclipse Ts2R epifluorescence microscope. Scalebar = 1 mm. The renal capsule, cortex and medulla are identified and labelled. A nephron schematic is positioned in its physiological location and highlighted with a green rectangle. **(B)** The structure of a nephron, a functional unit of the kidney, showing the flow of the filtrate. **(C)** The structure of a renal corpuscle. **(D)** Organotypic kidney cultures were fixed in 4% paraformaldehyde, embedded in optimal cutting temperature solution and cryosectioned at 10 µm thickness. Sections were immunostained to visualize endothelial cells, podocytes and proximal tubular epithelial cells with **(D1)** anti-CD34 (endothelial cells), **(D2)** anti-nephrin (podocytes) and **(D3)** anti-aquaporin1 (proximal tubular epithelial cells) primary antibodies. Scalebar = 1 mm. Images were reconstructed using the Stitching plugin in ImageJ (Preibisch et al., 2009).

Figure 2. Viability of hamster organotypic slices in culture.

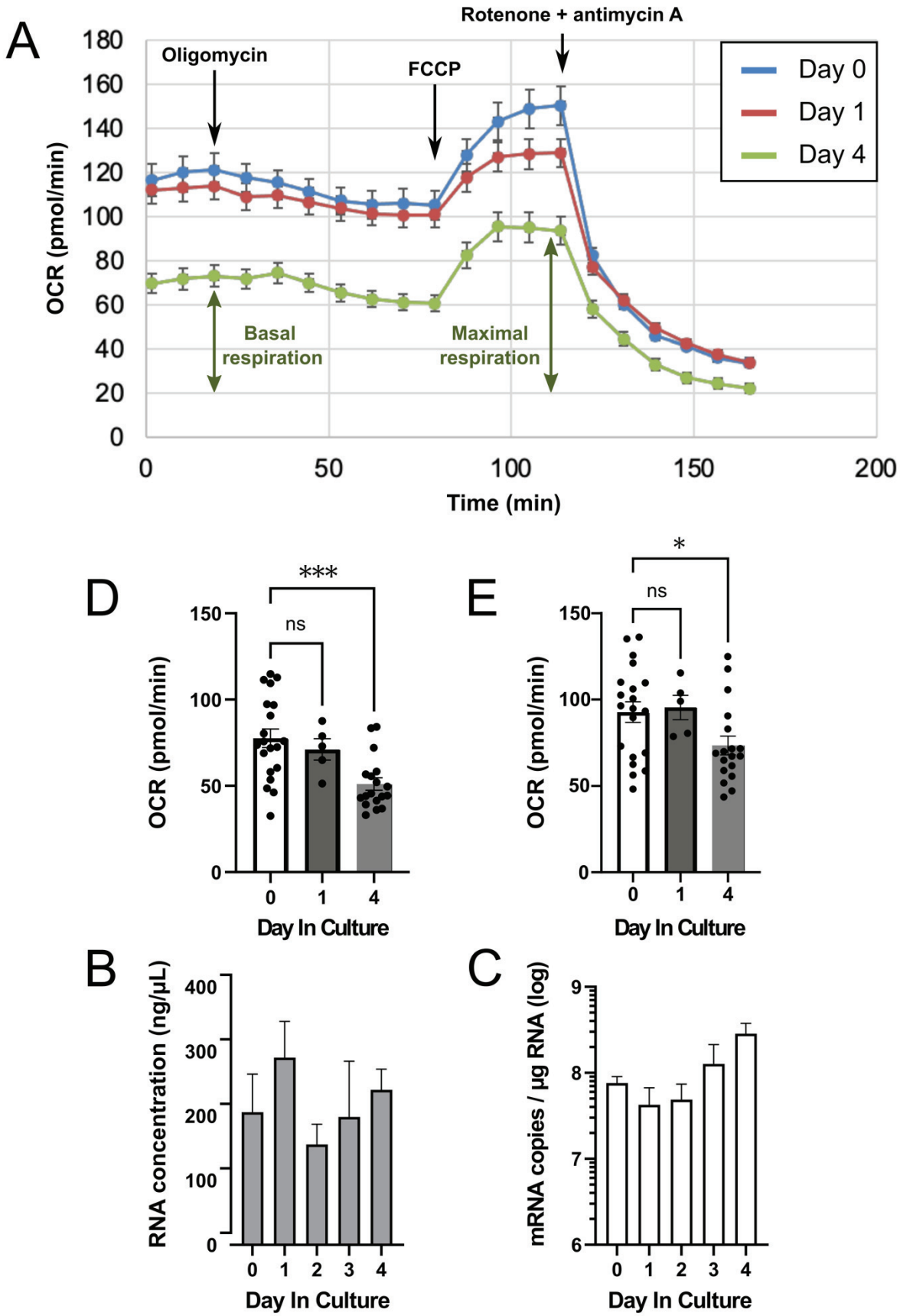

(A) The workflow of the Seahorse XF Analyzer metabolic activity assay performed on 1 mm punches of 400-nm thick organotypic kidney cultures maintained on an air-liquid interface in the OKC medium for 0, 1 or 4 days prior to measurement. The oxygen consumption rate (OCR) of punches was quantified. The basal respiration rate was measured prior to any drug administration. Oligomycin was added to inhibit ATP production and to allow distinguishing between ATP-linked and proton leak respiration (results not shown). The uncoupling agent FCCP disrupted the proton gradient, while rotenone and antimycin A completely inhibited mitochondrial respiration. Altogether, this allowed quantifying the maximal respiratory capacity of punches. (Divakaruni et al., 2014). The calculation methods of the basal and maximal respiration are indicated with green arrows on the example of the curve corresponding to 4-day old punches. **(B)** The basal and **(C)** maximal respiration rates of organotypic kidney cultures. OCR on days 1 and 4 was compared to that of day 0 using ordinary one-way ANOVA. *, $P < 0.05$; **, $P < 0.01$; ***, $P < 0.001$. **(D)** The concentration of RNA extracted from non-infected OKCs collected after 0 to 4 days of culture. **(E)** The expression of GAPDH in non-infected OKCs collected after 0 to 4 days of culture.

Figure 3. Permissiveness of and progression in hamster organotypic kidney cultures.

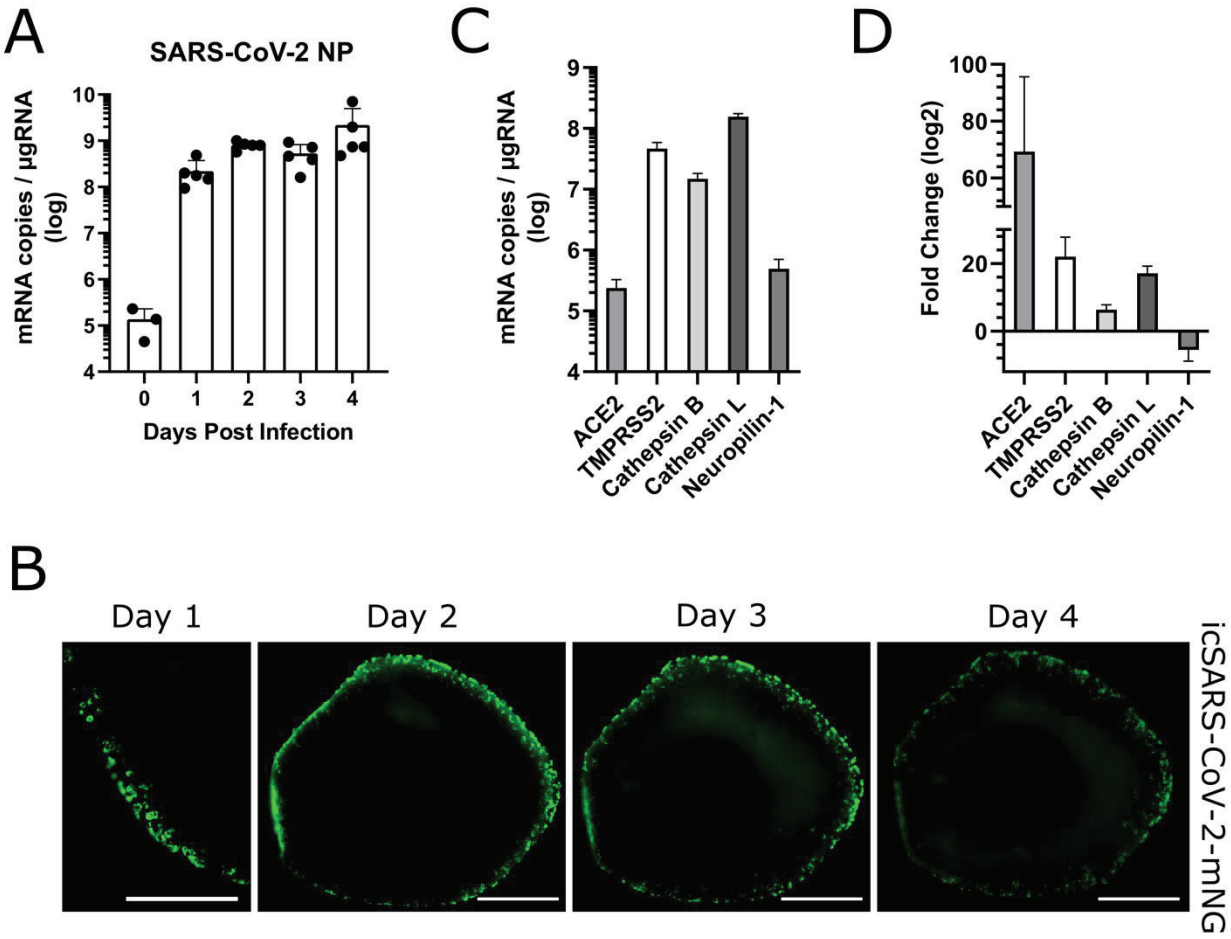

(A) Hamster organotypic cultures were infected with 1000 pfu of wild-type SARS-CoV-2 (2019-nCoV/USA_WA1/2020) and collected every day from day 0 (2 hours post-infection) to day 4 post-infection. The number of SARS-CoV-2 genomes was measured by quantifying the amount of SARS-CoV-2 nucleocapsid (NP) mRNA per µg of total mRNA via RT-qPCR and normalizing it by the expression of a housekeeping gene (GAPDH). **(B)** Hamster organotypic cultures infected with 10,000 pfu of SARS-CoV-2_mNeon Green (icSARS-CoV-2-mNG) were imaged from day 0 to day 1 post-infection using a Nikon Eclipse Ts2R epifluorescence microscope. Scalebar = 1 mm. The virus expresses mNeon Green after cell entry, rendering only successfully infected cells fluorescent. Non-infected slices, as well as infected slices at day 0 post-infection, could be visualized only at exposure levels significantly higher than those permitting the visualization of slices with advanced infection and are therefore not shown. **(C–D)** Gene expression was quantified in non-infected OKCs and hamster

organotypic lung cultures collected on the day of dissection via RT-qPCR as the number of mRNA copies per µg of total RNA and normalized by the standard deviation in GAPDH expression. **(C)** mRNA copy numbers of candidate SARS-CoV-2 entry factors per µg of total RNA. **(D)** Fold change of SARS-CoV-2 entry factor mRNA copy numbers per µg of total RNA in OKCs compared to organotypic lung cultures.

Figure 4. Tropism and dissemination of SARS-CoV-2 in hamster organotypic kidney cultures.

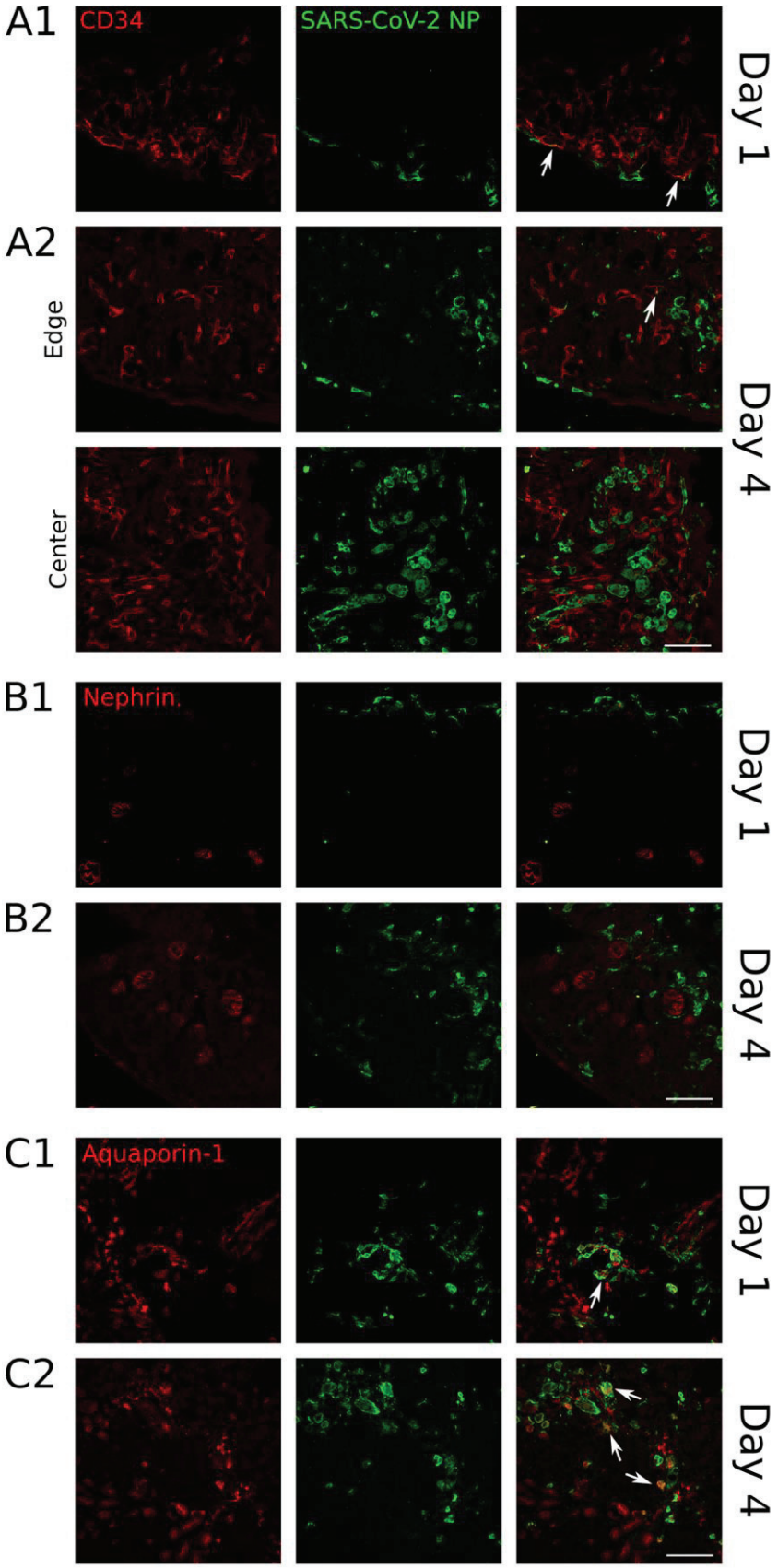

Organotypic kidney cultures infected with wild-type SARS-CoV-2 were fixed in 4% paraformaldehyde, embedded in optimal cutting temperature solution and cryosectioned at 10 µm thickness. Sections were immunostained with primary antibodies against SARS-CoV-2 nucleoprotein (NP) and renal cell population markers. Images were acquired using the Zeiss Axio Observer.Z1 microscope with confocal unit LSM980. Colocalization of cell type markers (red) with SARS-CoV-2 NP (green) is denoted with arrows. Scalebar = 100 µm. **(A)** OKC sections stained against SARS-CoV-2 NP and CD34 (marker of endothelial cells) on **(A1)** day 1 post-infection at the edge of the slice and **(A2)** day 4 (A2) post-infection at the edge of the slice and in its center, demonstrating the spread of infection towards the center. **(B–C)** OKC sections stained against SARS-CoV-2 NP and **(B)** nephrin (marker of podocytes), and **(C)** aquaporin-1 (marker of proximal tubular epithelial cells).

Figure 5. Transcriptomic analysis of hamster organotypic kidney cultures challenged with SARS-CoV-2.

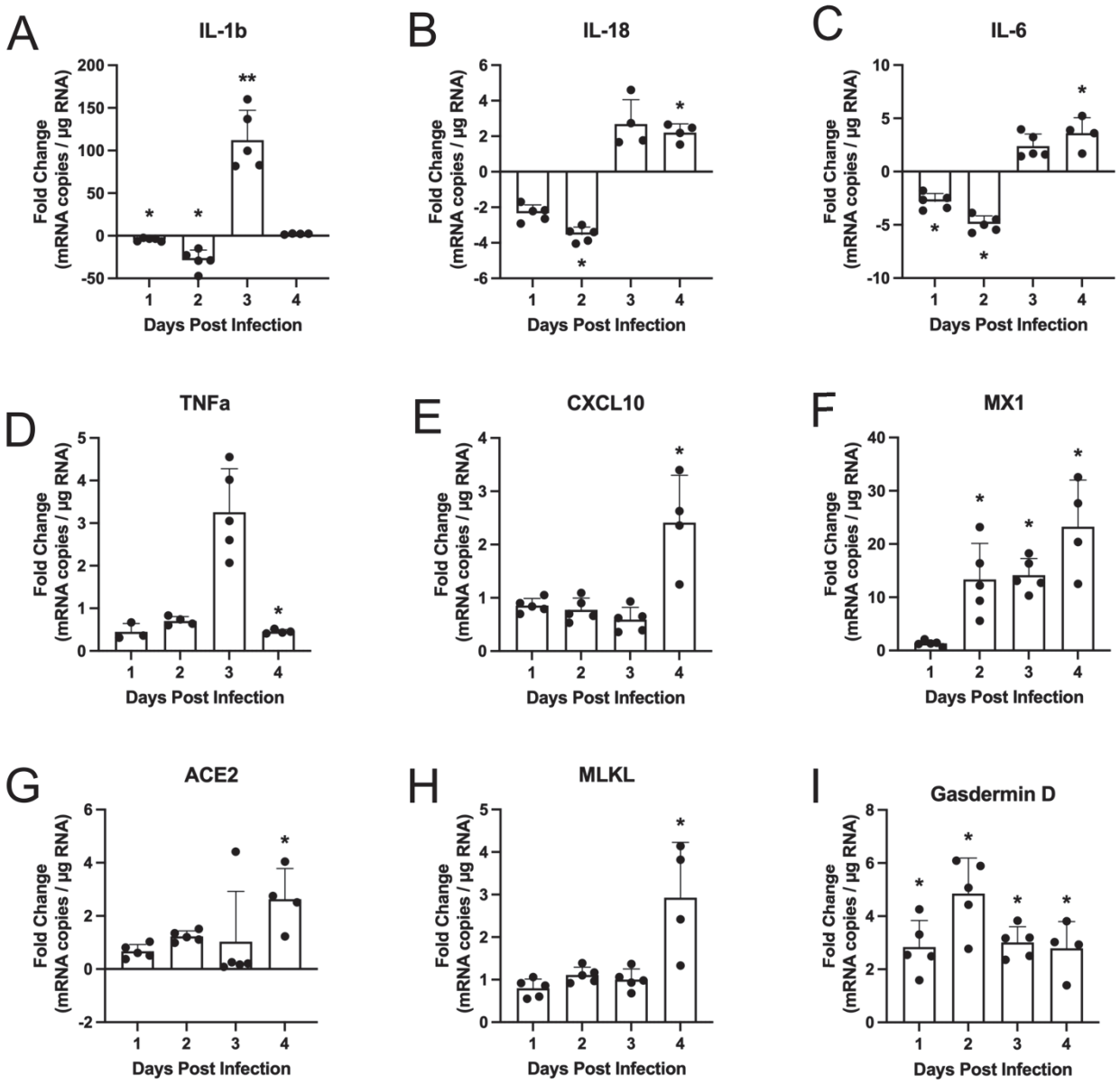

Hamster organotypic kidney cultures were cultured uninfected or infected with 1000 pfu of wild-type SARS-CoV-2 (2019-nCoV/USA_WA/2020) and collected every day from day 0 to day 4 post-infection. In both infected and non-infected slices, gene expression was measured via quantitative RT-PCR (RT-qPCR) as the number of mRNA copies per µg of total RNA and normalized by the standard deviation of GAPDH expression from its average across all days. To calculate the fold changes, values from infected slices were divided by the average values of non-infected slices from the corresponding day. **(A to I)** Fold change in the expression of **(A)** IL-1β, **(B)** IL-18, **(C)** IL-6, **(D)** TNFα, **(E)** CXCL10 **(F)** MX1 **(G)** ACE2 **(H)** MLKL **(I)** gasdermin D from

day 0 to day 4 post-infection. For each day, mRNA copy numbers per 1 µg of RNA of infected and non-infected samples were compared using the Mann-Whitney U-test. * = $p < 0.05$; ** = $p < 0.01$.

3) Tropisme précoce et dissémination du virus de la rougeole dans le CNS

a. Article de vulgarisation : Interféron de type I et sélectivité de l'infection des cellules du système nerveux central par le virus de la rougeole

Marion Ferren, Branka Horvat, Denis Gerlier et Cyrille Mathieu

Publié dans Médecine/sciences, 2021

Facteur d'impact : 0,818

Cet article de vulgarisation scientifique reprend les conclusions de l'étude publiée par Welsch et al. en 2019 dans Journal of Virology[274]*. Sur demande du journal « Medecine/sciences » j'ai présenté les résultats de cette étude différemment afin de les rendre plus accessibles à un public de médecins qui sont la cible principale de ce journal. Ayant apporté un support technique lors des révisions demandées pour la publication de l'article original j'ai saisi cette opportunité de pouvoir discuter les conclusions de cette étude. L'article est disponible en Annexe 1.*

Résumé de l'article :

Dans les études post-mortem, les victimes de MIBE et PESS présentent des antigènes viraux du VR majoritairement dans les neurones et les oligodendrocytes et quelquefois dans les astrocytes et les microglies. L'objectif de cette étude a été d'étudier si le tropisme du VR dans le SNC dépend des mécanismes de l'immunité innée. Cette question a été adressée dans des cultures organotypiques d'hippocampes de souriceaux génétiquement modifiés exprimant le récepteur SLAM de façon ubiquitaire (souris SLAM) et de souriceaux exprimant SLAM et étant rendues génétiquement déficientes pour le récepteur à l'interféron (souris SLAM IFNARKO). Les cultures ont été infectées le jour de la coupe et 7 jours après la coupe et les étapes précoces de l'infection ont été analysées. Dans les cultures organotypiques de souris SLAM les neurones constituent la population contribuant majoritairement à l'infection tandis que dans les cultures de souris SLAM IFNARKO tous les types cellulaires contribuent à l'infection. Enfin, lors de l'infection des cultures 7 jours après la coupe on observe une perte de susceptibilité à l'infection par le virus de la rougeole dans les cultures provenant des deux lignées de souris. Cette perte de susceptibilité globale est corrélée à une induction inversement proportionnelle d'IFN-β et des marqueurs de l'activation globale des systèmes tissulaires de défense et de réparation (S100B) et de l'activation spécifique des astrocytes, indiquant la mise en place d'une astrogliose. Cependant, dans les cultures provenant des souris immunocompétentes SLAM l'analyse révèle la résistance des astrocytes et des cellules microgliales via la signalisation IFNAR.

Ces résultats ont permis de mettre en évidence plusieurs caractéristiques des réponses inflammatoires liées aux interférons de type I, et de l'astrogliose impliqués dans la différence de susceptibilité des cellules à l'infection par le VR.

Cette étude a été réalisée avec le virus sauvage, or les séquences virales retrouvées dans les cerveaux de cas de MIBE et de PESS comportent des mutations associées à un phénotype hyperfusogène. Il serait donc intéressant de comparer ces observations avec des virus mutants porteurs de ces mutations.

b. Revue : Les encéphalites rougeoleuses : vers de nouveaux traitements

Marion Ferren, Branka Horvat et Cyrille Mathieu

Publié dans Viruses, 2019

Facteur d'impact : 5,048

Résumé de la revue :

L'objectif principal de cette revue (Annexe 2) était de faire l'état de l'art des encéphalites rougeoleuses et de faire le lien avec les traitements potentiels qui ont été testés dans ces contextes d'encéphalites ou qui pourraient être prometteurs. Pour illustrer le caractère hyperfusogène du VR conféré par les mutations dans la F retrouvées chez les patients souffrants de PESS (IC323-eGFP-F-T461I) ou de MIBE (IC323-eGFP-F-L454W) j'ai inclus des données originales obtenues après infection des cultures organotypiques de cervelet d'animaux plus ou moins susceptibles à l'infection en comparaison avec le virus sauvage. Des COC de souris n'exprimant pas de récepteur connu (C57BL/6 sauvage et IFNAR KO), des COC de souris SLAM-IFNAR KO et des COC de hamster ont été infectées par 1000 PFU de virus. L'infection a été suivie pendant 3 jours par microscopie à épifluorescence. Les images confirment la dissémination massive des virus portant les mutations L454W et T461I même en l'absence de récepteur connu tandis que le virus sauvage a besoin de l'expression du récepteur SLAM pour pouvoir se disséminer efficacement dans ce contexte d'infection neurale.

4) Traitements antiviraux contre le virus de la rougeole

a. Article 3 : Des fragments uniques des chaines variables d'anticorps neutralisent l'infection par le virus de la rougeole in vitro et *in vivo*

Cyrille Mathieu, Marion Ferren, Olivia Harder, Francesca T. Bovier, Tara C. Marcink, Camilla Predella, Fabrizio Angius, Jennifer Drew-Bear, Valerio N. Dorrello, Alex L. Greninger, Anne Moscona, Stefan Niewiesk , Branka Horvat et Matteo Porotto

Publié dans Cellular & Molecular Immunology, 2021
Facteur d'impact : 11,53

Malgré l'existence d'un vaccin efficace contre la rougeole il est nécessaire de développer des traitements pour prévenir la transmission de l'infection au sein des populations non-vaccinées et pour traiter les personnes immunodéprimées. Dans cette étude nous avons identifié plusieurs anticorps neutralisants monoclonaux de souris (mAbs) qui ciblent la protéine de fusion du VR dans son état de préfusion. Ces anticorps se sont montrés efficaces pour inhiber la fusion et l'infection virale in vitro des souches IC323 et G954 (isotypes D8 et B3). A partir de l'anticorps le plus efficace, nommé 77.4, nous avons conçu un fragment unique des régions variables en fusionnant celles des chaînes lourdes et légères en scFv (single-chain antibody fragment). Le scFv conserve la capacité d'inhiber la fusion et empêche l'infection in vitro par le VR. De plus, son administration intranasale en pré-traitement dans des rats des cotonniers prévient l'infection par le VR *in vivo*. Un effet synergique avec le peptide inhibiteur de fusion HRC4 a également été mis en lumière. Bien que le peptide HRC4 n'induit aucune toxicité *in vivo* l'utilisation synergique du scFV et du HRC4 permettrait non seulement de diminuer les doses administrées et donc de réduire les coûts mais surtout d'inhiber la fusion de 2 façons différentes, en neutralisant la F en pré-fusion et en empêchant le repliement de la F après son déclenchement. La combinaison de HRC4 avec le scFv permettrait ainsi de prévenir l'éventuelle émergence de mutants d'échappement.

Cellular & Molecular Immunology www.nature.com/cmi

CORRESPONDENCE

Single-chain variable fragment antibody constructs neutralize measles virus infection in vitro and in vivo

Cyrille Mathieu[1,2,3], Marion Ferren[1,2,3], Olivia Harder[4], Francesca T. Bovier[1,2,5], Tara C. Marcink[1,2], Camilla Predella[2], Fabrizio Angius[1,2], Jennifer Drew-Bear[1,2], N. Valerio Dorrello[2], Alex L. Greninger[6,7], Anne Moscona[1,2,8,9], Stefan Niewiesk[4], Branka Horvat[3] and Matteo Porotto[1,2,5]

Cellular & Molecular Immunology (2021) 18:1835–1837; https://doi.org/10.1038/s41423-021-00691-y

Despite the availability of an effective measles virus (MeV) vaccine and efforts to increase vaccine coverage by the WHO, UNICEF, and their partners, MeV has not been eradicated, and the estimated global measles death rose from 89,780 in 2016 to 207,500 in 2019.[1] Because there is an effective measles vaccine, antiviral development for measles has not been prioritized, but recent outbreaks have highlighted the need for drugs to prevent transmission in unvaccinated populations and to protect and treat immunocompromised individuals. We identified several neutralizing mouse monoclonal antibodies (mAbs) that target the MeV fusion (F) protein in its prefusion state[2] and inhibit fusion and viral infection. We engineered a single-chain variable fragment (scFv) from the most potent anti-MeV F mAb. The scFv retains the ability to inhibit fusion and prevents infection in vitro, and intranasal administration of the scFv antibody construct prevents infection in vivo.

MeV infects activated SLAM/CD150-expressing immune cells in the respiratory tract, from which the virus invades immune tissues.[3] Upon attachment of MeV to cell surface receptors, entry is mediated by the MeV receptor-binding (H) and F proteins, which comprise the H/F viral fusion complex on the surface of the virus[3–5] (Fig. 1a). Viral infection can be blocked at several steps during entry. MAbs that block H-receptor interaction and thereby interfere with entry have been described.[6] Entry can also be inhibited by interfering with the refolding step whereby the F protein attains a stable postfusion state—the process that drives membrane fusion during viral entry. This step relies on interaction between the complementary heptad repeat (HR) regions at the N- and C-termini of the protein (HRN and HRC). In previous studies, we demonstrated the potential of HR-targeting peptides as antiviral agents in vivo.[6] Several mAbs with neutralizing activity against MeV F have been identified,[7,8] and for one of these mAbs (mAb 186), neutralization potency correlated with recognition of the prefusion state of F.[9] However, mutation at F position 70 resulted in a naturally occurring mAb 186 escape mutant[7,8] (Fig. 1a and SFigs. 1–2); the IC323 strain has a K at F position 70, while the F of the circulating strain G954 has an R at this position and is not recognized by mAb 186 (see SFigs. 1–3).

We assessed viral neutralization by two mouse mAbs that target the prefusion F protein (77.4 and Y503, SFig. 3H-K). From the most potent antibody—77.4—we engineered an scFv by fusing the variable regions of the heavy (VH) and light chains (VL) of mAb 77.4 (SFig. 4A). The scFv construct was expressed in eukaryotic cells and affinity purified using a 6x histidine tag (see SI). The neutralizing activity of the scFv is shown in Fig. 1b, c (62.5 µg/ml or 2280 nM scFv is shown in 1 C; additional data are shown in SFig. 4). The scFv inhibited viral infection (Fig. 1b, c) and specifically bound to MeV F (SFig. 4E-F). Finally, we assessed whether the scFv blocked cell-cell fusion mediated by either MeV IC323 or G954 H/F fusion complexes using a beta-galactosidase (β-Gal) complementation assay[6] that measures the fusion of cells that express viral envelope glycoproteins (MeV IC323 or G954 H/F) with cells that express SLAM (Fig. 1d). The scFv inhibited cell fusion mediated by both the IC323 and G954 H/F fusion complexes (Fig. 1d).

To assess anti-MeV prophylaxis by the scFv in vivo, we used cotton rats as an infection model. The scFv antibody construct was administered intranasally 24 and 12 h before infection. Four days after infection, the animals were euthanized, and lung viral titers were measured. Treatment with scFv significantly reduced lung viral titers compared with those of untreated controls (Fig. 1e). We assessed three doses (0.25, 0.5 and 1 mg/ml) and observed that the two highest doses of scFv completely inhibited lung infection. The inhibition of infection in vivo after intranasal administration of scFv suggests that targeting the prefusion state of MeV F protein is a feasible anti-MeV strategy.

Next, we investigated the possibility of synergy between the scFv construct, which targets the early prefusion state of F, and HR-targeting antiviral peptides (HRC4) that target a later step, the refolding of the F protein after activation (Fig. 1f, g). Fusion of cells that express viral envelope glycoproteins with cells that express Nectin-4, a second MeV receptor, was quantified as shown in Fig. 1d. The results were analyzed with Combenefit software to obtain the additive curve based on the curves of the two

[1]Center for Host-Pathogen Interaction, Columbia University Vagelos College of Physicians and Surgeons, New York, NY, USA; [2]Department of Pediatrics, Columbia University Vagelos College of Physicians and Surgeons, New York, NY, USA; [3]CIRI, Centre International de Recherche en Infectiologie, Team IBIV, Univ Lyon, Inserm, U1111, Université Claude Bernard Lyon 1, CNRS, UMR5308, ENS de Lyon, F-69007 Lyon, France; [4]Department of Veterinary Biosciences, College of Veterinary Medicine, The Ohio State University, Columbus, OH, USA; [5]Department of Experimental Medicine, Università Vanvitelli, Caserta, Italy; [6]Department of Laboratory Medicine, University of Washington School of Medicine, Seattle, WA, USA; [7]Vaccine and Infectious Disease Division, Fred Hutchinson Cancer Research Center, Seattle, WA, USA; [8]Department of Microbiology & Immunology, Columbia University Vagelos College of Physicians and Surgeons, New York, NY, USA and [9]Department of Physiology & Cellular Biophysics, Columbia University Vagelos College of Physicians and Surgeons, New York, NY, USA
Correspondence: Cyrille Mathieu (cyrille.mathieu@inserm.fr) or Matteo Porotto (mp3509@cumc.columbia.edu)

Received: 16 April 2021 Accepted: 20 April 2021
Published online: 18 May 2021

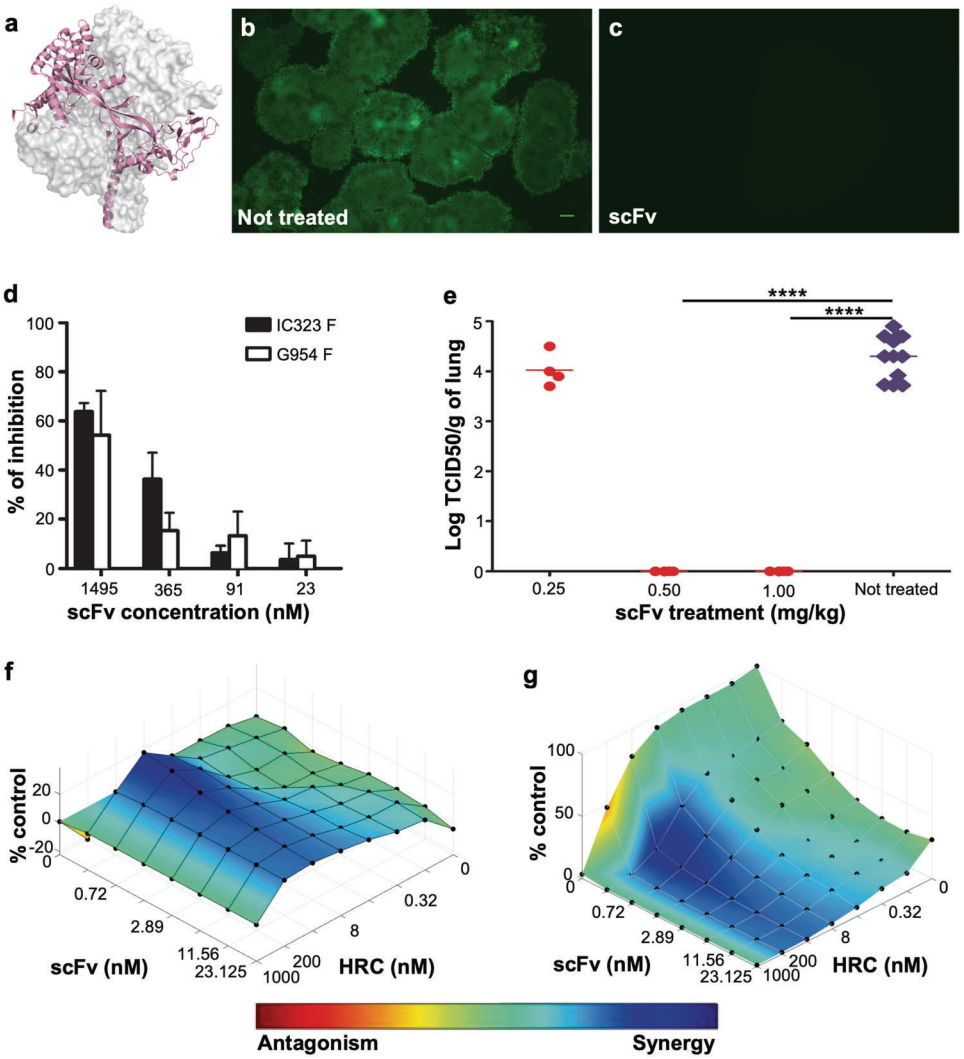

Fig. 1 A single-chain variable fragment (scFv) derived from mAb 77.4 inhibits MeV infection in vitro and in vivo. **a** Measles virus (MeV) fusion (F) protein in PyMOL (Schrödinger) using the crystal structure of MeV prefusion F ectodomain[2] (PDBID: 5YXW). **b**–**c** scFv inhibits MeV infection: Vero-SLAM cells treated with the indicated concentration of scFv (or not treated) were infected with MeV IC323-EGFP at a multiplicity of infection of 0.001. Images were obtained using epifluorescence microscopy 48 h after infection (scale bar = 200 µm). **d** scFv inhibits MeV H/F-mediated fusion: Fusion of MeV G954 or IC323 H/F-coexpressing cells with SLAM-bearing cells in the presence of the scFv at the indicated concentrations was quantified at 6 h. The results are presented as the percent reduction in luminescence (*Y*-axis) compared to no treatment. Each bar represents the mean (±standard error) of results from at least three separate experiments. **e** scFv blocks MeV in vivo: Cotton rats were infected intranasally with 10^5 $TCID_{50}$/mL MeV WTFb. Animals received either the indicated amount of the mAb 77.4-derived scFv construct ($n = 4$) or vehicle ($n = 8$) 24 h and 12 h prior to infection. Animals were euthanized 5 days after infection. The results are presented as $TCID_{50}$/g of lung tissue. Statistical analyses were performed using the Mann–Whitney U test. **f**–**g** The mAb 77.4-derived scFv and HRC4 peptide inhibitor were synergistic in fusion assays. The effects of mAb 77.4-derived scFv and the HRC4 inhibitor on MeV H/F-mediated cell fusion were assessed and analyzed using Combenefit software. **f** Loewe synergy and antagonism response surface for scFv and HRC4 at the indicated concentrations. **g** Multicolor synergism response surface in comparison to the additive outcome. Data are from three independent experiments

inhibitors alone and to compare this with the result of the inhibitors added together (see also SFig. 5), revealing significant synergy between scFv and HRC4 for inhibiting viral fusion. Similar results were obtained when we assessed the combined effects of mAb 77.4 and HRC4 on viral fusion (see SFig. 6).

Grafting the variable region to a single-chain antibody would reduce the size of the inhibitor and may permit the construct to cross the blood-brain barrier to address central nervous system manifestations of disease. Intranasal administration of the scFv construct was sufficient to neutralize MeV infection, suggesting that these modifications may be tolerated without loss of efficacy. Targeting viral entry is an ideal approach to prevent transmission of respiratory viruses.[10] Future strategies will entail either combination of the two entry inhibitors or conjugation of HRC4 and scFv (or a single-chain antibody) into a single bifunctional inhibitor.

ACKNOWLEDGEMENTS

We thank J. S. Orange and S. G. Kernie for their contributions to this study.

FUNDING

The work was supported by grants from the NIH: AI121349, NS091263, and NS105699, AI146980 to M.P., from the French ANR NITRODEP (ANR-13-PDOC-0010-01) to C.M. and from the Region Auvergne Rhone Alpes and LABEX ECOFECT (ANR-11-LABX-0048) of Lyon University within the program "Investissements d'Avenir" (ANR-11-IDEX-0007),

operated by the French National Research Agency (ANR) to B.H. The Sharon Golub Fund at Columbia University Irving Medical Center (CUIMC).

ADDITIONAL INFORMATION

Supplementary information The online version contains supplementary material available at https://doi.org/10.1038/s41423-021-00691-y.

Competing interests: C.M., A.M., B.H., and M.P. have submitted a provisional on the use of the scFv.

REFERENCES

1. Durrheim, D. N. et al. A dangerous measles future looms beyond the COVID-19 pandemic. *Nat. Med.* **27**, 360–361 (2021). https://doi.org/10.1038/s41591-021-01237-5.
2. Hashiguchi, T. et al. Structures of the prefusion form of measles virus fusion protein in complex with inhibitors. *Proc. Natl Acad. Sci. USA* **115**, 2496–2501 (2018).
3. Tatsuo, H., Ono, N., Tanaka, K. & Yanagi, Y. SLAM (CDw150) is a cellular receptor for measles virus. *Nature* **406**, 893–897 (2000).
4. Chang, A. & Dutch, R. E. Paramyxovirus fusion and entry: multiple paths to a common end. *Viruses* **4**, 613–636 (2012).
5. Harrison, S. C. Viral membrane fusion. *Nat. Struct. Mol. Biol.* **15**, 690–698 (2008).
6. Welsch, J. C. et al. Fatal measles virus infection prevented by brain-penetrant fusion inhibitors. *J. Virol.* **87**, 13785–13794 (2013).
7. Malvoisin, E. & Wild, F. Contribution of measles virus fusion protein in protective immunity: anti-F monoclonal antibodies neutralize virus infectivity and protect mice against challenge. *J. Virol.* **64**, 5160–5162 (1990).
8. Fayolle, J., Verrier, B., Buckland, R. & Wild, T. F. Characterization of a natural mutation in an antigenic site on the fusion protein of measles virus that is involved in neutralization. *J. Virol.* **73**, 787–790 (1999).
9. Avila, M. et al. Molecular determinants defining the triggering range of prefusion F complexes of canine distemper virus. *J. Virol.* **88**, 2951–2966 (2014).
10. Czuppon, P. et al. Success of prophylactic antiviral therapy for SARS-CoV-2: Predicted critical efficacies and impact of different drug-specific mechanisms of action. *PLoS Comput Biol.* **17**, e1008752 (2021).

b. Inhibition de l'infection par des virus de la rougeole mutants neuropathogènes par un fragment unique des chaines variables d'anticorps

Les encéphalites rougeoleuses de type MIBE et PESS sont incurables et entrainent systématiquement la mort des patients. Le développement de traitement permettant de stopper la progression de l'infection par le VR dans le SNC est donc un enjeu de taille. Pour compléter l'étude prometteuse sur le scFv, j'ai donc testé l'efficacité du scFv en cultures organotypiques de cervelet de souris IFNARKO infectées par le virus mutant hyperfusogène portant la mutation L454W dans la F retrouvée chez des patients souffrant de MIBE, MeV-IC323-eGFP-F-L454W. Les COC ont été traitées un jour après infection par le scFv et par le peptide HRC4 (figure 14). Le scFv a permis de diminuer la dissémination virale en inhibant plus de 60% de l'infection après 4 jours d'infection. Ce résultat est particulièrement encourageant car les anticorps correspondants n'ont aucune efficacité antivirale lors des précédents tests dans le même tissu sans doute à cause de leur taille les empêchant d'accéder aux couches internes de la culture (résultats ANR NITRODEP-2013-2017).

L'effet synergique entre le peptide HRC4 et le scFv a été testé dans ce même contexte de tissu cérébral, dans des COC infectées par le virus sauvage ou par le virus mutant hyperfusogène MeV-IC323-eGFP-F-L454W (figure 15). Le virus sauvage n'est pas capable de se disséminer dans les COC de souris IFNAR KO en absence du récepteur SLAM, ainsi l'expérience a été réalisée en COC provenant de souris SLAM IFNAR KO exprimant SLAM de façon ubiquitaire. Les résultats confirment l'effet synergique de HRC4 et du scFv pour inhiber l'infection par le virus sauvage dans ce contexte. En revanche un effet synergique n'a pas pu être vérifié pour le virus mutant portant la mutation L454W dans la F. En effet, le peptide HRC4 est particulièrement efficace pour bloquer l'infection par ce virus et il faudrait à l'avenir répéter cette expérience en diminuant la dose de HRC4, 50 nM au lieu de 250 nM par exemple, afin de pouvoir observer cet effet synergique. La dose de virus pour réaliser l'infection pourrait aussi être réduite à 100 PFU au lieu de 1000 PFU pour permettre une collection des échantillons lorsque l'infection est encore en phase ascendante.

La taille du scFv reste trop grande (approximativement 30 kilodaltons) pour traverser passivement la barrière hématoencéphalique mais son efficacité a pu être vérifiée *ex vivo*. Les résultats obtenus sont prometteurs pour ralentir l'infection par des mutants hyperfusogènes du VR dans le SNC. La structure du scFv peut être optimisée afin d'être encore réduite et conjuguée au peptide HRC4 déjà très puissant pour bloquer l'infection du VR. La présence de la molécule de cholestérol dans le peptide HRC4 permettrait au scFv de cibler le cerveau.

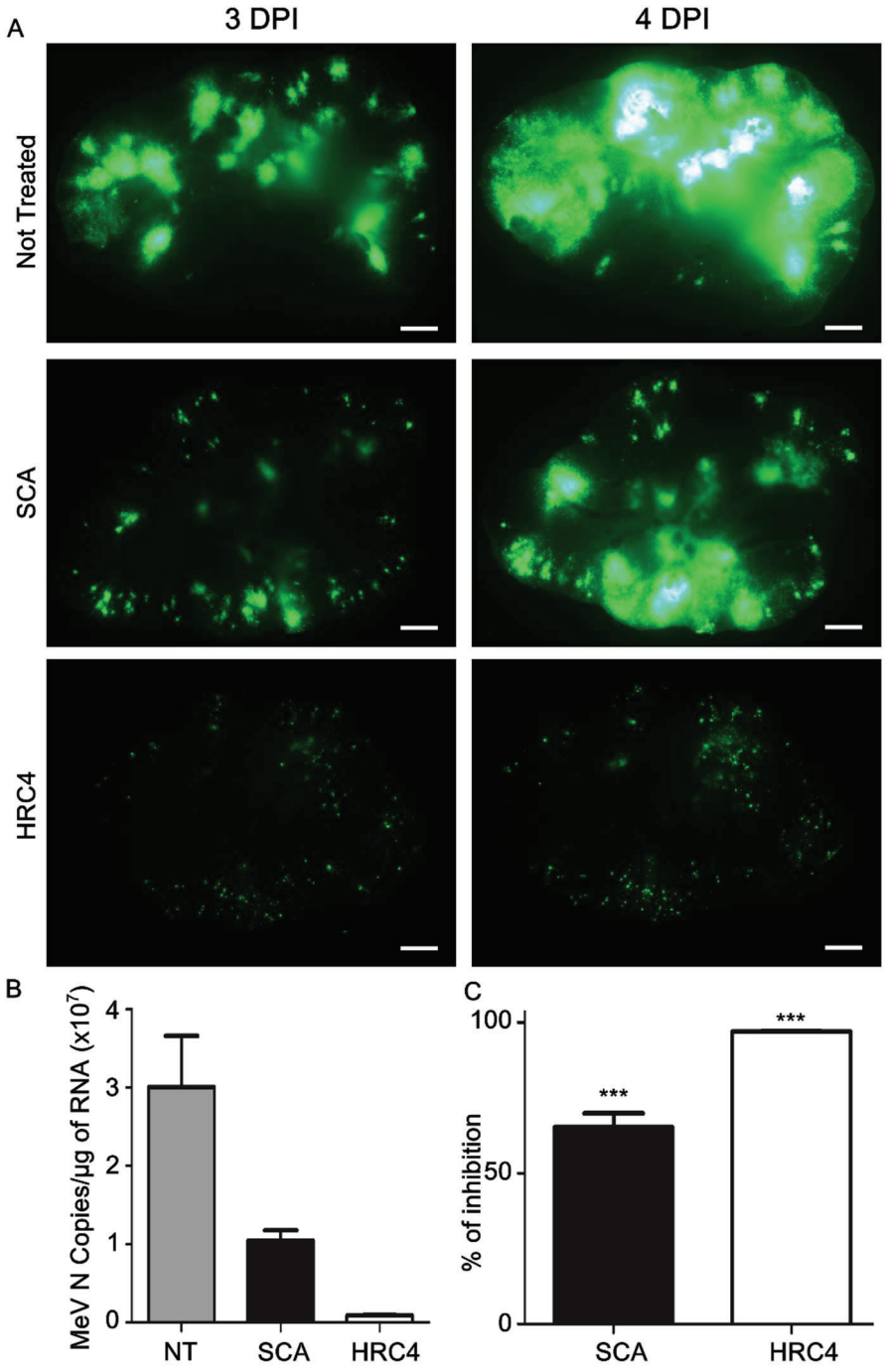

Figure 14 : Le scFv issu de l'anticorps monoclonal mAb77.4 bloque en partie la dissémination de MeV IC323-eGFP-F-L454W en cultures organotypiques de cervelet (COC) de souris IFNARKO.

Les COC provenant de souris IFNAR KO ont été infectées avec 1000 PFU par le mutant hyperfusogène MeV IC323-eGFP-F-L454W. Les COC ont ensuite été traitées quotidiennement à partir du jour 1 jusqu'au jour 4 après infection, soit par le scFV dérivé de mAb77.4 (10µg/ml) soit par le peptide inhibiteur de fusion HRC4 à 1µM, ou par un véhicule (Non traitées, NT). A) les images ont été obtenues à 3 et 4 jours post infection (dpi) par microscopie à épifluorescence (échelle = 1mm). B) et C) Quatre jours après infection les COC ont été collectées et l'ARN total a été extrait. Le nombre de copies de N du virus de la rougeole par µg d'ARN total et le pourcentage

d'inhibition de l'infection des cultures traitées comparées aux cultures non-traitées ont été obtenus par RT-qPCR (n=4 minimum). L'analyse statistique a été obtenue par un « one sample t-test » (***p<0.001). SCA = Single-chain antibody.

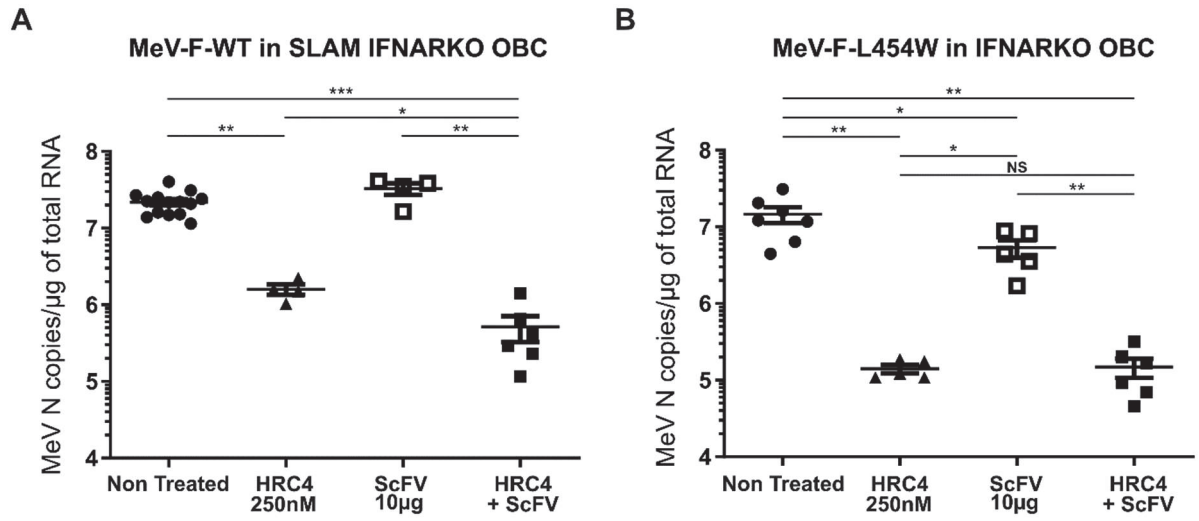

Figure 15 : Le scFv issus de l'anticorps monoclonal mAb77.4 en combinaison avec le peptide HRC4 a un effet synergique pour bloquer la dissémination du virus de la rougeole en cultures organotypiques de cervelet (COC) de souris.

Les COC issues de souris A, SLAM IFNAR KO A) ou B, IFNAR KO ont été infectées avec 1000 PFU par le virus sauvage A, MeV IC323-eGFP-F-WT, ou par le mutant hyperfusogène B, MeV IC323-eGFP-F-L454W. Les COC ont ensuite été traitées quotidiennement à partir du jour 1 jusqu'au jour 4 après infection, par le scFV dérivé de mAb77.4 (10µg/ml), par le peptide HRC4 à 250nM, ou par un véhicule (Non traitées). Les COC ont été collectées 4 jours après infection et l'ARN total a été extrait. Le nombre de copies de N du virus de la rougeole par µg d'ARN total et le pourcentage d'inhibition de l'infection des cultures traitées comparées aux cultures non-traitées ont été obtenus par RT-qPCR (n=4 minimum). L'analyse statistique a été obtenue par un one sample t-test (***p<0.001).

II. Hyperfusogénicité et infection du SNC par le virus de la rougeole

1) Impacte de la déstabilisation de la F dans l'invasion du SNC

a. Etude de l'impact des mutations dans la F et la H de souches du virus de la rougeole issu de cas SSPE dans la machinerie de fusion

Les résultats obtenus dans ce paragraphe ont été publiés dans Journal of Virology en 2019 par Fabrizio Angius et collègues (Analysis of a Subacute Sclerosing Panencephalitis genotype B3 virus from the 2009-2010 South African Measles epidemic shows that hyperfusogenic F proteins contribute to Measles virus infection in the brain) (Annexe 3). Je suis co-auteure de cette publication et j'ai réalisé une partie des expériences publiées dans cette étude en 2018 juste avant de commencer cette thèse. L'article complet est disponible en Annexe. J'ai présenté ces résultats dans une communication orale lors d'un mini symposium sur la rougeole à Rochester en 2019 et dans un poster au congrès de la société américaine de virologie (ASV) en 2019 à Minneapolis. Ces résultats permettent d'introduire la suite de cette partie sur l'étude de la machinerie de fusion des mutants hyperfusogènes du virus de la rougeole.

A la suite d'une épidémie du virus de la rougeole en 2009 en Afrique du Sud des enfants ont développé des PESS. Dans le but d'étudier les caractéristiques des infections du SNC par le VR, nous avons analysé les séquences virales provenant d'échantillons de tissu cérébral d'un cas de PESS. Ces séquences ont été comparées à celles provenant de cas de MIBE précédemment obtenues à partir de patients infectés au cours de la même épidémie.

Dans les deux cas, des substitutions d'acides aminés ont été identifiées dans l'ectodomaine de la protéine F et confèrent des propriétés de fusion améliorées. Parmi les mutations retrouvées dans la séquence F-PESS du patient sud-africain (G168R/E170G/S262G/A440P/R520C/L550P et X551G), la mutation S262G (position déjà associée à l'hyperfusogénicité avec une mutation S262R) située à l'interface de trois protomères, impliquée dans l'activation de la fusion, et la mutation X551G conférant la longue queue cytoplasmique peuvent conférer seules un phénotype hyperfusogène à la F sans avoir besoin d'aucune autre mutation. D'une façon générale, l'état de pré-fusion est généralement moins stable dans les isolats du SNC. L'analyse fonctionnelle du virus MeV_IC323 portant cette F-SSPE avec les 7 mutations a confirmé qu'une souche PESS peut se disséminer de cellule à cellule dans les cellules Vero, en l'absence de récepteurs connus.

Nos résultats suggèrent que les altérations du complexe de fusion du VR qui favorisent la fusion et la propagation de cellule à cellule en l'absence de récepteurs MeV connus sont une propriété clé pour l'infection du cerveau.

b. Article 4 : Caractéristiques moléculaires du complexe de fusion de virus de la rougeole favorisant l'infection et la propagation dans le cerveau

Cyrille Mathieu, Francesca T Bovier, Marion Ferren, Nicole A P Lieberman, Camilla Predella, Alexandre Lalande, Vikas Peddu, Michelle J Lin, Amin Addetia, Achchhe Patel, Victor Outlaw, Barbara Corneo, Valerio N Dorrello, Thomas Briese, Diana Hardie, Branka Horvat, Anne Moscona, Alexander L Greninger et Matteo Porotto.

Publié dans mBio, 2021

https://doi.org/10.1128/mBio.00799-21.

Facteur d'impact : 7,867

Résumé de l'article :

La mutation L454W dans la protéine de fusion du VR a été retrouvée dans des séquences d'ARN issues de cerveaux de patients décédés d'une MIBE. Dans cette étude nous avons infecté des cultures organotypiques de cervelet de souris génétiquement modifiées IFNAR KO ou SLAM/IFNAR KO et des organoïdes de cerveau humain générés à partir de cellules souches pluripotentes induites humaines avec différents VR mutants au niveau du domaine HRC de la F.

Remarquablement, le VR recombinant portant la mutation L454W tend à évoluer très rapidement en cellules Vero exprimant le récepteur SLAM humain (Vero hSLAM), sans la pression de sélection du SNC, et acquiert la double mutation L454W/E455G qui confère au virus un phénotype sauvage en rétablissant la stabilité de la F. A l'inverse, la mutation E455G présente partiellement (55%) dans ce virus L454W est contre-sélectionnée après passage en organoïdes de cerveau humain et en cultures organotypiques de souris IFNAR KO au profit de la mutation L454W seule. Les tests de fusogénicité et de stabilité thermique ont montré que la mutation E455G augmente considérablement la stabilité de F au point d'empêcher totalement la fusion tandis que la mutation L454W déstabilise la F et donc induit la fusion sans l'engagement de la protéine d'attachement H du virus, même en l'absence de récepteur. En revanche la double mutation L454W/E455G nécessite l'engagement de la H au récepteur afin de médier la fusion. Bien qu'elles résultent d'un artefact de laboratoire, cette mutation compensatoire fournit une preuve directe que les virus capables de fusionner en l'absence de récepteurs connus sont positivement sélectionnés dans le SNC. En effet, d'autres mutations associées à la mutation L454W déstabilisant encore plus la F sont également présentées dans cet article. De plus, dans un contexte neural, la propagation du virus portant la F L454W est totalement bloquée par un peptide dérivé du domaine HRC de la F visant à bloquer la fusion en capturant la protéine F dans son état métastable après avoir été

déclenchée. Ce résultat confirme que la dissémination dans le tissu cérébral est attribuable à la F.

Dans cet article, nous montrons que les virus portant la F mutée L454W observée dans des cas de MIBE et la F mutée dérivée T461I dérivée de SSPE sont avantagés pour infecter et se propager de cellule à cellule dans des modèles d'infection du SNC. Seuls les virus porteurs d'un complexe de fusion dérégulé particulièrement instable ont été sélectionnés positivement dans le SNC.

AMERICAN SOCIETY FOR MICROBIOLOGY | mBio®

RESEARCH ARTICLE

Molecular Features of the Measles Virus Viral Fusion Complex That Favor Infection and Spread in the Brain

Cyrille Mathieu,[a,b,c] Francesca T. Bovier,[a,b,d] Marion Ferren,[a,b,c] Nicole A. P. Lieberman,[e] Camilla Predella,[b] Alexandre Lalande,[c] Vikas Peddu,[e] Michelle J. Lin,[e] Amin Addetia,[e] Achchhe Patel,[f] Victor Outlaw,[g] Barbara Corneo,[f] N. Valerio Dorrello,[b] Thomas Briese,[h,i] Diana Hardie,[j] Branka Horvat,[c] Anne Moscona,[a,b,k,l] Alexander L. Greninger,[e] Matteo Porotto[a,b,d]

[a]Center for Host-Pathogen Interaction, Columbia University Vagelos College of Physicians and Surgeons, New York, New York, USA
[b]Department of Pediatrics, Columbia University Vagelos College of Physicians and Surgeons, New York, New York, USA
[c]CIRI, Centre International de Recherche en Infectiologie, Team Immuno-Biology of Viral Infections, University of Lyon, Inserm, U1111, Université Claude Bernard Lyon 1, CNRS, UMR5308, ENS de Lyon, Lyon, France
[d]Department of Experimental Medicine, University of Study of Campania "Luigi Vanvitelli", Naples, Italy
[e]Department of Laboratory Medicine, University of Washington Medical Center, Seattle, Washington, USA
[f]Stem Cell Core Facility, Columbia University Vagelos College of Physicians and Surgeons, New York, New York, USA
[g]Department of Chemistry, University of Wisconsin–Madison, Madison, Wisconsin, USA
[h]Center for Infection and Immunity, Mailman School of Public Health, Columbia University, New York, New York, USA
[i]Department of Epidemiology, Mailman School of Public Health, Columbia University, New York, New York, USA
[j]Division of Medical Virology, Department of Clinical Laboratory Sciences, University of Cape Town and National Health Laboratory Service, Cape Town, South Africa
[k]Department of Microbiology, Columbia University Vagelos College of Physicians and Surgeons, New York, New York, USA
[l]Department of Physiology and Cellular Biophysics, Columbia University Vagelos College of Physicians and Surgeons, New York, New York, USA

ABSTRACT Measles virus (MeV) bearing a single amino acid change in the fusion protein (F)—L454W—was isolated from two patients who died of MeV central nervous system (CNS) infection. This mutation in F confers an advantage over wild-type virus in the CNS, contributing to disease in these patients. Using murine *ex vivo* organotypic brain cultures and human induced pluripotent stem cell-derived brain organoids, we show that CNS adaptive mutations in F enhance the spread of virus *ex vivo*. The spread of virus in human brain organoids is blocked by an inhibitory peptide that targets F, confirming that dissemination in the brain tissue is attributable to F. A single mutation in MeV F thus alters the fusion complex to render MeV more neuropathogenic.

IMPORTANCE Measles virus (MeV) infection can cause serious complications in immunocompromised individuals, including measles inclusion body encephalitis (MIBE). In some cases, MeV persistence and subacute sclerosing panencephalitis (SSPE), another severe central nervous system (CNS) complication, develop even in the face of a systemic immune response. Both MIBE and SSPE are relatively rare but lethal. It is unclear how MeV causes CNS infection. We introduced specific mutations that are found in MIBE or SSPE cases into the MeV fusion protein to test the hypothesis that dysregulation of the viral fusion complex—comprising F and the receptor binding protein, H—allows virus to spread in the CNS. Using metagenomic, structural, and biochemical approaches, we demonstrate that altered fusion properties of the MeV H-F fusion complex permit MeV to spread in brain tissue.

KEYWORDS viral fusion, central nervous system infection, host-pathogen interaction, viral evolution

Despite the availability of an effective measles virus (MeV) vaccine, MeV has not been eradicated and has caused 100,000 to 140,000 deaths globally every year since 2010 (1–3). MeV eradication by vaccination is hindered in part by low vaccination

Citation Mathieu C, Bovier FT, Ferren M, Lieberman NAP, Predella C, Lalande A, Peddu V, Lin MJ, Addetia A, Patel A, Outlaw V, Corneo B, Dorrello NV, Briese T, Hardie D, Horvat B, Moscona A, Greninger AL, Porotto M. 2021. Molecular features of the measles virus viral fusion complex that favor infection and spread in the brain. mBio 12:e00799-21. https://doi.org/10.1128/mBio.00799-21.

Invited Editor W. Paul Duprex, University of Pittsburgh School of Medicine

Editor Michael S. Diamond, Washington University School of Medicine

Address correspondence to Cyrille Mathieu, cyrille.mathieu@inserm.fr, Alexander L. Greninger, agrening@uw.edu, or Matteo Porotto, mp3509@columbia.edu.

Received 23 March 2021
Accepted 23 April 2021
Published 1 June 2021

coverage, in part related to hesitancy about vaccine safety (4). Since the current vaccine is a live attenuated viral vaccine, it cannot be used in most immunocompromised people. Measles has been undergoing a global resurgence which may worsen since the SARS-CoV-2 pandemic has led to reduced routine childhood vaccination coverage and may expose more vulnerable individuals to infection (5).

MeV infection can result in fatal complications days to years after the acute phase of the infection when it infects the central nervous system (CNS) (6–8). In a small percentage of cases, subacute sclerosing panencephalitis (SSPE) develops several years after the initial infection, characterized by persistent infection of the brain associated with hypermutated MeV genomic RNA and viral transcripts and defective viral particle assembly (9–11). Measles inclusion body encephalitis (MIBE) occurs in immunocompromised patients weeks to months after infection with wild-type (WT) viruses and, in rare cases, has followed previous versions of the attenuated MeV vaccine that are no longer used (6, 12, 13). MIBE may be associated with viral fusion complexes that do not require cell surface receptors, referred to as hyperfusogenic MeV fusion complexes (14, 15). To date, the mechanisms governing MeV infection and spread in the CNS remain poorly understood, although CNS invasion seems to require the viral fusion (F) protein and may be inhibited by fusion inhibitors (16–19).

MeV initially infects activated CD150(SLAM)-expressing immune cells in the respiratory tract, gaining access to the immune system (20). After reaching the draining lymph nodes, MeV proliferates in CD150-expressing lymphocytes and proceeds to cause viremia. Late in infection, MeV infects respiratory epithelial cells via nectin 4 expressed on the basolateral membranes of these cells; from this location MeV exits the host's respiratory tract and may be transmitted (21, 22). Infection of a cell by MeV starts with attachment to cell surface receptors, and entry is then mediated by the concerted actions of the MeV receptor binding protein hemagglutinin (H) and F that form a protein complex on the surface of the virus (23, 24). Infected cells synthesize F as a precursor (F0) that is cleaved within the cell to yield the prefusion F complex, comprising three C-terminal F1 subunits that are associated via disulfide bonds with three N-terminal F2 subunits. On the surface of viral particles, this trimeric F structure is kinetically trapped in a metastable conformation (16). F is primed for fusion activation when H glycoprotein engages a target cell entry receptor (i.e., CD150 or nectin 4 for wild-type strains) (20–22). After receptor engagement, H triggers the prefusion F protein to undergo a structural transition, extending to insert its hydrophobic fusion peptide into the host cell membrane. F then refolds into a stable postfusion 6-helix bundle structure, which brings the viral and target cell membranes together to initiate formation of the fusion pore. This refolding is based on the interaction between two complementary heptad repeat (HR) regions located at the N- and C termini of the protein (HRN and HRC). This refolding step can be inhibited by peptides corresponding to these HR regions (25).

MeV bearing F proteins with mutations in the HRC domain have been isolated during CNS infection in several patients (14, 15, 26, 27). A viral sequence recovered from two patients who died from MIBE contained F with the mutation L454W (14), which conferred thermal lability to the metastable F. We have previously shown that this F mutation affects entry into target cells. Recombinant MeV (IC323 strain) expressing green fluorescent protein and bearing the L454W F (MeV-IC323-EGFP-F L454W) spreads in cells that lack a known MeV receptor. In cell-to-cell fusion assays, F bearing the L454W mutation alone mediates fusion independently of the H protein (15). In contrast, other hyperfusogenic viruses are dependent on the H protein for membrane fusion (28). The L454W mutation in F of the MIBE patients could have arisen *de novo* in the CNS (14) or could have been present in the WT viral population and undergone positive selection in the CNS. The origin of this virus could not be determined. One report showed that a virus bearing L454W F can emerge under the selective pressure of certain fusion inhibitors (29), indicating that viruses bearing this neuropathogenic F protein can be found outside the CNS. In recent work, we showed that a virus bearing

the L454W F outcompetes WT MeV in the lungs of cotton rats, is 10-fold more lethal in a suckling hCD150 transgenic mouse model of MeV CNS infection, and infects the mouse CNS faster than WT MeV (30).

In an effort to explain the CNS impact of the alteration in MeV F, we studied MeV bearing CNS-adapted fusion complexes in two *ex vivo* models of CNS infection—murine organotypic brain cultures (cerebellum slices from suckling mice) and human brain organoids (fetal 8- to 13-week stage of development). The hyperfusogenic variants from cases of encephalitis spread more efficiently than WT MeV in these models. The infection does not require any known measles receptor, and the extent of infection is inversely correlated with the stability of the MeV F (WT or mutant) in its prefusion state. Spread of virus is blocked by fusion inhibitors that inhibit the refolding of F. An innate immune response is induced in both models, but this response does not block viral spread. Viral evolution in these CNS models led—by distinct routes—toward similarly labile and receptor-independent F proteins, highlighting the critical nature of these features in regulating CNS infection.

RESULTS

Measles virus bearing the F glycoprotein bearing L454W is not stable in cell culture. We and others have previously described mutations in the MeV F glycoprotein (L454W, T461I, and N462K) associated with neuropathogenic measles strains that were either isolated from patients or generated in laboratory settings (14, 15, 27, 30). These mutations made the prefusion state of the F protein less stable. To explore the molecular determinants for altered stability, these mutations were mapped onto structures of the prefusion conformation of MeV F (PDB 5YXW; [16]). The three mutations (L454W, T461I, and N462K) are all located within the HRC domain. Based on the prefusion structure, the side chain of L454 binds within a cleft comprising T314 within the same protomer and L457 within an adjacent protomer (Fig. S1A). The larger tryptophan (W) side chain in the L454W mutant could cause steric hindrance with disruption of this interaction. The T461I and N462K mutations occur in a well-ordered α-helical region of the HRC domain (Fig. S1B). The side chain of T461 resides within a cleft between L354 and L355, and T461I would likely lead to steric clashes between these residues. The side chain of N462 hydrogen bonds with the side chain of S352 in an adjacent helix, and N462K would likely disrupt this H-bond interaction. These three mutations occur in the portion of the HRC domain where the head and stalk regions of the prefusion conformation meet. Interactions at this junction are likely to be important for stabilizing the prefusion state, and consequently, mutations in this region could lead to decreased stability of the MeV-F prefusion structure (15).

The MeV F L454W was found in viruses from two separate clinical cases. The mutation decreases the stability of the fusion protein, producing a hyperfusogenic phenotype that allows MeV to spread in Vero cells even in the absence of known receptors. In order to assess the impact of the mutation on viral fitness, we generated a recombinant infectious clone of MeV IC323-EGFP bearing F L454W and grew the recombinant virus in Vero-CD150 cells at either 37°C or 32°C (the lower temperature stabilizes the F protein in its prefusion state [15]). In the course of this process of generating recombinant viruses bearing the L454W F by reverse genetics, a process expected to be routine, an unexpected set of mutations emerged. For both viral preparations, titers remained low, reaching only 2×10^5 PFU/ml at 32°C and $\sim 5 \times 10^5$ PFU/ml at 37°C, compared to WT virus stocks, which generally grow to over 5.10^6 PFU/ml. We previously noted that the mutant grows to lower titers than WT virus at 37°C (30), suggesting that the F protein harboring the L454W mutation is detrimental for viral growth in cell culture. Next-generation sequencing of these two viral stocks rescued from the same initial plasmid but grown at different temperatures for 3 passages revealed two different viral quasipsecies (31, 32); in addition to the L454W that was present in 100% of the sequences, a G506E mutation emerged at 32°C with an allele frequency of ~36%, and an E455G mutation emerged at 37°C with an allele frequency of ~22% (see Table 1). The E455G mutation can be observed in Fig. 1, but G506 is not resolved in the available crystal structures. The G506 resides toward the

TABLE 1 Allele frequencies of the indicated viral quasispecies in OBC and in human brain organoids infected with the indicated viruses

Allele frequencies (%) for:											
OBC at 7 dpi for:					**Brain organoids at 10 dpi for:**				**Brain organoids at 20 dpi for:**		
Input virus	Sample CM005	Sample CM006	Sample CM007	Sample CM008	Input virus	FA10	FA11				
66% L454W, 34% L454W/G506E	3% L454W, 97% L454W/G506E	11% L454W, 89% L454W/G506E	4% L454W, 96% L454W/G506E	22% L454W, 78% L454W/G506E	62% L454W, 38% L454W/G506E	4% L454W, 96% L454W/G506E	23% L454W, 77% L454W/G506E				
	Sample CM017					FA11	FA11 + HRC4	FA11 + 3g	FA11	FA11	FA11
78% L454W, 22% L454W/E455G	96% L454W, 4% L454W/E455G				78% L454W, 22% L454W/E455G	100% L454W, 0% L454W/E455G	100% L454W, 0% L454W/E455G	98% L454W, 2% L454W/E455G	100% L454W, 0% L454W/E455G	76% L454W, 24% L454W/E455G	100% L454W, 0% L454W/E455G
						FA10	FA11		FA11	FA11	FA11
					0% L454W, 100% L454W/E455G	8% L454W, 92% L454W/E455G	0% L454W, 100% L454W/E455G		0.1% L454W, 99.9% L454W/E455G	1.1% L454W, 98.9% L454W/E455G	0.1% L454W, 99.9% L454W/E455G

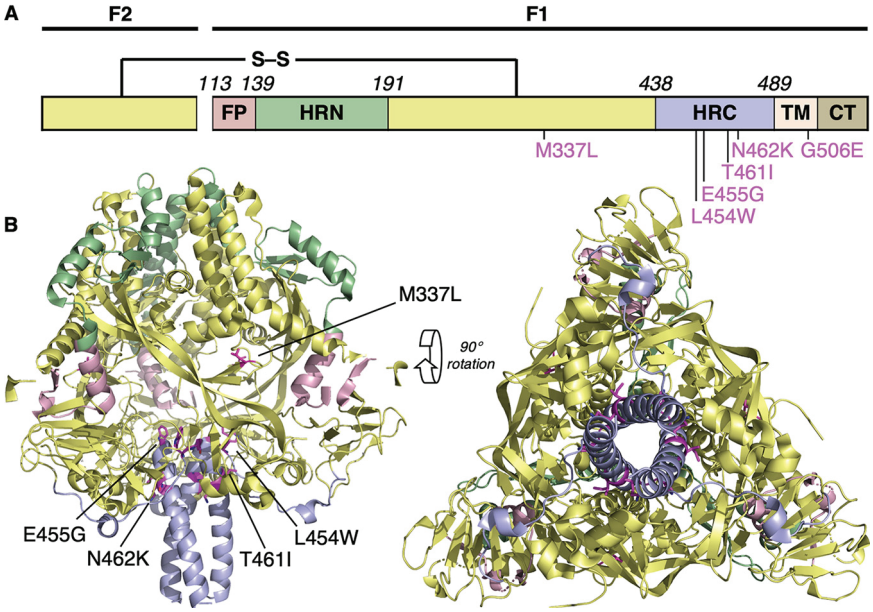

FIG 1 Location of substitutions within the F protein from CNS-adapted virus. (A) Schematic of MeV F with fusion peptide (FP), N-terminal heptad repeat (HRN), C-terminal heptad repeat (HRC), transmembrane (TM), and cytoplasmic (CT) domains indicated. (B) Ribbon diagrams of the prefusion MeV F protein (MeV F; PDB 5YXW [16]). Five substitutions (M337L, L454W, E455G, T461I, and N462K) in the F protein structure are shown.

end of the transmembrane (TM) domain, and mutation to a charged residue within this membrane-embedded segment is very unusual. We are pursuing further studies to determine the structural and functional impact of this finding. We hypothesized that the instability of the L454W F variant favors the emergence of these two new mutations in cell culture. These unexpected mutations provided remarkable investigative tools as discussed below.

Growth of MeV-IC323-EGFP-F L454W versus WT virus in murine organotypic brain cultures (OBC) in the absence of known receptor. The viruses bearing F L454W were isolated from the CNS, and we hypothesized that this mutation would be under positive selective pressure in brain models. We previously used mouse cerebellar organotypic brain cultures (OBC) from IFNAR1 knockout (KO) (IFNAR1^{KO}) mice to assess viral infection and spread in the absence of a type 1 interferon (IFN) response (33) (see Fig. 2A). OBC from mice that express the human CD150 F1 transgene sustain WT virus infection and spread (34), but the WT virus does not spread in the absence of known MeV receptors (33, 35). In the experiment shown in Fig. 2B to E OBC were derived from IFNAR1^{KO} mice that do not express any known measles receptor. The WT virus (expressing enhanced green fluorescent protein, EGFP) fails to spread over 96 h (Fig. 2B and C). In Fig. 2D and E OBC from IFNAR1^{KO} mice were coinfected with 5,000 PFU of WT virus expressing the red fluorescent protein (tdTomato) and MeV-IC323-EGFP-FL454W (a mixed population containing the two F allele sequences—L454W and L454W/G506E—that emerged in culture). Infection was monitored at 24 h (Fig. 2D) and 96 h (Fig. 2E). While the WT virus did not (as expected) spread well in the OBC, the virus bearing L454W (EGFP) infected and spread, and the G506E mutation allele frequency increased from ~36% to ~70%.

Blocking fusion inhibits spread of all variants. MeV vaccine strain infection studies have suggested that interfering with F protein function can reduce CNS spread (17). We previously showed that a MeV F-derived dimeric cholesterol-conjugated fusion inhibitory peptide ("HRC4") blocks infection with WT MeV *in vitro*, *ex vivo*, and *in vivo* in cotton rats and mice (30, 34, 36). The HRC4 peptide's effect on virus dissemination in IFNAR1^{KO} OBC (no known MeV receptor [33]) after exposure to virus was

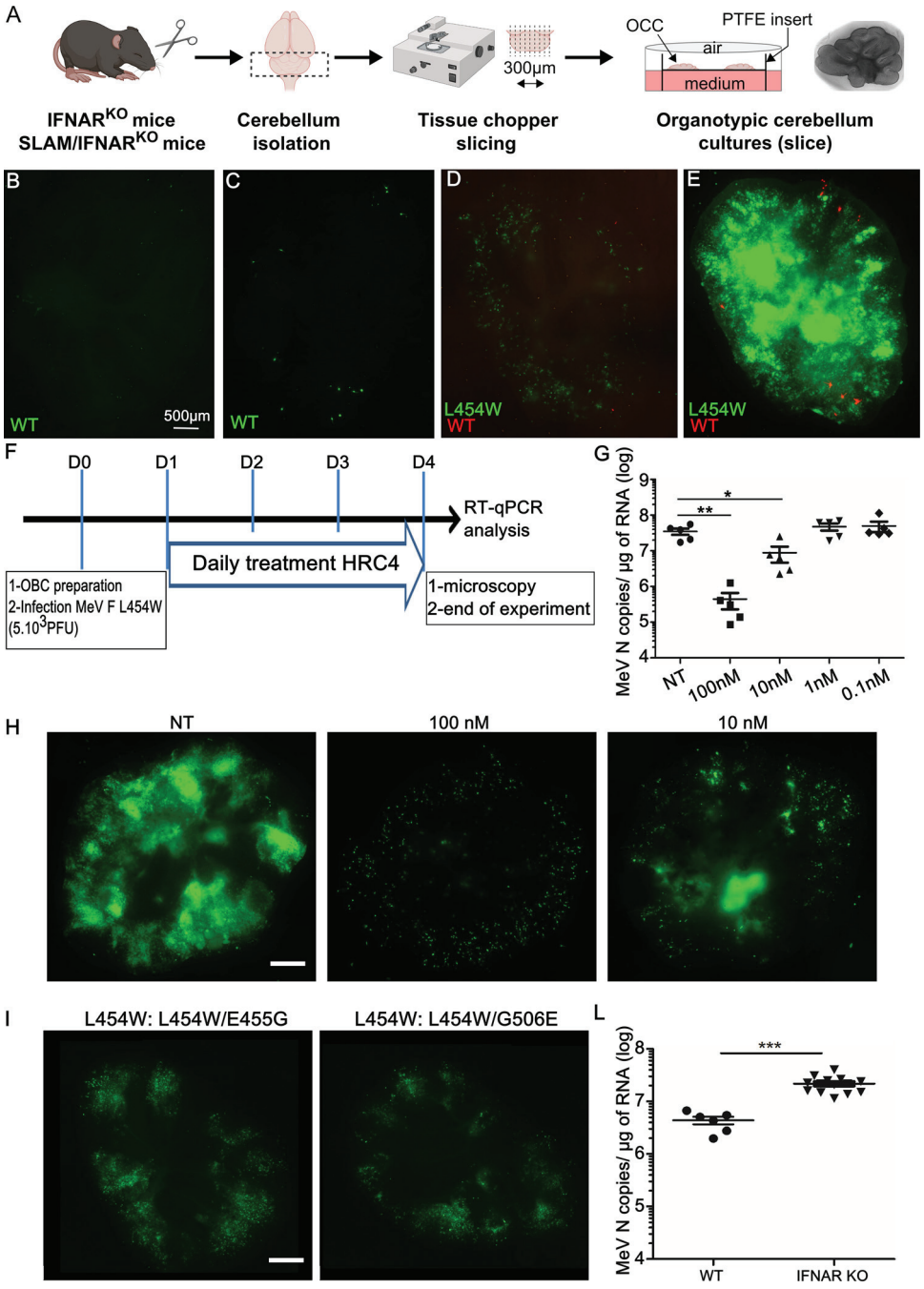

FIG 2 Infection with wild-type (WT) versus virus bearing the L454W F; the CNS-adapted virus outcompetes the WT virus in organotypic brain cultures (OBC). (A) Schematic representation of OBC preparation from the organ, slicing using a tissue chopper II device, and transfer of slices on insert for further culture and infection. (B and C) OBC from IFNAR^{KO} murine brains were infected with 5,000 PFU/slice WT virus bearing EGFP (green fluorescence). (D and E) OBC from IFNAR^{KO} murine brains were coinfected with 5,000 PFU/slice of WT virus bearing tdTomato (red fluorescence) and MeV IC323-EGFP-F L454W (green fluorescence) at 5,000 PFU/slice and monitored over 96 h. Photos were taken at 24 h (D) and 96 h (E). Scale bar = 500 μm. (F to H) MeV F-derived fusion inhibitor peptide (HRC4) inhibits the dissemination of MeV bearing L454W F in OBC. OBC from IFNAR^{KO} murine brains were infected with MeV IC323-EGFP-F L454W at 5,000 PFU/slice for 4 days. OBC were treated at the indicated concentrations or left untreated (NT control) by adding HRC4 fusion inhibitory peptide 24, 48, and 72 h after initial infection. (F) Schematic of the procedure. (G) Total RNA was harvested from organotypic slices at 4 days postinfection (dpi), and the level of MeV N gene expression was quantified by RT-qPCR. Results are expressed as means ± standard deviations of cultures from 5 different mice (**, $P < 0.01$; ***, $P < 0.001$ [Mann-Whitney-U test]). (H) Green fluorescence related to infection was observed 4 dpi by epifluorescence microscopy in OBC treated at the indicated concentrations (scale bar = 500 μm). (I) *Ex vivo* virus bearing the L454W F infection in fully immunocompetent OBC. OBC from C57BL/6 murine brains were infected with L454W

(Continued on next page)

assessed in Fig. 2F to H. The amount of MeV N RNA copies—reflecting the viral load present in the OBC at the end of the experiment—was quantified using reverse transcriptase quantitative PCR (RT-qPCR). Figure 2G shows the significant 2-log reduction in viral load in the cultures treated postinfection with 100 nM HRC4 peptide (**, $P = 0.008$, Mann-Whitney U-test) and a 4-fold significant reduction in the number of MeV N RNA copies in the group treated with 10 nM peptide (*, $P = 0.03$, Mann-Whitney U-test), compared to the viral load in untreated samples. MeV IC323-EGFP-F L454W virus invaded the OBC, forming extensive areas of fusion throughout the culture 4 days after infection (Fig. 2H). The HRC4 peptide (100 nM or 10 nM) blocks the spread of MeV-IC323-EGFP-F L454W over the same time period (Fig. 2H). At the highest concentration used (100 nM), only isolated single infected cells were observed. The lower concentration (10 nM) was partially inhibitory, with a few focal areas of dissemination (Fig. 2H). The peptide was ineffective at concentrations below 10 nM (Fig. 2G and H). Since the fusion inhibitor was added 24 h after infection, these results indicate that the HRC4 peptides block cell-to-cell spread in three-dimensional CNS-derived OBC, suggesting that MeV dissemination in brain depends on MeV F protein. Even when using OBC from IFNAR1^{KO} mice that express the human CD150 (SLAM) receptor, peptide (100 nM) blocked dissemination of both MeV IC323-EGFP-F L454W and WT (Fig. S2A).

Evolution of the L454W-bearing viruses in immunocompetent OBC. To explore the determinants of MeV fitness in the CNS, we evaluated the evolution of the two viruses bearing a double population of L454W F plus either L454W/E455G F or L454W/G506E F. RNA virus populations, including MeV, are present as quasispecies which can undergo rapid adaptation to their growth environment (31, 32). The MeV L454W F stocks represent viral quasispecies in which the E455G and G506E variants are major components. To assess the evolution of these viruses under the selective pressure of growth in fully immunocompetent mouse CNS models, we derived OBC from WT mice. OBC from C57BL/6 suckling mice were infected with MeV WT and the set of L454W F viruses. We previously observed that WT virus did not spread in this model (35), and this finding was confirmed here, but in contrast, both viruses bearing the L454W F spread in the C57BL/6 OBC with similar levels of infection after 7 days (Fig. 2I). Infected OBC were lysed at 7 days for sequencing to assess the transcriptome, quantify viral RNA, and evaluate viral evolution during infection. In C57BL/6 OBC, viruses bearing the L454W F induced a gene expression pattern associated with intense interferon signaling compared to the OBC infected with WT virus (with minimal spread), where the gene pattern was indistinguishable from that of uninfected OBC (see Fig. S3 for immune staining with specific neuronal markers and Fig. S4A for differential gene expression analysis). Despite this strong innate immune response, the spread of L454W F bearing-virus was not halted (see difference between viral genome in WT versus IFNAR^{KO} murine OBC in Fig. 2L). Viral sequence analysis is presented in Table 1 and in the LAVA plots in Data Sets S1 and S2 in the supplemental material (37). Table 1 and the murine OBC LAVA plot in the supplemental material show the allele frequency for L454W/G506E in four samples (CM005-8) and for L454W/E455G in one sample (CM017). The L454W/G506E input virus had an allele frequency for the double mutant of ~36% that rose after 7 days in OBC to 97%, 89%, 96%, and 78%. For the L454W/E455G, however, the input virus had an allele frequency for the double mutant of ~22%, and after *ex vivo* growth the double mutant decreased to ~4%.

Infection of human induced pluripotent stem cell (hiPSC)-derived brain organoids—CNS adapted variants versus WT virus. To validate the pattern of immune gene response and explore the surprising finding that the L454W/G506E virus—

FIG 2 Legend (Continued)

F-bearing virus (using both viral preparations, one with the additional E455G in F and the one with G506E in F) at 1,000 PFU/slice for 7 days. Pictures were taken at 4 days after infection as indicated. (L) L454W-bearing virus growth in WT and IFNAR^{KO} OBC. OBC from WT or IFNAR^{KO} murine brains were infected with 1,000 PFU/slice MeV IC323-EGFP-F L454W for 7 days. Total RNA was harvested from OBC at 4 days postinfection, and the level of MeV N gene expression was quantified by RT-qPCR. Results are expressed as means ± standard deviations in cultures from at least 5 different mice (*, $P < 0.05$; ***, $P < 0.001$ [Mann-Whitney-U test]). Pictures where reconstituted using the Stitching plugin with ImageJ software.

originally identified as a laboratory adaptation—underwent positive selection in mouse OBC, we used human brain organoids. For this human tissue model, we differentiated hiPSC from two separate donors—one male (FA10) and one female (FA11)—into brain organoids (38). Ninety-day old organoids were infected with viruses bearing WT or L454W F and also for comparison with MeV bearing N462K F (a lab adaptive mutation previously found to grow well in hamster brains) and T461I F (from an SSPE case) (27) (see Fig. 1). Infection and spread of fluorescent virus were monitored over a 10-day period (Fig. 3A and Fig. S1B show photos at day 10). To ensure that equal amounts of virus were used, the inocula used in the human brain organoids were assessed in parallel in Vero cells expressing CD150 (Vero-CD150) (Fig. 3B). All the viral titers (PFU/ml) were similar, with the MeV L454W F being slightly lower. After 10 days, the human brain organoids were lysed for RNA sequencing to assess the transcriptome, quantify viral RNA, and evaluate viral evolution during infection (Fig. 3C to E, Fig. S4C and D). The viruses bearing L454W F spread more than the virus bearing the WT F (Fig. 3A and C) and were blocked by the HRC4 fusion inhibitor added 24 h after infection (Fig. S2B and C). The MeV T461I F (SSPE patient) also spread, but in contrast, the MeV N462K F (lab adapted) spread only slightly better than WT virus (Fig. 3A and C).

The differential gene expression in uninfected or infected human brain organoids (WT MeV or MeV L454W F) is shown in Fig. 3D. MeV L454W F was present at severalfold higher reads per million (RPM) values than MeV WT (Fig. 3E). MeV L454W F induced a gene expression pattern that was associated with interferon signaling, compared to organoids infected with WT virus and control samples ($P = 2.6 \times 10^{-17}$, see Fig. S4C and D for the differential gene expression analysis). This difference seems likely related to the differences in viral growth, since it seems to correlate with viral genome count regardless of the specific F mutation. Fig. S4C shows the gene expression in organoids infected with the MeV variants shown in Fig. 3A). For both sets of human brain organoids, the highest gene-level expression coefficient correlated with the youngest fetal development stages (8 to 13 postconception weeks) and with brain tissues derived from the amygdala (Fig. S5A) with specific CNS markers (Fig. S6), as noted previously (39, 40). The developmental stage was not affected by infection. Pathway analysis of differentially expressed genes common to the two human brain organoid infection series confirmed that a strong interferon response was evoked by measles infection in human brain organoids (Fig. S5B).

Viral sequence analysis from growth in human brain organoids is presented in Table 1 and the LAVA plots (see supplemental material). For the infection with MeV L454W/G506E, the input virus had an allele frequency for the double mutant of ~38%, and this increased to ~96% in FA10 and ~77% in FA11 brain organoids (see Table 1 and human brain organoid LAVA plots in the supplemental material). For the MeV L454W/E455G, the input virus had an allele frequency for the double mutant of ~22%, and during infection of a second set of brain organoids (derived from FA11 iPSC), the allele frequency of the E455G F decreased to lower than 2% (see Table 1 and human brain organoid LAVA plots in the supplemental material). MeV WT did not show any alteration (see Table 1 and human brain organoid LAVA plots in the supplemental material).

Additional mutations in the L454W F background stabilize the prefusion state of the F protein. Since positive selection of G506E F and negative selection of E455G F were observed in both murine OBC and human brain organoids, we compared the functional properties of these F proteins bearing the additional mutations, both alone and in combination with L454W. All the F proteins bearing mutations that were selected in the CNS can mediate cell-to-cell fusion when expressed on transfected cell surfaces, without receptor (Fig. 4A and C). The L454W/G506E F was still significantly less stable than WT F in our functional assays, while the L454W/E455G F was more stable than WT F (Fig. 4B). The hallmark of the neuropathogenic variants is the ability to fuse without a known viral receptor, and the L454W/G506E F can mediate fusion without any of the known receptors (CD150/SLAM or nectin 4). However, the L454W/E455G

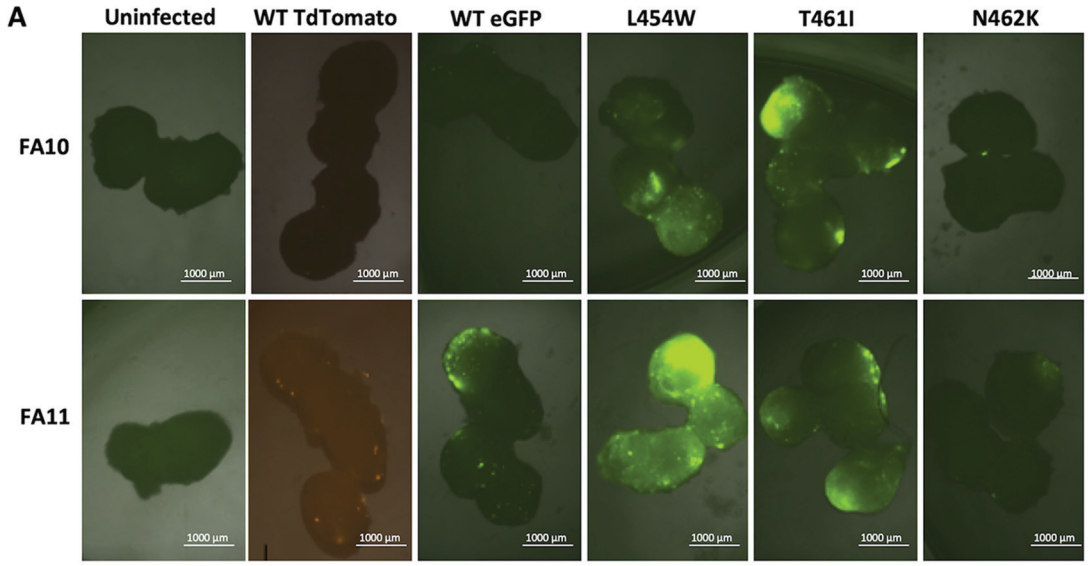

B

MeV virus	PFU/mL (log)
WT TdTomato	5.4
WT eGFP	5.2
L454W	4.6
T461I	5.4
N462K	5.1

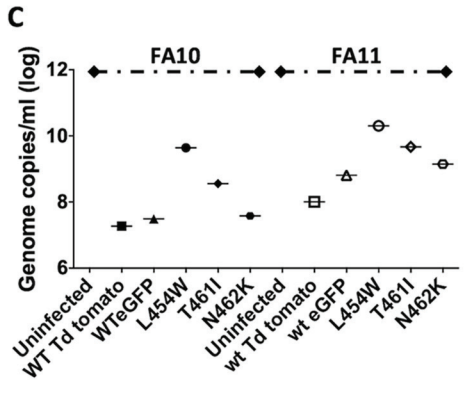

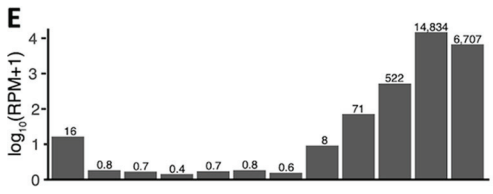

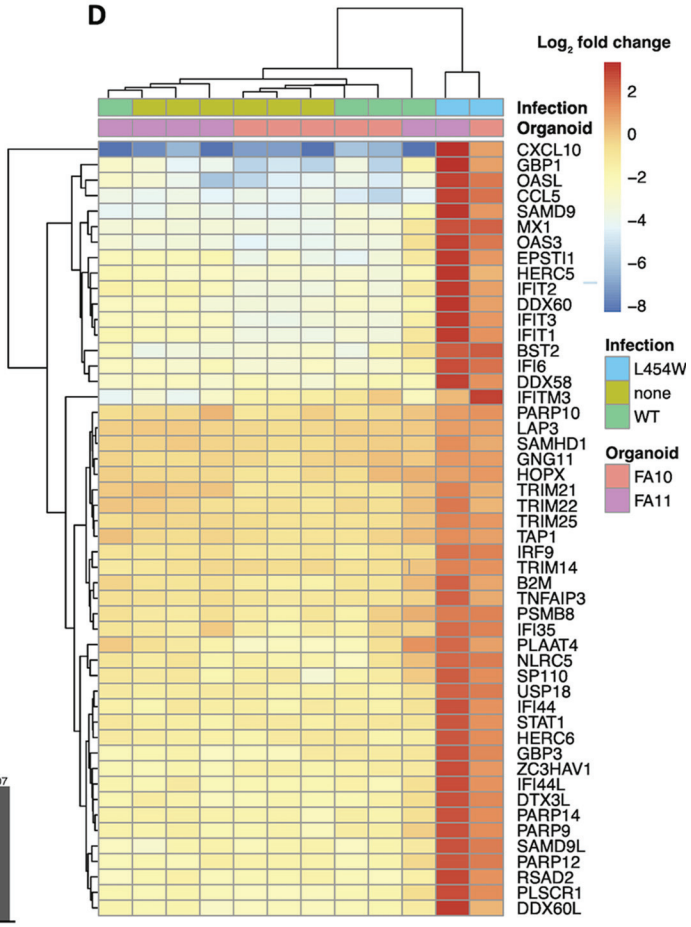

FIG 3 CNS-adapted MeV variants spread efficiently in human pluripotent stem cell (hiPSC)-derived brain organoids. (A) Two separate sets of 90-day-old human brain organoids (derived from two hiPSCs, FA10 and FA11) were infected with recombinant MeV viruses (with either EGFP or tdTomato fluorescent protein) bearing the indicated MeV fusion (F) proteins. For each virus, 3 separate wells each containing 2 to 4 organoids were infected (5,000 PFU/well). The brain organoids were monitored over time, and the fluorescence shown here reflects the infection after 10 days. Bar = 1,000 μm. (B) Viral titer of the inoculum used for infection was assessed on Vero CD150 cells (PFU/ml, log). (C) Total RNA was harvested from the human brain organoids at 10 days postinfection, and the level of MeV N gene expression was quantified by RT-qPCR. (D) RNA-Seq analysis of WT versus L454W F-bearing virus infection in brain organoids (data from three separate experiments). Seven replicates of uninfected and MeV-infected brain organoids were transcriptionally profiled ($n = 6$ uninfected, $n = 5$ WT, $n = 2$ L454W F-bearing virus). (E) RPM values

(Continued on next page)

F, bearing the E455G mutation that dramatically decreased in frequency during growth in brain organoids, does not mediate fusion without a known receptor.

Based on the finding (Fig. 4A to C) that the frequency of E455G decreased during growth in pressure in organoids and that this mutation conferred a receptor dependency on the L454W F, we hypothesized that a homogenous viral population of MeV L454W/E455G F behaves like WT MeV in the organotypic brain slices and in brain organoid models and that E455G would be subject to negative selection pressure in these neural models. We thus attempted to generate recombinant viruses bearing either the L454W/E455G F or the E455G F to analyze their growth and spread in brain organoids. The recombinant virus bearing L454W/E455G F grew similarly to WT virus in Vero-CD150. However, a recombinant virus bearing the singly mutated E455G F could not be recovered, suggesting that it is detrimental in culture. To determine whether the double mutant's phenotype resembles that of the WT, we coinfected with WT F (red)- and L454W/E455G F (green)-bearing viruses in OBC as shown in Fig. 2D. Figure 4D shows the extent of viral spread 96 h postinfection. In clear contrast to the results shown Fig. 2D (where the MeV L454W F invaded the entire OBC and WT infection was limited) the coinfection resulted in similar (limited) spread for both MeV WT and MeV L454W/E455G F viruses. Infection with fluorescent MeV L454W/E455G F in 90-day-old human brain organoids was monitored for 10 days (Fig. 4E). To ensure that infection was performed with the intended amount of virus (5, 000 PFU/well), the inocula used in the human brain organoids were assessed in parallel in Vero-CD150 cells (Fig. 4G). The MeV L454W/E455G F had only limited spread in both FA10 and FA11 hiPSC-derived brain organoids after 10 days (Fig. 4E) but infected and destroyed Vero-CD150 cell monolayers in 2 days (Fig. 4G). After 10 days, the human brain organoids were lysed for RNA sequencing to assess the transcriptome, quantify viral RNA, and evaluate viral evolution and differential gene expression during infection (Fig. 4F, Fig. S3C and D, Fig. S5A and supplemental material). The amount of viral genome of the infection from MeV L454W/E455G F was similar to what we observed for the WT virus (Fig. 3). After 10 days, the double mutation remained stable in the brain organoids derived from hiPSC FA11, but an ~8% reversion to E455 in the brain organoids derived from hiPSC FA10 was observed (Table 1 and human brain organoid LAVA plots in the supplemental material). We therefore differentiated another set of brain organoids from hiPSC FA11 and infected them with MeV WT, MeV L454W F (the mixed population of MeV L454W F and MeV L454W/E455G F), and MeV L4545/E455G F, each in triplicate. At 20 days postinfection the brain organoids were lysed, and RNA was extracted for viral sequencing (Table 1). The WT virus underwent only a change in the P gene (R77C) with an allele frequency of ~30% in all three samples. The results for the MeV L454W F-bearing virus (mixed population of MeV L454W F and MeV L454W/E455G F) were different among the triplicate samples. In two samples, the E455G mutation was totally eliminated. In the third sample, E455G remained at ~24%. The double mutant MeV L454W/E455G F remained stable with minor changes (the single-population L454W increased 0.1% to 1.1.%).

In light of the surprising finding that an F-stabilizing mutation like G506E (Fig. 4) does not necessarily interfere with CNS adaptation, we searched for evidence of such a phenotype *in vivo*. A clinical sample isolated from the original MIBE cohort that revealed the L454W mutation in F (14) bore an additional mutation in F (M337L). We assessed the effect of M337L on fusion and stability of F, both singly and in combination with L454W (Fig. 4A–C). The expressed M337L F did not mediate fusion in the absence of receptor, and its prefusion state was more stable than that of WT F. The M337L/L454W F promoted fusion in the absence of receptor and was significantly less thermostable than WT F. Evolution *in vivo* led—through a different mutated residue—

FIG 3 Legend (Continued)
for MeV for each sample are depicted in the same order as for the heatmap in panel D. Raw counts were normalized across all samples, and differential expression analysis was performed. The 50 genes with the lowest adjusted *P* value between MeV IC323-EGFP-F L454W and uninfected are depicted in the heatmap, colored by $\log_2$ fold change of each sample relative to the mean normalized counts for each gene.

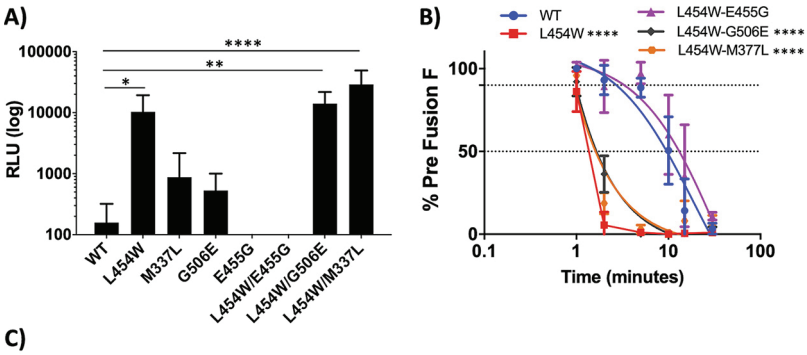

C)

F protein	Nectin4	CD150	w/o receptor	TS_{50} (min)	TS_{10} (min)
WT	100	100	100	10 ± 3	17 ± 8
L454W	104 ± 46	48 ± 17	6500 ± 2000	1 ± 0.3	3 ± 0.7
M337L	116 ± 22	130 ± 38	1200 ± 300	19	>30
G506E	136 ± 24	160 ± 80	500 ± 120	>30	>30
E455G	10 ± 3	9 ± 3	10 ± 2	>30	>30
L454W/E455G	95 ± 50	162 ± 50	40 ± 23	14 ± 5	24 ± 9
L454W/G506E	56 ± 26	52 ± 30	8900 ± 1600	2 ± 0.3	4 ± 0.2
L454W/M337L	104 ± 18	150 ± 24	10200 ± 1200	1.6 ± 0.2	6.6 ± 1.2

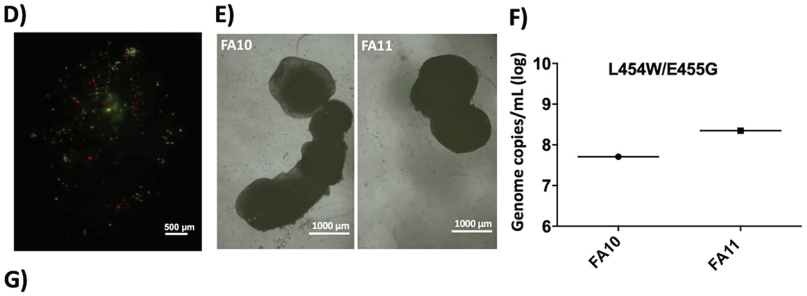

G)

MeV Virus	PFU/mL (log)
L454W/E455G	4.9

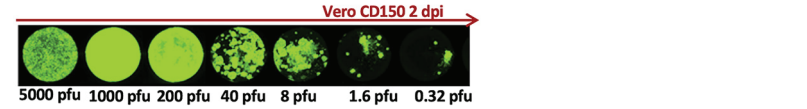

FIG 4 Fusion activity and thermal stability of MeV fusion (F) proteins bearing the indicated mutations. (A) Cell-to-cell fusion between HEK293T cells coexpressing the indicated MeV F proteins + MeV WT hemagglutinin (H) and HEK293T cells (no known measles receptor) was assessed by a B-gal complementation assay. The values on the *y* axis are expressed as relative luminescence unit (RLU) averages (with standard error, SE) of results from three independent experiments. ****, $P < 0.0001$ (2-way analysis of variance [ANOVA]). (B) HEK293T cells were transfected with MeV F protein bearing the indicated mutations and incubated at 37°C for 24 h and then raised to 55°C for the indicated times (*x* axis). The values on the *y* axis represent the percentages of prefusion conformation specific antibody binding to the indicated F proteins (compared to the WT F protein at time zero). The values are the average of three independent experiments. ****, $P < 0.0001$ (2-way ANOVA). (C) Fusion mediated by cells coexpressing MeV H and F proteins bearing the indicated F mutation in the presence of nectin 4, CD150, or no receptor compared to WT F (100%). HEK293T cells were transfected with MeV F protein bearing the indicated mutations and incubated at 37°C for 24 h and then raised to 55°C. The time (minutes) at 55°C that decreases the fraction of prefusion epitope to 50% (TS_{50}) and to 10% (TS_{10}) is indicated compared to the WT F at time zero (100%). Data are averages from three experiments +/− SE. (D) OBC from $IFNAR^{KO}$ murine brains were coinfected with 5,000 PFU/slice of WT virus bearing tdTomato (red fluorescence) and MeV-IC323-EGFP-F L454W/E455G (green fluorescence) and monitored over 96 h. Photos were taken at 96 h. Pictures where reconstituted using the Stitching plugin with ImageJ software. Scale bar = 500 μm. (E) Two separate sets of 90-day-old human brain organoids (derived from two hiPSCs, FA10 and FA11) were infected with recombinant MeV viruses bearing the L4545W/E455G F. Three separate wells containing 2 to 4 organoids were infected (5 000 PFU/well). The brain organoids were monitored over time, and the fluorescence shown here reflects infection after 10 days. Bar = 1,000 μm. (F) Total RNA was harvested from the human brain organoids

(Continued on next page)

to a similar functional alteration to that caused by G506E in F. These results reflect a CNS-specific pattern of adaptation.

DISCUSSION

In a South African MeV outbreak, 8 HIV-infected patients died of MeV CNS manifestations (41). The fusion complexes of MeV isolated from the CNS of patients with MIBE are altered so that F is activated without a known entry receptor (15). The F proteins of the isolates from two separate patients contain one specific amino acid alteration at position 454 (L454W) that increases F's ability to mediate fusion with any heterotypic attachment protein and markedly decreases F's thermal stability (15). An unexpectedly informative set of mutations emerged from the process of generating recombinant viruses bearing the L454W F by reverse genetics. The standard methods carried out at 37°C resulted in a mixed population of viruses bearing either L454W F or L454W/E455G F. Lowering the temperature of viral production to 32°C to stabilize the F resulted in a population containing both L454W and L454W/G506E. While E455 is located in the HRC domain of F (see Fig. 1), the residue G506 is in the transmembrane domain and is not resolved in the available crystal structures of MeV F. Placing a charged residue into the transmembrane domain would likely have a drastic impact on protein folding and activity, and yet this mutation was positively selected in our *ex vivo* models. The HRC mutation E455G increases the stability of F, and the L454W/E455G F (in contrast to L454W) requires engagement of H (MeV receptor binding protein) to the receptor in order to mediate fusion. This second HRC domain mutation thus confers a requirement for H-receptor interaction during infection, onto the receptor-independent L454W F. The G506E transmembrane domain mutation slightly restored F's stability; however, the double mutant L454W/G506 F is still less stable than the WT and mediates fusion in the absence of a known receptor. Although arising as a result of a technical process, these compensatory mutations provided direct evidence that viruses that can fuse without known receptors are positively selected in the CNS.

Fusion-inhibitory peptides inhibit MeV L454W F infection in murine OBC and human brain organoids, in support of the role of F-mediated fusion in CNS spread. Therapies designed to stabilize the prefusion F are in an advanced stage of development for a related virus, respiratory syncytial virus (42). For MeV, in previous work, a small F-targeting molecule (3G) that inhibited WT MeV infection *in vitro* was identified using WT MeV F for screening, and resistance to this inhibitor quickly arose via mutation at position 462 (N462K), one of the mutants we analyzed here (43–47). The mutated F was inherently destabilized but retained in the prefusion state in the presence of the inhibitor 3G (43, 44). The 3G inhibitor did not block spread of MeV L454W F in the human brain organoids (Fig. S2B and C). Another fusion inhibitor, FIP (29), which has a mechanism of action similar to that of 3G (16, 29), has also been shown to exert selective pressure for the emergence of L454W F. We asked whether the selective pressure of FIP would favor MeV L454W F over the double mutant MeV L454W/E455G F in immortalized cells, thereby suggesting that its instability is a disadvantage in culture. We grew viruses bearing L454W and L454W/E455G F in the presence of FIP, and the allele frequency of L454W/E455G decreased from ~22% to ~10%. FIP provided a selective pressure that reduced the population of the double mutant. This virus stock bearing L454W F and 10% double mutant was then used to infect Vero cells that bear no known receptor, and the double mutant population rose again, indicating that the lack of receptor is not the primary or only necessary selective pressure to maintain the unstable F phenotype.

Recombinant MeV bearing the L454W/E455G F behaved similarly to WT virus, in that infection in brain organoids was limited, and in the 10- to 20-day span of two sep-

FIG 4 Legend (Continued)
at 10 days postinfection, and the level of MeV N gene expression was quantified by RT-qPCR. (G) Viral titer of the viral inoculum used for infection was assessed on Vero CD150 cells (PFU/ml). Photos show the extent of infection after 2 days (PFU/well are indicated). Pictures were reconstituted using the Stitching plugin with ImageJ software.

arate experiments resulted in partial negative selection of the E455G mutation. It is possible that a longer infection could result in complete elimination of the E455G mutation or introduction of additional mutations. Despite several attempts, a virus bearing purely E455G F could not be recovered, and we gather that the increased stability of the E455G F may be detrimental to fitness. The factor(s) that leads to positive selection of viruses bearing the L454W F over the L454W/E455G F in *ex vivo* models remains to be explored.

The MeV bearing an N462K F, which is far less stable than WT F and grows well in cultured cells, surprisingly, was not well suited to growth in human brain organoids. The double mutant MV L454W/G506E F seems to have reached a "balance" that makes it fit for both culture conditions. We previously described a virus from an SSPE case in which the consensus F (SSPE F) had 6 amino acid changes (G168R, E170G, S262G, A440P, R520C, L550P) (48). The SSPE F was less thermally stable than the WT F and could mediate fusion in the absence of a known receptor. When we assessed the effect of the mutations individually, we observed that no mutation alone could confer the fusion property. Some of the mutations increased the stability of the prefusion F (e.g., E170G), while others decreased it (e.g., S262G). We speculate that *in vivo* evolution leading to the fully CNS-adapted SSPE F may have occurred in the clinical case.

Deep sequencing of one of the clinical samples from the patient cohort where the L454W mutation in F was first identified revealed the presence of several other mutations in the F protein. One of these (M337L) had an allele frequency similar to that of L454W, and the F protein bearing M337L/L454W matched the fusion phenotype of the F bearing the L454W/G506 mutations, suggesting *in vivo* viral evolution toward a similar functional phenotype of F to that observed in the brain organoids. Distinct mutations that arrive at a similarly labile and receptor-independent F may be positively selected in the CNS. Mapping the M337L mutation onto the prefusion structure of MeV F (Fig. S1) reveals that this residue could form hydrophobic interactions with L256 and L257 to stabilize the prefusion conformation of MeV F.

MeV is a uniquely human pathogen, and there is no *in vivo* model that faithfully reproduces the CNS sequelae of MeV infection. The best model for acute measles infection is the nonhuman primate; however, in rhesus monkeys, cynomolgus macaques, and squirrel monkeys, no CNS manifestations have been described (21, 49–55). The murine organotypic brain culture and the human brain organoid models described here contain the four major types of CNS cells (see Fig. S3 and S6) and offer the advantage that viral spread can be monitored in real time (35). Infection in human brain organoids reveals that the single L454W mutation in MeV F is sufficient to drive human CNS infection. Infection of human brain organoids induced an innate immune response that correlated with the intensity of infection but did not prevent spread of the MeV variants with hyperfusogenic F proteins.

Infection of mouse OBC also produced an innate immune response, and in these OBC, viral titers were reduced compared to those of IFNAR1^{KO} OBC (Fig. 2L), suggesting that the innate antiviral response in the immunocompetent OBC slowed viral spread (Fig. S4A and B). The increased innate antiviral response to the L454W F MeV variant, in both human brain organoids and murine cerebellar OBC, is likely related to the higher viral titer and spread, given that most of the upregulated genes are type I interferon-inducible genes (i.e., MX1, OAS, IFIT1, etc.) (56). However, we did not have the opportunity to compare these findings to infection with other viruses, and this is an area for future investigation. An enhanced type I IFN response in viral encephalitides has been observed to correlate with the severity of CNS infection (57), and we speculate that the L454W F MeV variant may induce a brisk innate immune response by infecting a larger area of CNS tissue.

In human cases of MeV infection of the CNS, it is unclear how MeV gains access to this site. The pathway may rely on lymphocytes that cross the blood-brain barrier (BBB) (58), on infection of endothelial cells of the BBB (59, 60), or on nectin 1-positive cells from the CNS capturing membranes and cytoplasm from the surface of adjacent cells

via a transendocytosis mechanism (61). To date, such mechanisms do not explain how cell-to-cell spread occurs within the CNS. Alterations in the viral fusion complex have been linked to CNS adaptation and neuropathogenesis (27). The timing of these alterations (whether they occur within the CNS or facilitate CNS infection) is also unclear. Here, we show that viruses bearing the MIBE-derived L454W F and the SSPE-derived T461I F are advantaged in infecting and spreading from cell to cell in models of CNS infection. Only the viruses bearing a dysregulated fusion complex were positively selected in the CNS.

MATERIALS AND METHODS

Ethical statement. All *ex vivo* experiments with mice were performed by C.M. and M.F. (accredited by the French veterinary service) according to the French National Charter on the ethics of animals. Animals used for *ex vivo* tissues in this study were directly euthanized by decapitation according to the AAALAC recommendations and according to French Ethical Committee (CECCAPP) regulations, accreditation no. CECCAPP_ENS_2014_034. All experiments involving human cells were approved by the Columbia University Institutional Review Board (IRB) and Embryonic Stem Cell Research Oversight (ESCRO) committees.

Peptides and chemicals. MeV F-derived fusion inhibitory peptides were previously described (36). Briefly 36-amino acid (aa) peptides derived from the heptad repeat region at the C terminus of the MeV F protein were synthesized. Dimeric cholesterol conjugated (HRC4) forms of the peptides were used in this study. *N*-(3-cyanophenyl)-2-phenylacetamide (also known as 3G) was commercially acquired from ZereneX Molecular Limited (United Kingdom). The purity of 3G was tested by high-pressure liquid chromatography (HPLC) and shown to be >95% pure.

Plasmids and reagents. The genes of MeV IC323 H and F proteins were codon optimized, synthesized, and subcloned into the mammalian expression vector pCAGGS. Plasmids encoding nectin 4, CD150, were commercially acquired.

Cells. HEK293T (human kidney epithelial), 293-3-46 (62, 63), Vero, and Vero-SLAM/CD150 (African green monkey kidney) cells were grown in Dulbecco's modified Eagle's medium (DMEM; Life Technologies, Thermo Fisher Scientific) supplemented with 10% fetal bovine serum (FBS; Life Technologies, Thermo Fisher Scientific) and antibiotics at 37°C in 5% CO_2. The 293-3-46 and Vero-SLAM/CD150 culture media were supplemented with 1 mg/ml Geneticin (Thermo Fisher Scientific).

Recombinant virus production and analysis. MeV IC323-EGFP (64) is a recombinant MeV expressing the gene encoding EGFP. All variants with the mutations T461I, N462K, L454W, and L454W/E455G were generated in the MeV IC323-EGFP background using reverse genetics (using the plasmid encoding MeV IC323-EGFP, kindly provided by Yanagi, Kyushu University, Fukyoka, Japan). MeV IC323-TdTomato was generated by replacing the EGFP expression cassette with the sequence coding for tdTomato red fluorescent protein. MeV IC323 recombinant viruses were rescued in 293-3-46 cells as previously described (63). Production of the virus bearing the L454W was performed at either 37°C or 32°C. All viruses were propagated and titrated in Vero-SLAM/CD150 cells.

Structural modeling. Twenty models were produced for the wild-type (WT) measles virus fusion glycoprotein (MeV F) using the protein homology server Phyre2 (65). Bad local geometries of each model for prefusion and postfusion states of MeV F were manually fixed using the program XtalView (66). The resulting models were subsequently refined using CNS-1.3 (67) against the electron density of 5EVM for the prefusion state. The same methodology was used for the production of models for all MeV-F mutant proteins. All structural figures were produced using PyMol (http://www.pymol.org/).

Beta-Galactosidase (Beta-Gal) complementation-based fusion assay. The Beta-Gal complementation-based fusion assay was performed as previously described (15). Briefly, HEK293T cells transiently transfected with the constructs indicated above and the omega reporter subunit were incubated for the indicated period with cells coexpressing viral glycoproteins and the alpha reporter subunit (36).

Cell surface staining with F-conformation-specific MAbs. HEK293T cells transiently transfected with viral glycoprotein constructs were incubated overnight at 37°C in complete medium (DMEM, 10% FBS). Then, 20 h posttransfection, cells were transferred to 55°C for the times indicated in the figures. Thereafter, cells were incubated with mouse monoclonal antibodies (MAbs) that specifically detect MeV F in its prefusion conformation (1:1,000) (44, 68, 69) for 1 h on ice. Cells were washed with phosphate-buffered saline (PBS) and then incubated for 1 h on ice with Alexa-488 anti-mouse secondary antibody (1:500; Life Technologies). Cells were washed with PBS and then fixed for 10 min on ice with 4% paraformaldehyde (PFA) with a 1:1,000 dilution of DAPI (4′,6-diamidino-2-phenylindole; Thermo Fisher) for 60 min. Plates were washed, 0.01% sodium azide was added, and plates were imaged via the use of an IN Cell Analyzer. The percentages of positively recognized cells were determined using Cell Profiler.

Organotypic cerebellar culture preparation and treatment postinfection. Cerebellar slices were prepared from IFNAR1^{KO} (and SLAM/CD150tg-IFNAR1^{KO}) or C57BL/6 mice and maintained in culture as detailed elsewhere (33). Briefly, cerebella were isolated from the brains of 7-day-old mice and cut with a McIlwain tissue chopper (WPI-Europe) to obtain 350-μm-thick progressive slices. The brain slices were then dissociated in cold Hibernate-A/5 g/liter D-glucose/1× kynurenic acid buffer and laid out on Millipore cell culture insert membranes (Millicell cell culture insert, 30 mm, hydrophilic polytetrafluoroethylene). Slices were subsequently cultured in GlutaMAX minimal essential medium supplemented with 25% horse serum, 5 g/liter glucose, 1% HEPES (all Thermo Fisher Scientific), and 0.1 mg/liter human

recombinant insulin (R&D Systems) at 37°C in 5% CO_2 in a humidified atmosphere. The medium was changed every day after the slicing procedure. Slices from 5 mice were infected on the day of slicing with the indicated recombinant viruses (5.10^3 PFU/slice from IFNAR1^{KO} and 100 PFU/slice from SLAM/CD150tg x IFNAR1^{KO} mice). Cultures were then treated daily from day 1 to day 4 either with serial dilutions of HRC4 fusion inhibitor in neurobasal medium or with vehicle (untreated condition; "NT"). Then, 2 μl of 10,000 nM, 1,000 nM, or 100 nM HRC4 was added on top of each of the 5 slices in each well. After several minutes, the drops containing the peptides were completely absorbed and reached the lower compartment of the system that contains the feeding medium. The final concentration in the culture medium (1 ml) was 100 nM, 10 nM, or 1 nM. At each time point, slices were collected, RNA extracted, and RT-qPCR performed as previously described (34).

Human brain organoid differentiation. Human brain organoids were generated as previously described (38) from two iPSC lines (FA0000010 and FA0000011, for brevity called FA10 and FA11). Briefly, cells were dissociated into single cell suspension with Accutase (Stem Cell Technologies; catalog [cat.] no. 7920) and seeded at 4,500 cells/well in 96-well low-attachment U-bottom plates, using embryoid body (EB) medium (DMEM/F12; Thermo Fisher Scientific; cat. no. 11330-032) supplemented with 20% knockout serum replacement (Thermo Fisher Scientific; cat. no. 10828-028), 3% embryonic stem cell (ES)-quality batch-tested fetal bovine serum (Thermo Fisher Scientific; cat. no. 10439024), 1% Glutamax (Thermo Fisher Scientific; cat. no. 35050-038), 1× nonessential amino acids, 0.1 mM 2-mercaptoethanol, 4 ng/ml basic fibroblast growth factor (bFGF; R&D Systems; cat. no. 233FB01M), and 50 μM Y-27632. Fresh medium was replaced every other day until day 6. On day 6, EB medium was replaced with neural induction (NI) medium (DMEM/F12, 1× N2 supplement, 1× Glutamax, 1× nonessential amino acid [NEAA], and 1 μg/ml heparin [Sigma-Aldrich; cat. no. H3149]), and the organoids were transferred to 60- mm or 100-mm low-attachment plates. The organoids were allowed to form neuroepithelium tissue until day 11 to 14, with medium changes every other day. Between day 11 and 24, the organoids were coated with Matrigel droplets and allowed to gel by keeping them at 37°C for 30 min. Matrigel-coated organoids were transferred to differentiation medium (1:1 DMEM/F12:neurobasal, 0.5% N2 supplement, 2% B27 supplement without vitamin A [Life Technologies; cat. no. 12587010], 0.25% insulin solution [Life Technologies; cat. no. 12585014], 50 μM 2-mercaptoethanol, 1% Glutamax, 0.5% NEAA, 1% penicillin-streptomycin), for 4 days. After 4 days, organoids were transferred to differentiation medium containing B27 supplement with vitamin A (Thermo Fisher Scientific; cat. no. 17504-044). Brain organoids were cultured for an additional 60 days with medium changes every 7 days and used for experiments at 90 days.

Immunofluorescent staining. Murine organotypic brain cultures (OBC) from 7-day-old SLAM mice were fixed for 1 hour in 4% paraformaldehyde (PFA), washed in 1× Dulbecco's phosphate-buffered saline (DPBS), dehydrated, clarified in xylene, and embedded in paraffin. Slices 10 μm thick were dewaxed thrice for 3 min in xylene and rehydrated following this protocol: ethanol 100% twice for 3 min, ethanol 95% for 3 min, ethanol 70% for 3 min, ethanol 30% for 3 min, and PBS 1× (twice for 3 min). Antigen unmasking was performed in sodium citrate buffer (at 100°C for 20 min) and slowly cooled down to room temperature (RT). The slices were permeabilized and blocked in 1× DPBS-3% BSA-0.3% Triton X-100 (permeabilization and block solution) for 1 h at RT. Slices were incubated in the permeabilization and block solution containing the primary antibodies overnight at 4°C. After 3 washes (for 5 min each) in 1× DPBS, slices were incubated in the permeabilization and block solution containing the secondary antibodies (1:750) and the DAPI (1:1,000) for 1 h at RT. After 3 washes in 1× DPBS, slices were mounted with Fluoromount-G aqueous mounting medium (SouthernBiotech; catalog no. 0100-01). Images were taken with the microscope set at epifluorescence (Eclipse Ts2R Nikon) and analyzed using ImageJ software.

Human brain organoids were picked from culture and embedded in optimum cutting temperature compound (OCT; Tissue Tek) and then cryosectioned (5 to 8 μm thickness). Brain organoid sections were thawed at room temperature for 5 min, fixed in 4% PFA for 10 min and permeabilized with 0.25% Triton X-100 in PBS for 20 min. Subsequently, the slides were blocked with 10% donkey serum in PBS for at least 1 h. All the steps were performed at RT unless stated otherwise. Sections were incubated overnight at 4°C with primary antibodies. After 3 washes for 5 min each on gentle rocking, in 0.025% Triton X-100 in PBS, sections were stained with fluorescently conjugated secondary antibodies for 1 h. Cell nuclei were stained with DAPI (1:1,000; Sigma-Aldrich), and the sections were mounted with Vectashield mounting medium (Vector Laboratories, Inc., Burlingame, CA), covered, and imaged with DMi8 (Leica Microsystems, Buffalo Grove, IL).

Antibodies used for immunofluorescent staining. See Table 2 for a list of antibodies.

Tiled images. For Fig. 2B to E, H and I and Fig. 4D and G, the fluorescence signal emitted was acquired from several different fields. Then, the images were analyzed with the Stitching plugin for ImageJ (70), which reconstructs images/stacks from an arbitrary number of tiled input images/stacks, yielding the best overlap in terms of the cross-correlation measure. In Fig. S7, the individual pictures used for Fig. 2I and Fig. 4G are presented.

Brain organoid RNA-Seq and analysis. RNA from uninfected and infected brain organoids was extracted using Direct-zol RNA MicroPrep (Zymo) and submitted to the JP Sulzberger Columbia Genome Center for library preparation and sequencing. Strand-specific RNA-Seq libraries were prepared using a poly-A enrichment and were sequenced on an Illumina NovaSeq instrument with paired-end 2 × 100-bp reads. After quality and adapter trimming, transcript abundance quantification was performed using Kallisto v0.44.0 (71) with GRCh38 as the reference genome.

To understand the brain organoid developmental stage, we used the BrainSpan data set (79). Since BrainSpan offers normalized reads per kilobase per million (RPKM) expression values based on Gencode

TABLE 2 Antibodies used for immunofluorescent staining

Antibody and manufacturer	Source
Murine organotypic brain cultures (OBC)	
Rabbit polyclonal anti-NeuN; EMD Millipore	Cat. no. ABN78
Rabbit polyclonal anti-calbindin D-28K (CB28K); Swant	Cat. no. CB38
Mouse monoclonal anti-myelin basic protein (MBP101); Abcam	Cat. no. ab62631
Rabbit polyclonal anti-iba1; Wako	Cat. no. 016-20001
Rabbit polyclonal anti-glial fibrillary acidic protein (GFAP); Agilent Technologies, Dakonumber	Cat. no. Z0334
Goat polyclonal anti-Olig2; R&D system	Cat. no. AF2418
Alexa Fluor 555 donkey anti-mouse IgG (H + L); Thermo Fisher Scientific	Cat. no. A31570
Alexa Fluor 555 donkey anti-rabbit IgG (H + L); Thermo Fisher Scientific	Cat. no. A31572
Alexa Fluor 555 donkey anti-goat IgG (H + L); Thermo Fisher Scientific	Cat. no. A21432
4-,6/diamidino/2/phenylindole, DAPI; Thermo Fisher Scientific	Cat. no. 62248
Human brain organoids	
Rabbit anti-NeuN; Abcam	No. ab177487
Rabbit anti-Olig1; Abcam	No. ab68105
Rabbit anti-nestin; Abcam	No. ab105389
Rabbit anti- anti-glial fibrillary acidic protein (GFAP); Cell Signaling	No. 12389
Rabbit polyclonal anti-Olig2; Proteintech	No. 13999-1-AP
Chicken anti-microtubule-associated protein 2 (MAP2); Abcam	No. ab5392
Rabbit anti-Pax6; Biolegend	No. 901301
Alexa Fluor 647 donkey anti-mouse IgG (H + L); Invitrogen	No. A31573
Alexa Fluor 594 goat anti-chicken IgG (H + L); Invitrogen	No. A11042
2-(4-amidinophenyl)-6-indolecarbamidine dihydrochloride (DAPI); Sigma-Aldrich	No. D9542

v10 annotations, we mapped R1 sequencing reads to GRCh37 annotation of the human genome using Bowtie2 (72) and quantified gene-level RPKM levels using featureCounts (73). Genes were filtered based on an arbitrary gene-level RPKM sum of greater than 1,000 across all 539 RNA-Seq experiments (524 BrainSpan, 15 MeV infections). All-by-all correlation matrices of $\log_2$-transformed RPKM values with a pseudocount of 1 were generated in R v3.6.2. The top 100 BrainSpan samples with the highest correlation coefficients with uninfected FA10 brain organoid replicate 1 were pulled, and a heatmap of correlation coefficients was generated using pheatmap (https://github.com/raivokolde/pheatmap).

Differential gene expression analysis was performed using the Kallisto transcript abundances and the R Bioconductor package DESeq2 (74). The code for analysis is available at http://www.github.com/greninger-lab/MeV-brain-organoids. Low-count filtering was performed on genes with an average of less than one count per sample. Batch effects and biological differences between organoids were incorporated into the design formula as confounders, and normalization and differential expression analysis was performed using DESeq2 with default parameters. The expression of the 50 genes with the lowest Benjamini-Hochberg adjusted *P* value between MeV IC323-EGFP-F L454W and uninfected organoids was plotted on a heatmap generated using the R package pheatmap, with bar graphs generated in the R package ggplot. Enrichment of differentially expressed genes (padj, <0.0001, absolute value $\log_2$ fold change, >1) between MeV IC323-EGFP-F L454W and those uninfected in KEGG pathways was evaluated using the R package ReactomePA (75). To calculate the reads per million (RPM) values for MeV reads, each sample was aligned against the NC_001498 MeV reference sequence using Bowtie2 with default parameters (72). MeV RPM values were calculated using the number of mapped reads in the resulting BAM file.

RNAseq of mouse brain slices. RNA extracted from brain slices was prepared and sequenced as for organoids, as described above. Reads were pseudoaligned with Kallisto v0.44 to mouse reference transcriptome mmGRCm38. Differential expression analysis was performed in DESeq2, incorporating batch effects into the design formula. An expression heatmap was generated as for brain organoids, described above. MeV RPMs were calculated as described above.

Brain organoid genome-specific RT-qPCR. Specific reverse transcription targeting the MeV genomic strand was performed with the SuperScript III first-strand synthesis system (Thermo Fisher), according to the manufacturer's instructions, on 500 ng of total RNA using reverse primer for human GAPDH and forward (FW) 5′ tagged-MeV primer 5′-gcagggcaatctcacaatcaggAAAACTGGTGTTCTACAACAA-3′ containing MeV sequence of the antigenomic strand with a TAG sequence from Nipah virus. The obtained cDNAs were then diluted 1:10. qPCRs were then performed as described previously (76) using MeV reverse (Rev) 5′-TGAAGGCCACTGCATT-3′ and Tag FW 5′-gcagggcaatctcacaatcagg-3′ primers. All results were normalized to human GAPDH deviation.

Metagenomic Next-Generation Sequencing (mNGS) and variant calling. The mNGS was performed as previously described (76). Briefly, RNA was extracted from 50 μl of viral culture using the Quick-RNA viral kit (Zymo) and treated with TURBO DNase I (Thermo Fisher). cDNA was generated from the DNase-treated RNA using Superscript IV reverse transcriptase (Thermo Fisher) and random hexamers (IDT), followed by second-strand synthesis via Sequenase v2.0 DNA polymerase. The resulting double-stranded cDNA was then purified with the DNA Clean & Concentrator kit (Zymo). Libraries were

constructed from 2 μl of cDNA using the Nextera XT kit (Illumina) and sequenced on 1 × 192-bp Illumina MiSeq runs.

Sequencing reads were adapter and quality trimmed using Trimmomatic v0.38 (77). Variants present at a frequency greater than 10% and coverage greater than 10× were identified with LAVA (https://github.com/greninger-lab/lava) using the MeV reference genome (GenBank accession no. NC_001498). All variants were manually confirmed by mapping sequencing reads to the same MeV reference strain in Geneious v11.1.4 (78). Those variants present in intergenic region between the matrix and fusion proteins as well as in homopolymeric tracts were excluded from the analysis. Sequencing reads are available under NCBI BioProject number PRJNA594952.

Statistical analysis. All other statistical comparisons were performed using the Mann-Whitney U-test. All analyses were performed in GraphPad Prism v5 software. Statistical analysis of RNAseq data was performed in R.

SUPPLEMENTAL MATERIAL

Supplemental material is available online only.

DATA SET S1, ZIP file, 0.4 MB.

DATA SET S2, ZIP file, 1.3 MB.

FIG S1, PDF file, 2.9 MB.

FIG S2, TIF file, 2.4 MB.

FIG S3, PDF file, 0.2 MB.

FIG S4, PDF file, 0.2 MB.

FIG S5, PDF file, 0.4 MB.

FIG S6, PDF file, 1 MB.

FIG S7, JPG file, 0.3 MB.

ACKNOWLEDGMENTS

The work was supported by grants from the NIH (AI121349, NS091263, NS105699, and AI146980) to M.P., from French ANR NITRODEP (ANR-13-PDOC-0010-01) to C.M., and from Region Auvergne Rhône-Alpes and LABEX ECOFECT (ANR-11-LABX-0048) of Lyon University, within the program "Investissements d'Avenir" (ANR-11-IDEX-0007) operated by the French National Research Agency (ANR) to B.H. This research was funded in part through the NIH/NCI Cancer Center Support grant P30CA013696.

The research was conducted using the Genomics and High Throughput Screening Shared Resource.

REFERENCES

1. Moss WJ, Griffin DE. 2012. Measles. Lancet 379:153–164. https://doi.org/10.1016/S0140-6736(10)62352-5.
2. Perry RT, Murray JS, Gacic-Dobo M, Dabbagh A, Mulders MN, Strebel PM, Okwo-Bele J-M, Rota PA, Goodson JL. 2015. Progress toward regional measles elimination: worldwide, 2000-2014. MMWR Morb Mortal Wkly Rep 64:1246–1251. https://doi.org/10.15585/mmwr.mm6444a4.
3. Simons E, Ferrari M, Fricks J, Wannemuehler K, Anand A, Burton A, Strebel P. 2012. Assessment of the 2010 global measles mortality reduction goal: results from a model of surveillance data. Lancet 379:2173–2178. https://doi.org/10.1016/S0140-6736(12)60522-4.
4. Jansen VAA, Stollenwerk N, Jensen HJ, Ramsay ME, Edmunds WJ, Rhodes CJ. 2003. Measles outbreaks in a population with declining vaccine uptake. Science 301:804. https://doi.org/10.1126/science.1086726.
5. Durrheim DN, Andrus JK, Tabassum S, Bashour H, Githanga D, Pfaff G. 2021. A dangerous measles future looms beyond the COVID-19 pandemic. Nature Medicine 27:360–361. https://doi.org/10.1038/s41591-021-01237-5.
6. Buchanan R, Bonthius DJ. 2012. Measles virus and associated central nervous system sequelae. Semin Pediatr Neurol 19:107–114. https://doi.org/10.1016/j.spen.2012.02.003.
7. Hosoya M. 2006. Measles encephalitis: direct viral invasion or autoimmune-mediated inflammation? Intern Med 45:841–842. https://doi.org/10.2169/internalmedicine.45.0161.
8. Allen IV, McQuaid S, McMahon J, Kirk J, McConnell R. 1996. The significance of measles virus antigen and genome distribution in the CNS in SSPE for mechanisms of viral spread and demyelination. J Neuropathol Exp Neurol 55:471–480. https://doi.org/10.1097/00005072-199604000-00010.
9. Schmid A, Spielhofer P, Cattaneo R, Baczko K, ter Meulen V, Billeter MA. 1992. Subacute sclerosing panencephalitis is typically characterized by alterations in the fusion protein cytoplasmic domain of the persisting measles virus. Virology 188:910–915. https://doi.org/10.1016/0042-6822(92)90552-z.
10. Cattaneo R, Schmid A, Billeter MA, Sheppard RD, Udem SA. 1988. Multiple viral mutations rather than host factors cause defective measles virus gene expression in a subacute sclerosing panencephalitis cell line. J Virol 62:1388–1397. https://doi.org/10.1128/JVI.62.4.1388-1397.1988.
11. Rima BK, Duprex WP. 2005. Molecular mechanisms of measles virus persistence. Virus Res 111:132–147. https://doi.org/10.1016/j.virusres.2005.04.005.
12. Baldolli A, Dargère S, Cardineau E, Vabret A, Dina J, de La Blanchardière A, Verdon R. 2016. Measles inclusion-body encephalitis (MIBE) in a immunocompromised patient. J Clin Virol 81:43–46. https://doi.org/10.1016/j.jcv.2016.05.016.
13. Hughes I, Jenney ME, Newton RW, Morris DJ, Klapper PE. 1993. Measles encephalitis during immunosuppressive treatment for acute lymphoblastic leukaemia. Arch Dis Child 68:775–778. https://doi.org/10.1136/adc.68.6.775.
14. Hardie DR, Albertyn C, Heckmann JM, Smuts HEM. 2013. Molecular characterisation of virus in the brains of patients with measles inclusion body encephalitis (MIBE). Virol J 10:283. https://doi.org/10.1186/1743-422X-10-283.
15. Jurgens EM, Mathieu C, Palermo LM, Hardie D, Horvat B, Moscona A, Porotto M. 2015. Measles fusion machinery is dysregulated in neuropathogenic variants. mBio 6:e02528-14. https://doi.org/10.1128/mBio.02528-14.
16. Hashiguchi T, Fukuda Y, Matsuoka R, Kuroda D, Kubota M, Shirogane Y, Watanabe S, Tsumoto K, Kohda D, Plemper RK, Yanagi Y. 2018. Structures of the prefusion form of measles virus fusion protein in complex with

inhibitors. Proc Natl Acad Sci U S A 115:2496–2501. https://doi.org/10.1073/pnas.1718957115.
17. Makhortova NR, Askovich P, Patterson CE, Gechman LA, Gerard NP, Rall GF. 2007. Neurokinin-1 enables measles virus trans-synaptic spread in neurons. Virology 362:235–244. https://doi.org/10.1016/j.virol.2007.02.033.
18. Watanabe M, Hashimoto K, Abe Y, Kodama EN, Nabika R, Oishi S, Ohara S, Sato M, Kawasaki Y, Fujii N, Hosoya M. 2016. A novel peptide derived from the fusion protein heptad repeat inhibits replication of subacute sclerosing panencephalitis virus in vitro and in vivo. PLoS One 11:e0162823. https://doi.org/10.1371/journal.pone.0162823.
19. Young VA, Rall GF. 2009. Making it to the synapse: measles virus spread in and among neurons. Curr Top Microbiol Immunol 330:3–30. https://doi.org/10.1007/978-3-540-70617-5_1.
20. Tatsuo H, Ono N, Tanaka K, Yanagi Y. 2000. SLAM (CDw150) is a cellular receptor for measles virus. Nature 406:893–897. https://doi.org/10.1038/35022579.
21. Mühlebach MD, Mateo M, Sinn PL, Prüfer S, Uhlig KM, Leonard VHJ, Navaratnarajah CK, Frenzke M, Wong XX, Sawatsky B, Ramachandran S, McCray PB, Cichutek K, von Messling V, Lopez M, Cattaneo R. 2011. Adherens junction protein nectin-4 is the epithelial receptor for measles virus. Nature 480:530–533. https://doi.org/10.1038/nature10639.
22. Noyce RS, Bondre DG, Ha MN, Lin L-T, Sisson G, Tsao M-S, Richardson CD. 2011. Tumor cell marker PVRL4 (nectin 4) is an epithelial cell receptor for measles virus. PLoS Pathog 7:e1002240. https://doi.org/10.1371/journal.ppat.1002240.
23. Chang A, Dutch RE. 2012. Paramyxovirus fusion and entry: multiple paths to a common end. Viruses 4:613–636. https://doi.org/10.3390/v4040613.
24. Harrison SC. 2008. Viral membrane fusion. Nat Struct Mol Biol 15:690–698. https://doi.org/10.1038/nsmb.1456.
25. Lambert DM, Barney S, Lambert AL, Guthrie K, Medinas R, Davis DE, Bucy T, Erickson J, Merutka G, Petteway SR. 1996. Peptides from conserved regions of paramyxovirus fusion (F) proteins are potent inhibitors of viral fusion. Proc Natl Acad Sci U S A 93:2186–2191. https://doi.org/10.1073/pnas.93.5.2186.
26. Ayata M, Takeuchi K, Takeda M, Ohgimoto S, Kato S, Sharma LB, Tanaka M, Kuwamura M, Ishida H, Ogura H. 2010. The F gene of the Osaka-2 strain of measles virus derived from a case of subacute sclerosing panencephalitis is a major determinant of neurovirulence. J Virol 84:11189–11199. https://doi.org/10.1128/JVI.01075-10.
27. Watanabe S, Shirogane Y, Suzuki SO, Ikegame S, Koga R, Yanagi Y. 2013. Mutant fusion proteins with enhanced fusion activity promote measles virus spread in human neuronal cells and brains of suckling hamsters. J Virol 87:2648–2659. https://doi.org/10.1128/JVI.02632-12.
28. Sato Y, Watanabe S, Fukuda Y, Hashiguchi T, Yanagi Y, Ohno S. 2018. Cell-to-cell measles virus spread between human neurons is dependent on hemagglutinin and hyperfusogenic fusion protein. J Virol 92:e02166-17. https://doi.org/10.1128/JVI.02166-17.
29. Ha MN, Delpeut S, Noyce RS, Sisson G, Black KM, Lin L-T, Bilimoria D, Plemper RK, Privé GG, Richardson CD. 2017. Mutations in the fusion protein of measles virus that confer resistance to the membrane fusion inhibitors carbobenzoxy-d-Phe-l-Phe-Gly and 4-nitro-2-phenylacetyl aminobenzamide. J Virol 91:e01026-17. https://doi.org/10.1128/JVI.01026-17.
30. Mathieu C, Ferren M, Jurgens E, Dumont C, Rybkina K, Harder O, Stelitano D, Madeddu S, Sanna G, Schwartz D, Biswas S, Hardie D, Hashiguchi T, Moscona A, Horvat B, Niewiesk S, Porotto M. 2019. Measles virus bearing measles inclusion body encephalitis-derived fusion protein is pathogenic after infection via the respiratory route. J Virol 93:e01862-18. https://doi.org/10.1128/JVI.01862-18.
31. Domingo E. 2020. Interaction of virus populations with their hosts, p 123–166. *In* Domingo E (ed), Virus as populations, 2nd ed. Academic Press, San Diego, CA.
32. Donohue RC, Pfaller CK, Cattaneo R. 2019. Cyclical adaptation of measles virus quasispecies to epithelial and lymphocytic cells: to V, or not to V. PLoS Pathogens 15:e1007605. https://doi.org/10.1371/journal.ppat.1007605.
33. Welsch JC, Lionnet C, Terzian C, Horvat B, Gerlier D, Mathieu C. 2017. Organotypic brain cultures: a framework for studying CNS infection by neurotropic viruses and screening antiviral drugs. Bio-protocol 7:e2605. https://doi.org/10.21769/BioProtoc.2605.
34. Welsch JC, Talekar A, Mathieu C, Pessi A, Moscona A, Horvat B, Porotto M. 2013. Fatal measles virus infection prevented by brain-penetrant fusion inhibitors. J Virol 87:13785–13794. https://doi.org/10.1128/JVI.02436-13.
35. Ferren M, Horvat B, Mathieu C. 2019. Measles encephalitis: towards new therapeutics. Viruses 11:1017. https://doi.org/10.3390/v11111017.
36. Mathieu C, Huey D, Jurgens E, Welsch JC, DeVito I, Talekar A, Horvat B, Niewiesk S, Moscona A, Porotto M. 2015. Prevention of measles virus infection by intranasal delivery of fusion inhibitor peptides. J Virol 89:1143–1155. https://doi.org/10.1128/JVI.02417-14.
37. Lin MJ, Shean RC, Makhsous N, Greninger AL. 2019. LAVA: a streamlined visualization tool for longitudinal analysis of viral alleles. bioRxiv https://doi.org/10.1101/2019.12.17.879320.
38. Lancaster MA, Knoblich JA. 2014. Generation of cerebral organoids from human pluripotent stem cells. Nat Protoc 9:2329–2340. https://doi.org/10.1038/nprot.2014.158.
39. Luo C, Lancaster MA, Castanon R, Nery JR, Knoblich JA, Ecker JR. 2016. Cerebral organoids recapitulate epigenomic signatures of the human fetal brain. Cell Rep 17:3369–3384. https://doi.org/10.1016/j.celrep.2016.12.001.
40. Qian X, Nguyen HN, Song MM, Hadiono C, Ogden SC, Hammack C, Yao B, Hamersky GR, Jacob F, Zhong C, Yoon K-J, Jeang W, Lin L, Li Y, Thakor J, Berg DA, Zhang C, Kang E, Chickering M, Nauen D, Ho C-Y, Wen Z, Christian KM, Shi P-Y, Maher BJ, Wu H, Jin P, Tang H, Song H, Ming G-L. 2016. Brain-region-specific organoids using mini-bioreactors for modeling ZIKV exposure. Cell 165:1238–1254. https://doi.org/10.1016/j.cell.2016.04.032.
41. Albertyn C, van der Plas H, Hardie D, Candy S, Tomoka T, Leepan EB, Heckmann JM. 2011. Silent casualties from the measles outbreak in South Africa. S Afr Med J 101:313–317. https://doi.org/10.7196/SAMJ.4616.
42. Battles MB, Langedijk JP, Furmanova-Hollenstein P, Chaiwatpongsakorn S, Costello HM, Kwanten L, Vranckx L, Vink P, Jaensch S, Jonckers THM, Koul A, Arnoult E, Peeples ME, Roymans D, McLellan JS. 2016. Molecular mechanism of respiratory syncytial virus fusion inhibitors. Nat Chem Biol 12:87–93. https://doi.org/10.1038/nchembio.1982.
43. Ader N, Brindley M, Avila M, Örvell C, Horvat B, Hiltensperger G, Schneider-Schaulies J, Vandevelde M, Zurbriggen A, Plemper RK, Plattet P. 2013. Mechanism for active membrane fusion triggering by morbillivirus attachment protein. J Virol 87:314–326. https://doi.org/10.1128/JVI.01826-12.
44. Avila M, Alves L, Khosravi M, Ader-Ebert N, Origgi F, Schneider-Schaulies J, Zurbriggen A, Plemper RK, Plattet P. 2014. Molecular determinants defining the triggering range of prefusion F complexes of canine distemper virus. J Virol 88:2951–2966. https://doi.org/10.1128/JVI.03123-13.
45. Plemper RK, Doyle J, Sun A, Prussia A, Cheng L-T, Rota PA, Liotta DC, Snyder JP, Compans RW. 2005. Design of a small-molecule entry inhibitor with activity against primary measles virus strains. Antimicrob Agents Chemother 49:3755–3761. https://doi.org/10.1128/AAC.49.9.3755-3761.2005.
46. Prussia AJ, Plemper RK, Snyder JP. 2008. Measles virus entry inhibitors: a structural proposal for mechanism of action and the development of resistance. Biochemistry 47:13573–13583. https://doi.org/10.1021/bi801513p.
47. Sun A, Prussia A, Zhan W, Murray EE, Doyle J, Cheng L-T, Yoon J-J, Radchenko EV, Palyulin VA, Compans RW, Liotta DC, Plemper RK, Snyder JP. 2006. Nonpeptide inhibitors of measles virus entry. J Med Chem 49:5080–5092. https://doi.org/10.1021/jm0602559.
48. Angius F, Smuts H, Rybkina K, Stelitano D, Eley B, Wilmshurst J, Ferren M, Lalande A, Mathieu C, Moscona A, Horvat B, Hashiguchi T, Porotto M, Hardie D. 2018. Analysis of a subacute sclerosing panencephalitis genotype B3 virus from the 2009–2010 South African measles epidemic shows that hyperfusogenic F proteins contribute to measles virus infection in the brain. J Virol 93:e01700-18. https://doi.org/10.1128/JVI.01700-18.
49. Devaux P, Hodge G, McChesney MB, Cattaneo R. 2008. Attenuation of V- or C-defective measles viruses: infection control by the inflammatory and interferon responses of rhesus monkeys. J Virol 82:5359. https://doi.org/10.1128/JVI.00169-08.
50. Frenzke M, Sawatsky B, Wong XX, Delpeut S, Mateo M, Cattaneo R, von Messling V. 2013. Nectin-4-dependent measles virus spread to the cynomolgus monkey tracheal epithelium: role of infected immune cells infiltrating the lamina propria. J Virol 87:2526–2534. https://doi.org/10.1128/JVI.03037-12.
51. Lemon K, de Vries RD, Mesman AW, McQuaid S, van Amerongen G, Yüksel S, Ludlow M, Rennick LJ, Kuiken T, Rima BK, Geijtenbeek TBH, Osterhaus ADME, Duprex WP, de Swart RL. 2011. Early target cells of measles virus after aerosol infection of non-human primates. PLoS Pathog 7:e1001263. https://doi.org/10.1371/journal.ppat.1001263.
52. Leonard VHJ, Sinn PL, Hodge G, Miest T, Devaux P, Oezguen N, Braun W, McCray PB, McChesney MB, Cattaneo R. 2008. Measles virus blind to its epithelial cell receptor remains virulent in rhesus monkeys but cannot cross the airway epithelium and is not shed. J Clin Invest 118:2448–2458. https://doi.org/10.1172/JCI35454.

53. Leonard VHJ, Hodge G, Reyes-del Valle J, McChesney MB, Cattaneo R. 2010. Measles virus selectively blind to signaling lymphocytic activation molecule (SLAM; CD150) is attenuated and induces strong adaptive immune responses in rhesus monkeys. J Virol 84:3413. https://doi.org/10.1128/JVI.02304-09.
54. Delpeut S, Sawatsky B, Wong X-X, Frenzke M, Cattaneo R, von Messling V. 2017. Nectin-4 interactions govern measles virus virulence in a new model of pathogenesis, the squirrel monkey (Saimiri sciureus). J Virol 91:e02490-16. https://doi.org/10.1128/JVI.02490-16.
55. Devaux P, Hudacek AW, Hodge G, Reyes-Del Valle J, McChesney MB, Cattaneo R. 2011. A recombinant measles virus unable to antagonize STAT1 function cannot control inflammation and is attenuated in rhesus monkeys. J Virol 85:348–356. https://doi.org/10.1128/JVI.00802-10.
56. Lin J-Y, Kuo R-L, Huang H-I. 2019. Activation of type I interferon antiviral response in human neural stem cells. Stem Cell Res Ther 10:387. https://doi.org/10.1186/s13287-019-1521-5.
57. Delhaye S, Paul S, Blakqori G, Minet M, Weber F, Staeheli P, Michiels T. 2006. Neurons produce type I interferon during viral encephalitis. Proc Natl Acad Sci U S A 103:7835–7840. https://doi.org/10.1073/pnas.0602460103.
58. Griffin DE, Lin W-H, Pan C-H. 2012. Measles virus, immune control, and persistence. FEMS Microbiol Rev 36:649–662. https://doi.org/10.1111/j.1574-6976.2012.00330.x.
59. Cosby SL, Brankin B. 1995. Measles virus infection of cerebral endothelial cells and effect on their adhesive properties. Vet Microbiol 44:135–139. https://doi.org/10.1016/0378-1135(95)00006-v.
60. Esolen LM, Takahashi K, Johnson RT, Vaisberg A, Moench TR, Wesselingh SL, Griffin DE. 1995. Brain endothelial cell infection in children with acute fatal measles. J Clin Invest 96:2478–2481. https://doi.org/10.1172/JCI118306.
61. Generous AR, Harrison OJ, Troyanovsky RB, Mateo M, Navaratnarajah CK, Donohue RC, Pfaller CK, Alekhina O, Sergeeva AP, Indra I, Thornburg T, Kochetkova I, Billadeau DD, Taylor MP, Troyanovsky SM, Honig B, Shapiro L, Cattaneo R. 2019. Trans-endocytosis elicited by nectins transfers cytoplasmic cargo, including infectious material, between cells. J Cell Sci 132:jcs235507. https://doi.org/10.1242/jcs.235507.
62. Radecke F, Billeter MA. 1995. Appendix: measles virus antigenome and protein consensus sequences. Curr Top Microbiol Immunol 191:181–192. https://doi.org/10.1007/978-3-642-78621-1_12.
63. Radecke F, Spielhofer P, Schneider H, Kaelin K, Huber M, Dötsch C, Christiansen G, Billeter MA. 1995. Rescue of measles viruses from cloned DNA. EMBO J 14:5773–5784. https://doi.org/10.1002/j.1460-2075.1995.tb00266.x.
64. Hashimoto K, Ono N, Tatsuo H, Minagawa H, Takeda M, Takeuchi K, Yanagi Y. 2002. SLAM (CD150)-independent measles virus entry as revealed by recombinant virus expressing green fluorescent protein. J Virol 76:6743–6749. https://doi.org/10.1128/jvi.76.13.6743-6749.2002.
65. Kelley LA, Mezulis S, Yates CM, Wass MN, Sternberg MJE. 2015. The Phyre2 Web portal for protein modeling, prediction and analysis. Nat Protoc 10:845–858. https://doi.org/10.1038/nprot.2015.053.
66. McRee DE. 1999. XtalView/Xfit: a versatile program for manipulating atomic coordinates and electron density. J Struct Biol 125:156–165. https://doi.org/10.1006/jsbi.1999.4094.
67. Brünger AT, Adams PD, Clore GM, DeLano WL, Gros P, Grosse-Kunstleve RW, Jiang JS, Kuszewski J, Nilges M, Pannu NS, Read RJ, Rice LM, Simonson T, Warren GL. 1998. Crystallography & NMR system: a new software suite for macromolecular structure determination. Acta Crystallogr D Biol Crystallogr 54:905–921. https://doi.org/10.1107/s0907444998003254.
68. Fayolle J, Verrier B, Buckland R, Wild TF. 1999. Characterization of a natural mutation in an antigenic site on the fusion protein of measles virus that is involved in neutralization. J Virol 73:787–790. https://doi.org/10.1128/JVI.73.1.787-790.1999.
69. Malvoisin E, Wild F. 1990. Contribution of measles virus fusion protein in protective immunity: anti-F monoclonal antibodies neutralize virus infectivity and protect mice against challenge. J Virol 64:5160–5162. https://doi.org/10.1128/JVI.64.10.5160-5162.1990.
70. Preibisch S, Saalfeld S, Tomancak P. 2009. Globally optimal stitching of tiled 3D microscopic image acquisitions. Bioinformatics 25:1463–1465. https://doi.org/10.1093/bioinformatics/btp184.
71. Bray NL, Pimentel H, Melsted P, Pachter L. 2016. Near-optimal probabilistic RNA-seq quantification. Nat Biotechnol 34:525–527. https://doi.org/10.1038/nbt.3519.
72. Langmead B, Salzberg SL. 2012. Fast gapped-read alignment with Bowtie 2. Nat Methods 9:357–359. https://doi.org/10.1038/nmeth.1923.
73. Liao Y, Smyth GK, Shi W. 2014. featureCounts: an efficient general purpose program for assigning sequence reads to genomic features. Bioinformatics 30:923–930. https://doi.org/10.1093/bioinformatics/btt656.
74. Love MI, Huber W, Anders S. 2014. Moderated estimation of fold change and dispersion for RNA-seq data with DESeq2. Genome Biol 15:550. https://doi.org/10.1186/s13059-014-0550-8.
75. Yu G, He Q-Y. 2016. ReactomePA: an R/Bioconductor package for reactome pathway analysis and visualization. Mol Biosyst 12:477–479. https://doi.org/10.1039/c5mb00663e.
76. Iketani S, Shean RC, Ferren M, Makhsous N, Aquino DB, Des Georges A, Rima B, Mathieu C, Porotto M, Moscona A, Greninger AL. 2018. Viral entry properties required for fitness in humans are lost through rapid genomic change during viral isolation. mBio 9:e00898-18. https://doi.org/10.1128/mBio.00898-18.
77. Bolger AM, Lohse M, Usadel B. 2014. Trimmomatic: a flexible trimmer for Illumina sequence data. Bioinformatics 30:2114–2120. https://doi.org/10.1093/bioinformatics/btu170.
78. Kearse M, Moir R, Wilson A, Stones-Havas S, Cheung M, Sturrock S, Buxton S, Cooper A, Markowitz S, Duran C, Thierer T, Ashton B, Meintjes P, Drummond A. 2012. Geneious Basic: an integrated and extendable desktop software platform for the organization and analysis of sequence data. Bioinformatics 28:1647–1649. https://doi.org/10.1093/bioinformatics/bts199.
79. Kang HJ, Kawasawa YI, Cheng F, Zhu Y, Xu X, Li M, Sousa AMM, Pletikos M, Meyer KA, Sedmak G, Guennel T, Shin Y, Johnson MB, Krsnik Ž, Mayer S, Fertuzinhos S, Umlauf S, Lisgo SN, Vortmeyer A, Weinberger DR, Mane S, Hyde TM, Huttner A, Reimers M, Kleinman JE, Šestan N. 2011. Spatio-temporal transcriptome of the human brain. Nature 478:483–489. https://doi.org/10.1038/nature10523.

c. Article 5 : Complexes de fusion du virus de la rougeole provenant d'isolats cliniques du système nerveux central : diminution de l'interaction entre l'hémagglutinine et les protéines de fusion

Cyrille Mathieu, Tiago Nascimento Figueira, Amanda R. Decker, Marion Ferren, Tiziana F. Bovier, Eric M. Jurgens, Tara C. Marcink, Anne Moscona, Matteo Porotto

bioRxiv 2021.06.18.449082; doi: https://doi.org/10.1101/2021.06.18.449082

Les mutations retrouvées dans les séquences des F provenant d'infections du SNC par le VR chez des patients confèrent aux virus un complexe de fusion dérégulé et permettent aux virus hyperfusogènes de promouvoir la fusion en l'absence de l'interaction de la H avec un récepteur connu. Pour le mutant portant la mutation L454W dans la F l'expression même de la H s'est avérée facultative et ce virus est capable de fusionner en absence de H et en absence de récepteur.

Pour aller plus loin, l'objectif de cette étude a été d'étudier l'interaction entre la H et la F portant des mutations dans le domaine HRC, en comparaison avec une F conférant un phénotype hyperfusogène également mais portant la mutation S262R à l'interface des 3 protomères dans la région de la tête de la structure pré-fusion de la F.

J'ai réalisé les expériences d'analyse de la fusion reposant sur un test de complémentation de la β-galactosidase. Des cellules 293T co-transfectées avec la F portant la mutation souhaitée, la H sauvage, et la sous-unité alpha de la β-galactosidase ont été mises en contact avec des cellules exprimant la sous-unité omega de la β-galactosidase et le récepteur SLAM. Les cellules ont été traitées par un peptide inhibiteur de fusion (monomère non conjugué du domaine HRC) et la luminescence a été quantifiée 1 heure, 3 heures et 6 heures après traitement. Les résultats montrent que le peptide bloque complètement la fusion de la F portant la mutation L454W, même 6 heures après traitement, contrairement aux F sauvages et mutantes S262R.

Les mutations du domaine HRC entrainent une diminution de l'interaction entre H et F. Une des conséquences est la perte de protection de la F par la H qui permet le déclenchement intempestif de la F en absence de récepteur. La fusion des virus portant ces mutations est toutefois plus lente. On peut expliquer ce phénomène par un repliement plus lent des F mutées en l'absence de l'effet de poussée de la H et par une réduction de l'interaction HRN-HRC. Lorsque la mutation L454W est associée à la mutation E455G, l'interaction entre la H et la F est restaurée et le virus portant cette double mutation retrouve alors un phénotype sauvage. De plus la F portant la mutation L454W, bien que hyperfusogène, entraine la fusion plus lentement que la F sauvage, laissant plus de temps aux peptides HRC inhibiteurs de fusion pour interagir avec le domaine HRN de la F et bloquer ainsi la fusion de façon efficace.

Ces observations sont associées à une diminution de l'interaction entre les protéines H et F pour les virus hyperfusogènes mutants du domaine HRC.

Les données présentées dans cette étude suggèrent que la fusion en l'absence d'interaction avec le récepteur est l'effet combiné d'une diminution de la stabilité de F ainsi que d'une diminution de l'interaction de F avec H.

Measles fusion complexes from central nervous system clinical isolates: decreased interaction between hemagglutinin and fusion proteins

Cyrille Mathieu[1,2,3*], Tiago Nascimento Figueira[1,2], Amanda R. Decker[1,2], Marion Ferren[1,2,3], Tiziana F. Bovier[1,2,4], Eric M. Jurgens[1,2,5] , Tara C. Marcink [1,2], Anne Moscona[1,2,6,7], and Matteo Porotto[1,2,4*]

[1]Center for Host-Pathogen Interaction, Columbia University Vagelos College of Physicians and Surgeons, New York, New York USA.

[2]Department of Pediatrics, Columbia University Vagelos College of Physicians and Surgeons, New York, New York USA.

[3]CIRI, Centre International de Recherche en Infectiologie, Team Immunobiology of the Viral infections, Univ Lyon, Inserm, U1111, CNRS, UMR5308, Université Claude Bernard Lyon 1, Ecole Normale Supérieure de Lyon, 69007, Lyon, France.

[4]Department of Experimental Medicine , University of Campania, 81100 Caserta , Caserta , Italy.

[5]Weill Cornell Medical College, New York, New York, USA.

[6]Department of Microbiology & Immunology, Columbia University Vagelos College of Physicians and Surgeons, New York, New York, USA.

[7]Department of Physiology & Cellular Biophysics, Columbia University Vagelos College of Physicians and Surgeons, New York, New York, United States.

[*]To whom correspondence should be addressed: Cyrille Mathieu (cyrille.mathieu@inserm.fr) and Matteo Porotto (mp3509@cumc.columbia.edu).

One Sentence Summary: Measles CNS adapted fusion complexes have altered H/F interaction.

Key words: Viral fusion; CNS adaptation; viral infectivity.

Abstract:

Measles virus (MeV) viral entry is mediated by a fusion complex comprised of a receptor binding protein (hemagglutinin, H) and a fusion protein (F). The wild type H/F complex requires interaction with specific proteinaceous receptors (CD150/SLAM and nectin-4) in order to be activated. In contrast the H/F complexes isolated from viruses infecting the central nervous system (CNS) do not require a specific receptor. A single amino acid change in the F protein (L454W) was previously identified in two patients with lethal sequelae of MeV CNS infection, and the F bearing this mutation mediates fusion even without the H protein. We show here that viruses bearing the L454W fusion complex are less efficient than wt virus at targeting receptor expressing cells and that this defect is associated with a decreased interaction between the H and the F proteins.

Importance:

Measles (Mev) infection can cause serious complications including measles inclusion body encephalitis (MIBE) and subacute sclerosing panencephalitis (SSPE). MIBE and SSPE are relatively rare but lethal. We have shown that the fusion complex of CNS adapted clinical samples can spread in the absence of known receptor. We now provide evidence that HRC mutations leading to CNS adaptation come at a cost to the efficiency of viral entry.

Introduction:

Despite the availability of an effective measles virus (MeV) vaccine and efforts to increase vaccine coverage by the WHO, UNICEF, and their partners, MeV has not been eradicated and the estimated global measles death toll rose from 89,780 in 2016 to 207,500 in 2019(1). The SARS-CoV-2 pandemic and associated countermeasures reduced the incidence

of other respiratory viral infections but also halted vaccination, increasing the risk of measles outbreaks in the future(1).

MeV is the most infectious virus known to humans, transmits via the air, and causes systemic infection. The virus enters cells via two cellular receptors: CD150/SLAM expressed by subsets of immune cells(2) and nectin-4 expressed by epithelial cells(3, 4). Central nervous system (CNS) sequelae associated with active viral infection include subacute sclerosing panencephalitis (SSPE) and measles inclusion body encephalitis (MIBE) (5-10). These CNS complications have been associated with viral evolution and specific CNS adaptation, specifically with alterations in the viral fusion mechanism(11, 12).

MeV expresses two envelope glycoproteins that make up the fusion complex. The H protein mediates receptor binding, followed by triggering of the F protein, which leads to merger of the viral envelope with target cell membranes. We refer to the H/F pairs of MeV as the viral fusion complex, since these proteins act in concert. F is synthesized as a precursor ($\mathbf{F_0}$) that is cleaved within the cell to yield the pre-fusion F complex comprising three C-terminal $\mathbf{F_1}$ subunits associated non-covalently with three N-terminal $\mathbf{F_2}$ subunits. This trimeric F structure is kinetically trapped in a metastable conformation, primed for fusion activation upon engagement of the H glycoprotein by the cell-surface receptor (either CD150/SLAM or nectin-4)(2-4, 13-15). After receptor engagement by H, the pre-fusion F undergoes a structural transition, extending and inserting its hydrophobic “fusion peptide” into the target cell. During entry, F refolds into a so-called “trimer of hairpins” (or 6-helix bundle) post-fusion structure that brings together the N-terminal heptad repeat (HRN) and the C-terminal heptad repeat (HRC), and the viral and cell membranes fuse(16-23). Peptides derived from the HRC region of the $\mathbf{F_2}$ ectodomain inhibit paramyxovirus entry with varying activity(19, 24-32). We and others have shown that fusion complexes from CNS isolated clinical samples are dysregulated and do not require H-receptor interaction for mediating fusion(8, 10, 33, 34), and for a

specific mutated F (L454W) even the presence of the H was dispensable for cell-to-cell fusion in transfected cells(8, 10, 34). Here we investigated whether this phenotype was correlated with dimished H-F interaction and we highlight that fusion in the absence of receptor interaction is the combined effect of a decrease in the stability of F as well as a decrease in F's interaction with H.

Results:

Measles virus F glycoprotein from neuropathogenic viruses

MeV F glycoproteins with specific single residue alterations (S262R, L454W, T461I, and N462K) have been associated with neuropathogenic measles strains that were either isolated from patients or generated in laboratory settings (9, 12, 34, 35). We mapped these mutations onto x-ray structures of the pre-fusion (36) conformations of F (Fig.1A), highlighting the locations of these mutations in MeV F. The S262R mutation occurs at the interface of three protomers in the head region of the pre-fusion structure. The mutation from Ser to Arg at residue 262 results in a clash within each monomer in the existing crystal structure . These microenvironmental changes are likely to affect the conformational stability of the F. The other three mutations (L454W, T461I, and N462K) were located within the C-terminal heptad repeat domain (HRC). In the pre-fusion structure, the L454W mutation would also perturbs the current pre-fusion structure. The T461I and N462K mutations occur in a well-ordered α-helical region of the HRC domain. These three mutations (L454W, T461I, and N462K) occur in the portion of the HRC domain where the head and stalk regions of the pre-fusion conformation meet. Interactions at this region may be important for stabilizing the pre-fusion state and mutations in this junction would affect stability of the MeV-F prefusion structure, as our previous data have shown (12, 34).

Impact of hyperfusogenic mutations in F on H-F interaction

We previously suggested that the ability of HRC mutants to fuse in the absence of known receptors could be at least partly due to reduced interaction between H and F(34). The interaction between F and H and the impact of mutations in the HRC domain (*i.e.,* L454W, T461I and N462 may be affected by thermal instability – obscuring the effect of the specific mutations -- we included the highly unstable mutant F-S262R (11, 12, 33, 35) which interacts efficiently with H. H-F interaction was assessed with both the cleavable F proteins (Fig. 2A) and the cleavage site mutant (CSM) version of these F proteins (Fig. 2B), to distinguish between effects on the $\mathbf{F_0}$ and the $\mathbf{F_1}$ form of F. Results are presented as the average of 3 separate experiments ± SD (Fig.2C). Densitometric analysis was used to normalize the results to total protein content and to convert the data to graphs (average of 3 separate experiments ± standard deviation; Fig. 2C). There is significant reduction in the amount of $\mathbf{F_1}$ co-immunoprecipitated with H for the HRC hyperfusogenic mutants (*i.e. ,* L454W, T461I and N462K) compared to the *wt* F ($P = 0.0023$, $P = 0.0030$ and $P = 0.0014$, respectively; two-way ANOVA with multiple comparisons against *wt* F, corrected with the Dunnett hypothesis test). For the other hyperfusogenic mutant, F S262R, there was more co-immunoprecipitated $\mathbf{F_1}$ protein when compared to the HRC mutants. There were no differences in co-immunoprecipitation of $\mathbf{F_0}$. Thus, mutations in HRC associated with a hyperfusogenic phenotype decrease the ability of H to interact with the active $\mathbf{F_1}$ form of F.

Viral evolution leads to compensatory mutation

MeV bearing the L454W F protein, when grown at 37^{o}C in cell culture, acquired a compensatory mutation (E455G) that re-balanced F's stability and dependence on H and cellular receptor for mediating fusion (12). The E455G mutation is shown in Fig. 3A, alone and in combination with L454W. Tryptophan (W454) contains a bulky aromatic sidechain

when compared to leucine (L454), while glutamic acid (E455) is larger than glycine (G455). We determined whether the E455G mutation restored H-F interaction (Fig. 3). H-F interaction for wt ,L454W, E455G, and L454W/E455G F proteins is shown in Fig. 3 . Densitometric analysis was used to normalize the results to total protein content and to convert the data to graphs (average of 3 separate experiments ± SD; Fig. 3C). The *wt* versus the L454W F was significantly different (as seen in Fig.2), however the mutant E455G F and the double mutant L454W/E455G F co-immunoprecipitated similarly to the *wt* F. The E455G compensatory mutation in the HRC domain of the F resulted in a *wt* phenotype. We previously showed that E455G restored F's stability (as measured by sensitivity to thermal activation) and restored F's dependence on H-receptor interaction for fusion(12). Fig. 3 reveals that E455G also reestablished interaction of H with the active $\mathbf{F_1}$ form of F.

Loss of H-F interaction delays viral entry.

One of the consequences of the loss of interaction between F and H is the loss of protection of F from spontaneous triggering(37). Additionally, hyperfusogenic MeV F HRC mutants proteins are less stable in their pre-fusion state, as measured by their temperature sensitivity, compared to the wt F protein. The hyperfusogenic F proteins mediate fusion even in the absence of either CD150/SLAM or nectin-4 receptors(10, 34). We have shown that this decreased F stability, however, results in viruses that are inactivated at lower temperatures than wt virus (10), because F transitions to its post-fusion state more readily, rendering the viral particle non-infectious. We asked whether the destabilizing mutations in F of the neuropathogenic variants affect viral entry into SLAM-expressing cells (38). To do so, we used an assay developed for a related paramyxovirus, human parainfluenza virus 3 (HPIV3). For HPIV3 we have shown that the kinetics of F protein activation and viral entry modulate the potency of HR derived peptides(37, 39), and therefore this modulation can be used as a

tool to quantitate F activation and entry. Applying this strategy to MeV, we determined the sensitivity of MeV F to inhibition by MeV HR derived peptides, using a previously described dimeric HR lipopeptide, HRC4. In Fig. 4A, 1μM of HRC4 peptide was added at time points from 0 to 2 hours during infection of Vero-SLAM cells. Peptide addition at time zero inhibited 100% of infection for all the viruses (wt and the three viruses bearing the mutated F proteins). Peptides added after 1 hour decreased inhibition to 30% for wt virus, meaning that most of the wt virus had already entered, while the mutants bearing F T461I and N462K were 50% inhibited and the mutant bearing F L454W was 70% inhibited. After 90 min, the peptide continued to inhibit the mutants (from 20 to 30% of viral entry). No inhibitory effect was observed after 2 hours. This experiment reveals that for wt viruses, the window of HRC4 inhibitor sensitivity is significantly shorter than that of the viruses bearing the mutated Fs. The longer time of inhibitor susceptibility of the HRC mutant Fs suggests that wt H-F is more efficient for entry in the presence of receptors.

Easier triggering of HRC hyperfusogenic mutants correlates with longer time to completion of fusion.

For HPIV3, fusion requires engagement of the receptor binding protein (the hemagglutinin neuraminidase, HN) beyond initial triggering of the F protein. This engagement of HN is essential for F's function until membrane merger (37). A similar mechanism of ongoing activation of the fusion process by receptor-engaged H could explain our observations for MeV. We showed that constant interaction with F by receptor-engaged H may allow wt H-F to fuse even in the presence of F-targeted anti-MeV peptides (40). As above, we also previously showed that for HRC peptide fusion inhibitors, adding a lipid moiety improves antiviral potency over time(40). In this case a cholesterol-conjugated dimeric

peptide (HRC4) was inhibitory as long as 6h after *in vitro* (41). Without a lipid moiety (HRC1), peptide was effective only at early time points after infection.

We hypothesize that the loss of of H-F interaction affects both the triggering of HRC mutants and their ability to fuse in the presence of inhibitor. In Fig. 4B we assessed weak peptide inhibitor (HRC1) for inhibition of wt and mutant F fusion. The assay measures the fusion of cells that express viral envelope glycoproteins (MeV IC323 H/F) with cells that express the MeV receptor SLAM. HRC1 peptide inhibited fusion at early time points (1h, Fig. 4 B). As expected, this inhibition decreased below 70% after 3h and below 40% for the wt F and S262R F respectively after 6h. In contrast, for the H/L454W F fusion complex, HRC1 peptide inhibited over the time course of this fusion assay, significantly better than for the wt complex (**p value, Mann-Whitney U-Test). A parallel assay was performed with the HRC4 peptide, which completely inhibited fusion of all MeV Fs (Fig. S1).

HRC peptides are thought to stabilize F protein intermediates during the fusion process after insertion into the target cell membrane but before refolding to the post-fusion state. The stabilization of the transient intermediate state of F by HRC peptides was used to identify discrete steps in the fusion process (37, 42). In Fig. 4C we determined whether the HRC1 fusion blockade for the HRC mutated F occurs at the same transitional state. Red blood cells (RBCs) were allowed to interact with cells expressing the MeV F hyperfusogenic mutants along with a chimeric receptor binding protein expressing the MeV H stalk and the globular head of HPIV3 HN. This chimeric protein can engage the sialic acid receptor on the RBCs and initiate MeV F-activation for the neuropathogenic F proteins (8, 34, 43). The read-out for peptide inhibition is irreversible binding of the RBCs to the F-expressing cells and/or fusion. This assay provides a measure of the efficiency with which HRC1 binds and retains F in its transitional intermediate state, preventing membrane merger (Fig.4C). 293T cells co-expressing the chimeric receptor binding protein MeV H-HN and MeV F (hyperfusogenic

mutants) were incubated with RBCs at 4 °C, then transferred to 37 °C in the presence of HRC1 peptides (1μM). Zanamivir, a small molecule sialic acid analog that blocks HN-receptor interaction was added after 1 h to disengage cells that were bound by HN-globular head engagement alone. Note that wt F was not used in this assay since it is too stable to be activated under these conditions. The proportion of RBCs either free, reversibly bound by HN-receptor interaction (and therefore released by zanamivir), irreversibly bound by F protein bridging (following insertion of the fusion peptide in the target cell membrane), or fused was quantified. For all three MeV F HRC mutants the larger majority of the cell population remained irreversibly bound and very little fusion was observed, confirming the ability of HRC1 to block F in its transitional state after insertion of the fusion peptide in the target cell membrane. In contrast, the percentage of irreversibly bound cells decreased to 30% concomitantly with an increase in fusion up to 50% for the S262R hyperfusogenic mutant, confirming that this F can "override" inhibition by the peptide. The HRC1 peptide stabilizes the intermediate fusion state for all the F proteins that bear mutations in the heptad repeat domain. Taken together, these results confirm that while the reduction in H-F interaction allows HRC hyperfusogenic mutants to fuse in the absence of receptor — which seems to be a benefit in the CNS— it also decreases their fusion compared to wt virus in presence of receptor by reducing complete fusion after triggering. Outside the CNS, this reduced fusion is a disadvantage.

Discussion

The altered HRC region of the CNS-adapted MeV F proteins produced viruses that can fuse and infect without known receptors for H. While H-F interaction is essential for fusion and infection by wt MeV, these F proteins (L454W, T461I and N462K; fig 1A) interact less with H but nevertheless mediate infection *in vitro* (L454W, T461I and N462K) (10, 34), in models

of CNS infection (L454W, and T461I)(12) and *in vivo* (L454W) (10) more effectively than wt virus in the absence of SLAM or Nectin-4 receptors. As anticipated based on previous data(10, 12, 34), the hyperfusogenicity conferred by the alterations in the MeV F HRC region affects both functional and physical interactions with H. The E455G revertant restored wt-like properties in the context of the L454W-bearing F , and when introduced singly into the F protein led to an extremely stable F(12) . We speculate that introducing W454 into the prefusion F stalk results in local destabilization that enhances F activation, even in the absence of receptor. The nearby mutation G455 may alter the structure sufficiently to restore the "wt" properties. When the viral quasispecies formed by L454W and L454W/E455G F bearing viruses is cultivated in human brain organoids , the L454W/E455G F bearing virus is eliminated within 10 days confirming that the L454W F bearing virus is fit for growth in CNS tissues(12). The virus bearing the S262R mutation in F is neuropathogenic *in vivo* (11, 35), and we observed no significant differences in H-F interaction. A S262G mutation in F (along with several other mutations) was found in virus from a SSPE clinical case (8). Thus, while destabilizing the F protein significantly improves MeV's ability to spread in the brain, the loss of H-F interaction may not be necessary for CNS adaptation.

MeV H-F interaction is key for the steps after F insertion in the target membrane, to complete fusion. The viruses bearing F mutations that lead to CNS spread are more susceptible to fusion inhibitory peptides(10). We attribute this, at least in part, to the fact that the H does not continue to activate F after initial triggering.

In Fig. 5 we propose models of viral infection with wt MeV and the CNS adapted variants, incorporating the findings in this work as well as work from others. A common pattern for neuropathogenic F variants is decreased stability of F (as assessed by sensitivitiy to heat) and a fusion complex that mediates cell-to-cell fusion in the absence of either CD150/SLAM or nectin-4(8, 10, 12, 34, 44). These properties confer an infectivity cost, since

249 they are significantly slower to complete the fusion process after inital triggering. These
250 features together with lower viability (10) make these viruses adapt to cell-to cell transmission
251 after initial infection but also likely mean that they are less transmissible.
252
253
254 **Funding sources:** The work was supported by grant from NIH AI121349, NS091263, and
255 NS105699 to MP, from French ANR NITRODEP (ANR-13-PDOC-0010-01) to CM.
256

Figure legends

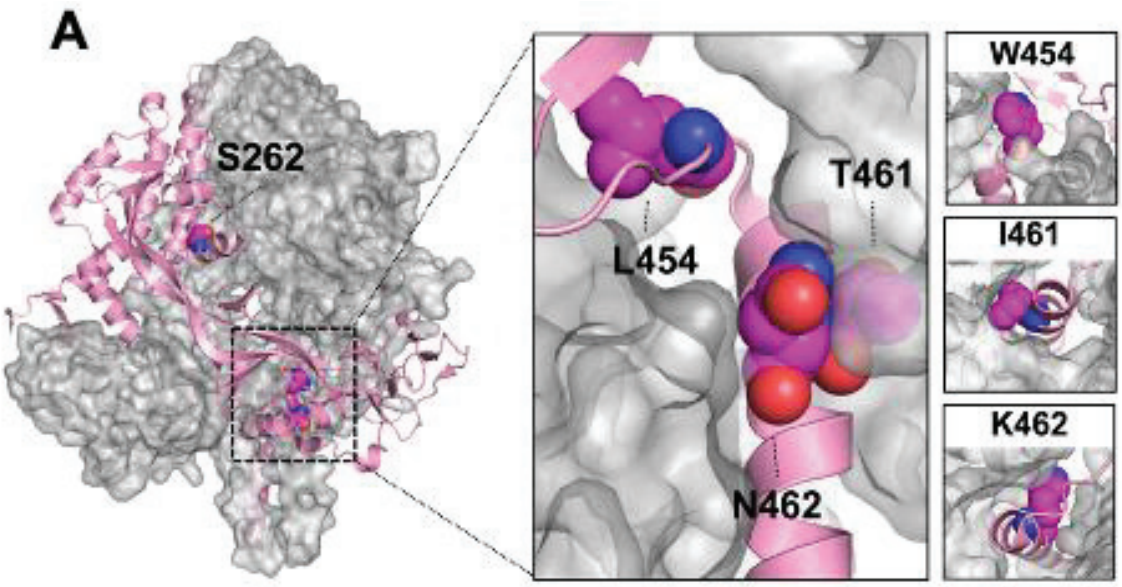

Figure 1 – Crystal structure of the trimeric measles F (PDBID:5YXW) in the prefusion state. Monomer is shown in pink. Zoomed in view shows close proximity of residues L454, T461, and N462 near the top of the prefusion F stalk. Left-most panels show potential orientations of mutations W454, I461, and K462 as modeled by pymol with minimal sculpting to reduce steric clashes. Three substitutions (L454W, T461I and N462K) in the HRC domain in neuropathogenic strains are shown. The residue S262 (mutated here to R) was previously described in the hyperfusogenic F variant.

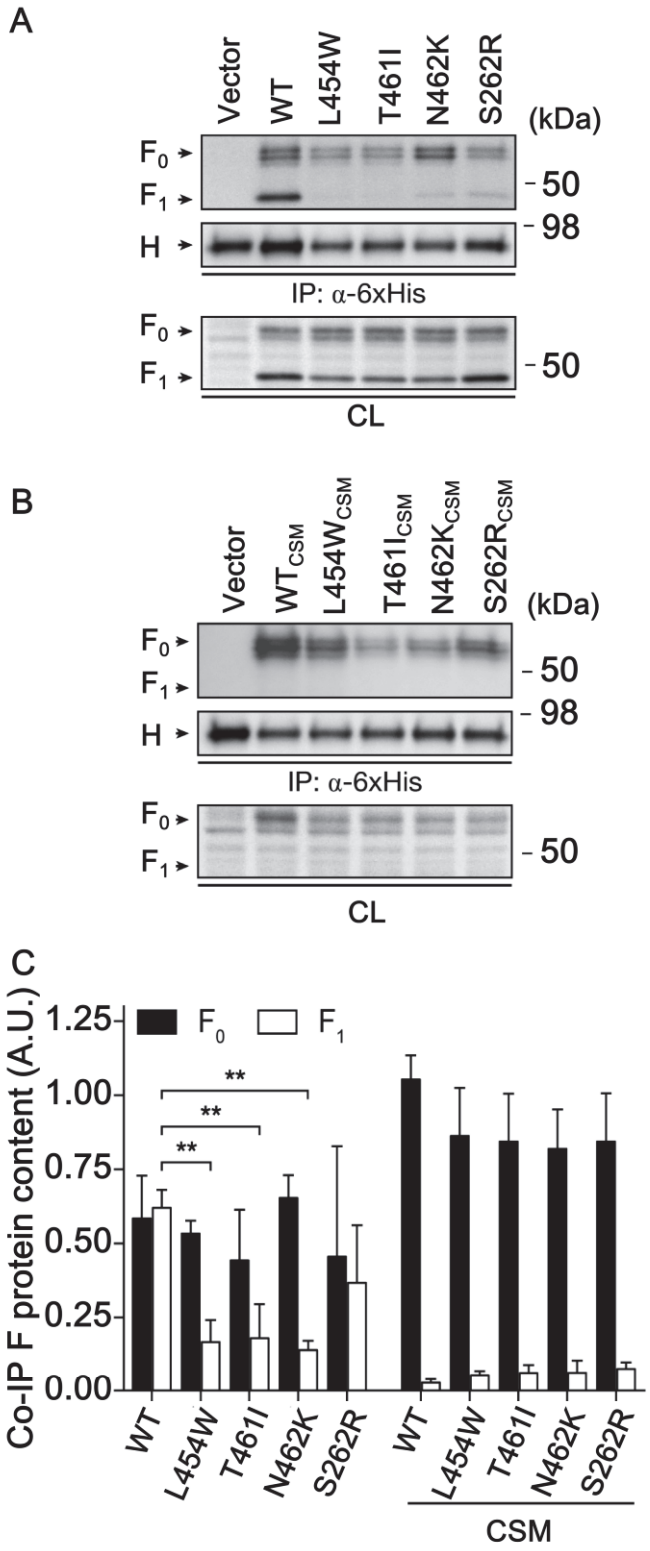

Figure 2 – The effect of hyperfusogenic MeV F HRC domain mutations on MeV H functional and physical interactions with F_0 and F_1. (A-B) Cell lysates from 293T cell cultures co-expressing MeV H-6xHis and F *wt*, L454W, T461I, N462K or S262R proteins were immunoprecipitated with an anti-6xHis antibody. Cleavable (A) and non-cleavable (B)

273 forms of F were included in the experiment. Precipitates were analyzed by western blotting
274 using anti-MeV F HRC and anti-6xHis (top panels) while cell lysates were blotted using anti-
275 MeV F HRC (bottom panels). **(C)** Densitometry measurements of co-immunoprecipitated
276 MeV F protein detected through western blot analysis. Protein content was normalized for the
277 total F protein in cell lysates and the immunoprecipitated H protein. Results are the average of
278 three independent replicates. Error bars correspond to the standard deviation. **, $P \leq 0.01$.
279

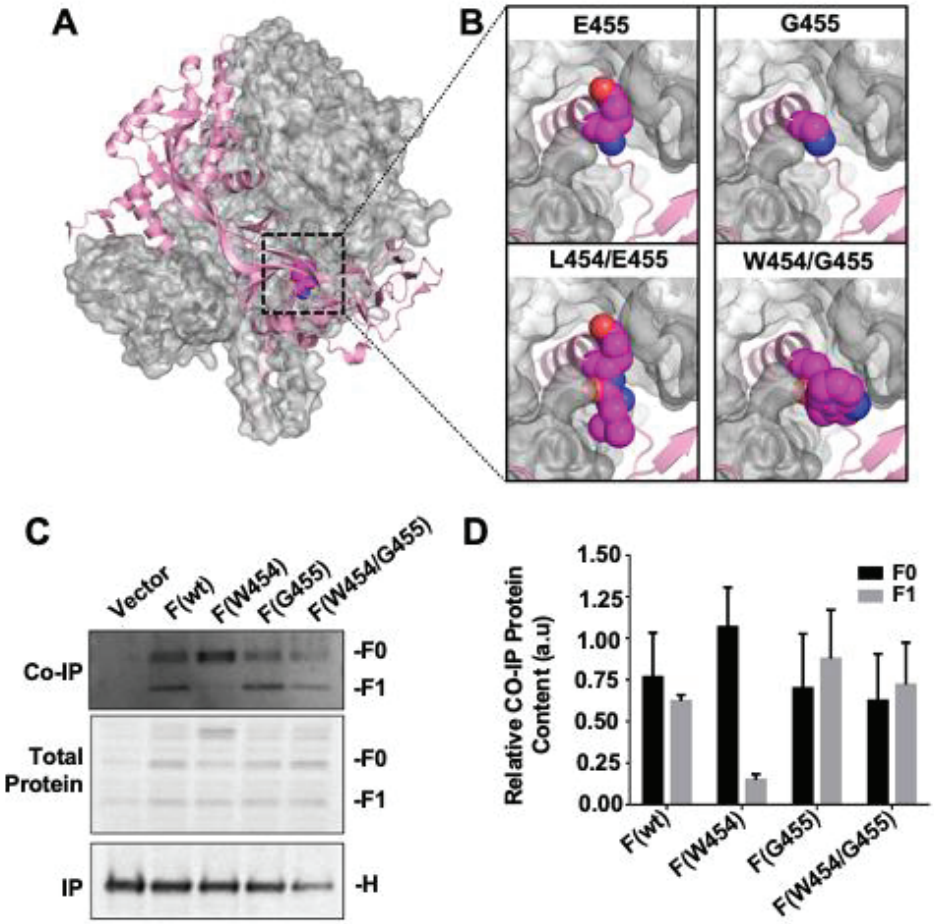

Figure 3 – The effect of F protein's E455G compensatory mutation on H protein's interaction with F_0 and F_1.(A) Prefusion F crystal structure (PDBID: 5YXW). (B) Zoomed in views near the top of the prefusion F stalk region with E455 (top left) and L454/E455 (bottom left) shown as spheres. Mutations G455 (top right) and W454/G455 (bottom right) were substituted in pymol with minimal sculpting to reduce steric clashes. **(C and D)** Cell lysates from 293T cell cultures co-expressing MeV H-6xHis and F *wt*, L454W, E455G, or L454W/E455G proteins were immunoprecipitated with an anti-6xHis antibody. Cleavable (B) and non-cleavable (C) forms of F were included in the experiment. Precipitates were analyzed through western blotting using anti-MeV F HRC and anti-6xHis (top panels) while cell lysates were blotted using anti-MeV F HRC (bottom panels). **(D)** Densitometry measurements of co-immunoprecipitated MeV F protein detected by western blot analysis. Protein content was

293 normalized for the total F protein in cell lysates and the immunoprecipitated H protein. There
294 was no statistical difference (unpaired T-test) between the levels of $\mathbf{F_0}$ that were co-
295 immunoprecipitated for each allele. There was also no statistical difference between F(*wt*) and
296 either allele that contained E455G (single and double mutant) for $\mathbf{F_1}$ levels. However, the
297 difference between the F(*wt*) and F(L454W) $\mathbf{F_1}$ that co-immunoprecipitated with H was
298 extremely statistically significant (P = 0.0007). Error equals +/- SEM. N = 3 biological
299 replicates
300
301

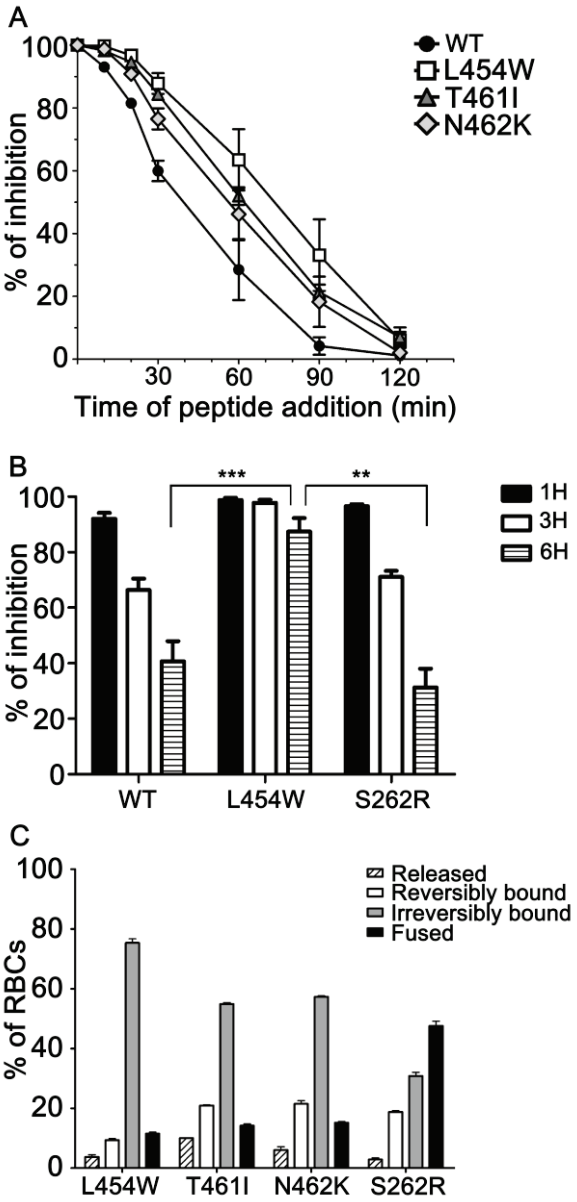

Figure 4 – HRC hyperfusogenic mutants fuse less in presence of entry receptor- (**A**) Inhibition by MeV HRC4 peptides added at different times after infection reveals differences in the rate of F activation. Vero-SLAM cells were infected with wt or the indicated viruses at a multiplicity of infection of 6.7×10^{-4}. The MeV HRC4 fusion inhibitory peptide was added at the time points noted to a final concentration of 1 μM. Cells were overlaid with agarose at 90 min and plaques were stained and counted at 36 h. The percent inhibition of viral entry, normalized to 100% inhibition at time zero, is shown as a function of the time of peptide addition. Data points are means (± standard error) for triplicate experiments. - (**B**) Fusion of MeV H/F co-expressing cells with SLAM-bearing cells in the presence of unconjugated

peptides (HRC1 at 1 μM) was quantitated at 1 h , 3h or 6 h using a β-galactosidase complementation assay. Results are presented as percent reduction in luminescence (*y* axis) compared with no treatment. Each point is the mean (± standard error) of results from 3 to 5 separate experiments (**, $P < 0.01$; ***, $P < 0.001$ [Mann-Whitney-U test]). (**C**) Role of receptor binding protein (H-HN) after F has inserted its hydrophobic fusion peptide into the target cell: progression to membrane merger in the presence of H-F interaction. If H-F interaction is functional, processed F is activated to the stage of fusion peptide insertion captured by unconjugated peptides, and then proceeds to membrane merger. Monolayers of cells co-expressing H-HN and processed F proteins (as indicated on the axis) were allowed to bind to receptor-bearing RBCs at 4°C. Unbound RBCs were washed away, and cells were incubated with standard HRC1 peptides (1 μM) at 37°C for 60 min. The values on the *y* axis reflect the quantity of RBCs that were released by H-HN neuraminidase (striped bar), reversibly bound by H-HN-receptor interaction (white bar), irreversibly bound (gray bar), or fused (black bar). The values are means (±standard deviations) of results from triplicate samples and are representative of the experiment repeated at least four times.

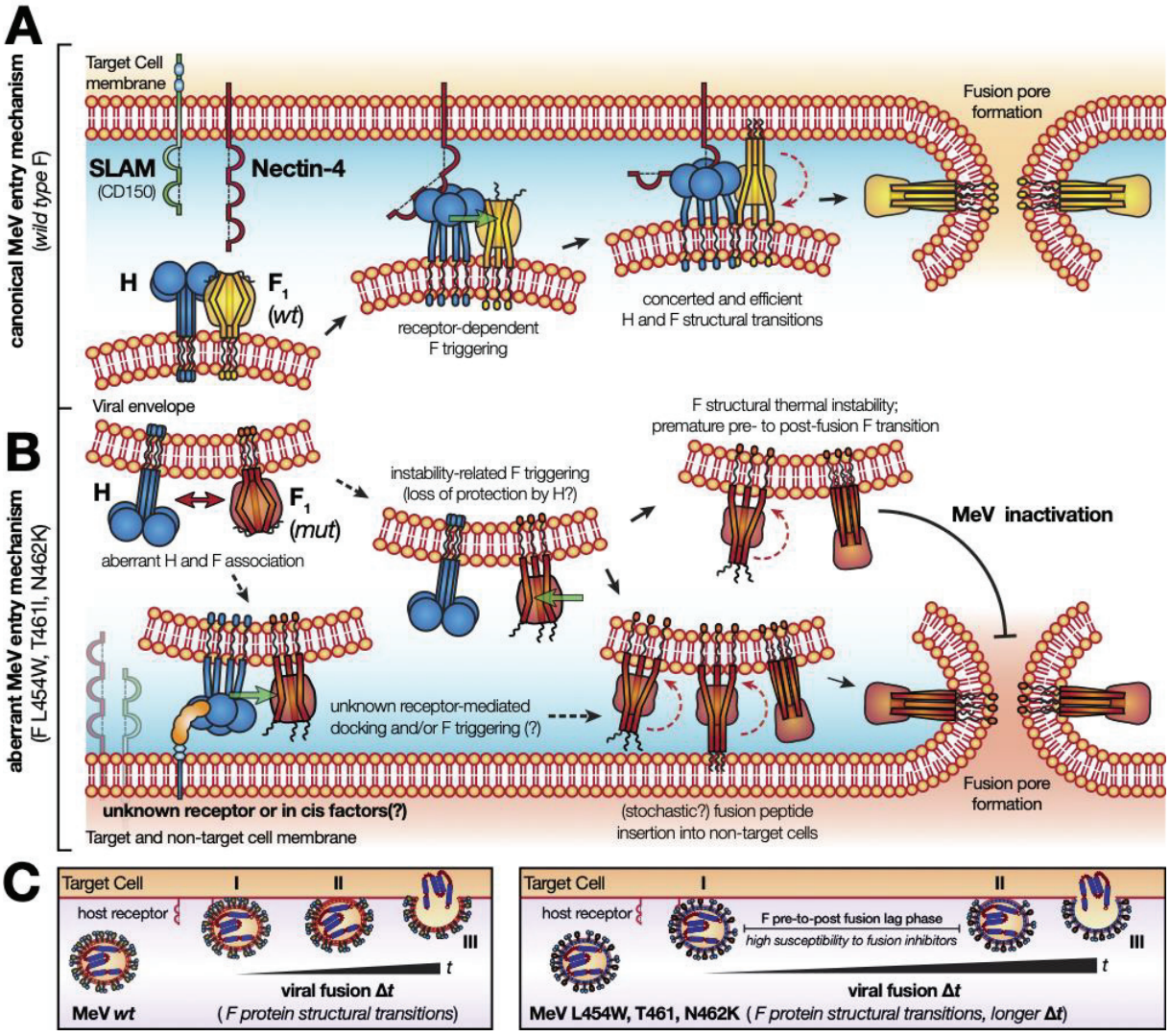

Figure 5 – Model for the hyperfusogenic entry mechanism of neuropathogenic MeV mutant strains. (A) The *wt* MeV entry mechanism is characterized by the concerted action of the H and F glycoprotein complex. Upon H-mediated CD150/SLAM or Nectin-4 receptor recognition, and subsequent F triggering, both H and F undergo a series of conformational changes that guide fusion of the cell membrane and viral envelope. H anchors the virus to the cell surface and activates the F to insert its fusion peptide trimers into the cell membrane and undergo a conformational transition, the driving force for lipid mixing and fusion. **(B)** The hyperfusogenic phenotype of neuropathogenic MeV variants is associated with single amino acid mutations in F (L454W, T461I and N462K). Altered association with H triggers the mutated F into unstable fusogenic conformations. The lower energy barrier between the pre-

and post-fusion (6HB) conformations leads to premature structural transitions of F and consequent viral attenuation/inactivation. Yet, the mutated F can insert into non-targeted cell types, such as neurons, promoting MeV aberrant infection. **(C)** The coordinated structural transitions of H and F promote entry by *wt* MeV after receptor engagement (left panel). In hyperfusogenic MeV variants, with loss of H-to-F interaction, entry kinetics are slower, with a lag between the F pre- and post-fusion conformations (right panel). This feature enhanges susceptibility to F-specific fusion inhibitory peptides acting at this stage.

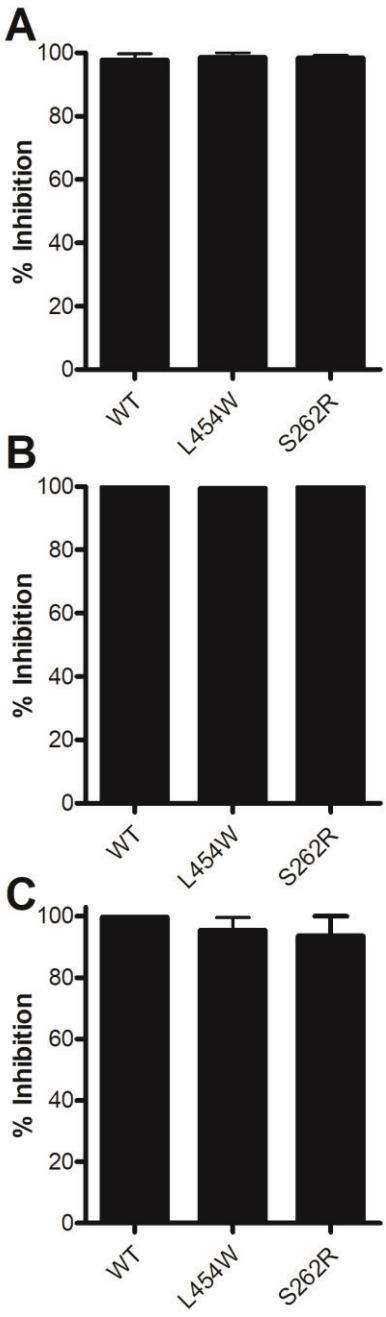

345

346 **FIG S1.** Fusion of MeV H/F co-expressing cells with SLAM-bearing cells in the presence of
347 unconjugated peptides (HRC4, dimer peptide with cholesterol, 1 μM) was quantitated at 1 h
348 (**A**) 3h (**B**) or 6 h (**C**), using a β-galactosidase complementation assay. Results are presented
349 as percent reduction in luminescence (*y* axis) compared with no treatment. Each point is the
350 mean (± standard error) of results from 3 to 5 experiments.

351

Materials and Methods

Peptides: MeV F derived fusion inhibitor peptides HRC1 and HRC4 were previously described (40). Briefly 36aa long peptides derived from the heptad repeat region at the C-terminal of the MeV F protein were synthesized (using the wt sequence or the L454W sequence). Monomeric unconjugated (HRC1) or dimeric cholesterol conjugated (HRC4) forms of the peptides were used in this study.

Plasmids and reagent. The genes of MeV IC323 H and F proteins were codon optimized, synthesized, and sub cloned into the mammalian expression vector pCAGGS. Plasmids encoding nectin 4 and CD150/SLAM were commercially acquired.

Cells. 293T (human kidney epithelial) and Vero-SLAM (African green monkey kidney) cells were grown in Dulbecco's modified Eagle's medium (DMEM; Gibco, Invitrogen) supplemented with 10% fetal bovine serum (FBS) and antibiotics in 5% CO_2. The Vero-SLAM culture medium was supplemented with Geneticin.

HRC4 Peptide time addition related inhibition. Dulbecco's Modified Eagle's medium (DMEM) containing the indicated viruses (MeV IC323-EGFP, MeV IC323-EGFP-F L454W, MeV IC323-EGFP-F T461I, MeV IC323-EGFP-F N462K all these viruses are from(34)) was used to infect sub-confluent VERO-SLAM cells in 6 well plates (100pfu/well) for 2h at 32°C. MeV HRC4 dimeric fusion inhibitory peptide (1μM) was added to the medium at time points from 15 to 120 min after the beginning of infection. After 2h of incubation with the virus, medium was replaced with medium containing Avicel. Viral titers were assessed after 3 days of incubation at 32°C by immune staining.

Beta-Galactosidase (Beta-gal) complementation-based fusion assay. The beta-gal complementation-based fusion assay was performed as described previously(34). Briefly, 293T cells transiently transfected with the constructs indicated above and the omega reporter

subunit were incubated for the indicated period with cells coexpressing viral glycoproteins and the alpha reporter subunit in presence or not of MeV F HRC derived peptide (40).

RBC fusion assay. RBC fusion assays were performed on HEK 293T cells transiently expressing MV H_Y17H HPIV3_T193A chimerae (43) and the indicated MeV Fs. Cell monolayers were washed three times with serum-free medium, placed at 4°C with 1% RBC in DMEM for 30 min, then treated with the indicated peptide and placed at 37°C. Zanamivir was added at a final concentration of 10 mM and the cells were incubated at 4°C, rocked, and the liquid phase was collected in V-bottomed 96-well plates for measurement of reversibly bound RBCs. The cells were then incubated at 4°C with ACK-Lysing buffer, and the liquid phase was collected in V-bottomed 96-well plates for measurement of irreversibly bound RBCs. The cells were then lysed in lysis buffer and transferred to flat-bottom 96 well plates for quantification of fused RBCs. The amount of RBCs in each of the four compartments (released, reversibly bound, irreversibly bound, and fused) was determined by measurement of absorption at 410 nm.

Co-Immunoprecipitation. 293T cells were seeded in biocoated 6-well plates (Corning) at $5x10^5$ cells/well and incubated for 24h, at 37^o C. Cells were transfected with plasmid vectors encoding for MeV H-6xHis, MeV F (*wt*, L454W, T461I, N462K ,E455G, L454W/E455G and S262R) and mCherry (6:4:1 mixtures; 2.2 µg/well) using Lipofectamine® 2000 (Invitrogen), according to the manufacturer's recommendations. Transfected cultures were grown at 32^o C, overnight, in the presence of HRC1 peptide (1 µM), to minimize cell-cell fusion. mCherry fluorescence was used to monitor cell transfection efficiency after 18h. Prior to cell lysis, cell protein expression was synchronized with cycloheximide (Sigma, 0.1 mg/mL), followed by membrane protein cross-linking with 3,3'-dithiobis(sulfosuccinimidyl propionate) (Sigma; 1 mM), at low temperature. The cross-linking reaction was quenched with 20 mM Tris, 150 mM NaCl, pH 7.5. Cells were lysed with 50 mM HEPES, 100 mM NaCl, 0.05 g/mL dodecyl

maltoside, pH 7.5, supplemented with complete protease inhibitor cocktail (Roche). Lysates were centrifuged at 16000 *g* for 10 min to remove nuclei and cell debris, and the supernatant was collected for immunoprecipitation and total protein content analysis. MeV H-6xHis protein was immunoprecipitated from cell lysates using Dynabeads® (Thermo, 1 mg/mL) coated with a 6xHis tag-specific antibody (mouse monoclonal, Thermo, MA1-21315).

For Fig.2: Co-immunoprecipitated and cell lysate proteins were analyzed by western blotting, using primary antibodies specific for MeV F HRC (rabbit polyclonal, Genscript, 503028-1) and 6xHis tag (rabbit polyclonal, Thermo, PA1-983B), followed by an HRP-conjugated anti-rabbit secondary antibody (Kindle Biosceiences, R1006). Western blots were developed using the SuperSignal West Femto substrate (Thermo) and imaged on a *Kwik*Quant^{TM} Imager UV (Kindle Biosciences).

For Fig. 3: Co-immunoprecipitated and cell lysate proteins were analyzed by western blotting, using primary antibodies specific for MeV F HRC (rabbit polyclonal, Genscript, 503028-1) and 6xHis tag (rabbit polyclonal, Thermo, PA1-983B), followed by WesternBreeze Chromogenic Immunodetection Protocol for detection.

Literature cited

1. Durrheim DN, Andrus JK, Tabassum S, Bashour H, Githanga D, Pfaff G. 2021. A dangerous measles future looms beyond the COVID-19 pandemic. Nat Med 27:360-361.
2. Tatsuo H, Ono N, Tanaka K, Yanagi Y. 2000. SLAM (CDw150) is a cellular receptor for measles virus. Nature 406:893-7.
3. Noyce RS, Bondre DG, Ha MN, Lin LT, Sisson G, Tsao MS, Richardson CD. 2011. Tumor cell marker PVRL4 (nectin 4) is an epithelial cell receptor for measles virus. PLoS Pathog 7:e1002240.
4. Muhlebach MD, Mateo M, Sinn PL, Prufer S, Uhlig KM, Leonard VH, Navaratnarajah CK, Frenzke M, Wong XX, Sawatsky B, Ramachandran S, McCray PB, Jr., Cichutek K, von Messling V, Lopez M, Cattaneo R. 2011. Adherens junction protein nectin-4 is the epithelial receptor for measles virus. Nature 480:530-3.
5. Griffin DE, Lin WH, Pan CH. 2012. Measles virus, immune control, and persistence. FEMS microbiology reviews 36:649-62.
6. Rota PA, Moss WJ, Takeda M, de Swart RL, Thompson KM, Goodson JL. 2016. Measles. Nat Rev Dis Primers 2:16049.

7. Kija E, Ndondo A, Spittal G, Hardie DR, Eley B, Wilmshurst JM. 2015. Subacute sclerosing panencephalitis in South African children following the measles outbreak between 2009 and 2011. S Afr Med J 105:713-8.
8. Angius F, Smuts H, Rybkina K, Stelitano D, Eley B, Wilmshurst J, Ferren M, Lalande A, Mathieu C, Moscona A, Horvat B, Hashiguchi T, Porotto M, Hardie D. 2019. Analysis of a Subacute Sclerosing Panencephalitis Genotype B3 Virus from the 2009-2010 South African Measles Epidemic Shows That Hyperfusogenic F Proteins Contribute to Measles Virus Infection in the Brain. J Virol 93:e01700-18.
9. Hardie DR, Albertyn C, Heckmann JM, Smuts HE. 2013. Molecular characterisation of virus in the brains of patients with measles inclusion body encephalitis (MIBE). Virology journal 10:283.
10. Mathieu C, Ferren M, Jurgens E, Dumont C, Rybkina K, Harder O, Stelitano D, Madeddu S, Sanna G, Schwartz D, Biswas S, Hardie D, Hashiguchi T, Moscona A, Horvat B, Niewiesk S, Porotto M. 2019. Measles Virus Bearing Measles Inclusion Body Encephalitis-Derived Fusion Protein Is Pathogenic after Infection via the Respiratory Route. J Virol 93:e01862-18.
11. Watanabe S, Shirogane Y, Sato Y, Hashiguchi T, Yanagi Y. 2019. New Insights into Measles Virus Brain Infections. Trends Microbiol 27:164-175.
12. Mathieu C, Bovier FT, Ferren M, Lieberman NAP, Predella C, Lalande A, Peddu V, Lin MJ, Addetia A, Patel A, Outlaw V, Corneo B, Dorrello NV, Briese T, Hardie D, Horvat B, Moscona A, Greninger AL, Porotto M. 2021. Molecular Features of the Measles Virus Viral Fusion Complex That Favor Infection and Spread in the Brain. mBio doi:10.1128/mBio.00799-21:e0079921.
13. Yanagi Y, Ono N, Tatsuo H, Hashimoto K, Minagawa H. 2002. Measles virus receptor SLAM (CD150). Virology 299:155-61.
14. Yanagi Y, Takeda M, Ohno S, Hashiguchi T. 2009. Measles virus receptors. Current topics in microbiology and immunology 329:13-30.
15. Hashiguchi T, Maenaka K, Yanagi Y. 2011. Measles virus hemagglutinin: structural insights into cell entry and measles vaccine. Frontiers in microbiology 2:247.
16. Yin HS, Paterson RG, Wen X, Lamb RA, Jardetzky TS. 2005. Structure of the uncleaved ectodomain of the paramyxovirus (hPIV3) fusion protein. Proc Natl Acad Sci U S A 102:9288-93.
17. Lamb RA, Paterson RG, Jardetzky TS. 2006. Paramyxovirus membrane fusion: lessons from the F and HN atomic structures. Virology 344:30-7.
18. Yin HS, Wen X, Paterson RG, Lamb RA, Jardetzky TS. 2006. Structure of the parainfluenza virus 5 F protein in its metastable, prefusion conformation. Nature 439:38-44.
19. Harrison SC. 2008. Viral membrane fusion. Nat Struct Mol Biol 15:690-8.
20. Chang A, Dutch RE. 2012. Paramyxovirus fusion and entry: multiple paths to a common end. Viruses 4:613-36.
21. Plemper RK, Brindley MA, Iorio RM. 2011. Structural and mechanistic studies of measles virus illuminate paramyxovirus entry. PLoS pathogens 7:e1002058.
22. White JM, Delos SE, Brecher M, Schornberg K. 2008. Structures and mechanisms of viral membrane fusion proteins: multiple variations on a common theme. Crit Rev Biochem Mol Biol 43:189-219.
23. Sapir A, Avinoam O, Podbilewicz B, Chernomordik LV. 2008. Viral and developmental cell fusion mechanisms: conservation and divergence. Dev Cell 14:11-21.
24. Eckert DM, Kim PS. 2001. Design of potent inhibitors of HIV-1 entry from the gp41 N-peptide region. Proc Natl Acad Sci U S A 98:11187-92.

25. Porotto M, Carta P, Deng Y, Kellogg GE, Whitt M, Lu M, Mungall BA, Moscona A. 2007. Molecular determinants of antiviral potency of paramyxovirus entry inhibitors. J Virol 81:10567-74.
26. Schmidt AG, Yang PL, Harrison SC. 2010. Peptide inhibitors of flavivirus entry derived from the E protein stem. J Virol 84:12549-54.
27. Vigant F, Lee B. 2011. Hendra and nipah infection: pathology, models and potential therapies. Infectious disorders drug targets 11:315-36.
28. Pessi A, Langella A, Capito E, Ghezzi S, Vicenzi E, Poli G, Ketas T, Mathieu C, Cortese R, Horvat B, Moscona A, Porotto M. 2012. A general strategy to endow natural fusion-protein-derived peptides with potent antiviral activity. PLoS One 7:e36833.
29. Steffen DL, Xu K, Nikolov DB, Broder CC. 2012. Henipavirus mediated membrane fusion, virus entry and targeted therapeutics. Viruses 4:280-309.
30. Miyamoto F, Kodama EN. 2012. Novel HIV-1 fusion inhibition peptides: designing the next generation of drugs. Antiviral chemistry & chemotherapy 22:151-8.
31. Tan JJ, Ma XT, Liu C, Zhang XY, Wang CX. 2012. The Current Status and Challenges in the Development of Fusion Inhibitors as Therapeutics for HIV-1 Infection. Current pharmaceutical design.
32. Lee KK, Pessi A, Gui L, Santoprete A, Talekar A, Moscona A, Porotto M. 2011. Capturing a fusion intermediate of influenza hemagglutinin with a cholesterol-conjugated peptide, a new antiviral strategy for influenza virus. J Biol Chem 286:42141-9.
33. Sato Y, Watanabe S, Fukuda Y, Hashiguchi T, Yanagi Y, Ohno S. 2018. Cell-to-Cell Measles Virus Spread between Human Neurons Is Dependent on Hemagglutinin and Hyperfusogenic Fusion Protein. J Virol 92.
34. Jurgens EM, Mathieu C, Palermo LM, Hardie D, Horvat B, Moscona A, Porotto M. 2015. Measles fusion machinery is dysregulated in neuropathogenic variants. mBio 6.
35. Watanabe S, Shirogane Y, Suzuki SO, Ikegame S, Koga R, Yanagi Y. 2013. Mutant fusion proteins with enhanced fusion activity promote measles virus spread in human neuronal cells and brains of suckling hamsters. Journal of virology 87:2648-59.
36. Hashiguchi T, Fukuda Y, Matsuoka R, Kuroda D, Kubota M, Shirogane Y, Watanabe S, Tsumoto K, Kohda D, Plemper RK, Yanagi Y. 2018. Structures of the prefusion form of measles virus fusion protein in complex with inhibitors. Proc Natl Acad Sci U S A 115:2496-2501.
37. Porotto M, Devito I, Palmer SG, Jurgens EM, Yee JL, Yokoyama CC, Pessi A, Moscona A. 2011. Spring-loaded model revisited: paramyxovirus fusion requires engagement of a receptor binding protein beyond initial triggering of the fusion protein. J Virol 85:12867-80.
38. Figueira TN, Palermo LM, Veiga AS, Huey D, Alabi CA, Santos NC, Welsch JC, Mathieu C, Horvat B, Niewiesk S, Moscona A, Castanho M, Porotto M. 2017. In Vivo Efficacy of Measles Virus Fusion Protein-Derived Peptides Is Modulated by the Properties of Self-Assembly and Membrane Residence. J Virol 91.
39. Porotto M, Yokoyama CC, Orefice G, Kim HS, Aljofan M, Mungall BA, Moscona A. 2009. Kinetic dependence of paramyxovirus entry inhibition. J Virol 83:6947-51.
40. Mathieu C, Huey D, Jurgens E, Welsch JC, DeVito I, Talekar A, Horvat B, Niewiesk S, Moscona A, Porotto M. 2015. Prevention of measles virus infection by intranasal delivery of fusion inhibitor peptides. J Virol 89:1143-55.
41. Welsch JC, Talekar A, Mathieu C, Pessi A, Moscona A, Horvat B, Porotto M. 2013. Fatal measles virus infection prevented by brain-penetrant fusion inhibitors. J Virol 87:13785-94.

42. Mathieu C, Augusto MT, Niewiesk S, Horvat B, Palermo LM, Sanna G, Madeddu S, Huey D, Castanho MA, Porotto M, Santos NC, Moscona A. 2017. Broad spectrum antiviral activity for paramyxoviruses is modulated by biophysical properties of fusion inhibitory peptides. Sci Rep 7:43610.
43. Talekar A, Moscona A, Porotto M. 2013. Measles virus fusion machinery activated by sialic acid binding globular domain. J Virol 87:13619-27.
44. Watanabe S, Ohno S, Shirogane Y, Suzuki SO, Koga R, Yanagi Y. 2015. Measles virus mutants possessing the fusion protein with enhanced fusion activity spread effectively in neuronal cells, but not in other cells, without causing strong cytopathology. J Virol 89:2710-7.

2) Pathogénicité des mutants hyperfosogènes du virus de la rougeole dans les voies respiratoires

a. Article 6 : Le virus de la rougeole portant une protéine de fusion dérivée d'encéphalite rougeoleuse à corps d'inclusion est pathogène après une infection par voie respiratoire

Cyrille Mathieu, Marion Ferren, Eric Jurgens, Claire Dumont, Ksenia Rybkina, Olivia Harder, Debora Stelitano, Sylvia Madeddu, Giuseppina Sanna, Dayna Schwartz, Sudipta Biswas, Diana Hardie, Takao Hashiguchi, Anne Moscona, Branka Horvat, Stefan Niewiesk et Matteo Porotto

Publié dans Journal of Virology, 2019

https://doi.org/10.1128/JVI .01862-18

Facteur d'impact : 5,103

Résumé de l'article :

La mutation L454W dans la F du virus de la rougeole (VR) a été précédemment identifiée chez deux patients présentant des séquelles mortelles d'une infection du SNC au VR. Il a été montré que cette mutation seule entrainait la dérégulation de la machinerie de fusion virale en permettant la fusion des membranes en l'absence de récepteurs connus du virus de la rougeole. En 2017, Ha. MN et collègues 1 ont retrouvé cette même mutation dans le contexte de l'échappement au traitement par des petites molécules inhibitrices de fusion qui augmentent la stabilité de la F telles que le FIP, l'AS-48 et le 3G (respectivement Carbobenzoxy-d-Phe-l-Phe-Gly, 4-Nitro-2-Phenylacetyl Amino-Benzamide, N-[3-cyanophenyl]-2-phenylacetamide). Alors que les peptides dérivés du domaine HRC tel que HRC4 bloquent la fusion après l'activation de la F, les molécules mentionnées plus haut telles que le FIP, l'AS-48 et la 3G stabilise l'état de préfusion de la protéine F en s'insérant dans une poche entre la tête et la tige de la conformation en pré-fusion de la F. Ces molécules s'avèrent inefficaces pour stabiliser la F du mutant neuroadapté portant la mutation L454W et comportent un risque de sélectionner des mutants neuroadaptés du VR.

Puisque cette mutation a pu émerger sous pression de sélection d'un traitement nous nous sommes donc demandé si un virus portant cette mutation pouvait infecter des animaux par voie respiratoire. En effet, les données de la littérature suggèrent que les mutations d'adaptations du VR au SNC sont défavorables à la propagation inter-hôtes.

Ici nous avons posé l'hypothèse selon laquelle, malgré un complexe de fusion viral dérégulé, un virus de la rougeole adapté au SNC pourrait, en dehors du contexte cérébral, infecter et se propager dans un hôte après une infection intranasale. L'idée sous-jacente étant de vérifier si un tel virus perd ou non son pouvoir pathogène et donc si sa « non-circulation » repose davantage sur son incapacité à ressortir du SNC. Nous avons donc investigué cette piste en infectant deux modèles animaux par

voie intranasale avec le virus portant la mutation L454W dans la F. Nous avons montré que les souris génétiquement modifiées exprimant le récepteur SLAM de façon ubiquitaire et les rats des cotonniers peuvent être facilement infectés par ce mutant neuroadapté via les voies respiratoires. Ce virus a été retrouvé dans les poumons et dans le cerveau de ces deux modèles et s'est avéré plus pathogène que le virus sauvage. De plus, l'administration du peptide inhibiteur de fusion dimérique conjugué au cholestérol dérivé du domaine HRC (HRC4) par voie intranasale a permis de protéger 100% des animaux infectés par le mutant L454W confirmant ainsi la grande efficacité du HRC4 ce pour bloquer la fusion du variant viral L454W, in vitro, indépendamment de la présence du récepteur d'entrée.

AMERICAN SOCIETY FOR MICROBIOLOGY | Journal of Virology®

VIRUS-CELL INTERACTIONS

Measles Virus Bearing Measles Inclusion Body Encephalitis-Derived Fusion Protein Is Pathogenic after Infection via the Respiratory Route

Cyrille Mathieu,[a,b,c] Marion Ferren,[a,b,c] Eric Jurgens,[a,b] Claire Dumont,[c] Ksenia Rybkina,[a,b] Olivia Harder,[d] Debora Stelitano,[a,b] Silvia Madeddu,[a,b,e] Giuseppina Sanna,[a,b,e] Dayna Schwartz,[a,b] Sudipta Biswas,[a,b] Diana Hardie,[f] Takao Hashiguchi,[g] Anne Moscona,[a,b,h,i] Branka Horvat,[c] Stefan Niewiesk,[d] Matteo Porotto[a,b,j]

[a]Center for Host-Pathogen Interaction, Columbia University Medical Center, New York, New York, USA
[b]Department of Pediatrics, Columbia University Medical Center, New York, New York, USA
[c]CIRI, International Center for Infectiology Research, Inserm, U1111, University Claude Bernard Lyon 1, CNRS, UMR5308, Ecole Normale Supérieure de Lyon, Lyon, France
[d]Department of Veterinary Biosciences, College of Veterinary Medicine, The Ohio State University, Columbus, Ohio, USA
[e]Department of Biomedical Sciences, University of Cagliari, Cittadella Universitaria, Monserrato, Cagliari, Italy
[f]Division of Medical Virology, Department of Clinical Laboratory Sciences, University of Cape Town and National Health Laboratory Service, Cape Town, South Africa
[g]Department of Virology, Faculty of Medicine, Kyushu University, Fukuoka, Japan
[h]Department of Microbiology and Immunology, Columbia University Medical Center, New York, New York, USA
[i]Department of Physiology and Cellular Biophysics, Columbia University Medical Center, New York, New York, USA
[j]Department of Experimental Medicine, University of Study of Campania Luigi Vanvitelli, Naples, Italy

ABSTRACT A clinical isolate of measles virus (MeV) bearing a single amino acid alteration in the viral fusion protein (F; L454W) was previously identified in two patients with lethal sequelae of MeV central nervous system (CNS) infection. The mutation dysregulated the viral fusion machinery so that the mutated F protein mediated cell fusion in the absence of known MeV cellular receptors. While this virus could feasibly have arisen via intrahost evolution of the wild-type (wt) virus, it was recently shown that the same mutation emerged under the selective pressure of small-molecule antiviral treatment. Under these conditions, a potentially neuropathogenic variant emerged outside the CNS. While CNS adaptation of MeV was thought to generate viruses that are less fit for interhost spread, we show that two animal models can be readily infected with CNS-adapted MeV via the respiratory route. Despite bearing a fusion protein that is less stable at 37°C than the wt MeV F, this virus infects and replicates in cotton rat lung tissue more efficiently than the wt virus and is lethal in a suckling mouse model of MeV encephalitis even with a lower inoculum. Thus, either during lethal MeV CNS infection or during antiviral treatment *in vitro*, neuropathogenic MeV can emerge, can infect new hosts via the respiratory route, and is more pathogenic (at least in these animal models) than wt MeV.

IMPORTANCE Measles virus (MeV) infection can be severe in immunocompromised individuals and lead to complications, including measles inclusion body encephalitis (MIBE). In some cases, MeV persistence and subacute sclerosing panencephalitis (SSPE) occur even in the face of an intact immune response. While they are relatively rare complications of MeV infection, MIBE and SSPE are lethal. This work addresses the hypothesis that despite a dysregulated viral fusion complex, central nervous system (CNS)-adapted measles virus can spread outside the CNS within an infected host.

KEYWORDS central nervous system infections, *in vivo* infection, pathogenesis, viral fusion

Citation Mathieu C, Ferren M, Jurgens E, Dumont C, Rybkina K, Harder O, Stelitano D, Madeddu S, Sanna G, Schwartz D, Biswas S, Hardie D, Hashiguchi T, Moscona A, Horvat B, Niewiesk S, Porotto M. 2019. Measles virus bearing measles inclusion body encephalitis-derived fusion protein is pathogenic after infection via the respiratory route. J Virol 93:e01862-18. https://doi.org/10.1128/JVI.01862-18.

Editor Rebecca Ellis Dutch, University of Kentucky College of Medicine

Address correspondence to Cyrille Mathieu, cyrille.mathieu@inserm.fr, or Matteo Porotto, mp3509@cumc.columbia.edu.

Received 29 October 2018
Accepted 30 January 2019
Accepted manuscript posted online 6 February 2019
Published 3 April 2019

Despite the availability of a measles virus (MeV) vaccine and ongoing efforts by the Measles Initiative to increase vaccine coverage, MeV has not been eradicated and has caused 100,000 to 140,000 deaths globally every year since 2010 (1–3). MeV eradication by vaccination is complicated by several biological and societal factors, including incomplete protection in the presence of maternal antibodies (4) and decreasing vaccination rates, often related to parental concerns over safety (5). These factors contribute to the recent resurgence of MeV infection in Europe and the United States (6).

MeV initially infects activated SLAM/CD150-expressing immune cells in the respiratory tract and thereby enters the lymphatic circulation (7). Viral replication occurs in SLAM/CD150-expressing lymphocytes in draining lymph nodes and is followed by viremia. Late in infection, MeV infects respiratory epithelial cells after attaching to nectin-4 expressed on the basolateral membranes of these cells and exits the host for interhost transmission from the respiratory tract (8, 9).

Cellular infection by MeV starts with attachment to cell surface receptors, followed by entry that is mediated by fusion between the viral and host membranes. Both initial steps rely on the concerted actions of the MeV receptor binding (H) and fusion (F) surface glycoproteins, which together make up the viral fusion complex (10, 11). F is synthesized as a precursor (F_0) that is cleaved within the infected cell prior to egress to yield the prefusion F, which exists as a homotrimer composed of three C-terminal F_1 subunits associated via disulfide bonds with three N-terminal F_2 subunits. The newly produced viral particles bear the trimeric F structure kinetically trapped in a metastable conformation on the surface of the viral membrane (12). In this metastable conformation, F can be activated to mediate fusion when the H glycoprotein engages a target cell surface entry receptor (SLAM/CD150 or nectin-4 for wild-type [wt] strains) (7–9). Upon receptor engagement, H triggers the prefusion F protein to undergo a conformational change, extending to expose the hydrophobic fusion peptide that inserts into the host cell membrane. Following insertion, F refolds into a stable postfusion 6-helix bundle structure, bringing the viral and target cell membranes together to initiate the formation of the fusion pore. The propensity of F to refold to the postfusion state relies on the interaction between two complementary heptad repeat (HR) regions at the N and C termini of the protein (HRN and HRC, respectively). This step of fusion can be inhibited by peptides corresponding to these HR regions (13).

Days to years after the acute phase of infection, central nervous system (CNS) MeV infection can lead to fatal complications (14–16). Subacute sclerosing panencephalitis (SSPE) develops in a small percentage of immune-competent patients several years after initial infection. SSPE is characterized by persistent infection of the brain and hypermutated MeV genomic RNA and viral transcripts, as well as defective viral particle assembly (17–19). Measles inclusion body encephalitis (MIBE) occurs in immunocompromised patients days to months after infection or vaccination with the live-attenuated MeV vaccine (15, 20, 21) and has been suggested to be associated with hyperfusogenic viral fusion complexes that can mediate viral entry in the absence of known MeV receptors (22, 23). Mechanisms governing MeV infection and spread in the CNS remain poorly understood, although CNS invasion seems to require the F protein and thus may feasibly be targeted by fusion inhibitors (12, 24–26).

MeV CNS infection by viruses bearing F proteins mutated in the HRC domain has been observed (22, 23, 27, 28), but growth of these viruses outside the CNS was thought to be impaired (29). Viral isolates from two patients with fatal MIBE contained F with an L454W mutation (22) that increased the thermal lability of the F protein in its metastable state. We previously showed that the L454W mutation in F affects cell entry and that recombinant MeV IC323-F L454W expressing green fluorescent protein spread in cells that lack a known MeV receptor. In cell-cell fusion assays, transfection with L454W F alone mediates fusion independently of the H protein (23). This is in distinction to other hyperfusogenic MeV isolates that depend on H for membrane fusion (30).

Virus bearing L454W F that was isolated from patients could either have arisen *de novo* in the CNS or have been present in the circulating wild-type viral population;

either way, this mutation appears to have undergone positive selection in the CNS. The virus's origin could not be determined. A recent report showed that a virus bearing L454W F emerges under the selective pressure of certain small-molecule fusion inhibitors, including fusion inhibitory peptide (FIP) (31). These findings raised the question of whether a virus bearing this neuropathogenic F protein can be found outside the CNS and spread within an individual. To address this question, we assessed the L454W F variant virus *in vivo*, using an engineered virus expressing enhanced green fluorescent protein (EGFP) with the mutated F on the background of the IC323 wt MeV strain (MeV IC323-EGFP-F L454W) and an identical control engineered virus bearing wt F. In cotton rat lungs, MeV IC323-EGFP-F L454W replicates better than the wt virus. The lethal dose for MeV IC323-EGFP-F L454W virus in a suckling transgenic mouse model is significantly lower than for wt virus but similar to the wt virus, and infection can be blocked by fusion inhibitory peptides. The F L454W mutation thus enhances viral growth in cotton rat lung tissue and correlates with increased pathogenicity in mice. We pursued the striking finding that this neuropathogenic MeV with a dysregulated fusion complex is pathogenic outside the CNS and can infect two animal models by the respiratory route.

RESULTS

F glycoproteins from neuropathogenic measles viruses. We and others have previously described several mutations in the MeV F glycoprotein (L454W, T461I, and N462K) in neuropathogenic MeV strains either isolated from patients or generated in laboratory settings (22, 23, 28). These mutations were associated with decreased thermal stability of the prefusion metastable state of the F protein. We mapped these mutations onto structures of the prefusion (MeV F; PDB identifier [ID] 5YXW [12]) and postfusion (modeled on HPIV3 F; PDB ID 1ZTM [32]) conformations of MeV F (Fig. 1). The three mutated residues (L454W, T461I, and N462K) were all located within the C-terminal heptad repeat domain (HRC). In the prefusion structure, the L454W mutation causes steric hindrance within the same protomer. The T461I and N462K mutations map in an α-helical region of the HRC domain. These three mutations occur at the portion of the HRC domain where the head and stalk regions of the prefusion conformation meet. Interactions at this junction are likely to be important for stabilizing the prefusion state, and consequently, mutations in this region would lead to decreased stability of the MeV F prefusion structure, as our data have previously suggested (23).

Thermal stability and fusion inhibitor susceptibility of neuropathogenic MeV variants. Hyperfusogenic variants of MeV F mutated in the HRC domain are less thermostable than viruses with the wild-type F protein (23). To determine whether viruses bearing the mutated F proteins are less stable than wt virus, thermal inactivation profiles were obtained (Fig. 2). Viruses ($\sim$1,000 PFU in 100 μl) were incubated at various temperatures (from 4 to 55°C for the times indicated in Fig. 2). The viral titers were not affected by 30 min at 4°C. At 37°C, the infectivity of only the F-L454W and F-N462K variants decreased significantly (to 50% and 12%, respectively). This decrease correlates with the lower thermal stability of these F proteins (23). Thirty minutes at 45°C abrogated the infectivity of the three mutant viruses by more than 90% compared to that of the wt, which retained more than 40% of its original viral titer ($P < 0.001$, two-way analysis of variance [ANOVA] with Bonferroni's posttest). After 10 min at 50°C, only the wt virus was still infectious, becoming noninfectious only after 10 min at 55°C. These results confirm that the infectivity of recombinant viruses harboring the hyperfusogenic mutated F HRC correlates with the lower thermal stability of their respective fusion proteins (23).

HRC4 fusion inhibitory peptide inhibits fusion and spread by the CNS-adapted variants. We have shown that a dimeric cholesterol-conjugated fusion inhibitory peptide (HRC4) blocks infection with wt MeV (G954, WTFb, and IC323 strains) *in vitro*, *ex vivo*, and *in vivo* in cotton rats and mice (33, 34). Here, fusion inhibition by HRC4 was assessed in an *in vitro* cell-cell fusion assay using 293T cell targets expressing either of the two known MeV receptors (CD150/SLAM and nectin-4) (Fig. 3). We have noted

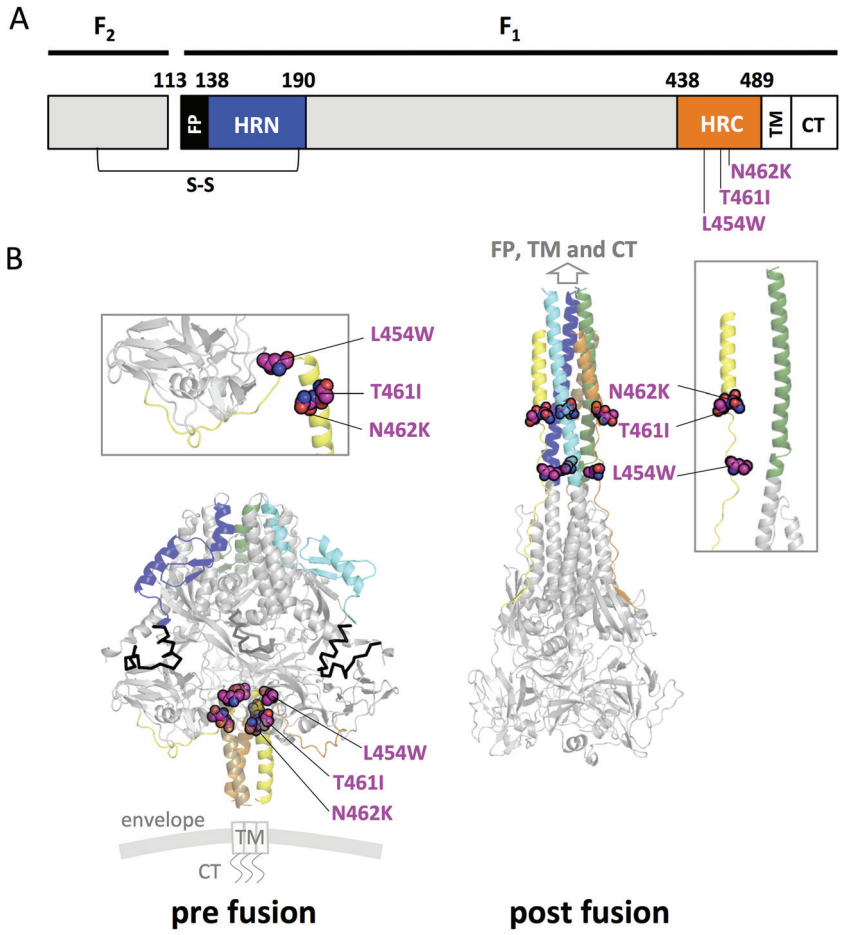

FIG 1 Location of substitutions within the F protein from CNS-adapted virus. (A) Schematic of MeV F fusion peptide (FP) with N-terminal heptad repeat (HRN), C-terminal heptad repeat (HRC), transmembrane (TM), and cytoplasmic (CT) domains indicated. (B) Ribbon diagrams representing a crystal structure of the prefusion conformation of MeV F (left, PDB 5YXW) and a model of a postfusion conformation of F (right, based on the postfusion HPIV3 F; PDB 1ZTM). The HRN (blue, green, and cyan) and the HRC (orange, brown, and yellow) domains are identified. Three substitutions (L454W, T461I, and N462K) in the HRC domain in neuropathogenic strains that side residues of the indicated amino acid position are represented as a sphere model. Color coding of substitutions: magenta, carbon; blue, nitrogen; and red, oxygen.

this assay to be the most stringent *in vitro* quantitative measure of viral inhibition. For these experiments, a small-molecule fusion protein inhibitor, *N*-(3-cyanophenyl)-2-phenylacetamide (3G) was assessed in parallel with HRC4. In contrast to the HRC-derived peptides, which block fusion after F activation, 3G stabilizes the prefusion state of the F protein (35, 36). The latter mechanism of action is shared by a previously described fusion inhibitory peptide (FIP; carbobenzoxy [Z]-D-Phe-Phe-Gly), an inhibitor that elicited resistant viruses, including one bearing an L454W F (31); therefore, we expected the L454W to be resistant to 3G.

Effector cells transfected with H and either wt F or F L454W were allowed to fuse with target cells expressing CD150/SLAM, nectin-4, or no known receptor (mock transfected) in the presence of the HRC4 or 3G fusion inhibitors. After 24 h, fusion was evaluated using beta-galactosidase complementation (37). The 50% inhibitory concentration (IC_{50}) of HRC4 for MeV F wt was between 10 and 50 nM in the presence of the SLAM/CD150 or nectin-4. The IC_{50} of HRC4 for MeV F L454W was below 0.2 nM in the presence of the SLAM/CD150 or nectin-4 transfected cells, while in the presence of mock-transfected target cells, we observed almost 100% inhibition even at the lowest concentration tested (0.2 nM). Note that wt F did not mediate fusion with mock-

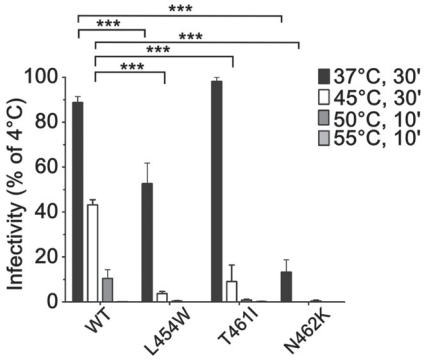

FIG 2 Thermal stability of MeV IC323 viruses bearing wild-type and mutant F proteins. Viruses bearing the indicated F proteins (*x* axis) were incubated at the indicated temperatures and times. The *y* axis represents the percentage infectivity (on Vero SLAM) compared to viruses incubated at 4°C. Results are expressed as means ± standard deviations from 3 separate experiments performed in triplicates. ***, $P < 0.001$ by two-way ANOVA with Bonferroni's posttest.

transfected cells. The IC_{50} of 3G for MeV F wt was around 10,000 to 20,000 nM in the presence of the SLAM/CD150 or nectin-4. With 3G for MeV F L454W in the presence of the SLAM/CD150 or nectin-4 transfected cells, the IC_{50} was reached only at the highest concentration used (100,000 nM). The IC_{50} dropped in the presence of mock-transfected target cells to ~50,000 nM. Thus, susceptibility to HRC-derived fusion inhibitors was higher for the F L454W than for the wt F. For 3G, we confirmed the previous findings that the L454W mutation in F confers resistance to this fusion inhibitor (12, 31, 35, 36).

The antiviral activity of HRC4 and 3G was next assessed against MeV IC323-EGFP-F L454W live virus infection (Fig. 4). Since the virus bearing L454W F spreads in the absence of a known MeV entry receptor (23), we compared the inhibitory efficacies in Vero cells expressing SLAM/CD150 (Vero-SLAM) and Vero cells that express no known MeV receptor (Fig. 4). After a 90-min infection with either wt IC323-EGFP or IC323-EGFP-F L454W viruses, cells were treated with the compounds and visualized at several time points (24, 48, and 72 h). Without treatment, the two viruses spread and formed large syncytia after 48 h in Vero-SLAM cells. In Vero cells (without receptor), MeV wt did not spread, while MeV IC323-EGFP-F L454W formed syncytia that were smaller than those formed in the presence of CD150/SLAM. The 3G posttreatment at 2,000 nM resulted in a reduction of syncytium size formed by wt MeV in Vero-SLAM cells but had no significant effect on the F L454W mutant in either cell type. HRC4 peptide treatment blocked both viruses in the presence or absence of receptor. The finding that HRC4 but not 3G inhibits MeV IC323-EGFP-F L454W suggests that HRC4 minimizes viral spread by inhibiting activated F from proceeding to fusion. Additional data are shown in Fig. S1 in the supplemental material.

Pathogenesis and protection against lethal infection with MeV IC323-EGFP-F L454W *in vivo*. Growth of MeV IC323-EGFP-F L454W in lung tissue was assessed in cotton rats (Fig. 5A). Cotton rats were infected intranasally with 10^5 50% tissue culture infective dose ($TCID_{50}$) of recombinant MeV IC323 bearing the wt F or the mutated L454W F. Four days postinfection, the animals were sacrificed and the lung viral titers were assessed. There were significantly more infectious particles in the lungs of animals infected with the hyperfusogenic mutant (L454W F) than in those infected with the wt virus ($P < 0.001$, Mann-Whitney U test).

As a complementary infection model, we assessed wt MeV IC323-EGFP and MeV IC323-EGFP-F L454W infection in a SLAM transgenic suckling mouse model of MeV lethal encephalitis that we have previously used for wt MeV infection (33) (Fig. 5B). Suckling mice were infected intranasally with either 5,000 or 10,000 PFU of wt MeV IC323-EGFP. Half of the animals died with the lowest dose (4 of 8) and only 1 of 7 animals survived the highest viral dose, suggesting that 5,000 PFU was approximately

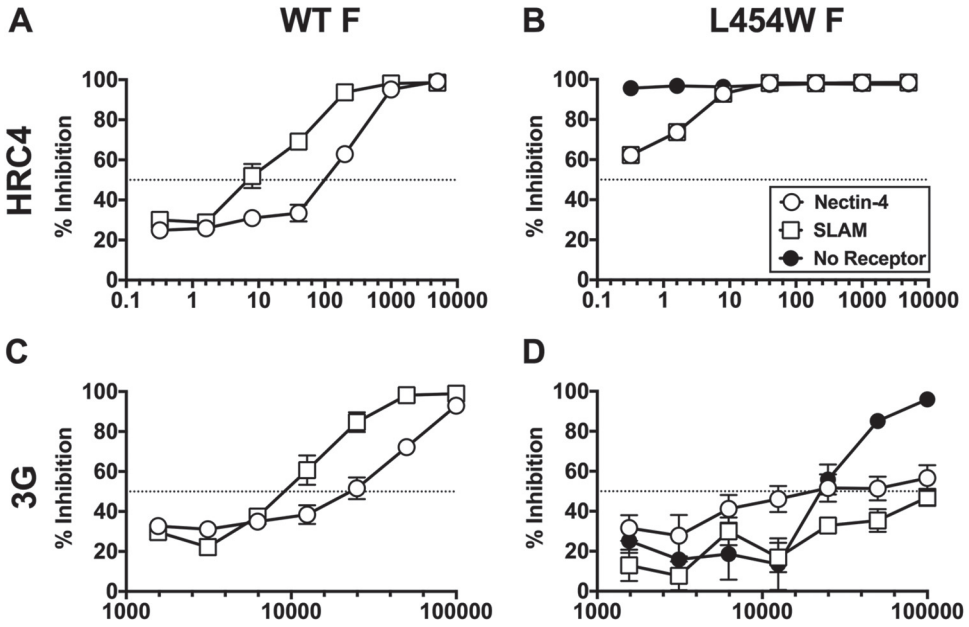

FIG 3 Inhibition of cell fusion of cells transiently expressing MeV F and MeV receptors. HEK 293T cells were cotransfected with either MeV IC323-WT F (A, C) or MeV IC323-F L454W (B, D), α-subunit of β-galactosidase, and wt IC323 MeV H. Transfected cells were subsequently overlaid 3 h posttransfection with HEK 293T cells expressing the indicated receptors (nectin-4, SLAM/CD150, or no receptor; only for F L454W, since wt F does not mediate fusion in the absence of receptor) and the ω-subunit of β-galactosidase in the presence of decreasing concentrations of HRC4 (A, B) or 3G (C, D). Cells were then incubated overnight to permit fusion. Resulting luminescence from β-galactosidase activity was quantified using Tecan Infinite M1000 Pro. Results depict means and standard errors of the means (SEMs) from two (3G) or three (HRC4) biological replicates of three technical replicates each. Dotted lines indicate 50% inhibition.

the 50% lethal dose (LD_{50}) for the wt virus. Suckling mice were infected with 500 PFU of the MeV IC323-EGFP-F L454W variant (Fig. 5C). This dose led to 80% lethality within 12 days, suggesting that this dose was above the LD_{50}. To better understand whether F L454W mutation would confer the ability to MeV to propagate faster *in vivo*, we intranasally coinfected SLAM transgenic suckling animals with 1,000 PFU of both MeV IC323-tdTomato-F wt and the MeV IC323-EGFP-F L454W variant. After 4 days, we only detected EGFP (by immune staining) in lungs, in meninges, and in neural cells in brain parenchyma (i.e., ventricle, cortex, and cerebellum areas) in all animals (Fig. 5D to G). Infection with MeV IC323-tdTomato-F wt was not detected after 4 days, a result that is consistent with the late infection observed with other wt MeV (38) These results suggest that virus bearing the F L454W mutation infects better and spreads more efficiently in both lung and CNS than the wt in this animal model.

Intranasal administration of HRC4 fusion inhibitory peptides protected SLAM transgenic suckling mice from fatal CNS infection with wt MeV (33). To evaluate the efficacy of HRC4 prophylaxis against MeV IC323-EGFP-F L454W *in vivo*, an infection was performed with 5,000 PFU of virus either with or without intranasal administration of HRC4 peptide 24 h before and 4 h after infection (33) (Fig. 6). Although 5,000 PFU infection was 100% lethal for untreated mice between day 7 and day 14 after infection, all infected animals that were treated with HRC4 24 h before and 4 h after infection survived. Thus, the pretreatment with HRC4 resulted in 100% survival ($P < 0.0001$, Mantel-Cox test) despite the very high viral inoculum, and the treated animals had no clinical manifestations.

DISCUSSION

Central nervous system (CNS) complications may occur soon after acute MeV infection in the case of acute encephalomyelitis or years after infection, as a result of viral persistence in SSPE. SSPE has recently been noted to be more common than

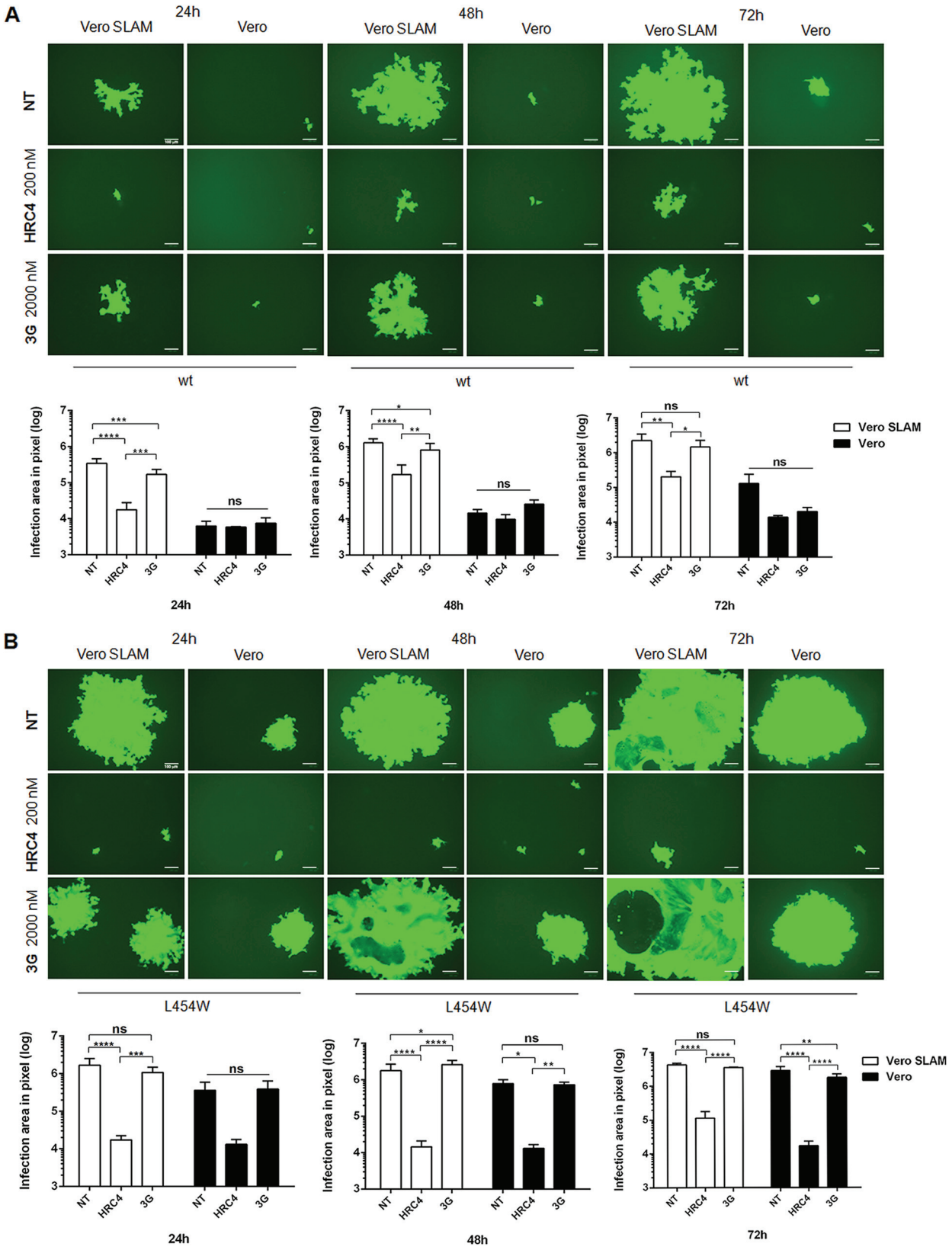

FIG 4 Inhibition of viral spread. Effect of fusion inhibitors on the areas of plaques formed by the MeV wt (A) and CNS-adapted variant virus bearing the L454W F (B) in infected Vero or Vero SLAM cells. The indicated fusion inhibitors were added after the 120-min adsorption period. Pictures were taken 24, 48, and 72 h postinfection using a ZOE Fluorescent cell imager (Bio-Rad) (bars, 100 μm). Areas of infection in pixels were measured using ImageJ software on images randomly acquired from separate experiments. ns, not significant; *, $P < 0.05$; **, $P < 0.01$; ***, $P < 0.001$; ****, $P < 0.0001$ (two-way ANOVA, $n = 3$ at least).

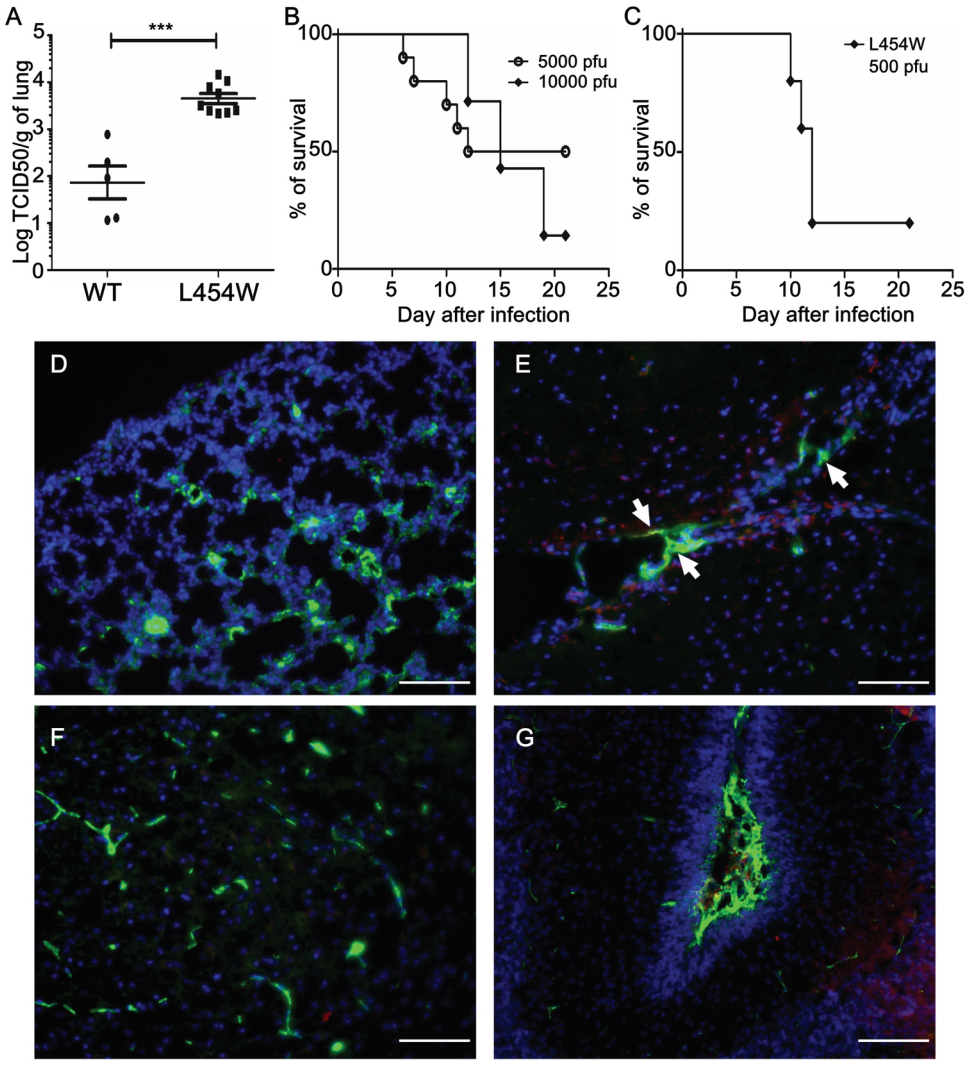

FIG 5 *In vivo* infection with virus bearing the L454W F. (A) Cotton rats ($n = 8$) were infected intranasally with MeV IC323-EGFP and MeV IC323-EGFP F L454W F viruses and were euthanized at 4 days postinfection. MeV titration of lung homogenates showed that L454W F bearing virus grew to a significantly higher titer than wt virus in cotton rats ($P = 0.001$ by the Mann-Whitney U test). The limit of viral detection was 10^2 median tissue culture infective dose per gram of tissue ($TCID_{50}$/g). (B) CD150/SLAM suckling mice were infected intranasally with either 5,000 ($n = 10$) or 10,000 ($n = 7$) PFU of MeV IC323-EGFP. (C) CD150/SLAM suckling mice were infected intranasally with 500 PFU of MeV IC323-EGFP-F L454W ($n = 5$). Cryosections of lungs (D) and brain areas (E to G) collected from CD150/SLAM suckling mice ($n = 3$) coinfected intranasally with 1,000 PFU of both MeV IC323-tdTomato and MeV IC323-EGFP-F L454W (at day 4 postinfection) were stained using anti-GFP (green) and anti-tdTomato (red) antibodies. Nuclei were counterstained with DAPI (blue). (D) Lung section. (E) Brain ventricle area (white arrows indicate the infection in meninges). (F) Cortex parenchyma. (G) Cerebellum. Scale bars, 100 μm.

previously thought and may occur in up to 1 in 600 children infected under 1 year of age (1). The third form of MeV-induced CNS disease, progressive infectious encephalitis or measles inclusion body encephalitis (MIBE), occurs in immunosuppressed patients several months after MeV infection (22, 39, 40). Acute encephalomyelitis does not seem to be associated with active viral growth in the CNS, while both SSPE and MIBE are associated with viral propagation in the CNS.

In a recent South African MeV outbreak (2014), 8 HIV-infected patients died of fatal MeV CNS manifestations (41). The F protein component of the MeV virus fusion complex recovered from the CNS of patients who suffered fatal MIBE is altered, so that F is activated in the absence of a known receptor for H (23). The usual balance maintained by F between stability of the prefusion state and activation is skewed towards activation in these isolates. The F proteins from two separate patient isolates

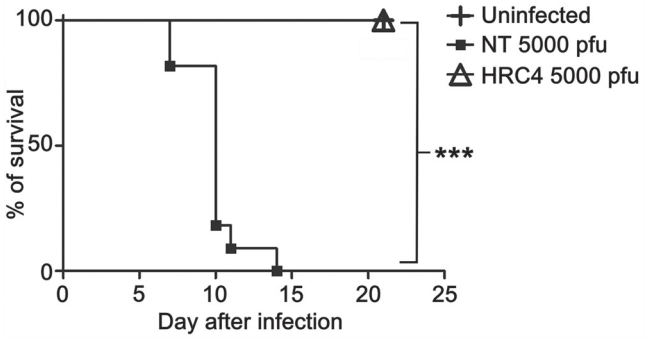

FIG 6 Fusion inhibitory peptides protect from lethal infection with virus bearing the L454W F *in vivo*. SLAM suckling mice were infected intranasally with 5,000 PFU of MeV IC323-EGFP-F L454W. A subset of animals infected with 5,000 PFU ($n = 9$) was treated with HRC4 peptide intranasally (6 mg/kg) the day before and 4 h after infection (as we have previously done for wt virus [33]). The mock-infected group received vehicle at the same time ($n = 11$). The Mantel-Cox test was used for the survival comparison analysis. ***, $P = 0.0007$.

from the outbreak contained one specific amino acid alteration at position 454 (L454W) that increased fusion even in the absence of H and markedly decreased the thermal stability of F (23). Alterations in the fusion complex have been linked to CNS adaptation and to increased neuropathogenesis (28).

MeV is a uniquely human pathogen, and none of the currently available *in vivo* models completely represent the CNS sequelae. The best current model for acute measles infection is the nonhuman primate. However, in studies in rhesus, cynomolgus, and squirrel monkeys, CNS manifestations have not been described (8, 42–48). We showed here that MeV bearing the MIBE-derived L454W F infects two animal models of MeV infection via the respiratory route. In cotton rat lungs, the mutant virus grew at even higher titers than the wt virus, indicating that L454W F may confer an advantage in this model. The lethal dose in suckling mice for L454W F bearing virus was lower than 500 PFU, in contrast to a lethal dose of around 5,000 PFU for wt virus. These two animal models suggest that the virus bearing the L454W F is pathogenic *in vivo*.

Previous experiments with MeV F proteins bearing mutations at position T461I and S103I/N462S/N465S—found in virus isolates from patients with SSPE—showed that these mutations permit the spread of virus in the CNS after intracranial inoculation in small animal models lacking known MeV receptors (28, 29). However, those viruses did not spread after intraperitoneal inoculation (29). In this study, intranasal infection of suckling SLAM transgenic mice led to viral spread in the CNS. This difference might be explained by factors, including the specific virus used, the animal model, receptor expression, and/or infection route. Our results in suckling CD150/SLAM receptor transgenic mice show that the MeV bearing F L454W can infect via the natural route of MeV infection, reach the CNS, and cause lethal disease. The wt virus in this model requires a significantly higher viral load and more time to achieve CNS infection and lethality. Host-to-host transmission was not assessed here, but the lower thermal stability of the viruses bearing the unstable F suggests that these viruses may be at a disadvantage for transmission, as they may more readily become inactivated before reaching the correct target cells. Future work will assess the pathogenicity of the L454W mutation in the context of the original B3 strain, where this mutation was initially found, with and without the additional coding and noncoding mutations found in the clinical samples (22, 23).

There are no specific therapies for acute complications of MeV or for persistent MeV CNS infections (24, 26, 49–51). For MeV cerebral infection, the only available antiviral therapy is ribavirin, which is unlikely to offer significant benefit. Ribavirin prophylaxis in a mouse model of MeV infection resulted in only 60% survival (52), in contrast with HRC4 peptide prophylaxis, which resulted in 100% survival in a similar model (34). A peptide-based prophylactic approach prevents lethal infection in CD150/SLAM trans-

genic suckling mice infected with wt MeV (33) and MeV bearing L454W F (Fig. 6). An anti-MeV strategy that combines vaccines and antivirals would contribute to better management of infected individuals and prevention and treatment of complications and could support public health objectives, including that of global eradication (53, 54).

The CNS-adapted viruses we describe are sensitive to the fusion inhibitory peptides, which act after the activation of conformational transformation in F. However, these viruses are resistant to antivirals that stabilize the prefusion state of F (35). Therapies designed to stabilize prefusion F protein are in an advanced stage of development for a related virus, respiratory syncytial virus (55). For MeV, small molecules targeting prefusion F have been identified, but resistance to these inhibitors quickly arose. For 3G—the inhibitor used in this study alongside the inhibitory peptides—resistance occurred due to a mutation at position 462 (N462K) in F, one of the mutants we analyzed here (35, 36, 56–58). The N462K F was inherently destabilized but was retained in the prefusion state in the presence of inhibitor (35, 36). FIP was reported to have a mechanism of action similar to 3G (12, 31), suggesting that MeV with L454W F may emerge under the selective pressure of a fusion inhibitor (31), and MeV bearing the L454W F was resistant to the inhibitory activity of 3G (Fig. 3 and 4; see also Fig. S1 in the supplemental material). These findings suggest that an antiviral strategy based on retaining F in its prefusion state, at least for MeV, may carry the risk of eliciting the emergence of neurotropic variant viruses.

MATERIALS AND METHODS

Ethical statement. All *in vivo* experiments with mice were performed by C. M. and C. D. (accredited by the French veterinary service) according to the French national charter on the ethics of animals, class 2, 3, and 4 genetically modified organisms (GMO) authorization number 5854. The *in vivo* protocol was also according to French ethical committee (CECCAPP) regulations, accreditation number CECCAPP_ENS_2015_011. All experiments performed in cotton rats were approved by the Institutional Animal Care and Use Committee of The Ohio State University.

Peptides and chemicals. MeV F-derived fusion inhibitory peptide HRC4 was previously described (33). Briefly, peptide dissolved in dimethyl sulfoxide (DMSO) was added to cholesterol-polyethylene glycol 4 (PEG4)-bis-maleimide dissolved in tetrahydrofuran followed by addition of *N*,*N*-diisopropylethylamine to the solution. The solution was left stirring at room temperature for 3 h and then purified by C_4 prep column (Phenomenex Jupiter C_4 liquid chromatography [LC] column, 300 Å) using as eluents 0.1% trifluoroacetic acid in water (A) and 0.1% trifluoroacetic acid in acetonitrile (B) and the following linear gradient: 30% to 80% in 20 min to 100% in 3 min, washing step at 100% for 5 min, flow 20 ml/min. The product of lyophilization was a white powder confirmed by matrix-assisted laser desorption ionization (MALDI) to be HRC4: HRC4 expected mass, 10076.4; HRC4 observed mass, 10075.4. *N*-(3-cyanophenyl)-2-phenylacetamide (also known as 3G [35, 36]) was commercially acquired from ZereneX Molecular Limited (UK). The purity of 3G was tested by high-pressure liquid chromatography (HPLC) and shown to be >95% pure.

Cells. Vero and Vero-SLAM (African green monkey kidney) (7) cells were grown in Dulbecco's modified Eagle's medium (DMEM; Invitrogen, Thermo Fisher Scientific) supplemented with 10% fetal bovine serum (FBS) and antibiotics in 5% CO_2. The 293-3-46 (59) and Vero-SLAM culture media were supplemented with Geneticin 1 mg/ml (Thermo Fisher Scientific).

Recombinant virus production and analysis. MeV IC323-EGFP (60) is a recombinant virus generated by reverse genetics using a plasmid (kindly provided by Yusuke Yanagi, Kyushu University, Fukyoka, Japan) coding for the IC323 MeV strain consensus sequence and containing an EGFP expression cassette between the leader sequence and the N viral gene.

To generate the L454W variant, the mutated F fragment was generated by PCR, inserted into the p(+)MeV_IC323-EGFP plasmid, and digested with the restriction enzymes NruI and PacI. For the MeV IC323-tdTomato plasmid, the EGFP fragment was removed from the p(+)MeV_IC323-EGFP plasmid by digestion with AscI and AatII and replaced by a PCR fragment encoding tdTomato. The PCR fragments were inserted using the In-Fusion HD Cloning kit (TaKaRa). Modified plasmids were then amplified in *Escherichia coli* Stellar bacterial cells, extracted using the NucleoBond Xtra plasmid Midiprep kit (Macherey-Nagel), and sequenced.

MeV IC323 recombinant viruses were rescued in 293-3-46 cells as previously described (59). All viruses were propagated and the titers determined in Vero-SLAM cells. Briefly, 2×10^5 293-3-46 cells were seeded in 6-well plates. The following day, cells were transfected using a ProFection mammalian transfection system, calcium phosphate kit (Promega) according to manufacturer's recommendations with 10 μg of plasmid encoding the full-length viral genome and 40 ng of pEMC-MeV-L. The next day, supernatant fluids were replaced with DMEM supplemented with 10% FBS, incubated at 42°C for 3 h, and replaced at 37°C in 5% CO_2. Three days after transfection, cells were mechanically detached by pipetting up and down and overlaid onto Vero-SLAM cells in a 10-cm culture dish. The cells were incubated for 3 to 4 days at 37°C in 5% CO_2 until the appearance of syncytia. For the production of the initial passage (i.e., P0), single syncytia were collected by scraping using a tip and pipetting in 20 μl and transferred onto

fresh Vero-SLAM cells in a well of a 6-well plate. When syncytia covered approximately 80% of the well's surface, the cells and the supernatant fluid were collected by scraping and were frozen at −80°C until use (P0 production). The passage 1 (P1) stock was made by using 300 μl of the P0 to infect a 70% confluent T150 flask of Vero-SLAM in 15 ml of Opti-MEM (2 h at 37°C). After 2 h, 15 ml of DMEM-10% FBS was added to the culture, and cells were incubated for 2 to 4 days at 32°C in 5% CO_2 until 70% to 90% infection. The virus was collected in a small volume of Opti-MEM by scraping the cells and exposed to 2 cycles of freezing and thawing at −80°C to lyse cells and detach the virus particles. Cell debris was removed by centrifugation for 10 min at 400 × g, and the viral stock in the supernatant fluid was aliquoted and kept at −80°C. After titration, the passage 2 (P2) stock was made by infecting Vero-SLAM at a multiplicity of infection (MOI) of 0.03 using the P1 viral stock and collected the same way as for the P1.

Structural modeling. Twenty models were produced for the wild-type (wt) measles virus fusion glycoprotein (MeV F) using the protein homology server Phyre2 (61) based on the postfusion structure of hPIV3-F as a template (PDB ID 1ZTM) (62). The resulting models were subsequently optimized via Dunbrack rotamer library and the REF15 scoring function through the PyRosetta (63, 64), resulting in a model for the conformation of the postfusion MeV-F. The crystal structure is represented for the prefusion MeV-F (PDB ID 5YXW) (12). All structural figures were produced using PyMol (http://www.pymol.org/).

Infectivity of MeV variants. Aliquots of equal volumes of DMEM containing 1,000 PFU of virus (MeV IC323-EGFP, MeV IC323-EGFP-F L454W, MeV IC323-EGFP-F T461I, and MeV IC323-EGFP-F N462K) were incubated at a range of temperatures from 4 to 55°C for 5 to 30 min. The titers from samples were then determined on Vero-SLAM cells in triplicates. Results are presented as means ± standard deviations from 3 separate experiments.

β-Gal complementation-based fusion assay. To quantify cell-to-cell fusion, we used a fusion assay based on alpha-omega complementation of β-galactosidase (β-Gal) that was previously described (37, 65). Briefly, 293T cells transiently transfected with the omega reporter subunit and the receptor plasmids were incubated with cells coexpressing viral glycoproteins and the alpha reporter subunit in the presence or absence of MeV F HRC4 dimeric fusion inhibitory peptide or 3G. Cell fusion, which leads to β-Gal complementation, was stopped by lysing the cells, and the luminescence after adding the Galacton-Star substrate (Applied Biosystems) was measured on an Infinite M1000 Pro (Tecan) microplate reader.

Plaque enlargement assay. Vero or Vero-SLAM cells were plated in 12-well plates (2×10^5 cells/well). The following day, cells were infected either with MeV IC323-EGFP or with MeV IC323-EGFP-F L454W (100 PFU/well for Vero-SLAM and 500 PFU/well for Vero cells) for 2 h at 32°C. The medium was replaced with medium containing 2% of methylcellulose Avicel/2× complete medium (1:1) and serial dilutions of either *N*-(3-cyanophenyl)-2-phenylacetamide, referred to as 3G (35), or MeV F-derived HRC4 dimeric fusion inhibitory peptide (33, 34). After 24 h, 48 h, or 72 h, medium was removed, cells were rinsed with phosphate-buffered saline (PBS), and pictures were obtained on a ZOE Fluorescent cell imager (Bio-Rad). Areas of infection in pixels were measured using ImageJ software on images randomly acquired from separated experiments ($n = 3$ at least; analyzed by two-way ANOVA).

***In vivo* experiments. (i) Mice.** One-week-old SLAM transgenic (tg) mice, highly susceptible to MeV infection (33, 38), were infected intranasally (i.n.) by inoculation of 5 μl of Opti-MEM (Thermo Fisher Scientific) containing either 500 or 5,000 PFU of MeV IC323-EGFP-F L454W. Infection with MeV IC323-EGFP F wt was performed with 5,000 or 10,000 PFU. Animals were treated with HRC4 i.n. (6 mg/kg) 24 h before and 4 h after infection (5 μl of peptide). Mock groups received vehicle (Milli-Q water containing 10% DMSO). All animals were observed daily for 21 days, and those showing clinical signs, including neurological symptoms, ataxia, or lethargy, were euthanized. SLAM tg mice (male and female, bred at the Institute's animal facility, PBES, ENS-Lyon) were handled in strict accordance with good animal practice as defined by the French National Charter on the Ethics of Animal Experimentation.

(ii) Cotton rats. Inbred cotton rats (*Sigmodon hispidus*) were purchased from Envigo, Inc., Indianapolis. Both male and female cotton rats aged 5 to 7 weeks were used. For i.n. infection, 10^5 $TCID_{50}$ of MeV IC323-EGFP F wt or MeV IC323-EGFP-F L454W in PBS was inoculated intranasally to isoflurane-anesthetized cotton rats in a volume of 100 μl. Four days after infection, the animals were euthanized by CO_2 inhalation, and their lungs were collected and weighed. Lung tissue was minced with scissors and homogenized with a glass dounce homogenizer. Serial 10-fold dilutions of supernatant fluids were assessed for the presence of infectious virus in 48-well plates using cytopathic effect (CPE) in Vero SLAM cells as the endpoint. Plates were scored for CPE microscopically after 7 days. The $TCID_{50}$ was calculated as described previously (33).

Coinfection and immunofluorescence. One-week-old SLAM tg mice ($n = 3$) received 1,000 PFU of both MeV IC323-tdTomato F wt and MeV IC323-EGFP-F L454W intranasally in 5 μl of Opti-MEM. After 4 days, the animals were euthanized by cervical dislocation, and the brains and lungs were collected. Organs were fixed overnight in 4% paraformaldehyde (PFA), washed in 1× Dulbecco's phosphate-buffered saline (DPBS), placed in 30% sucrose, and frozen in cold isopentane on dry ice. Cryosections (7-μm thick) were dried for 30 min at room temperature (RT) and permeabilized and blocked in 1× DPBS-4% FBS-0.3% Triton X-100 for 20 min at RT. Sections were incubated in 1× DPBS-4% FBS-0.3% Triton X-100 containing mouse anti-GFP (catalog number AB1218; Abcam) (1:500) and goat anti-tdTomato (catalog number AB8181-200; Sicgen antibodies) (1:500) for 1 h at RT. After 3 washes (5 min each) in 1× DPBS, tissue sections were incubated in 1× DPBS-4% FBS-0.3% Triton X-100 containing the secondary donkey anti-rabbit conjugated with Alexa 488 and donkey anti-goat conjugated with Alexa

555 antibodies (1:500 each) for 1 h at RT. Nuclei were counterstained with DAPI (4′,6-diamidino-2-phenylindole).

Statistical analysis. The Mantel-Cox test was used for the survival comparison analysis. The two-way ANOVA with Bonferroni's posttest was used to compare the thermal stability of the different viruses and to compare plaque enlargement in the presence or absence of receptor and/or antiviral compound. All other statistical comparisons were performed using the Mann-Whitney U test. All analyses were performed with GraphPad Prism 5 software.

SUPPLEMENTAL MATERIAL

Supplemental material for this article may be found at https://doi.org/10.1128/JVI.01862-18.

SUPPLEMENTAL FILE 1, PDF file, 0.4 MB.

ACKNOWLEDGMENTS

The work was supported by NIH AI121349, NS091263, and NS105699 to M.P., by French ANR NITRODEP (ANR-13-PDOC-0010-01) to C.M., by Region Auvergne Rhone Alpes and LABEX ECOFECT (ANR-11-LABX-0048) of Lyon University, within the program "Investissements d'Avenir" (ANR-11-IDEX-0007) operated by the French National Research Agency (ANR), to B.H., and by Japan AMED J-PRIDE (JP18fm0208022h) to T.H.

REFERENCES

1. Moss WJ, Griffin DE. 2012. Measles. Lancet 379:153–164. https://doi.org/10.1016/S0140-6736(10)62352-5.
2. Perry RT, Murray JS, Gacic-Dobo M, Dabbagh A, Mulders MN, Strebel PM, Okwo-Bele J-M, Rota PA, Goodson JL. 2015. Progress toward regional measles elimination - worldwide, 2000–2014. MMWR Morb Mortal Wkly Rep 64:1246–1251.
3. Simons E, Ferrari M, Fricks J, Wannemuehler K, Anand A, Burton A, Strebel P. 2012. Assessment of the 2010 global measles mortality reduction goal: results from a model of surveillance data. Lancet 379:2173–2178. https://doi.org/10.1016/S0140-6736(12)60522-4.
4. Niewiesk S. 2014. Maternal antibodies: clinical significance, mechanism of interference with immune responses, and possible vaccination strategies. Front Immunol 5:446. https://doi.org/10.3389/fimmu.2014.00446.
5. Jansen VA, Stollenwerk N, Jensen HJ, Ramsay ME, Edmunds WJ, Rhodes CJ. 2003. Measles outbreaks in a population with declining vaccine uptake. Science 301:804. https://doi.org/10.1126/science.1086726.
6. Melenotte C, Zandotti C, Gautret P, Parola P, Raoult D. 2018. Measles: is a new vaccine approach needed? Lancet Infect Dis 18:1060–1061. https://doi.org/10.1016/S1473-3099(18)30543-7.
7. Tatsuo H, Ono N, Tanaka K, Yanagi Y. 2000. SLAM (CDw150) is a cellular receptor for measles virus. Nature 406:893–897. https://doi.org/10.1038/35022579.
8. Mühlebach MD, Mateo M, Sinn PL, Prüfer S, Uhlig KM, Leonard VHJ, Navaratnarajah CK, Frenzke M, Wong XX, Sawatsky B, Ramachandran S, McCray PB, Cichutek K, von Messling V, Lopez M, Cattaneo R. 2011. Adherens junction protein nectin-4 is the epithelial receptor for measles virus. Nature 480:530–533. https://doi.org/10.1038/nature10639.
9. Noyce RS, Bondre DG, Ha MN, Lin L-T, Sisson G, Tsao M-S, Richardson CD. 2011. Tumor cell marker PVRL4 (nectin 4) is an epithelial cell receptor for measles virus. PLoS Pathog 7:e1002240. https://doi.org/10.1371/journal.ppat.1002240.
10. Chang A, Dutch RE. 2012. Paramyxovirus fusion and entry: multiple paths to a common end. Viruses 4:613–636. https://doi.org/10.3390/v4040613.
11. Harrison SC. 2008. Viral membrane fusion. Nat Struct Mol Biol 15:690–698. https://doi.org/10.1038/nsmb.1456.
12. Hashiguchi T, Fukuda Y, Matsuoka R, Kuroda D, Kubota M, Shirogane Y, Watanabe S, Tsumoto K, Kohda D, Plemper RK, Yanagi Y. 2018. Structures of the prefusion form of measles virus fusion protein in complex with inhibitors. Proc Natl Acad Sci U S A 115:2496–2501. https://doi.org/10.1073/pnas.1718957115.
13. Lambert DM, Barney S, Lambert AL, Guthrie K, Medinas R, Davis DE, Bucy T, Erickson J, Merutka G, Petteway SR. 1996. Peptides from conserved regions of paramyxovirus fusion (F) proteins are potent inhibitors of viral fusion. Proc Natl Acad Sci U S A 93:2186–2191. https://doi.org/10.1073/pnas.93.5.2186.
14. Allen IV, McQuaid S, McMahon J, Kirk J, McConnell R. 1996. The significance of measles virus antigen and genome distribution in the CNS in SSPE for mechanisms of viral spread and demyelination. J Neuropathol Exp Neurol 55:471–480. https://doi.org/10.1097/00005072-199604000-00010.
15. Buchanan R, Bonthius DJ. 2012. Measles virus and associated central nervous system sequelae. Semin Pediatr Neurol 19:107–114. https://doi.org/10.1016/j.spen.2012.02.003.
16. Hosoya M. 2006. Measles encephalitis: direct viral invasion or autoimmune-mediated inflammation? Intern Med 45:841–842. https://doi.org/10.2169/internalmedicine.45.0161.
17. Cattaneo R, Schmid A, Billeter MA, Sheppard RD, Udem SA. 1988. Multiple viral mutations rather than host factors cause defective measles virus gene expression in a subacute sclerosing panencephalitis cell line. J Virol 62:1388–1397.
18. Rima BK, Duprex WP. 2005. Molecular mechanisms of measles virus persistence. Virus Res 111:132–147. https://doi.org/10.1016/j.virusres.2005.04.005.
19. Schmid A, Spielhofer P, Cattaneo R, Baczko K, ter Meulen V, Billeter MA. 1992. Subacute sclerosing panencephalitis is typically characterized by alterations in the fusion protein cytoplasmic domain of the persisting measles virus. Virology 188:910–915. https://doi.org/10.1016/0042-6822(92)90552-Z.
20. Baldolli A, Dargère S, Cardineau E, Vabret A, Dina J, de La Blanchardière A, Verdon R. 2016. Measles inclusion-body encephalitis (MIBE) in a immunocompromised patient. J Clin Virol 81:43–46. https://doi.org/10.1016/j.jcv.2016.05.016.
21. Hughes I, Jenney ME, Newton RW, Morris DJ, Klapper PE. 1993. Measles encephalitis during immunosuppressive treatment for acute lymphoblastic leukaemia. Arch Dis Child 68:775–778. https://doi.org/10.1136/adc.68.6.775.
22. Hardie DR, Albertyn C, Heckmann JM, Smuts HEM. 2013. Molecular characterisation of virus in the brains of patients with measles inclusion body encephalitis (MIBE). Virol J 10:283. https://doi.org/10.1186/1743-422X-10-283.
23. Jurgens EM, Mathieu C, Palermo LM, Hardie D, Horvat B, Moscona A, Porotto M. 2015. Measles fusion machinery is dysregulated in neuropathogenic variants. mBio 6:e02528-14. https://doi.org/10.1128/mBio.02528-14.
24. Makhortova NR, Askovich P, Patterson CE, Gechman LA, Gerard NP, Rall GF. 2007. Neurokinin-1 enables measles virus trans-synaptic spread in neurons. Virology 362:235–244. https://doi.org/10.1016/j.virol.2007.02.033.
25. Watanabe M, Hashimoto K, Abe Y, Kodama EN, Nabika R, Oishi S, Ohara S, Sato M, Kawasaki Y, Fujii N, Hosoya M. 2016. A novel peptide derived from the fusion protein heptad repeat inhibits replication of subacute sclerosing panencephalitis virus *in vitro* and *in vivo*. PLoS One 11:e0162823. https://doi.org/10.1371/journal.pone.0162823.

26. Young VA, Rall GF. 2009. Making it to the synapse: measles virus spread in and among neurons. Curr Top Microbiol Immunol 330:3–30.
27. Ayata M, Takeuchi K, Takeda M, Ohgimoto S, Kato S, Sharma LB, Tanaka M, Kuwamura M, Ishida H, Ogura H. 2010. The F gene of the Osaka-2 strain of measles virus derived from a case of subacute sclerosing panencephalitis is a major determinant of neurovirulence. J Virol 84:11189–11199. https://doi.org/10.1128/JVI.01075-10.
28. Watanabe S, Shirogane Y, Suzuki SO, Ikegame S, Koga R, Yanagi Y. 2013. Mutant fusion proteins with enhanced fusion activity promote measles virus spread in human neuronal cells and brains of suckling hamsters. J Virol 87:2648–2659. https://doi.org/10.1128/JVI.02632-12.
29. Watanabe S, Ohno S, Shirogane Y, Suzuki SO, Koga R, Yanagi Y. 2015. Measles virus mutants possessing the fusion protein with enhanced fusion activity spread effectively in neuronal cells, but not in other cells, without causing strong cytopathology. J Virol 89:2710–2717. https://doi.org/10.1128/JVI.03346-14.
30. Sato Y, Watanabe S, Fukuda Y, Hashiguchi T, Yanagi Y, Ohno S. 2018. Cell-to-cell measles virus spread between human neurons is dependent on hemagglutinin and hyperfusogenic fusion protein. J Virol 92:e02166-17. https://doi.org/10.1128/JVI.02166-17.
31. Ha MN, Delpeut S, Noyce RS, Sisson G, Black KM, Lin L-T, Bilimoria D, Plemper RK, Privé GG, Richardson CD. 2017. Mutations in the fusion protein of measles virus that confer resistance to the membrane fusion inhibitors carbobenzoxy-D-Phe-L-Phe-Gly and 4-nitro-2-phenylacetyl amino-benzamide. J Virol 91:e01026-17. https://doi.org/10.1128/JVI.01026-17.
32. Yin H-S, Paterson RG, Wen X, Lamb RA, Jardetzky TS. 2005. Structure of the uncleaved ectodomain of the paramyxovirus (hPIV3) fusion protein. Proc Natl Acad Sci U S A 102:9288–9293. https://doi.org/10.1073/pnas.0503989102.
33. Mathieu C, Huey D, Jurgens E, Welsch JC, DeVito I, Talekar A, Horvat B, Niewiesk S, Moscona A, Porotto M. 2015. Prevention of measles virus infection by intranasal delivery of fusion inhibitor peptides. J Virol 89:1143–1155. https://doi.org/10.1128/JVI.02417-14.
34. Welsch JC, Talekar A, Mathieu C, Pessi A, Moscona A, Horvat B, Porotto M. 2013. Fatal measles virus infection prevented by brain-penetrant fusion inhibitors. J Virol 87:13785–13794. https://doi.org/10.1128/JVI.02436-13.
35. Avila M, Alves L, Khosravi M, Ader-Ebert N, Origgi F, Schneider-Schaulies J, Zurbriggen A, Plemper RK, Plattet P. 2014. Molecular determinants defining the triggering range of prefusion F complexes of canine distemper virus. J Virol 88:2951–2966. https://doi.org/10.1128/JVI.03123-13.
36. Ader N, Brindley M, Avila M, Örvell C, Horvat B, Hiltensperger G, Schneider-Schaulies J, Vandevelde M, Zurbriggen A, Plemper RK, Plattet P. 2013. Mechanism for active membrane fusion triggering by morbillivirus attachment protein. J Virol 87:314–326. https://doi.org/10.1128/JVI.01826-12.
37. Porotto M, Fornabaio M, Kellogg GE, Moscona A. 2007. A second receptor binding site on human parainfluenza virus type 3 hemagglutinin-neuraminidase contributes to activation of the fusion mechanism. J Virol 81:3216–3228. https://doi.org/10.1128/JVI.02617-06.
38. Sellin CI, Davoust N, Guillaume V, Baas D, Belin M-F, Buckland R, Wild TF, Horvat B. 2006. High pathogenicity of wild-type measles virus infection in CD150 (SLAM) transgenic mice. J Virol 80:6420–6429. https://doi.org/10.1128/JVI.00209-06.
39. Fox A, Hung TM, Wertheim H, Hoa LNM, Vincent A, Lang B, Waters P, Ha NH, Trung NV, Farrar J, Van Kinh N, Horby P. 2013. Acute measles encephalitis in partially vaccinated adults. PLoS One 8:e71671. https://doi.org/10.1371/journal.pone.0071671.
40. Mahil SK, Fleming J, Robson A, Sarkany R. 2014. Measles in a previously vaccinated human immunodeficiency virus-positive adult. Clin Exp Dermatol 39:117–118. https://doi.org/10.1111/ced.12238.
41. Albertyn C, van der Plas H, Hardie D, Candy S, Tomoka T, Leepan EB, Heckmann JM. 2011. Silent casualties from the measles outbreak in South Africa. S Afr Med J 101:313–317. https://doi.org/10.7196/SAMJ.4616.
42. Devaux P, Hodge G, McChesney MB, Cattaneo R. 2008. Attenuation of V- or C-defective measles viruses: infection control by the inflammatory and interferon responses of rhesus monkeys. J Virol 82:5359–5367. https://doi.org/10.1128/JVI.00169-08.
43. Frenzke M, Sawatsky B, Wong XX, Delpeut S, Mateo M, Cattaneo R, von Messling V. 2013. Nectin-4-dependent measles virus spread to the cynomolgus monkey tracheal epithelium: role of infected immune cells infiltrating the lamina propria. J Virol 87:2526–2534. https://doi.org/10.1128/JVI.03037-12.
44. Lemon K, de Vries RD, Mesman AW, McQuaid S, van Amerongen G, Yüksel S, Ludlow M, Rennick LJ, Kuiken T, Rima BK, Geijtenbeek TBH, Osterhaus ADME, Duprex WP, de Swart RL. 2011. Early target cells of measles virus after aerosol infection of non-human primates. PLoS Pathog 7:e1001263. https://doi.org/10.1371/journal.ppat.1001263.
45. Leonard VHJ, Sinn PL, Hodge G, Miest T, Devaux P, Oezguen N, Braun W, McCray PB, McChesney MB, Cattaneo R. 2008. Measles virus blind to its epithelial cell receptor remains virulent in rhesus monkeys but cannot cross the airway epithelium and is not shed. J Clin Invest 118:2448–2458. https://doi.org/10.1172/JCI35454.
46. Leonard VHJ, Hodge G, Reyes-Del Valle J, McChesney MB, Cattaneo R. 2010. Measles virus selectively blind to signaling lymphocytic activation molecule (SLAM; CD150) is attenuated and induces strong adaptive immune responses in rhesus monkeys. J Virol 84:3413–3420. https://doi.org/10.1128/JVI.02304-09.
47. Delpeut S, Sawatsky B, Wong X-X, Frenzke M, Cattaneo R, von Messling V. 2017. Nectin-4 interactions govern measles virus virulence in a new model of pathogenesis, the squirrel monkey (*Saimiri sciureus*). J Virol 91:e02490-16. https://doi.org/10.1128/JVI.02490-16.
48. Devaux P, Hudacek AW, Hodge G, Reyes-del Valle J, McChesney MB, Cattaneo R. 2011. A recombinant measles virus unable to antagonize STAT1 function cannot control inflammation and is attenuated in rhesus monkeys. J Virol 85:348–356. https://doi.org/10.1128/JVI.00802-10.
49. Chiu MH, Meatherall B, Nikolic A, Cannon K, Fonseca K, Joseph JT, MacDonald J, Pabbaraju K, Tellier R, Wong S, Koch MW. 2016. Subacute sclerosing panencephalitis in pregnancy. Lancet Infect Dis 16:366–375. https://doi.org/10.1016/S1473-3099(15)00524-1.
50. O'Donnell LA, Rall GF. 2010. Blue moon neurovirology: the merits of studying rare CNS diseases of viral origin. J Neuroimmune Pharmacol 5:443–455. https://doi.org/10.1007/s11481-010-9200-4.
51. Reuter D, Schneider-Schaulies J. 2010. Measles virus infection of the CNS: human disease, animal models, and approaches to therapy. Med Microbiol Immunol 199:261–271. https://doi.org/10.1007/s00430-010-0153-2.
52. Jeulin H, Venard V, Carapito D, Finance C, Kedzierewicz F. 2009. Effective ribavirin concentration in mice brain using cyclodextrin as a drug carrier: evaluation in a measles encephalitis model. Antiviral Res 81:261–266. https://doi.org/10.1016/j.antiviral.2008.12.006.
53. Plemper RK, Hammond AL. 2014. Synergizing vaccinations with therapeutics for measles eradication. Expert Opin Drug Discov 9:201–214. https://doi.org/10.1517/17460441.2014.867324.
54. Plemper RK, Snyder JP. 2009. Measles control–can measles virus inhibitors make a difference? Curr Opin Investig Drugs 10:811–820.
55. Battles MB, Langedijk JP, Furmanova-Hollenstein P, Chaiwatpongsakorn S, Costello HM, Kwanten L, Vranckx L, Vink P, Jaensch S, Jonckers THM, Koul A, Arnoult E, Peeples ME, Roymans D, McLellan JS. 2016. Molecular mechanism of respiratory syncytial virus fusion inhibitors. Nat Chem Biol 12:87–93. https://doi.org/10.1038/nchembio.1982.
56. Plemper RK, Doyle J, Sun A, Prussia A, Cheng L-T, Rota PA, Liotta DC, Snyder JP, Compans RW. 2005. Design of a small-molecule entry inhibitor with activity against primary measles virus strains. Antimicrob Agents Chemother 49:3755–3761. https://doi.org/10.1128/AAC.49.9.3755-3761.2005.
57. Prussia AJ, Plemper RK, Snyder JP. 2008. Measles virus entry inhibitors: a structural proposal for mechanism of action and the development of resistance. Biochemistry 47:13573–13583. https://doi.org/10.1021/bi801513p.
58. Sun A, Prussia A, Zhan W, Murray EE, Doyle J, Cheng L-T, Yoon J-J, Radchenko EV, Palyulin VA, Compans RW, Liotta DC, Plemper RK, Snyder JP. 2006. Nonpeptide inhibitors of measles virus entry. J Med Chem 49:5080–5092. https://doi.org/10.1021/jm0602559.
59. Radecke F, Spielhofer P, Schneider H, Kaelin K, Huber M, Dötsch C, Christiansen G, Billeter MA. 1995. Rescue of measles viruses from cloned DNA. EMBO J 14:5773–5784. https://doi.org/10.1002/j.1460-2075.1995.tb00266.x.
60. Hashimoto K, Ono N, Tatsuo H, Minagawa H, Takeda M, Takeuchi K, Yanagi Y. 2002. SLAM (CD150)-independent measles virus entry as revealed by recombinant virus expressing green fluorescent protein. J Virol 76:6743–6749. https://doi.org/10.1128/JVI.76.13.6743-6749.2002.
61. Kelley LA, Mezulis S, Yates CM, Wass MN, Sternberg MJE. 2015. The

Phyre2 web portal for protein modeling, prediction and analysis. Nat Protoc 10:845–858. https://doi.org/10.1038/nprot.2015.053.
62. McRee DE. 1999. XtalView/Xfit–A versatile program for manipulating atomic coordinates and electron density. J Struct Biol 125:156–165. https://doi.org/10.1006/jsbi.1999.4094.
63. Alford RF, Leaver-Fay A, Jeliazkov JR, O'Meara MJ, DiMaio FP, Park H, Shapovalov MV, Renfrew PD, Mulligan VK, Kappel K, Labonte JW, Pacella MS, Bonneau R, Bradley P, Dunbrack RL, Das R, Baker D, Kuhlman B, Kortemme T, Gray JJ. 2017. The Rosetta all-atom energy function for macromolecular modeling and design. J Chem Theory Comput 13:3031–3048. https://doi.org/10.1021/acs.jctc.7b00125.
64. Roberts E, Eargle J, Wright D, Luthey-Schulten Z. 2006. MultiSeq: unifying sequence and structure data for evolutionary analysis. BMC Bioinformatics 7:382. https://doi.org/10.1186/1471-2105-7-382.
65. Moosmann P, Rusconi S. 1996. Alpha complementation of LacZ in mammalian cells. Nucleic Acids Res 24:1171–1172. https://doi.org/10.1093/nar/24.6.1171.

b. Tropisme initial de mutants hyperfusogènes du virus de la rougeole dans le système nerveux central

L'objectif de cette partie est de déterminer le tropisme précoce de l'infection du système nerveux central par les mutants hyperfusogènes du VR en comparaison avec le virus sauvage. Pour répondre à cette question j'ai infecté des cultures organotypiques de cervelet de hamster avec différents VR recombinants MeV-IC323-eGFP-exprimant la F sauvage (wt), ou la F avec des mutations dans la F identifiées dans des cas d'encéphalites PESS ou MIBE : F-T461I, F-L454W, F-L454W/E455G, F-G168R/E170G, F-G168R/E170G/S262G et F-S262G. Tous ces virus ont été reconstitués au laboratoire par génétique inverse et amplifiés en cellules Vero-SLAM à 32°C. Les plasmides utilisés pour générer ces virus ont été clonés à partir du plasmide codant pour le virus sauvage MeV-IC323-eGFP-F-WT.

Tout d'abord la susceptibilité des COC à l'infection par ces mutants a été vérifiée. Les COC ont été infectées par 1000 PFU de virus le jour de la coupe. La dissémination virale a été suivie par microscopie à épifluorescence et a été quantifiée (réplication et transcription) par RT-qPCR (Figure 16). Quatre jours après l'infection, dans le cas des virus Fwt et F-L454W/E455G seules quelques particules sont rentrées dans quelques cellules (identifiables par la fluorescence de la GFP) sans parvenir à infecter les cellules voisines (Figure 16, A et D). Par contre, à 4 jours, les virus F-T461I et F-L454W se sont largement disséminés dans les coupes (Figure 16, B et C) et les virus F-G168R/E170G et F-G168R/E170G/S262G ont aussi formé des foyers d'infection bien que plus petits. Les quantifications des copies de N par µg d'ARN confirment ces observations avec notamment une augmentation de 2 log pour le virus F-L454W. (Figure 16, I). Ces résultats confirment que les mutations retrouvées dans les séquences virales isolées de cerveaux de patients souffrant de SSPE ou MIBE favorisent la dissémination virale dans le SNC en absence de récepteur connu alors que le virus sauvage ou un virus portant une mutation de compensation capable de rétablir la stabilité de la F (E455G) est incapable de se disséminer dans ces conditions.

Dans le but de comparer le tropisme précoce des mutants hyperfusogènes avec le virus de la rougeole sauvage dans le SNC des COC de hamsters ont été infectées par 10^4 PFU avec les virus F-wt, F-L454W et F-T461I. Les premières cellules infectées ont été analysées par marquages immunofluorescents (Figures 17, 18, 19, 20) et par cytométrie en flux. L'observation en microscopie à fluorescence a montré l'infection de neurones et d'astrocytes par le virus F-wt (Figure 17, B, C). De plus le marquage Tuj-1 (clone de l'anticorps marquant la beta-III-Tubuline), marqueur de neurones, colocalise rarement avec l'eGFP des cellules les plus infectées même si l'apparence des cellules porte à croire qu'il s'agit bien d'un neurone. Les zones de colocalisations sont visibles lorsque l'infection est très faible (Figure 17, C3, D3) et on peut émettre l'hypothèse que l'infection entraine une désorganisation du cytosquelette des cellules, expliquant une perte d'expression de la beta-III-Tubuline. Dans le cas de l'infection par les virus hyperfusogénes F-L454W et F-T461I les 4 populations microglies, astrocytes, oligodendrocytes et neurones sont infectées (Figure 18 et Figure 19). Par contre l'absence de colocalisation de l'eGFP avec le

marquage NeuN représentant les neurones granulaires ou le marquage CB28K représentant les neurones de Purkinje indiquent que ces types de neurone seraient non permissifs au VR. Seuls les neurones exprimant la beta-III-tubuline semblent positifs à l'infection par les variants hyperfusogènes. Le fait que l'on retrouve de l'infection dans les 4 types cellulaires pour les virus hyperfusogènes F-L454W et F-T461I n'est pas surprenant étant donné leur capacité à infecter indépendamment de l'expression des récepteurs d'entrée connus et que ces mutations ont émergé dans des cas d'encéphalites rougeoleuses chez l'Homme. Les résultats des marquages immunofluorescents sont résumés dans le Tableau 3 ci-dessous. Il est important de noter cependant que les résultats négatifs représentent l'absence d'observation de colocalisation de l'eGFP avec les types cellulaires marqués ne sont qu'une indication qualitative qui ne permet pas de garantir l'absence totale d'infection de ces types cellulaires.

Tableau 3 : Infection des différents types cellulaires du SNC par des mutants du virus de la rougeole à un temps précoce après infection

	IC323-eGFP-F-WT	IC323-eGFP-F-L454W	IC323-eGFP-F-T461I
Tubuline des neurones	+	+	+
Astrocytes	+	+	+
Oligodendrocytes	-	+	+
Microglies	-	+	+
Neurones granulaires	-	-	-
Neurones de Purkinje	-	-	-

(+) observation de colocalisation entre les cellules infectées et les cellules d'intérêt,
(-) pas de colocalisation observée.

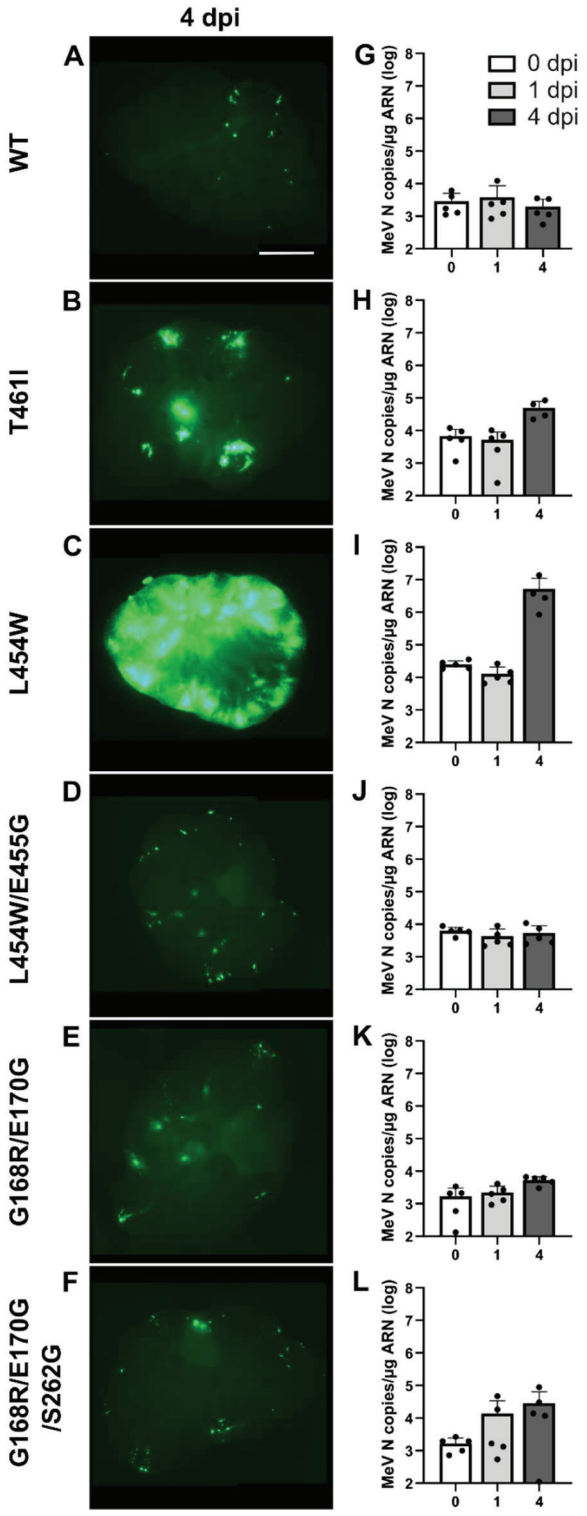

Figure 16 : Dissémination virale des virus mutants dans leur protéine F en cultures organotypiques de cervelet de hamster.

Les cultures organotypiques de cervelet (COC) de hamster ont été infectées le jour de la coupe avec 1000 PFU de virus de la rougeole sauvage ou comportant des mutations dans la F. A-F) Photos des COC 4 jours post infection. Les cellules exprimant l'eGFP témoignent de la réplication virale. Les photos ont été prises par le mircroscope Nikon Eclipse Ts2R microscope à 200 millisecondes (ms) d'exposition

pour A, D, E, F et 50 ms d'exposition pour B et C et reconstituées en utilisant le plug-in Stitching plug-in avec le logiciel ImageJ [494]. G-L) Quantification des copies de N par µg d'ARN pour chaque virus à 0, 1 et 4 jours post infection (n=5). Barre d'échelle = 1mm.

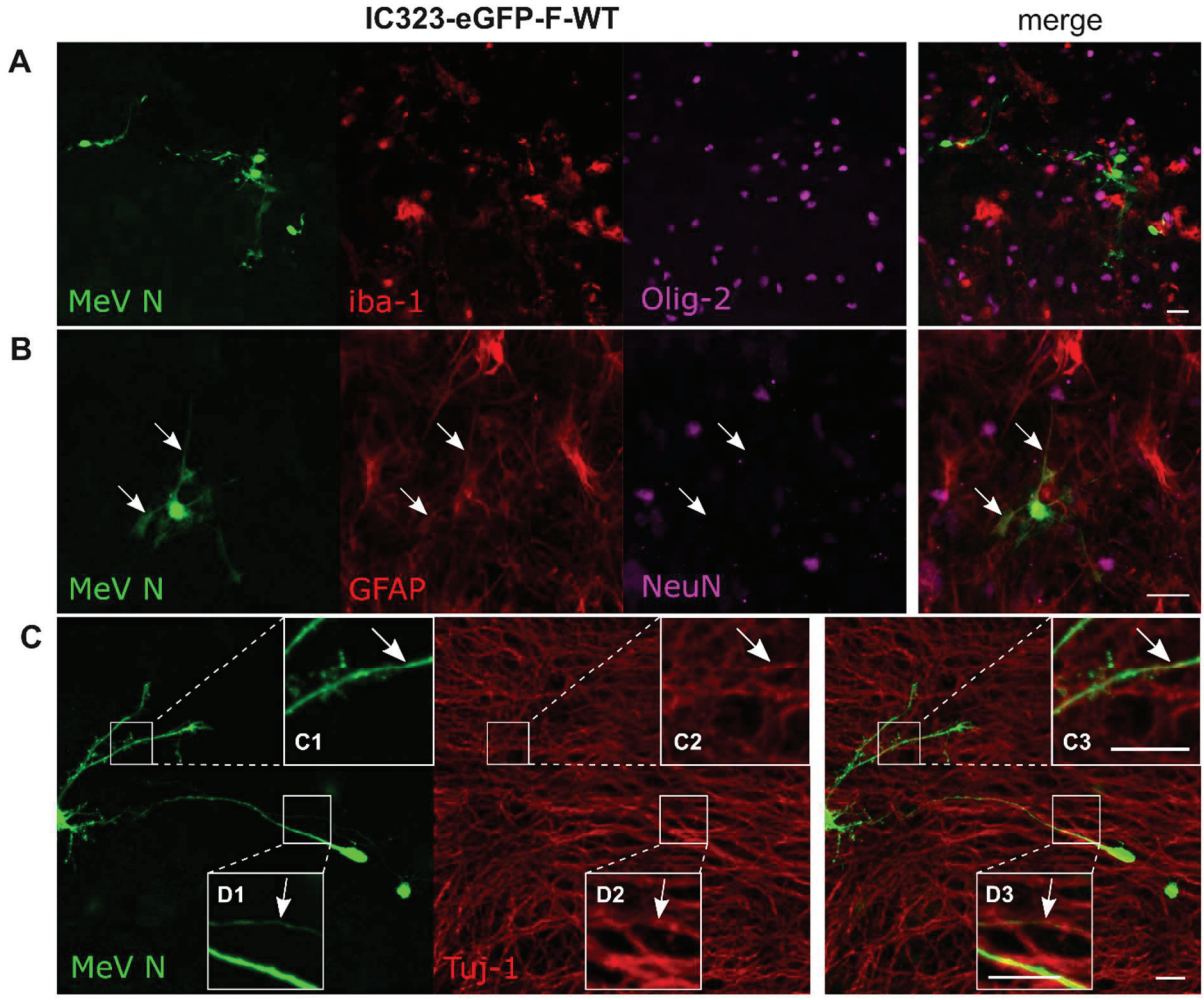

Figure 17 : Tropisme précoce de l'infection par le virus de la rougeole sauvage en cultures organotypiques de cervelet de hamster.

Les cultures organotypiques de cervelet (COC) ont été infectées par 10^4 PFU du virus IC323-eGFP-F-wt le jour de la coupe, traitées par 1µM de peptide inhibiteur de fusion à 24 heures post infection et fixées en formaldéhyde 4% à 48 heures post infection. A) Marquages immunofluorescents (IF) des microglies (iba1) et des oligodendrocytes (Olig-2). B) Marquages IF des astrocytes (GFAP) et des neurones granulaires. C) Marquages IF de la tubuline présente dans les neurones (Beta-III-Tubulin, clone TUJ1), C1, C2, C3) et D1, D2, D3) zoom sur les zones de colocalisations de la fluorescence eGFP et du marquage Beta-III-Tubulin. La fluorescence verte correspond aux cellules infectées exprimant l'eGFP. Les images ont été prises avec le microscope Zeiss Axio Observer avec le système confocal LSM 980 et analysées avec le logiciel ImageJ. Les flèches pointent les zones de colocalisations entre les cellules infectées et le marquage d'intérêt. Barres d'échelles = 20µm.

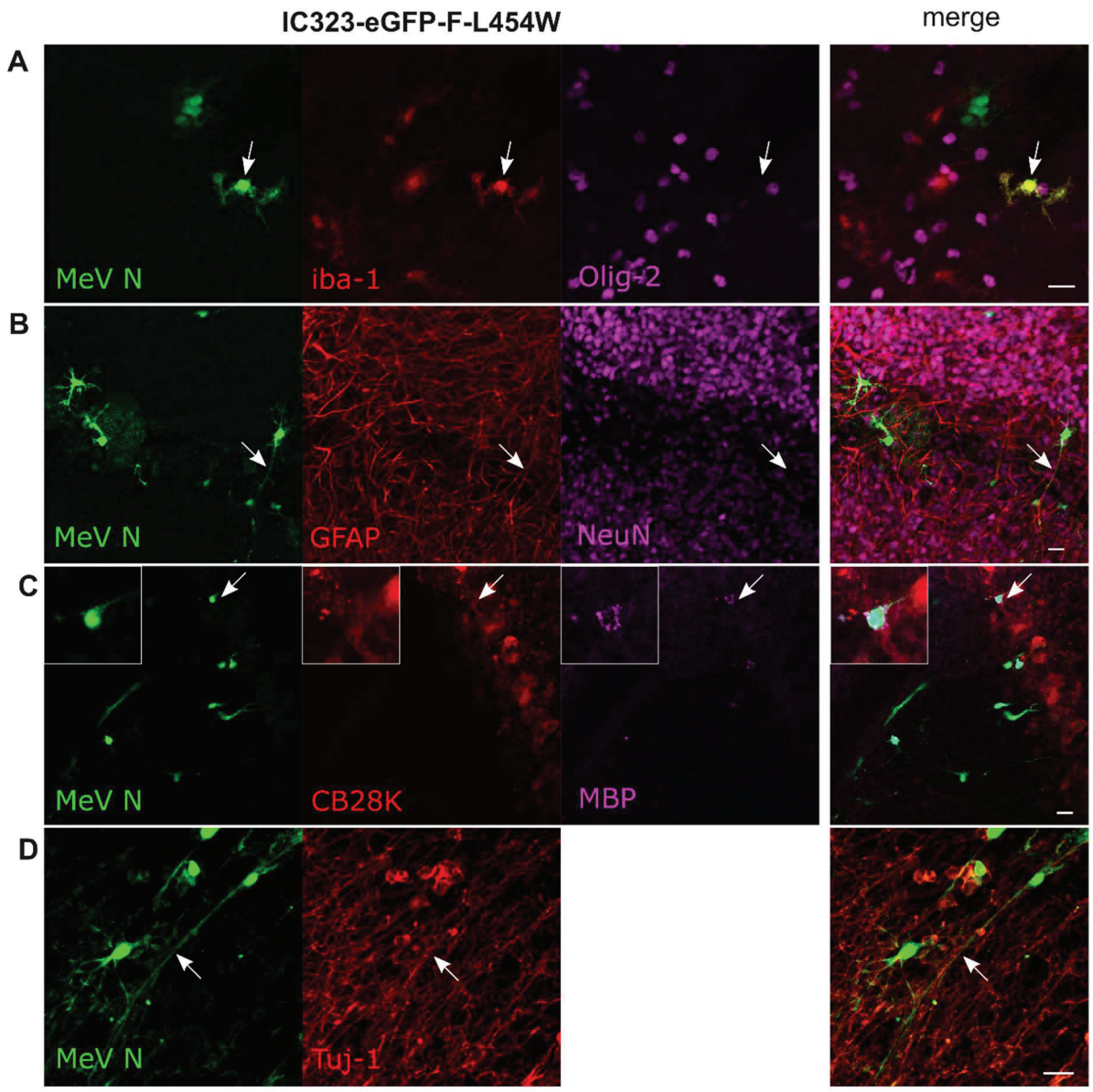

Figure 18 : Tropisme précoce de l'infection par le virus mutant IC323-eGFP-F-L454W en cultures organotypiques de cervelet de hamster.

Les cultures organotypiques de cervelet (COC) ont été infectées par 10^4 PFU du virus IC323-eGFP-F-L454W le jour de la coupe et fixées en formaldéhyde 4% 24 heures post infection. A) Marquages immunofluorescents (IF) des microglies (iba1) et des oligodendrocytes (Olig-2). B) Marquages IF des astrocytes (GFAP) et des neurones granulaires. C) Marquages IF des neurones de Purkinje (CB-28k) et de la protéine de myéline basique (MBP) des oligodendrocytes. D) Marquages IF de la tubuline présente dans les neurones (Beta-III-Tubulin, clone TUJ1). La fluorescence verte correspond aux cellules infectées exprimant l'eGFP. Les images ont été prises avec le microscope Zeiss Axio Observer avec le système confocal LSM 980 et analysées avec le logiciel ImageJ. Les flèches pointent les zones de colocalisations entre les cellules infectées et le marquage d'intérêt. Barres d'échelles = 20µm.

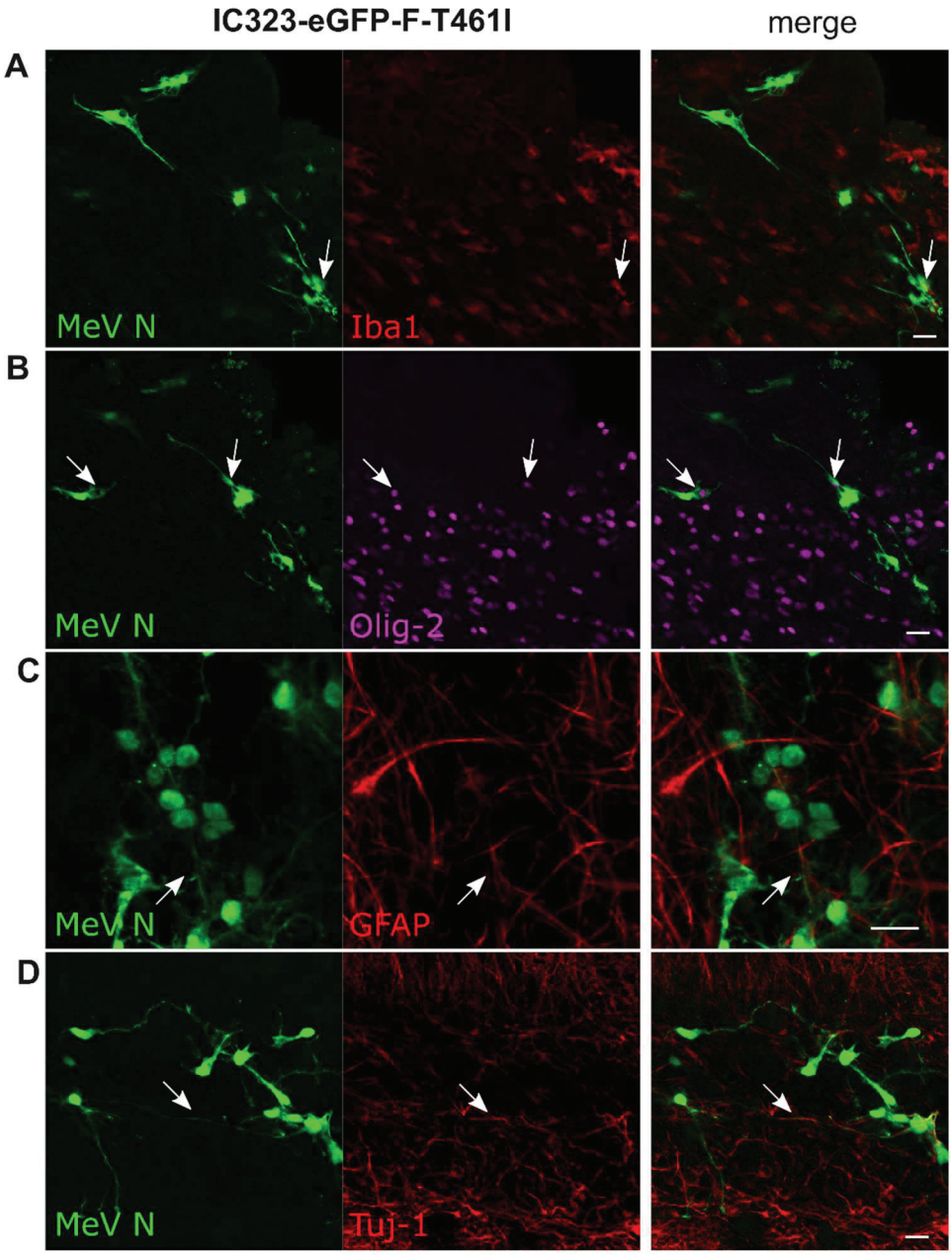

Figure 19 : Tropisme précoce de l'infection par le virus mutant IC323-eGFP-F-T461I en cultures organotypiques de cervelet de hamster.

Les cultures organotypiques de cervelet (COC) ont été infectées par 10^4 PFU du virus IC323-eGFP-F-T461I le jour de la coupe et fixées en formaldéhyde 4% 24 heures post infection. A) Marquages immunofluorescents des microglies (iba1), B) des oligodendrocytes (Olig-2), C) des astrocytes (GFAP) et D) de la tubuline présente dans les neurones (Beta-III-Tubulin, clone TUJ1). La fluorescence verte correspond aux cellules infectées exprimant l'eGFP. Les images ont été prises avec le microscope Zeiss Axio Observer avec le système confocal LSM 980 et analysées avec le logiciel ImageJ. Les flèches pointent les zones de colocalisations entre les cellules infectées et le marquage d'intérêt. Barres d'échelles = 20µm.

Pour évaluer de façon quantitative la distribution des cellules infectées et la contribution des cellules du SNC au début de l'infection par les virus mutants F-L454W et F-T461I une analyse par cytométrie en flux a été réalisée. Les cultures organotypiques de cervelet de hamster (COC) ont été infectées par 10^4 PFU. 24 heures post infection, les cultures ont été dissociées par une digestion à la papaïne et les cellules vivantes ont été marquées en surface par des anticorps anti-GABA, anti-Glast, anti-GalC et anti-CD68 ciblant respectivement les neurones, les astrocytes les oligodendrocytes, et les microglies (Figure 20). L'analyse de la distribution de l'infection, c'est-à-dire le pourcentage de chaque type cellulaire parmi les cellules infectées montre que les virus F-L454W et F-T461I ciblent majoritairement les neurones avec plus de 55% de cellules infectées positives au marquage GABA (Figure 20, A). Les astrocytes sont la deuxième population cellulaire la plus ciblée par l'infection suivis des oligodendrocytes et des microglies pour F- L454W et des microglies puis des oligodendrocytes pour le F-T461I. La somme des pourcentages supérieure à 100% s'explique par le fait que la dissociation du tissu conduit à la libération de fragments myélinisés d'oligodendrocytes se collant à toutes les cellules, ce qui implique une surévaluation potentielle de cette population et une difficulté d'exclure finement ces faux positifs. De plus, à une moindre échelle, certaines cellules expriment les différents marqueurs utilisés ici à différents niveaux pouvant légèrement biaiser l'observation. Cependant la proportion de chaque catégorie de cellules est identique dans les contrôles non infectés et cette surévaluation de certaines populations n'est donc pas une conséquence de l'infection.

Le pourcentage de cellules infectées au sein de chaque population cellulaire a été analysé également. Les résultats montrent que les microglies, bien que représentant seulement 0,5% des cellules totales contribuent grandement à l'infection avec plus de 30% d'infection des microglies infectées, aussi bien par le mutant L454W que par le mutant T461I (Figure 20, B).

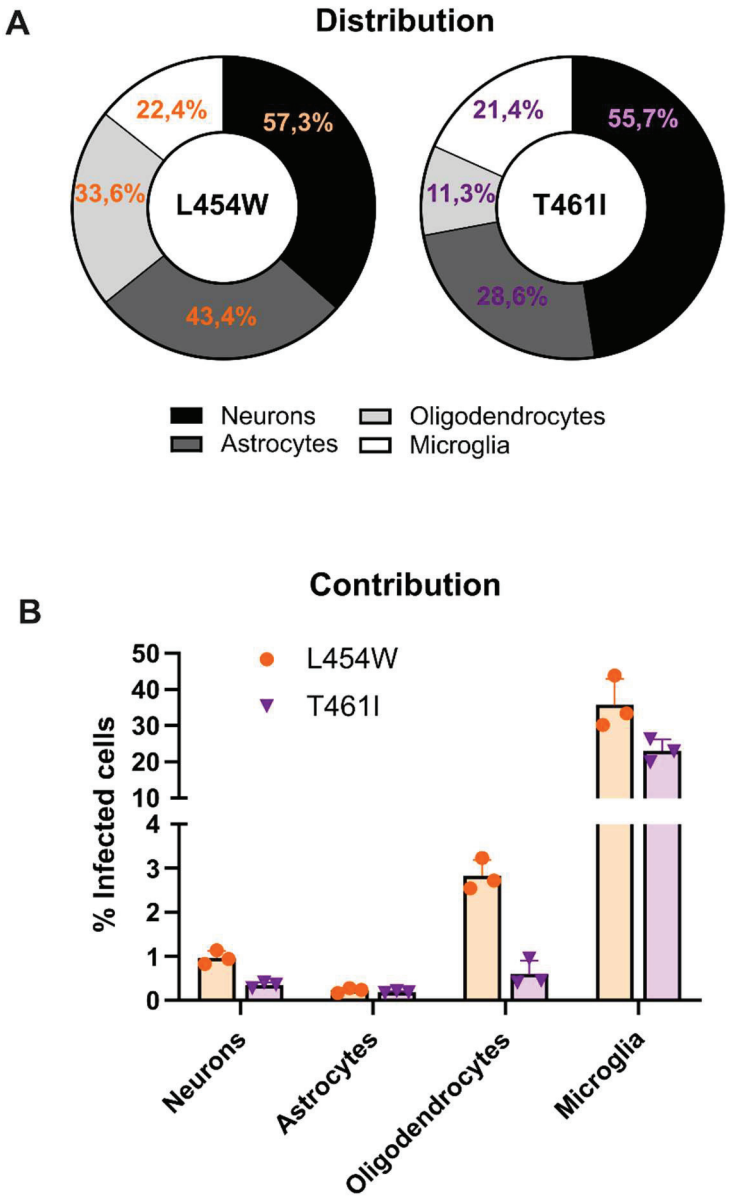

Figure 20 : Evaluation de la distribution des cellules infectées et de la contribution des cellules du SNC au début de l'infection par les virus mutants IC323-eGFP-F-L454W et IC323-eGFP-F-T461I.

Les cultures organotypiques de cervelet de hamster ont été infectées par 10^4 PFU des virus IC323-eGFP-F-L454W ou IC323-eGFP-F-T461I. 24 heures post infection, les neurones, les astrocytes, les oligodendrocytes, et les microglies ont été marqués pour une analyse en cytométrie en flux par des anticorps conjugués à des fluorochromes, anti-Gaba, anti-Glast, anti-GalC et anti-CD68, respectivement. A) La distribution de l'infection, c'est-à-dire le pourcentage de chaque type cellulaire parmi les cellules infectées a été quantifiée, et B) la contribution de chaque type cellules à l'infection, c'est-à-dire le pourcentage de cellules infectées au sein de chaque population cellulaire a été analysé également.

Les résultats de cette partie permettent de confirmer que le modèle de COC de hamster est un bon modèle pour étudier le tropisme initial par le VR et a permis de conclure que les mutants hyperfusogènes sont capables d'entrer dans tous les types cellulaires du SNC mais ciblent tout de même préférentiellement les neurones. La somme des pourcentages de cellules infectées au sein des populations cellulaires (distribution) est supérieure à 100% (environ 150% en moyenne) et est explicable par le fait que les oligodendrocytes myélinisent potentiellement tous les types cellulaires, entrainant des cellules doublement ou triplement positives.

L'analyse de cytométrie en flux avec le virus sauvage n'a pu être réalisée car trop peu de cellules sont infectées 24 heures après infection, même en infectant les cultures avec 10^6 PFU.

Les expériences de cytométrie en flux ont fait l'objet de la mise au point d'un cocktail d'anticorps permettant de réaliser les marquages de surface dans ce modèle. Nous avons été confrontés à la difficulté d'analyser des cellules neurales en cytométrie en flux de par leur morphologie et aux contraintes de l'espèce du hamster contre laquelle il n'existe presque pas d'anticorps commercialisés. Ce cocktail ainsi que le déroulement de l'expérience ont été conçus pour répondre également à un autre objectif sur le plus long terme consistant à comparer le tropisme précoce de l'infection du SNC par les Henipavirus dans ce même modèle.

III. Transposition du savoir moléculaire pour évaluer les différences d'encéphalitogenèse entre les Henipavirus

1) Différences génomiques entre les Henipavirus

En 2020 nous avons publié dans le journal « Emerging Infectious Deseases » une étude portant sur la caractérisation d'un isolat de NiV provenant d'une chauve-souris Preropus lylei au Cambodge en 2003 nommé CSUR381 [495]. L'article est disponible en Annexe 4. J'ai présenté ces résultats sous forme de poster au cours de la conférence internationale sur le virus Nipah en décembre 2019 à Singapour. L'objectif était de comparer la pathogénicité de cet isolat à NiV Mal et NiV Ban pour évaluer le risque d'épidémie du CSUR381 au Cambodge.

Le génome de ce virus a été séquencé par RNA-Seq (MiSeq Nano v2, Illumina). Je suis intervenue pour obtenir les séquences des extrémités 5' et 3' en utilisant le système 5' RACE pour une amplification des extrémités d'ADN complémentaire. La séquence complète a ainsi pu être publiée sur GenBank (numéro d'accession MK801755).

Les résultats sont que l'isolat cambodgien appartient au même génotype que NiV Mal avec lequel il partage 97,7% d'identité nucléotidique. NiV Mal et CSUR381 sont très proches dans leur cinétique de réplication et leur permissivité dans différents types cellulaires. De plus, ces deux virus présentent une pathogénicité similaire lors de l'infection de hamsters dorés, ce qui ne justifie donc pas de qualifier l'isolat cambodgien de nouveau génotype.

La même année j'ai également obtenu les séquences des extrémités 5' et 3' de l'isolat de HeV que nous utilisons au laboratoire et qui n'étaient pas encore publiées. Mes résultats associés aux résultats du séquençage RNA-Seq m'ont permis de publier la séquence complète du génome de la souche HeV/Australia/1994/Horse18 (numéro d'accession MN062017.1).

J'ai ainsi pu comparer les séquences des F des isolats de NiV Mal, NiV Ban et HeV utilisés au laboratoire. J'ai notamment détecté une différence au niveau de l'acide aminé 273 dans la région située entre le domaine HRN et HRC où l'on observe une sérine pour NiV Mal et HeV tandis que NiV B présente une glycine. Le résidu en position 42 dans le fragment F2 est une valine pour NiV Mal et une isoleucine pour NiV Ban et pour HeV. Les régions HRN sont identiques pour NiV Mal, NiV Ban et HeV. En revanche, dans le domaine HRC, en positions 479 et 478 les deux souches de NiV portent une arginine et une leucine respectivement alors que HeV porte une lysine et une isoleucine. L'impact de ces différences de séquences sur les différences de pathogénicité dans le SNC par ces 3 virus n'a pas encore été étudié. Enfin, des différences d'actions du peptide HRC inhibiteur de fusion (VIKI-PEG4-

Cholestérol) dans des cultures organotypiques de cervelet de hamster face à ces trois virus (données non montrées) suggèrent l'importance de la F pour une dissémination dans le SNC.

2) Les facteurs influençant l'infection du système nerveux central par les Henipavirus

a. Article 7 : Comparaison de l'infection des Henipavirus dans le système nerveux central : tropisme précoce, entrée et machineries de fusion

Marion Ferren, Alexandre Lalande, Olivier Reynard, Mathieu Iampietro, Branka Horvat, Cyrille Mathieu

En préparation, 2022.

Abstract:

Nipah virus (NiV) and Hendra virus (HeV) are highly pathogenic zoonotic Henipavirus that exhibit great differences in pathogenicity and clinical symptoms, in receptor and tissue tropism, fusion machinery and replication mechanism. NiV Malaysia (NiV Mal) and NiV Bangladesh (NiV Ban) strains as well as HeV. In human, NiV Mal tends to induce more encephalitis while NiV Ban leads primarily to respiratory disease. HeV induces as many encephalitis and respiratory syndrome but is the least transmissible virus to human.

The early stages of the central nervous system (CNS) infection by these three viruses remain poorly documented because most of the data come from post-mortem analyzes. Here we identified factors influencing the CNS invasion by these viruses. The initial tropism, the dissemination, as well as the involvement of viral surface glycoproteins were analyzed for NiV Mal, NiV Ban and HeV at the organic, cellular, and molecular levels.

Organotypic cultures from hamster cerebellum, brainstem and lung are susceptible to the infection with these three viruses. We show that NiV Ban replicates faster than NiV Mal and HeV in CNS, however with more cytopathic effect rapidly limiting brain neuroinvasion. In these *ex vivo* cultures NiV Mal primarily targets granular neurons while NiV Ban and HeV infect neural cells more broadly without targeting a particular cell type.

We analyzed the binding and the fusion of NiV Mal, NiV Ban et HeV in presence of binding receptors. Moreover, we identified EFNB1 as a low affinity receptor allowing the binding of these three viruses as well as viral entry.

The comparative study of the organotypic culture infections by these respiratory viruses with high pathogenicity differences illustrated how the fusion machinery can influence the viral dissemination in the brain.

Henipavirus fusion machinery comparison and early tropism in the central nervous system

Marion Ferren, Alexandre Lalande, Olivier Reynard, Mathieu Iampietro, Branka Horvat, Cyrille Mathieu

Introduction

The emerging zoonotic paramyxoviruses Nipah virus (NiV) and Hendra virus (HeV) cause lethal encephalitis, with case fatality rates ranging from 50 to 100% [1,2]. Post mortem analysis clearly show the infection of the central nervous system (CNS). However, the early tropism of Henipavirus within neural cells remains poorly documented.

HeV first emerged in 1994 in Australia [3] and NiV emerged in Malaysia in 1998 [4]. The main natural reservoirs of Henipavirus are *Pteropodidae* fruit bats [5,6]. To date there is neither commercialized treatment nor vaccine available in human against these lethal infections with a global pandemic and bioterrorism potential [7,8]. Thus, NiV and HeV are classified as biosafety level 4 (BSL4) pathogens and in 2015 the World Health Organization (WHO) listed NiV among the top 8 diseases and pathogens to prioritize for research and development in public health emergency contexts [9]. All the data about the tropism of the infection within the CNS are from are originated from post mortem studies or late infection in animal models.

Despite their high sequence relatedness, NiV isolates and HeV exhibit great differences in pathogenicity and clinical symptoms. Among NiV isolates, the Malaysian strain (NiV Mal) appears to be highly encephalitogenic with a case fatality rate about 40%. NiV Mal can cause relapse encephalitis for 7.5% of the surviving patient without any re-exposure to the virus but also asymptomatic infection leading to late onset encephalitis years after infection [10], suggesting a potential viral persistence in the brain already observed in other encephalitic *Paramyxoviridae* such as Measles virus and canine distemper virus (CDV). The Bangladesh strain (NiV Ban) can be transmitted human to human. Moreover, NiV Ban is slightly less neuropathogenic and 70 to 100% of the patients are principally dying from the severe acute respiratory syndrome. Other NiV isolates have been described in fruit bats only in Ghana and in Cambodia but no human cases have been clearly identified [11–13]. Four of the 7 HeV infected patients died either from respiratory disease or either from acute encephalitis or for one case, from relapse encephalitis [14,15]. *In vivo*, in human, in hamster and in non-human primates, NiV Mal seems to initiate the infection in the trachea and progresses down the respiratory tract while HeV infection started mainly in the small airways of the lungs [16,17].NiV Mal and HeV acute encephalitis cause cerebellar atrophy, brainstem lesions, cortical nervous transmission abnormalities and white matter damage [15,18,19]. Surviving patients often showed neurological complication and motor dysfunctions [20]. For both viruses, the acute encephalitis started with the infection of endothelial cells leading to syncytia formation and generalized vasculitis, mainly in the lung but also in the brain, the heart and kidney

as well as a parenchymal inflammation and necrosis un the lung [19,21]. Then, the brain invasion is characterized by a direct neural infection in the brain that can be explained by the disruption of the blood brain barrier (BBB) due to the vascular inflammation or through infected dendritic cells crossing the BBB. Alternatively, another ways of infection through the olfactory nerve [22] or through the transinfection of neural cells from the circulating immune cells [23] have been validated in animal studies but none of these hypotheses has been confirmed in human who always develop generalized vasculitis. Viral RNA and antigens are found in neurons and in rare cases, in ependyma and blood vessels of patients that develop acute encephalitis [15,19].

For both NiV Mal and HeV, at the time of the relapses or late onset encephalitis, no systemic sign of infection is observed except in the brain; no vasculitis, no syncytia formation of endothelial cells and no inflammation of any other organ. NiV relapse or late onset encephalitis are characterized by large lesions with virus inclusions in neurons and in the neuropil, as a result of severe neuronal necrosis, gliosis, perivascular cuffing and inflammatory infiltrate. Viral RNA and antigens were found in neurons and also in glial and ependymal cells contrary to acute NiV infection and no demyelination has been observed [19]. The case of relapsing HeV encephalitis displayed a meningitis, an inflammation of the cerebral cortex, a perivascular cuffing, glial proliferation, reactive blood vessels and neuronal loss, associate with the detection of viral RNA and antigens in neurons and some glial cells [15].

Henipavirus infection starts by the fusion of the viral membrane with the cell host membrane. The glyocoprotein (G) binds to its receptor and allows the triggering of the pre-fusion F protein. The F undergoes a structural transition, extending and inserting its hydrophobic “fusion peptide” into the target cell. During entry, F refolds into a so-called “trimer of hairpins” (or 6-helix bundle) post-fusion structure that brings together the N-terminal heptad repeat (HRN) and the C-terminal heptad repeat (HRC), leading to the formation of the fusion pore between the viral and cell membranes. The G protein takes part at different level in this process: prior the binding to his receptor the G prevents the triggering of the F, after the binding the G triggers the F in the meta-stable conformation, and then pushes the F to accelerate the refolding of the F into the post-fusion stage.

Ephrin-B2 (EFN B2) and Ephrin-B3 act as entry receptor for both NiV and HeV [24,25]. The interaction between EFN B2 and EFN B3 with the monomeric soluble NiV Mal G and HeV G have been analyzed by surface plasmon resonance technology using a BIACORE 1000 with purified proteins or by quantifying the fusion after the transfection of F and G in presence of soluble monomeric EFN B2. EFN B3 has a lower affinity for NiV than EFN B2 [26]. It is speculated that the higher expression of EFN B3 in the brainstem could be linked with the severity of the neuron dysfunctions during NiV encephalitis [27]. EFN B2 is expressed in microvascular endothelial cells and smooth muscle cells in arterial vessels [28]. Within the brain, EFN B2 is mainly expressed in the cortex and neuroepithelial cells, but can also be detected in the olfactory bulb and the amygdala [29,30]. EFN B3 expression is mostly restricted to the CNS. EFN B3 has been highly detected in the occipital lobe, the prefrontal cortex, and the amygdala. At a lower levels EFN B3 can also be found in the pons, the globus pallidus, the subthalamic nucleus, the temporal lobe, the hypothalamus, the corpus callosum and the hippocampus [29–31]. Despite strong homology with Ephrin B2

and B3, Ephrin B1 (EFN B1) is not considered an entry receptor for NiV and HeV. Indeed, the two critical residues for the entry of the virus at position 121 and 122 (leucine and tryptophan) are common to EFN B2 and B3 and differ for EFN B1 (tyrosine and methionine). The data also show that EFN B1 binds 10 times less efficiently to NiV Mal G compared to EFN B2 [26].

To date, post mortem analysis performed in human and in animal models about the tropism of the Henipavirus infection within the CNS suggest that neurons are the major target for NiV Mal and HeV [32,33]. However, very little is known about the Henipavirus initial tropism and dissemination within the CNS.
Golden Syrian hamster is considered as a relevant small animal model that reflect the pathogenesis observed in human for several viruses [34] and more specifically for respiratory viruses that also target the CNS, such as NiV and HeV [32,35]. Hamster cerebellar organotypic cultures have been characterized and are relevant for studying CNS infection by neurotropic viruses and screening antiviral drugs [36–38]. These *ex vivo* cultures are particularly suitable to study the viral tropism at the beginning of the infection.
In this study, we compare the binding, the entry and the stability of the F of three different Henipavirus as well as their behaviors in *ex vivo* organotypic cultures from hamster lung, cerebellum and brainstem cultures.

Results

1) Differences of susceptibility and viral dissemination in hamster organotypic lung, cerebellum and brainstem cultures

Part of the differences in pathogenesis may rely on variation in organ susceptibility to the infection. First, in order to further characterize the organotypic cultures the mRNA expression of the EFN B1, B2 and B3 receptors have been quantified by RT-qPCR in the cerebellum and the brainstem cultures (Figure 1, A). Consistent with the literature, fewer EFN B2 mRNA expression has been quantified in the brainstem than in the cerebellum cultures. However, EFN B3 mRNA expression in similar in both brain substructures and can be attributed to the fact that EFN B3 is known to be less express in the pons than in other brain area. Based on this, we compare the viral dissemination of NiV Mal, NiV Ban and HeV in the hamster organotypic lung, cerebellum and brainstem cultures. The number of N copies per µg of total RNA of the three viruses, reflecting the viral load in cultures, has been quantified daily by RT-qPCR from the day 0 to the day 4 post infection (dpi). All viruses replicate faster and higher in brain cultures than lung cultures with 10 to 1000 times more N copies quantified per µg of RNA in the cerebellum and brainstem cultures compare to the lung (Figure 1, B). The viral growth has been expressed in fold change of the number of copies of N RNA at day 0 (Figure 1, C, D, E). Consistently with the pathogenesis, at 1dpi NiV Mal replicates significantly slower in the lung compared to NiV Ban and HeV (P values = 0.0159 and 0.0079, respectively). At 3 and 4 dpi the N copies numbers do not increase anymore for all viruses in the lung cultures, meaning that the maximum replication is reached (Figure

1, C). In the three substructures, the viral growth is faster for NiV Mal and HeV compared to NiV Ban. However, the total amount of RNA we have been able to extract from each sample of cerebellum (but not of the brainstem) was lower for NiV Ban from 2dpi to 4 dpi suggesting a cytopathic effect of the infection and cell death (data not shown).

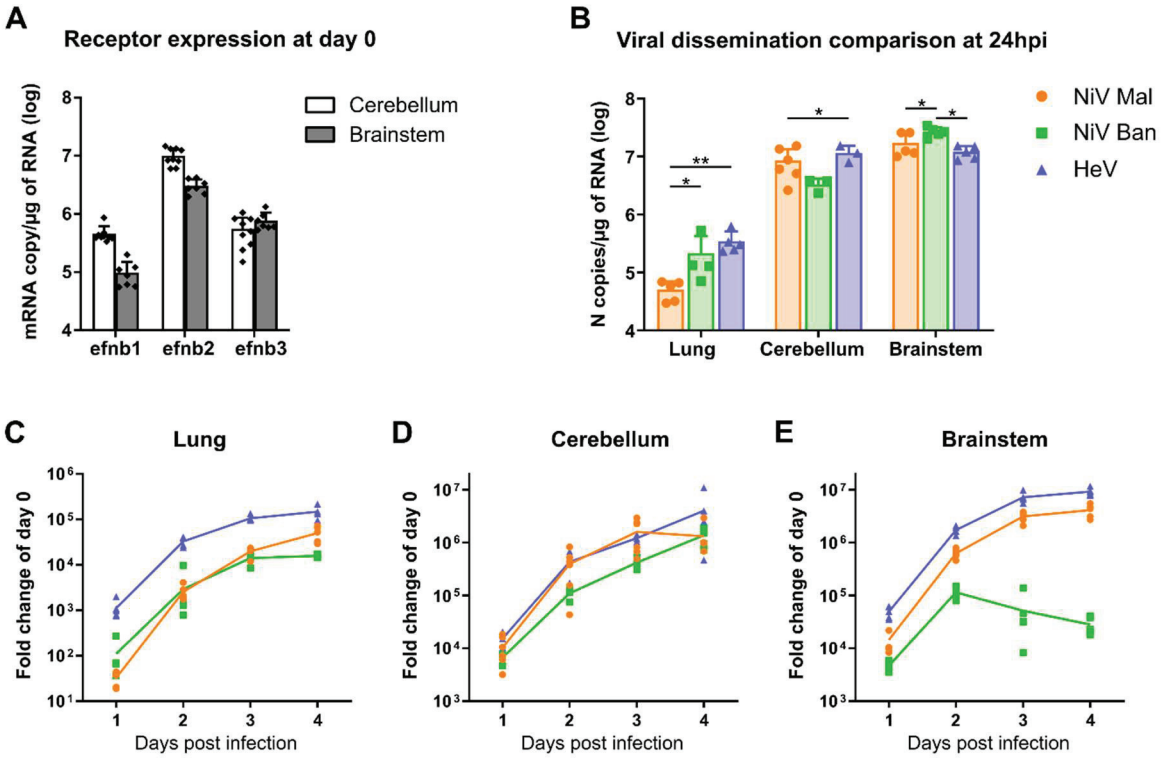

Figure 1: Viral dissemination of three Henipavirus in hamster organotypic cultures.

A, EFN 1, EFN B2 and EFN B3 basal mRNA expression in hamster organotypic cerebellum and brainstem cultures were quantified by RT-qPCR (day 0 of culture) (n = 10 biologically independent animals). **B, C, D, E,** Hamster organotypic cultures were infected with 500 PFU of NiV Mal, NiV Ban and HeV. NiV N and HeV N mRNA copies per µg of total RNA were quantified by RT-qPCR in the lung, cerebellum and brainstem organotypic cultures at 90 min post infection and 1–4 days post infection (dpi) and normalized to the standard deviation for GAPDH mRNA (n = 5 biologically independent animals). **B,** comparison of the N mRNA copies per µg of RNA quantified at 24 hours post infection for NiV Mal, NiV Ban and HeV (n = 5 biologically independent animals). **C, D, E,** Viral growth expressed in fold change of N mRNA copies per µg of RNA compared to the input from the day 0. Error bars represent SD. Statistical analyses were performed using the Mann–Whitney test two-sided. *P < 0.05.

2) **Differences in binding and viral entry between the three different Henipavirus**

Infection starts with the attachment to the target cells, thus to evaluate the binding of NiV Mal, NiV Ban and HeV, viral particles labeled with Atto-488 were incubated for 15min on ice with PGSA cells expressing EFNB1, EFNB2 or EFNB3. The percentage of cells bearing fluorescent viral particles was quantified by flow cytometry (Figure 2, A, B). The results showed that NiV Mal binding to all receptors is faster than NiV Ban and HeV binding. HeV binds only to 12,4% of cells, even in EFNB2 expressing cells. Interestingly, for all Henipavirus similar binding was observed on cells expressing only EFNB3 or EFNB1. In the EFNB1 expressing cells NiV Mal binds to 28,4% of cells and NiV Ban binds to 10,2% of cells.
The kinetic of entry of NiV Mal, NiV Ban and HeV was also compared after several binding time-lengths (Supplementary Figure 1). CHO-PGSA-745 cells expressing EFNB1, EFNB2 or EFNB3 were infected with the three viruses on ice and the viral replication was quantified by RT-qPCR 24 hours post infection. The results reflect the entry of the viruses that were able to bind during the indicated time. For all cell types, the kinetic showed a slower infection for NiV Mal compared to NiV Ban and HeV. In opposition to both NiV, HeV infection already reached the plateau when the binding with EFNB2 was only 5 min. Under these conditions, even if fewer viral particles have bound, the strong replication quickly saturates the system.

Regardless the binding, the entry of the three Henipaviruses was analyzed. NiV Mal, NiV Ban and HeV were bound for 1 hour on ice with PGSA-745 cells expressing similar level of human EFNB1, EFNB2 or EFNB3 (Supplementary Table 1). Then, the cells were either treated directly with pronase in order to remove all bound viral particles from the cell surface and incubated at 37°C in presence of fusion inhibitory peptide to block further entry and dissemination [39] or incubated for 30min at 37°C to allow the entry of bound particles and then treated with pronase and incubated at 37°C overnight in presence of peptide to prevent any viral dissemination (Figure 2, C). The percentage of infected cells reflecting the entry (and thus fusion) was quantified by intra cellular nucleoprotein staining by flow cytometry 24 hours post infection (Figure 2, D, E). In opposition with the binding results, NiV Ban and HeV entered better and faster than NiV Mal in presence of EFNB2 and EFNB3 expression and were able to infect up to 20% of EFNB2 expressing cells and up to 10% of EFNB3 expressing cells. Some infected cells were counted in the PGSA-EFNB1, especially for NiV Ban (4% of infected cells).

Taken together these data show that NiV Mal is the fastest to bind but the slowest to fuse with the target cells while the slow binding of HeV is balanced by its especially fast fusion capacity. NiV Ban displays an intermediate phenotype. In addition, EFNB1 is not described in the literature as an entry receptor for NiV and HeV. However, these results show that NiV Mal, NiV Ban and HeV are all able to use EFNB1 for binding and for entry at least to a low extend. The infection of CHO-K1 and CHO-PGSA-745 cells in comparison with PGSA-EFNB1 and EFNB2 confirm that the entry shown here is specific (Supplementary Figure 2).

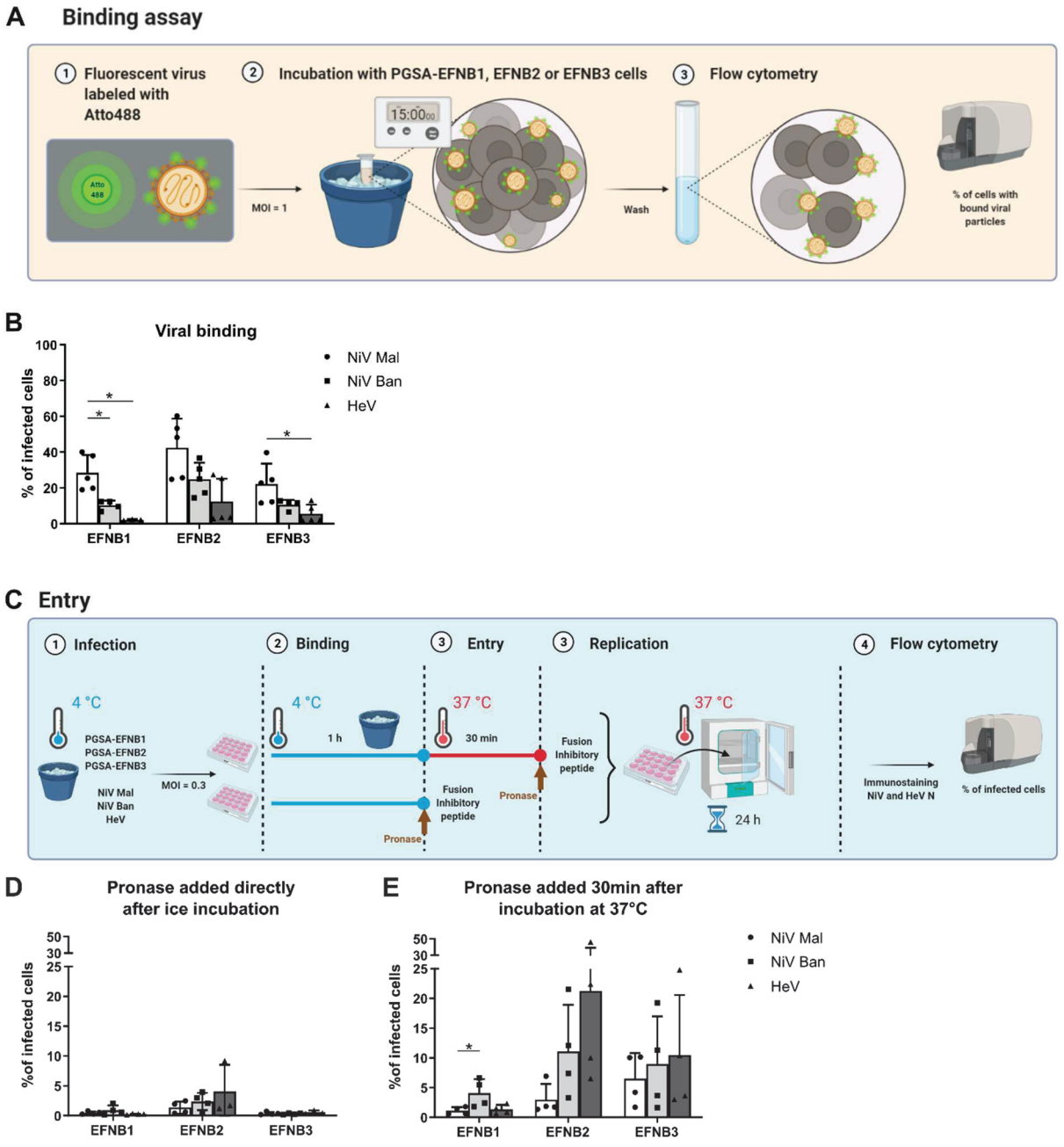

Figure 2 : Comparison of the viral binding and viral entry. A, Schematic of the procedure to evaluate the binding of NiV Mal, NiV Ban and HeV. Atto-488-labeled viruses were incubated for 15 min on ice with PGSA cells expressing EFNB1, EFNB2 or EFNB3 at MOI=1. **B,** The percentage of cells bearing a fluorescent viral particle was quantified by flow cytometry. (n=5 biologically independent samples over 3 independent experiments). **C,** Schematic of the procedure to evaluate the entry of NiV Mal, NiV Ban and HeV. Viruses were incubated for 1 hour on ice with PGSA cells expressing EFNB1, EFNB2 or EFNB3 to allow binding at MOI=0.3. The cells were then either treated directly with pronase in order to remove all bound viral particles at the cell surface and incubated at 37°C in presence of fusion inhibitory peptide or incubated for 30min at 37°C to allow the entry of bound particles and then treated with pronase and incubated at 37°C overnight in presence of peptide to prevent any

dissemination. **D-E,** The percentage of infected cells was quantified by flow cytometry 24 hours post infection (n=4 biologically independent samples over 4 independent experiments). Error bars represent SD. Statistical analyses were performed using the Mann–Whitney test two-sided. *P < 0.05.

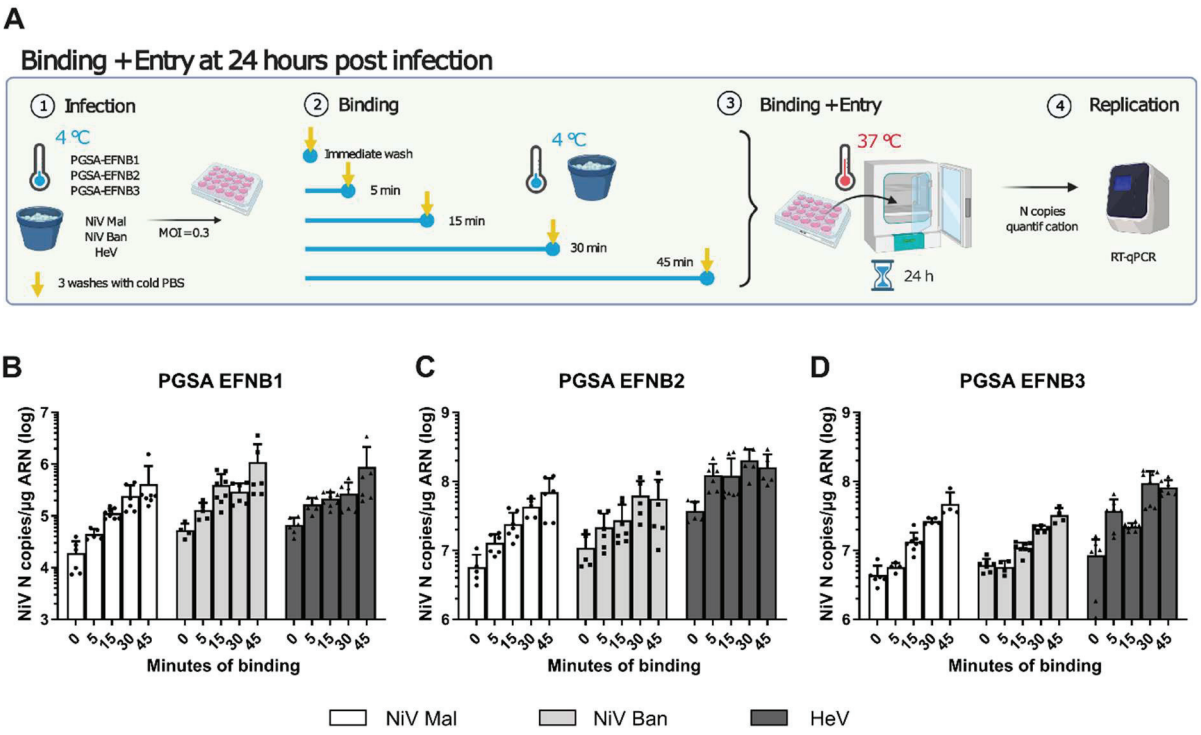

Supplementary figure 1 : Binding and Entry of Henipaviruses in presence of EFNB1, EFNB2 or EFNB3 expression. A, Schematic of the experiment. Cells were infected with NiV Mal, NiV Ban and HeV on ice. The cells were immediately washed with cold PBS or incubated with the viral supernatants for 5, 15, 30 and 45 min on ice. The cells were washed 3 times and incubated at 37°C. 24 hours post infection the cells were collected in order to quantify the N copies of NiV or HeV per µg of ARN by RT-qPCR. The results reflect the entry among the viruses that was able to bind in the indicated time in presence of **B,** EFNB1 expression, **C,** EFNB2 expression or **D,** EFNB3 expression. (n=5 to 8 biologically independent samples over 5 independent experiments). Error bars represent SD.

3) Differences in the fusion machinery of the Henipavirus

Paramyxovirus surface glycoproteins are known to be sensitive to increase of temperature which affect infectivity. Here, the comparison of the thermal stability of viruses allows a better characterization of the fusion machinery. 10^4 PFU of viral supernatants were incubated for 5 or 15 min at 50°C, cool down, and titrated by TCID50. The decrease of infectivity by NiV Mal, NiV Ban and HeV was quantified by comparison to the non-heated viral supernatant kept at 4°C (Figure 3, A). 75% of the infection was already inhibited after 5 min incubation at 50°C for HeV while only 20 to 40% of the infection was inhibited for both NiV Mal and NiV Ban, respectively (Figure 3, B, C). After 15 min incubation at 50°C HeV was fully inactivated and 75% of NiV Mal and NiV Ban infections were inhibited. These results show that, at 50°C, the

fusion machineries of NiV Mal and NiV Ban are significantly more stable than HeV. In order to assess the thermal stability of the F independently of the G proteins a cell surface ELISA using an antibody that recognize the F in their prefusion conformation was performed. 293T cells were transfected with NiV Mal F, NiV Ban F and HeV F and the prefusion F were stained after 30 min incubation at 32°C or at 55°C (Figure 3, D). The preliminary qualitative results analyzed using an epifluorescence microscope show, despite a similar level of transfection, a stronger reduction of the prefusion F staining for NiV Mal F and NiV Ban F compared to HeV F after 10 min incubation at 55°C. This data suggests that in absence of the protection of the G protein NiV Mal F and NiV Ban F are less stable than HeV F. On the contrary, HeV F seems to need the interaction with G in order to be triggered and to reach its post fusion conformation. This experiment will be repeated and a quantitative analysis will be performed using the spinning disk confocal microscope HCS Yokogawa CQ1 in order to confirm these data. In order to better characterize the exact role of G in the triggering of the F we will also repeat this experiment in presence of G in the same assay and in PGSA-745 cells that does not express any high affinity or secondary binding receptor. However, transfection of wild type HeV G does not allow its appropriate expression at the cell surface because of retention in the Golgi. We will have to use instead a plasmid encoding for the HeV G ΔCT32 lacking the cytoplasmic domain of the G which might induce a bias in the experiment.

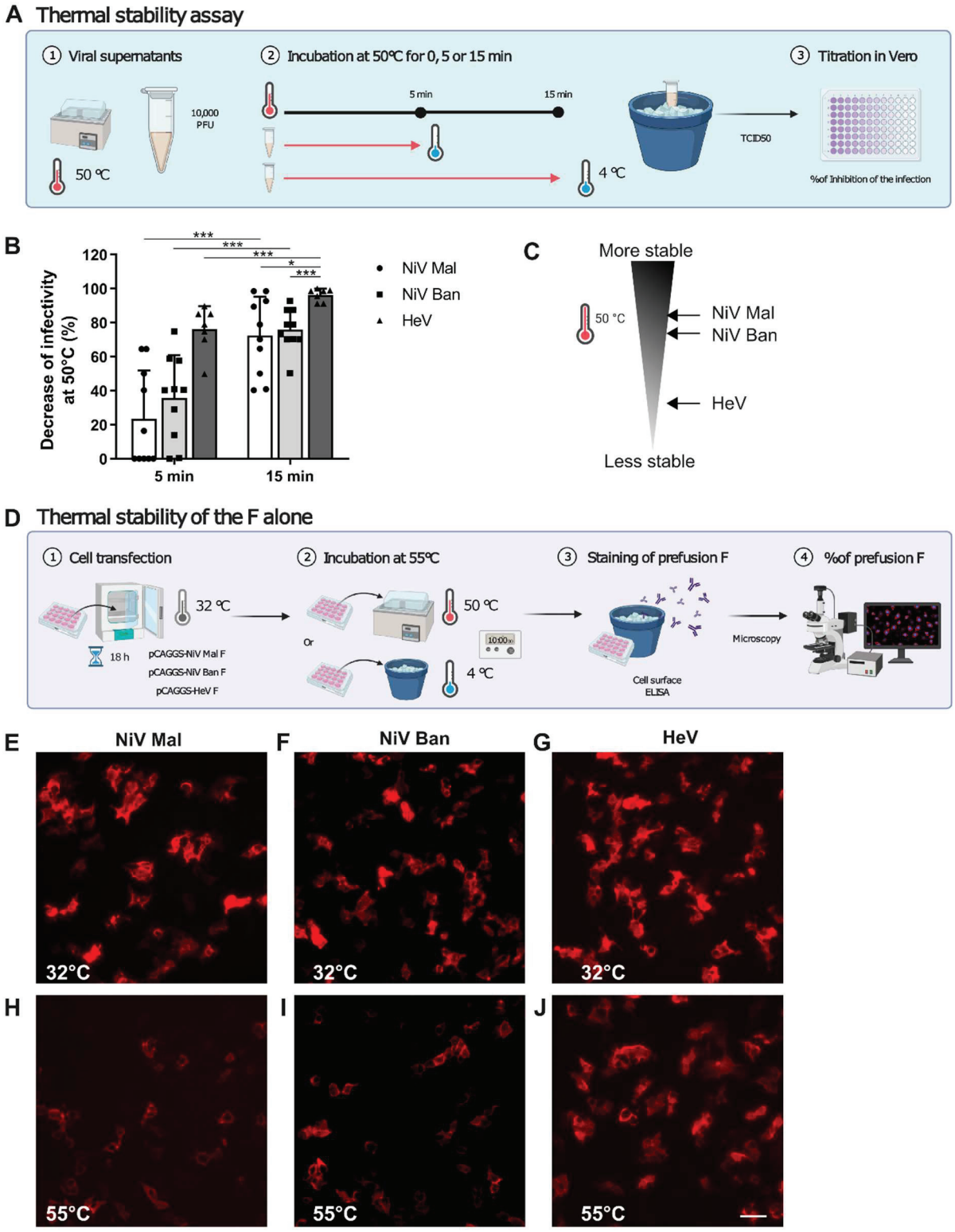

Figure 3 : Differences in the thermal stability of the Henipavirus. **A,** Schematic of the experiment. 10^4 PFU of viral supernatants were incubated for 5 or 15min at 50°C, cool down, and tittered by TCID50. **B,** The decrease of the infectivity by NiV Mal, NiV Ban and HeV was quantified by comparison to the non-heated viral supernatant containing the exact same number of PFU. (n=7 to 10 biologically independent samples over 7 to 10 independent experiments). Error bars represent SD. Statistical analyses were performed using the Mann–Whitney test two-sided. *P < 0.05. **C,**

schematic showing the thermal stability of NiV Mal, NiV Ban and HeV with live viruses. **D, E, F, G, H, I, J,** 293T cells were transfected with NiV Mal F, NiV Ban F and HeV F and incubated at 32°C. 16 hours later, cells were incubated at 32°C or 55°C during 10min and the F in the prefusion stages were stained by cell surface ELISA using the antibody SN hybridoma Nip GIP35 (1/500). Fluorescent staining was observed under the epifluorescence Nikon Eclipse Ts2R microscope. Scale bar 20µm.

4) NiV Malaysia preferentially targets neurons while NiV Bangladesh and HeV tropism is broader

To determine the most susceptible cells to NiV Mal, NiV Ban and HeV infection, the viral tropism was evaluated 24 hours post infection in hamster OCC by immunofluorescent staining analyzed by confocal microscopy (Figure 4). For all Henipaviruses NiV N staining colocalized with NeuN- positive cells (Figure 4, A, D, G), confirming the infection of granular neurons. NiV N staining was commonly found in astrocytes (GFAP staining), and Oligodendrocytes (Olig-2 staining) in OCC infected with HeV and NiV Ban (Figure 4, B, C, H, I) but not in OCC infected with NiV Mal (Figure 4, E, F). We did not observe any infection of Purkinje neurons (using anti-CB28K antibody, data not shown), suggesting that under the given conditions the viruses targeted specific neuronal subtypes but not all. The microglia will be stained in the future to assess their susceptibility in hamster OCC. The results are summarized in the Table 1.

Table 1 : Summary of the Henipavirus infection in several central nervous system cell types in hamster organotypic cerebellum cultures at 1 day post infection

	NiV Mal	NiV Ban	HeV
Granular neurons	**+**	**+**	**+**
Oligodendrocytes	-	**+**	**+**
Astrocytes	**-**	**+**	**+**
Microglia	Not done	Not done	Not done
Purkijne neurons	**-**	**-**	**-**

Supplementary table 1 : EFN mRNA expression in PGSA-EFNB1, EFNB2 and EFNB3 cells

mRNA copies/µg of RNA	EFNB1	EFNB2	EFNB3
PGSA-EFNB1 cells	**$1{,}1.10^6$**	BQL	BQL
PGSA-EFNB2 cells	BQL	**$4{,}7.10^6$**	BQL
PGSA-EFNB3 cells	BQL	BQL	**$8{,}4.10^6$**

BQL = Bellow Quantification Limit

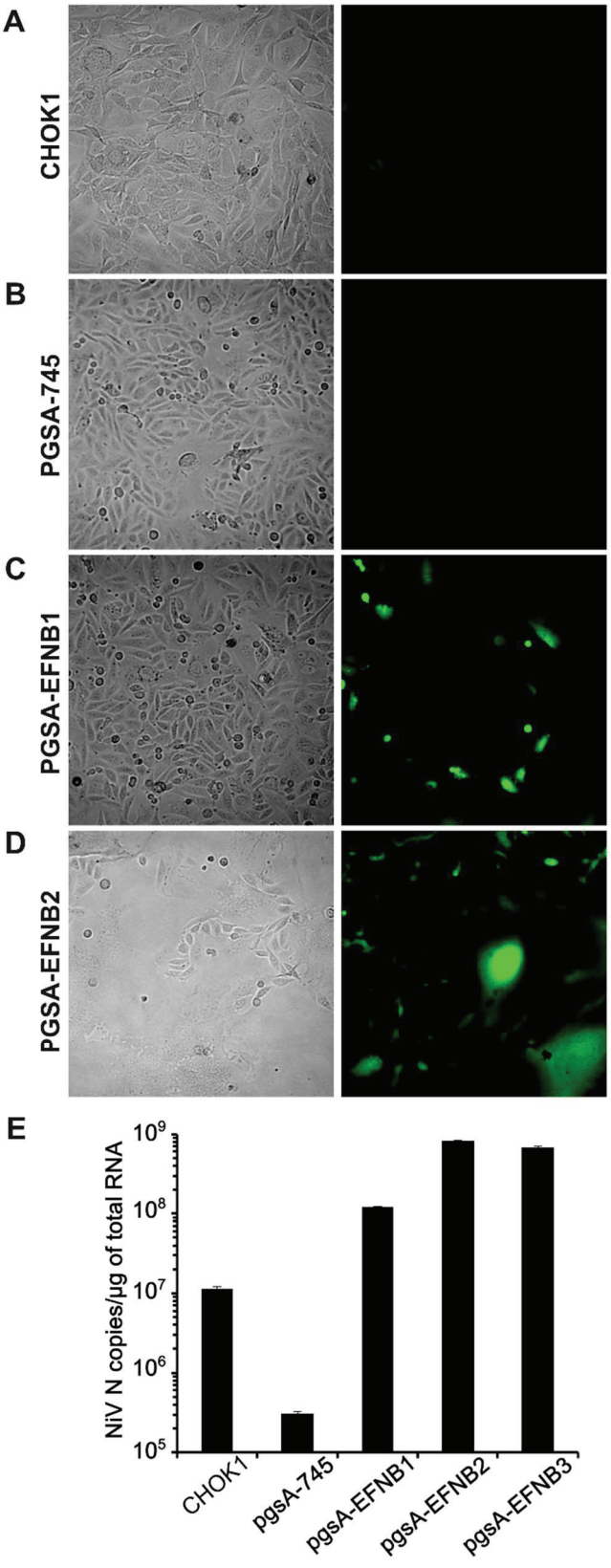

Supplementary figure 2 : NiV Malaysia replication in presence or in absence of known receptor. **A-D,** CHOK1, PGSA-745, PGSA-EFNB1 and PGSA-EFNB2, respectively, were infected with rNiV-eGFP at MOI=1. Pictures were taken one day post infection using a Zeiss Axiovert 100M microscope. **E,** 24 hours post infection the

RNA were extracted from the cells in order to quantify NiV N copies µg of ARN by RT-qPCR. Error bars represent SD.

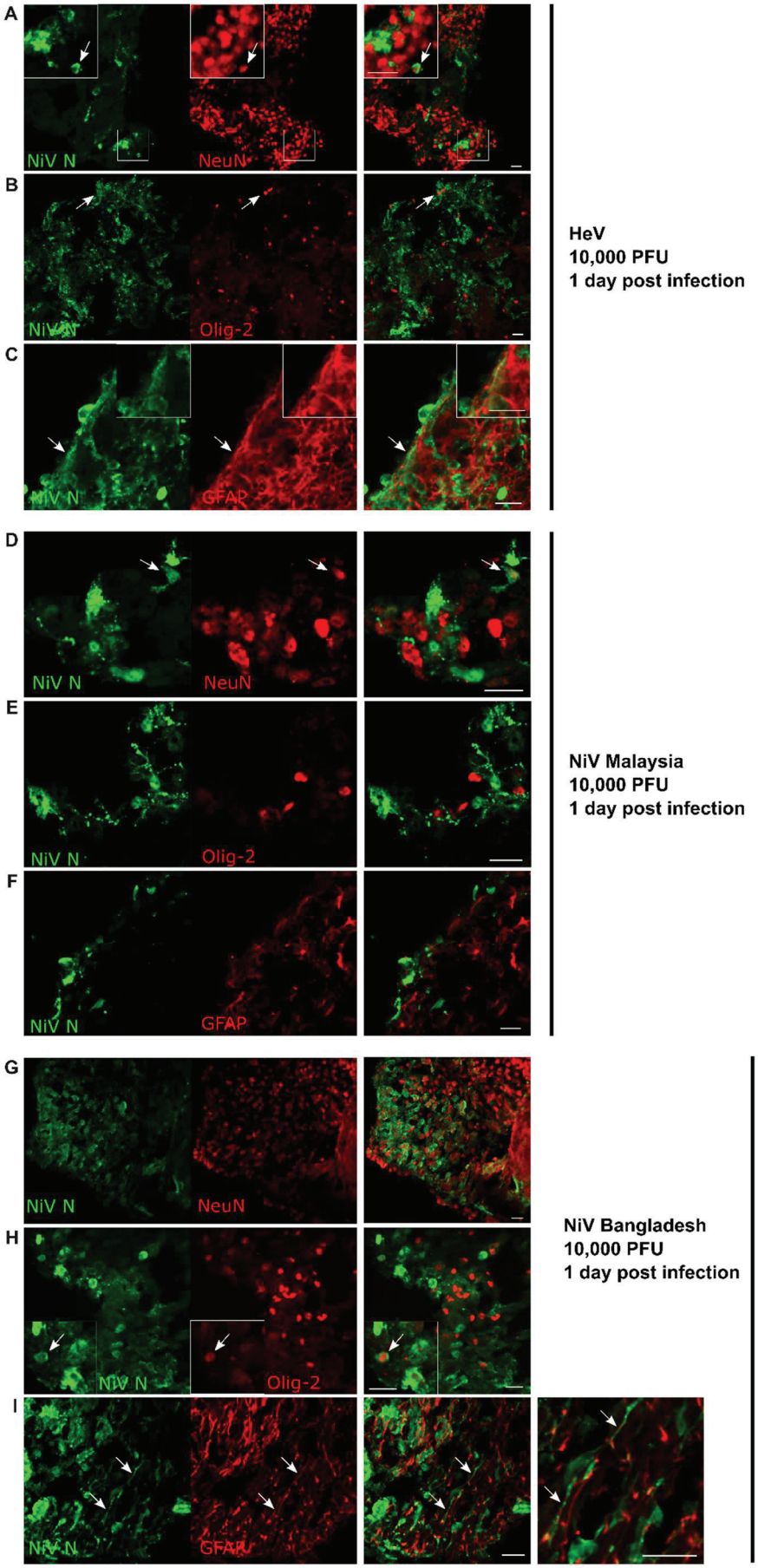
A
NiV N
NeuN
B
NiV N
Olig-2
C
NiV N
GFAP
HeV
10,000 PFU
1 day post infection
D
NiV N
NeuN
E
NiV N
Olig-2
F
NiV N
GFAP
NiV Malaysia
10,000 PFU
1 day post infection
G
NiV N
NeuN
H
NiV N
Olig-2
I
NiV N
GFAP
NiV Bangladesh
10,000 PFU
1 day post infection

Figure 4 : Henipaviruses tropism in hamster cerebellum organotypic cultures one day post infection. Cultures were infected with 10^4 PFU of HeV, NiV Mal or NiV Ban and fixed with formaldehyde 4% 24 hours post infection. Cryosections of the cultures were stained with antibodies anti-NiV_N cross reacting with HeV N and **A, D, G,** anti-NeuN, **B, E, H,** anti-Olig2 and **C, F, I,** anti-glial fibrillary acidic protein (GFAP). Images were taken using an inverted microscope Zeiss Axio Observer. Z1 with confocal unit LSM 980 and analyzed using ImageJ software. White arrows are pointing colocalization area between the NiV-N staining and the staining of interest. Scale bar 20 µm.

Discussion

NiV isolates and HeV exhibit great differences in pathogenicity and clinical symptoms, in receptor and tissue tropism, fusion machinery and replication mechanism. Here we aimed to understand the factors influencing these differences and to do so we compared NiV Mal, NiV Ban et HeV infection in hamster organotypic cultures from lung, cerebellum, and brainstem as well as their binding and entry properties in absence and in presence of the receptors.

We hypothesized that the differences in pathogenicity between strains could be explained by a difference in susceptibility at the organic scale explained by the distribution of the expression of the input receptors. In the literature EFNB1 is not presented as an input receptor for NiV Mal, NiV Ban or HeV. However, it has been shown that the binding of NiV Mal G to EFNB1 is 10 times lower than EFNB2 [26]. In this study Ephrin-B1 was included as a comparison to study the binding and the entry of NiV Malaysia, NiV Bangladesh and HeV. However, our data clearly show in that the context of infection with live viruses NiV Mal, NiV Ban and HeV are able to use EFNB1 (Figure 2, B, G, and Supplementary Figure 1). It seems that EFNB1 is a low affinity receptor allowing the binding of these three viruses as well as viral entry. A recent study has shown that NiV Mal can replicate without any cytopathic effect in smooth muscle cells that lack the expression of EFNB2 and EFNB3 receptors[40]. These cells express EFNB1 and the results of this study confirm that the expression of EFNB1 is sufficient for NiV permissiveness.

EFNB3 is also described as being a receptor of lower affinity for NiV Mal and NiV Ban compared to HeV[26]. In our model, the quantification of EFN mRNA expression level in hamster organotypic cultures do not witness a higher expression of EFNB3 in the brainstem compared to EFNB2 mRNA expression cultures in opposition with one unmissable publication[27] (Figure 1, A). The overexpression of EFNB3 in the brainstem compared to EFNB2 is not described in other publications. However, it is known that EFNB2 and EFNB3 expressions are both very high in the developmental stages of the CNS, and our organotypic cultures from suckling animals may contain some remaining immature cells. In addition, although our models lack any blood circulation, the cultures still contain the endothelial cells of the blood vessels which express very strongly Ephrin B2 and potentially bias the results of this experiment.

In hamster organotypic cerebellum and brainstem cultures NiV Ban viral replication is faster at early times in comparison with NiV Mal and HeV while this virus is the least encephalitogenic of the three (Figure 1, B-E). This result goes along with a decline in viral growth from the third day of infection. In the brainstem, no difference of the RNA quantification can explain the drop of the viral dissemination at 3 and 4 dpi for NiV Ban and this result has to be investigated more deeply in the future. These results demonstrate that if NiV Ban reaches the CNS, this virus is able to replicate there very strongly.

We then aimed to establish a link between the early tropism of each Henipavirus in the CNS that could explain some differences in the pathogenicity (Figure 4). NiV Mal primarily targets granular neurons while NiV Ban and HeV appear to infect neural cells more broadly without targeting a particular cell type [41 42]. NiV Ban is, however, poorly encephalitogenic and the massive infection of CNS cells is consistent with the strong viral replication and cytopathic effect observed in brain tissue. This dispersive tropism for NiV Ban and HeV leads to a very strong infection of the CNS. The fact that encephalitis is much less common for NiV Ban than for NiV Mal despite its strong ability to invade the CNS is suggests that NiV Ban generally does not have time to reach the CNS.

In order to better understand the differences between the fusion machineries of NiV Mal, NiV Ban et HeV we compared their ability to bind and to fuse in presence of each known receptors and we compared the thermal stability of the Fusion proteins.

Our results showed that NiV Mal binds faster to any binding receptors than NiV Ban and HeV. However, the analysis of the entry into the target cells highlights that HeV is the fastest virus, which suggests that its fusion is more efficient. NiV Ban exhibits an intermediate phenotype both for the binding and the entry, except in the cells expressing EFNB1. Indeed, NiV Ban is the fastest virus to fuse in cells expressing the EFNB1 receptor. The importance of this observation should be compared to its more pulmonary pathogenesis to see if this could explain why this strain generates more SARS than lethal encephalitis.

The thermal stability of Henipavirus viral particles in the context of infection indicates that HeV is much less stable than NiV Mal and NiV Ban. However, in the context of transfection in the absence of G we obtained the opposite results. HeV F remains in a prefusion state even after 10 min at 55 °C while NiV Mal and NiV Ban F can be triggered very quickly.

Taken together, my results have led us to the following interpretation. Both NiV F are very unstable in the absence of G, moreover it is easily observed by the appearance of syncytia when cells are transfected with F alone, even at 37 °C. This suggests that NiV Mal and NiV Ban G particularly assumes their protective function on the F to prevent its inadvertent triggering. Following the F triggering, the fusion seems slower, meaning that the refolding of the F to promote the fusion could be similar as the F from hyperfusogenic MeV mutants of the HRC domain[43]. It can be explained by the slower triggering of the F by the G or by a slower triggering followed by a lower pushing from the G. However, HeV F is naturally much more stable but can refold in

post fusion state extremely fast, probably due to the triggering and "pushing" action of the G which allows the fusion to be completed more quickly. This would result in a very rapid entry, despite a lower binding to the receptors. This theory would also explain the better efficiency of the fusion inhibitory HRC peptides on both NiV strains compared to HeV. Indeed, in the case of the hyperfusogenic F of MeV the fusion is slower and gives more time to the HRC peptides to associate with the HRN of the F and block the fusion. Alternatively, since the peptide has to compete with the HRC domain from the F when the latter is in its metastable state the very rapid refolding of HeV F would not allow the peptides to interpose quickly enough.

Method

Viruses

NiV-Bangladesh isolate SPB200401066 (GenBank accession no. AY988601, passage 3) was isolated from oropharyngeal swabs from a patient in Rajbari and obtained from the Centers for Disease Control and Prevention in Atlanta.
NiV Malaysia isolate UMMC1 (GenBank accession no. AY029767, passage 7) was isolated from the cerebrospinal fluid of a patient was obtained from Drs. K. B. Chua and S. K. Lam (University of Malaya, Kuala Lumpur).
Hendra virus isolate Australia/1994/Horse18, (GenBank accession number MN062017.1) [44] was isolated from a horse and obtained from Porton Down Laboratory, United Kingdom.
The recombinant NiV (rNiv)–enhanced green fluorescent protein (eGFP) (rNiV-EGFP) was generated using reverse genetic in 293 cells and prepared as previously described [45].
All viruses were produced and titrated at 37°C in Vero E6 cells. Briefly, for stock production, cells were infected with MOI=0.001 in OptiMEM. After 60min incubation at 37°C, medium was replaced with DMEM-5% FBS and the cells were incubated at 37°C in 5% CO2 atmosphere for 48 hours. Viral supernatants were collected and centrifuged (400g, 5min), aliquoted and titrated in plaque forming unit by classic dilution limit assay.
All infections were carried out at the INSERM Jean Mérieux biosafety level 4 (BSL-4) laboratory in Lyon, France.

Cell culture

293T and Vero E6 cells were grown in Dulbecco's modified Eagle's medium (DMEM, Gibco) supplemented with 10% fetal calf serum (FCS) at 37°C in 5% CO2 atmosphere.

The CHO-pgsA745-EFNB1, CHO-pgsA745-EFNB2 and CHO-pgsA745-EFNB3 were stably transfected with human ephrin-B1, B2 and -B3 and generously provided by Benhur Lee (UCLA, United States) [26].

These cells were maintained in DMEM/Nutrient Mixture F-12 Ham medium (Sigma-Aldrich, # D6421) supplemented with 10% FCS, NEAA, NaPy and L-Glutamin 10 mM HEPES, and 2 mM L-glutamine at 37°C in 5% CO2 atmosphere.

All cells were routinely tested negative for mycoplasma every month (MycoAlert Detection Kit; Lonza).

Binding Assay for viruses labeled with Atto-488

In order to produce viral stocks labeled with Atto-488 (Sigma-Aldrich, # 41051) the first step was to produce purified and concentrated viral stocks. Viral stocks were produced as described above except that after the quick centrifugation (400g, 5min) the supernatants were ultra-centrifuged on a 20% sucrose cushion during 1 hour at 175,000 g at 4°C using the SW 32 Ti rotor (Beckman Coulter, # 344058) and resuspended in PBS. Ultracentrifugated viral solutions were then titrated in PFU by classic dilution limit assay and conjugated with Atto-488 following Hoffmann et al. recommendations [46]. Briefly, 1.10^9 PFU purified viral solutions were incubated at room temperature for 2 hours protected from light while gently mixing on a shaker with 200µl of a solution of 0.5mg/ml of Atto-488. Freshly labeled viruses were then purified by ultracentrifugated on a 20% sucrose cushion to eliminate the excess of Atto-488 during 1 hour at 175,000 g at 4°C (acceleration and deceleration set to max and min, respectively). Pellets were then resuspended in PBS and these new virus stocks were aliquoted, frozen at -80°C and titrated as described above.
In order to compare the binding capacity of the three Henipaviruses, CHO-pgsA745-EFNB1, CHO-pgsA745-EFNB2 and CHO-pgsA745-EFNB3 were gently detached using Versene (Gibco, # 15040066) and infected with the Atto-488 labeled viruses on ice at a MOI of 1 in OptiMEM. Unbound particles were washed twice by centrifugation with cold PBS and fixed with 4% methanol-free Formaldehyde (ThermoFisher Scientific, # 28906) for 20min. After 2 washes cells were resuspended in PBS and the number of cells carrying a labeled viral particle was quantified by flow cytometry.

Henipaviruses entry comparison assay

CHO-pgsA745-EFNB1, CHO-pgsA745-EFNB2 and CHO-pgsA745-EFNB3 were infected on ice at MOI=0.3 and incubated on ice for 1h to allow binding. Then, cells were incubated at 37°C for 0 or 30min and treated with 1µM of the fusion inhibitory peptide VIKI-PEG4-Chol to block the viral entry. In order to detach all the viral particles that were bound at the cell membranes but did not enter the cells a pronase treatment (200µg/ml) was performed during 10min (4min at room temperature and then 6min at 37°C because of the BSL4 constraints). Cells were washed with the complete DMEM/Nutrient Mixture F-12 Ham medium and incubate in a fresh culture plate at 37°C in 5% CO2 atmosphere in presence of 1µM VIKI-PEG4-Chol peptide.

24 hours after infection cells were detached using a P1000 pipet and stained using the BD Cytofix/Cytoperm Kit, (BD biosciences, # 554714). First the cells were centrifuged at 1000g for 2min and resuspended in the Fixation/Permeabilization solution during 30min. After 2 washes in PBS, cells were stained with the primary rabbit anti-NiV N purified antibody (ValBex, France) (cross reacting with HeV N) diluted 1/1000 during 30min. Cells were washed in PBS and incubated with the secondary antibody Alexa FluorTM 647 Donkey anti-Rabbit IgG (H+L); (ThermoFisher Scientific, # **A32795) diluted 1/1000 during 30min. Cells were washed and resuspended in PBS. Infected cells were quantified by flow cytometry using a** Gallios cytometer from Beckman Coulter.

Henipavirus thermal stability assay

In order to compare the termal stability of NiV Malaysia, NiV Bangladesh and HeV, 1.10^5 PFU of viruses were heated at 50°C for 0min, 5min, 10min and 15min and 20min in a water bath. Virus solutions where then cool down on ice and tittered by TCID50 on Vero cells. Titrations were revealed 5 days post infection using a Crystal violet solution (Sigma-aldrich, # HT90132) containing 4% Formaldehyde. The percentage of infection remaining after 5min, 10min and 15min heat at 50°C was calculated compared to the non-heated condition.

Henipaviruses binding and entry comparison

To compare the binding and the entry of NiV Malaysia, NiV Bangladesh and HeV in CHO-pgsA745-EFNB1, CHO-pgsA745-EFNB2 and CHO-pgsA745-EFNB3, cells were infected on ice at a MOI of 0.1 and washed 3 times with cold PBS at 0, 5, 15, 30 and 45min after infection. Cells were then incubated 37°C in 5% CO2 atmosphere. 24 hours post infection cells were collected in the lysis buffer RLT (Qiagen, # 79216) in order to quantify NiV N and HeV N RNA copies by RT-qPCR.

RNA Extraction and quantitative RT-PCR

Total RNA from organotypic cultures or from cell lysates were extracted using the NucleoSpin RNA Kit (Macherey-Nagel) and quantified with a spectrophotometer (DS-11-FX, DeNovix). 100 ng of total RNA were reverse-transcribed using the iScript cDNA Synthesis Kit (Bio-Rad), based on oligo-dT and random hexamer primers. Obtained cDNAs were diluted 1:10. Quantitative PCR was performed using Platinum SYBR Green qPCR SuperMix-UDG (Invitrogen) on a StepOnePlus Real-Time PCR System (Applied Biosystems). NiV N copies were quantified using the NiV N primers, forward primer 5' GGCAGGATTCTTCGCAACCATC 3', reverse primer 5' GGCTCTTGGGCCAATTTCTCTG 3' [47]. HeV N copies were quantified using the HeV N primers, forward primer 5' GGCCGGCTTCTTTGCGACTATC 3', reverse primer 5' CGCTCGAGGCCCTATTTCTCTG 3. The primer used to quantify hamster EFN B1, B2 and B3 were respectively: hamster_efnb1 froward 5' CTCACCTTCGGCATCTAT 3' and reverse 5' GTGTGCTTTCTCGTACTG 3'; hamster_efnb2 froward 5' GCTTTGGGAGATGGTTTA 3' and reverse 5' GTGGTGATGGACTTACAG 3';

hamster_efnb2 froward 5' CGAAAACCTGTGTCTGAAATG 3' and reverse 5' GTCACCTGGTAGGCTGTC 3'.
All primer were designed using the Beacon Designer (version 8) software and chosen after validation that their efficacy was close to 100% according to the MIQE checklist [48]. All samples were run in duplicates and results were analyzed using StepOne version 2.3 (Applied Biosystems). All results were normalized to the standard deviation (SD) for *GAPDH* (Glyceraldehyde 3-phosphate dehydrogenase) mRNA using mouse-GAPDH primers (forward primer 5' GCATGGCCTTCCGTGTCC 3' and reverse primer 5' TGTCATCATACTTGGCAGGTTTCT 3' [23]), and the calculations were performed using the 2ΔΔCT model [49].

Animals

Suckling Syrian golden hamsters (Mesocricetus auratus) used in this study were obtained from Janvier Labs (53940 Le Genest-Saint-Isle, France) with clean health monitoring report. C57BL/6 suckling mice are coming from the animal facility "Plateau de Biologie Expérimentale de la Souris" (PBES) in Lyon.
All animals were used at seven days old. The sex of the animals were random and dependent of the litter threw by the mother.

Organotypic culture preparation and treatment

Organotypic cultures were prepared from suckling hamsters (*Mesocricetus auratus*, Janvier lab) or C57BL/6 mice and maintained in culture as detailed elsewhere [37]. Briefly, organ substructures (i.e. cerebellum, brainstem, left lung) were isolated from 7-day-old animals (n=5; sex non-discriminated) and cut with a McIlwain tissue chopper (WPI-Europe): 350-µm-thick progressive slices were prepared for brainstems and cerebella, and 500-µm-thick slices for the lungs. The cultures were then separated from each other in cold Hibernate®-A/5 g/L D-Glucose/1x Kynurenic acid buffer and laid out on hydrophilic polytetrafluoroethylene cell culture insert membranes (PICM0RG50, Millipore). Slices were subsequently cultured in Minimal Essential Medium GlutaMAX supplemented with 25% horse serum, 5 g/L glucose, 1% HEPES (all Thermo Fisher Scientific), and 0.1 mg/L human recombinant insulin (Sigma-Aldrich) at 37°C in 5% CO_2. The medium was changed every other day after the slicing procedure. Slices from 5 different animals were infected on the day of slicing. When using the rNiV-EGFP the fluorescence was followed by microscopy using a Zeiss Axiovert 100M.

Immunofluorescent staining

Organotypic cultures from seven-day-old hamsters were infected with 10,000 PFU. 24 hours post infection, the slices were fixed in 4% paraformaldehyde (PFA) during 14 days, washed 3 times in PBS and immerged in a 20% sucrose solution at 4°C during 24 hours. Sunk slices were then frozen in dry-iced cold Isopentane (VWR, # 24872.298), embedded in Optimal cutting temperature (OCT) solution (Neg-50, ThermoFisher, # 6502) and kept at -80°C. 10µM section were performed using a Cryostat, placed on Superfrost Plus Gold microscope slides (Thermoscientific ;

#K5800AMNZ72) and warmed during 1 hour at 45°C. Sections were then cirle with a hydrophobic PAP pen (KISKER, #MKP-1), permeabilized and blocked in 1× PBS-4% horse serum- Triton X-100 (perm and block solution) during 30min at 4°C. Slices were incubated in the perm and block solution containing the primary antibodies overnight at 4°C. After 3 washes (5 min each) in PBS, slices were incubated in the perm and block solution containing the secondary antibodies for 1 hour at RT (Table 2). After 3 washes in PBS, slices were mounted with Fluoromount-G® aqueous mounting medium (SouthernBiotech, #0100-01) and coverslipped. Images were taken using an inverted microscope Zeiss Axio Observer.Z1 with confocal unit LSM 980 and analyzed using ImageJ software. All primary antibodies used in this study were validated previously for the use in hamster tissue or the sequence homology of the epitopes were more that 85%.

Table 2 : Antibodies used for Immunofluorescent staining

Antibody	Dilution used	Reference
Mouse monoclonal anti-NeuN (clone A-60); Merk	1/200	Cat# MAB377
Rabbit, purified polyclonal anti-NiV N and HeV H	1/1000	ValBex, France
Goat polyclonal anti-GFAP; Abcam	1/200	Cat# Ab53554
Goat polyclonal anti-Olig2; R&D system	1/200	Cat#AF2418
Alexa FluorTM 488 Donkey anti-rabbit IgG (H+L); ThermoFisher Scientific	1/500	Cat# A21206
Alexa FluorTM 555 Donkey anti-mouse IgG (H+L); ThermoFisher Scientific	1/500	Cat# A31570
Alexa FluorTM 647 Donkey anti-goat IgG (H+L); ThermoFisher Scientific	1/500	Cat# A21447

References

1. Mathieu, C. & Horvat, B. Henipavirus pathogenesis and antiviral approaches. *Expert Rev. Anti. Infect. Ther.* **13**, 343–354 (2015).
2. Wong, K. T. & Tan, C. T. Clinical and pathological manifestations of human henipavirus infection. *Curr. Top. Microbiol. Immunol.* **359**, 95–104 (2012).
3. Murray, K. *et al.* A morbillivirus that caused fatal disease in horses and humans. *Science (80-.).* **268**, 94–97 (1995).
4. Chua, K. B. *et al.* Fatal encephalitis due to Nipah virus among pig-farmers in Malaysia. *Lancet (London, England)* **354**, 1257–9 (1999).
5. Middleton, D. J. *et al.* Experimental Nipah virus infection in pteropid bats (Pteropus poliocephalus). *J. Comp. Pathol.* **136**, 266–72 (2007).
6. Drexler, J. F. *et al.* Bats host major mammalian paramyxoviruses. *Nat. Commun.* **3**, (2012).
7. Luby, S. P. The pandemic potential of Nipah virus. *Antiviral Res.* **100**, 38–43 (2013).
8. Plotkin, S. A. Vaccines for epidemic infections and the role of CEPI. *Hum. Vaccin. Immunother.* **13**, 2755–2762 (2017).
9. Sweileh, W. M. Global research trends of World Health Organization's top eight emerging pathogens. *Global. Health* **13**, 9 (2017).
10. Tan, C. T. *et al.* Relapsed and late-onset Nipah encephalitis. *Ann. Neurol.* **51**, 703–8 (2002).
11. Lo, M. K. & Rota, P. A. The emergence of Nipah virus, a highly pathogenic paramyxovirus. *J. Clin. Virol.* **43**, 396–400 (2008).
12. Reynes, J.-M. *et al.* Nipah virus in Lyle's flying foxes, Cambodia. *Emerg. Infect. Dis.* **11**, 1042–7 (2005).
13. Gaudino, M. *et al.* High pathogenicity of nipah virus from pteropus lylei fruit bats, Cambodia. *Emerg. Infect. Dis.* **26**, 104–113 (2020).
14. Ong, K. C. & Wong, K. T. Henipavirus encephalitis: Recent developments and advances. *Brain Pathol.*

25, 605–613 (2015).
15. Wong, K. T. *et al.* Human Hendra virus infection causes acute and relapsing encephalitis. *Neuropathol. Appl. Neurobiol.* **35**, 296–305 (2009).
16. Rockx, B. *et al.* Clinical Outcome of Henipavirus Infection in Hamsters Is Determined by the Route and Dose of Infection. *J. Virol.* **85**, 7658–7671 (2011).
17. Escaffre, O. *et al.* Henipavirus Pathogenesis in Human Respiratory Epithelial Cells. *J. Virol.* **87**, 3284–3294 (2013).
18. Ng, B.-Y., Lim, C. C. T., Yeoh, A. & Lee, W. L. Neuropsychiatric sequelae of Nipah virus encephalitis. *J. Neuropsychiatry Clin. Neurosci.* **16**, 500–4 (2004).
19. Wong, K. T. *et al.* Nipah virus infection: pathology and pathogenesis of an emerging paramyxoviral zoonosis. *Am. J. Pathol.* **161**, 2153–67 (2002).
20. Sejvar, J. J. *et al.* Long-term neurological and functional outcome in Nipah virus infection. *Ann. Neurol.* **62**, 235–42 (2007).
21. Marsh, G. A. & Wang, L.-F. Hendra and Nipah viruses: why are they so deadly? *Curr. Opin. Virol.* **2**, 242–7 (2012).
22. Tiong, V., Shu, M. H., Wong, W. F., Abubakar, S. & Chang, L. Y. Nipah virus infection of immature dendritic cells increases its transendothelial migration across human brain microvascular endothelial cells. *Front. Microbiol.* **9**, (2018).
23. Mathieu, C. *et al.* Nipah Virus Uses Leukocytes for Efficient Dissemination within a Host. *J. Virol.* **85**, 7863–7871 (2011).
24. Bonaparte, M. I. *et al.* Ephrin-B2 ligand is a functional receptor for Hendra virus and Nipah virus. *Proc. Natl. Acad. Sci. U. S. A.* **102**, 10652–10657 (2005).
25. Negrete, O. A. *et al.* EphrinB2 is the entry receptor for Nipah virus, an emergent deadly paramyxovirus. *Nature* **436**, 401–405 (2005).
26. Negrete, O. A. *et al.* Two Key Residues in EphrinB3 Are Critical for Its Use as an Alternative Receptor for Nipah Virus. *PLoS Pathog.* **2**, e7 (2006).
27. Negrete, O. A., Chu, D., Aguilar, H. C. & Lee, B. Single amino acid changes in the Nipah and Hendra virus attachment glycoproteins distinguish ephrinB2 from ephrinB3 usage. *J. Virol.* **81**, 10804–14 (2007).
28. Gale, N. W. *et al.* Ephrin-B2 selectively marks arterial vessels and neovascularization sites in the adult, with expression in both endothelial and smooth-muscle cells. *Dev. Biol.* **230**, 151–160 (2001).
29. Su, Z., Xu, P. & Ni, F. Single phosphorylation of Tyr304 in the cytoplasmic tail of ephrin B2 confers high-affinity and bifunctional binding to both the SH2 domain of Grb4 and the PDZ domain of the PDZ-RGS3 protein. *Eur. J. Biochem.* **271**, 1725–1736 (2004).
30. Liebl, D. J., Morris, C. J., Henkemeyer, M. & Parada, L. F. mRNA expression of ephrins and Eph receptor tyrosine kinases in the neonatal and adult mouse central nervous system. *J. Neurosci. Res.* **71**, 7–22 (2003).
31. Benson, M. D. *et al.* Ephrin-B3 is a myelin-based inhibitor of neurite outgrowth. *Proc. Natl. Acad. Sci. U. S. A.* **102**, 10694–10699 (2005).
32. Wong, K. T. *et al.* A golden hamster model for human acute Nipah virus infection. *Am. J. Pathol.* **163**, 2127–37 (2003).
33. Weingartl, H. *et al.* Invasion of the central nervous system in a porcine host by nipah virus. *J. Virol.* **79**, 7528–34 (2005).
34. Miao, J., Chard, L. S., Wang, Z. & Wang, Y. Syrian Hamster as an Animal Model for the Study on Infectious Diseases. *Frontiers in Immunology* **10**, (2019).
35. Guillaume, V. *et al.* Acute Hendra virus infection: Analysis of the pathogenesis and passive antibody protection in the hamster model. *Virology* **387**, 459–465 (2009).
36. Ferren, M. *et al.* Organotypic modeling of SARS-CoV-2 lung and brainstem infection. *Nature Communications* **12**, 1–17 (2021).
37. Welsch, J. *et al.* Organotypic Brain Cultures: A Framework for Studying CNS Infection by Neurotropic Viruses and Screening Antiviral Drugs. *Bio-protocol* **7**, (2017).
38. Ferren, M., Horvat, B. & Mathieu, C. Measles encephalitis: Towards new therapeutics. *Viruses* **11**, (2019).
39. Porotto, M. *et al.* Inhibition of Nipah virus infection in vivo: targeting an early stage of paramyxovirus fusion activation during viral entry. *PLoS Pathog.* **6**, e1001168 (2010).
40. Debuysscher, B. L. *et al.* Nipah virus efficiently replicates in human smooth muscle cells without cytopathic effect. *Cells* **10**, (2021).
41. Dawes, B. E. & Freiberg, A. N. Henipavirus infection of the central nervous system. *Pathog. Dis.* **77**, (2019).
42. Pernet, O., Wang, Y. E. & Lee, B. Henipavirus Receptor Usage and Tropism. in 59–78 (2012). doi:10.1007/82_2012_222
43. Mathieu, C. *et al.* Measles fusion complexes from central nervous system clinical isolates: decreased interaction between hemagglutinin and fusion proteins. *bioRxiv* 2021.06.18.449082 (2021). doi:10.1101/2021.06.18.449082
44. Ferren, M. *et al.* Hendra henipavirus strain HeV/Australia/1994/Horse18, complete genome. *Nucleotide - NCBI* (2019). Available at: https://www-ncbi-nlm-nih-gov.proxy.insermbiblio.inist.fr/nuccore/1701710593. (Accessed: 11th September 2021)
45. Yoneda, M. *et al.* Establishment of a Nipah virus rescue system. *Proc. Natl. Acad. Sci. U. S. A.* **103**, 16508–16513 (2006).

46. Hoffmann, A. B., Mazelier, M., Léger, P. & Lozach, P. Y. Deciphering Virus Entry with Fluorescently Labeled Viral Particles. in *Methods in Molecular Biology* **1836**, 159–183 (Methods Mol Biol, 2018).
47. Mathieu, C. *et al.* Nonstructural Nipah Virus C Protein Regulates both the Early Host Proinflammatory Response and Viral Virulence. *J. Virol.* **86**, 10766–10775 (2012).
48. Bustin, S. A. *et al.* The MIQE Guidelines: Minimum Information for Publication of Quantitative Real-Time PCR Experiments. *Clin. Chem.* **55**, 611–622 (2009).
49. Pfaffl, M. W. A new mathematical model for relative quantification in real-time RT-PCR. *Nucleic Acids Res.* **29**, (2001).

b. Comparaison de l'infection d'organoïdes de cerveau humain par les Henipavirus

Les souches d'Henipavirus présentent des différences de pathogénicité. NiV Malaysie (NiV Mal) s'avère être le plus encéphalitogène tandis que NiV Bangladesh (NiV Ban) atteint plus les voies respiratoires. Comme pour le SARS-CoV-2 et le VR, les résultats publiés décrivant l'infection du SNC par les Henipavirus chez l'Homme sont tous issus d'études post-mortem.

L'objectif principal de cette partie est de comparer l'infection par trois Henipavirus, NiV Mal, NiV Ban et HeV, dans un contexte de tissu cérébral humain. Des organoïdes de cerveau humain de 63 jours ont ainsi été infectés par 50 FPU de chaque virus ou du véhicule. Les organoïdes ont été différentiés à partir de cellules souches pluripotentes par Noémie Aurine dans l'équipe de Bertrand Pain à l'institut de la cellule souche et du cerveau comme décrit la revue publiée par Bertrand Pain et collègues (2021) [496]. La première question était de savoir si ce modèle était susceptible à l'infection par les Henipavirus. L'infection des organoïdes par le virus codant pour l'eGFP, rNiV-eGFP a été suivie par microscopie (Figure 21, A). La susceptibilité du modèle à l'infection par NiV Mal a été vérifée et les images mettent en évidence une grande hétérogénéité entre les différents échantillons. Dans le but de comparer la dissémination des Henipavirus dans ce modèle les organoïdes ont été collectés, le jour de l'infection ainsi que les jours 1, 2, 4 et 7 post infection, les ARN totaux ont été extraits et les copies d'ARNm N par µg d'ARN ont été quantifiées par RT-qPCR (Figure 21, B). Les résultats montrent une dissémination virale pour les 3 virus jusqu'au 7ème jour post infection. Cependant, dans les premiers jours après l'infection, la transcription et de la réplication virale augmentent plus rapidement pour NiV Ban. Le nombre de copies de N par µg d'ARN atteint déjà 1,8*10^7 pour NiV Ban à 2 jours post infection alors que l'on compte 2,3*10^6 copies de N pour NiV Mal et seulement 3,9*10^5 copies de N pour HeV. La croissance virale ralentit pour NiV Ban à partir de 4 jours post infection comparée à NiV Mal et HeV qui suivent une cinétique similaire. On remarque cependant une baisse des quantités d'ARN à 4 jours pour NiV Ban avec 1,6 µg d'ARN extrait au total en moyenne par échantillon contre 2,8 µg en moyenne par échantillon pour NiV Mal et HeV (données non montrées), témoignant d'un effet cytopathique plus élevé pour NiV Ban.

Dans le but d'évaluer l'efficacité du peptide inhibiteur de fusion VIKI dans un contexte neural humain les surnageants des organoïdes infectés ont été traités les jours 0, 2 et 4 par 1µM du peptide. Le suivi de la fluorescence pour les organoïdes infectés par le rNiV-eGFP (Figure 21, C) a été analysé. Les ARN ont été extraits et les copies de N par µg d'ARN ont été quantifiées par RT-qPCR. Le peptide a été capable d'inhiber 99,5% à 99,9% de l'infection aussi bien après 4 jours que après 7 jours en comparaison aux échantillons non traités (Figure 21, D). Les images avec les organoïdes infectés et traités ainsi que les quantifications des copies de N témoignent d'une grande variabilité. De façon intéressante on observe très nettement sur l'organoïde 1 traité infecté par le rNiV-eGFP (Figure 21, C) un début d'infection. Parmi les objectifs la question de l'évolution virale sous pression de sélection dans un contexte neural humain en présence ou en absence de traitement fait partie des

priorités. La prochaine étape consistera donc à séquencer les ARN viraux des organoïdes collectés aux temps tardifs (4 et 7 jours) afin d'identifier l'émergence de mutations dans ce modèle. Les séquences virales issues des organoïdes traités seront également analysées dans le but d'identifier l'apparition d'éventuelles mutations d'adaptation.

Le tropisme précoce des Henipavirus dans les organoïdes sera comparé prochainement par marquages immunofluorescents. De plus une analyse transcriptomique pour comparer les réponses immunitaires, inflammatoires et immunométaboliques à 1 jour après infection est en cours. Les résultats seront confirmés par RT-qPCR.

Ces résultats, bien que préliminaires permettent de confirmer que les organoïdes offrent l'opportunité d'étudier l'infection du SNC par les Henipavirus. Il s'agit de résultats inédits car c'est la première fois qu'une équipe infecte des organoïdes de cerveau humain par des Henipavirus. Ce modèle comporte des limites telles que l'absence de cellules microgliales ou de barrière hématoencéphalique. Cependant il existe aujourd'hui des systèmes permettant de rajouter des microglies en cis et de mimer la barrière hématoencéphalique sur les organoïdes. Etant donné le potentiel des organoïdes pour la recherche de nombreuses équipes partout dans le monde travaillent à l'amélioration de ce modèle.

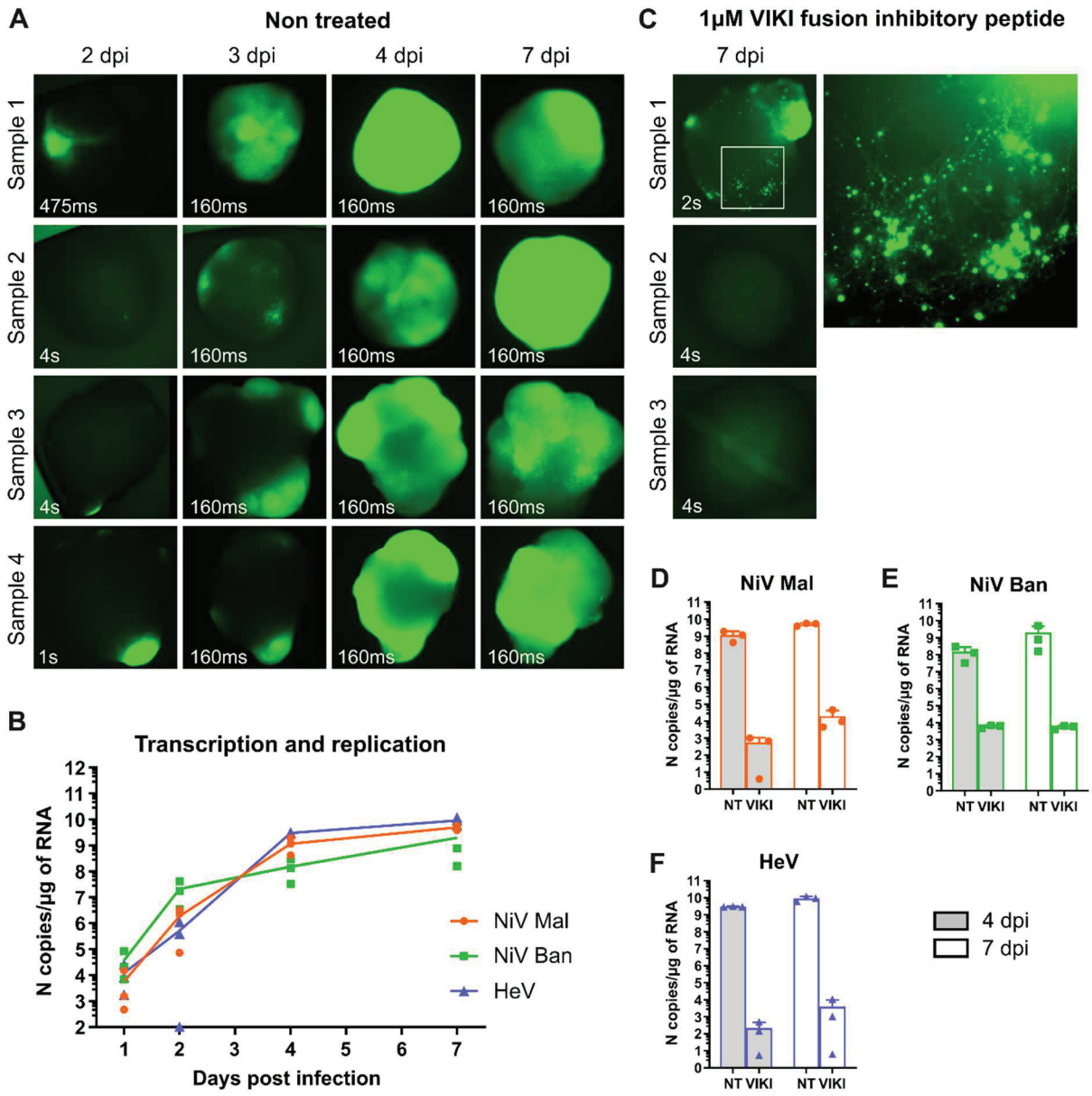

Figure 21 : Infection d'organoïdes de cerveau humain par des Henipavirus.

Les organoïdes de cerveau humain ont été infectés par 50 PFU de rNiV-eGFP, Nipah Malaisie (NiV Mal), Nipah Bangladesh (NiV Ban) et Hendra. A) L'infection de 4 organoïdes par le rNiV-eGFP a été suivie par microscopie à épifluorescence à 2, 3, 4 et 7 jours post infection (dpi = days post infection). B) Le nombre de copies de N par µg d'ARN total a été quantifié par RT-qPCR pour les trois virus (n=3). C), D), E), F) Les organoïdes infectés on été traités par 1µM du peptide inhibiteur de fusion. C) L'infection des organoïdes traités a été suivie par microscopie à épifluorescence pour le rNiV-eGFP et les copies de N par µg d'ARN ont été quantifiées par RT-qPCR à 4 dpi et à 7 dpi dans les organoïdes infectés par D) NiV Mal, E) NiV Ban et F) HeV (n=3). Les photos ont été prises par le microscope Zeiss Axiovert 100M aux temps d'expositions indiqués en millisecondes (ms) ou en secondes (s) en bas de chaque image et reconstituées en utilisant le plug-in Stitching plug-in avec le logiciel ImageJ [494].

DISCUSSION GENERALE

Le SARS-CoV-2, le VR, NiV Mal, NiV Ban et HeV étudiés ici sont tous des virus ciblant initialement les voies respiratoires. Cependant ils sont tous capables d'infecter le SNC et d'induire des encéphalites dont la fréquence et la sévérité sont très variables. A ce jour très peu d'études permettent de déterminer les étapes précoces de l'infection du SNC par ces virus. Dans la littérature, les données concernant l'infection du SNC sont généralement issues d'analyses post mortem chez l'Homme et chez l'animal ou obtenues dans des modèles *in vitro* spécifiques ne permettant pas de conclure sur les étapes précoces de l'infection du SNC à l'échelle organique. La comparaison de l'infection du SNC par trois genres de virus plus ou moins encéphalitogènes m'a permis d'apporter des éléments permettant de mieux comprendre les facteurs influençant l'infection du SNC.

1) L'infection du SNC : un circuit fermé ?

Il est communément admis dans la littérature que les patients atteints de PESS ne sont pas contagieux, l'infection étant cantonnée au SNC. Dans les cas de MIBE, on retrouve le virus de la rougeole circulant mais les mutations conférant un caractère hyperfusogène au virus n'ont été retrouvées que dans le cerveau des patients. Néanmoins, nos résultats tendent à confirmer que si l'hyperfusogénie est une marque de neuroadaptation, cet avantage devient contre-productif pour le virus en dehors du SNC. En effet, les mutations de compensation semblent ramener la machinerie de fusion vers la stabilité pour augmenter l'efficacité d'infection et limiter le déclenchement accidentel de la protéine F. Dans ce cas le circuit n'est peut-être pas fermé mais les pressions tissulaires lors du retour vers les autres organes pourraient conduire au retour vers le virus le plus efficace qui serait le virus sauvage. Une étude de l'évolution du virus mutant F L454W en multi-passages en cellules immunitaires permettrait peut-être de répondre à cette question.

Dans les cas d'encéphalites tardives à NiV Mal on retrouve le même schéma que dans les PESS. En revanche, l'émergence de mutations dans les séquences de NiV Mal et HeV retrouvées dans le cerveau des patients n'est pas clairement décrite dans la littérature. Le nombre de séquences est cependant très restreint, et les séquençages effectués manquaient sans doute de profondeur rendant impossible d'affirmer qu'il n'y ait pas eu d'évolution génétique des séquences dans le SNC. Les souches du VR portant une M hypermutée sont incapables de bourgeonner. Pourtant, dans le SNC, ces mêmes souches sont tout à fait capables de se propager. Tout porte à croire que l'infection cellule à cellule est suffisante pour envahir le SNC. Dans l'hypothèse où des particules virales aux propriétés hyperfusogènes seraient libérées dans le SNC il serait étonnant, compte tenu de leur effet cytopathique et de la permissivité des cellules endothéliales à l'infection, qu'elles n'atteignent pas les autres systèmes. De plus, aucun isolat clinique provenant de cerveau de patients décédés de PESS ou de MIBE n'a pu être collecté et seules des séquences virales ont pu être séquencées.

2) Neuroadaptation ou neurosélection?

Les expériences de passages multiples du virus de la rougeole *in vivo* dans le système nerveux central (historiquement chez le rat de Lewis) ou dans des modèles adaptés reflétant le SNC tels que les cultures organotypiques ou les organoïdes de cerveaux aboutissent systématiquement à l'émergence de mutations. Parmi ces mutations, celles retrouvées dans la F ou la H, confèrent souvent au virus un avantage pour envahir le SNC. Cependant aucune étude ne permet de spéculer que les cas de PESS et de MIBE soient liés à un même phénomène de neuroadaptation chez les patients. En effet, l'hypothèse inverse selon laquelle certaines mutations seraient déjà présentes à bas bruit dans le pool de virus sauvages (quasi-espèces) lors de l'infection n'est pas exclue. On parlerait alors de neurosélection. Cette hypothèse, pourrait expliquer la redondance de certaines mutations (ou des zones mutées) spécifiques observées chez des patients souffrant de MIBE ou de SSPE mais ne présentant aucun lien les uns avec les autres. En particulier, la mutation

L454W dans la protéine F a été retrouvée chez 4 patients totalement indépendants (deux en Afrique du Sud et deux en Italie dans deux villes différentes depuis 2008). La mutation du résidu 262 est également souvent retrouvée dans des cas de PESS ou sous pression de sélection de traitements sensés stabiliser la F en préfusion (S262R ou S262G). La neurosélection pourrait aussi expliquer l'atteinte du SNC mais il serait cependant surprenant que de tels virus atteignent le SNC au cours de la phase aiguë de l'infection sans pour autant induire directement une encéphalite. D'autant plus que d'après nos résultats, les mutations qui confèrent un caractère hyperfusogène ont tendance à muter rapidement en dehors du système nerveux central pour revenir vers un phénotype sauvage par le biais de mutation de compensation (cf. mutation E455G), elles-mêmes contre-sélectionnées dans le SNC. Impossible pour l'instant de dire si le VR parvient à atteindre le SNC parce qu'il contient déjà des mutations qui lui permettent d'évoluer dans cet environnement (neurosélection) ou si le VR sauvage a accidentellement atteint le SNC sans pour autant pouvoir s'y disséminer jusqu'à l'émergence d'une mutation d'adaptation qui déclencherait alors l'invasion du SNC.

Pour le SARS-CoV-2, malgré l'immense nombre de publications et l'émergence de nouveaux variants je n'ai pas trouvé d'études dans lesquelles les auteurs auraient séquencé les séquences virales retrouvées dans les cerveaux de patients. Nous ne savons donc pas si le virus retrouvé dans ces patients comporte des mutations d'adaptation. Le séquençage de nos cultures organotypiques de cerveau de hamster infectées par le SARS-CoV-2 sur une longue durée (plus de 7 jours) pourraient nous apporter des réponses quant à la possible neuroadaptation.

Dans le cas des encéphalites tardives et des rechutes de l'infection par NiV Malaisie aucune publication n'indique la recherche de mutations dans ce contexte. Malheureusement les études ont souvent plus de 20 ans et les échantillons ne sont probablement plus accessibles. Cependant, tout comme pour les cas de PESS avec le VR il serait important de comprendre ce qui permet la « réactivation » du virus des années après exposition. L'apparition de ces encéphalites tardives semble aléatoire et à ce jour aucun stimulus n'a été identifié. Toutefois il est envisageable que le déclenchement de ces encéphalites virales fasse suite à une autre infection ou à un facteur environnemental.

Les voies d'entrées et d'infection du SNC restent très difficiles à déterminer à ce jour. Pour le VR la voie hématogène est la plus probable. Cependant, l'infection indirecte par l'infiltration de cellules immunitaires infectées dans le SNC est également tout à fait possible comme démontrée pour le virus de l'immunodéficience simienne [318,497]. Ce mécanisme du cheval de Troie est fortement suspecté pour le VR et semble majeure (mais on exclusive) pour les Henipavirus par transinfection réalisé des cellules immunitaires chargées de virus en suface [452]. Certains virus utilisent plusieurs voies d'entrée comme par exemple le virus CDV qui utilise aussi bien la voie hématogène que le système nerveux périphérique pour atteindre le SNC [498]. Pour le VR, les Henipavirus et le SARS-CoV-2 tout porte à croire que plusieurs voies d'entrées sont également possibles. La rupture de la BHE provoquée par un fort effet

cytopathique ou par la tempête cytokinique semble être la voie d'entrée majoritaire pour les Henipavirus et le SARS-CoV-2.

3) Avantages et limites des cultures organotypiques et des organoïdes

a. Les cultures organotypiques

Les cultures organotypiques issues de cerveau ou de poumon de hamsters ou de souris présentent l'avantage unique d'offrir une fenêtre ouverte directement sur l'organe d'intérêt et permet ainsi de suivre une infection en temps réel à l'échelle organique. Ces modèles comportent toutes les cellules de la zone tranchée en conservant une bonne organisation tridimensionnelle. Les cultures organotypiques sont le seul modèle existant permettant d'étudier les étapes précoces d'une infection dans un organe. Ces cultures *ex vivo* ne permettent cependant pas de déterminer comment les virus atteignent le SNC. De plus, même si les vaisseaux sanguins sont présents lors de la coupe il n'y a plus de fluides circulants une fois les cultures déposées sur la membrane de PTFE. Les images des cultures organotypiques de cervelets infectées par le VR prises au microscope confocal montrent fréquemment l'infection des vaisseaux sanguins et indiquent l'existence d'un tropisme endothélial possible lorsque les vaisseaux sont accessibles à l'infection. Dans ces modèles *ex vivo* toutes les cellules sont exposées au virus tandis que lors d'une infection *in vivo* certaines d'entre elles ne sont peut-être pas disponibles. Les cultures organotypiques permettent cependant de déterminer la permissivité des cellules à l'infection. L'astrogliose modérée à sévère qui se met en place plusieurs jours après la coupe dans les cultures organotypiques de cervelet notamment est contournée en infectant les cultures le jour de la coupe. Pour l'étude de l'infection précoce par les virus où les cultures sont collectées seulement après 24 heures d'infection l'astrogliose n'a pas eu le temps de se mettre en place. Dans des études visant à comparer différents virus ou l'impact de mutations sur le tropisme initial de l'infection ces modèles sont particulièrement pertinents. Une autre limite est la restriction du modèle animal, cependant des cultures organotypiques similaires peuvent tout à fait être réalisées à partir d'animaux plus gros tels que des macaques, des furets et des chiens [306]. L'obtention de tissus humains constitue en France un véritable défi mais n'est toutefois pas impossible et on peut également envisager de réaliser des cultures organotypiques à partir de reins, de poumons, ou de cerveaux de patients lors d'interventions chirurgicales. Il serait particulièrement intéressant de collaborer davantage avec le personnel hospitalier pour obtenir des échantillons d'organes provenant d'autopsie de patients ou de fœtus abortifs par exemple.

Au cours de ma thèse j'ai pu démontrer le grand potentiel de ces modèles pour une application dans le monde de la virologie. Le fait que les cultures peuvent être réalisées à partir d'animaux sauvages immunocompétents ou génétiquement modifiés pour surexprimer un récepteur d'entrée ou déficientes pour le récepteur à

l'interféron par exemple ouvre un large champ de possibilités. L'étude des étapes précoces d'une infection dans un organe donné ainsi que les réponses transcriptomiques et la mort cellulaire induite par l'infection sont très intéressantes pour étudier la pathogénèse d'un virus émergeant à l'échelle organique. Cependant, l'utilisation des cultures organotypiques dans des études pré-cliniques pour cribler l'efficacité et la toxicité de traitements est particulièrement prometteuse. L'inefficacité de l'Hydroxychloroquine sur les cultures de poumons infectées par le SARS-CoV-2 en comparaison aux cultures de cerveaux ainsi que la toxicité observée avec le 17DMAG illustrent ce fort potentiel. A partir d'un animal de la taille d'un hamster de 7 jours on peut obtenir une quinzaine de coupes de cervelet, une dizaine de coupes de tronc cérébral, une vingtaine de coupes de poumon et une dizaine de coupes de reins. On peut également générer des cultures organotypiques à partir d'hippocampes et de bulbes olfactifs. 5 animaux suffisent pour obtenir des résultats avec suffisamment de réplicas biologiques indépendants permettant d'effectuer des analyses statistiques convaincantes. Indépendamment de tous les avantages mentionnés précédemment, ces modèles *ex vivo* apportent une solution éthique à la recherche en permettant de tester un nombre de conditions inégalables avec des expériences *in vivo* et respectent très largement la règle des 3R. De plus, les cultures organotypiques sont rapidement modélisables à moindre coût et répondent donc aux contraintes financières et temporelles. Enfin, les études actuelles visant à comprendre les manifestations neurologiques du COVID-19 comportent toutes des limites. Même les résultats provenant d'autopsies ou de rapports de cas se basent sur des panels trop petits pour pouvoir apporter des conclusions fiables [499] .

b. Organoïdes de cerveau humain

Contrairement aux cultures organotypiques les organoïdes de cerveau humain offrent la possibilité unique de travailler sur du tissu cérébral humain. En revanche ces modèles ne permettent pas de répondre aux mêmes questions. Ils sont particulièrement pertinents pour étudier l'évolution génétique des virus sous pression de sélection dans le SNC et les réponses transcriptomiques mises en place. A ce jour la majorité des organoïdes de cerveau humain sont constitués de neurones, d'astrocytes, d'oligodendrocytes et de cellules progénitrices. Ils sont générés à partir de cellules souches humaines pluripotentes induites ou embryonnaires. La différenciation des cellules en organoïdes se fait par l'exposition successive à des facteurs de croissances sur un support non adhérent ou en agitation dans des bioréacteurs miniatures pour permettre l'organisation tridimensionnelle. Les organoïdes de cerveau sont exempts de toute vascularisation, incluant l'absence de la BHE et ne présentent pas de cellules microgliales [500]. De plus, ils sont encore immatures et comprennent beaucoup de cellules progénitrices.

Bien qu'encore incomplets, les organoïdes de cerveau humain sont très prometteurs. La grande force de ce modèle réside dans le fait qu'on peut réaliser les organoïdes à partir de plusieurs espèces différentes et à partir de différents donneurs. Les cellules

souches peuvent être modifiées afin d'introduire des mutations et les possibilités sont donc infinies. Les organoïdes sont idéaux pour tester l'efficacité de traitements ciblant l'infection du SNC, l'évolution génétique des virus dans le SNC et les réponses inflammatoires mises en place suite à l'infection. Pour étudier l'infection du SNC par des virus tels que Nipah ou Hendra pour lesquels il est impossible de se procurer des échantillons de patients, l'utilisation d'organoïdes permet d'adresser beaucoup de questions laissées en suspens.

4) Pathogénèse du SARS-CoV-2, du virus de la rougeole et des Henipavirus à l'échelle organique

L'infection du tronc cérébral par le SARS-CoV-2 pourrait expliquer les cas d'arrêts cardiaques ou d'arrêts respiratoires des patients décédés du COVID-19. Cependant la présence du SARS-CoV-2 dans le tronc cérébral de patients humains n'a été que rarement suggérée. Mes données dans les cultures organotypiques de cervelet et de tronc cérébral de hamster confirment la susceptibilité de ces sous-structures à l'infection par le SARS-CoV-2. Toutefois les niveaux de réplication virale sont plus de 10 fois plus faibles que dans le poumon. Si le virus parvient à se disséminer dans le SNC il induit une forte mortalité cellulaire dans les neurones qu'il cible, ce qui explique peut-être sa rareté dans le SNC. Alternativement, l'infection de la zone du nerf vague pourrait aussi expliquer la défaillance multiple par des lésions plus basses que dans le tronc cérébral.

Pour le virus de la rougeole les virus neuroadaptés se disséminent difficilement dans les lignées cellulaires habituellement utilisées pour cultiver les souches sauvages ou dans les tissus pulmonaires. La formation de trop larges syncytia entraine la mort des cellules voisines et n'est donc pas du tout un avantage pour l'infection qui est du coup trop cytopathique. Au contraire, nous avons montré que dans le contexte du système nerveux central ces virus neuroadaptés se propagent avec relativement peu d'effets cytopathiques. L'infection de motoneurones humains par le virus MeV-IC232-eGFP-F-L454W illustre particulièrement ce phénomène où l'infection des neurones, bien que très rapide, devient persistante.

Pour les Henipavirus nous avons émis l'hypothèse que les différences de pathogénicité entre les souches pourraient s'expliquer par une différence de susceptibilité à l'échelle organique explicable par la distribution de l'expression des récepteurs d'entrée. Dans la littérature EFNB1 n'est pas présenté comme un récepteur d'entrée pour NiV Mal, NiV Ban ou HeV. Cependant il a tout de même été montré que la liaison de EFNB1 à la G de NiV Mal est 10 fois moins forte que EFNB2 mais pas nulle pour autant [443]. Les interactions entre les EFN et les G des Henipavirus ont été analysées dans la littérature à partir des protéines solubles purifiées ou dans des contextes de transfection. J'ai inclus initialement EFNB1 dans mes travaux de thèse pour avoir un élément de comparaison à EFNB2 et EFNB3.

Cependant mes résultats montrent clairement que NiV Mal, NiV Ban et HeV sont capables d'utiliser EFNB1. En opposition avec la littérature il semblerait donc que EFNB1 soit un récepteur de faible affinité permettant la liaison de la G de ces trois virus ainsi que l'entrée virale. Une étude récente a montré que NiV Mal peut se répliquer intensément et sans aucun effet cytopathique dans les cellules du muscle lisse pourtant dépourvues de l'expression des récepteurs EFNB2 et EFNB3 [501]. Ces cellules expriment EFNB1 et les résultats de cette étude confirment que l'expression de EFNB1 suffit à rendre des cellules permissives à l'infection par NiV. EFNB3 est également décrit comme étant un récepteur de plus faible affinité pour HeV comparé à NiV [443]. EFNB3 serait exprimé plus fortement dans le tronc cérébral et de nombreuses publications suggèrent un lien entre l'expression de EFNB3 dans le tronc cérébral et la sévérité du dysfonctionnement neuronal au cours des encéphalites causées par NiV [445]. Cependant, cette surexpression de EFNB3 dans le tronc cérébral par rapport à EFNB2 n'a été décrite que dans les publications d'une équipe de recherche et n'est pas relevée dans des articles plus spécialisés. Mes résultats de quantifications des ARN messagers des EFN dans mes cultures organotypiques de cervelet de hamster en comparaison aux cultures organotypiques de tronc cérébral de hamster ne permettent pas de confirmer une plus forte expression d'EFNB3 dans le tronc cérébral non plus. Il est connu toutefois que l'expression des EFN est très élevée dans les stades de développement du SNC, or nos cultures sont réalisées à partir de jeunes animaux et il n'est pas impossible que leur SNC contienne encore des cellules immatures. De plus comme mentionné précédemment, bien que dépourvues de circulation sanguine, les cultures contiennent tout de même les cellules endothéliales des vaisseaux sanguins qui expriment très fortement Ephrin B2 et biaisent potentiellement les résultats de cette expérience.

Il est remarquable que dans les études menées dans les modèles COC de hamster et organoïdes humains, les virus NiV Mal, NiV Ban et HeV se comportent de manière semblable. Dans les cultures organotypiques de cervelet, de tronc cérébral de hamster et dans les organoïdes de cerveau humain la réplication virale de NiV Ban est plus rapide aux temps précoces en comparaison avec NiV Mal et HeV alors que ce virus est le moins encéphalitogène des trois. Ce résultat s'accompagne d'une baisse de croissance virale à partir des 2ème ou 3ème jour d'infection, souvent associée à de la mortalité cellulaire. Ces résultats démontrent que NiV Ban, s'il atteint le SNC, est capable de s'y répliquer très fortement. Mon interprétation de ces résultats est que le fort effet cytopathique induit par l'infection par NiV Ban associé à sa dissémination particulièrement rapide (un cycle viral toutes les 4 heures observé in vitro) limite la progression du virus vers le système nerveux central.

De façon intéressante les cultures organotypiques de poumons de hamster ne sont pas susceptibles à l'infection par le variant de rougeole portant la mutation L454W. Cette mutation permet pourtant une infection et une dissémination virale en absence de récepteur connu, aussi bien in vitro dans des cellules Vero qu'*ex vivo* dans les cultures organotypiques de cerveau ou dans des cultures primaires d'épithélium

humain des voies respiratoires. Cette absence de permissivité de ce modèle de poumon par ce virus pourtant capable d'infecter le poumon *in vivo* (Article 7) peut s'expliquer par l'implication de mécanismes supplémentaires. L'entrée virale dans l'épithélium pulmonaire ne pourrait se produire que via le récepteur Nectin-4 exprimé sur les pôles basolatéraux des cellules ou en utilisant un autre récepteur de basse affinité. Nectin-4 serait alors inaccessible pour la H du virus et on peut envisager que dans ce contexte une infection des poumons n'est possible que par contact avec une cellule infectée en accord avec l'hypothèse prévalant chez l'humain. Des expériences supplémentaires pourraient être réalisées en réalisant une co-culture de cultures organotypique de poumon avec des splénocytes, des PBMC ou des microglies préalablement infectés isolés du même animal. On pourrait aussi simplement observer la liaison ou l'entrée des particules virales par microscopie électronique en transmission.

5) Infection par le SARS-CoV-2, le virus de la rougeole et les Henipavirus à l'échelle cellulaire

a. Tropisme dans le SNC

Dans le système nerveux central le SARS-CoV-2 envahit peu et cible majoritairement les neurones granulaires et les neurones de golgi. NiV Mal cible en priorité les neurones positifs pour le marquage NeuN tandis que NiV Ban et HeV semblent infecter les cellules neurales de façon plus large sans cibler un type cellulaire en particulier. NiV Ban est pourtant peu encéphalitogène et l'infection massive des cellules du SNC est cohérente avec la forte réplication virale et l'effet cytopathique observés dans les tissus cérébraux. Ce tropisme dispersif pour NiV Ban et HeV entraine une infection très forte du SNC. Le fait que les encéphalites soient beaucoup moins courantes pour NiV Ban que pour NiV Mal malgré sa capacité à envahir le SNC très rapidement est une raison de plus de penser que dans les cas où l'infection entraine la mort à cause du syndrome respiratoire aigu ce virus n'a simplement pas eu le temps d'accéder au SNC. De plus cette infection massive peut entrainer une réponse très forte dans les cellules alors que les neurones induisent une plus faible réponse.

Les mutants HRC du VR sont pourtant capables d'infecter, dès les premières étapes de l'infection les neurones, les astrocytes, les oligodendrocytes et les microglies contrairement au virus sauvage qui se concentre sur l'infection des neurones et des microglies. Cependant les conditions chez l'homme sont différentes puisqu'il est possible que les mutations ne soient apparues qu'une fois le virus infiltré dans le SNC à la façon d'un cheval de Troie. L'analyse du tropisme des mutants hyperfusogènes confirme ces résultats et le fait que 50% des microglies contribuent à l'infection apporte une fenêtre de réflexion sur le mode d'infection de ces mutants dans le SNC.

L'observation de l'infection des cellules endothéliales par le VR dans les cultures organotypiques de cerveaux et plus particulièrement des zones ressemblant très fortement à la BHE ouvre également le débat sur la possible infection du SNC par le VR via la BHE.

b. Persistance virale

Dans les cas de COVID-longs on observe un syndrome multi-systémique une virémie persistante et la présence de particules virales dans différents tissus. Les publications récentes suggèrent la mise en place de cette persistance virale par une mauvaise réponse immunitaire, une réinfection ou une rechute [94,502,503] mais ce ne sont à ce jour que des hypothèses.

Malgré un effet cytopathique moindre dans le système nerveux central nous avons démontré que le caractère hyperfusogène des virus les plus encéphalitogènes (mutants du domaine HRC du VR et NiV Mal) est un facteur clé pour l'invasion du SNC. Il est donc particulièrement surprenant que de tels virus puissent persister dans le SNC des patients sans symptomatologie pendant de longues périodes allant jusqu'à plus de 10 ans. De tels virus à ARN sont cytoplasmiques et on s'attend à ce qu'ils soient rapidement éliminés en l'absence de réplication. Une hypothèse serait que les génomes viraux pourraient rester quiescents dans des cellules qui ne se répliquent pas ou très peu telles que les cellules de la glie radiaire ou les cellules souches hématopoïétiques. Le déclenchement des encéphalites pourrait avoir lieu au moment où ces cellules sont sollicitées pour se différencier.

6) Infection par le SARS-CoV-2, le virus de la rougeole et les Henipavirus à l'échelle moléculaire

Au cours de ma thèse j'ai essayé de comprendre les facteurs qui pourraient expliquer les différences d'effet cytopathique et de tropisme entre des virus ciblant initialement toutes les voies respiratoires.

Aussi bien pour SARS-CoV-2, le VR et les trois Henipavirus, les expériences visant à bloquer la fusion virale par le biais de peptides HRC inhibiteurs de fusion visant la F montrent que la F est essentielle pour la dissémination virale dans le SNC. En revanche on a pu voir que dans les organoïdes de cerveau humain infectés par NiV l'infection parvient tout de même ponctuellement à envahir le tissu après 7 jours de traitement, suggérant une possible émergence de mutation ou une autre voie de dissémination. De plus, on ne sait pas si les Henipavirus peuvent se disséminer en absence de la G.

Dans le but de comprendre dans quelle mesure les différences dans les séquences des glycoprotéines de surface des différents Henipavirus influencent le tropisme dans le SNC on pourrait envisager de générer des virus mutants en interchangeant les F et/ou les G de NiV Mal, NiV Ban et HeV. On pourrait également envisager d'intégrer le virus Cedar dans les expériences. Il pourrait d'ailleurs être utile de

générer ces virus recombinants à partir du génome du virus Cedar afin de s'affranchir de la contrainte du travail en laboratoire P4.

Dans mon article en préparation je vise une meilleure compréhension des différences des machineries de fusion des différents Henipavirus en me basant sur l'attachement, l'entrée, la stabilité de la F et le tropisme.

Mes résultats montrent que NiV Mal est plus efficace pour se lier rapidement aux récepteurs d'entrée que NiV Ban et HeV alors que lorsque l'on analyse l'entrée seule dans les cellules cibles, HeV est au contraire le virus le plus rapide pour fusionner. NiV Ban présente un phénotype intermédiaire autant au niveau de la liaison aux récepteurs que pour l'entrée, sauf dans les cellules exprimant EFNB1. En effet, NiV B est le virus qui fusionne le plus rapidement dans les cellules exprimant le récepteur EFNB1.

La stabilité thermique des F dans un contexte d'infection indique que HeV est beaucoup plus instable que NiV Mal et NiV Ban. Dans un contexte de transfection en l'absence de la G j'obtiens les résultats inverses ; la F de HeV demeure en état de pré-fusion même après 10 min à 55°C contrairement aux F de NiV Mal et NiV Ban qui se déclenchent très vite.

L'ensemble de mes résultats m'ont menée à l'interprétation suivante. La F des deux NiV est très instable en l'absence de la G, on l'observe d'ailleurs facilement par l'apparition de syncytia lorsqu'on transfecte des cellules avec la F seule, même à 37°C. La G de NiV Mal et de NiV Ban assume particulièrement sa fonction protectrice sur la F pour prévenir son déclenchement intempestif (Figure 22, A, B). Après le déclenchement de la F la fusion est en revanche longue et il semblerait que le repliement de la F pour promouvoir la fusion soit à l'image des mutants du VR hyperfusogènes du domaine HRC. Il peut s'agir du déclenchement plus long de la F par la G ou de l'effet cumulé du déclenchement de la F suivie de sa « poussée » par la G. En revanche la F de HeV est naturellement beaucoup plus stable mais son repliement est extrêmement rapide, probablement grâce à l'action de déclenchement et de « poussée » de la G qui permettent d'achever plus rapidement la fusion (Figure 22, C). Ceci aurait pour conséquence une entrée très rapide, malgré une moins bonne liaison aux récepteurs. Cette théorie expliquerait également la meilleure efficacité des peptides HRC inhibiteurs de fusion sur les souches de NiV en comparaison à HeV car comme dans le cas des F hyperfusogènes de rougeole la fusion est plus lente et donne plus de temps aux peptides HRC pour s'associer au HRN de la F et bloquer la fusion. Alternativement, le peptide devant entrer en compétition avec le HRC de la F lorsque celle-ci est dans son état métastable, le repliement très rapide de la F de HeV ne permettrait pas aux peptides de s'interposer assez rapidement.

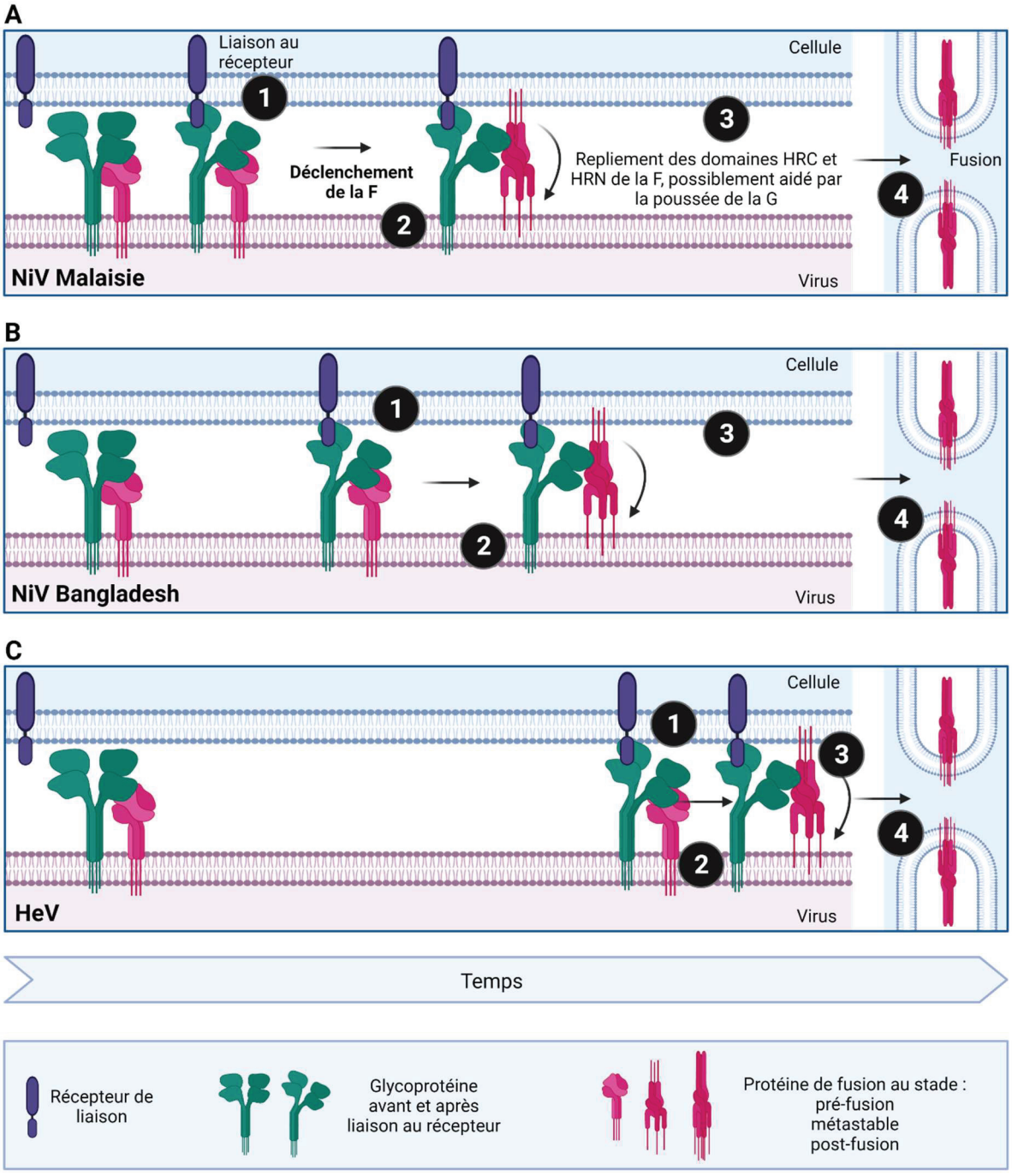

Figure 22 : Proposition d'un modèle de fusion pour NiV Malaisie, NiV Bangladesh et HeV.

Schéma proposant la cinétique de liaison au récepteur (1), du déclenchement de la F (2), du repliement de la F (3) et de la création du pore de fusion (3) pour NiV Mal (A), NiV Ban (B) et HeV (C).

7) Conclusion et perspectives

La meilleure compréhension des mécanismes de fusion de ces virus ouvre des perspectives pour le développement d'inhibiteurs de fusion. Par exemple, dans le cadre des peptides HRC inhibiteurs de fusion pour le VR, le remplacement de la séquence HRC sauvage par la séquence portant la mutation E455G améliore significativement l'efficacité de ces peptides. De plus une telle mutation stabilisant la F pourrait permettre de réaliser des analyses de co-cristallographie de la F dans son état de pré-fusion avec d'autres molécules visant à bloquer la fusion à ce niveau et de mieux comprendre les interactions avec ces traitements éventuels.

L'étape suivante consiste à déterminer comment les virus respiratoires décrits dans cette thèse atteignent le SNC. Pour répondre à cette question des études plus poussées *in vivo* chez l'animal seront nécessaires afin de trouver des explications potentielles à cette invasion du SNC.

REFERENCES

1. Nichols, W. G., Peck Campbell, A. J. & Boeckh, M. Respiratory viruses other than influenza virus: Impact and therapeutic advances. *Clinical Microbiology Reviews* **21**, 274–290 (2008).

2. Jubelt, B. & Lipton, H. L. Enterovirus/Picornavirus infections. in *Handbook of Clinical Neurology* **123**, 379–416 (Handb Clin Neurol, 2014).

3. Griffin, D. E., Lin, W. H. & Pan, C. H. Measles virus, immune control, and persistence. *FEMS Microbiology Reviews* **36**, 649–662 (2012).

4. Eugenin, E. A. *et al.* CCL2/monocyte chemoattractant protein-1 mediates enhanced transmigration of human immunodeficiency virus (HIV)-infected leukocytes across the blood-brain barrier: A potential mechanism of HIV-CNS invasion and NeuroAIDS. *J. Neurosci.* **26**, 1098–1106 (2006).

5. Shimohata, T. Neuro-COVID-19. *Clinical and Experimental Neuroimmunology* (2021). doi:10.1111/cen3.12676

6. Ludlow, M. *et al.* Neurotropic virus infections as the cause of immediate and delayed neuropathology. *Acta Neuropathol.* **131**, 159–184 (2016).

7. Organisation Mondiale de la Santé. *Weekly epidemiological update on COVID-19 - 22 June 2021*. *World Health Organization* (2020).

8. Worldometer. Coronavirus Cases. *Worldometer* (2021). Available at: https://www.worldometers.info/coronavirus/. (Accessed: 20th April 2021)

9. Weiss, S. R. Forty years with coronaviruses. *Journal of Experimental Medicine* **217**, (2020).

10. van der Hoek, L. *et al.* Identification of a new human coronavirus. *Nat. Med.* **10**, 368–373 (2004).

11. Fouchier, R. A. M. *et al.* A previously undescribed coronavirus associated with respiratory disease in humans. *Proc. Natl. Acad. Sci. U. S. A.* **101**, 6212 (2004).

12. Woo, P. C. Y. *et al.* Characterization and Complete Genome Sequence of a Novel Coronavirus, Coronavirus HKU1, from Patients with Pneumonia. *J. Virol.* **79**, 884–895 (2005).

13. Walsh, E. E., Shin, J. H. & Falsey, A. R. Clinical Impact of Human Coronaviruses 229E and OC43 Infection in Diverse Adult Populations. *J. Infect. Dis.* **208**, 1634 (2013).

14. Lina, B. *et al.* Surveillance of community-acquired viral infections due to respiratory viruses in Rhone-Alpes (France) during winter 1994 to 1995. *J. Clin. Microbiol.* **34**, 3007–3011 (1996).

15. Mäkelä, M. J. *et al.* Viruses and bacteria in the etiology of the common cold. *J. Clin. Microbiol.* **36**, 539–542 (1998).

16. Drosten, C. *et al.* Identification of a Novel Coronavirus in Patients with Severe Acute Respiratory Syndrome. *N. Engl. J. Med.* **348**, 1967–1976 (2003).

17. Zhong, N. S. *et al.* Epidemiology and cause of severe acute respiratory syndrome (SARS) in Guangdong, People's Republic of China, in February, 2003. *Lancet* **362**, 1353–1358 (2003).

18. Zaki, A. M., van Boheemen, S., Bestebroer, T. M., Osterhaus, A. D. M. E. & Fouchier, R. A. M. Isolation of a Novel Coronavirus from a Man with Pneumonia in Saudi Arabia. *N. Engl. J. Med.* **367**, 1814–1820 (2012).

19. Memish, Z. A., Perlman, S., Van Kerkhove, M. D. & Zumla, A. Middle East respiratory syndrome. *The Lancet* **395**, 1063–1077 (2020).

20. Zhou, P. *et al.* A pneumonia outbreak associated with a new coronavirus of probable bat origin. *Nature* **579**, 270–273 (2020).

21. Cui, J., Li, F. & Shi, Z. L. Origin and evolution of pathogenic coronaviruses. *Nature Reviews Microbiology* **17**, 181–192 (2019).

22. Guo, H. *et al.* Identification of a novel lineage bat SARS-related coronaviruses that use bat ACE2 receptor. *bioRxiv* 2021.05.21.445091 (2021). doi:10.1080/22221751.2021.1956373

23. Lu, R. *et al.* Genomic characterisation and epidemiology of 2019 novel coronavirus: implications for virus origins and receptor binding. *Lancet* **395**, 565–574 (2020).

24. Dhama, K. *et al.* Coronavirus disease 2019–COVID-19. *Clin. Microbiol. Rev.* **33**, 1–48 (2020).

25. Turoňová, B. *et al.* In situ structural analysis of SARS-CoV-2 spike reveals flexibility mediated by three hinges. *Science (80-.).* **370**, 203–208 (2020).

26. Shang, J. *et al.* Cell entry mechanisms of SARS-CoV-2. *Proc. Natl. Acad. Sci. U. S. A.* **117**, (2020).

27. Hoffmann, M. *et al.* SARS-CoV-2 Cell Entry Depends on ACE2 and TMPRSS2 and Is Blocked by a Clinically Proven Protease Inhibitor. *Cell* **181**, 271-280.e8 (2020).

28. Coutard, B. *et al.* The spike glycoprotein of the new coronavirus 2019-nCoV contains a furin-like cleavage site absent in CoV of the same clade. *Antiviral Res.* **176**, (2020).

29. Cantuti-Castelvetri, L. *et al.* Neuropilin-1 facilitates SARS-CoV-2 cell entry and infectivity. *Science (80-.).* **370**, (2020).

30. Daly, J. L. *et al.* Neuropilin-1 is a host factor for SARS-CoV-2 infection. *Science (80-.).* **370**, 861–865 (2020).

31. Qiao, J. *et al.* The expression of SARS-CoV-2 receptor ACE2 and CD147, and protease TMPRSS2 in human and mouse brain cells and mouse brain tissues. *Biochem. Biophys. Res. Commun.* (2020). doi:10.1016/j.bbrc.2020.09.042

32. Wang, K. *et al.* CD147-spike protein is a novel route for SARS-CoV-2 infection to host cells. *Signal Transduct. Target. Ther.* **5**, (2020).

33. Machhi, J. *et al.* The Natural History, Pathobiology, and Clinical Manifestations of SARS-CoV-2 Infections. *Journal of Neuroimmune Pharmacology* **15**, 359–386 (2020).

34. V'kovski, P., Kratzel, A., Steiner, S., Stalder, H. & Thiel, V. Coronavirus biology and replication: implications for SARS-CoV-2. *Nature Reviews Microbiology* **19**, 155–170 (2021).

35. Ghosh, S. *et al.* β-Coronaviruses Use Lysosomes for Egress Instead of the Biosynthetic Secretory Pathway. *Cell* **183**, 1520-1535.e14 (2020).

36. Organisation Mondiale de la Santé. Weekly epidemiological update on COVID-19 - 23 March 2021. *Who* 31 (2021). Available at: https://www.who.int/publications/m/item/weekly-epidemiological-update-on-covid-19---10-august-2021. (Accessed: 28th August 2021)

37. Hoffmann, M. *et al.* SARS-CoV-2 variants B.1.351 and P.1 escape from neutralizing antibodies. *Cell* **184**, 2384-2393.e12 (2021).

38. Zhang, L. *et al.* SARS-CoV-2 spike-protein D614G mutation increases virion spike density and infectivity. *Nat. Commun.* **11**, 1–9 (2020).

39. Kuzmina, A. *et al.* SARS-CoV-2 spike variants exhibit differential infectivity and neutralization resistance to convalescent or post-vaccination sera. *Cell Host Microbe* **29**, 522-528.e2 (2021).

40. Kirchdoerfer, R. N. *et al.* Stabilized coronavirus spikes are resistant to conformational changes induced by receptor recognition or proteolysis. *Sci. Rep.* **8**, (2018).

41. Pallesen, J. *et al.* Immunogenicity and structures of a rationally designed prefusion MERS-CoV spike antigen. *Proc. Natl. Acad. Sci. U. S. A.* **114**, E7348–E7357 (2017).

42. Wrapp, D. *et al.* Cryo-EM structure of the 2019-nCoV spike in the prefusion conformation. *Science* **367**, 1260 (2020).

43. Polack, F. P. *et al.* Safety and Efficacy of the BNT162b2 mRNA Covid-19 Vaccine. *N. Engl. J. Med.* **383**, 2603–2615 (2020).

44. Jeong, D.-E. *et al.* Assemblies of putative SARS-CoV2-spike-encoding mRNA sequences for vaccines BNT-162b2 and mRNA-1273. *GitHub* (2021). Available at: https://github.com/NAalytics/Assemblies-of-putative-SARS-CoV2-spike-encoding-mRNA-sequences-for-vaccines-BNT-162b2-and-mRNA-1273/blob/main/Assemblies of putative SARS-CoV2-spike-encoding mRNA sequences for vaccines BNT-162b2 and mRNA-1273.docx.pdf. (Accessed: 7th September 2021)

45. Xia, X. Domains and functions of spike protein in sars-cov-2 in the context of vaccine design. *Viruses* **13**, (2021).

46. Watanabe, Y. *et al.* Native-like SARS-CoV-2 Spike Glycoprotein Expressed by ChAdOx1 nCoV-19/AZD1222 Vaccine. *ACS Cent. Sci.* **7**, 594–602 (2021).

47. Geers, D. *et al.* SARS-CoV-2 variants of concern partially escape humoral but not T-cell responses in COVID-19 convalescent donors and vaccinees. *Sci. Immunol.* **6**, (2021).

48. Brown, C. M. *et al.* Outbreak of SARS-CoV-2 Infections, Including COVID-19 Vaccine Breakthrough Infections, Associated with Large Public Gatherings — Barnstable County, Massachusetts, July 2021. *MMWR. Morb. Mortal. Wkly. Rep.* **70**, 1059–1062 (2021).

49. Public Health England. SARS-CoV-2 variants of concern and variants under investigation in England. *Sage* 1–50 (2021).

50. Buchan, S. A. *et al.* Increased Household Secondary Attacks Rates With Variant of Concern Severe Acute Respiratory Syndrome Coronavirus 2 Index Cases. *Clin. Infect. Dis.* (2021). doi:10.1093/cid/ciab496

51. Sims, A. C. *et al.* Severe Acute Respiratory Syndrome Coronavirus Infection of Human Ciliated Airway Epithelia: Role of Ciliated Cells in Viral Spread in the Conducting Airways of the Lungs. *J. Virol.* **79**, 15511–15524 (2005).

52. Guan, W. *et al.* Clinical Characteristics of Coronavirus Disease 2019 in China. *N. Engl. J. Med.* **382**, 1708–1720 (2020).

53. Letko, M., Marzi, A. & Munster, V. Functional assessment of cell entry and receptor usage for SARS-CoV-2 and other lineage B betacoronaviruses. *Nat. Microbiol.* **5**, 562–569 (2020).

54. Blanco-Melo, D. *et al.* Imbalanced Host Response to SARS-CoV-2 Drives Development of COVID-19. *Cell* **181**, 1036-1045.e9 (2020).

55. Han, H. *et al.* Profiling serum cytokines in COVID-19 patients reveals IL-6 and IL-10 are disease severity predictors. *Emerg. Microbes Infect.* **9**, 1123–1130 (2020).

56. Patra, T. *et al.* SARS-CoV-2 spike protein promotes IL-6 transsignaling by activation of angiotensin II receptor signaling in epithelial cells. *PLoS Pathog.* **16**, e1009128 (2020).

57. Frisoni, P. *et al.* Cytokine storm and histopathological findings in 60 cases of COVID-19-related death: from viral load research to immunohistochemical quantification of major players IL-1β, IL-6, IL-15 and TNF-α. *Forensic Sci. Med. Pathol.* (2021). doi:10.1007/s12024-021-00414-9

58. Jiménez-Gastélum, G. R. *et al.* More Evidence of the Link of Interleukin-6 and Interleukin-10 with Critical COVID-19: A Report in Mexican Patients. *Iran. J. Immunol.* **18**, 331–337 (2021).

59. Tutal Gursoy, G. *et al.* Neurological Presentations in Patients with COVID-19 in Cytokine Storm. *Can. J. Neurol. Sci. / J. Can. des Sci. Neurol.* 1–7 (2021). doi:10.1017/cjn.2021.247

60. Orsucci, D., Ienco, E. C., Nocita, G., Napolitano, A. & Vista, M. Neurological features of COVID-19 and their treatment: A review. *Drugs in Context* **9**, (2020).

61. Khoo, A. *et al.* Postinfectious brainstem encephalitis associated with SARS-CoV-2. *J. Neurol. Neurosurg. Psychiatry* **91**, jnnp-2020-323816 (2020).

62. Rábano-Suárez, P. *et al.* Generalized myoclonus in COVID-19. *Neurology* **95**, 10.1212/WNL.0000000000009829 (2020).

63. Solomon, I. H. *et al.* Neuropathological Features of Covid-19. *N. Engl. J. Med.* **383**, 989–992 (2020).

64. Bougakov, D., Podell, K. & Goldberg, E. Multiple Neuroinvasive Pathways in COVID-19. *Molecular Neurobiology* (2020). doi:10.1007/s12035-020-02152-5

65. Jafari Khaljiri, H. *et al.* Comprehensive Review on Neuro-COVID-19 Pathophysiology and Clinical Consequences. *Neurotox. Res.* 1 (2021). doi:10.1007/s12640-021-00389-z

66. Chigr, F., Merzouki, M. & Najimi, M. Comment on “The neuroinvasive potential of SARS-CoV-2 may play a role in the respiratory failure of COVID-19 patients”. *Journal of Medical Virology* **92**, 703–704 (2020).

67. Li, Y. C., Bai, W. Z. & Hashikawa, T. The neuroinvasive potential of SARS-CoV2 may play a role in the respiratory failure of COVID-19 patients. *Journal of Medical Virology* **92**, 552–555 (2020).

68. Smith, J. C., Ellenberger, H. H., Ballanyi, K., Richter, D. W. & Feldman, J. L. Pre-Bötzinger complex: A brainstem region that may generate respiratory rhythm in mammals. *Science (80-.).* **254**, 726–729 (1991).

69. Netland, J., Meyerholz, D. K., Moore, S., Cassell, M. & Perlman, S. Severe Acute Respiratory Syndrome Coronavirus Infection Causes Neuronal Death in the Absence of Encephalitis in Mice Transgenic for

Human ACE2. *J. Virol.* **82**, 7264–7275 (2008).

70. Meinhardt, J. *et al.* Olfactory transmucosal SARS-CoV-2 invasion as a port of central nervous system entry in individuals with COVID-19. *Nat. Neurosci.* **24**, 168–175 (2021).

71. Alwan, N. A. The road to addressing Long Covid. *Science* **373**, 491–493 (2021).

72. Nalbandian, A. *et al.* Post-acute COVID-19 syndrome. *Nature Medicine* **27**, 601–615 (2021).

73. Liu, K., Pan, M., Xiao, Z. & Xu, X. Neurological manifestations of the coronavirus (SARS-CoV-2) pandemic 2019-2020. *Journal of Neurology, Neurosurgery and Psychiatry* **91**, 669–670 (2020).

74. Bulfamante, G. *et al.* First ultrastructural autoptic findings of sars-cov-2 in olfactory pathways and brainstem. *Minerva Anestesiologica* **86**, 678–679 (2020).

75. Xiang, P. *et al.* Case Report: Identification of SARS-CoV-2 in Cerebrospinal Fluid by Ultrahigh-Depth Sequencing in a Patient With Coronavirus Disease 2019 and Neurological Dysfunction. *Front. Med.* **8**, (2021).

76. Domingues, R. B. *et al.* First case of SARS-COV-2 sequencing in cerebrospinal fluid of a patient with suspected demyelinating disease. *Journal of Neurology* **267**, 3154–3156 (2020).

77. Huang, Y. H., Jiang, D. & Huang, J. T. SARS-CoV-2 Detected in Cerebrospinal Fluid by PCR in a Case of COVID-19 Encephalitis. *Brain, Behavior, and Immunity* **87**, 149 (2020).

78. Färber, K., Stäbler, P., Getzinger, T. & Uhlig, T. Suspected sepsis in a 10-week-old infant and SARS-CoV-2 detection in cerebrospinal fluid and pharynx. *Monatsschr. Kinderheilkd.* **169**, 312–316 (2021).

79. Fadakar, N. *et al.* A First Case of Acute Cerebellitis Associated with Coronavirus Disease (COVID-19): a Case Report and Literature Review. *Cerebellum* **19**, 911–914 (2020).

80. Khodamoradi, Z. *et al.* COVID-19 meningitis without pulmonary involvement with positive cerebrospinal fluid PCR. *Eur. J. Neurol.* **27**, 2668–2669 (2020).

81. Destras, G. *et al.* Systematic SARS-CoV-2 screening in cerebrospinal fluid during the COVID-19 pandemic. *The Lancet Microbe* **1**, e149 (2020).

82. Westhoff, T. H. *et al.* Allograft infiltration and meningoencephalitis by SARS-CoV-2 in a pancreas-kidney transplant recipient. *Am. J. Transplant.* **20**, 3216–3220 (2020).

83. Yachou, Y., El Idrissi, A., Belapasov, V. & Ait Benali, S. Neuroinvasion, neurotropic, and neuroinflammatory events of SARS-CoV-2: understanding the neurological manifestations in COVID-19 patients. *Neurol. Sci.* **41**, 2657–2669 (2020).

84. Yi, S. A. *et al.* Infection of Brain Organoids and 2D Cortical Neurons with SARS-CoV-2 Pseudovirus. *Viruses* **12**, (2020).

85. Zhang, B. Z. *et al.* SARS-CoV-2 infects human neural progenitor cells and brain organoids. *Cell Research* 1–4 (2020). doi:10.1038/s41422-020-0390-x

86. Bullen, C. K. *et al.* Infectability of human BrainSphere neurons suggests neurotropism of SARS-CoV-2. *ALTEX* **37**, 665–671 (2020).

87. Pellegrini, L. *et al.* SARS-CoV-2 Infects the Brain Choroid Plexus and Disrupts the Blood-CSF Barrier in Human Brain Organoids. *Cell Stem Cell* **27**, 951-961.e5 (2020).

88. Moriguchi, T. *et al.* A first case of meningitis/encephalitis associated with SARS-Coronavirus-2. *Int. J. Infect. Dis.* **94**, 55–58 (2020).

89. Song, E. *et al.* Neuroinvasive potential of SARS-CoV-2 revealed in a human brain organoid model. *bioRxiv* 2020.06.25.169946 (2020). doi:10.1101/2020.06.25.169946

90. Manosso, L. M. *et al.* Microbiota-Gut-Brain Communication in the SARS-CoV-2 Infection. *Cells* **10**, 1993 (2021).

91. Buzhdygan, T. P. *et al.* The SARS-CoV-2 spike protein alters barrier function in 2D static and 3D microfluidic in-vitro models of the human blood–brain barrier. *Neurobiol. Dis.* **146**, (2020).

92. Uversky, V. N. *et al.* Severe acute respiratory syndrome coronavirus 2 infection reaches the human nervous system: How? *Journal of Neuroscience Research* **99**, 750–777 (2021).

93. Zhang, L. *et al.* SARS-CoV-2 crosses the blood-brain barrier accompanied with basement membrane disruption without tight junctions alteration. *Signal Transduct. Target. Ther.* **6**, 337 (2021).

94. Bratosiewicz-Wąsik, J. Neuro-COVID-19: an insidious virus in action. *Neurol. Neurochir. Pol.* (2021). doi:10.5603/pjnns.a2021.0072

95. Lee, C.-Y. & Lowen, A. C. Animal Models for SARS-CoV-2. *Curr. Opin. Virol.* (2021). doi:10.1016/j.coviro.2021.03.009

96. de Vries, R. D. *et al.* Animal models of SARS-CoV-2 transmission. *Current Opinion in Virology* **50**, 8–16 (2021).

97. Miao, J., Chard, L. S., Wang, Z. & Wang, Y. Syrian Hamster as an Animal Model for the Study on Infectious Diseases. *Frontiers in Immunology* **10**, (2019).

98. Wong, K. T. *et al.* A golden hamster model for human acute Nipah virus infection. *Am. J. Pathol.* **163**, 2127–37 (2003).

99. Watanabe, S. *et al.* Mutant fusion proteins with enhanced fusion activity promote measles virus spread in human neuronal cells and brains of suckling hamsters. *J. Virol.* **87**, 2648–2659 (2013).

100. Roberts, A. *et al.* Severe Acute Respiratory Syndrome Coronavirus Infection of Golden Syrian Hamsters. *J. Virol.* **79**, 503–511 (2005).

101. Roberts, A. *et al.* Animal models and vaccines for SARS-CoV infection. *Virus Res.* **133**, 20–32 (2008).

102. Imai, M. *et al.* Syrian hamsters as a small animal model for SARS-CoV-2 infection and countermeasure development. *Proc. Natl. Acad. Sci. U. S. A.* **117**, 16587–16595 (2020).

103. Chan, J. F. W. *et al.* Simulation of the clinical and pathological manifestations of Coronavirus Disease 2019 (COVID-19) in golden Syrian hamster model: implications for disease pathogenesis and transmissibility. *Clin. Infect. Dis.* (2020). doi:10.1093/cid/ciaa325

104. Bryche, B. *et al.* Massive transient damage of the olfactory epithelium associated with infection of sustentacular cells by SARS-CoV-2 in golden Syrian hamsters. *Brain. Behav. Immun.* (2020). doi:10.1016/j.bbi.2020.06.032

105. Sia, S. F. *et al.* Pathogenesis and transmission of SARS-CoV-2 in golden hamsters. *Nature* **583**, 834–838 (2020).

106. Abbas Rizvi, Z. *et al.* Immunological and cardio-vascular pathologies associated with SARS-CoV-2 infection 1 in golden syrian hamster Summary. *Transl. Heal. Sci. Technol. Inst.* 2021.01.11.426080 (2021). doi:10.1101/2021.01.11.426080

107. Nouailles, G. *et al. Longitudinal omics in Syrian hamsters integrated with human data unravel 1 cellular effector responses to moderate COVID-19 2 3*. (2021). doi:10.21203/RS.3.RS-148392/V1

108. Pizzorno, A. *et al.* In vitro evaluation of antiviral activity of single and combined repurposable drugs against SARS-CoV-2. *Antiviral Res.* **181**, (2020).

109. Wang, M. *et al.* Remdesivir and chloroquine effectively inhibit the recently emerged novel coronavirus (2019-nCoV) in vitro. *Cell Research* **30**, 269–271 (2020).

110. Yao, X. *et al.* In vitro antiviral activity and projection of optimized dosing design of hydroxychloroquine for the treatment of severe acute respiratory syndrome coronavirus 2 (SARS-CoV-2). *Clin. Infect. Dis.* **71**, 732–739 (2020).

111. Kivrak, A., Ulaş, B. & Kivrak, H. A comparative analysis for anti-viral drugs: Their efficiency against SARS-CoV-2. *International Immunopharmacology* **90**, (2021).

112. Axfors, C. *et al.* Mortality outcomes with hydroxychloroquine and chloroquine in COVID-19 from an international collaborative meta-analysis of randomized trials. *Nat. Commun.* **12**, (2021).

113. Wang, Y. *et al.* Remdesivir in adults with severe COVID-19: a randomised, double-blind, placebo-controlled, multicentre trial. *Lancet* **395**, 1569–1578 (2020).

114. Beigel, J. H. *et al.* Remdesivir for the Treatment of Covid-19 — Final Report. *N. Engl. J. Med.* (2020). doi:10.1056/nejmoa2007764

115. NIH Clinical Trial Shows Remdesivir Accelerates Recovery from Advanced COVID-19 | NIH: National Institute of Allergy and Infectious Diseases. Available at: https://www.niaid.nih.gov/news-events/nih-clinical-trial-shows-remdesivir-accelerates-recovery-advanced-covid-19. (Accessed: 18th April 2021)

116. Lo, M. K. *et al.* GS-5734 and its parent nucleoside analog inhibit Filo-, Pneumo-, and Paramyxoviruses. *Sci. Rep.* **7**, 43395 (2017).

117. Schooley, R. T. *et al.* Rethinking Remdesivir: Synthesis, Antiviral Activity and Pharmacokinetics of Oral Lipid Prodrugs. *Antimicrob. Agents Chemother.* (2021). doi:10.1128/aac.01155-21

118. Outlaw, V. K. *et al.* Inhibition of coronavirus entry in vitro and ex vivo by a lipid-conjugated peptide derived from the sars-cov-2 spike glycoprotein hrc domain. *MBio* **11**, 1–14 (2020).

119. de Vries, R. D. *et al.* Intranasal fusion inhibitory lipopeptide prevents direct-contact SARS-CoV-2 transmission in ferrets. *Science (80-.).* **371**, 1379–1382 (2021).

120. Holzmann, H., Hengel, H., Tenbusch, M. & Doerr, H. W. Eradication of measles: remaining challenges. *Medical Microbiology and Immunology* **205**, 201–208 (2016).

121. Strebel, P. M. & Orenstein, W. A. Measles. *N. Engl. J. Med.* **381**, 349–357 (2019).

122. Organisation Mondiale de la Santé. Plus de 140 000 personnes meurent de la rougeole tandis que le nombre de cas augmente dans le monde entier. *Joint News Release* (2019). Available at: https://www.who.int/fr/news-room/detail/05-12-2019-more-than-140-000-die-from-measles-as-cases-surge-worldwide. (Accessed: 28th June 2020)

123. Moss, W. J. Measles. *Lancet* **390**, 2490–2502 (2017).

124. Waaijenborg, S. *et al.* Waning of maternal antibodies against measles, mumps, rubella, and varicella in communities with contrasting vaccination coverage. *J. Infect. Dis.* **208**, 10–6 (2013).

125. Guerra, F. M. *et al.* The basic reproduction number (R0) of measles: a systematic review. *Lancet. Infect. Dis.* **17**, e420–e428 (2017).

126. Organisation Mondiale de la Santé. Selon de nouvelles données de l'OMS et de l'UNICEF, la pandémie de COVID-19 entraîne un net recul des vaccinations chez l'enfant. (2020). Available at: https://www.who.int/fr/news/item/15-07-2021-covid-19-pandemic-leads-to-major-backsliding-on-childhood-vaccinations-new-who-unicef-data-shows. (Accessed: 13th August 2021)

127. WHO. New measles surveillance data for 2019. (2019). Available at: https://www.who.int/immunization/newsroom/measles-data-2019/en/. (Accessed: 23rd October 2019)

128. Paules, C. I., Marston, H. D. & Fauci, A. S. Measles in 2019 — Going Backward. *N. Engl. J. Med.* **380**, 2185–2187 (2019).

129. Brechot, C. *et al.* 2018 international meeting of the Global Virus Network. *Antiviral Res.* **163**, 140–148 (2019).

130. Organisation Mondiale de la Santé. Les décès dus à la rougeole ont augmenté de 50 % dans le monde entre 2016 et 2019, pour atteindre 207 500 morts en 2019. (2020). Available at: https://www.who.int/fr/news/item/12-11-2020-worldwide-measles-deaths-climb-50-from-2016-to-2019-claiming-over-207-500-lives-in-2019. (Accessed: 13th August 2021)

131. Griffin, D. E. Measles virus. in *Fields Virology. volume 6* (eds. D.M., K. & P.M., H.) 1042–1069 (2013).

132. Thibault, P. A., Watkinson, R. E., Moreira-Soto, A., Drexler, J. F. & Lee, B. Zoonotic Potential of Emerging Paramyxoviruses: Knowns and Unknowns. in *Advances in Virus Research* **98**, 1–55 (Adv Virus Res, 2017).

133. Bellini, W. J., Englund, G., Rozenblatt, S., Arnheiter, H. & Richardson, C. D. Measles virus P gene codes for two proteins. *J. Virol.* **53**, 908–19 (1985).

134. Shaffer, J. A., Bellini, W. J. & Rota, P. A. The C protein of measles virus inhibits the type I interferon response. *Virology* **315**, 389–97 (2003).

135. Schuhmann, K. M., Pfaller, C. K. & Conzelmann, K.-K. The measles virus V protein binds to p65 (RelA) to suppress NF-kappaB activity. *J. Virol.* **85**, 3162–71 (2011).

136. Gotoh, B., Komatsu, T., Takeuchi, K. & Yokoo, J. Paramyxovirus accessory proteins as interferon antagonists. *Microbiol. Immunol.* **45**, 787–800 (2001).

137. Griffin, D. E., Lin, W.-H. & Pan, C.-H. Measles virus, immune control, and persistence. *FEMS Microbiol. Rev.* **36**, 649–62 (2012).

138. Tatsuo, H., Ono, N., Tanaka, K. & Yanagi, Y. SLAM (CDw150) is a cellular receptor for measles virus. *Nature* **406**, 893–897 (2000).

139. Noyce, R. S. *et al.* Tumor cell marker PVRL4 (nectin 4) is an epithelial cell receptor for measles virus. *PLoS Pathog.* **7**, e1002240 (2011).

140. Mühlebach, M. D. *et al.* Adherens junction protein nectin-4 is the epithelial receptor for measles virus. *Nature* **480**, 530–3 (2011).

141. Naniche, D. *et al.* Human membrane cofactor protein (CD46) acts as a cellular receptor for measles virus. *J. Virol.* **67**, 6025–32 (1993).

142. Dörig, R. E., Marcil, A., Chopra, A. & Richardson, C. D. The human CD46 molecule is a receptor for measles virus (Edmonston strain). *Cell* **75**, 295–305 (1993).

143. Lamb, R. A. & Parks, G. D. Paramyxoviridae: the viruses and their replication. 1449–1496 (2007).

144. Gonçalves-Carneiro, D., McKeating, J. A. & Bailey, D. The Measles Virus Receptor SLAMF1 Can Mediate Particle Endocytosis. *J. Virol.* **91**, (2017).

145. Delpeut, S., Sisson, G., Black, K. M. & Richardson, C. D. Measles Virus Enters Breast and Colon Cancer Cell Lines through a PVRL4-Mediated Macropinocytosis Pathway. *J. Virol.* **91**, (2017).

146. Jurgens, E. M. *et al.* Measles fusion machinery is dysregulated in neuropathogenic variants. *MBio* **6**, 1–12 (2015).

147. Mathieu, C. *et al.* Prevention of Measles Virus Infection by Intranasal Delivery of Fusion Inhibitor Peptides. *J. Virol.* **89**, 1143–1155 (2015).

148. Singh, B. K. *et al.* Cell-to-Cell Contact and Nectin-4 Govern Spread of Measles Virus from Primary Human Myeloid Cells to Primary Human Airway Epithelial Cells. *J. Virol.* **90**, 6808–6817 (2016).

149. Duprex, W. P., McQuaid, S., Hangartner, L., Billeter, M. A. & Rima, B. K. Observation of measles virus cell-to-cell spread in astrocytoma cells by using a green fluorescent protein-expressing recombinant virus. *J. Virol.* **73**, 9568–75 (1999).

150. Rima, B. K. & Duprex, W. P. The measles virus replication cycle. *Curr. Top. Microbiol. Immunol.* **329**, 77–102 (2009).

151. Iwasaki, M. *et al.* The matrix protein of measles virus regulates viral RNA synthesis and assembly by interacting with the nucleocapsid protein. *J. Virol.* **83**, 10374–83 (2009).

152. Bhella, D., Ralph, A., Murphy, L. B. & Yeo, R. P. Significant differences in nucleocapsid morphology within the Paramyxoviridae. *J. Gen. Virol.* **83**, 1831–1839 (2002).

153. Radecke, F. *et al.* Rescue of measles viruses from cloned DNA. *EMBO J.* **14**, 5773–84 (1995).

154. Calain, P. & Roux, L. The rule of six, a basic feature for efficient replication of Sendai virus defective interfering RNA. *J. Virol.* **67**, 4822–30 (1993).

155. Kim, Y. H. *et al.* Capture and imaging of a prehairpin fusion intermediate of the paramyxovirus PIV5. *Proc. Natl. Acad. Sci. U. S. A.* **108**, 20992–20997 (2011).

156. Hashiguchi, T. *et al.* Structures of the prefusion form of measles virus fusion protein in complex with inhibitors. *Proc. Natl. Acad. Sci. U. S. A.* **115**, 2496–2501 (2018).

157. Watanabe, S., Shirogane, Y., Sato, Y., Hashiguchi, T. & Yanagi, Y. New Insights into Measles Virus Brain Infections. *Trends Microbiol.* (2018). doi:10.1016/j.tim.2018.08.010

158. Plattet, P., Alves, L., Herren, M. & Aguilar, H. C. Measles Virus Fusion Protein: Structure, Function and Inhibition. *Viruses* **8**, 112 (2016).

159. Angius, F. *et al.* Analysis of a Subacute Sclerosing Panencephalitis Genotype B3 Virus from the 2009-2010 South African Measles Epidemic Shows That Hyperfusogenic F Proteins Contribute to Measles Virus Infection in the Brain. *J. Virol.* **93**, (2019).

160. Lambert, D. M. *et al.* Peptides from conserved regions of paramyxovirus fusion (F) proteins are potent inhibitors of viral fusion. *Proc. Natl. Acad. Sci. U. S. A.* **93**, 2186–91 (1996).

161. Mathieu, C. *et al.* Measles Virus Bearing Measles Inclusion Body Encephalitis-Derived Fusion Protein Is Pathogenic after Infection via the Respiratory Route. *J. Virol.* **93**, (2019).

162. Palgen, J. L., Jurgens, E. M., Moscona, A., Porotto, M. & Palermo, L. M. Unity in diversity: Shared mechanism of entry among paramyxoviruses. in *Progress in Molecular Biology and Translational Science* **129**, 1–32 (NIH Public Access, 2015).

163. Navaratnarajah, C. K., Generous, A. R., Yousaf, I. & Cattaneo, R. Receptor-mediated cell entry of paramyxoviruses: Mechanisms, and consequences for tropism and pathogenesis. *Journal of Biological*

Chemistry **295**, 2771–2786 (2020).

164. Corey, E. A. & Iorio, R. M. Mutations in the Stalk of the Measles Virus Hemagglutinin Protein Decrease Fusion but Do Not Interfere with Virus-Specific Interaction with the Homologous Fusion Protein. *J. Virol.* **81**, 9900–9910 (2007).

165. Lee, B. & Ataman, Z. A. Modes of paramyxovirus fusion: A Henipavirus perspective. *Trends in Microbiology* **19**, 389–399 (2011).

166. Lorio, R. M., Melanson, V. R. & Mahon, P. J. Glycoprotein interactions in paramyxovirus fusion. *Future Virology* **4**, 335–351 (2009).

167. Ader-Ebert, N. *et al.* Sequential Conformational Changes in the Morbillivirus Attachment Protein Initiate the Membrane Fusion Process. *PLoS Pathog.* **11**, (2015).

168. Porotto, M. *et al.* Spring-loaded model revisited: paramyxovirus fusion requires engagement of a receptor binding protein beyond initial triggering of the fusion protein. *J. Virol.* **85**, 12867–12880 (2011).

169. Russell, C. J., Jardetzky, T. S. & Lamb, R. A. Membrane fusion machines of paramyxoviruses: Capture of intermediates of fusion. *EMBO J.* **20**, 4024–4034 (2001).

170. Bose, S. *et al.* Fusion activation by a headless parainfluenza virus 5 hemagglutinin- neuraminidase stalk suggests a modular mechanism for triggering. *Proc. Natl. Acad. Sci. U. S. A.* **109**, (2012).

171. Porotto, M. *et al.* The Second Receptor Binding Site of the Globular Head of the Newcastle Disease Virus Hemagglutinin-Neuraminidase Activates the Stalk of Multiple Paramyxovirus Receptor Binding Proteins To Trigger Fusion. *J. Virol.* **86**, 5730–5741 (2012).

172. Porotto, M., Palmer, S. G., Palermo, L. M. & Moscona, A. Mechanism of fusion triggering by human parainfluenza virus type III: Communication between viral glycoproteins during entry. *J. Biol. Chem.* **287**, 778–793 (2012).

173. van der Vlist, M. *et al.* Human Langerhans cells capture measles virus through Langerin and present viral antigens to CD4 + T cells but are incapable of cross-presentation. *Eur. J. Immunol.* **41**, 2619–2631 (2011).

174. Cannons, J. L., Tangye, S. G. & Schwartzberg, P. L. SLAM family receptors and SAP adaptors in immunity. *Annu. Rev. Immunol.* **29**, 665–705 (2011).

175. Coughlin, M. M., Beck, A. S., Bankamp, B. & Rota, P. A. Perspective on Global Measles Epidemiology and Control and the Role of Novel Vaccination Strategies. *Viruses* **9**, (2017).

176. Bankamp, B., Takeda, M., Zhang, Y., Xu, W. & Rota, P. A. Genetic characterization of measles vaccine strains. *J. Infect. Dis.* **204 Suppl 1**, S533-48 (2011).

177. Vaccine for Measles (MMR Shot) | CDC. Available at: https://www.cdc.gov/measles/vaccination.html. (Accessed: 15th September 2019)

178. McLean, H. Q., Fiebelkorn, A. P., Temte, J. L., Wallace, G. S. & Centers for Disease Control and Prevention. Prevention of measles, rubella, congenital rubella syndrome, and mumps, 2013: summary recommendations of the Advisory Committee on Immunization Practices (ACIP). *MMWR. Recomm. reports Morb. Mortal. Wkly. report. Recomm. reports* **62**, 1–34 (2013).

179. Haralambieva, I. H. *et al.* A large observational study to concurrently assess persistence of measles specific B-cell and T-cell immunity in individuals following two doses of MMR vaccine. *Vaccine* **29**, 4485–91 (2011).

180. Haralambieva, I. H., Kennedy, R. B., Ovsyannikova, I. G., Whitaker, J. A. & Poland, G. A. Variability in Humoral Immunity to Measles Vaccine: New Developments. *Trends Mol. Med.* **21**, 789–801 (2015).

181. Laksono, B. M. *et al.* Studies into the mechanism of measles-associated immune suppression during a measles outbreak in the Netherlands. *Nat. Commun.* **9**, 4944 (2018).

182. Sindhu, T. G., Geeta, M. G., Krishnakumar, P., Sabitha, S. & Ajina, K. K. Clinical profile of measles in children with special reference to infants. *Trop. Doct.* **49**, 20–23 (2019).

183. Ben-Chetrit, E. *et al.* Measles-related hospitalizations and associated complications in jerusalem, 2018-2019. *Clin. Microbiol. Infect.* (2019). doi:10.1016/j.cmi.2019.08.022

184. Marie, J. C. *et al.* Cell Surface Delivery of the Measles Virus Nucleoprotein: a Viral Strategy To Induce Immunosuppression. *J. Virol.* **78**, 11952–11961 (2004).

185. Mina, M. J., Metcalf, C. J. E., de Swart, R. L., Osterhaus, A. D. M. E. & Grenfell, B. T. Long-term measles-induced immunomodulation increases overall childhood infectious disease mortality. *Science (80-.).* **348**, 694–699 (2015).

186. Sellin, C. I. *et al.* Interplay between Virus-Specific Effector Response and Foxp3+ Regulatory T Cells in Measles Virus Immunopathogenesis. *PLoS One* **4**, e4948 (2009).

187. Moss, W. J. & Griffin, D. E. Measles. *Lancet (London, England)* **379**, 153–164 (2012).

188. Rima, B. K. & Duprex, W. P. Morbilliviruses and human disease. *J. Pathol.* **208**, 199–214 (2006).

189. Enders, J. F., McCarthy, K., Mitus, A. & Cheatham, W. J. Isolation of measles virus at autopsy in cases of giant-cell pneumonia without rash. *N. Engl. J. Med.* **261**, 875–81 (1959).

190. D'Souza, R. M. Vitamin A for the Treatment of Children with Measles--A Systematic Review. *J. Trop. Pediatr.* **48**, 323–327 (2002).

191. Ellison, J. B. Intensive vitamin therapy in measles. *Br. Med. J.* **2**, 708–11 (1932).

192. Imdad, A., Mayo-Wilson, E., Herzer, K. & Bhutta, Z. A. Vitamin A supplementation for preventing morbidity and mortality in children from six months to five years of age. *Cochrane Database Syst. Rev.* (2017). doi:10.1002/14651858.CD008524.pub3

193. Avota, E., Koethe, S. & Schneider-Schaulies, S. Membrane dynamics and interactions in measles virus dendritic cell infections. *Cell. Microbiol.* **15**, 161–9 (2013).

194. Ferreira, C. S. A. *et al.* Measles virus infection of alveolar macrophages and dendritic cells precedes spread to lymphatic organs in transgenic mice expressing human signaling lymphocytic activation molecule (SLAM, CD150). *J. Virol.* **84**, 3033–42 (2010).

195. de Vries, R. D., Mesman, A. W., Geijtenbeek, T. B., Duprex, W. P. & de Swart, R. L. The pathogenesis of measles. *Curr. Opin. Virol.* **2**, 248–255 (2012).

196. Delpeut, S. *et al.* Nectin-4 Interactions Govern Measles Virus Virulence in a New Model of Pathogenesis, the Squirrel Monkey (Saimiri sciureus). *J. Virol.* **91**, (2017).

197. Frenzke, M. *et al.* Nectin-4-dependent measles virus spread to the cynomolgus monkey tracheal epithelium: role of infected immune cells infiltrating the lamina propria. *J. Virol.* **87**, 2526–34 (2013).

198. Gourru-Lesimple, G. *et al.* Measles virus infection of human keratinocytes: Possible link between measles and atopic dermatitis. *J. Dermatol. Sci.* **86**, 97–105 (2017).

199. Lemon, K. *et al.* Early target cells of measles virus after aerosol infection of non-human primates. *PLoS Pathog.* **7**, e1001263 (2011).

200. Cohen, B. E., Durstenfeld, A. & Roehm, P. C. Viral causes of hearing loss: a review for hearing health professionals. *Trends Hear.* **18**, 233121651454136 (2014).

201. Dunmade, A., Segun-Busari, S., Olajide, T. & Ologe, F. Profound Bilateral Sensorineural Hearing Loss in Nigerian Children: Any Shift in Etiology? *J. Deaf Stud. Deaf Educ.* **12**, 112–118 (2006).

202. Stephenson, J. Will the current measles vaccines ever eradicate measles? *Expert Rev. Vaccines* **1**, 355–362 (2002).

203. Semba, R. D. & Bloem, M. W. Measles blindness. *Surv. Ophthalmol.* **49**, 243–55 (2004).

204. Shinoda, K. *et al.* Detection of measles virus genomic RNA in tear samples from a patient with measles keratitis. *Cornea* **21**, 610–2 (2002).

205. Ludlow, M. *et al.* Wild-type measles virus infection of primary epithelial cells occurs via the basolateral surface without syncytium formation or release of infectious virus. *J. Gen. Virol.* **91**, 971–9 (2010).

206. Muñoz-Alía, M. Á., Muller, C. P. & Russell, S. J. Hemagglutinin-specific neutralization of subacute sclerosing panencephalitis viruses. *PLoS One* **13**, e0192245 (2018).

207. Pratakpiriya, W. *et al.* Expression of canine distemper virus receptor nectin-4 in the central nervous system of dogs. *Sci. Rep.* **7**, 349 (2017).

208. Pratakpiriya, W. *et al.* Nectin4 is an epithelial cell receptor for canine distemper virus and involved in neurovirulence. *J. Virol.* **86**, 10207–10 (2012).

209. Generous, A. R. *et al.* Trans-endocytosis elicited by nectins transfers cytoplasmic cargo, including infectious material, between cells. *J. Cell Sci.* **132**, jcs235507 (2019).

210. Griffin, D. E. Measles virus and the nervous system. in *Handbook of clinical neurology* **123**, 577–590 (2014).

211. Zachariah, P. & Stockwell, M. S. Measles vaccine: Past, present, and future. *J. Clin. Pharmacol.* **56**, 133–140 (2016).

212. Johnson, R. T. *et al.* Measles encephalomyelitis--clinical and immunologic studies. *N. Engl. J. Med.* **310**, 137–41 (1984).

213. Moench, T. R., Griffin, D. E., Obriecht, C. R., Vaisberg, A. J. & Johnson, R. T. Acute measles in patients with and without neurological involvement: distribution of measles virus antigen and RNA. *J. Infect. Dis.* **158**, 433–42 (1988).

214. Reuter, D. & Schneider-Schaulies, J. Measles virus infection of the CNS: Human disease, animal models, and approaches to therapy. *Medical Microbiology and Immunology* **199**, 261–271 (2010).

215. Garg, R. K. Acute disseminated encephalomyelitis. *Postgrad. Med. J.* **79**, 11–7 (2003).

216. Miller, H. G., Stanton, J. B. & Gibbons, J. L. Acute disseminated encephalomyelitis and related syndromes. *Br. Med. J.* **1**, 668–72 (1957).

217. Griffin, D. E. *et al.* Changes in plasma IgE levels during complicated and uncomplicated measles virus infections. *J. Allergy Clin. Immunol.* **76**, 206–13 (1985).

218. Esolen, L. M. *et al.* Brain endothelial cell infection in children with acute fatal measles. *J. Clin. Invest.* **96**, 2478–81 (1995).

219. Hosoya, M. Measles encephalitis: direct viral invasion or autoimmune-mediated inflammation? *Intern. Med.* **45**, 841–2 (2006).

220. Baldolli, A. *et al.* Measles inclusion-body encephalitis (MIBE) in a immunocompromised patient. *J. Clin. Virol.* **81**, 43–46 (2016).

221. Hughes, I., Jenney, M. E., Newton, R. W., Morris, D. J. & Klapper, P. E. Measles encephalitis during immunosuppressive treatment for acute lymphoblastic leukaemia. *Arch. Dis. Child.* **68**, 775–778 (1993).

222. Hardie, D. R., Albertyn, C., Heckmann, J. M. & Smuts, H. E. M. Molecular characterisation of virus in the brains of patients with measles inclusion body encephalitis (MIBE). *Virol. J.* **10**, 283 (2013).

223. Roos, R. P., Graves, M. C., Wollmann, R. L., Chilcote, R. R. & Nixon, J. Immunologic and virologic studies of measles inclusion body encephalitis in an immunosuppressed host: the relationship to subacute sclerosing panencephalitis. *Neurology* **31**, 1263–70 (1981).

224. Bitnun, A. *et al.* Measles inclusion-body encephalitis caused by the vaccine strain of measles virus. *Clin. Infect. Dis.* **29**, 855–61 (1999).

225. Ohuchi, M., Ohuchi, R., Mifune, K., Ishihara, T. & Ogawa, T. Characterization of the measles virus isolated from the brain of a patient with immunosuppressive measles encephalitis. *J. Infect. Dis.* **156**, 436–41 (1987).

226. Mekki, M., Eley, B., Hardie, D. & Wilmshurst, J. M. Subacute sclerosing panencephalitis: clinical phenotype, epidemiology, and preventive interventions. *Dev. Med. Child Neurol.* dmcn.14166 (2019). doi:10.1111/dmcn.14166

227. Young, V. A. & Rall, G. F. Making it to the synapse: measles virus spread in and among neurons. *Curr. Top. Microbiol. Immunol.* **330**, 3–30 (2009).

228. Wendorf, K. A. *et al.* Subacute Sclerosing Panencephalitis: The Devastating Measles Complication That Might Be More Common Than Previously Estimated. *Clin. Infect. Dis.* **65**, 226–232 (2017).

229. Nakamura, Y., Iinuma, K., Oka, E. & Nihei, K. [Epidemiologic features of subacute sclerosing panencephalitis from clinical data of patients receiving a public aid for treatment]. *No to hattatsu = Brain Dev.* **35**, 316–20 (2003).

230. Miller, C. *et al.* The epidemiology of subacute sclerosing panencephalitis in England and Wales 1990-2002. *Arch. Dis. Child.* **89**, 1145–8 (2004).

231. Prashanth, L. K., Taly, A. B., Ravi, V., Sinha, S. & Rao, S. Long term survival in subacute sclerosing panencephalitis: an enigma. *Brain Dev.* **28**, 447–52 (2006).

232. Oldstone, M. B. A., Dales, S., Tishon, A., Lewicki, H. & Martin, L. A role for dual viral hits in causation of subacute sclerosing panencephalitis. *J. Exp. Med.* **202**, 1185–90 (2005).

233. Bellini, W. J. *et al.* Subacute sclerosing panencephalitis: more cases of this fatal disease are prevented by measles immunization than was previously recognized. *J. Infect. Dis.* **192**, 1686–93 (2005).

234. Forcić, D. *et al.* Detection and characterization of measles virus strains in cases of subacute sclerosing panencephalitis in Croatia. *Virus Res.* **99**, 51–6 (2004).

235. Moulin, E. *et al.* Molecular characterization of measles virus strains causing subacute sclerosing panencephalitis in France in 1977 and 2007. *J. Med. Virol.* **83**, 1614–23 (2011).

236. Cattaneo, R. *et al.* Biased hypermutation and other genetic changes in defective measles viruses in human brain infections. *Cell* **55**, 255–65 (1988).

237. Pfaller, C. K., Donohue, R. C., Nersisyan, S., Brodsky, L. & Cattaneo, R. Extensive editing of cellular and viral double-stranded RNA structures accounts for innate immunity suppression and the proviral activity of ADAR1p150. *PLoS Biol.* **16**, e2006577 (2018).

238. Rima, B. K. & Duprex, W. P. Molecular mechanisms of measles virus persistence. *Virus Res.* **111**, 132–47 (2005).

239. Liebert, U. G., Baczko, K., Budka, H. & ter Meulen, V. Restricted expression of measles virus proteins in brains from cases of subacute sclerosing panencephalitis. *J. Gen. Virol.* **67 (Pt 11)**, 2435–44 (1986).

240. Cathomen, T. *et al.* A matrix-less measles virus is infectious and elicits extensive cell fusion: consequences for propagation in the brain. *EMBO J.* **17**, 3899–3908 (1998).

241. Patterson, J. B. *et al.* Evidence that the hypermutated M protein of a subacute sclerosing panencephalitis measles virus actively contributes to the chronic progressive CNS disease. *Virology* **291**, 215–25 (2001).

242. Reuter, T., Weissbrich, B., Schneider-Schaulies, S. & Schneider-Schaulies, J. RNA interference with measles virus N, P, and L mRNAs efficiently prevents and with matrix protein mRNA enhances viral transcription. *J. Virol.* **80**, 5951–7 (2006).

243. Maisner, A., Klenk, H. & Herrler, G. Polarized budding of measles virus is not determined by viral surface glycoproteins. *J. Virol.* **72**, 5276–8 (1998).

244. Cathomen, T. *et al.* A matrix-less measles virus is infectious and elicits extensive cell fusion: Consequences for propagation in the brain. *EMBO J.* **17**, 3899–3908 (1998).

245. Kühne, M., Brown, D. W. G. & Jin, L. Genetic variability of measles virus in acute and persistent infections. *Infect. Genet. Evol.* **6**, 269–76 (2006).

246. Kweder, H. *et al.* Mutations in the H, F, or M Proteins Can Facilitate Resistance of Measles Virus to Neutralizing Human Anti-MV Sera. *Adv. Virol.* **2014**, 205617 (2014).

247. Homma, M. *et al.* Isolation and characterization of subacute sclerosing panencephalitis virus (Yamagata-1 strain) from a brain autopsy. *Microbiol. Immunol.* **26**, 1195–202 (1982).

248. Ito, N. *et al.* Comparison of the neuropathogenicity of two SSPE sibling viruses of the Osaka-2 strain isolated with Vero and B95a cells. *J. Neurovirol.* **8**, 6–13 (2002).

249. Makino, S., Sasaki, K., Nakagawa, M., Saito, M. & Shinohara, Y. Isolation and biological characterization of a measles virus-like agent from the brain of an autopsied case of subacute sclerosing panencephalitis (SSPE). *Microbiol. Immunol.* **21**, 193–205 (1977).

250. Ogura, H. *et al.* Efficient isolation of subacute sclerosing panencephalitis virus from patient brains by reference to magnetic resonance and computed tomographic images. *J. Neurovirol.* **3**, 304–9 (1997).

251. Cathomen, T., Naim, H. Y. & Cattaneo, R. Measles viruses with altered envelope protein cytoplasmic tails gain cell fusion competence. *J. Virol.* **72**, 1224–34 (1998).

252. Schmid, A. *et al.* Subacute sclerosing panencephalitis is typically characterized by alterations in the fusion protein cytoplasmic domain of the persisting measles virus. *Virology* **188**, 910–915 (1992).

253. Watanabe, S. *et al.* Measles virus mutants possessing the fusion protein with enhanced fusion activity spread effectively in neuronal cells, but not in other cells, without causing strong cytopathology. *J. Virol.* **89**, 2710–2717 (2015).

254. Ader, N. *et al.* Mechanism for active membrane fusion triggering by morbillivirus attachment protein. *J. Virol.* **87**, 314–26 (2013).

255. Avila, M. *et al.* Molecular determinants defining the triggering range of prefusion F complexes of canine distemper virus. *J. Virol.* **88**, 2951–2966 (2014).

256. Doyle, J. *et al.* Two Domains That Control Prefusion Stability and Transport Competence of the Measles Virus Fusion Protein. *J. Virol.* **80**, 1524–1536 (2006).

257. Sato, Y. *et al.* Cell-to-Cell Measles Virus Spread between Human Neurons Is Dependent on Hemagglutinin and Hyperfusogenic Fusion Protein. *J. Virol.* **92**, (2018).

258. Moeller-Ehrlich, K. *et al.* Two functionally linked amino acids in the stem 2 region of measles virus haemagglutinin determine infectivity and virulence in the rodent central nervous system. *J. Gen. Virol.* **88**, 3112–20 (2007).

259. Moeller, K. *et al.* Recombinant measles viruses expressing altered hemagglutinin (H) genes: functional separation of mutations determining H antibody escape from neurovirulence. *J. Virol.* **75**, 7612–20 (2001).

260. Hotta, H. *et al.* Full-length sequence analysis of subacute sclerosing panencephalitis (SSPE) virus, a mutant of measles virus, isolated from brain tissues of a patient shortly after onset of SSPE. *Microbiol. Immunol.* **50**, 525–34 (2006).

261. Jehmlich, U., Ritzer, J., Grosche, J., Härtig, W. & Liebert, U. G. Experimental measles encephalitis in Lewis rats: dissemination of infected neuronal cell subtypes. *J. Neurovirol.* **19**, 461–470 (2013).

262. Parhad IM, Johnson KP, Wolinsky JS & Swoveland P. Measles retinopathy. A hamster model of acute and chronic lesions. *Lab Invest.* **43(1):52**–**6**, (1980).

263. Oldstone, M. B. *et al.* Measles virus infection in a transgenic model: virus-induced immunosuppression and central nervous system disease. *Cell* **98**, 629–40 (1999).

264. Rall, G. F. *et al.* A transgenic mouse model for measles virus infection of the brain. *Proc. Natl. Acad. Sci. U. S. A.* **94**, 4659–63 (1997).

265. Blixenkrone-Møller, M. *et al.* Role of CD46 in Measles Virus Infection in CD46 Transgenic Mice. *Virology* **249**, 238–248 (1998).

266. Horvat, B. *et al.* Transgenic mice expressing human measles virus (MV) receptor CD46 provide cells exhibiting different permissivities to MV infections. *J. Virol.* **70**, 6673–81 (1996).

267. Evlashev, A. *et al.* Productive Measles Virus Brain Infection and Apoptosis in CD46 Transgenic Mice. *J. Virol.* **74**, 1373–1382 (2000).

268. Mrkic, B. *et al.* Measles virus spread and pathogenesis in genetically modified mice. *J. Virol.* **72**, 7420–7 (1998).

269. Sellin, C. I. *et al.* High pathogenicity of wild-type measles virus infection in CD150 (SLAM) transgenic mice. *J. Virol.* **80**, 6420–9 (2006).

270. Hahm, B., Arbour, N. & Oldstone, M. B. . Measles virus interacts with human SLAM receptor on dendritic cells to cause immunosuppression. *Virology* **323**, 292–302 (2004).

271. Hahm, B., Cho, J.-H. & Oldstone, M. B. A. Measles virus-dendritic cell interaction via SLAM inhibits innate immunity: selective signaling through TLR4 but not other TLRs mediates suppression of IL-12 synthesis. *Virology* **358**, 251–7 (2007).

272. Shingai, M. *et al.* Wild-type measles virus infection in human CD46/CD150-transgenic mice: CD11c-positive dendritic cells establish systemic viral infection. *J. Immunol.* **175**, 3252–61 (2005).

273. Ohno, S. *et al.* Measles virus infection of SLAM (CD150) knockin mice reproduces tropism and immunosuppression in human infection. *J. Virol.* **81**, 1650–9 (2007).

274. Welsch, J. C. *et al.* Type I Interferon Receptor Signaling Drives Selective Permissiveness of Astrocytes and Microglia to Measles Virus during Brain Infection. *J. Virol.* **93**, (2019).

275. Welstead, G. G. *et al.* Measles virus replication in lymphatic cells and organs of CD150 (SLAM) transgenic mice. *Proc. Natl. Acad. Sci. U. S. A.* **102**, 16415–20 (2005).

276. Makhortova, N. R. *et al.* Neurokinin-1 enables measles virus trans-synaptic spread in neurons. *Virology* **362**, 235–244 (2007).

277. Chan, S. P. K. Induction of Chronic Measles Encephalitis in C57BL/6 Mice. *J. Gen. Virol.* **66**, 2071–2076 (1985).

278. Ehrengruber, M. U., Ehler, E., Billeter, M. A. & Naim, H. Y. Measles virus spreads in rat hippocampal neurons by cell-to-cell contact and in a polarized fashion. *J. Virol.* **76**, 5720–8 (2002).

279. Liebert, U. G. Measles virus infections of the central nervous system. *Intervirology* **40**, 176–84 (1997).

280. Bankamp, B. *et al.* Measles virus nucleocapsid protein protects rats from encephalitis. *J. Virol.* **65**, 1695–700 (1991).

281. Niewiesk, S. Cotton rats (Sigmodon hispidus): an animal model to study the pathogenesis of measles virus infection. *Immunol. Lett.* **65**, 47–50 (1999).

282. Niewiesk, S. *et al.* CD46 expression does not overcome the intracellular block of measles virus replication in transgenic rats. *J. Virol.* **71**, 7969–73 (1997).

283. Liebert, U. G. & Meulen, V. T. Virological Aspects of Measles Virus-induced Encephalomyelitis in Lewis and BN Rats. *J. Gen. Virol.* **68**, 1715–1722 (1987).

284. Katz, M., Rorke, L. B., Masland, W. S., Brodano, G. B. & Koprowski, H. Subacute sclerosing panencephalitis: isolation of a virus encephalitogenic for ferrets. *J. Infect. Dis.* **121**, 188–95 (1970).

285. Thormar, H., Mehta, P. D., Lin, F. H., Brown, H. R. & Wisniewski, H. M. Presence of oligoclonal immunoglobulin G bands and lack of matrix protein antibodies in cerebrospinal fluids and sera of ferrets with measles virus encephalitis. *Infect. Immun.* **41**, 1205–11 (1983).

286. da Fontoura Budaszewski, R. & von Messling, V. Morbillivirus Experimental Animal Models: Measles Virus Pathogenesis Insights from Canine Distemper Virus. *Viruses* **8**, 274 (2016).

287. Burnstein, T., Jensen, J. H. & Waksman, B. H. The Development of a Neurotropic Strain of Measles Virus in Hamsters and Mice. *J. Infect. Dis.* **114**, 265–272 (1964).

288. Neighbour, P. A., Rager-Zisman, B. & Bloom, B. R. Susceptibility of mice to acute and persistent measles infection. *Infect. Immun.* **21**, 764–70 (1978).

289. Schubert, S. *et al.* A mouse model of persistent brain infection with recombinant Measles virus. *J. Gen. Virol.* **87**, 2011–9 (2006).

290. Abe, Y. *et al.* Characteristics of viruses derived from nude mice with persistent measles virus infection. *J. Virol.* **87**, 4170–5 (2013).

291. Figueira, T. N. *et al. In Vivo* Efficacy of Measles Virus Fusion Protein-Derived Peptides Is Modulated by the Properties of Self-Assembly and Membrane Residence. *J. Virol.* **91**, (2017).

292. Welsch, J. C. *et al.* Fatal measles virus infection prevented by brain-penetrant fusion inhibitors. *J. Virol.* **87**, 13785–94 (2013).

293. van Binnendijk, R. S., van der Heijden, R. W. J., Amerongen, G. v., UytdeHaag, F. G. C. M. & Osterhaus, A. D. M. E. Viral Replication and Development of Specific Immunity in Macaques after Infection with Different Measles Virus Strains. *J. Infect. Dis.* **170**, 443–448 (1994).

294. Devaux, P. *et al.* A Recombinant Measles Virus Unable To Antagonize STAT1 Function Cannot Control Inflammation and Is Attenuated in Rhesus Monkeys. *J. Virol.* **85**, 348–356 (2011).

295. Leonard, V. H. J. *et al.* Measles virus blind to its epithelial cell receptor remains virulent in rhesus monkeys but cannot cross the airway epithelium and is not shed. *J. Clin. Invest.* **118**, 2448–58 (2008).

296. El Mubarak, H. S. *et al.* Infection of cynomolgus macaques (Macaca fascicularis) and rhesus macaques (Macaca mulatta) with different wild-type measles viruses. *J. Gen. Virol.* **88**, 2028–2034 (2007).

297. Remfry, J. A measles epizootic with 5 deaths in newly-imported rhesus monkeys (*Macaca mulatta*). *Lab. Anim.* **10**, 49–57 (1976).

298. Choi, Y. K. *et al.* Fatal Measles Virus Infection in Japanese Macaques (Macaca fuscata). *Vet. Pathol.* **36**, 594–600 (1999).

299. Schumacher, H. P., Albrecht, P., Clark, R. G., Kirschstein, R. L. & Tauraso, N. M. Intracerebral inoculation of rhesus monkeys with a strain of measles virus isolated from a case of subacute sclerosing panencephalitis. *Infect. Immun.* **4**, 419–24 (1971).

300. Albrecht, P., Shabo, A. L., Burns, G. R. & Tauraso, N. M. Experimental measles encephalitis in normal and cyclophosphamide-treated rhesus monkeys. *J. Infect. Dis.* **126**, 154–61 (1972).

301. Lorenz, D. & Albrecht, P. Susceptibility of tamarins (Saguinus) to measles virus. *Lab. Anim. Sci.* **30**, 661–5 (1980).

302. Albrecht, P., Lorenz, D., Klutch, M. J., Vickers, J. H. & Ennis, F. A. Fatal measles infection in marmosets

pathogenesis and prophylaxis. *Infect. Immun.* **27**, 969–78 (1980).

303. Albrecht, P., Lorenz, D. & Klutch, M. J. Encephalitogenicity of measles virus in marmosets. *Infect. Immun.* **34**, 581–7 (1981).

304. Welsch, J. *et al.* Organotypic Brain Cultures: A Framework for Studying CNS Infection by Neurotropic Viruses and Screening Antiviral Drugs. *Bio-protocol* **7**, (2017).

305. Sheppard, R. D., Raine, C. S., Burnstein, T., Bornstein, M. B. & Feldman, L. A. Cell-associated subacute sclerosing panencephalitis agent studied in organotypic central nervous system cultures: viral rescue attempts and morphology. *Infect. Immun.* **12**, 891–900 (1975).

306. Laksono, B. M. *et al.* Comparable infection level and tropism of measles virus and canine distemper virus in organotypic brain slice cultures obtained from natural host species. *Viruses* **13**, (2021).

307. Lawrence, D. M. *et al.* Measles virus spread between neurons requires cell contact but not CD46 expression, syncytium formation, or extracellular virus production. *J. Virol.* **74**, 1908–18 (2000).

308. Duprex, W. P. *et al.* In vitro and in vivo infection of neural cells by a recombinant measles virus expressing enhanced green fluorescent protein. *J. Virol.* **74**, 7972–9 (2000).

309. Ludlow, M. *et al.* Measles virus superinfection immunity and receptor redistribution in persistently infected NT2 cells. *J. Gen. Virol.* **86**, 2291–2303 (2005).

310. McQuaid, S., Campbell, S., Wallace, I. J., Kirk, J. & Cosby, S. L. Measles virus infection and replication in undifferentiated and differentiated human neuronal cells in culture. *J. Virol.* **72**, 5245–50 (1998).

311. Brawner, A. T., Xu, R., Liu, D. & Jiang, P. Generating CNS organoids from human induced pluripotent stem cells for modeling neurological disorders. *Int. J. Physiol. Pathophysiol. Pharmacol.* **9**, 101–111 (2017).

312. Qian, X. *et al.* Brain-Region-Specific Organoids Using Mini-bioreactors for Modeling ZIKV Exposure. *Cell* **165**, 1238–1254 (2016).

313. Cosby, S. L. & Brankin, B. Measles virus infection of cerebral endothelial cells and effect on their adhesive properties. *Vet. Microbiol.* **44**, 135–9 (1995).

314. Laksono, B. M., de Vries, R. D., McQuaid, S., Duprex, W. P. & de Swart, R. L. Measles virus host invasion and pathogenesis. *Viruses* **8**, 210 (2016).

315. Bechmann, I., Galea, I. & Perry, V. H. What is the blood-brain barrier (not)? *Trends Immunol.* **28**, 5–11 (2007).

316. Allen, I. V, McQuaid, S., McMahon, J., Kirk, J. & McConnell, R. The significance of measles virus antigen and genome distribution in the CNS in SSPE for mechanisms of viral spread and demyelination. *J. Neuropathol. Exp. Neurol.* **55**, 471–80 (1996).

317. Delpeut, S., Noyce, R. S., Siu, R. W. C. & Richardson, C. D. Host factors and measles virus replication. *Curr. Opin. Virol.* **2**, 773–83 (2012).

318. McQuaid, S. & Cosby, S. L. An immunohistochemical study of the distribution of the measles virus receptors, CD46 and SLAM, in normal human tissues and subacute sclerosing panencephalitis. *Lab. Invest.* **82**, 403–9 (2002).

319. Thormar, H., Brown, H. R., Goller, N. L., Barshatzky, M. R. & Wisniewski, H. M. Transmission of measles virus encephalitis to ferrets by intracardiac inoculation of a cell-associated SSPE virus strain. *APMIS* **96**, 1125–8 (1988).

320. Woyciechowska, J., Breschkin, A. M. & Rapp, F. Measles virus meningoencephalitis. Immunofluorescence study of brains infected with virus mutants. *Lab. Invest.* **36**, 233–6 (1977).

321. Hofman, F. M., Hinton, D. R., Baemayr, J., Weil, M. & Merrill, J. E. Lymphokines and immunoregulatory molecules in subacute sclerosing panencephalitis. *Clin. Immunol. Immunopathol.* **58**, 331–42 (1991).

322. Manchester, M., Eto, D. S. & Oldstone, M. B. Characterization of the inflammatory response during acute measles encephalitis in NSE-CD46 transgenic mice. *J. Neuroimmunol.* **96**, 207–17 (1999).

323. Bispo da Silva, A. *et al.* The flavonoid rutin modulates microglial/macrophage activation to a CD150/CD206 M2 phenotype. *Chem. Biol. Interact.* **274**, 89–99 (2017).

324. O'Donnell, L. A. *et al.* STAT1-independent control of a neurotropic measles virus challenge in primary neurons and infected mice. *J. Immunol.* **188**, 1915–23 (2012).

325. Shirogane, Y. *et al.* CADM1 and CADM2 Trigger Neuropathogenic Measles Virus-Mediated Membrane Fusion by Acting in cis. *J. Virol.* **95**, (2021).

326. Sabella C. Measles: Not just a childhood rash. *Cleve. Clin. J. Med.* **77**, 207–213 (2010).

327. Ordman, C. W., Jennings, C. G. & Janeway, C. A. Chemical, clinical, and immunological studies on the products of human plasma fractionation. XII. The use of concentrated normal human serum gamma globulin (human immune serum globulin) in the prevention and attenuation of measles. *J. Clin. Invest.* **23**, 541–9 (1944).

328. Bigham, M. *et al.* Estimated protective effectiveness of intramuscular immune serum globulin post-exposure prophylaxis during a measles outbreak in British Columbia, Canada, 2014. *Vaccine* **35**, 2723–2727 (2017).

329. Rammohan, K. W., McFarland, H. F. & McFarlin, D. E. Subacute sclerosing panencephalitis after passive immunization and natural measles infection: Role of antibody in persistence of measles virus. *Neurology* **32**, 390–394 (1982).

330. Liebert, U. G., Schneider-Schaulies, S., Baczko, K. & ter Meulen, V. Antibody-induced restriction of viral gene expression in measles encephalitis in rats. *J. Virol.* **64**, 706–13 (1990).

331. Rammohan, K. W., McFarland, H. F. & McFarlin, D. E. Induction of subacute murine measles encephalitis by monoclonal antibody to virus haemagglutinin. *Nature* **290**, 588–9 (1981).

332. Wear, D. J. & Rapp, F. Latent measles virus infection of the hamster central nervous system. *J. Immunol.* **107**, 1593–8 (1971).

333. Mori, K. *et al.* Adenosine kinase is a key determinant for the anti-HCV activity of ribavirin. *Hepatology* **58**, 1236–1244 (2013).

334. Crotty, S., Cameron, C. & Andino, R. Ribavirin's antiviral mechanism of action: lethal mutagenesis? *J. Mol. Med. (Berl).* **80**, 86–95 (2002).

335. Stogner, S. W., King, J. W., Black-Payne, C. & Bocchini, J. Ribavirin and Intravenous Immune Globulin Therapy for Measles Pneumonia in HIV Infection. *South. Med. J.* **86**, 1415–1418 (1993).

336. Numasaki, M., Tomioka, Y., Takahashi, H. & Sasaki, H. IL-17 and IL-17F modulate GM-CSF production by lung microvascular endothelial cells stimulated with IL-1β and/or TNF-α. *Immunol. Lett.* **95**, 175–184 (2004).

337. Shigeta, S. *et al.* Antiviral activities of ribavirin, 5-ethynyl-1-β-D- ribofuranosylimidazole-4-carboxamide, and 6'-(R)-6'-C-methylneplanocin A against several ortho- and paramyxoviruses. *Antimicrob. Agents Chemother.* **36**, 435–439 (1992).

338. Hosoya, M., Shigeta, S., Nakamura, K. & De Clercq, E. Inhibitory effect of selected antiviral compounds on measles (SSPE) virus replication in vitro. *Antiviral Res.* **12**, 87–97 (1989).

339. Solomon, T. *et al.* Treatment of subacute sclerosing panencephalitis with interferon-alpha, ribavirin, and inosiplex. *J. Child Neurol.* **17**, 703–5 (2002).

340. Hosoya, M. *et al.* Pharmacokinetics and Effects of Ribavirin following Intraventricular Administration for Treatment of Subacute Sclerosing Panencephalitis. *Antimicrob. Agents Chemother.* **48**, 4631–4635 (2004).

341. Tomoda, A. *et al.* Trial of intraventricular ribavirin therapy for subacute sclerosing panencephalitis in Japan. *Brain Dev.* **25**, 514–7 (2003).

342. Kwak, M. *et al.* A long-term subacute sclerosing panencephalitis survivor treated with intraventricular interferon-alpha for 13 years. *Korean J. Pediatr.* **62**, 108–112 (2019).

343. Gokcil, Z., Odabasi, Z., Demirkaya, S., Eroglu, E. & Vural, O. Alpha-interferon and isoprinosine in adult-onset subacute sclerosing panencephalitis. *J. Neurol. Sci.* **162**, 62–4 (1999).

344. Gutierrez, J., Issacson, R. S. & Koppel, B. S. Subacute sclerosing panencephalitis: an update. *Dev. Med. Child Neurol.* **52**, 901–907 (2010).

345. Miyazaki, K. *et al.* Maintaining Concentration of Ribavirin in Cerebrospinal Fluid by a New Dosage Method; 3 Cases of Subacute Sclerosing Panencephalitis Treated Using a Subcutaneous Continuous Infusion Pump. *Pediatr. Infect. Dis. J.* **38**, 496–499 (2019).

346. Ravikumar, S. & Crawford, J. R. Role of carbamazepine in the symptomatic treatment of subacute sclerosing panencephalitis: a case report and review of the literature. *Case Rep. Neurol. Med.* **2013**,

327647 (2013).

347. Blank, T. & Prinz, M. Type I interferon pathway in CNS homeostasis and neurological disorders. *Glia* **65**, 1397–1406 (2017).

348. Bello, S., Meremikwu, M. M., Ejemot-Nwadiaro, R. I. & Oduwole, O. Routine vitamin A supplementation for the prevention of blindness due to measles infection in children. *Cochrane Database Syst. Rev.* (2016). doi:10.1002/14651858.CD007719.pub4

349. Barclay, A. J., Foster, A. & Sommer, A. Vitamin A supplements and mortality related to measles: a randomised clinical trial. *Br. Med. J. (Clin. Res. Ed).* **294**, 294–6 (1987).

350. Coutsoudis, A., Broughton, M. & Coovadia, H. M. Vitamin A supplementation reduces measles morbidity in young African children: a randomized, placebo-controlled, double-blind trial. *Am. J. Clin. Nutr.* **54**, 890–5 (1991).

351. Hussey, G. D. & Klein, M. Routine High-dose Vitamin A Therapy for Children Hospitalized with Measles. *J. Trop. Pediatr.* **39**, 342–345 (1993).

352. Measles vaccines: WHO position paper – April 2017. *Wkly Epidemiol Rec.* **92**, 205–27 (2017).

353. Loo, Y.-M. & Gale, M. Immune signaling by RIG-I-like receptors. *Immunity* **34**, 680–92 (2011).

354. Gerlier, D. & Lyles, D. S. Interplay between innate immunity and negative-strand RNA viruses: towards a rational model. *Microbiol. Mol. Biol. Rev.* **75**, 468–90 (2011).

355. Plumet, S. *et al.* Cytosolic 5'-triphosphate ended viral leader transcript of measles virus as activator of the RIG I-mediated interferon response. *PLoS One* **2**, e279 (2007).

356. Yoneyama, M., Onomoto, K., Jogi, M., Akaboshi, T. & Fujita, T. Viral RNA detection by RIG-I-like receptors. *Curr. Opin. Immunol.* **32**, 48–53 (2015).

357. Trottier, C. *et al.* Retinoids inhibit measles virus in vitro via nuclear retinoid receptor signaling pathways. *Antiviral Res.* **80**, 45–53 (2008).

358. Soye, K. J., Trottier, C., Richardson, C. D., Ward, B. J. & Miller, W. H. RIG-I is required for the inhibition of measles virus by retinoids. *PLoS One* **6**, e22323 (2011).

359. Trottier, C., Colombo, M., Mann, K. K., Miller, W. H. & Ward, B. J. Retinoids inhibit measles virus through a type I IFN-dependent bystander effect. *FASEB J.* **23**, 3203–12 (2009).

360. Barnard, D. L. Inhibitors of measles virus. *Antivir. Chem. Chemother.* **15**, 111–9 (2004).

361. Schönberger, K., Ludwig, M.-S., Wildner, M. & Weissbrich, B. Epidemiology of subacute sclerosing panencephalitis (SSPE) in Germany from 2003 to 2009: a risk estimation. *PLoS One* **8**, e68909 (2013).

362. Otaki, M., Sada, K., Kadoya, H., Nagano-Fujii, M. & Hotta, H. Inhibition of measles virus and subacute sclerosing panencephalitis virus by RNA interference. *Antiviral Res.* **70**, 105–111 (2006).

363. Keita, D., Servan de Almeida, R., Libeau, G. & Albina, E. Identification and mapping of a region on the mRNA of Morbillivirus nucleoprotein susceptible to RNA interference. *Antiviral Res.* **80**, 158–167 (2008).

364. Brunel, J. *et al.* Sequence of Events in Measles Virus Replication: Role of Phosphoprotein-Nucleocapsid Interactions. *J. Virol.* **88**, 10851–10863 (2014).

365. Zinke, M. *et al.* Clearance of Measles Virus from Persistently Infected Cells by Short Hairpin RNA. *J. Virol.* **83**, 9423–9431 (2009).

366. Plumet, S., Duprex, W. P. & Gerlier, D. Dynamics of Viral RNA Synthesis during Measles Virus Infection. *J. Virol.* **79**, 6900–6908 (2005).

367. Bloyet, L.-M. *et al.* HSP90 Chaperoning in Addition to Phosphoprotein Required for Folding but Not for Supporting Enzymatic Activities of Measles and Nipah Virus L Polymerases. *J. Virol.* **90**, 6642–6656 (2016).

368. Geller, R., Andino, R. & Frydman, J. Hsp90 Inhibitors Exhibit Resistance-Free Antiviral Activity against Respiratory Syncytial Virus. *PLoS One* **8**, e56762 (2013).

369. Jordan, P. C. *et al.* Initiation, extension, and termination of RNA synthesis by a paramyxovirus polymerase. *PLoS Pathog.* **14**, e1006889 (2018).

370. Warren, T. K. *et al.* Therapeutic efficacy of the small molecule GS-5734 against Ebola virus in rhesus monkeys. *Nature* **531**, 381–5 (2016).

371. White, L. K. *et al.* Nonnucleoside inhibitor of measles virus RNA-dependent RNA polymerase complex activity. *Antimicrob. Agents Chemother.* **51**, 2293–303 (2007).

372. Yoon, J.-J. *et al.* Target analysis of the experimental measles therapeutic AS-136A. *Antimicrob. Agents Chemother.* **53**, 3860–70 (2009).

373. Ndungu, J. M. *et al.* Non-nucleoside inhibitors of the measles virus RNA-dependent RNA polymerase: synthesis, structure-activity relationships, and pharmacokinetics. *J. Med. Chem.* **55**, 4220–30 (2012).

374. Tahara, M. *et al.* The receptor-binding site of the measles virus hemagglutinin protein itself constitutes a conserved neutralizing epitope. *J. Virol.* **87**, 3583–6 (2013).

375. Tadokoro, T. *et al.* Biophysical characterization and single-chain Fv construction of a neutralizing antibody to measles virus. *FEBS J.* febs.14991 (2019). doi:10.1111/febs.14991

376. Plemper, R. K. *et al.* A target site for template-based design of measles virus entry inhibitors. *Proc. Natl. Acad. Sci.* **101**, 5628–5633 (2004).

377. Ha, M. N. *et al.* Mutations in the Fusion Protein of Measles Virus That Confer Resistance to the Membrane Fusion Inhibitors Carbobenzoxy-d-Phe-l-Phe-Gly and 4-Nitro-2-Phenylacetyl Amino-Benzamide. *J. Virol.* **91**, (2017).

378. LaBonte, J., Lebbos, J. & Kirkpatrick, P. Enfuvirtide. *Nature Reviews Drug Discovery* **2**, 345–346 (2003).

379. Ding, X. *et al.* Enfuvirtide (T20)-Based Lipopeptide Is a Potent HIV-1 Cell Fusion Inhibitor: Implications for Viral Entry and Inhibition. *J. Virol.* **91**, (2017).

380. Dingens, A. S., Arenz, D., Overbaugh, J. & Bloom, J. D. Massively parallel profiling of HIV-1 resistance to the fusion inhibitor enfuvirtide. *Viruses* **11**, (2019).

381. Mathieu, C. *et al.* Prevention of measles virus infection by intranasal delivery of fusion inhibitor peptides. *J. Virol.* **89**, 1143–1155 (2015).

382. Porotto, M. *et al.* Viral Entry Inhibitors Targeted to the Membrane Site of Action. *J. Virol.* **84**, 6760–6768 (2010).

383. Porotto, M. *et al.* Inhibition of Nipah virus infection in vivo: targeting an early stage of paramyxovirus fusion activation during viral entry. *PLoS Pathog.* **6**, e1001168 (2010).

384. Murray, K. *et al.* A morbillivirus that caused fatal disease in horses and humans. *Science (80-.).* **268**, 94–97 (1995).

385. Mayo, M. A. A summary of taxonomic changes recently approved by ICTV. *Archives of Virology* **147**, 1655–1656 (2002).

386. Queensland Goverment. Hendra virus | Business Queensland. *Hendra virus* (2018). Available at: https://www.business.qld.gov.au/industries/farms-fishing-forestry/agriculture/livestock/animal-welfare/pests-diseases-disorders/hendra-virus. (Accessed: 22nd October 2021)

387. Khusro, A., Aarti, C., Pliego, A. B. & Cipriano-Salazar, M. Hendra Virus Infection in Horses: A Review on Emerging Mystery Paramyxovirus. *Journal of Equine Veterinary Science* **91**, 103149 (2020).

388. Yuen, K. Y. *et al.* Hendra virus: Epidemiology dynamics in relation to climate change, diagnostic tests and control measures. *One Health* **12**, (2021).

389. Business Queensland. Summary of Hendra virus incidents in horses. *Queensland Government* (2019). Available at: https://www.business.qld.gov.au/industries/service-industries-professionals/service-industries/veterinary-surgeons/guidelines-hendra/incident-summary. (Accessed: 8th September 2021)

390. Middleton, D. J. *et al.* Experimental Hendra virus infection of dogs: virus replication, shedding and potential for transmission. *Aust. Vet. J.* **95**, 10–18 (2017).

391. Li, M., Embury-Hyatt, C. & Weingartl, H. M. Experimental inoculation study indicates swine as a potential host for Hendra virus. *Vet. Res.* **41**, (2010).

392. Guillaume, V. *et al.* Acute Hendra virus infection: Analysis of the pathogenesis and passive antibody protection in the hamster model. *Virology* **387**, 459–465 (2009).

393. Williamson, M. M., Hooper, P. T., Selleck, P. W., Westbury, H. A. & Slocombe, R. F. S. A guinea-pig model of hendra virus encephalitis. *J. Comp. Pathol.* **124**, 273–279 (2001).

394. Pallister, J. *et al.* A recombinant Hendra virus G glycoprotein-based subunit vaccine protects ferrets from

lethal Hendra virus challenge. *Vaccine* **29**, 5623–5630 (2011).

395. Rockx, B. *et al.* A Novel Model of Lethal Hendra Virus Infection in African Green Monkeys and the Effectiveness of Ribavirin Treatment. *J. Virol.* **84**, 9831–9839 (2010).

396. Williamson, M. M. *et al.* Transmission studies of Hendra virus (equine morbillivirus) in fruit bats, horses and cats. *Aust. Vet. J.* **76**, 813–818 (1998).

397. Marsh, G. A. *et al.* Experimental infection of horses with Hendra virus/Australia/horse/2008/Redlands. *Emerg. Infect. Dis.* **17**, 2232–2238 (2011).

398. Dhondt, K. P. *et al.* Type I interferon signaling protects mice from lethal henipavirus infection. *J. Infect. Dis.* **207**, 142–151 (2013).

399. Chua, K. B. *et al.* Fatal encephalitis due to Nipah virus among pig-farmers in Malaysia. *Lancet (London, England)* **354**, 1257–9 (1999).

400. Centers for Disease Control and Prevention (CDC). Outbreak of Hendra-like virus - Malaysia and Singapore, 1998-1999. *J. Am. Med. Assoc.* **281**, 1787–1788 (1999).

401. Goh, K. J. *et al.* Clinical Features of Nipah Virus Encephalitis among Pig Farmers in Malaysia. *N. Engl. J. Med.* **342**, 1229–1235 (2000).

402. Paton, N. I. *et al.* Outbreak of Nipah-virus infection among abattoir workers in Singapore. *Lancet* **354**, 1253–1256 (1999).

403. Lam, S. K. Nipah virus - A potential agent of bioterrorism? *Antiviral Res.* **57**, 113–119 (2003).

404. Hsu, V. P. *et al.* Nipah Virus Encephalitis Reemergence, Bangladesh. *Emerg. Infect. Dis.* **10**, 2082–2087 (2004).

405. Gurley, E. S. *et al.* Person-to-person transmission of Nipah virus in a Bangladeshi community. *Emerg. Infect. Dis.* **13**, 1031–1037 (2007).

406. Chadha, M. S. *et al.* Nipah virus-associated encephalitis outbreak, Siliguri, India. *Emerg. Infect. Dis.* **12**, 235–240 (2006).

407. Chua, K. *et al.* Nipah virus: A recently emergent deadly paramyxovirus. *Science (80-.).* **288**, 1432–1435 (2000).

408. Halpin, K. *et al.* Pteropid bats are confirmed as the reservoir hosts of henipaviruses: A comprehensive experimental study of virus transmission. *Am. J. Trop. Med. Hyg.* **85**, 946–951 (2011).

409. Chua, K. B. *et al.* Isolation of Nipah virus from Malaysian Island flying-foxes. *Microbes Infect.* **4**, 145–151 (2002).

410. Reynes, J.-M. *et al.* Nipah virus in Lyle's flying foxes, Cambodia. *Emerg. Infect. Dis.* **11**, 1042–7 (2005).

411. Luby, S. P. *et al.* Foodborne transmission of Nipah virus, Bangladesh. *Emerg. Infect. Dis.* **12**, 1888–1894 (2006).

412. Islam, M. S. *et al.* Nipah virus transmission from bats to humans associated with drinking traditional liquor made from date palm sap, Bangladesh, 2011-2014. *Emerg. Infect. Dis.* **22**, 664–670 (2016).

413. Montgomery, J. M. *et al.* Risk factors for Nipah virus encephalitis in Bangladesh. *Emerg. Infect. Dis.* **14**, 1526–1532 (2008).

414. Wacharapluesadee, S. *et al.* Bat Nipah virus, Thailand. *Emerg. Infect. Dis.* **11**, 1949–1951 (2005).

415. Anderson, D. E. *et al.* Isolation and full-genome characterization of nipah viruses from bats, Bangladesh. *Emerg. Infect. Dis.* **25**, 166–170 (2019).

416. Yob, J. M. *et al.* Nipah Virus Infection in Bats (Order Chiroptera) in Peninsular Malaysia. *Emerg. Infect. Dis.* **7**, 439–441 (2001).

417. Yadav, P. D. *et al.* Short report: Detection of Nipah virus RNA in fruit bat (Pteropus giganteus) from India. *Am. J. Trop. Med. Hyg.* **87**, 576–578 (2012).

418. Iehlé, C. *et al.* Henipavirus and tioman virus antibodies in pteropodid bats, Madagascar. *Emerg. Infect. Dis.* **13**, 159–161 (2007).

419. Hayman, D. T. S. *et al.* Evidence of henipavirus infection in West African fruit bats. *PLoS One* **3**, (2008).

420. Ching, P. K. G. *et al.* Outbreak of henipavirus infection, Philippines, 2014. *Emerg. Infect. Dis.* **21**, 328–331 (2015).

421. Arunkumar, G. *et al.* Outbreak investigation of nipah virus disease in Kerala, India, 2018. *J. Infect. Dis.* **219**, 1867–1878 (2019).

422. Nikolay, B. *et al.* Transmission of Nipah Virus — 14 Years of Investigations in Bangladesh. *N. Engl. J. Med.* **380**, 1804–1814 (2019).

423. Spiropoulou, C. F. Nipah virus outbreaks: Still small but extremely lethal. *Journal of Infectious Diseases* **219**, 1855–1857 (2019).

424. Plowright, R. K. *et al.* Ecological dynamics of emerging bat virus spillover. *Proceedings of the Royal Society B: Biological Sciences* **282**, (2014).

425. Chua, K. B., Chua, B. H. & Wang, C. W. Anthropogenic deforestation, El Niño and the emergence of Nipah virus in Malaysia. *Malays. J. Pathol.* **24**, 15–21 (2002).

426. Pillai, V. S., Krishna, G. & Veettil, M. V. Nipah virus: Past outbreaks and future containment. *Viruses* **12**, (2020).

427. Broder, C. C., Weir, D. L. & Reid, P. A. Hendra virus and Nipah virus animal vaccines. *Vaccine* **34**, 3525–3534 (2016).

428. Dhondt, K. P. & Horvat, B. Henipavirus infections: Lessons from animal models. *Pathogens* **2**, 264–287 (2013).

429. Geisbert, T. W. *et al.* Development of an acute and highly pathogenic nonhuman primate model of nipah virus infection. *PLoS One* **5**, (2010).

430. Wang, L., Mackenzie, J. & Broder, C. C. Henipaviruses. in *Fields virology* (ed. Knipe DM, H. P.) 286–313 (Lippincott Williams & Wilkins, 2013).

431. Eaton, B. T., Mackenzie, J. & Wang, L. Henipavirus. in *Fields virology* (ed. Knipe DM, H. P.) (Lippincott Williams & Wilkins, 2007).

432. Halpin, K., Bankamp, B., Harcourt, B. H., Bellini, W. J. & Rota, P. A. Nipah virus conforms to the rule of six in a minigenome replication assay. *J. Gen. Virol.* **85**, 701–707 (2004).

433. Horikami, S. M. & Moyer, S. A. Synthesis of leader RNA and editing of the P mRNA during transcription by purified measles virus. *J. Virol.* **65**, 5342–5347 (1991).

434. Bowden, T. A. *et al.* Structural basis of Nipah and Hendra virus attachment to their cell-surface receptor ephrin-B2. *Nat. Struct. Mol. Biol.* **15**, 567–572 (2008).

435. Bennett, K. M. *et al.* Ephrin-B2 reverse signaling increases α5β1 integrin-mediated fibronectin deposition and reduces distal lung compliance. *Am. J. Respir. Cell Mol. Biol.* **49**, 680–687 (2013).

436. Hafner, C. *et al.* Differential Gene Expression of Eph Receptors and Ephrins in Benign Human Tissues and Cancers. *Clin. Chem.* **50**, 490–499 (2004).

437. Gale, N. W. *et al.* Ephrin-B2 selectively marks arterial vessels and neovascularization sites in the adult, with expression in both endothelial and smooth-muscle cells. *Dev. Biol.* **230**, 151–160 (2001).

438. Lee, B. Envelope-receptor interactions in Nipah virus pathobiology. *Ann. N. Y. Acad. Sci.* **1102**, 51–65 (2007).

439. Zimmer, M., Palmer, A., Köhler, J. & Klein, R. EphB-ephrinB bi-directional endocytosis terminates adhesion allowing contact mediated repulsion. *Nat. Cell Biol.* **5**, 869–878 (2003).

440. Wang, H. U., Chen, Z. F. & Anderson, D. J. Molecular distinction and angiogenic interaction between embryonic arteries and veins revealed by ephrin-B2 and its receptor Eph-B4. *Cell* **93**, 741–753 (1998).

441. Negrete, O. A. *et al.* EphrinB2 is the entry receptor for Nipah virus, an emergent deadly paramyxovirus. *Nature* **436**, 401–405 (2005).

442. Bonaparte, M. I. *et al.* Ephrin-B2 ligand is a functional receptor for Hendra virus and Nipah virus. *Proc. Natl. Acad. Sci. U. S. A.* **102**, 10652–10657 (2005).

443. Negrete, O. A. *et al.* Two Key Residues in EphrinB3 Are Critical for Its Use as an Alternative Receptor for Nipah Virus. *PLoS Pathog.* **2**, e7 (2006).

444. Xu, K., Broder, C. C. & Nikolov, D. B. Ephrin-B2 and ephrin-B3 as functional henipavirus receptors.

Seminars in Cell and Developmental Biology **23**, 116–123 (2012).

445. Negrete, O. A., Chu, D., Aguilar, H. C. & Lee, B. Single amino acid changes in the Nipah and Hendra virus attachment glycoproteins distinguish ephrinB2 from ephrinB3 usage. *J. Virol.* **81**, 10804–14 (2007).

446. Pryce, R. *et al.* A key region of molecular specificity orchestrates unique ephrin-B1 utilization by Cedar virus. *Life Sci. Alliance* **3**, (2020).

447. Marsh, G. A. *et al.* Cedar Virus: A Novel Henipavirus Isolated from Australian Bats. *PLoS Pathog.* **8**, (2012).

448. Laing, E. D. *et al.* Rescue and characterization of recombinant cedar virus, a non-pathogenic Henipavirus species. *Virol. J.* **15**, (2018).

449. Laing, E. D. *et al.* Structural and functional analyses reveal promiscuous and species specific use of ephrin receptors by Cedar virus. *Proc. Natl. Acad. Sci. U. S. A.* **116**, 20707–20715 (2019).

450. Mathieu, C. *et al.* Heparan Sulfate-Dependent Enhancement of Henipavirus Infection. *MBio* **6**, e02427-14 (2015).

451. Bishop, J. R., Schuksz, M. & Esko, J. D. Heparan sulphate proteoglycans fine-tune mammalian physiology. *Nature* **446**, 1030–1037 (2007).

452. Mathieu, C. *et al.* Nipah Virus Uses Leukocytes for Efficient Dissemination within a Host. *J. Virol.* **85**, 7863–7871 (2011).

453. Guillaume, V. *et al.* Evidence of a Potential Receptor-Binding Site on the Nipah Virus G Protein (NiV-G): Identification of Globular Head Residues with a Role in Fusion Promotion and Their Localization on an NiV-G Structural Model. *J. Virol.* **80**, 7546–7554 (2006).

454. Pernet, O., Pohl, C., Ainouze, M., Kweder, H. & Buckland, R. Nipah virus entry can occur by macropinocytosis. *Virology* **395**, 298–311 (2009).

455. Garten, W. *et al.* Processing of viral glycoproteins by the subtilisin-like endoprotease furin and its inhibition by specific peptidylchloroalkylketones. *Biochimie* **76**, 217–225 (1994).

456. Watanabe, M. *et al.* Engineered serine protease inhibitor prevents furin-catalyzed activation of the fusion glycoprotein and production of infectious measles virus. *J. Virol.* **69**, 3206–3210 (1995).

457. Pager, C. T. & Dutch, R. E. Cathepsin L Is Involved in Proteolytic Processing of the Hendra Virus Fusion Protein. *J. Virol.* **79**, 12714–12720 (2005).

458. Pager, C. T., Craft, W. W., Patch, J. & Dutch, R. E. A mature and fusogenic form of the Nipah virus fusion protein requires proteolytic processing by cathepsin L. *Virology* **346**, 251–257 (2006).

459. Diederich, S., Moll, M., Klenk, H. D. & Maisner, A. The Nipah virus fusion protein is cleaved within the endosomal compartment. *J. Biol. Chem.* **280**, 29899–29903 (2005).

460. Lamb, R. A. & Jardetzky, T. S. Structural basis of viral invasion: lessons from paramyxovirus F. *Current Opinion in Structural Biology* **17**, 427–436 (2007).

461. Mathieu, C. & Horvat, B. Henipavirus pathogenesis and antiviral approaches. *Expert Rev. Anti. Infect. Ther.* **13**, 343–354 (2015).

462. Tiong, V., Shu, M. H., Wong, W. F., Abubakar, S. & Chang, L. Y. Nipah virus infection of immature dendritic cells increases its transendothelial migration across human brain microvascular endothelial cells. *Front. Microbiol.* **9**, (2018).

463. Wong, K. T. *et al.* Human Hendra virus infection causes acute and relapsing encephalitis. *Neuropathol. Appl. Neurobiol.* **35**, 296–305 (2009).

464. Tan, C. T. *et al.* Relapsed and late-onset Nipah encephalitis. *Ann. Neurol.* **51**, 703–8 (2002).

465. Ng, B.-Y., Lim, C. C. T., Yeoh, A. & Lee, W. L. Neuropsychiatric sequelae of Nipah virus encephalitis. *J. Neuropsychiatry Clin. Neurosci.* **16**, 500–4 (2004).

466. Sejvar, J. J. *et al.* Long-term neurological and functional outcome in Nipah virus infection. *Ann. Neurol.* **62**, 235–42 (2007).

467. Dawes, B. E. & Freiberg, A. N. Henipavirus infection of the central nervous system. *Pathog. Dis.* **77**, (2019).

468. Wong, K. T. *et al.* Nipah virus infection: pathology and pathogenesis of an emerging paramyxoviral

zoonosis. *Am. J. Pathol.* **161**, 2153–67 (2002).

469. Weingartl, H. *et al.* Invasion of the central nervous system in a porcine host by nipah virus. *J. Virol.* **79**, 7528–34 (2005).

470. Pallister, J. A. *et al.* Vaccination of ferrets with a recombinant G glycoprotein subunit vaccine provides protection against Nipah virus disease for over 12 months. *Virol. J.* **10**, (2013).

471. Guillaume, V. *et al.* Nipah virus: vaccination and passive protection studies in a hamster model. *J. Virol.* **78**, 834–40 (2004).

472. Weingartl, H. M. *et al.* Recombinant Nipah Virus Vaccines Protect Pigs against Challenge. *J. Virol.* **80**, 7929–7938 (2006).

473. Pickering, B. S. *et al.* Protection against henipaviruses in swine requires both, cell-mediated and humoral immune response. *Vaccine* **34**, 4777–86 (2016).

474. Ploquin, A. *et al.* Protection Against Henipavirus Infection by Use of Recombinant Adeno-Associated Virus–Vector Vaccines. *J. Infect. Dis.* **207**, 469–478 (2013).

475. Yoneda, M. *et al.* Recombinant Measles Virus Vaccine Expressing the Nipah Virus Glycoprotein Protects against Lethal Nipah Virus Challenge. *PLoS One* **8**, (2013).

476. Mire, C. E. *et al.* Single injection recombinant vesicular stomatitis virus vaccines protect ferrets against lethal Nipah virus disease. *Virol. J.* **10**, (2013).

477. Mire, C. E. *et al.* Use of single-injection recombinant vesicular stomatitis virus vaccine to protect nonhuman primates against lethal nipah virus disease. *Emerg. Infect. Dis.* **25**, 1144–1152 (2019).

478. Walpita, P. *et al.* A VLP-based vaccine provides complete protection against Nipah virus challenge following multiple-dose or single-dose vaccination schedules in a hamster model. *npj Vaccines* **2**, (2017).

479. Lo, M. K. *et al.* Evaluation of a Single-Dose Nucleoside-Modified Messenger RNA Vaccine Encoding Hendra Virus-Soluble Glycoprotein Against Lethal Nipah virus Challenge in Syrian Hamsters. *J. Infect. Dis.* **221**, S493–S498 (2020).

480. Hauser, N., Gushiken, A. C., Narayanan, S., Kottilil, S. & Chua, J. V. Evolution of nipah virus infection: Past, present, and future considerations. *Tropical Medicine and Infectious Disease* **6**, (2021).

481. Dawes, B. E. *et al.* Favipiravir (T-705) protects against Nipah virus infection in the hamster model /631/326/22/1295 /631/326/596/1296 /13/106 /14/35 /38/77 /82/51 /96/63 article. *Sci. Rep.* **8**, (2018).

482. Lo, M. K. *et al.* Remdesivir (GS-5734) protects African green monkeys from Nipah virus challenge. *Sci. Transl. Med.* **11**, eaau9242 (2019).

483. Bossart, K. N. *et al.* A neutralizing human monoclonal antibody protects against lethal disease in a new ferret model of acute nipah virus infection. *PLoS Pathog.* **5**, e1000642 (2009).

484. Geisbert, T. W. *et al.* Therapeutic treatment of Nipah virus infection in nonhuman primates with a neutralizing human monoclonal antibody. *Sci. Transl. Med.* **6**, (2014).

485. Bossart, K. N. *et al.* Infectious disease: A neutralizing human monoclonal antibody protects African green monkeys from Hendra virus challenge. *Sci. Transl. Med.* **3**, (2011).

486. Mire, C. E. *et al.* A Cross-Reactive Humanized Monoclonal Antibody Targeting Fusion Glycoprotein Function Protects Ferrets Against Lethal Nipah Virus and Hendra Virus Infection. *J. Infect. Dis.* **221**, S471–S479 (2020).

487. Playford, E. G. *et al.* Safety, tolerability, pharmacokinetics, and immunogenicity of a human monoclonal antibody targeting the G glycoprotein of henipaviruses in healthy adults: a first-in-human, randomised, controlled, phase 1 study. *Lancet Infect. Dis.* **20**, 445–454 (2020).

488. Porotto, M. *et al.* Molecular Determinants of Antiviral Potency of Paramyxovirus Entry Inhibitors. *J. Virol.* **81**, 10567–10574 (2007).

489. Mathieu, C., Porotto, M., Figueira, T. N., Horvat, B. & Moscona, A. Fusion inhibitory lipopeptides engineered for prophylaxis of nipah virus in primates. *J. Infect. Dis.* **218**, 218–227 (2018).

490. Mathieu, C. *et al.* Broad spectrum antiviral activity for paramyxoviruses is modulated by biophysical properties of fusion inhibitory peptides. *Sci. Rep.* **7**, 43610 (2017).

491. Chong, H. T. *et al.* Treatment of acute Nipah encephalitis with ribavirin. *Ann. Neurol.* **49**, 810–813 (2001).

492. Freiberg, A. N., Worthy, M. N., Lee, B. & Holbrook, M. R. Combined chloroquine and ribavirin treatment does not prevent death in a hamster model of Nipah and Hendra virus infection. *J. Gen. Virol.* **91**, 765–772 (2010).

493. Pallister, J. *et al.* Chloroquine Administration Does Not Prevent Nipah Virus Infection and Disease in Ferrets. *J. Virol.* **83**, 11979–11982 (2009).

494. Preibisch, S., Saalfeld, S. & Tomancak, P. Globally optimal stitching of tiled 3D microscopic image acquisitions. *Bioinformatics* **25**, 1463–1465 (2009).

495. Gaudino, M. *et al.* High pathogenicity of nipah virus from pteropus lylei fruit bats, Cambodia. *Emerg. Infect. Dis.* **26**, 104–113 (2020).

496. Pain, B., Baquerre, C. & Coulpier, M. Cerebral organoids and their potential for studies of brain diseases in domestic animals. *Veterinary Research* **52**, (2021).

497. Clay, C. C. *et al.* Neuroinvasion of Fluorescein-Positive Monocytes in Acute Simian Immunodeficiency Virus Infection. *J. Virol.* **81**, 12040–12048 (2007).

498. Rudd, P. A., Cattaneo, R. & von Messling, V. Canine Distemper Virus Uses both the Anterograde and the Hematogenous Pathway for Neuroinvasion. *J. Virol.* **80**, 11416–11416 (2006).

499. Doyle, M. F. Central Nervous System Outcomes of COVID-19. *Transl. Res.* (2021). doi:10.1016/j.trsl.2021.09.002

500. Qian, X., Song, H. & Ming, G. L. Brain organoids: Advances, applications and challenges. *Development (Cambridge)* **146**, (2019).

501. Debuysscher, B. L. *et al.* Nipah virus efficiently replicates in human smooth muscle cells without cytopathic effect. *Cells* **10**, (2021).

502. Di Toro, A. *et al.* Long COVID: long-term effects? *Eur. Hear. J. Suppl.* **23**, E1–E5 (2021).

503. Viszlayová, D. *et al.* SARS-CoV-2 RNA in the Cerebrospinal Fluid of a Patient with Long COVID. *Ther. Adv. Infect. Dis.* **8**, 204993612110485 (2021).

ANNEXES

1) Annexe 1 : Interféron de type I et sélectivité de l'infection des cellules du système nerveux central par le virus de la rougeole

NOUVELLE

Interféron de type I et sélectivité de l'infection des cellules du système nerveux central par le virus de la rougeole

Marion Ferren, Branka Horvat, Denis Gerlier, Cyrille Mathieu

Centre international de recherche en infectiologie (CIRI), équipe d'immunobiologie des infections virales, Univ Lyon, Inserm U1111, Université Claude Bernard Lyon 1, CNRS UMR5308, ENS de Lyon, 21 avenue Tony-Garnier, 69007, Lyon, France.
marion.ferren@inserm.fr
cyrille.mathieu@inserm.fr

> L'infection par le virus de la rougeole reste une cause majeure de morbidité et de mortalité dans le monde [1]. Malgré la disponibilité d'un vaccin, ce virus n'a pas été éradiqué et a encore causé plus de 140 000 décès en 2018, un nombre en augmentation par rapport aux années précédentes [2]. Aucun traitement n'est disponible pour guérir l'infection par le virus de la rougeole. La maladie commence dans les voies respiratoires par l'infection des macrophages pulmonaires ou des cellules dendritiques exprimant le récepteur cellulaire de la molécule d'activation lymphocytaire F1 (*signaling lymphocyte-activating molecule*, SLAM/CD150). En ce qui concerne les cellules dendritiques infectées, celles-ci migrent alors vers les ganglions lymphatiques et transmettent le virus aux lymphocytes B et T activés exprimant SLAM, qui propagent l'infection par les systèmes vasculaires lymphatique et sanguin. Au stade avancé de l'infection, le virus de la rougeole infecte la surface baso-latérale des cellules épithéliales respiratoires par la protéine des jonctions d'adhérence nectine-4, ce qui permet l'excrétion du virus par voie aérienne et la propagation de l'épidémie [3]. À l'échelle moléculaire, les glycoprotéines d'attachement H et de fusion F forment la machinerie de fusion à la surface de la membrane virale. L'engagement du récepteur d'entrée par la protéine H déclenche la transition structurale de la protéine F qui gouverne le processus de fusion des membranes virale et cellulaire, donc l'entrée de la ribonucléocapside virale dans le cytoplasme [4].

Le virus de la rougeole peut également se propager au système nerveux central et causer une encéphalite, presque toujours létale. La myéloencéphalite rougeoleuse à corps d'inclusions (MIBE) survient chez les patients immunodéprimés plusieurs semaines ou mois après l'infection, et la panencéphalite subaiguë sclérosante (PESS) se produit chez les patients immunocompétents encore plus tardivement, jusqu'à plusieurs décennies après l'exposition au virus survenant le plus souvent chez le très jeune enfant [5, 6]. Les étapes précoces de la neuro-invasion restent particulièrement peu documentées faute d'outils disponibles, et la plupart des données proviennent d'analyses *post mortem*. Les infections pathologiques du système nerveux central conduisent généralement à une démyélinisation et sont associées à des lésions du cortex cérébral, de l'hippocampe, du thalamus, du tronc cérébral, et du cortex cérébelleux [6]. Les antigènes viraux sont généralement détectés dans les neurones et les oligodendrocytes, et beaucoup plus rarement dans les acteurs immunitaires majeurs du système nerveux central, les astrocytes et les cellules microgliales [7, 8]. Le récepteur d'entrée du virus de la rougeole dans les cellules du système nerveux central est inconnu.

Des souris transgéniques exprimant artificiellement le récepteur humain du virus de la rougeole de façon ubiquitaire (souris SLAMtg) permettent de s'affranchir de toute variation liée à l'entrée du virus dans les cellules. En particulier, l'infection intranasale, par le virus de la rougeole, de souriceaux SLAMtg provoque une invasion virale du système nerveux central conduisant à un syndrome neurologique aigu létal, associé histologiquement à une astrogliose et

m/s n° 1, vol. 37, janvier 2021
https://doi.org/10.1051/medsci/2020252

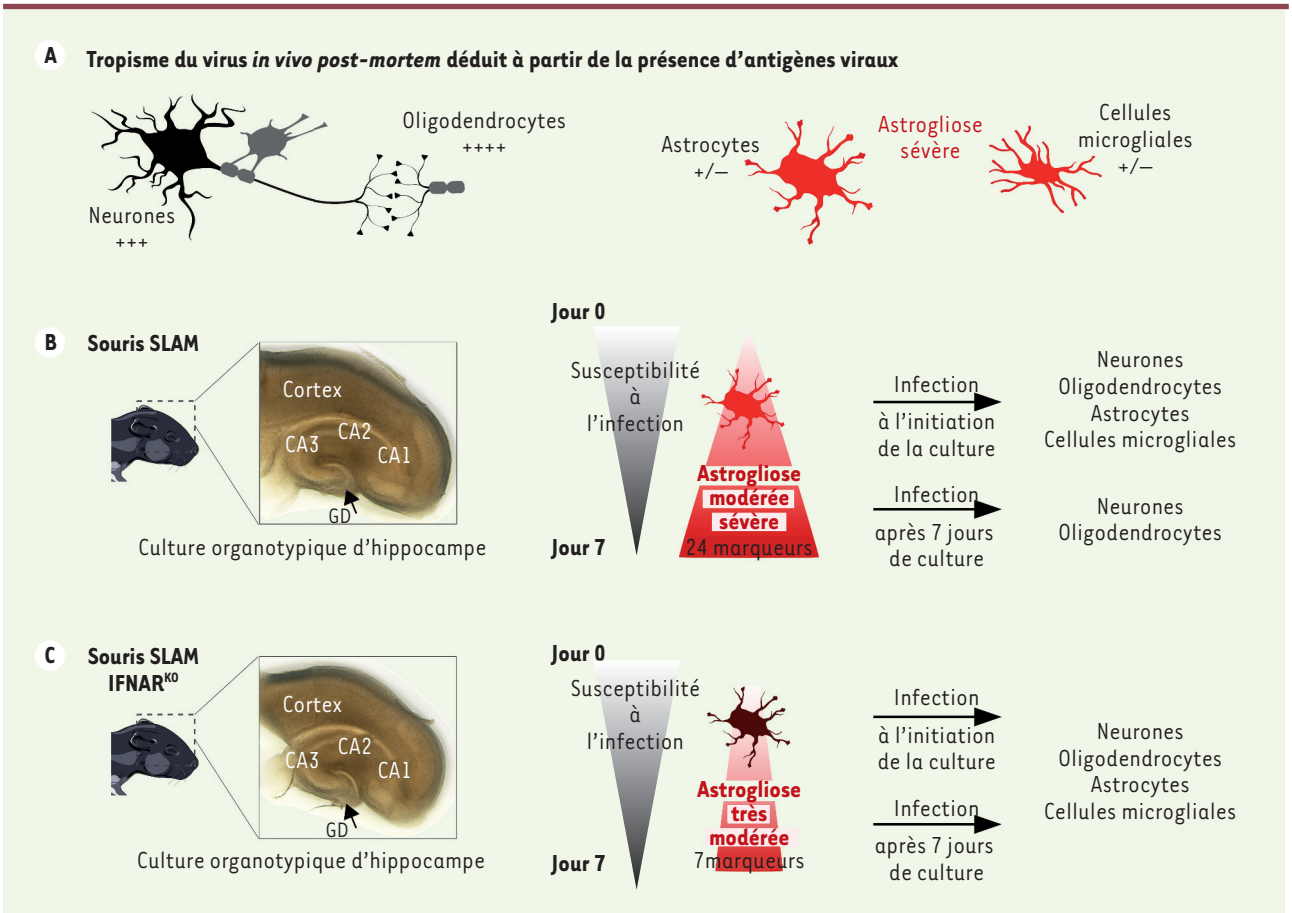

Figure 1. ***(A) Pathologie de l'infection par le virus de la rougeole dans le système nerveux central chez l'homme au moment du décès et chez la souris transgénique au moment de l'euthanasie. (B, C) Différence de développement d'une astrogliose dans les cultures organotypiques d'hippocampe, en l'absence de virus, de souris SLAMtg (B) et de souris SLAM IFNARKO (C), et impact sur la susceptibilité de ces cultures à l'infection par le virus de la rougeole.*** GD : gyrus denté, CA : corne d'Ammon.

un tropisme cellulaire du virus similaire à celui observé chez l'homme *post mortem* (*Figure 1A*). L'interféron de type I (IFN-I) joue un rôle important dans la lutte contre les infections virales [9]. Les souris SLAMtg ont été très utiles pour étudier le rôle clé de la signalisation par le récepteur de IFN-I (IFNAR) dans l'invasion du système nerveux central par le virus de la rougeole. Cette atteinte est en effet exacerbée chez des souris SLAMtg rendues génétiquement déficientes pour IFNAR (souris SLAM IFNAR^{KO}). Elle est alors létale même chez des animaux adultes, ce qui confirme le rôle crucial de la signalisation IFN-I dans le contrôle de l'infection *in vivo* [8].

Grâce aux souris SLAM IFNAR^{KO}, nous avons pu étudier si le tropisme du virus dépendait des mécanismes de l'immunité innée du cerveau [8]. Dans ce contexte, les cultures organotypiques cérébrales de rongeurs — des coupes standardisées de sous-structures cérébrales, issues de jeunes animaux et maintenues en culture pendant plusieurs jours voire semaines — offrent une opportunité unique d'étudier *ex vivo* les étapes précoces de l'infection dans des régions particulières du cerveau, non encore accessibles à l'expérimentation sous la forme d'organoïdes humains. De plus, ces cultures constituent le seul outil préservant les quatre types cellulaires du système nerveux central dans une organisation tridimensionnelle, avec des connexions physiologiques entre les cellules [10]. Nous avons observé une perte de susceptibilité à l'infection par le virus de la rougeole des cultures organotypiques d'hippocampe de souris SLAMtg et de souris SLAM IFNAR^{KO} après une semaine de culture. Cette perte de susceptibilité globale est corrélée à une induction inversement proportionnelle d'IFN-β et des marqueurs de l'activation globale des systèmes tissulaires de défense et de réparation (S100B) et de l'activation spécifique des astrocytes (protéine acide fibrillaire gliale, GFAP). Ce résultat, associé au changement phénotypique des astrocytes, est indicateur de la mise en place d'une astrogliose. L'analyse du protéome associé aux cultures organotypiques d'hippocampe de souris SLAMtg après 7 jours de culture en l'absence d'infection a montré la surexpression de 84 des 111 protéines sécrétées testées, dont 18 des 24 marqueurs majeurs généralement

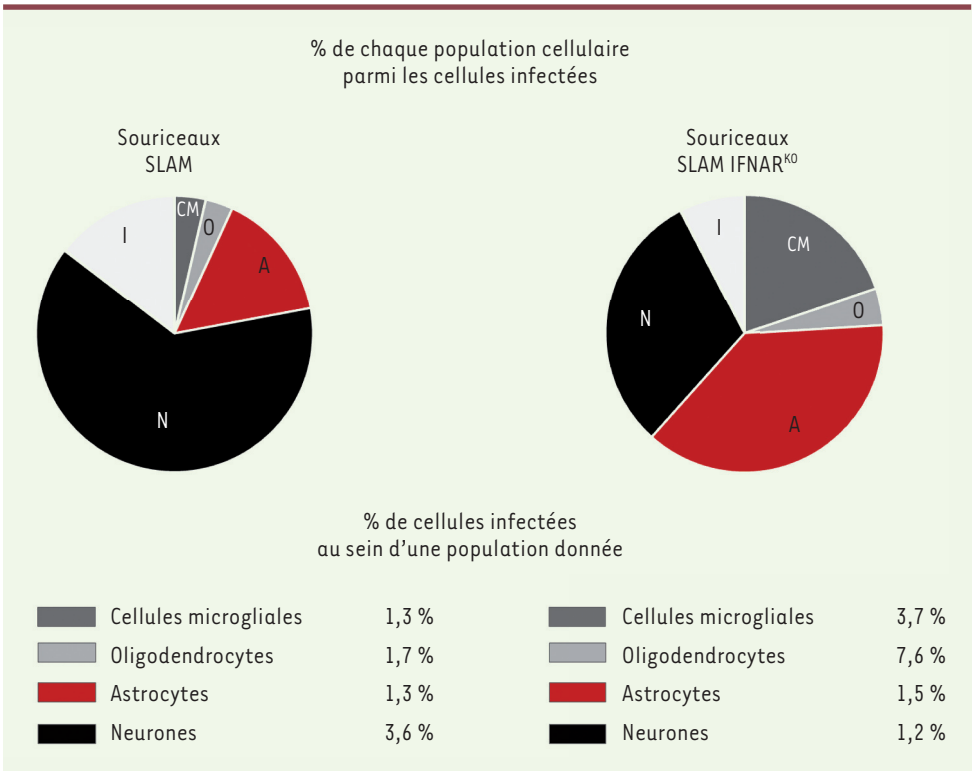

Figure 2. ***Permissivité des cellules neurales à l'infection par le virus de la rougeole dans des cultures organotypiques d'hippocampe de souris SLAMtg et de souris SLAM IFNAR^{KO}.*** Les cultures organotypiques d'hippocampe ont été infectées avec 2 x 10^4 unités infectieuses (*plaque-forming units*, PFU) du virus de la rougeole (souche IC323) exprimant la protéine de fluorescence verte VR-IC323-eGFP. Les cellules isolées, obtenues après digestion enzymatique par la papaïne, suivie d'une dissociation mécanique des cultures 24 heures après l'infection, ont été marquées avec des anticorps spécifiques pour effectuer une analyse par cytométrie en flux. La distribution cellulaire de l'infection (diagrammes circulaires) représente le pourcentage de chaque population cellulaire parmi l'ensemble des cellules infectées : neurones (N), astrocytes (A), oligodendrocytes (O), cellules microgliales (CM), et cellules de nature indéterminée (I). Le pourcentage de cellules infectées au sein de chacune des quatre populations cellulaires (neurones, astrocytes, oligodendrocytes, et cellules microgliales) est également indiqué pour évaluer comparativement la contribution de chaque population à l'infection dans les deux modèles organotypiques murins.

observés dans le développement de l'astrogliose modérée à sévère *(Figure 1B)*. En l'absence d'IFNAR, seules 27 protéines sécrétées étaient surexprimées (après 7 jours de culture en l'absence d'infection), dont seulement 7 associées à l'astrogliose, et aucune n'était associée à une activité antivirale connue *(Figure 1C)*. En revanche, l'infection des cultures organotypiques d'hippocampe de souris SLAMtg par le virus de la rougeole a conduit à la surexpression significative de 50 protéines sécrétées, dont 44 comptent parmi les protéines induites naturellement dans les cultures. Ainsi, l'infection par ce virus a exacerbé la part de réponse de l'astrogliose sous la dépendance de l'IFN-I.

L'analyse en microscopie à fluorescence, après 24 heures, des cultures organotypiques d'hippocampe de souris SLAMtg ou SLAM IFNAR^{KO} infectées le jour de leur préparation a montré la permissivité des neurones, oligodendrocytes, astrocytes, et cellules microgliales à l'infection. La distribution de l'infection dans les cellules des cultures issues de souris SLAMtg, suivie par cytométrie en flux après digestion enzymatique des coupes tissulaires par la papaïne, dissociation des cellules et immunomarquages, montre que les neurones constituent plus de 60 % des cellules infectées, loin devant les astrocytes infectés (15 %), et les quelques pourcents d'oligodendrocytes et de cellules microgliales infectés, tandis que dans les cultures issues de souris SLAM IFNAR^{KO}, dépourvues de IFNAR, on observe une homogénéisation de la distribution des cellules infectées, avec presque autant de neurones que d'astrocytes infectés (30 % et 38 % respectivement), environ 20 % de cellules microgliales infectées, environ 5 % d'oligodendrocytes infectés, et autant de cellules « indéterminées » (comportant simultanément le marqueur oligodendrocytaire et un des autres marqueurs) *(Figure 2)*. En tenant compte des proportions des différents types cellulaires dans la culture organotypique, nous avons confirmé que, dans le modèle de souris SLAMtg, les neurones constituent la population contribuant majoritairement à l'infection. En revanche, en l'absence de IFNAR, les astrocytes sont aussi permissifs à l'infection que les neurones, les oligodendrocytes et cellules microgliales devenant alors des contributeurs majeurs de l'infection. Enfin, si l'infection par le virus de la rougeole est effectuée 7 jours après la mise en culture organotypique, aucune cellule astrocytaire ou microgliale des cultures issues de souris SLAMtg n'est infectée, contrairement à ce qui est observé dans les cultures issues des souris SLAM IFNAR^{KO} *(Figure 1B, C)*.

Cette étude met en évidence plusieurs caractéristiques des réponses inflammatoires liées aux interférons de type I, et de l'astrogliose des explants cérébraux, faisant suite à l'infection par le virus de la rougeole. Elle révèle la différence de susceptibilité des cellules à l'infection, notamment la résistance des astrocytes et des cellules microgliales *via* la signalisation IFNAR, même lorsque l'entrée du virus dans les cellules cérébrales murines est artificiellement rendue possible par l'expression ectopique du récepteur SLAM humain. Sans que l'on puisse exclure la possibilité d'une différence de mécanisme d'entrée entre les différentes populations cellulaires cérébrales, ces observations expliquent au moins partiellement l'inconstance des données *post mortem* concernant la présence d'antigènes du virus de la rougeole dans les astrocytes et des cellules microgliales chez l'homme. Par ailleurs, si l'infection dans nos deux modèles animaux, souris SLAMtg et souris SLAM IFNAR^{KO}, se termine par un syndrome neurologique mortel dans les deux cas, les premiers évènements conduisant à une encéphalite sont différents en termes de sensibilité cellulaire et de molécules sécrétées dans le parenchyme du système nerveux central. Il reste à déterminer si cette plus faible susceptibilité des astrocytes et des cellules microgliales à l'infection par le virus de la rougeole et leur capacité à contrôler l'infection par la voie IFN jouent un rôle dans la sélection ou l'acquisition des mutations caractéristiques observées dans les séquences virales isolées de patients décédés d'une encéphalite rougeoleuse. Il faudra pour cela étudier en détail l'évolution virale à long terme au cours d'une propagation de l'infection du système nerveux central. ◊

Type I interferon and selective permissiveness of central nervous system to measles virus infection

LIENS D'INTÉRÊT

Les auteurs déclarent n'avoir aucun lien d'intérêt concernant les données publiées dans cet article.

RÉFÉRENCES

1. Holzmann H, Hengel H, Tenbusch M, *et al.* Eradication of measles: remaining challenges. *Med Microbiol Immunol* 2016 ; 205 : 201-8.
2. Organisation mondiale de la santé. Plus de 140 000 personnes meurent de la rougeole tandis que le nombre de cas augmente dans le monde entier. 2019, *Joint News Release.*
3. Laksono BM, Vries RD de, McQuaid S, *et al.* Measles virus host invasion and pathogenesis. *Viruses* 2016 ; 8 : 210.
4. Jurgens EM, Mathieu C, Palermo LM, *et al.* Measles fusion machinery is dysregulated in neuropathogenic variants. *MBio* 2015 ; 6 : 1-12.
5. Griffin DE. Measles virus and the nervous system. In : Tselis AC, John B, eds. *Handbook of clinical neurology*. New York :Elsevier, 2014 : 577-90.
6. Ferren M, Horvat B, Mathieu C. Measles encephalitis: towards new therapeutics. *Viruses* 2019 ; 11 : 1017.
7. Duprex WP, McQuaid S, Hangartner L, *et al.* Observation of measles virus cell-to-cell spread in astrocytoma cells by using a green fluorescent protein-expressing recombinant virus. *J Virol* 1999 ; 73 : 9568-75.
8. Welsch JC, Charvet B, Dussurgey S, *et al.* Type I interferon receptor signaling drives selective permissiveness of astrocytes and microglia to measles virus during brain infection. *J Virol* 2019 ; 93.
9. Gerlier D, Lyles DS. Interplay between innate immunity and negative-strand RNA viruses: towards a rational model. *Microbiol Mol Biol Rev* 2011 ; 75 : 468-90.
10. Welsch J, Lionnet C, Terzian C, *et al.* Organotypic brain cultures: a framework for studying CNS infection by neurotropic viruses and screening antiviral drugs. *Bio-protocol* 2017 ; 7.

2) Annexe 2 : Measles Encephalitis: Towards New Therapeutics

viruses

MDPI

Review

Measles Encephalitis: Towards New Therapeutics

Marion Ferren *, Branka Horvat and Cyrille Mathieu *

CIRI, International Center for Infectiology Research, INSERM U1111, University of Lyon, University Claude Bernard Lyon 1, CNRS, UMR5308, Ecole Normale Supérieure de Lyon, France; branka.horvat@inserm.fr

* Correspondence: marion.ferren@inserm.fr (M.F.); cyrille.mathieu@inserm.fr (C.M.)

Received: 30 September 2019; Accepted: 31 October 2019; Published: 2 November 2019

Abstract: Measles remains a major cause of morbidity and mortality worldwide among vaccine preventable diseases. Recent decline in vaccination coverage resulted in re-emergence of measles outbreaks. Measles virus (MeV) infection causes an acute systemic disease, associated in certain cases with central nervous system (CNS) infection leading to lethal neurological disease. Early following MeV infection some patients develop acute post-infectious measles encephalitis (APME), which is not associated with direct infection of the brain. MeV can also infect the CNS and cause sub-acute sclerosing panencephalitis (SSPE) in immunocompetent people or measles inclusion-body encephalitis (MIBE) in immunocompromised patients. To date, cellular and molecular mechanisms governing CNS invasion are still poorly understood. Moreover, the known MeV entry receptors are not expressed in the CNS and how MeV enters and spreads in the brain is not fully understood. Different antiviral treatments have been tested and validated in vitro, ex vivo and in vivo, mainly in small animal models. Most treatments have high efficacy at preventing infection but their effectiveness after CNS manifestations remains to be evaluated. This review describes MeV neural infection and current most advanced therapeutic approaches potentially applicable to treat MeV CNS infection.

Keywords: measles virus; central nervous system; tropism; treatments

1. Measles Virus Epidemiology

Measles virus (MeV) is the etiologic agent responsible for measles disease. Humans are the only known reservoir for MeV. Despite the availability of a very efficient vaccine [1], measles remains one of the most contagious diseases with a R0 ranking from 12 to 18 [2] meaning that (in a fully susceptible population) an infected patient will on average transmit the infection to 12 to 18 individuals. This propagation rate may even increase among people with low or compromised immunity [3]. Viral transmission generally occurs from person to person through aerosols [3] and precedes onset of skin rash, making the disease even more difficult to contain. After decades of emergences mainly restricted to the poorest countries, measles has made a strong comeback and re-emerged in industrialized countries [4] where access to the vaccine was supposed to be easier. Measles killed more than 100,000 people every year [5] since 2010. In 2017, 110,000 people died from measles, mostly children under five years old [3]. Indeed, in the absence of vaccination, children are the main targets of MeV [6], although adults can be infected as well [3]. Last year, WHO documented 268,038 confirmed cases. Nevertheless, according to other estimations, there are 7 to 20 million people getting infected by measles each year [7,8].

In most developed countries measles was considered eliminated, in recent years. However the rate of vaccination decreased due to a vaccination hesitancy, and as consequence the decreased herd immunity led to large outbreaks and today measles is considered re-emerged [4,9]. This year, in many developed countries including USA and France, there is a 300% increase in reported MeV cases compared to last year [10]. Notably, 1250 cases have been reported in the USA in 2019 (from January to

October) [11]. Those outbreaks confirm the re-emergence of measles, already announced by the NIAID following MeV epidemics in 2014 (CDC).

2. Virus

MeV belongs to the Morbillivirus genus within the *Paramyxoviridae* family and *Mononegavirales* order. This enveloped virus produces pleiomorphic viral particles with an average size ranging from 150 to 300 nm and up to 900 nm [12]. Its genome is a negative-sense, single stranded RNA of 15,894 nucleotides that encodes six structural proteins: The nucleocapsid (N) protein, the phosphoprotein (P), the matrix (M) protein, the fusion (F) protein, the haemagglutinin (H) protein, and the polymerase (large, L) protein. Two non-structural proteins, V and C are produced from the P gene [13] and mainly alter the innate immune sensing and response [14–17].

Wild type MeV strains use signaling lymphocytic activation molecule 1 (SLAMF1, also called SLAM or CD150) and nectin-4 receptors to infect target cells [18–20]. MeV vaccine strains use the ubiquitously expressed CD46 molecule as an additional entry receptor in vitro [21,22]. MeV entry is pH-independent and occurs directly at the cell surface [23]. However, MeV entry may also occur by endocytosis mediated by SLAM in B-lymphoblastoid cells or A549-SLAM cells [24], and through a nectin-4-mediated macropinocytosis pathway, in breast and colon cancer cell lines (MCF7, HTB-20, and DLD-1) [25]. It was also suggested that MeV Edmonston or Hallé strains could use a macropinocytosis-like pathway in non-lymphoid and lymphoid cells when SLAM and CD46 are engaged but this remains poorly documented [26,27].

To initiate the infection of the main target cells, the MeV H protein binds to entry receptor on the surface. This attachment triggers the F protein and leads to exposure of its hydrophobic fusion peptide that then inserts into the host cell membrane. The F protein undergoes serial conformational changes allowing the merge of the host and viral membranes creating a fusion pore allowing the ribonucleocapsid (RNP) delivery in the cytoplasm (Figure 1A,B) [28,29]. Infection also spreads efficiently via cell-to-cell contact [30,31].

Transcription by the RNA-dependent RNA polymerase (RdRp) starts from a single promoter resulting in a transcriptional gradient from the most abundant mRNA for N to the least abundant mRNA for L in order to allow efficient viral cycles. These mRNAs are then translated into viral proteins. The accumulation of N and P leads to viral genome replication into positive stranded RNA anti-genome that will allow further synthesis of negative sense RNA strands that will be encapsidated by newly synthesized N, P, and L proteins [32]. Viral RNA synthesis and assembly are regulated through the interaction between M and N [33]. Viral proteins assemble to the plasma membrane and the budding of new virions can occur (Figure 1A). Alternatively, the surface glycoproteins are transported to the plasma membrane and allow cell-to-cell dissemination.

The viral RNA is encapsidated by the protein N and forms the helical nucleocapsid [34]. Each N protein covers six nucleotides, hence the genome length has to follow the "rule of 6" for being fully protected [35,36]. Together, the proteins L and P form the viral RdRp. That polymerase interacts with the nucleocapsid to progress on the viral RNA: Altogether they form the RNP.

The M protein generally ensures the viral particle integrity. The M protein also orchestrates the viral assembly at the plasma membrane and the budding of the new infectious viral particles [23].

The H and F proteins constitute the viral fusion complex that is responsible for the viral entry into the host cell. The H protein is a tetramer organized as a dimer of dimers responsible for the binding to the entry receptor. The F protein mediates the fusion between the virus and the host plasma membranes. The F is a trimer first produced as a precursor F0 that is cleaved in the trans-Golgi by a furin protease in F1 plus F2 subunits linked by a disulfide bond. The extracellular domain is constituted by the F1 and F2 subunits containing the fusion peptide at the N terminus followed by two complementary heptad repeat domains, respectively at the N terminus (HRN) and the C terminus (HRC). While the crystal structure of the prefusion form of the F protein has been described [37], the exact delimitations of the F sub-domains are still not completely defined [38–40].

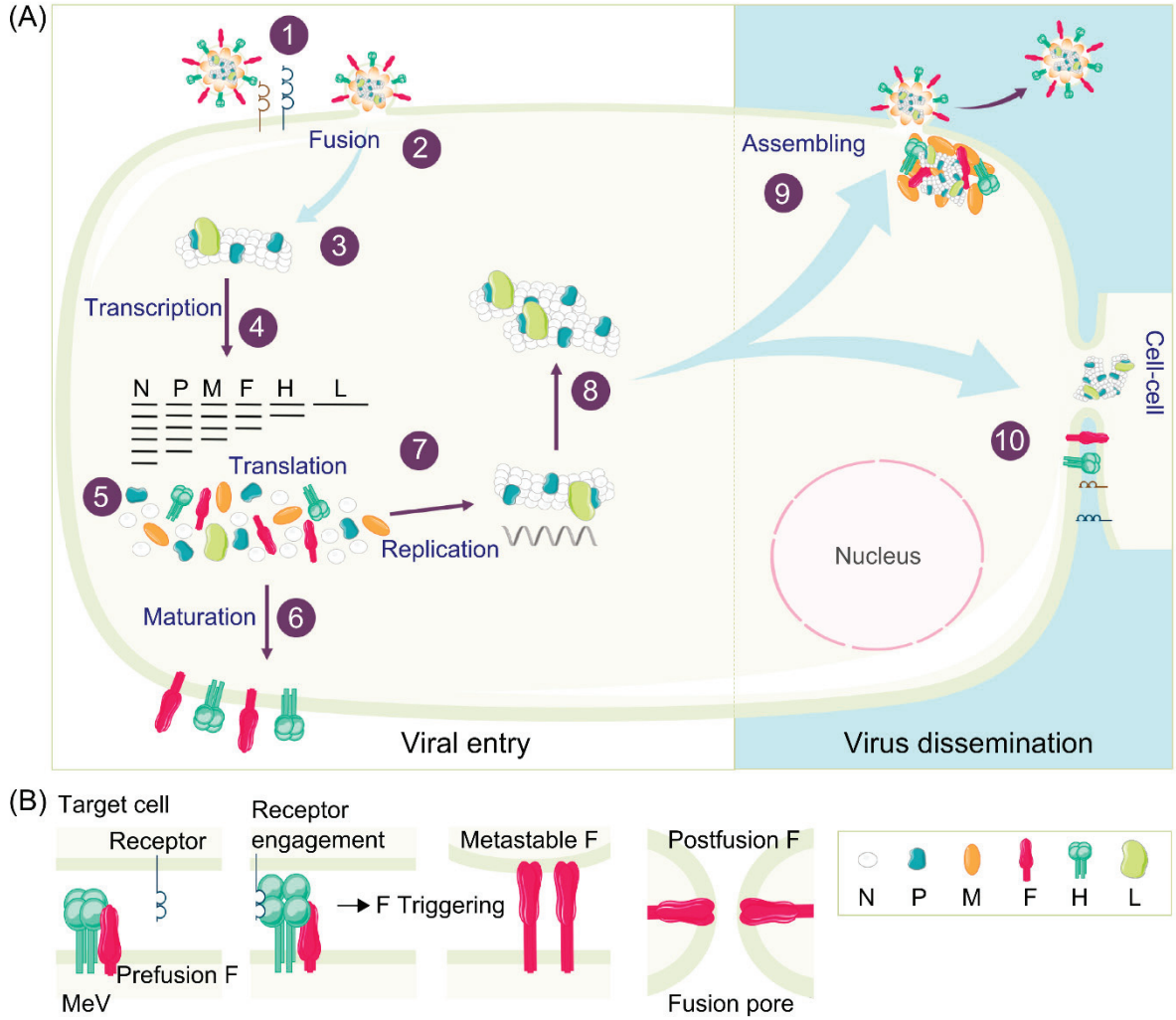

Figure 1. Measles Virus (MeV) replication cycle. (**A**) In order to infect a susceptible and permissive cell, MeV binds to its entry receptors on the cell surface (1) and initiates the virus-cell membrane fusion (2), as described in detail in (**B**). Virus and cell membranes fusion leads to genome delivery into the cytoplasm (3). Viral RNA is transcribed in mRNA (4) that is further translated into viral proteins (5). Viral glycoproteins maturate during their transport to the cell surface (6). The replication of positive stranded anti-genomic RNA starts in the cytoplasm (7) and serves as a template for synthesis of new negative stranded genomic RNA (8). Viral proteins assemble at the cell surface, leading either to budding of new virions (9) or cell-to-cell fusion (10). (**B**) The haemagglutinin (H) protein binds to the MeV receptor at the cell surface, allowing the triggering of fusion (F) which reaches a metastable conformation. Then, F protein anchors its fusion peptide in the target cell membrane, F undergoes serial conformational changes bringing the two membranes close enough to merge and form a pore throughout which the viral ribonucleocapsid (RNP) is delivered to the cytoplasm.

Based on bioinformatic tools the HRN domain encompasses residues 116/138 to residue 190 and the HRC domain is included between residues 438 and 488/489. The current crystal structure however shows the region between 438 and 458 as disorganized while a canonical heptad repeat is shown after residue 458 [41,42].

3. Vaccines

A highly efficient live-attenuated virus vaccine is available to prevent measles outbreaks. MeV transmissibility is very high and 95% of the population needs to possess anti-measles immunity for disease eradication [43]. In 1997, during a meeting co-sponsored by the World Health Organization

(WHO), the Pan American Health Organization (PAHO), and the Centers for Disease Control (CDC), the experts agreed that measles eradication was technically feasible by 2005–2010. Nevertheless, vaccination coverage decreased and led to a re-emergence of measles infection. Nowadays, measles global eradication is one of the top priorities of the expanded program on immunization (EPI) supported by the WHO. The Global Vaccine Action Plan aims to eliminate measles in five WHO Regions by 2020. Based on confirmed cases reported by the WHO, the countries with the most measles cases in 2018 were India, Ukraine, Philippines, Brazil, and Yemen. Recently, measles strongly re-emerged in industrialized countries due to the significant decrease in vaccination coverage [4,44].

Different MeV strains have been used for vaccine purpose starting with the Edmonston strain isolated in 1954 that was very reactogenic. Five vaccines were derived from Edmonston: Edmonston-Zagreb, AIK-C, Moraten, Schwarz, and Edmonston-B [45]. Some of them such as Edmonston-B remained too reactogenic. The Edmonston vaccine was replaced by the more attenuated Schwarz vaccine strain in early 60s and Moraten vaccine strains in 1968. Years later, studies have shown that Schwarz and Moraten were in fact the same virus [45]. Other vaccines derived from other strains have also been developed. Leningrad strain (isolated in 1957) attenuation successively led to Leningrad 4 and more recently to the Chinese vaccine Changchung-47. Shanghai isolate (1960) attenuation allowed production of shanghai-191 vaccine while Cam-70 which was currently produced and used in Indonesia and Japan, derived from the Tanabe (Japan, 1968) strain. All vaccines strains belong to the measles virus genotype A [45]. Measles vaccine is usually combined with mumps and rubella vaccines, known as MMR (Measles, Mumps, and Rubella) vaccine, or with mumps, rubella, and varicella (chickenpox) vaccines, called MMRV (Measles, Mumps, Rubella, and Varicella) vaccine. MMR is a live-attenuated measles virus [46]. MMR vaccination is given in a two-dose schedule, with a first dose generally administered to 12–15 months old children, and a second one three to five years later [4]. While MMR vaccine cannot be used in immunocompromised patients (with low CD4+ cell count, or severely immunedepressed), the WHO strongly recommends the vaccination of human immunodeficiency virus (HIV) positive patients without severe immunosuppression [47].

Generally, vaccinated people develop a strong humoral and cellular immunity. Only 2–10% of people who received the two vaccine doses do not produce protective measles antibodies. However, most of them remain protected by their T cell immunity [48,49].

Taken together, the too low vaccination coverage combined with the increasing proportion of immunocompromised and other non-vaccinable people call for the development of an efficient, preventive, and/or curative treatment.

4. Disease/Generalities

4.1. Symptoms and Complications

During the acute phase of MeV infection, the patients develop several symptoms, including fever, cough, nasal congestion, characteristic erythematous maculopapular rash, conjunctivitis, and pathognomonic Koplik spots on oral mucosa. Diarrhea and vomiting are often observed in infected children during the disease [50,51] or appear as a complication following the disease [5,52]. Additionally, MeV infection leads to a strong immunosuppression that can last for several months and lead to severe secondary infections [53,54]. Moreover, MeV seems to impact FoxP3 T regulatory cells homeostasis by increasing their frequency and attenuating the hypersensitivity cellular response [55]. A more recent study suggests a MeV-induced immune amnesia relying on the depletion of pre-existing memory lymphocytes [50].

MeV infection can lead to several complications such as pneumonia, which is the main cause of measles mortality [56] or to central nervous system (CNS) complications, and to a lower extent to thrombocytopenia, blindness, or hearing loss [57]. Briefly, interstitial pneumonitis associated with mucosal inflammation due to large syncytia formations in the lungs are mainly observed

in immunocompromised patients (Hecht's pneumonia) [56,58]. This cytopathic effect leads to bronchio-epithelial destruction generally resolved within few days of hospitalization (Figure 2A).

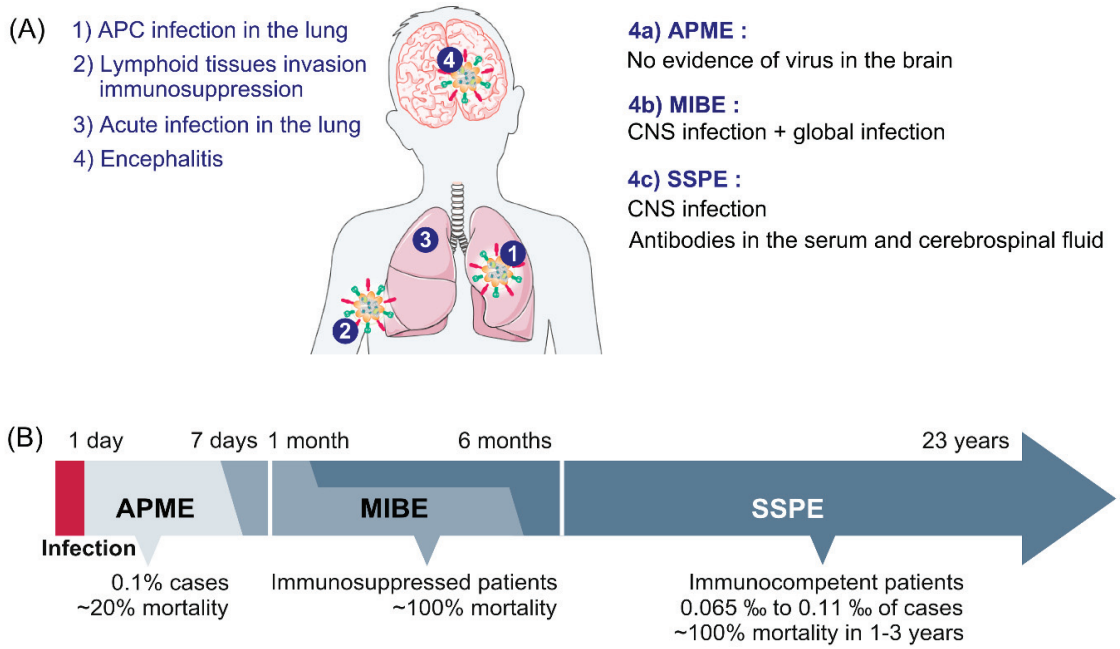

Figure 2. Course of MeV infection leading to measles encephalitis. (**A**) Initially, MeV infects myeloid cells in the respiratory tract. Then, MeV-infected lymphocytes disseminate the infection via the lymphatic and vascular systems. As a consequence of transient immunosuppression or autoimmunity, patients can develop acute post-infectious measles encephalitis (APME) shortly after exposure without systematic central nervous system (CNS) infection. However, measles inclusion-body encephalitis (MIBE) and subacute sclerosing panencephalitis (SSPE) are associated with MeV infection of the CNS. (**B**) The occurrence of MeV encephalitis may range from one day to 15 years following initial infection.

4.2. Associated Factors (Age/Nutrition)

Multiple factors such as malnutrition and vitamin A deficiency seem to increase measles associated morbidity and mortality. Indeed, regardless of vaccination coverage, MeV-infected people in poorest countries are more likely to develop complications leading to severe disease [3,59–61].

4.3. Pathogenesis

Pathogenesis starts with MeV infection of myeloid cells in the respiratory tract. As mentioned in Section 2, the two known entry receptors for MeV wild-type strains are SLAM/CD150 and nectin-4 [18,19]. Wild-type (wt) viruses generally target lung resident macrophages and/or dendritic cells, expressing SLAM [62–64]. These antigen presenting cells (APCs) migrate to the lymph nodes and transmit the viral infection to SLAM expressing lymphocytes with subsequent spread of the virus in the lymphatic and vascular systems (viremia). During the late stages of the infection, circulating infected immune cells that reach the respiratory tract and the skin can transmit the infection in cis to epithelial cells expressing nectin-4 on their basolateral side [20,65–67]. Then, the virions produced at the apical membrane can be shed into the respiratory mucus or aerosolized in the respiratory tract through coughing [68].

5. Disabilities and Nervous System

MeV can also cause damages to the nervous system.

5.1. Hearing Loss

MeV can induce hearing loss [69]. Before the introduction of mass vaccination, hearing loss was observed in 5% to 10% of measles cases in the USA. This remains highly frequent in under-developed countries where vaccination coverage is low [70]. One possible explanation is that otitis associated with measles in up to 25% of infected patients could cause hearing loss [71]. This pathology seems related to a super infection due to MeV-related transient immune-suppression.

Alternatively, hearing loss can occur immediately after the acute phase of the infection or later following measles acute encephalitis (described in paragraph 6.1) with typical bilateral and moderate to profound sensorineural hearing loss [69]. The mechanism associated with MeV-induced hearing loss remains unclear since neither viral antigen nor RNA have been detected in samples from the inner ear [57].

5.2. Blindness

Eye related symptoms such as conjunctivitis or corneal inflammation (keratitis) are commonly associated with measles [57]. Corneal complications are often more serious when superinfection (bacterial or viral) occurs during MeV-induced immune-suppression. However, there is a correlation between vitamin A deficiency and measles-induced blindness. Indeed, vitamin A deficiency is associated with severe keratitis and considerably increases the risk of xerophthalmia, corneal ulceration, and blindness [72]. This may explain why measles related blindness is more common in areas where children are already suffering of malnutrition.

Viral RNA can be detected in tear secretions [73]. In addition, human ex vivo cornea rim tissue is susceptible to MeV infection on its basolateral pole but neither syncytium formation nor released infectious particle have been found [74].

The relationship between MeV infection of ocular epithelial cells and the potential relationship with neural cell infection with cases of blindness is still unclear.

6. Central Nervous System (CNS) Infection

How the virus enters the CNS remains unclear since the known MeV receptors are not expressed. While its expression in the CNS seems to be only transient, nectin-4 has also been suggested to play a crucial role in MeV neuroinvasion based on observations made on closely related canine distemper virus whose neurotropism directly depends on nectin-4 specific patterns of expression [65,75–77]. Nectin-1 positive cells have recently been shown to be able to capture membranes and their cytoplasm from the surface of adjacent cells expressing nectin-4 at their surface via a trans-endocytosis mechanism [78]. In this context, viral RNP could transit from nectin-4 positive cells in nasal turbinate or meninges to neural cells expressing nectin-1 in olfactory bulb or brain parenchyma, respectively. The following key elements involved in the neural cell-to-cell dissemination and successful CNS invasion remain to be investigated (Figure 2A).

Three main CNS complications are associated with measles: The acute and the chronic forms, the latter being subdivided in two sub-types, the first as a measles inclusion-body encephalitis (MIBE) in immunocompromised patients and the second as a subacute sclerosing panencephalitis (SSPE) occurring in immunocompetent patients [79,80] (Figure 2B).

6.1. Acute Encephalitis

The acute post-infectious measles encephalitis (APME) occurs in 0.1% of measles cases, about a week following the appearance of first clinical signs. The APME is also called post-infection encephalitis (PIE), acute demyelinating encephalomyelitis, or acute disseminated encephalomyelitis.

APME is associated with 20% mortality and severe neurological sequelae, mainly in adults. Symptoms include fever, headaches, seizures, and consciousness alterations. APME is a complication associated with MeV infection that seems to be related to an auto-immune reaction against the myelin

basic protein mainly expressed by oligodendrocytes [81–83]. APME causes CNS lesions in both white and grey matters and is characterized by brain inflammation and perivenous demyelination [68,84–86]. Moreover, APME is often associated with more immunological abnormalities such as high levels of IgE antibodies in the serum [87]. The binding of infected leukocytes to brain microvascular endothelial cells, or a direct infection of endothelial cells themselves in the brain may also partially contribute to this inflammatory immune reaction [88]. Overall, MeV acute encephalitis is poorly described in the recent literature. Note that there is a total lack of evidence of the virus presence in the brain parenchyma compared to that in the blood circulation. Based on the absence of virus detection in certain cases, multiple groups have suggested that the encephalitis could be caused by an autoimmune-like response [89]. While the presence of myelin basic protein (MBP) in the cerebrospinal fluid (CSF) suggests autoimmune-mediated encephalitis, oligodendrocytes viability and neurons myelination have not been explored yet [89].

6.2. MIBE

MIBE occurs in immunosuppressed patients ranging from three weeks to six months following wild-type MeV infection or in some rare cases after inappropriate vaccination with former vaccine strains [90–92]. MIBE is characterized by the presence of intracytoplasmic or intranuclear inclusion bodies composed of nucleocapsids, mainly in neurons, oligodendrocytes, and astrocytes [93,94]. Patients develop febrile focal seizures and behavior disorders before lapsing into coma. At a molecular level, mutations have sometimes been observed in the intracytoplasmic domain of MeV F protein and lead to the expression of hyperfusogenic viral phenotypes. Some mutations similar to those observed in SSPE have also been detected in the N gene and it has been hypothesized that MIBE and SSPE might be very similar, apart from the more rapid development of MIBE in immunocompromised subjects [95]. Recently, other MIBE- associated mutant viruses have also been described and present an hyperfusogenic phenotype [42,92]. Notably, the mutation L454W in the HRC domain of the F protein emerged in two patients that contracted MIBE in South Africa. This mutation confers the ability of entry without the presence of known receptor even at 25 °C. The mutation L454W leads to a highly unstable F protein potentially due to a lower interaction with the H protein which loses its protection role from random triggering of the fusion protein. This finding suggests that hyperfusogenicity of these neurotropic variants allows better viral dissemination, without the need of H binding to a high affinity receptor [37,96,97].

6.3. SSPE

Subacute sclerosing panencephalitis (SSPE) cases occur in 6.5 to 11 cases per 100,000 [97,98] in immunocompetent patients that contracted measles in their childhood, with a mortality rate close to 100%. Within children infected by MeV before the age of 12 months, the incidence for SSPE rises to 1/609, while reaching 1/1367 for children under five years old [99]. There is a latency period ranging from one to 15 years following primary infection and before appearance of symptoms [100,101]. In addition, because of the non-specificity of the first symptoms, SSPE diagnosis is generally delayed [102]. In most of the cases, patients do not survive more than 1–3 years following appearance of the symptoms associated with important neurological signs and dementia. Patients are developing severe physical and mental impairments but also a loss of motor control that tends to evolve in myoclonic jerks and spasms, seizures, and coma. Patients that underwent primary infection below the age of two are more at risk of developing SSPE. It was suggested that an immature immune system before two years old could contribute to persistent brain infection [83]. A dual viral hit was suggested to play a role in SSPE development. In this model, authors proposed that during classical first exposure to MeV immunocompetent patients do not develop encephalitis. However, a first exposure to a virus different from MeV, but capable of inducing an immunosuppression, which is followed with MeV infection later in the life, may favor development of CNS disease such as SSPE, as shown in the model of transgenic mice susceptible to MeV infection [103]. Most epidemiological studies are pointing that young boys are

more often affected by SSPE than girls [17,104]. In one study in Germany from 2003 to 2009, the authors counted 21 males within 31 SSPE cases. SSPE is characterized by an excessive intrathecal synthesis of MeV specific antibodies. Most of the time, in the brain of SSPE patients, the genes that are encoding for MeV matrix protein (M), fusion protein (F), and attachment protein (H) are mutated [28,105,106] (Figure 3A).

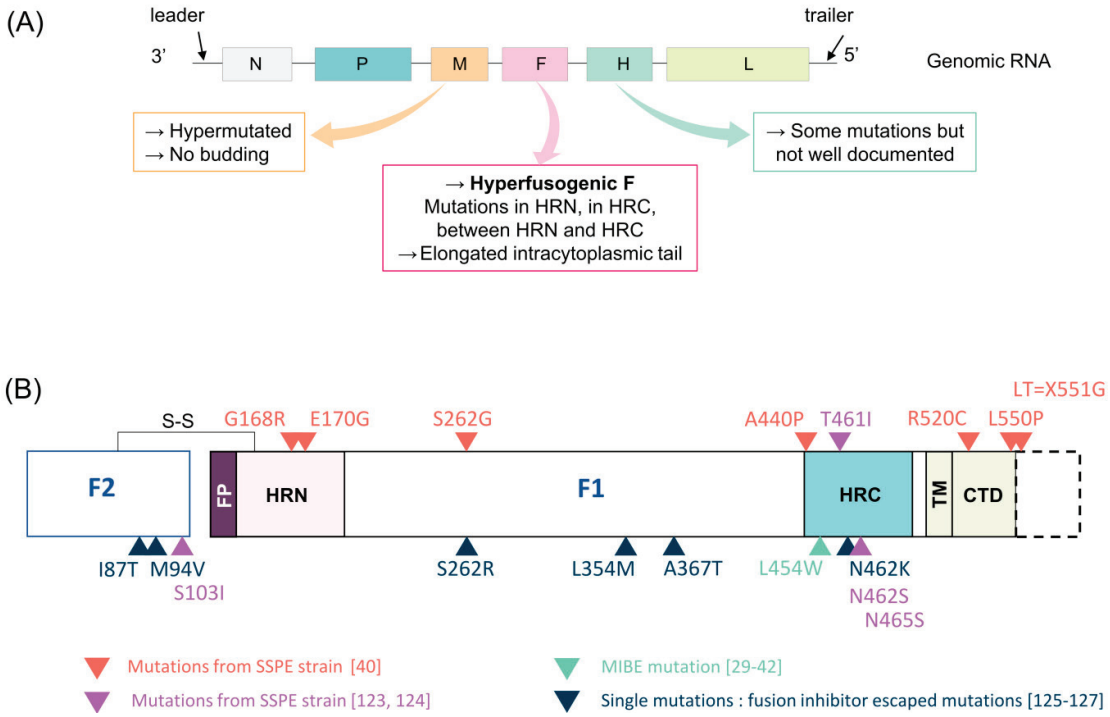

Figure 3. MeV F gene mutations related to CNS infection. (**A**) Schematic of MeV genome showing the most common mutations found in SSPE cases. (**B**) Details of MeV mutations in F protein leading to a hyperfusogenic phenotype and/or CNS infection.

7. Mutations Associated with MeV CNS Infection

7.1. M Protein

In SSPE, uridine-to-cytidine biased hypermutations of M protein are characteristic [107]. Studies have shown that MeV can evade the innate immunity control by taking advantage of the adenosine deaminase acting on RNA 1 (ADAR1), an IFN-stimulated gene that binds double-stranded RNA and converts adenosine to inosine by deamination [108]. The biased hypermutations in M (and other) gene in SSPE (or MIBE) cases might also be related to ADAR1 activity. Hypermutation of M protein leads to an unstable and defective M protein in viral particles assembly [109]. As a result, the virus is defective in budding from the plasma membranes and cannot produce viral particles. Among the large number of mutations in mRNA, the lack of the AUG initiation codon is leading to a low expression of M protein [110]. Nevertheless, in the context of brain invasion, the hypermutated M gene still allows MeV to replicate, spread, and cause disease [111,112]. Indeed, M protein negatively regulates the viral polymerase activity and thus to impact mRNA transcription and genome replication [113]. One of the roles of M protein is the distribution of both F and H glycoproteins at the apical cell surface [114]. Thereby, mutations in M protein could impact the virus fusion (and F stabilization), through association with surface glycoproteins tails, and thus influence the virus dissemination through the brain. Although in transgenic mice the infection with a M hypermutated MeV induces a more fusogenic phenotype despite attenuated budding, resulting in a more suitable virus for brain infection [111]. Other mutations impact interactions with the viral nucleocapsid and surface glycoproteins [115,116]. This provides

another explanation for the absence of viral particle productions in SSPE-patient brains. This lack of budding is a key property highlighting that patients are non-contagious [93]. While numerous studies report the isolation of SSPE infectious viral particles from patient brains, none of them have physically shown whether classic infectious viral particles or virus RNP-containing apoptotic bodies expressing surface glycoproteins were effectively isolated [107,117–120].

7.2. F protein

The F proteins observed in SSPE cases present several mutations conferring a hyperfusogenic phenotype. F is produced as metastable protein in its pre-fusion state. This pre-fusion state is generally less stable in the CNS isolates. The F can also fuse without H engagement to any known receptor. Thus, it is suggested that these mutations facilitate CNS spread [40].

Mutations can occur in the HRC domain (T461I, A440P, N462S, N465S, and L454W), in the HRN domain (G168R/E170G), in between HRC and HRN domains (S262G), in the cytoplasmic tail domain (CTD) (R520C, L550P), and in the F2 subunit of F protein. Among the mutations found in the F-SSPE sequence from South African patient (G168R/E170G/S262G/A440P/R520C/L550P and X551G), only the mutation S262G (position already associated to hyperfusogenicity with a mutation S262R) located at the interface of three protomers, involved in fusion activation, may independently confer an hyperfusogenic phenotype to F without needing any other mutation. The functional analysis of MeV_IC323 virus carrying this F-SSPE with all seven mutations confirmed the finding that an SSPE strain can disseminate via cell-to-cell spreading in Vero cells, in the absence of known receptors [40] (Figure 3B).

The mutation of stop codon (X551G) in F-SSPE strains has been frequently observed previously [107] and leads to an elongated cytoplasmic tail (called LT for Long Tail) that can enhance the incorporation of F and nonspecific cellular protein in the virion [121,122].

Other mutations found in F extracellular domain from SSPE sequences isolated from patients brain (T461I and S103I/N462S/N465S) also confer hyperfusogenicity and can spread in human neuroblastoma cell lines and suckling hamster brains in the absence of known MeV receptors [123,124].

Fusion inhibitors such as 3G or FIP are tested on MeV and it has been documented that several mutations emerged in F protein in order to escape the treatment. The impact of these mutations (I87T, M94V, S262R, L354M, A367T, N462K) on the fusion machinery is of great interest [125–127]. One of the most interesting mutations that emerged is located at the residue 262. The escape mutation S262R confers hyperfusogenicity, as well as the mutant S262G that has been described in a real case of SSPE [40,123]. These data highlight the fact that emergence of mutations under a selective pressure can lead to viral adaptation to CNS. This can also allow a better design of inhibitors that could counteract these adaptation mutations.

As discussed in Section 6.2. the hyperfusogenicity correlates with a lower thermal stability of the pre-fusion state of F [28,125]. As an example, the L454W F is highly unstable and this characteristic could be sufficient to trigger F in a postfusion state by itself, allowing the fusion to occur without any receptor engagement. In the context of a circulating viral particle outside the brain, that property might not be an advantage for the virus, which could explain why any hyperfusogenic form of MeV has never been found in circulating viruses.

7.3. H Protein

The H protein of SSPE strains is often mutated as well and contributes to neurovirulence [128]. In a recent study, three mutations were found in the H gene of South African SSPE strain, in the cytoplasmic tail, the stalk domain, and β5 blade of the head domain, associated with substitutions R7Q, R62Q, and D530E, respectively [40]. The residue D530 is necessary for cell entry through SLAM, so the mutation D530E could compromise the use of infection through SLAM [129,130].

In a modified Edmonston strain expressing a murine-adapted H protein from a neurovirulent strain CAM/RB, the substitutions G195R and S200N lead to complete loss of neurovirulence in mice

C57BL/B6 [83,131,132]. Due to questionable strains and animal model used in this study, these data have to be considered carefully and these findings might be difficult to transpose to human SSPE cases. Nevertheless, it highlights the potential existence of a specific site in H involved in neurovirulence or a site of an unknown neuron-specific receptor.

C-terminus elongation of the H protein due to single-point mutation at the stop codon have also been reported multiple times in SSPE cases [75,133]. Contrarily to deletions of the cytoplasmic tail of H which were shown to enhance fusion activity [121], elongation of the extracellular domain of H seemed to impact binding, targeting, and may explain at least partially the high level of antibodies in SSPE cases [75,133].

Unlike SSPE, mutations in H gene of MIBE virus sequences seem to be less frequent and further investigations for their potential impact in CNS infection is required [92].

7.4. Mutations in Other Genes

In SSPE cases, some mutations have also been found in N, P, and L proteins but most of the recent studies focused on F and M proteins. Some P genes from SSPE cases exhibit an impaired editing system that lead to less V protein production. Most of the time, the viral cycle does not seem compromised but the lower expression level of V could contribute to the viral persistence by reduced inhibition of interferon (IFN) response [134]. Is has also been shown that the P gene of the multi-mutated rodent brain-adapted strain CAMR40 is largely involved in neurovirulence, suggesting that MeV P gene could also play a role in CNS infection [135].

8. Animal Models for Neuro-Invasion Studies

Humans are the only natural reservoir for MeV. Thus, the choice of the best animal model remains a challenge and depends on the type of scientific questions asked, to be faithfully representative of the CNS infection in humans. A summary of the most used small animal models and their related application is presented in Table 1. Several genetically modified mice have been used, mainly to study tropism, dissemination, and to develop new treatments. Historically, the Lewis rat was commonly used to study viral tropism and dissemination through the CNS [136]. More recently, the Golden Hamsters are preferred to study MeV neurovirulence because of the similarities in the brain lesions observed by MeV in this model compared to human cases of SSPE. Moreover, unlike mice, suckling hamsters are naturally susceptible to MeV infection, especially in the brain, despite the lack of expression of any known receptors as reported in human [123,137] (Table 1). Numerous studies have been done using neurotropic strains obtained following multiple passages in Hamster brains. Nowadays, these strains, supposed to mimic persistent infection in the brain, are not used anymore. Indeed, the strains CAM/RB or HNT were highly virulent in mice, rat and hamster but the induced infection was not representative of a persistent MeV infection in the brain. These hypermutated neuro-adapted strains led to an acute infection in the brain that was not representative of the slow and progressive infection seen in SSPE [136,138,139]. Such type of infection cannot be representative of an APME or MIBE since there is no CNS infection in the first case, and there are very distinctive inclusion bodies in the brains in the second one. Nevertheless, it may allow a better understanding of the behavior of MeV once these mutations have emerged in the CNS.

Multiple murine models have been developed to address specific question about MeV pathogenesis, CNS invasion, antiviral treatments, and persistence (Table 1). Notably, MeV persistence has been demonstrated in mice infected with the Edmonston strain or a recombinant MeV expressing H from CAM/RB strain up to two months [140,141] and in nude mice with Edmonston strain highlighting the emergence of mutations [142]. SLAM transgenic (tg) ant CD46 tg mice models and derivates expressing stably and ubiquitously or not the human receptors for wt or vaccine MeV strains were also extensively used [143,144]. When these receptors are ubiquitously expressed (notably in the CNS) these very artificial models highly facilitate MeV entry. In SLAM transgenic suckling mice infected intranasally, MIBE-related mutants such as MeV F L454W were able to propagate in lungs, meninges,

and neural cells in brain parenchyma confirming the maintenance of its ability to infect a host from the respiratory tract [42]. Additionally, such animal models allow not only the study of the key factors of the cells permissiveness independently of the entry step, but also to validate the efficacy of antiviral drugs in the most stringent context, since the virus spread is the most difficult to block [29,96,145,146] (Table 1).

Non-human primates represent faithful models of measles since they are fully susceptible to wild-type MeV infection [147]. Thus, rhesus and cynomolgus macaques or squirrel monkey are often used mainly for studies focusing on the acute pathogenesis [20,65,66,68,148–150]. These studies highlighted numerous similarities between measles pathogenesis in humans and primates. Particularly, they allowed confirming the essential role of nectin-4 for the shedding and inter-human transmission of MeV, but symptoms related to CNS infection have not been reported so far. Accidental transmission of the circulating MeV strain from human to primate have occurred notably causing five deaths out of 21 cases in rhesus monkey [151]. In this study CNS infection was not investigated and all deaths were due to secondary infection related to MeV-induced immunosuppression. In 1999, another natural outbreak led to the death of 12 Japanese macaques out of 53 cases. In the brain, demyelination was observed in one monkey and two monkeys showed neuronal inclusions with measles antigens [152] but no infectious viral particle has been isolated. In order to better characterize the CNS infection, rhesus monkeys were infected intracerebrally with a SSPE derived virus but animals did not develop any visible symptom and the virus was not detectable after three weeks, suggesting the resolution of the infection [153]. Another study reported that rhesus monkeys infected intracerebrally with hamster-brain-adapted strain developed encephalitis with morphological characteristics similar to those observed in the brain of human SSPE cases. However, as already observed in rodent, these brain infections induced by the hamster-brain-adapted strain evolved during the acute phase of infection and do not reflect the slow progression observed in the SSPE [154]. MeV CNS infection still has to be characterized in this model.

More recently, comparative analysis of MeV infection, tropism, and spread in human to canine distemper virus (CDV) in natural host species such as dog and ferrets suggested that studies of this closely related morbillivirus infection could shed light on key elements of MeV pathogenesis [155].

The tamarin (*Saguinus mystax*), often called marmoset in the literature, has been shown to be susceptible to MeV infection with Edmonston and JM strains [156,157]. The JM strain was highly pathogenic in this model, especially following cerebral inoculation [158].

Table 1. Small animal models used to study MeV infection. IFNAR stands for interferon alpha/beta receptor, Rag for recombination activating gene, and TLR for Toll-like receptor.

Animal	Purpose	Route of Infection
MICE		
NSE-CD46: Expression of BC1 isoform of human CD46 under the control of the neuron-specific enolase (NSE) [159,160] YAC-CD46: Similar expression level and location than in human [159] CD46 [143,161,162] CD46-IFNAR$^{-/-}$ [163]	Vaccinal MeV behavior in the brain. Ability to disseminate in the brain. Pathogenesis of MeV infection in the CNS. Permissiveness. Immune response.	Intranasally (i.n.)Intracranially (i.c.)
SLAM: Ubiquitous expression [144] SLAM: Dendritic cell expression only [164,165] CD46/TLR induced CD150 [166] CD46/TLR induced CD150-IFNAR$^{-/-}$	Innate immune response Spreading and pathogenicity of Edmonston and wild-type Ichinose (IC) strains	i.n. i.c.
SLAM IFNAR$^{-/-}$ [167] (Figure in Section 9.3) IFNAR$^{-/-}$ [42,168] (Figure in Section 9.3)	Tropism Dissemination within CNS	Intraperitoneal (i.p.) i.n.
SLAM$^{+/+}$/Stat 1$^{-/-}$: Same expression level than human [169]	Innate immune response	i.p. i.n.
CD46 IFN-α/βKO [163]	Induction of MeV encephalitis with Edmonston	i.c.
CD46 RagKO [96,103]	Study of the establishment of SSPE Role of the immunosuppression in the MeV persistence Drug testing	Multiple
CD46 Neurokinin-1 KO [96]	Trans-synaptic viral dissemination	i.c.
C57BL/6 [170] (Figure in Section 9.3)	Viral persistence Tropism	i.c.
RAT		
Lewis rat [136,139,171]	Tropism	i.c.
Cotton rat (Sigmodon hispidus) [12,172,173]	Treatment development. Respiratory infection MeV induced immunosuppression CNS infection Immune suppression	i.n.
CD46 Sprague-Dawley rat [174]	permissiveness	Multiple
Brown Norway rat [175]	Immune response in MeV associated neurologic disease	i.c.
HAMSTER		
Syrian Golden Hamster [123] (Figure in Section 9.3)	Tropism Dissemination and invasion by mutated viruses	i.c.
FERRET		
Ferret [97,155,176,177]	To mimic SSPE Transmission Pathogenesis of CDV infection to model MeV infection	i.c. i.n.

9. MeV Tropism

Although MeV is primary a lymphotropic virus it could also infect the CNS. One of the ways the virus might enter into CNS could be through the hematogenous way by crossing the blood-brain barrier (BBB) [17]. Since endothelial cells are susceptible to infection in vitro, in vivo and in SSPE cases, their infection at the BBB could also give an opportunity for MeV to reach the CNS [88,178]. In addition, lymphocytes are also able to pass the BBB meaning that MeV-infected lymphocytes could carry the virus across the BBB [179,180]. However, the specific mechanisms allowing the virus to enter the CNS remain unclear [88,105,181]. The hyperfusogenic phenotype seems to be necessary to allow viral dissemination through neurons even in the absence of known receptor. To date, the early tropism and dissemination of *Paramyxoviridae* within the CNS during early stages of infection remain poorly documented. There are also very few available data on cellular and molecular mechanisms governing CNS invasion. To date, investigations are mainly limited to clinical symptoms, serology, RNA sequencing, and tissue immunostaining. Moreover, most of the studies have been performed with MeV vaccinal strains such as Edmonston B strain or neuro-adapted strains in Hamster, using several wild type or transgenic rodents, or other in vitro models such as primary or immortalized neural cultures. Nowadays, whether these viruses and models perfectly reflect what occurs in human remains questionable, they allow addressing specific questions in obtaining important information regarding the tropism of MeV infection in the brain.

9.1. Post-Mortem Studies

Post-mortem analyses of MeV-infected human brains show lesions in almost all areas (Figure 4A). In the same late context, studies of brain infection in human and animal models described the cell types harboring viral antigens in the CNS, nevertheless the early targeted and permissive cells need to be clarified.

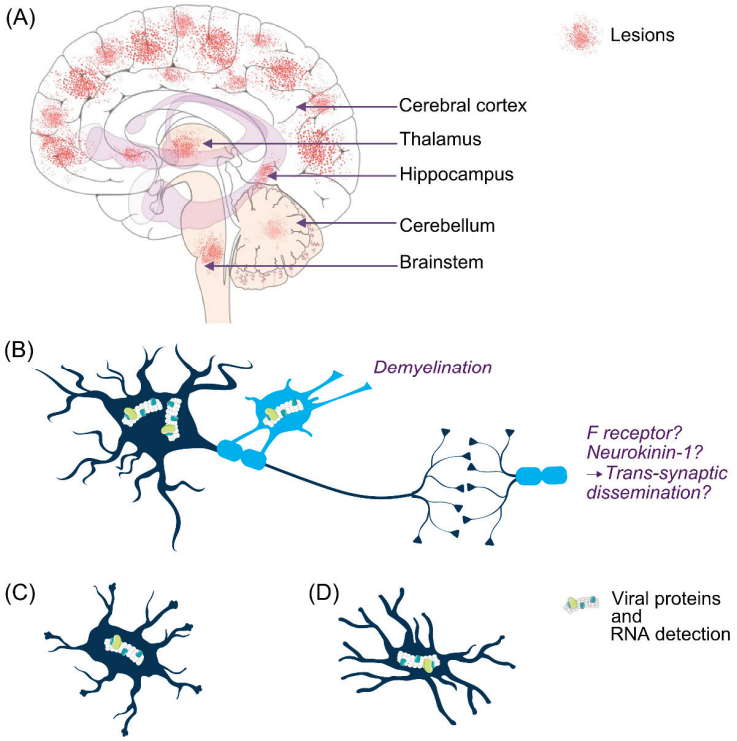

Figure 4. MeV central nervous system infection. Lesion areas are found in the brain of SSPE and MIBE patients but the specific areas associated with RNA detection are still poorly documented (**A**). Generally, MeV infects neurons and oligodendrocytes in humans (**B**). Occasionally, MeV RNA is also found in astrocytes (**C**) and microglia (**D**).

In the CNS, MeV infection occurs mainly in neurons but also in oligodendrocytes, astrocytes, and microglia [17,182,183] (Figure 4B–D). In MIBE and in SSPE cases, viral antigens and RNA have been found in neurons and oligodendrocytes [181]. In human SSPE cases, neurons are the main target with evidence of transneuronal viral spread [97]. Infected oligodendrocytes are often located near infected neurons, suggesting oligodendrocytes infection as a secondary infection from axons. The infection of oligodendrocytes is highly related to their demyelination. The authors suggest that MeV induces demyelination that could be a hallmark of SSPE (Figure 4A,B).

Viral genome and antigen have also been found in the perinuclear cytoplasm of astrocytes, albeit with lower frequency [181].

In a study using Edmonston B strain, infection of organotypic cultures of rat hippocampus ex vivo showed that the virus can infect neurons in the absence of CD46 receptor [139].

Meninges infection has been observed following intracranial MeV inoculation in ferrets [184] and hamsters [185], as well as following intranasal infection of SLAM transgenic mice [42]. Interestingly, MeV strains and mutants used in these studies were all known as hyperfusogenic. However, meninges infection has not been reported in humans yet.

9.2. Early Events in MeV Infection?

It is strongly suggested that MeV may use a third receptor or co-receptor yet unknown to enter the CNS. A parallel could be done with studies of CNS invasion with the closely related CDV conducted in dog and showing that astrocytes are neither expressing SLAM nor nectin-4, but remains permissive to the infection [76].

For MeV, the hypothesis that single or combination of mutations would be sufficient to confer adaptation in brain tissues for invasion without the engagement of any receptor is also relevant. Indeed, highly unstable F mutants such as L454W, observed in MIBE cases, do not need any communication with the H for triggering and fusion and thus cell-to-cell dissemination [28]. Alternatively, there is no proof that such a virus would be able to attach to any cell in absence of H and thus go through the first event allowing the entry in the CNS. Additionally, other hyperfusogenic mutants more stable and also observed in encephalitis cases were shown to conserve there dependence on H for F triggering [40], reinforcing the idea that at least a low affinity neural receptor should allow the initial entry in a CNS cell [186].

To date, the very first cell target of MeV infection in CNS, is unknown. A recent study focused on cell susceptibility during MeV infection in the CNS using hippocampus organotypic brain cultures (OBC) from IFNAR deficient genetically modified C57BL/6 mice expressing human SLAM receptor [168]. While all cell types were susceptible to infection in the absence of IFN-I response, the permissiveness of astrocytes and microglia strongly decreased when astrogliosis was observed in immunocompetent OBC. Astrogliosis and microgliosis have been observed in MeV encephalitis [144,187,188]. These data could explain why infection of astrocytes and microglia in post-mortem analysis are barely detectable.

9.3. Models to Study Tropism?

The main obstacle to study early tropism of MeV and other *Paramyxoviridae* is the lack of adequate models that could faithfully represent the infection in human brains. To date, ex vivo models seem to be a good compromise [189]. Organotypic brain cultures from mice, hamsters, and rats can be generated with several brain substructures such as cerebellum, cerebral cortex, or hippocampus [139,189,190]. The advantages of this model are the presence of all four cell types in the CNS (neurons, astrocytes, oligodendrocytes, and microglia), the possibility to produce OBC from any transgenic animal, and the unique opportunity to have a direct visibility of the CNS as an open window. Moreover, several slices can be made from each substructure. Therefore, a large number of conditions can be tested with a very limited number of animals, making this model ethically preferable, compared to in vivo experiments. The main weaknesses of OBC are the lack of a vascular system with circulating leukocytes and the decreasing susceptibility to infection through time concomitant to the development of astrogliosis [168].

Murine OBC offer many possibilities but mice are not susceptible to infection so their OBC would not be suitable to study early tropism. On the other hand, golden hamsters are susceptible to MeV infection. Thus, hamster OBC might be a more relevant *ex vivo* models but the lack of tools and available antibodies for this species still strongly slows down the study of the early tropism in this model.

Organotypic cerebellar cultures (OCC) from suckling SLAM-IFNARKO mice (Figure 5A), IFNARKO mice (Figure 5B), wild-type C57BL/6 mice (Figure 5C), and Syrian Hamster (Figure 5D) allows highlighting the hyperfusogenic phenotype of MeV-IC323 bearing a L454W or T461I mutated F protein compared to the wild-type in a CNS context. The fluorescence signal is used for tracking the infection and shows the massive dissemination of the viruses MeV-IC323-eGFP-F-L454W and MeV-IC323-eGFP-F-T461I in OCC even in the absence of known entry receptor (Figure 5B–D) while the MeV-IC323-eGFP-F-wt needs the expression of SLAM in order to disseminate efficiently in the OCC (Figure 5A).

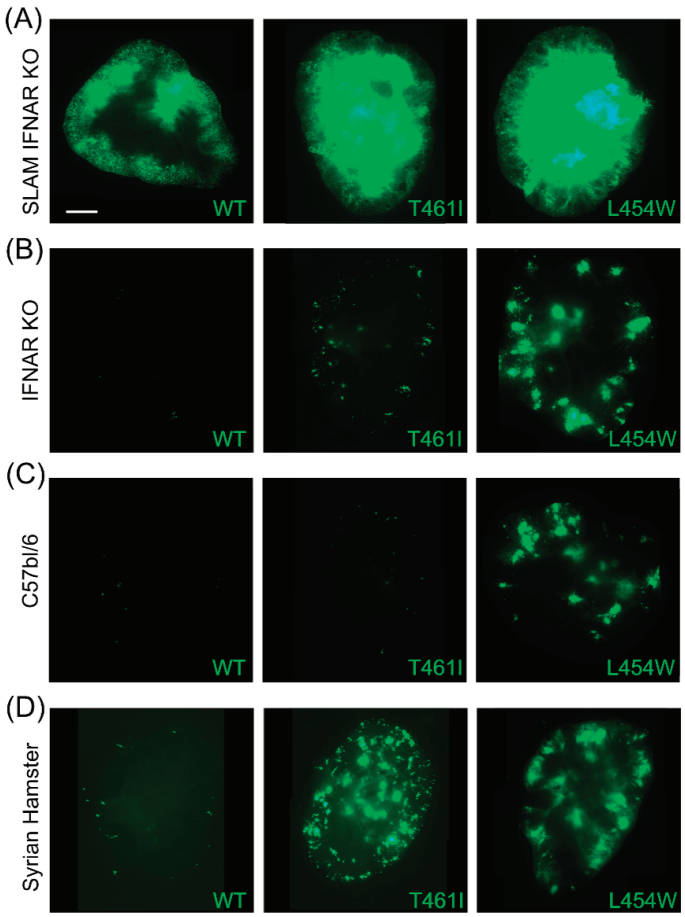

Figure 5. Wild-type and hyperfusogenic MeV growth in organotypic cerebellar cultures (OCC). OCC from suckling SLAM-IFNARKO mice (**A**), IFNARKO mice (**B**), wild-type C57BL/6 mice (**C**), and Syrian Hamster (**D**) were prepared as described elsewhere [189] and infected on the day of slicing with 10^3 PFU per slice with MeV-IC323-eGFP-F-wild-type (left side images), MeV-IC323-eGFP-F-L454W (right side images) and MeV-IC323-eGFP-F-T461I (middle images). Pictures were taken at day three post infection (dpi) and reconstituted using the Stitching plug-in with ImageJ software [191]. Scale bars, 1 mm.

10. MeV Dissemination in the CNS

In SSPE brain tissue, extracellular MeV has not been detected, suggesting that neuron-to-neuron viral dissemination can occur without released infectious viral particle [182]. MeV spread in mice and rat neurons is based on cell-to-cell contact [139,192,193]. The functional analysis of hyperfusogenic

MeV bearing a mutated F protein T461I confirmed this theory by being able to disseminate exclusively from cell-to-cell in human primary neurons [124,128]. The combination of mutations found in SSPE strains seems to enable viral fitness in the brain and neurovirulence [128]. Viruses with these mutations can spread in the brain of genetically modified mice [111].

It is suggested that MeV dissemination can be mediated by the microfusion at synaptic membranes [97,128]. In this theory, the F protein may interact with Neurokinin-1, the receptor of the P substance [96,139] (Figure 5B). This interaction would lead to the formation of a fusion micropore, allowing viral RNP to pass disseminate through neurons without the need of neither budding nor other receptor engagement. This could also explain the lack of syncytia formation in human primary neurons following infection with hyperfusogenic MeV forms. It has also been hypothesized that some supporting cells of myelinated nerves could block cell-to-cell contact between neurons and trans-synaptic spread in the brain could be the only way to allow viral dissemination [38].

It is strongly suggested that neurovirulent MeV strains are using a third receptor or co-receptor yet unknown. Nevertheless, the hypothesis that single or combination of mutations would be sufficient to confer adaptation in brain tissues for infection and dissemination without the engagement of any receptor is also relevant.

Models to Study the Dissemination?

Neuronal cell lines such as human cells NT2, human astrocytoma cells, or mouse neuroblastoma cells were also used, but their relevance remains difficult to appreciate when considering the important variation of behavior of cells out of their tissue context [31,97,192,194–196]. Primary neurons or neural polycultures were also often used [97] but are poorly representative of the neural population in human brain. In many studies, these cultures have been useful to investigate both intra and inter-neuronal spread of MeV [96], especially because they can be made from the brain of any transgenic mice.

The recently developed three-dimensional (3D) human brain organoid model has a high potential in order to investigate viral dissemination and evolution in the brain. The 3D brain organoids are generated from human pluripotent stem cells or human embryonic stem cells. This more ethical model offers a unique opportunity in generating relevant data that could be transposed faithfully to brain infection in humans [197]. Human brain organoids still require further development in order to overcome the lack of microglia and vascularization, but also their high cost and variability of the system [198]. However, to date, this model can be very useful in combination with ex vivo models, especially to test the efficacy of inhibitors in the context of brain infection, to follow viral dissemination and highlight the emergence of mutations.

11. Treatments

11.1. Symptomatic Treatment

Very few treatments are available against MeV infection and there is no therapeutic treatment for MeV-related encephalitis. The very first therapy administered after initial signs of infection are mainly supportive and focus on symptoms such as fever, dehydration, and diarrhea. Then, most of the treatments are generally dedicated to prevent or to cure from super infection such as pneumonia, often observed in infected patients. Antibiotics are commonly used to treat the complications related to bacterial superinfection [199].

11.2. Treatment Based on the Enhancement of Immune Response

In order to enhance the immune response, ribavirin, interferon alpha (IFN-α), and immune serum globulin can also be used clinically to treat MeV infection.

11.2.1. Immune Serum Globulin

From the 1940s, intramuscular injection of immune serum globulin was reported to confer up to 79% protection to unvaccinated patients having close contact with measles infected patients [200]. More recently, effectiveness of immune serum globulin as post-exposure prophylaxis was estimated from 50% to 69% during the 2014 measles outbreak in British Columbia in Canada. However, this estimation is highly controversial because many other factors could have contributed to prevent the appearance of the disease. Indeed, the potential pre-exposure immune status as well as the unknown exposure intensity and timing make the effectiveness of the immune serum globulin very difficult to quantify [201]. Moreover, the level of measles-specific antibodies has been shown to be lower when induced by the vaccine compared to the acquisition from a wild type measles infection [202]. This led to the necessity to increase the doses of immune serum globulin in order to maintain a protective level of measles antibodies [201]. However, as mentioned in paragraph 7.3, SSPE seems to develop mainly when the exposure to MeV occurs during the first years of age before the immune system is completely mature and when maternal antibodies are still lasting [17]. Additionally, administration of immunoglobulin may have led to SSPE cases [203] and the use of MeV-specific antibodies to treat rodents after infection via intracerebral route led to persistency of MeV infection and encephalitis [204–206]. Thus, the use of immunoglobulins to treat measles infection should be very carefully thought before introduction in therapies and would greatly benefit from the combination with other antivirals acting at different levels of the viral replication cycle in order to cure the infection instead of inducing persistency.

11.2.2. Ribavirin, IFN-α, Isoprinosine

Ribavirin is an antiviral drug with a broad antiviral activity, initially used for treatment of HCV [207]. It is a nucleic acid analog derived from guanosine and its main antiviral activity shown in vivo is its incorporation as a mutagenic nucleoside by the viral RNA polymerase [208]. The use of ribavirin and immune serum globulin seems to decrease respiratory symptoms in MeV-infected patients [209] but to date there is no standard protocol and doses recommended to treat patients.

IFN-α, ribavirin, and inosine pranobex are also used for SSPE treatment, with relative long-term effectiveness [210]. Many clinical reports show that Ribavirin can decrease measles antibody titers in cerebrospinal fluid (CSF) of SSPE patients and improve neurologic symptoms without side effects [211,212], especially when combined with IFN-α. In rare cases, long term IFN-α treatment stabilizes clinical symptoms of SSPE patients for years [213]. A recent study suggests also that continuous intraventricular administration of ribavirin and interferon-α in CSF by using a subcutaneous infusion pump, combined with oral administration of inosine pranobex, could limit the progression of SSPE [214]. Intrathecal IFN-α treatment combined with oral isoprinosine could also be effective to treat SSPE patients and is the most common treatment used nowadays [215,216]. Isoprinosine is a derivative of inosine and aims at blocking viral replication, probably through an immunoregulatory activity. Again, these treatments have rarely been shown to recover loss of function but they can stabilize the disease for several years [98,213,217]. Despite the benefits of IFN-α treatments, its use can be associated with side effects and could lead to interferonopathies [218]. Alternatively, there is induction of IFNα/β in vivo with MeV infection. This induction is associated at least partially to the presence of defective interfering (DI) particles which are also reducing the viral replication by occupying the proteins from the replication machinery and may thus constitute helpful complementary tool for treatments [219,220].

11.2.3. Vitamin A

Vitamin A deficiency is highly related to measles complications and the supplementation of vitamin A has been shown to decrease the morbidity and mortality related to MeV infection in children [59–61]. Vitamin A is also mainly used to prevent blindness due to MeV infection in children [72,221]. Thus, WHO recommends immediate vitamin A administration to MeV-infected children with two repeated doses of 200,000 IU especially as vitamin A deficiency is a public health

problem [3,222–225]. Nevertheless, vitamin A is also encouraged to be given in all severe cases, regardless of the country or patient age [225]. In severe cases of measles, the combination of vitamin A with ribavirin treatment can also decrease the morbidity [226].

At the beginning of the infection, the innate immune response relies on the detection of PAMPs (pathogen-associated molecular pattern) by pathogens recognition receptors (PRR) such as the RIG-I like Receptors (RLRs) in the cytoplasm [227]. This pathway allows the synthesis and the secretion of type-I interferon. Among the RLRs recognizing the double stranded RNA patterns for activation of the type I interferon response, RIG-I (Retinoic acid-inducible gene I) is activated by several RNA viruses including MeV [228–230].

Retinoic acid is a metabolic product of vitamin A (retinol) that inhibits MeV replication in vitro via a retinoid nuclear receptor-dependent pathway [231] and a type I interferon (IFN)-dependent mechanism [232].

The mechanism of action of vitamin A as an antiviral still needs to be better understood. Nevertheless, RIG-I is required for MeV inhibition by retinoids [233], suggesting an implication of RIG-I in the efficacy of vitamin A treatment.

11.2.4. Interferon-Stimulating Genes (ISGs) and Other Treatments

The antiviral response is mediated by the interferon-stimulated genes (ISGs) that lead to the cell-intrinsic immunity. Recently, the overexpression of the bone marrow stromal antigen 2 proteins, also called BST2, Tetherin, or CD317, have been shown to inhibit Morbilliviruses cell to cell fusion in vitro by targeting the H protein [234]. In addition, the interferon-inducible transmembrane protein 1 (IFTIM1) has been shown to inhibit infection by several RNA viruses *in vitro*. While MeV enters via the plasma membrane, the effect of IFTIM1 on MeV replication is low compared to other *paramyxoviruses* such as the respiratory syncytial virus (RSV) but might be of interest in combination with other treatments [235].

Numerous other treatments, such as immunomodulators, carbamazepineamantadine, steroids, cimetidine, and plasmapheresis have been tested to treat SSPE but their efficacy seems to be case-dependent and need to be confirmed [216,217]. In addition, several alternative inhibitors such as antisense molecules, adenosine, and guanosine nucleosides, including ring-expanded "fat" nucleoside analogues, brassinosteroids, coumarins, modulators of cholesterol synthesis, and a variety of natural products have been investigated on MeV-infected patients. All these inhibitors showed relative efficacy or toxicity in vitro and in vivo and remain to be improved [236]. Among patients who received two doses of vaccine after initial infection some developed SSPE suggesting that the vaccine may not act as a therapeutic cure and prevent from encephalitis in this particular case [237].

11.3. Transcription/Replication Inhibitors

In order to inhibit the MeV growth, a strategy is to silence mRNAs encoding one of the key polymerase complex, namely N, P or L using small interfering RNAs (siRNAs) or shRNAs, as synthetic oligonucleotides, encoded by plasmids, or transduced using lentiviral vectors. siRNAs targeting the mRNA of either L [238] or N [239] or P [240], or the three in combination [241] have shown their efficiency in preventing virus growth over few days without cytotoxic effect. However, MeV finally escapes the silencing even in cells that constitutively express the siRNAs without acquiring any mutation even those that could disrupt the siRNA target sequence [240]. This likely reflects the remarkable long half-life of the polymerase brought by the incoming virus particles that last at least over 24 h [242,243] and the saturation of the siRNA linked to the continuous viral mRNA synthesis by the incoming polymerases.

As mentioned in Section 2, MeV P interacts with L protein. Although this interaction is independent of heat shock proteins such as the heat shock protein 90 (HSP90), both MeV P and HSP90 are necessary to fold and stabilize functional MeV L proteins able to enter the polymerase complex [243]. This transient requirement of HSP90 constitutes a potential target for transcription inhibition. Indeed, Geldanamycin and derivates such as 17-DMAG blocking HSP90 chaperon activity by entering its ATP pocket. These compounds showed the ability to block the viral transcription in preventive and post infection treatment in vitro and ex vivo in organotypic brain cultures [243]. Moreover, it is unlikely that a HSP90 inhibitor leads to the emergence of escape mutant virus [244]. While already used in cancer treatment, antivirals directly targeting the chaperon activity of HSP90 might be too toxic for human application. Nevertheless, molecules interfering between HSP90 and L and thus its functional folding are of interest for antiviral cure development.

Nucleoside analogs such as Remdesivir (GS-5734) and R1479 exhibit a broad spectrum activity against *paramyxoviruses* infections, including MeV [245]. Briefly, in cells, Remdesivir is metabolically converted to active nucleoside triphosphate. Obtained metabolite specifically inhibits several polymerases from different *Mononegavirales* such as Filoviruses and Henipaviruses, but not host polymerases. Recently, Remdesivir has been shown to inhibit Nipah virus polymerase activity by delaying the chain termination synthesis, notably in vivo in the African green monkey model [245,246]. Based on the huge conservation of the polymerases among *Mononegavirales*, there is a high probability that Remdesivir may also inhibit measles virus polymerase activity. Interestingly, pharmakokinetic studies performed in non-human primates showed high and persistent levels of the active metabolite in peripheral blood mononuclear cells (PBMCs) mainly targeted by wt MeV during the early stages of the pathogenesis [247]. Additionally, Remdesivir and subsequent active nucleoside seem to be able to reach the brain and may thus also inhibit CNS adapted variants of MeV observed in MIBE and SSPE cases.

Finally, the compound 16677 (1-methyl-3-trifluoromethyl-5-pyrazolecarboxylic acid) has been described as a non-nucleoside inhibitor of the RNA-dependent RNA polymerase complex activity [248]. The way this compound interacts with the replication machinery as well as the emergence of resistant variants remain poorly documented. Nevertheless, when tested in combination with an entry inhibitor increasing the stability of the fusion protein, the use of such replication inhibitor offered a high potential as a specific treatment against MeV. More recently, the same group has shown that compound AS-136A, analog to 16677, was able to block viral RNA synthesis by targeting L protein. This compound has also been associated to three candidates' hotspots of mutation increasing the knowledge of L sequence adaptation [249]. In order to face its poor solubility in water, known to influence the antiviral activity, structure-activity relationship investigations were driven to discover analogs which could be used in vivo and resulted in the generation of orally bioavailable compound 2O (ERDRP-00519) more potent and aqueous soluble than former generation [250]. As the former candidates, this antiviral remains quite cytotoxic but could be particularly efficient in combination with fusion inhibitors or antiviral immune response activators.

11.4. Inhibitors of MeV Fusion and Entry

As mentioned in Section 2, the first step of the infection relies on entry of the virus into its target cell. Briefly, H protein engages entry receptor and triggers F protein. F exposes its highly hydrophobic fusion peptide which inserts into host cell plasma membrane. This transient intermediate stage is highly unstable. Consequently, F undergoes serial conformational changes leading to the interaction between the two heptad repeat domains that brings the two membranes close enough to merge and form the fusion pore. The viral RNP can thus enter in the cell host cytoplasm. In order to prevent viral entry, the main target is to block fusion of the virus. Blocking the interaction with the receptor or F serial conformational changes are the two mainly considered possibilities.

The receptor binding site of MeV H is considered as a potential neutralizing target. Indeed, the insertion of any compound in the H pocket responsible for the binding to the receptor could either prevent from the virus attachment to the host cell or pre-trigger the F protein leading to fusion dead viral particles. Several neutralizing antibodies targeting the H protein have been proposed mainly resulting in the emergence of resistant mutants not anymore able to bind either SLAM or nectin-4 [251]. While this loss of function should not exist in the wild, the question of the ability of such variants to invade the CNS which does not express SLAM or nectin-4 receptor under this selective pressure still needs to be investigated. More recently, neutralizing antibody-derived molecules such as single chain variable fragments targeting the H protein represent a major advance in the field of therapeutics design [252]. As for the corresponding neutralizing antibodies, the ability of such molecules to penetrate the brain parenchyma and to block hyperfusogenic variants depending less on the receptor engagement as those commonly observed in CNS infection has never been tested.

As described in Section 10, Neurokinin-1 has been shown to be a potential receptor for MeV F. As an antagonist of Neurokinin-1, Aprepitant has been shown to drastically limit the viral dissemination of vaccine strain in the brain of CD46+/RAG-2ko mice [96].

The fusion inhibitor peptide (FIP), Z-D-Phe-L-Phe Gly that is a small hydrophobic peptide and other small molecules such as AS-48 or 3G (an analogue of AS-48) can block the membrane fusion in vitro [125,126,253]. These inhibitors are known to stabilize the prefusion state of the F protein. Nevertheless the use of these inhibitors leads to the emergence of mutations in the HRC of the F that can evade their efficacy leading to the selection of MeV hyperfusogenic variants [254].

In contrast, HRC-derived peptides, aim at blocking the fusion by capturing the F protein in the post-triggering state and freezing the fusion process at an early stage (Figure 6A–D). The so-called HRC4 peptide is a MeV F HRC-derived dimeric peptide that interacts with the HRN domain during the structural transition of F (Figure 6C,D). Briefly, HRC4 peptide is a dimer constituted of the HRC derived peptide linked with two chains of PEG that acts as a spacer each conjugated with a molecule of cholesterol. The cholesterol allows the fusion peptide to anchor into the host membrane and thus increases the antiviral potency of the HRC-derived peptide by two logs [255]. The HRC-derived peptides conjugated to cholesterol as well as tocopherol have shown high efficacy in vitro, ex vivo and in vivo, even in the context of the CNS infection by crossing the blood-brain barrier [29,42,146]. Notably, dissemination of viruses bearing the L454W mutation in F can be efficiently blocked in vitro and in vivo by F HRC-derived fusion inhibitors, regardless of the presence of SLAM [42]. To date, these fusion inhibitors are the only system already tested against both the wt and hyperfusogenic variants observed in CNS infection, and figure thus among the priority candidates for preclinical studies, to test alone and in combination with treatments targeting other viral functions.

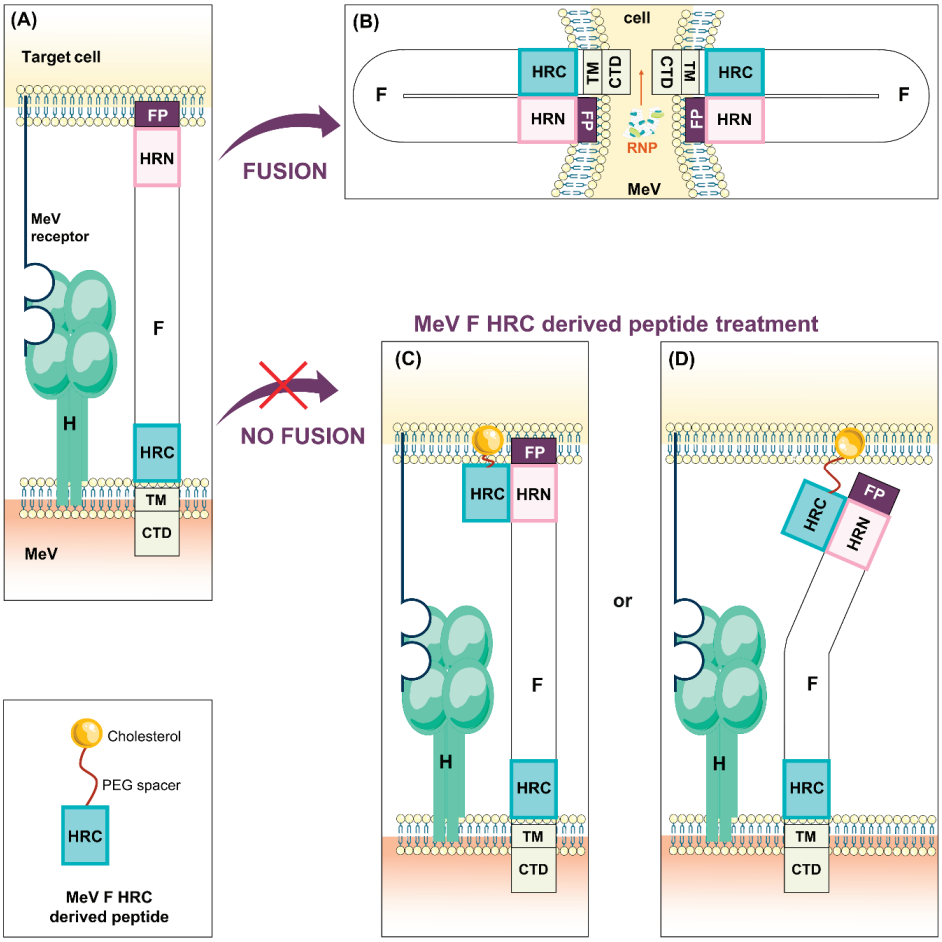

Figure 6. MeV F heptad repeats at the C terminal domain (HRC)-derived peptide. Following its engagement with any MeV receptor, H triggers F which inserts its fusion peptide in the host membrane (**A**). Then, F undergoes serial conformational changes to reach its post fusion state, bringing the two membranes close enough to form a fusion pore (**B**). MeV F HRC-derived peptides interact with MeV F HRN and catch the intermediate states of MeV F to block the fusion, regardless of the insertion of the fusion peptide in the host membrane (**C**,**D**).

12. Conclusions

A better understanding of MeV CNS invasion remains a priority in the field of MeV studies, especially because of the recent re-emergences of measles and the increasing number of associated fatal encephalitis [44,256]. While the vaccine remains the most efficient prevention against MeV infection, the decreasing coverage combined to the increasing number of immunocompromised people difficult to vaccinate confirm the necessity to develop efficient antiviral strategies.

To date, the emergence of the mutations observed in the brain of SSPE or MIBE patients is still poorly understood. These mutations could have emerged through an adaptation to the brain, leading to SSPE or MIBE, or through a selection of pre-existing mutations as a polymorphism among the circulating strains. Since MIBE only concerns immunocompromised patients and occurs usually very shortly after the primary MeV infection, one could speculate that it is more likely that a minor population of MeV, bearing the mutations that allow the virus grow in a neural context, gets selected and take the advantage of this immunological status for further propagation in the brain. Regardless of the type of encephalitis or MeV variant invading the brain, the high mortality rate associated to measles virus CNS complication highlight the requirement to validate antiviral molecules against these variants.

While the number of tested potential antiviral therapeutics keeps growing, a single molecule or treatment capable to block the major viral cycle steps is still not available. Ultimately, a combination of the treatments that could block the viral entry, the dissemination, the replication, and stimulate the immune system seems to be the most promising solution to prevent and cure MeV systemic infection and will be even more critical for the treatment of CNS infection.

Author Contributions: Conceptualization, M.F. and C.M.; methodology, M.F.; validation, C.M. and B.H.; investigation, M.F.; resources, C.M. and B.H..; writing—original draft preparation, M.F.; writing—review and editing, M.F., C.M. and B.H.; visualization, M.F.; supervision, C.M; project administration, B.H. and C.M.; funding acquisition, B.H. and C.M.

Funding: The work was supported by grant from NIH RO1-NS091263, from the French National Research Agency (ANR) NITRODEP (ANR-13-PDOC-0010-01) to C.M., from Region Auvergne Rhone Alpes (Pack Ambition Recherche) and LABEX ECOFECT (ANR-11-LABX-0048) of Lyon University, within the program "Investissements d'Avenir" (ANR-11-IDEX-0007) operated by the French National Research Agency (ANR) to BH.

Acknowledgments: The authors wish to thank M. Porotto and D. Gerlier for precious scientific advising and M. Iampietro for English proof-reading of the manuscript. We are grateful to SERVIER Medical Art, for their image bank which helped to create Figures 1, 2A, 4 and 6. SERVIER Medical Art is licensed by Creative Commons 3.0 -https://creativecommons.org/licenses/by/3.0/.

Conflicts of Interest: The authors declare no conflict of interest.

References

1. Holzmann, H.; Hengel, H.; Tenbusch, M.; Doerr, H.W. Eradication of Measles: Remaining Challenges. *Med. Microbiol. Immunol.* **2016**, *205*, 201–208. [CrossRef] [PubMed]
2. Guerra, F.M.; Bolotin, S.; Lim, G.; Heffernan, J.; Deeks, S.L.; Li, Y.; Crowcroft, N.S. The Basic Reproduction Number (R0) of Measles: A Systematic Review. *Lancet. Infect. Dis.* **2017**, *17*, e420–e428. [CrossRef]
3. Moss, W.J. Measles. *Lancet* **2017**, *390*, 2490–2502. [CrossRef]
4. Brechot, C.; Bryant, J.; Endtz, H.; Garry, R.F.; Griffin, D.E.; Lewin, S.R.; Mercer, N.; Osterhaus, A.; Picot, V.; Vahlne, A.; et al. 2018 International Meeting of the Global Virus Network. *Antivir. Res.* **2019**, *163*, 140–148. [CrossRef]
5. Strebel, P.M.; Orenstein, W.A. Measles. *N. Engl. J. Med.* **2019**, *381*, 349–357. [CrossRef]
6. Waaijenborg, S.; Hahné, S.J.M.; Mollema, L.; Smits, G.P.; Berbers, G.A.M.; van der Klis, F.R.M.; de Melker, H.E.; Wallinga, J. Waning of Maternal Antibodies against Measles, Mumps, Rubella, and Varicella in Communities with Contrasting Vaccination Coverage. *J. Infect. Dis.* **2013**, *208*, 10–16. [CrossRef]
7. LaVito, A.; John, S.W. Measles Infected up to 4 million a year in US before Vaccine. Available online: https://www.cnbc.com/2019/05/24/measles-infected-up-to-4-million-a-year-in-us-before-vaccine.html (accessed on 24 October 2019).
8. Tesini, B.L. Measles-Pediatrics—Merck Manuals Professional Edition. Available online: https://www.merckmanuals.com/professional/pediatrics/miscellaneous-viral-infections-in-infants-and-children/measles (accessed on 24 October 2019).
9. Paules, C.I.; Marston, H.D.; Fauci, A.S. Measles in 2019—Going Backward. *N. Engl. J. Med.* **2019**, *380*, 2185–2187. [CrossRef]
10. WHO. New Measles Surveillance Data for 2019. Available online: https://www.who.int/immunization/newsroom/measles-data-2019/en/ (accessed on 23 October 2019).
11. Measles Cases and Outbreaks|CDC. Available online: https://www.cdc.gov/measles/cases-outbreaks.html (accessed on 15 September 2019).
12. Griffin, D.E. Measles Virus. In *Fields Virology*; Knipe, D.M., Ed.; Wolters Kluwer: Philadelphia, PA, USA, 2013; Volume 6.
13. Bellini, W.J.; Englund, G.; Rozenblatt, S.; Arnheiter, H.; Richardson, C.D. Measles Virus P Gene Codes for Two Proteins. *J. Virol.* **1985**, *53*, 908–919.
14. Shaffer, J.A.; Bellini, W.J.; Rota, P.A. The C Protein of Measles Virus Inhibits the Type I Interferon Response. *Virology* **2003**, *315*, 389–397. [CrossRef]
15. Schuhmann, K.M.; Pfaller, C.K.; Conzelmann, K.-K. The Measles Virus V Protein Binds to P65 (RelA) to Suppress NF-KappaB Activity. *J. Virol.* **2011**, *85*, 3162–3171. [CrossRef]

16. Gotoh, B.; Komatsu, T.; Takeuchi, K.; Yokoo, J. Paramyxovirus Accessory Proteins as Interferon Antagonists. *Microbiol. Immunol.* **2001**, *45*, 787–800. [CrossRef] [PubMed]
17. Griffin, D.E.; Lin, W.-H.; Pan, C.-H. Measles Virus, Immune Control, and Persistence. *FEMS Microbiol. Rev.* **2012**, *36*, 649–662. [CrossRef] [PubMed]
18. Tatsuo, H.; Ono, N.; Tanaka, K.; Yanagi, Y. SLAM (CDw150) Is a Cellular Receptor for Measles Virus. *Nature* **2000**, *406*, 893–897. [CrossRef] [PubMed]
19. Noyce, R.S.; Bondre, D.G.; Ha, M.N.; Lin, L.-T.; Sisson, G.; Tsao, M.-S.; Richardson, C.D. Tumor Cell Marker PVRL4 (Nectin 4) Is an Epithelial Cell Receptor for Measles Virus. *PLoS Pathog.* **2011**, *7*, e1002240. [CrossRef] [PubMed]
20. Mühlebach, M.D.; Mateo, M.; Sinn, P.L.; Prüfer, S.; Uhlig, K.M.; Leonard, V.H.J.; Navaratnarajah, C.K.; Frenzke, M.; Wong, X.X.; Sawatsky, B.; et al. Adherens Junction Protein Nectin-4 Is the Epithelial Receptor for Measles Virus. *Nature* **2011**, *480*, 530–533. [CrossRef] [PubMed]
21. Naniche, D.; Varior-Krishnan, G.; Cervoni, F.; Wild, T.F.; Rossi, B.; Rabourdin-Combe, C.; Gerlier, D. Human Membrane Cofactor Protein (CD46) Acts as a Cellular Receptor for Measles Virus. *J. Virol.* **1993**, *67*, 6025–6032.
22. Dörig, R.E.; Marcil, A.; Chopra, A.; Richardson, C.D. The Human CD46 Molecule Is a Receptor for Measles Virus (Edmonston Strain). *Cell* **1993**, *75*, 295–305. [CrossRef]
23. Lamb, R.A.; Parks, G.D. *Paramyxoviridae: The Viruses and Their Replication*; Lippincott, Williams, and Wilkins: Philadelphia, PA, USA, 2007; pp. 1449–1496.
24. Gonçalves-Carneiro, D.; McKeating, J.A.; Bailey, D. The Measles Virus Receptor SLAMF1 Can Mediate Particle Endocytosis. *J. Virol.* **2017**, *91*. [CrossRef]
25. Delpeut, S.; Sisson, G.; Black, K.M.; Richardson, C.D. Measles Virus Enters Breast and Colon Cancer Cell Lines through a PVRL4-Mediated Macropinocytosis Pathway. *J. Virol.* **2017**, *91*. [CrossRef]
26. Crimeen-Irwin, B.; Ellis, S.; Christiansen, D.; Ludford-Menting, M.J.; Milland, J.; Lanteri, M.; Loveland, B.E.; Gerlier, D.; Russell, S.M. Ligand Binding Determines Whether CD46 Is Internalized by Clathrin-Coated Pits or Macropinocytosis. *J. Biol. Chem.* **2003**, *278*, 46927–46937. [CrossRef]
27. Frecha, C.; Lévy, C.; Costa, C.; Nègre, D.; Amirache, F.; Buckland, R.; Russell, S.J.; Cosset, F.-L.; Verhoeyen, E. Measles Virus Glycoprotein-Pseudotyped Lentiviral Vector-Mediated Gene Transfer into Quiescent Lymphocytes Requires Binding to Both SLAM and CD46 Entry Receptors. *J. Virol.* **2011**, *85*, 5975–5985. [CrossRef] [PubMed]
28. Jurgens, E.M.; Mathieu, C.; Palermo, L.M.; Hardie, D.; Horvat, B.; Moscona, A.; Porotto, M. Measles Fusion Machinery Is Dysregulated in Neuropathogenic Variants. *MBio* **2015**, *6*. [CrossRef] [PubMed]
29. Mathieu, C.; Huey, D.; Jurgens, E.; Welsch, J.C.; DeVito, I.; Talekar, A.; Horvat, B.; Niewiesk, S.; Moscona, A.; Porotto, M. Prevention of Measles Virus Infection by Intranasal Delivery of Fusion Inhibitor Peptides. *J. Virol.* **2015**, *89*, 1143–1155. [CrossRef] [PubMed]
30. Singh, B.K.; Li, N.; Mark, A.C.; Mateo, M.; Cattaneo, R.; Sinn, P.L. Cell-to-Cell Contact and Nectin-4 Govern Spread of Measles Virus from Primary Human Myeloid Cells to Primary Human Airway Epithelial Cells. *J. Virol.* **2016**, *90*, 6808–6817. [CrossRef] [PubMed]
31. Duprex, W.P.; McQuaid, S.; Hangartner, L.; Billeter, M.A.; Rima, B.K. Observation of Measles Virus Cell-to-Cell Spread in Astrocytoma Cells by Using a Green Fluorescent Protein-Expressing Recombinant Virus. *J. Virol.* **1999**, *73*, 9568–9575.
32. Rima, B.K.; Duprex, W.P. The Measles Virus Replication Cycle. *Curr. Top. Microbiol. Immunol.* **2009**, *329*, 77–102.
33. Iwasaki, M.; Takeda, M.; Shirogane, Y.; Nakatsu, Y.; Nakamura, T.; Yanagi, Y. The Matrix Protein of Measles Virus Regulates Viral RNA Synthesis and Assembly by Interacting with the Nucleocapsid Protein. *J. Virol.* **2009**, *83*, 10374–10383. [CrossRef]
34. Bhella, D.; Ralph, A.; Murphy, L.B.; Yeo, R.P. Significant Differences in Nucleocapsid Morphology within the Paramyxoviridae. *J. Gen. Virol.* **2002**, *83*, 1831–1839. [CrossRef]
35. Radecke, F.; Spielhofer, P.; Schneider, H.; Kaelin, K.; Huber, M.; Dötsch, C.; Christiansen, G.; Billeter, M.A. Rescue of Measles Viruses from Cloned DNA. *EMBO J.* **1995**, *14*, 5773–5784. [CrossRef]
36. Calain, P.; Roux, L. The Rule of Six, a Basic Feature for Efficient Replication of Sendai Virus Defective Interfering RNA. *J. Virol.* **1993**, *67*, 4822–4830.

37. Hashiguchi, T.; Fukuda, Y.; Matsuoka, R.; Kuroda, D.; Kubota, M.; Shirogane, Y.; Watanabe, S.; Tsumoto, K.; Kohda, D.; Plemper, R.K.; et al. Structures of the Prefusion Form of Measles Virus Fusion Protein in Complex with Inhibitors. *Proc. Natl. Acad. Sci. USA* **2018**, *115*, 2496–2501. [CrossRef] [PubMed]
38. Watanabe, S.; Shirogane, Y.; Sato, Y.; Hashiguchi, T.; Yanagi, Y. New Insights into Measles Virus Brain Infections. *Trends Microbiol.* **2018**. [CrossRef] [PubMed]
39. Plattet, P.; Alves, L.; Herren, M.; Aguilar, H.C. Measles Virus Fusion Protein: Structure, Function and Inhibition. *Viruses* **2016**, *8*, 112. [CrossRef] [PubMed]
40. Angius, F.; Smuts, H.; Rybkina, K.; Stelitano, D.; Eley, B.; Wilmshurst, J.; Ferren, M.; Lalande, A.; Mathieu, C.; Moscona, A.; et al. Analysis of a Subacute Sclerosing Panencephalitis (SSPE) Genotype B3 Virus from the 2009/10 South African Measles Epidemic Shows Hyperfusogenic F Proteins Contribute to Measles Virus Infection in the Brain. *J. Virol.* **2018**. [CrossRef] [PubMed]
41. Lambert, D.M.; Barney, S.; Lambert, A.L.; Guthrie, K.; Medinas, R.; Davis, D.E.; Bucy, T.; Erickson, J.; Merutka, G.; Petteway, S.R. Peptides from Conserved Regions of Paramyxovirus Fusion (F) Proteins Are Potent Inhibitors of Viral Fusion. *Proc. Natl. Acad. Sci. USA* **1996**, *93*, 2186–2191. [CrossRef]
42. Mathieu, C.; Ferren, M.; Jurgens, E.; Dumont, C.; Rybkina, K.; Harder, O.; Stelitano, D.; Madeddu, S.; Sanna, G.; Schwartz, D.; et al. Measles Virus Bearing Measles Inclusion Body Encephalitis-Derived Fusion Protein Is Pathogenic after Infection via the Respiratory Route. *J. Virol.* **2019**, *93*. [CrossRef]
43. Coughlin, M.M.; Beck, A.S.; Bankamp, B.; Rota, P.A. Perspective on Global Measles Epidemiology and Control and the Role of Novel Vaccination Strategies. *Viruses* **2017**, *9*, 11. [CrossRef]
44. Melenotte, C.; Zandotti, C.; Gautret, P.; Parola, P.; Raoult, D. Measles: Is a New Vaccine Approach Needed? *Lancet. Infect. Dis.* **2018**, *18*, 1060–1061. [CrossRef]
45. Bankamp, B.; Takeda, M.; Zhang, Y.; Xu, W.; Rota, P.A. Genetic Characterization of Measles Vaccine Strains. *J. Infect. Dis.* **2011**, *204*, S533–S548. [CrossRef]
46. Vaccine for Measles (MMR Shot)|CDC. Available online: https://www.cdc.gov/measles/vaccination.html (accessed on 15 September 2019).
47. McLean, H.Q.; Fiebelkorn, A.P.; Temte, J.L.; Wallace, G.S. Centers for Disease Control and Prevention. Prevention of Measles, Rubella, Congenital Rubella Syndrome, and Mumps, 2013: Summary Recommendations of the Advisory Committee on Immunization Practices (ACIP). *Morb. Mortal. Wkly.* **2013**, *62*, 1–34.
48. Haralambieva, I.H.; Ovsyannikova, I.G.; O'Byrne, M.; Pankratz, V.S.; Jacobson, R.M.; Poland, G.A. A Large Observational Study to Concurrently Assess Persistence of Measles Specific B-Cell and T-Cell Immunity in Individuals Following Two Doses of MMR Vaccine. *Vaccine* **2011**, *29*, 4485–4491. [CrossRef] [PubMed]
49. Haralambieva, I.H.; Kennedy, R.B.; Ovsyannikova, I.G.; Whitaker, J.A.; Poland, G.A. Variability in Humoral Immunity to Measles Vaccine: New Developments. *Trends Mol. Med.* **2015**, *21*, 789–801. [CrossRef] [PubMed]
50. Laksono, B.M.; de Vries, R.D.; Verburgh, R.J.; Visser, E.G.; de Jong, A.; Fraaij, P.L.A.; Ruijs, W.L.M.; Nieuwenhuijse, D.F.; van den Ham, H.-J.; Koopmans, M.P.G.; et al. Studies into the Mechanism of Measles-Associated Immune Suppression during a Measles Outbreak in the Netherlands. *Nat. Commun.* **2018**, *9*, 4944. [CrossRef] [PubMed]
51. Sindhu, T.G.; Geeta, M.G.; Krishnakumar, P.; Sabitha, S.; Ajina, K.K. Clinical Profile of Measles in Children with Special Reference to Infants. *Trop. Doct.* **2019**, *49*, 20–23. [CrossRef] [PubMed]
52. Ben-Chetrit, E.; Oster, Y.; Jarjou'i, A.; Megged, O.; Lachish, T.; Cohen, M.J.; Stein-Zamir, C.; Ivgi, H.; Rivkin, M.; Milgrom, Y.; et al. Measles-Related Hospitalizations and Associated Complications in Jerusalem, 2018-2019. *Clin. Microbiol. Infect.* **2019**. [CrossRef] [PubMed]
53. Marie, J.C.; Saltel, F.; Escola, J.-M.; Jurdic, P.; Wild, T.F.; Horvat, B. Cell Surface Delivery of the Measles Virus Nucleoprotein: A Viral Strategy To Induce Immunosuppression. *J. Virol.* **2004**, *78*, 11952–11961. [CrossRef] [PubMed]
54. Mina, M.J.; Metcalf, C.J.E.; de Swart, R.L.; Osterhaus, A.D.M.E.; Grenfell, B.T. Long-Term Measles-Induced Immunomodulation Increases Overall Childhood Infectious Disease Mortality. *Science* **2015**, *348*, 694–699. [CrossRef] [PubMed]
55. Sellin, C.I.; Jégou, J.-F.; Renneson, J.; Druelle, J.; Wild, T.F.; Marie, J.C.; Horvat, B. Interplay between Virus-Specific Effector Response and Foxp3+ Regulatory T Cells in Measles Virus Immunopathogenesis. *PLoS ONE* **2009**, *4*, e4948. [CrossRef]
56. Moss, W.J.; Griffin, D.E. Measles. *Lancet* **2012**, *379*, 153–164. [CrossRef]

57. Rima, B.K.; Duprex, W.P. Morbilliviruses and Human Disease. *J. Pathol.* **2006**, *208*, 199–214. [CrossRef]
58. Enders, J.F.; McCarthy, K.; Mitus, A.; Cheatham, W.J. Isolation of Measles Virus at Autopsy in Cases of Giant-Cell Pneumonia without Rash. *N. Engl. J. Med.* **1959**, *261*, 875–881. [CrossRef] [PubMed]
59. D'Souza, R.M. Vitamin A for the Treatment of Children with Measles—A Systematic Review. *J. Trop. Pediatr.* **2002**, *48*, 323–327. [CrossRef] [PubMed]
60. Ellison, J.B. Intensive Vitamin Therapy in Measles. *Br. Med. J.* **1932**, *2*, 708–711. [CrossRef] [PubMed]
61. Imdad, A.; Mayo-Wilson, E.; Herzer, K.; Bhutta, Z.A. Vitamin A Supplementation for Preventing Morbidity and Mortality in Children from Six Months to Five Years of Age. *Cochrane Database Syst. Rev.* **2017**. [CrossRef]
62. Avota, E.; Koethe, S.; Schneider-Schaulies, S. Membrane Dynamics and Interactions in Measles Virus Dendritic Cell Infections. *Cell. Microbiol.* **2013**, *15*, 161–169. [CrossRef]
63. Ferreira, C.S.A.; Frenzke, M.; Leonard, V.H.J.; Welstead, G.G.; Richardson, C.D.; Cattaneo, R. Measles Virus Infection of Alveolar Macrophages and Dendritic Cells Precedes Spread to Lymphatic Organs in Transgenic Mice Expressing Human Signaling Lymphocytic Activation Molecule (SLAM, CD150). *J. Virol.* **2010**, *84*, 3033–3042. [CrossRef]
64. De Vries, R.D.; Mesman, A.W.; Geijtenbeek, T.B.; Duprex, W.P.; de Swart, R.L. The Pathogenesis of Measles. *Curr. Opin. Virol.* **2012**, *2*, 248–255. [CrossRef]
65. Delpeut, S.; Sawatsky, B.; Wong, X.-X.; Frenzke, M.; Cattaneo, R.; von Messling, V. Nectin-4 Interactions Govern Measles Virus Virulence in a New Model of Pathogenesis, the Squirrel Monkey (Saimiri Sciureus). *J. Virol.* **2017**, *91*. [CrossRef]
66. Frenzke, M.; Sawatsky, B.; Wong, X.X.; Delpeut, S.; Mateo, M.; Cattaneo, R.; von Messling, V. Nectin-4-Dependent Measles Virus Spread to the Cynomolgus Monkey Tracheal Epithelium: Role of Infected Immune Cells Infiltrating the Lamina Propria. *J. Virol.* **2013**, *87*, 2526–2534. [CrossRef]
67. Gourru-Lesimple, G.; Mathieu, C.; Thevenet, T.; Guillaume-Vasselin, V.; Jégou, J.-F.; Boer, C.G.; Tomczak, K.; Bloyet, L.-M.; Giraud, C.; Grande, S.; et al. Measles Virus Infection of Human Keratinocytes: Possible Link between Measles and Atopic Dermatitis. *J. Dermatol. Sci.* **2017**, *86*, 97–105. [CrossRef]
68. Lemon, K.; de Vries, R.D.; Mesman, A.W.; McQuaid, S.; van Amerongen, G.; Yüksel, S.; Ludlow, M.; Rennick, L.J.; Kuiken, T.; Rima, B.K.; et al. Early Target Cells of Measles Virus after Aerosol Infection of Non-Human Primates. *PLoS Pathog.* **2011**, *7*, e1001263. [CrossRef] [PubMed]
69. Cohen, B.E.; Durstenfeld, A.; Roehm, P.C. Viral Causes of Hearing Loss: A Review for Hearing Health Professionals. *Trends Hear.* **2014**, *18*, 233121651454136. [CrossRef] [PubMed]
70. Dunmade, A.; Segun-Busari, S.; Olajide, T.; Ologe, F. Profound Bilateral Sensorineural Hearing Loss in Nigerian Children: Any Shift in Etiology? *J. Deaf Stud. Deaf Educ.* **2006**, *12*, 112–118. [CrossRef] [PubMed]
71. Stephenson, J. Will the Current Measles Vaccines Ever Eradicate Measles? *Expert Rev. Vaccines* **2002**, *1*, 355–362. [CrossRef] [PubMed]
72. Semba, R.D.; Bloem, M.W. Measles Blindness. *Surv. Ophthalmol.* **2004**, *49*, 243–255. [CrossRef] [PubMed]
73. Shinoda, K.; Kobayashi, A.; Higashide, T.; Shirao, Y.; Sakurai, M.; Shirota, Y.; Kagaya, M. Detection of Measles Virus Genomic RNA in Tear Samples from a Patient with Measles Keratitis. *Cornea* **2002**, *21*, 610–612. [CrossRef] [PubMed]
74. Ludlow, M.; Rennick, L.J.; Sarlang, S.; Skibinski, G.; McQuaid, S.; Moore, T.; de Swart, R.L.; Duprex, W.P. Wild-Type Measles Virus Infection of Primary Epithelial Cells Occurs via the Basolateral Surface without Syncytium Formation or Release of Infectious Virus. *J. Gen. Virol.* **2010**, *91*, 971–979. [CrossRef]
75. Muñoz-Alía, M.Á.; Muller, C.P.; Russell, S.J. Hemagglutinin-Specific Neutralization of Subacute Sclerosing Panencephalitis Viruses. *PLoS ONE* **2018**, *13*, e0192245. [CrossRef]
76. Pratakpiriya, W.; Ping Teh, A.P.; Radtanakatikanon, A.; Pirarat, N.; Thi Lan, N.; Takeda, M.; Techangamsuwan, S.; Yamaguchi, R. Expression of Canine Distemper Virus Receptor Nectin-4 in the Central Nervous System of Dogs. *Sci. Rep.* **2017**, *7*, 349. [CrossRef]
77. Pratakpiriya, W.; Seki, F.; Otsuki, N.; Sakai, K.; Fukuhara, H.; Katamoto, H.; Hirai, T.; Maenaka, K.; Techangamsuwan, S.; Lan, N.T.; et al. Nectin4 Is an Epithelial Cell Receptor for Canine Distemper Virus and Involved in Neurovirulence. *J. Virol.* **2012**, *86*, 10207–10210. [CrossRef]
78. Generous, A.R.; Harrison, O.J.; Troyanovsky, R.B.; Mateo, M.; Navaratnarajah, C.K.; Donohue, R.C.; Pfaller, C.K.; Alekhina, O.; Sergeeva, A.P.; Indra, I.; et al. Trans-Endocytosis Elicited by Nectins Transfers Cytoplasmic Cargo, Including Infectious Material, between Cells. *J. Cell Sci.* **2019**, *132*, jcs235507. [CrossRef] [PubMed]

79. Griffin, D.E. Measles Virus and the Nervous System. In *Handbook of Clinical Neurology*; Elsevier: Amsterdam, The Netherlands, 2014; Volume 123, pp. 577–590. [CrossRef]
80. Zachariah, P.; Stockwell, M.S. Measles Vaccine: Past, Present, and Future. *J. Clin. Pharmacol.* **2016**, *56*, 133–140. [CrossRef] [PubMed]
81. Johnson, R.T.; Griffin, D.E.; Hirsch, R.L.; Wolinsky, J.S.; Roedenbeck, S.; Lindo de Soriano, I.; Vaisberg, A. Measles Encephalomyelitis—Clinical and Immunologic Studies. *N. Engl. J. Med.* **1984**, *310*, 137–141. [CrossRef] [PubMed]
82. Moench, T.R.; Griffin, D.E.; Obriecht, C.R.; Vaisberg, A.J.; Johnson, R.T. Acute Measles in Patients with and without Neurological Involvement: Distribution of Measles Virus Antigen and RNA. *J. Infect. Dis.* **1988**, *158*, 433–442. [CrossRef] [PubMed]
83. Reuter, D.; Schneider-Schaulies, J. Measles Virus Infection of the CNS: Human Disease, Animal Models, and Approaches to Therapy. *Med. Microbiol. Immunol.* **2010**, *199*, 261–271. [CrossRef]
84. Garg, R.K. Acute Disseminated Encephalomyelitis. *Postgrad. Med. J.* **2003**, *79*, 11–17. [CrossRef]
85. Miller, H.G.; Stanton, J.B.; Gibbons, J.L. Acute Disseminated Encephalomyelitis and Related Syndromes. *Br. Med. J.* **1957**, *1*, 668–672. [CrossRef]
86. Ludlow, M.; Kortekaas, J.; Herden, C.; Hoffmann, B.; Tappe, D.; Trebst, C.; Griffin, D.E.; Brindle, H.E.; Solomon, T.; Brown, A.S.; et al. Neurotropic Virus Infections as the Cause of Immediate and Delayed Neuropathology. *Acta Neuropathol.* **2016**, *131*, 159–184. [CrossRef]
87. Griffin, D.E.; Cooper, S.J.; Hirsch, R.L.; Johnson, R.T.; Lindo de Soriano, I.; Roedenbeck, S.; Vaisberg, A. Changes in Plasma IgE Levels during Complicated and Uncomplicated Measles Virus Infections. *J. Allergy Clin. Immunol.* **1985**, *76*, 206–213. [CrossRef]
88. Esolen, L.M.; Takahashi, K.; Johnson, R.T.; Vaisberg, A.; Moench, T.R.; Wesselingh, S.L.; Griffin, D.E. Brain Endothelial Cell Infection in Children with Acute Fatal Measles. *J. Clin. Investig.* **1995**, *96*, 2478–2481. [CrossRef]
89. Hosoya, M. Measles Encephalitis: Direct Viral Invasion or Autoimmune-Mediated Inflammation? *Intern. Med.* **2006**, *45*, 841–842. [CrossRef] [PubMed]
90. Baldolli, A.; Dargère, S.; Cardineau, E.; Vabret, A.; Dina, J.; de La Blanchardière, A.; Verdon, R. Measles Inclusion-Body Encephalitis (MIBE) in a Immunocompromised Patient. *J. Clin. Virol.* **2016**, *81*, 43–46. [CrossRef] [PubMed]
91. Hughes, I.; Jenney, M.E.; Newton, R.W.; Morris, D.J.; Klapper, P.E. Measles Encephalitis during Immunosuppressive Treatment for Acute Lymphoblastic Leukaemia. *Arch. Dis. Child.* **1993**, *68*, 775–778. [CrossRef] [PubMed]
92. Hardie, D.R.; Albertyn, C.; Heckmann, J.M.; Smuts, H.E.M. Molecular Characterisation of Virus in the Brains of Patients with Measles Inclusion Body Encephalitis (MIBE). *Virol. J.* **2013**, *10*, 283. [CrossRef] [PubMed]
93. Roos, R.P.; Graves, M.C.; Wollmann, R.L.; Chilcote, R.R.; Nixon, J. Immunologic and Virologic Studies of Measles Inclusion Body Encephalitis in an Immunosuppressed Host: The Relationship to Subacute Sclerosing Panencephalitis. *Neurology* **1981**, *31*, 1263–1270. [CrossRef] [PubMed]
94. Bitnun, A.; Shannon, P.; Durward, A.; Rota, P.A.; Bellini, W.J.; Graham, C.; Wang, E.; Ford-Jones, E.L.; Cox, P.; Becker, L.; et al. Measles Inclusion-Body Encephalitis Caused by the Vaccine Strain of Measles Virus. *Clin. Infect. Dis.* **1999**, *29*, 855–861. [CrossRef]
95. Ohuchi, M.; Ohuchi, R.; Mifune, K.; Ishihara, T.; Ogawa, T. Characterization of the Measles Virus Isolated from the Brain of a Patient with Immunosuppressive Measles Encephalitis. *J. Infect. Dis.* **1987**, *156*, 436–441. [CrossRef]
96. Makhortova, N.R.; Askovich, P.; Patterson, C.E.; Gechman, L.A.; Gerard, N.P.; Rall, G.F. Neurokinin-1 Enables Measles Virus Trans-Synaptic Spread in Neurons. *Virology* **2007**, *362*, 235–244. [CrossRef]
97. Young, V.A.; Rall, G.F. Making It to the Synapse: Measles Virus Spread in and among Neurons. *Curr. Top. Microbiol. Immunol.* **2009**, *330*, 3–30.
98. Mekki, M.; Eley, B.; Hardie, D.; Wilmshurst, J.M. Subacute Sclerosing Panencephalitis: Clinical Phenotype, Epidemiology, and Preventive Interventions. *Dev. Med. Child Neurol.* **2019**, dmcn.14166. [CrossRef]
99. Wendorf, K.A.; Winter, K.; Zipprich, J.; Schechter, R.; Hacker, J.K.; Preas, C.; Cherry, J.D.; Glaser, C.; Harriman, K. Subacute Sclerosing Panencephalitis: The Devastating Measles Complication That Might Be More Common Than Previously Estimated. *Clin. Infect. Dis.* **2017**, *65*, 226–232. [CrossRef] [PubMed]

100. Nakamura, Y.; Iinuma, K.; Oka, E.; Nihei, K. Epidemiologic Features of Subacute Sclerosing Panencephalitis from Clinical Data of Patients Receiving a Public Aid for Treatment. *No to hattatsu = Brain Dev.* **2003**, *35*, 316–320.
101. Miller, C.; Andrews, N.; Rush, M.; Munro, H.; Jin, L.; Miller, E. The Epidemiology of Subacute Sclerosing Panencephalitis in England and Wales 1990-2002. *Arch. Dis. Child.* **2004**, *89*, 1145–1148. [CrossRef]
102. Prashanth, L.K.; Taly, A.B.; Ravi, V.; Sinha, S.; Rao, S. Long Term Survival in Subacute Sclerosing Panencephalitis: An Enigma. *Brain Dev.* **2006**, *28*, 447–452. [CrossRef] [PubMed]
103. Oldstone, M.B.A.; Dales, S.; Tishon, A.; Lewicki, H.; Martin, L. A Role for Dual Viral Hits in Causation of Subacute Sclerosing Panencephalitis. *J. Exp. Med.* **2005**, *202*, 1185–1190. [CrossRef]
104. Bellini, W.J.; Rota, J.S.; Lowe, L.E.; Katz, R.S.; Dyken, P.R.; Zaki, S.R.; Shieh, W.-J.; Rota, P.A. Subacute Sclerosing Panencephalitis: More Cases of This Fatal Disease Are Prevented by Measles Immunization than Was Previously Recognized. *J. Infect. Dis.* **2005**, *192*, 1686–1693. [CrossRef]
105. Forcić, D.; Baricević, M.; Zgorelec, R.; Kruzić, V.; Kaić, B.; Della Marina, B.M.; Sojat, L.C.; Tesović, G.; Mazuran, R. Detection and Characterization of Measles Virus Strains in Cases of Subacute Sclerosing Panencephalitis in Croatia. *Virus Res.* **2004**, *99*, 51–56. [CrossRef]
106. Moulin, E.; Beal, V.; Jeantet, D.; Horvat, B.; Wild, T.F.; Waku-Kouomou, D. Molecular Characterization of Measles Virus Strains Causing Subacute Sclerosing Panencephalitis in France in 1977 and 2007. *J. Med. Virol.* **2011**, *83*, 1614–1623. [CrossRef]
107. Cattaneo, R.; Schmid, A.; Eschle, D.; Baczko, K.; ter Meulen, V.; Billeter, M.A. Biased Hypermutation and Other Genetic Changes in Defective Measles Viruses in Human Brain Infections. *Cell* **1988**, *55*, 255–265. [CrossRef]
108. Pfaller, C.K.; Donohue, R.C.; Nersisyan, S.; Brodsky, L.; Cattaneo, R. Extensive Editing of Cellular and Viral Double-Stranded RNA Structures Accounts for Innate Immunity Suppression and the Proviral Activity of ADAR1p150. *PLoS Biol.* **2018**, *16*, e2006577. [CrossRef] [PubMed]
109. Rima, B.K.; Duprex, W.P. Molecular Mechanisms of Measles Virus Persistence. *Virus Res.* **2005**, *111*, 132–147. [CrossRef] [PubMed]
110. Liebert, U.G.; Baczko, K.; Budka, H.; ter Meulen, V. Restricted Expression of Measles Virus Proteins in Brains from Cases of Subacute Sclerosing Panencephalitis. *J. Gen. Virol.* **1986**, *67*, 2435–2444. [CrossRef]
111. Cathomen, T.; Mrkic, B.; le Spehner, D.; Drillien, R.; Naef, R.; Pavlovic, J.; Aguzzi, A.; ABilleter, M.; Cattaneo, R. A Matrix-Less Measles Virus Is Infectious and Elicits Extensive Cell Fusion: Consequences for Propagation in the Brain. *EMBO J.* **1998**, *17*, 3899–3908. [CrossRef] [PubMed]
112. Patterson, J.B.; Cornu, T.I.; Redwine, J.; Dales, S.; Lewicki, H.; Holz, A.; Thomas, D.; Billeter, M.A.; Oldstone, M.B. Evidence That the Hypermutated M Protein of a Subacute Sclerosing Panencephalitis Measles Virus Actively Contributes to the Chronic Progressive CNS Disease. *Virology* **2001**, *291*, 215–225. [CrossRef]
113. Reuter, T.; Weissbrich, B.; Schneider-Schaulies, S.; Schneider-Schaulies, J. RNA Interference with Measles Virus N, P, and L MRNAs Efficiently Prevents and with Matrix Protein MRNA Enhances Viral Transcription. *J. Virol.* **2006**, *80*, 5951–5957. [CrossRef]
114. Maisner, A.; Klenk, H.; Herrler, G. Polarized Budding of Measles Virus Is Not Determined by Viral Surface Glycoproteins. *J. Virol.* **1998**, *72*, 5276–5278. [PubMed]
115. Kühne, M.; Brown, D.W.G.; Jin, L. Genetic Variability of Measles Virus in Acute and Persistent Infections. *Infect. Genet. Evol.* **2006**, *6*, 269–276. [CrossRef]
116. Kweder, H.; Ainouze, M.; Cosby, S.L.; Muller, C.P.; Lévy, C.; Verhoeyen, E.; Cosset, F.-L.; Manet, E.; Buckland, R. Mutations in the H, F, or M Proteins Can Facilitate Resistance of Measles Virus to Neutralizing Human Anti-MV Sera. *Adv. Virol.* **2014**, *2014*, 205617. [CrossRef]
117. Homma, M.; Tashiro, M.; Konno, H.; Ohara, Y.; Hino, M.; Takase, S. Isolation and Characterization of Subacute Sclerosing Panencephalitis Virus (Yamagata-1 Strain) from a Brain Autopsy. *Microbiol. Immunol.* **1982**, *26*, 1195–1202. [CrossRef]
118. Ito, N.; Ayata, M.; Shingai, M.; Furukawa, K.; Seto, T.; Matsunaga, I.; Muraoka, M.; Ogura, H. Comparison of the Neuropathogenicity of Two SSPE Sibling Viruses of the Osaka-2 Strain Isolated with Vero and B95a Cells. *J. Neurovirol.* **2002**, *8*, 6–13. [CrossRef]
119. Makino, S.; Sasaki, K.; Nakagawa, M.; Saito, M.; Shinohara, Y. Isolation and Biological Characterization of a Measles Virus-like Agent from the Brain of an Autopsied Case of Subacute Sclerosing Panencephalitis (SSPE). *Microbiol. Immunol.* **1977**, *21*, 193–205. [CrossRef]

120. Ogura, H.; Ayata, M.; Hayashi, K.; Seto, T.; Matsuoka, O.; Hattori, H.; Tanaka, K.; Tanaka, K.; Takano, Y.; Murata, R. Efficient Isolation of Subacute Sclerosing Panencephalitis Virus from Patient Brains by Reference to Magnetic Resonance and Computed Tomographic Images. *J. Neurovirol.* **1997**, *3*, 304–309. [CrossRef]
121. Cathomen, T.; Naim, H.Y.; Cattaneo, R. Measles Viruses with Altered Envelope Protein Cytoplasmic Tails Gain Cell Fusion Competence. *J. Virol.* **1998**, *72*, 1224–1234. [PubMed]
122. Schmid, A.; Spielhofer, P.; Cattaneo, R.; Baczko, K.; ter Meulen, V.; Billeter, M.A. Subacute Sclerosing Panencephalitis Is Typically Characterized by Alterations in the Fusion Protein Cytoplasmic Domain of the Persisting Measles Virus. *Virology* **1992**, *188*, 910–915. [CrossRef]
123. Watanabe, S.; Shirogane, Y.; Suzuki, S.O.; Ikegame, S.; Koga, R.; Yanagi, Y. Mutant Fusion Proteins with Enhanced Fusion Activity Promote Measles Virus Spread in Human Neuronal Cells and Brains of Suckling Hamsters. *J. Virol.* **2013**, *87*, 2648–2659. [CrossRef] [PubMed]
124. Watanabe, S.; Ohno, S.; Shirogane, Y.; Suzuki, S.O.; Koga, R.; Yanagi, Y. Measles Virus Mutants Possessing the Fusion Protein with Enhanced Fusion Activity Spread Effectively in Neuronal Cells, but Not in Other Cells, without Causing Strong Cytopathology. *J. Virol.* **2015**, *89*, 2710–2717. [CrossRef]
125. Ader, N.; Brindley, M.; Avila, M.; Örvell, C.; Horvat, B.; Hiltensperger, G.; Schneider-Schaulies, J.; Vandevelde, M.; Zurbriggen, A.; Plemper, R.K.; et al. Mechanism for Active Membrane Fusion Triggering by Morbillivirus Attachment Protein. *J. Virol.* **2013**, *87*, 314–326. [CrossRef] [PubMed]
126. Avila, M.; Alves, L.; Khosravi, M.; Ader-Ebert, N.; Origgi, F.; Schneider-Schaulies, J.; Zurbriggen, A.; Plemper, R.K.; Plattet, P. Molecular Determinants Defining the Triggering Range of Prefusion F Complexes of Canine Distemper Virus. *J. Virol.* **2014**, *88*, 2951–2966. [CrossRef] [PubMed]
127. Doyle, J.; Prussia, A.; White, L.K.; Sun, A.; Liotta, D.C.; Snyder, J.P.; Compans, R.W.; Plemper, R.K. Two Domains That Control Prefusion Stability and Transport Competence of the Measles Virus Fusion Protein. *J. Virol.* **2006**, *80*, 1524–1536. [CrossRef]
128. Sato, Y.; Watanabe, S.; Fukuda, Y.; Hashiguchi, T.; Yanagi, Y.; Ohno, S. Cell-to-Cell Measles Virus Spread between Human Neurons Is Dependent on Hemagglutinin and Hyperfusogenic Fusion Protein. *J. Virol.* **2018**, *92*. [CrossRef] [PubMed]
129. Mateo, M.; Navaratnarajah, C.K.; Cattaneo, R. Structural Basis of Efficient Contagion: Measles Variations on a Theme by Parainfluenza Viruses. *Curr. Opin. Virol.* **2014**, *5*, 16–23. [CrossRef]
130. Vongpunsawad, S.; Oezgun, N.; Braun, W.; Cattaneo, R. Selectively Receptor-Blind Measles Viruses: Identification of Residues Necessary for SLAM- or CD46-Induced Fusion and Their Localization on a New Hemagglutinin Structural Model. *J. Virol.* **2004**, *78*, 302–313. [CrossRef]
131. Moeller-Ehrlich, K.; Ludlow, M.; Beschorner, R.; Meyermann, R.; Rima, B.K.; Duprex, W.P.; Niewiesk, S.; Schneider-Schaulies, J. Two Functionally Linked Amino Acids in the Stem 2 Region of Measles Virus Haemagglutinin Determine Infectivity and Virulence in the Rodent Central Nervous System. *J. Gen. Virol.* **2007**, *88*, 3112–3120. [CrossRef]
132. Moeller, K.; Duffy, I.; Duprex, P.; Rima, B.; Beschorner, R.; Fauser, S.; Meyermann, R.; Niewiesk, S.; ter Meulen, V.; Schneider-Schaulies, J. Recombinant Measles Viruses Expressing Altered Hemagglutinin (H) Genes: Functional Separation of Mutations Determining H Antibody Escape from Neurovirulence. *J. Virol.* **2001**, *75*, 7612–7620. [CrossRef]
133. Hotta, H.; Nihei, K.; Abe, Y.; Kato, S.; Jiang, D.-P.; Nagano-Fujii, M.; Sada, K. Full-Length Sequence Analysis of Subacute Sclerosing Panencephalitis (SSPE) Virus, a Mutant of Measles Virus, Isolated from Brain Tissues of a Patient Shortly after Onset of SSPE. *Microbiol. Immunol.* **2006**, *50*, 525–534. [CrossRef]
134. Millar, E.L.; Rennick, L.J.; Weissbrich, B.; Schneider-Schaulies, J.; Duprex, W.P.; Rima, B.K. The Phosphoprotein Genes of Measles Viruses from Subacute Sclerosing Panencephalitis Cases Encode Functional as Well as Non-Functional Proteins and Display Reduced Editing. *Virus Res.* **2016**, *211*, 29–37. [CrossRef]
135. Arai, T.; Terao-Muto, Y.; Uchida, S.; Lin, C.; Honda, T.; Takenaka, A.; Ikeda, F.; Sato, H.; Yoneda, M.; Kai, C. The P Gene of Rodent Brain-Adapted Measles Virus Plays a Critical Role in Neurovirulence. *J. Gen. Virol.* **2017**, *98*, 1620–1629. [CrossRef]
136. Jehmlich, U.; Ritzer, J.; Grosche, J.; Härtig, W.; Liebert, U.G. Experimental Measles Encephalitis in Lewis Rats: Dissemination of Infected Neuronal Cell Subtypes. *J. Neurovirol.* **2013**, *19*, 461–470. [CrossRef]
137. Parhad, I.M.; Johnson, K.P.; Wolinsky, J.S.; Swoveland, P. Measles Retinopathy. A Hamster Model of Acute and Chronic Lesions. *Lab Investig.* **1980**, *43*, 52–56.

138. Burnstein, T.; Jensen, J.H.; Waksman, B.H. The Development of a Neurotropic Strain of Measles Virus in Hamsters and Mice. *J. Infect. Dis.* **1964**, *114*, 265–272. [CrossRef]
139. Ehrengruber, M.U.; Ehler, E.; Billeter, M.A.; Naim, H.Y. Measles Virus Spreads in Rat Hippocampal Neurons by Cell-to-Cell Contact and in a Polarized Fashion. *J. Virol.* **2002**, *76*, 5720–5728. [CrossRef]
140. Neighbour, P.A.; Rager-Zisman, B.; Bloom, B.R. Susceptibility of Mice to Acute and Persistent Measles Infection. *Infect. Immun.* **1978**, *21*, 764–770.
141. Schubert, S.; Möller-Ehrlich, K.; Singethan, K.; Wiese, S.; Duprex, W.P.; Rima, B.K.; Niewiesk, S.; Schneider-Schaulies, J. A Mouse Model of Persistent Brain Infection with Recombinant Measles Virus. *J. Gen. Virol.* **2006**, *87*, 2011–2019. [CrossRef]
142. Abe, Y.; Hashimoto, K.; Watanabe, M.; Ohara, S.; Sato, M.; Kawasaki, Y.; Hashimoto, Y.; Hosoya, M. Characteristics of Viruses Derived from Nude Mice with Persistent Measles Virus Infection. *J. Virol.* **2013**, *87*, 4170–4175. [CrossRef]
143. Horvat, B.; Rivailler, P.; Varior-Krishnan, G.; Cardoso, A.; Gerlier, D.; Rabourdin-Combe, C. Transgenic Mice Expressing Human Measles Virus (MV) Receptor CD46 Provide Cells Exhibiting Different Permissivities to MV Infections. *J. Virol.* **1996**, *70*, 6673–6681.
144. Sellin, C.I.; Davoust, N.; Guillaume, V.; Baas, D.; Belin, M.-F.; Buckland, R.; Wild, T.F.; Horvat, B. High Pathogenicity of Wild-Type Measles Virus Infection in CD150 (SLAM) Transgenic Mice. *J. Virol.* **2006**, *80*, 6420–6429. [CrossRef]
145. Figueira, T.N.; Palermo, L.M.; Veiga, A.S.; Huey, D.; Alabi, C.A.; Santos, N.C.; Welsch, J.C.; Mathieu, C.; Horvat, B.; Niewiesk, S.; et al. In Vivo Efficacy of Measles Virus Fusion Protein-Derived Peptides Is Modulated by the Properties of Self-Assembly and Membrane Residence. *J. Virol.* **2017**, *91*. [CrossRef]
146. Welsch, J.C.; Talekar, A.; Mathieu, C.; Pessi, A.; Moscona, A.; Horvat, B.; Porotto, M. Fatal Measles Virus Infection Prevented by Brain-Penetrant Fusion Inhibitors. *J. Virol.* **2013**, *87*, 13785–13794. [CrossRef]
147. Van Binnendijk, R.S.; van der Heijden, R.W.J.; van Amerongen, G.; UytdeHaag, F.G.C.M.; Osterhaus, A.D.M.E. Viral Replication and Development of Specific Immunity in Macaques after Infection with Different Measles Virus Strains. *J. Infect. Dis.* **1994**, *170*, 443–448. [CrossRef]
148. Devaux, P.; Hudacek, A.W.; Hodge, G.; Reyes-del Valle, J.; McChesney, M.B.; Cattaneo, R. A Recombinant Measles Virus Unable To Antagonize STAT1 Function Cannot Control Inflammation and Is Attenuated in Rhesus Monkeys. *J. Virol.* **2011**, *85*, 348–356. [CrossRef]
149. Leonard, V.H.J.; Sinn, P.L.; Hodge, G.; Miest, T.; Devaux, P.; Oezguen, N.; Braun, W.; McCray, P.B.; McChesney, M.B.; Cattaneo, R.; et al. Measles Virus Blind to Its Epithelial Cell Receptor Remains Virulent in Rhesus Monkeys but Cannot Cross the Airway Epithelium and Is Not Shed. *J. Clin. Investig.* **2008**, *118*, 2448–2458. [CrossRef]
150. El Mubarak, H.S.; Yuksel, S.; van Amerongen, G.; Mulder, P.G.H.; Mukhtar, M.M.; Osterhaus, A.D.M.E.; de Swart, R.L. Infection of Cynomolgus Macaques (Macaca Fascicularis) and Rhesus Macaques (Macaca Mulatta) with Different Wild-Type Measles Viruses. *J. Gen. Virol.* **2007**, *88*, 2028–2034. [CrossRef]
151. Remfry, J. A Measles Epizootic with 5 Deaths in Newly-Imported Rhesus Monkeys (*Macaca Mulatta*). *Lab. Anim.* **1976**, *10*, 49–57. [CrossRef]
152. Choi, Y.K.; Simon, M.A.; Kim, D.Y.; Yoon, B.I.; Kwon, S.W.; Lee, K.W.; Seo, I.B.; Kim, D.Y. Fatal Measles Virus Infection in Japanese Macaques (Macaca Fuscata). *Vet. Pathol.* **1999**, *36*, 594–600. [CrossRef]
153. Schumacher, H.P.; Albrecht, P.; Clark, R.G.; Kirschstein, R.L.; Tauraso, N.M. Intracerebral Inoculation of Rhesus Monkeys with a Strain of Measles Virus Isolated from a Case of Subacute Sclerosing Panencephalitis. *Infect. Immun.* **1971**, *4*, 419–424.
154. Albrecht, P.; Shabo, A.L.; Burns, G.R.; Tauraso, N.M. Experimental Measles Encephalitis in Normal and Cyclophosphamide-Treated Rhesus Monkeys. *J. Infect. Dis.* **1972**, *126*, 154–161. [CrossRef]
155. da Fontoura Budaszewski, R.; von Messling, V. Morbillivirus Experimental Animal Models: Measles Virus Pathogenesis Insights from Canine Distemper Virus. *Viruses* **2016**, *8*, 274. [CrossRef]
156. Lorenz, D.; Albrecht, P. Susceptibility of Tamarins (Saguinus) to Measles Virus. *Lab. Anim. Sci.* **1980**, *30*, 661–665.
157. Albrecht, P.; Lorenz, D.; Klutch, M.J.; Vickers, J.H.; Ennis, F.A. Fatal Measles Infection in Marmosets Pathogenesis and Prophylaxis. *Infect. Immun.* **1980**, *27*, 969–978.
158. Albrecht, P.; Lorenz, D.; Klutch, M.J. Encephalitogenicity of Measles Virus in Marmosets. *Infect. Immun.* **1981**, *34*, 581–587.

159. Oldstone, M.B.; Lewicki, H.; Thomas, D.; Tishon, A.; Dales, S.; Patterson, J.; Manchester, M.; Homann, D.; Naniche, D.; Holz, A. Measles Virus Infection in a Transgenic Model: Virus-Induced Immunosuppression and Central Nervous System Disease. *Cell* **1999**, *98*, 629–640. [CrossRef]
160. Rall, G.F.; Manchester, M.; Daniels, L.R.; Callahan, E.M.; Belman, A.R.; Oldstone, M.B. A Transgenic Mouse Model for Measles Virus Infection of the Brain. *Proc. Natl. Acad. Sci. USA* **1997**, *94*, 4659–4663. [CrossRef] [PubMed]
161. Blixenkrone-Møller, M.; Bernard, A.; Bencsik, A.; Sixt, N.; Diamond, L.E.; Logan, J.S.; Wild, T.F. Role of CD46 in Measles Virus Infection in CD46 Transgenic Mice. *Virology* **1998**, *249*, 238–248. [CrossRef] [PubMed]
162. Evlashev, A.; Moyse, E.; Valentin, H.; Azocar, O.; Trescol-Biemont, M.-C.; Marie, J.C.; Rabourdin-Combe, C.; Horvat, B. Productive Measles Virus Brain Infection and Apoptosis in CD46 Transgenic Mice. *J. Virol.* **2000**, *74*, 1373–1382. [CrossRef] [PubMed]
163. Mrkic, B.; Pavlovic, J.; Rülicke, T.; Volpe, P.; Buchholz, C.J.; Hourcade, D.; Atkinson, J.P.; Aguzzi, A.; Cattaneo, R. Measles Virus Spread and Pathogenesis in Genetically Modified Mice. *J. Virol.* **1998**, *72*, 7420–7427.
164. Hahm, B.; Arbour, N.; Oldstone, M.B. Measles Virus Interacts with Human SLAM Receptor on Dendritic Cells to Cause Immunosuppression. *Virology* **2004**, *323*, 292–302. [CrossRef]
165. Hahm, B.; Cho, J.-H.; Oldstone, M.B.A. Measles Virus-Dendritic Cell Interaction via SLAM Inhibits Innate Immunity: Selective Signaling through TLR4 but Not Other TLRs Mediates Suppression of IL-12 Synthesis. *Virology* **2007**, *358*, 251–257. [CrossRef]
166. Shingai, M.; Inoue, N.; Okuno, T.; Okabe, M.; Akazawa, T.; Miyamoto, Y.; Ayata, M.; Honda, K.; Kurita-Taniguchi, M.; Matsumoto, M.; et al. Wild-Type Measles Virus Infection in Human CD46/CD150-Transgenic Mice: CD11c-Positive Dendritic Cells Establish Systemic Viral Infection. *J. Immunol.* **2005**, *175*, 3252–3261. [CrossRef]
167. Ohno, S.; Ono, N.; Seki, F.; Takeda, M.; Kura, S.; Tsuzuki, T.; Yanagi, Y. Measles Virus Infection of SLAM (CD150) Knockin Mice Reproduces Tropism and Immunosuppression in Human Infection. *J. Virol.* **2007**, *81*, 1650–1659. [CrossRef]
168. Welsch, J.C.; Charvet, B.; Dussurgey, S.; Allatif, O.; Aurine, N.; Horvat, B.; Gerlier, D.; Mathieu, C. Type I Interferon Receptor Signaling Drives Selective Permissiveness of Astrocytes and Microglia to Measles Virus during Brain Infection. *J. Virol.* **2019**, *93*. [CrossRef]
169. Welstead, G.G.; Iorio, C.; Draker, R.; Bayani, J.; Squire, J.; Vongpunsawad, S.; Cattaneo, R.; Richardson, C.D. Measles Virus Replication in Lymphatic Cells and Organs of CD150 (SLAM) Transgenic Mice. *Proc. Natl. Acad. Sci. USA* **2005**, *102*, 16415–16420. [CrossRef]
170. Chan, S.P.K. Induction of Chronic Measles Encephalitis in C57BL/6 Mice. *J. Gen. Virol.* **1985**, *66*, 2071–2076. [CrossRef]
171. Liebert, U.G. Measles Virus Infections of the Central Nervous System. *Intervirology* **1997**, *40*, 176–184. [CrossRef] [PubMed]
172. Bankamp, B.; Brinckmann, U.G.; Reich, A.; Niewiesk, S.; ter Meulen, V.; Liebert, U.G. Measles Virus Nucleocapsid Protein Protects Rats from Encephalitis. *J. Virol.* **1991**, *65*, 1695–1700. [PubMed]
173. Niewiesk, S. Cotton Rats (Sigmodon Hispidus): An Animal Model to Study the Pathogenesis of Measles Virus Infection. *Immunol. Lett.* **1999**, *65*, 47–50. [CrossRef]
174. Niewiesk, S.; Schneider-Schaulies, J.; Ohnimus, H.; Jassoy, C.; Schneider-Schaulies, S.; Diamond, L.; Logan, J.S.; ter Meulen, V. CD46 Expression Does Not Overcome the Intracellular Block of Measles Virus Replication in Transgenic Rats. *J. Virol.* **1997**, *71*, 7969–7973.
175. Liebert, U.G.; Meulen, V.T. Virological Aspects of Measles Virus-Induced Encephalomyelitis in Lewis and BN Rats. *J. Gen. Virol.* **1987**, *68*, 1715–1722. [CrossRef]
176. Katz, M.; Rorke, L.B.; Masland, W.S.; Brodano, G.B.; Koprowski, H. Subacute Sclerosing Panencephalitis: Isolation of a Virus Encephalitogenic for Ferrets. *J. Infect. Dis.* **1970**, *121*, 188–195. [CrossRef]
177. Thormar, H.; Mehta, P.D.; Lin, F.H.; Brown, H.R.; Wisniewski, H.M. Presence of Oligoclonal Immunoglobulin G Bands and Lack of Matrix Protein Antibodies in Cerebrospinal Fluids and Sera of Ferrets with Measles Virus Encephalitis. *Infect. Immun.* **1983**, *41*, 1205–1211.
178. Cosby, S.L.; Brankin, B. Measles Virus Infection of Cerebral Endothelial Cells and Effect on Their Adhesive Properties. *Vet. Microbiol.* **1995**, *44*, 135–139. [CrossRef]

179. Laksono, B.M.; de Vries, R.D.; McQuaid, S.; Duprex, W.P.; de Swart, R.L. Measles Virus Host Invasion and Pathogenesis. *Viruses* **2016**, *8*, 210. [CrossRef]
180. Bechmann, I.; Galea, I.; Perry, V.H. What Is the Blood-Brain Barrier (Not)? *Trends Immunol.* **2007**, *28*, 5–11. [CrossRef]
181. Allen, I.V.; McQuaid, S.; McMahon, J.; Kirk, J.; McConnell, R. The Significance of Measles Virus Antigen and Genome Distribution in the CNS in SSPE for Mechanisms of Viral Spread and Demyelination. *J. Neuropathol. Exp. Neurol.* **1996**, *55*, 471–480. [CrossRef] [PubMed]
182. Delpeut, S.; Noyce, R.S.; Siu, R.W.C.; Richardson, C.D. Host Factors and Measles Virus Replication. *Curr. Opin. Virol.* **2012**, *2*, 773–783. [CrossRef] [PubMed]
183. McQuaid, S.; Cosby, S.L. An Immunohistochemical Study of the Distribution of the Measles Virus Receptors, CD46 and SLAM, in Normal Human Tissues and Subacute Sclerosing Panencephalitis. *Lab. Investig.* **2002**, *82*, 403–409. [CrossRef] [PubMed]
184. Thormar, H.; Brown, H.R.; Goller, N.L.; Barshatzky, M.R.; Wisniewski, H.M. Transmission of Measles Virus Encephalitis to Ferrets by Intracardiac Inoculation of a Cell-Associated SSPE Virus Strain. *APMIS* **1988**, *96*, 1125–1128. [CrossRef]
185. Woyciechowska, J.; Breschkin, A.M.; Rapp, F. Measles Virus Meningoencephalitis. Immunofluorescence Study of Brains Infected with Virus Mutants. *Lab. Investig.* **1977**, *36*, 233–236.
186. Shirogane, Y.; Hashiguchi, T.; Yanagi, Y. Weak Cis and Trans Interactions of the Hemagglutinin with Receptors Trigger Fusion Proteins of Neuropathogenic Measles Virus Isolates. *J. Virol.* **2019**. [CrossRef]
187. Hofman, F.M.; Hinton, D.R.; Baemayr, J.; Weil, M.; Merrill, J.E. Lymphokines and Immunoregulatory Molecules in Subacute Sclerosing Panencephalitis. *Clin. Immunol. Immunopathol.* **1991**, *58*, 331–342. [CrossRef]
188. Manchester, M.; Eto, D.S.; Oldstone, M.B. Characterization of the Inflammatory Response during Acute Measles Encephalitis in NSE-CD46 Transgenic Mice. *J. Neuroimmunol.* **1999**, *96*, 207–217. [CrossRef]
189. Welsch, J.; Lionnet, C.; Terzian, C.; Horvat, B.; Gerlier, D.; Mathieu, C. Organotypic Brain Cultures: A Framework for Studying CNS Infection by Neurotropic Viruses and Screening Antiviral Drugs. *Bio-Protocol* **2017**, *7*. [CrossRef]
190. Sheppard, R.D.; Raine, C.S.; Burnstein, T.; Bornstein, M.B.; Feldman, L.A. Cell-Associated Subacute Sclerosing Panencephalitis Agent Studied in Organotypic Central Nervous System Cultures: Viral Rescue Attempts and Morphology. *Infect. Immun.* **1975**, *12*, 891–900. [PubMed]
191. Preibisch, S.; Saalfeld, S.; Tomancak, P. Globally Optimal Stitching of Tiled 3D Microscopic Image Acquisitions. *Bioinformatics* **2009**, *25*, 1463–1465. [CrossRef] [PubMed]
192. Lawrence, D.M.; Patterson, C.E.; Gales, T.L.; D'Orazio, J.L.; Vaughn, M.M.; Rall, G.F. Measles Virus Spread between Neurons Requires Cell Contact but Not CD46 Expression, Syncytium Formation, or Extracellular Virus Production. *J. Virol.* **2000**, *74*, 1908–1918. [CrossRef]
193. O'Donnell, L.A.; Conway, S.; Rose, R.W.; Nicolas, E.; Slifker, M.; Balachandran, S.; Rall, G.F. STAT1-Independent Control of a Neurotropic Measles Virus Challenge in Primary Neurons and Infected Mice. *J. Immunol.* **2012**, *188*, 1915–1923. [CrossRef]
194. Duprex, W.P.; McQuaid, S.; Roscic-Mrkic, B.; Cattaneo, R.; McCallister, C.; Rima, B.K. In Vitro and in Vivo Infection of Neural Cells by a Recombinant Measles Virus Expressing Enhanced Green Fluorescent Protein. *J. Virol.* **2000**, *74*, 7972–7979. [CrossRef]
195. Ludlow, M.; McQuaid, S.; Cosby, S.L.; Cattaneo, R.; Rima, B.K.; Duprex, W.P. Measles Virus Superinfection Immunity and Receptor Redistribution in Persistently Infected NT2 Cells. *J. Gen. Virol.* **2005**, *86*, 2291–2303. [CrossRef]
196. McQuaid, S.; Campbell, S.; Wallace, I.J.; Kirk, J.; Cosby, S.L. Measles Virus Infection and Replication in Undifferentiated and Differentiated Human Neuronal Cells in Culture. *J. Virol.* **1998**, *72*, 5245–5250.
197. Brawner, A.T.; Xu, R.; Liu, D.; Jiang, P. Generating CNS Organoids from Human Induced Pluripotent Stem Cells for Modeling Neurological Disorders. *Int. J. Physiol. Pathophysiol. Pharmacol.* **2017**, *9*, 101–111.
198. Qian, X.; Nguyen, H.N.; Song, M.M.; Hadiono, C.; Ogden, S.C.; Hammack, C.; Yao, B.; Hamersky, G.R.; Jacob, F.; Zhong, C.; et al. Brain-Region-Specific Organoids Using Mini-Bioreactors for Modeling ZIKV Exposure. *Cell* **2016**, *165*, 1238–1254. [CrossRef]
199. Sabella, C. Measles: Not Just a Childhood Rash. *Cleve. Clin. J. Med.* **2010**, *77*, 207–213. [CrossRef] [PubMed]

200. Ordman, C.W.; Jennings, C.G.; Janeway, C.A. Chemical, Clinical, and Immunological Studies on the Products of Human Plasma Fractionation. XII. The Use of Concentrated Normal Human Serum Gamma Globulin (Human Immune Serum Globulin) in the Prevention and Attenuation of Measles. *J. Clin. Investig.* **1944**, *23*, 541–549. [CrossRef] [PubMed]
201. Bigham, M.; Murti, M.; Fung, C.; Hemming, F.; Loadman, S.; Stam, R.; Van Buynder, P.; Lem, M. Estimated Protective Effectiveness of Intramuscular Immune Serum Globulin Post-Exposure Prophylaxis during a Measles Outbreak in British Columbia, Canada, 2014. *Vaccine* **2017**, *35*, 2723–2727. [CrossRef] [PubMed]
202. Maldonado, Y.A.; Lawrence, E.C.; DeHovitz, R.; Hartzell, H.; Albrecht, P. Early Loss of Passive Measles Antibody in Infants of Mothers with Vaccine-Induced Immunity. *Pediatrics* **1995**, *96*, 447–450. [PubMed]
203. Rammohan, K.W.; McFarland, H.F.; McFarlin, D.E. Subacute Sclerosing Panencephalitis after Passive Immunization and Natural Measles Infection: Role of Antibody in Persistence of Measles Virus. *Neurology* **1982**, *32*, 390–394. [CrossRef] [PubMed]
204. Liebert, U.G.; Schneider-Schaulies, S.; Baczko, K.; ter Meulen, V. Antibody-Induced Restriction of Viral Gene Expression in Measles Encephalitis in Rats. *J. Virol.* **1990**, *64*, 706–713. [PubMed]
205. Rammohan, K.W.; McFarland, H.F.; McFarlin, D.E. Induction of Subacute Murine Measles Encephalitis by Monoclonal Antibody to Virus Haemagglutinin. *Nature* **1981**, *290*, 588–589. [CrossRef]
206. Wear, D.J.; Rapp, F. Latent Measles Virus Infection of the Hamster Central Nervous System. *J. Immunol.* **1971**, *107*, 1593–1598.
207. Mori, K.; Hiraoka, O.; Ikeda, M.; Ariumi, Y.; Hiramoto, A.; Wataya, Y.; Kato, N. Adenosine Kinase Is a Key Determinant for the Anti-HCV Activity of Ribavirin. *Hepatology* **2013**, *58*, 1236–1244. [CrossRef]
208. Crotty, S.; Cameron, C.; Andino, R. Ribavirin's Antiviral Mechanism of Action: Lethal Mutagenesis? *J. Mol. Med.* **2002**, *80*, 86–95. [CrossRef]
209. Stogner, S.W.; King, J.W.; Black-Payne, C.; Bocchini, J. Ribavirin and Intravenous Immune Globulin Therapy for Measles Pneumonia in HIV Infection. *South. Med. J.* **1993**, *86*, 1415–1418. [CrossRef]
210. Solomon, T.; Hart, C.A.; Vinjamuri, S.; Beeching, N.J.; Malucci, C.; Humphrey, P. Treatment of Subacute Sclerosing Panencephalitis with Interferon-Alpha, Ribavirin, and Inosiplex. *J. Child Neurol.* **2002**, *17*, 703–705. [CrossRef]
211. Hosoya, M.; Mori, S.; Tomoda, A.; Mori, K.; Sawaishi, Y.; Kimura, H.; Shigeta, S.; Suzuki, H. Pharmacokinetics and Effects of Ribavirin Following Intraventricular Administration for Treatment of Subacute Sclerosing Panencephalitis. *Antimicrob. Agents Chemother.* **2004**, *48*, 4631–4635. [CrossRef]
212. Tomoda, A.; Nomura, K.; Shiraishi, S.; Hamada, A.; Ohmura, T.; Hosoya, M.; Miike, T.; Sawaishi, Y.; Kimura, H.; Takashima, H.; et al. Trial of Intraventricular Ribavirin Therapy for Subacute Sclerosing Panencephalitis in Japan. *Brain Dev.* **2003**, *25*, 514–517. [CrossRef]
213. Kwak, M.; Yeh, H.-R.; Yum, M.-S.; Kim, H.-J.; You, S.J.; Ko, T.-S. A Long-Term Subacute Sclerosing Panencephalitis Survivor Treated with Intraventricular Interferon-Alpha for 13 Years. *Korean J. Pediatr.* **2019**, *62*, 108–112. [CrossRef]
214. Miyazaki, K.; Hashimoto, K.; Suyama, K.; Sato, M.; Abe, Y.; Watanabe, M.; Kanno, S.; Maeda, H.; Kawasaki, Y.; Hosoya, M. Maintaining Concentration of Ribavirin in Cerebrospinal Fluid by a New Dosage Method; 3 Cases of Subacute Sclerosing Panencephalitis Treated Using a Subcutaneous Continuous Infusion Pump. *Pediatr. Infect. Dis. J.* **2019**, *38*, 496–499. [CrossRef]
215. Gokcil, Z.; Odabasi, Z.; Demirkaya, S.; Eroglu, E.; Vural, O. Alpha-Interferon and Isoprinosine in Adult-Onset Subacute Sclerosing Panencephalitis. *J. Neurol. Sci.* **1999**, *162*, 62–64. [CrossRef]
216. Gutierrez, J.; Issacson, R.S.; Koppel, B.S. Subacute Sclerosing Panencephalitis: An Update. *Dev. Med. Child Neurol.* **2010**, *52*, 901–907. [CrossRef]
217. Ravikumar, S.; Crawford, J.R. Role of Carbamazepine in the Symptomatic Treatment of Subacute Sclerosing Panencephalitis: A Case Report and Review of the Literature. *Case Rep. Neurol. Med.* **2013**, *2013*, 327647. [CrossRef]
218. Blank, T.; Prinz, M. Type I Interferon Pathway in CNS Homeostasis and Neurological Disorders. *Glia* **2017**, *65*, 1397–1406. [CrossRef]
219. Rima, B.K.; Davidson, W.B.; Martin, S.J. The Role of Defective Interfering Particles in Persistent Infection of Vero Cells by Measles Virus. *J. Gen. Virol.* **1977**, *35*, 89–97. [CrossRef] [PubMed]

220. Yount, J.S.; Gitlin, L.; Moran, T.M.; López, C.B. MDA5 Participates in the Detection of Paramyxovirus Infection and Is Essential for the Early Activation of Dendritic Cells in Response to Sendai Virus Defective Interfering Particles. *J. Immunol.* **2008**, *180*, 4910–4918. [CrossRef] [PubMed]
221. Bello, S.; Meremikwu, M.M.; Ejemot-Nwadiaro, R.I.; Oduwole, O. Routine Vitamin A Supplementation for the Prevention of Blindness Due to Measles Infection in Children. *Cochrane Database Syst. Rev.* **2016**. [CrossRef]
222. Barclay, A.J.; Foster, A.; Sommer, A. Vitamin A Supplements and Mortality Related to Measles: A Randomised Clinical Trial. *Br. Med. J. (Clin. Res. Ed).* **1987**, *294*, 294–296. [CrossRef]
223. Coutsoudis, A.; Broughton, M.; Coovadia, H.M. Vitamin A Supplementation Reduces Measles Morbidity in Young African Children: A Randomized, Placebo-Controlled, Double-Blind Trial. *Am. J. Clin. Nutr.* **1991**, *54*, 890–895. [CrossRef]
224. Hussey, G.D.; Klein, M. Routine High-Dose Vitamin A Therapy for Children Hospitalized with Measles. *J. Trop. Pediatr.* **1993**, *39*, 342–345. [CrossRef]
225. WHO. Measles Vaccines: WHO Position Paper—April 2017. *Wkly Epidemiol Rec.* **2017**, *92*, 205–227.
226. Bichon, A.; Aubry, C.; Benarous, L.; Drouet, H.; Zandotti, C.; Parola, P.; Lagier, J.-C. Case Report. *Medicine (Baltimore)* **2017**, *96*, e9154. [CrossRef]
227. Loo, Y.-M.; Gale, M. Immune Signaling by RIG-I-like Receptors. *Immunity* **2011**, *34*, 680–692. [CrossRef]
228. Gerlier, D.; Lyles, D.S. Interplay between Innate Immunity and Negative-Strand RNA Viruses: Towards a Rational Model. *Microbiol. Mol. Biol. Rev.* **2011**, *75*, 468–490. [CrossRef]
229. Plumet, S.; Herschke, F.; Bourhis, J.-M.; Valentin, H.; Longhi, S.; Gerlier, D. Cytosolic 5′-Triphosphate Ended Viral Leader Transcript of Measles Virus as Activator of the RIG I-Mediated Interferon Response. *PLoS ONE* **2007**, *2*, e279. [CrossRef]
230. Yoneyama, M.; Onomoto, K.; Jogi, M.; Akaboshi, T.; Fujita, T. Viral RNA Detection by RIG-I-like Receptors. *Curr. Opin. Immunol.* **2015**, *32*, 48–53. [CrossRef]
231. Trottier, C.; Chabot, S.; Mann, K.K.; Colombo, M.; Chatterjee, A.; Miller, W.H.; Ward, B.J. Retinoids Inhibit Measles Virus in Vitro via Nuclear Retinoid Receptor Signaling Pathways. *Antivir. Res.* **2008**, *80*, 45–53. [CrossRef]
232. Trottier, C.; Colombo, M.; Mann, K.K.; Miller, W.H.; Ward, B.J. Retinoids Inhibit Measles Virus through a Type I IFN-Dependent Bystander Effect. *FASEB J.* **2009**, *23*, 3203–3212. [CrossRef]
233. Soye, K.J.; Trottier, C.; Richardson, C.D.; Ward, B.J.; Miller, W.H. RIG-I Is Required for the Inhibition of Measles Virus by Retinoids. *PLoS ONE* **2011**, *6*, e22323. [CrossRef]
234. Kelly, J.T.; Human, S.; Alderman, J.; Jobe, F.; Logan, L.; Rix, T.; Gonçalves-Carneiro, D.; Leung, C.; Thakur, N.; Birch, J.; et al. BST2/Tetherin Overexpression Modulates Morbillivirus Glycoprotein Production to Inhibit Cell–Cell Fusion. *Viruses* **2019**, *11*, 692. [CrossRef]
235. Smith, S.E.; Busse, D.C.; Binter, S.; Weston, S.; Diaz Soria, C.; Laksono, B.M.; Clare, S.; Van Nieuwkoop, S.; Van den Hoogen, B.G.; Clement, M.; et al. Interferon-Induced Transmembrane Protein 1 Restricts Replication of Viruses That Enter Cells via the Plasma Membrane. *J. Virol.* **2018**, *93*. [CrossRef]
236. Barnard, D.L. Inhibitors of Measles Virus. *Antivir. Chem. Chemother.* **2004**, *15*, 111–119. [CrossRef]
237. Schönberger, K.; Ludwig, M.-S.; Wildner, M.; Weissbrich, B. Epidemiology of Subacute Sclerosing Panencephalitis (SSPE) in Germany from 2003 to 2009: A Risk Estimation. *PLoS ONE* **2013**, *8*, e68909. [CrossRef]
238. Otaki, M.; Sada, K.; Kadoya, H.; Nagano-Fujii, M.; Hotta, H. Inhibition of Measles Virus and Subacute Sclerosing Panencephalitis Virus by RNA Interference. *Antivir. Res.* **2006**, *70*, 105–111. [CrossRef]
239. Keita, D.; Servan de Almeida, R.; Libeau, G.; Albina, E. Identification and Mapping of a Region on the MRNA of Morbillivirus Nucleoprotein Susceptible to RNA Interference. *Antivir. Res.* **2008**, *80*, 158–167. [CrossRef]
240. Brunel, J.; Chopy, D.; Dosnon, M.; Bloyet, L.-M.; Devaux, P.; Urzua, E.; Cattaneo, R.; Longhi, S.; Gerlier, D. Sequence of Events in Measles Virus Replication: Role of Phosphoprotein-Nucleocapsid Interactions. *J. Virol.* **2014**, *88*, 10851–10863. [CrossRef]
241. Zinke, M.; Kendl, S.; Singethan, K.; Fehrholz, M.; Reuter, D.; Rennick, L.; Herold, M.J.; Schneider-Schaulies, J. Clearance of Measles Virus from Persistently Infected Cells by Short Hairpin RNA. *J. Virol.* **2009**, *83*, 9423–9431. [CrossRef]
242. Plumet, S.; Duprex, W.P.; Gerlier, D. Dynamics of Viral RNA Synthesis during Measles Virus Infection. *J. Virol.* **2005**, *79*, 6900–6908. [CrossRef]

243. Bloyet, L.-M.; Welsch, J.; Enchery, F.; Mathieu, C.; de Breyne, S.; Horvat, B.; Grigorov, B.; Gerlier, D. HSP90 Chaperoning in Addition to Phosphoprotein Required for Folding but Not for Supporting Enzymatic Activities of Measles and Nipah Virus L Polymerases. *J. Virol.* **2016**, *90*, 6642–6656. [CrossRef]
244. Geller, R.; Andino, R.; Frydman, J. Hsp90 Inhibitors Exhibit Resistance-Free Antiviral Activity against Respiratory Syncytial Virus. *PLoS ONE* **2013**, *8*, e56762. [CrossRef]
245. Lo, M.K.; Jordan, R.; Arvey, A.; Sudhamsu, J.; Shrivastava-Ranjan, P.; Hotard, A.L.; Flint, M.; McMullan, L.K.; Siegel, D.; Clarke, M.O.; et al. GS-5734 and Its Parent Nucleoside Analog Inhibit Filo-, Pneumo-, and Paramyxoviruses. *Sci. Rep.* **2017**, *7*, 43395. [CrossRef]
246. Jordan, P.C.; Liu, C.; Raynaud, P.; Lo, M.K.; Spiropoulou, C.F.; Symons, J.A.; Beigelman, L.; Deval, J. Initiation, Extension, and Termination of RNA Synthesis by a Paramyxovirus Polymerase. *PLoS Pathog.* **2018**, *14*, e1006889. [CrossRef]
247. Warren, T.K.; Jordan, R.; Lo, M.K.; Ray, A.S.; Mackman, R.L.; Soloveva, V.; Siegel, D.; Perron, M.; Bannister, R.; Hui, H.C.; et al. Therapeutic Efficacy of the Small Molecule GS-5734 against Ebola Virus in Rhesus Monkeys. *Nature* **2016**, *531*, 381–385. [CrossRef]
248. White, L.K.; Yoon, J.-J.; Lee, J.K.; Sun, A.; Du, Y.; Fu, H.; Snyder, J.P.; Plemper, R.K. Nonnucleoside Inhibitor of Measles Virus RNA-Dependent RNA Polymerase Complex Activity. *Antimicrob. Agents Chemother.* **2007**, *51*, 2293–2303. [CrossRef]
249. Yoon, J.-J.; Krumm, S.A.; Ndungu, J.M.; Hoffman, V.; Bankamp, B.; Rota, P.A.; Sun, A.; Snyder, J.P.; Plemper, R.K. Target Analysis of the Experimental Measles Therapeutic AS-136A. *Antimicrob. Agents Chemother.* **2009**, *53*, 3860–3870. [CrossRef]
250. Ndungu, J.M.; Krumm, S.A.; Yan, D.; Arrendale, R.F.; Reddy, G.P.; Evers, T.; Howard, R.; Natchus, M.G.; Saindane, M.T.; Liotta, D.C.; et al. Non-Nucleoside Inhibitors of the Measles Virus RNA-Dependent RNA Polymerase: Synthesis, Structure-Activity Relationships, and Pharmacokinetics. *J. Med. Chem.* **2012**, *55*, 4220–4230. [CrossRef]
251. Tahara, M.; Ohno, S.; Sakai, K.; Ito, Y.; Fukuhara, H.; Komase, K.; Brindley, M.A.; Rota, P.A.; Plemper, R.K.; Maenaka, K.; et al. The Receptor-Binding Site of the Measles Virus Hemagglutinin Protein Itself Constitutes a Conserved Neutralizing Epitope. *J. Virol.* **2013**, *87*, 3583–3586. [CrossRef]
252. Tadokoro, T.; Jahan, M.L.; Ito, Y.; Tahara, M.; Chen, S.; Imai, A.; Sugimura, N.; Yoshida, K.; Saito, M.; Ose, T.; et al. Biophysical Characterization and Single-chain Fv Construction of a Neutralizing Antibody to Measles Virus. *FEBS J.* **2019**, febs.14991. [CrossRef]
253. Plemper, R.K.; Erlandson, K.J.; Lakdawala, A.S.; Sun, A.; Prussia, A.; Boonsombat, J.; Aki-Sener, E.; Yalcin, I.; Yildiz, I.; Temiz-Arpaci, O.; et al. A Target Site for Template-Based Design of Measles Virus Entry Inhibitors. *Proc. Natl. Acad. Sci. USA* **2004**, *101*, 5628–5633. [CrossRef]
254. Ha, M.N.; Delpeut, S.; Noyce, R.S.; Sisson, G.; Black, K.M.; Lin, L.-T.; Bilimoria, D.; Plemper, R.K.; Privé, G.G.; Richardson, C.D. Mutations in the Fusion Protein of Measles Virus That Confer Resistance to the Membrane Fusion Inhibitors Carbobenzoxy-d-Phe-l-Phe-Gly and 4-Nitro-2-Phenylacetyl Amino-Benzamide. *J. Virol.* **2017**, *91*. [CrossRef]
255. Porotto, M.; Yokoyama, C.C.; Palermo, L.M.; Mungall, B.; Aljofan, M.; Cortese, R.; Pessi, A.; Moscona, A. Viral Entry Inhibitors Targeted to the Membrane Site of Action. *J. Virol.* **2010**, *84*, 6760–6768. [CrossRef]
256. Griffin, D.E. Emergence and Re-Emergence of Viral Diseases of the Central Nervous System. *Prog. Neurobiol.* **2010**, *91*, 95–101. [CrossRef]

3) Annexe 3 : Analysis of a Subacute Sclerosing Panencephalitis Genotype B3 Virus from the 2009-2010 South African Measles Epidemic Shows That Hyperfusogenic F Proteins Contribute to Measles Virus Infection in the Brain

AMERICAN SOCIETY FOR MICROBIOLOGY | Journal of Virology®

VIRUS-CELL INTERACTIONS

Analysis of a Subacute Sclerosing Panencephalitis Genotype B3 Virus from the 2009-2010 South African Measles Epidemic Shows That Hyperfusogenic F Proteins Contribute to Measles Virus Infection in the Brain

Fabrizio Angius,[a,b] Heidi Smuts,[j] Ksenia Rybkina,[a,b] Debora Stelitano,[a,b] Brian Eley,[c,k] Jo Wilmshurst,[d,k] Marion Ferren,[a,b] Alexandre Lalande,[e] Cyrille Mathieu,[a,b] Anne Moscona,[a,b,f,g] Branka Horvat,[e] Takao Hashiguchi,[h] Matteo Porotto,[a,b,i] Diana Hardie[j]

[a]Center for Host-Pathogen Interaction, Columbia University Medical Center, New York, New York, USA
[b]Department of Pediatrics, Columbia University Medical Center, New York, New York, USA
[c]Paediatric Infectious Diseases Unit, Red Cross War Memorial Children's Hospital, Cape Town, South Africa
[d]Paediatric Neurology Unit, Red Cross War Memorial Children's Hospital, Cape Town, South Africa
[e]CIRI, International Center for Infectiology Research, Inserm, U1111, University Claude Bernard Lyon 1, CNRS, UMR5308, Ecole Normale Supérieure de Lyon, Lyon, France
[f]Department of Microbiology and Immunology, Columbia University Medical Center, New York, New York, USA
[g]Department of Physiology and Cellular Biophysics, Columbia University Medical Center, New York, New York, USA
[h]Department of Virology, Faculty of Medicine, Kyushu University, Fukuoka, Japan
[i]Department of Experimental Medicine, University of Campania Luigi Vanvitelli, Naples, Italy
[j]Division of Medical Virology, Department of Pathology, University of Cape Town and National Health Laboratory Service, Cape Town, South Africa
[k]Department of Paediatrics and Child Health, Faculty of Health Sciences, University of Cape Town, Cape Town, South Africa

ABSTRACT During a measles virus (MeV) epidemic in 2009 in South Africa, measles inclusion body encephalitis (MIBE) was identified in several HIV-infected patients. Years later, children are presenting with subacute sclerosing panencephalitis (SSPE). To investigate the features of established MeV neuronal infections, viral sequences were analyzed from brain tissue samples of a single SSPE case and compared with MIBE sequences previously obtained from patients infected during the same epidemic. Both the SSPE and the MIBE viruses had amino acid substitutions in the ectodomain of the F protein that confer enhanced fusion properties. Functional analysis of the fusion complexes confirmed that both MIBE and SSPE F protein mutations promoted fusion with less dependence on interaction by the viral receptor-binding protein with known MeV receptors. While the SSPE F required the presence of a homotypic attachment protein, MeV H, in order to fuse, MIBE F did not. Both F proteins had decreased thermal stability compared to that of the corresponding wild-type F protein. Finally, recombinant viruses expressing MIBE or SSPE fusion complexes spread in the absence of known MeV receptors, with MIBE F-bearing viruses causing large syncytia in these cells. Our results suggest that alterations to the MeV fusion complex that promote fusion and cell-to-cell spread in the absence of known MeV receptors is a key property for infection of the brain.

IMPORTANCE Measles virus can invade the central nervous system (CNS) and cause severe neurological complications, such as MIBE and SSPE. However, mechanisms by which MeV enters the CNS and triggers the disease remain unclear. We analyzed viruses from brain tissue of individuals with MIBE or SSPE, infected during the same epidemic, after the onset of neurological disease. Our findings indicate that the emergence of hyperfusogenic MeV F proteins is associated with infection of the brain. We also demonstrate that hyperfusogenic F proteins permit MeV to enter cells and spread without the need to engage nectin-4 or CD150, known receptors for MeV that are not present on neural cells.

Citation Angius F, Smuts H, Rybkina K, Stelitano D, Eley B, Wilmshurst J, Ferren M, Lalanfde A, Mathieu C, Moscona A, Horvat B, Hashiguchi T, Porotto M, Hardie D. 2019. Analysis of a subacute sclerosing panencephalitis genotype B3 virus from the 2009-2010 South African measles epidemic shows that hyperfusogenic F proteins contribute to measles virus infection in the brain. J Virol 93:e01700-18. https://doi.org/10.1128/JVI.01700-18.

Editor Rebecca Ellis Dutch, University of Kentucky College of Medicine

Address correspondence to Matteo Porotto, mp3509@columbia.edu, or Diana Hardie, diana.hardie@uct.ac.za.

F.A., H.S., and K.R. contributed equally.

Received 9 October 2018
Accepted 20 November 2018
Accepted manuscript posted online 28 November 2018
Published 5 February 2019

KEYWORDS central nervous system infections, measles, viral fusion

In 2009-2010, a single measles virus (MeV) strain (genotype B3) was responsible for an extensive measles outbreak in South Africa (1). During this epidemic, numerous HIV-infected patients were diagnosed with measles inclusion body encephalitis (MIBE) (2), constituting the largest MIBE case series ever reported. Now, several years later, children who were infected with MeV during the outbreak are developing subacute sclerosing panencephalitis (SSPE) (3).

The early events enabling MeV to establish brain infection remain to be elucidated, since samples are mainly obtained postmortem. Neurons, which are particularly targeted by neurotropic MeV, do not express known MeV receptors (i.e., CD150 and nectin-4). However, neuroselected or neuroadapted variants spread in the central nervous system (CNS). Several mutations in the fusion complex (composed of the receptor binding protein H and the fusion protein F) have been reported, mainly in the fusion protein of neurotropic MeV (4–6). The viruses bearing these F proteins infect and spread without known measles receptors (4–6).

MIBE occurs shortly after exposure to MeV from several weeks to months following infection, typically in highly immunocompromised patients. In a previous study, viral sequences obtained from the brains of HIV-infected patients who died of MIBE were analyzed to identify mutations correlated with neurovirulence (7). In samples from two out of three MIBE patients, the extracellular domain of the F protein had an L454W substitution that conferred a hyperfusogenic phenotype to MeV (8). SSPE, in contrast, occurs much later after exposure, on average 6 to 8 years, in immunocompetent patients. This syndrome is characterized by MeV brain infection and is associated with hypermutated genomic RNA and viral transcripts, as well as defects in particle assembly (9–11). These mutations often affect the matrix protein responsible for viral assembly and budding (9, 12–15).

To investigate the genetic underpinnings of MeV brain infection, we analyzed viral sequences isolated from an HIV-infected male child with SSPE who contracted MeV (under 6 months of age) during the 2009-2010 South African outbreak and presented with intractable seizures and deteriorating nervous system function 4 years later. The infant had been vertically infected with HIV and was on antiretroviral therapy (ART) from the age of 2.5 months, with near-normal CD4 counts and suppressed HIV load at the time of clinical presentation (3). The SSPE diagnosis was based on high MeV antibody titers in blood and cerebrospinal fluid (CSF), a history of measles in the first 6 months of life, and compatible electroencephalogram and magnetic resonance imaging results. He experienced a rapid decline in neurological function and died from aspiration pneumonia 8 months after initial presentation.

Viral sequence analyses showed close homology with the epidemic wild-type and MIBE-related strains and additional genetic changes characteristic of SSPE.

We compared the functional effects of mutations in the MeV fusion complex in the SSPE, MIBE, and wild-type B3 viruses from the original outbreak. The F proteins of both SSPE and MIBE viruses have a lower thermal stability than the wild type and can promote fusion independently of H binding to known MeV receptors.

RESULTS

Phylogenetic analysis confirms close relationship to epidemic strain. The SSPE sequences were found to be closely related to the 2009-2010 B3 epidemic strain and MIBE sequences in a phylogenetic tree of the H gene (nucleotide positions 7496 to 9124) using maximum likelihood analysis (Fig. 1).

Sequence analysis reveals genetic features typical of SSPE. Sixty mutations were detected in the SSPE viral sequence relative to the epidemic B3 reference strain (28 U-C, 4 A-G, 10 C-U, 9 G-A, 1 U-G, 4 C-A, and 1 A-U), with 28 being nonsynonymous (all nucleotide substitutions are annotated in Table S1 in supplemental material). Variation relative to the reference consensus sequence was highest in the first 3 genes, increasing

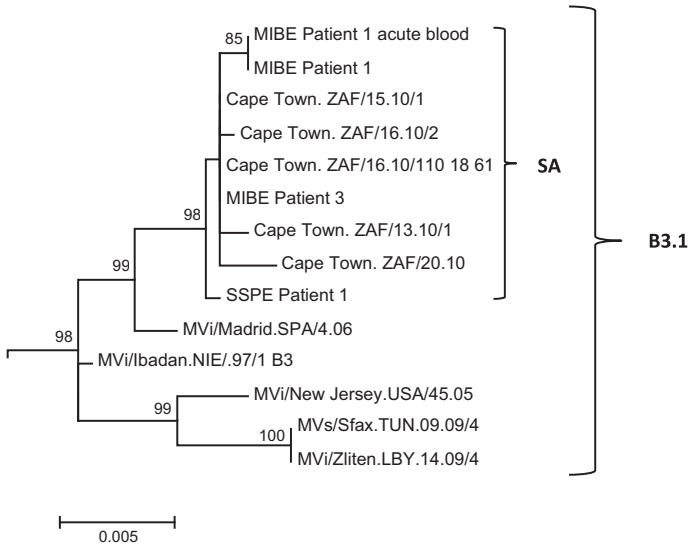

FIG 1 Phylogenetic tree of H gene (nucleotide positions 7496 to 9124) generated by maximum likelihood analysis of MeV from the SSPE case, patients with MIBE, patients who had acute measles infection during the measles epidemic of 2009-2010 in South Africa, and reference sequences. Reference sequences of other MeV genotype B3.1 viruses were retrieved from the NCBI GenBank database and are indicated by accession numbers. Bootstrap values greater than 75% are indicated at the nodes of the tree. The branch lengths are proportional to the evolutionary distances, as shown on the scale.

from 0.47% for N, 0.60% for P, and 0.89% for the M gene. The number of mutations declined progressively over the last 3 genes, namely, 0.38% for F, 0.31% for H, and 0.23% for the large protein (L) gene. In comparison, there were approximately 10 times fewer mutations in the MIBE sequences.

Hallmarks of the SSPE sequences included hypermutation, in particular U-to-C substitutions, in the N, P, and M genes. There appear to have been three events. One was at the N-P gene border (6 mutations between residues 1525 and 1778, of which 5 are silent). The second event occurs at the end of the P gene (4 mutations between residues 2722 and 2958, of which 2 are silent). The third is found in the M gene (9 mutations between residues 3450 and 4280, of which only 2 are silent; 4 of the 7 amino acid changes affect tyrosines). In all probability the last hypermutation event ablated the function of the matrix protein. U-to-C mutations occurred at a lower frequency in the latter part of the genome. In the MIBE-related sequences, U-to-C mutations were also most prominent in the N, P, and M genes.

Mutations in the H/F glycoproteins of MeV isolated from the brain of an SSPE patient. Mutations in the F proteins are shown on the sequence and on the prefusion structures (16) in Fig. 2. The F sequence from the clinical sample (SSPE F) had 6 amino acid changes (G168R, E170G, S262G, A440P, R520C, and L550P) compared to the sequence of wild-type epidemic strain B3 MeV F. One additional mutation abolished a stop codon, leading to a longer C-terminal cytoplasmic tail, referred to here as long tail (LT). In contrast to substitutions in the C-terminal heptad repeat (HRC) region of the F previously described in other neuropathogenic strains (i.e., L454W, T461I, and N462K) (6, 7), this SSPE sequence had two substitutions (G168R and E170G) in the N-terminal heptad repeat (HRN), one (A440P) in the N-terminal border of the HRC and two (R520C and L550P) in the C-terminal cytoplasmic domain (CTD). One additional substitution (S262G) was located at the interface of three protomers and two intramolecular domains near the HRN. This position has been shown to be involved in fusion activation and was previously described in a hyperfusogenic F variant (6). Conversely, compared to related MIBE sequences, only the L454W substitution in the HRC domain was present (Fig. 2). In the H gene of the South African SSPE sequence, 3 nonsynonymous mutations were identified in the cytoplasmic tail (R7Q), stalk domain (R62Q), and β5 blade of the

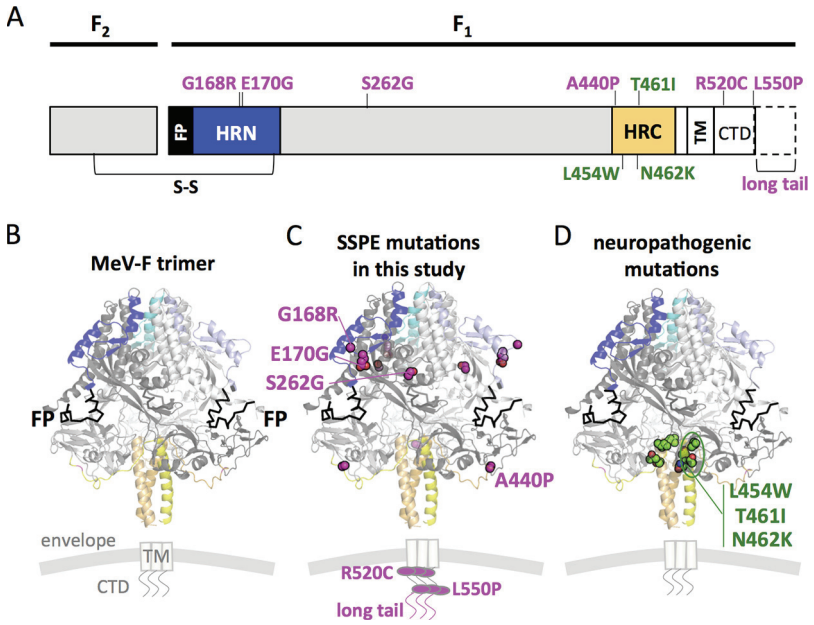

FIG 2 Location of substitutions within the F protein from CNS-adapted virus. (A) Schematic representation of fusion protein with relevant regions indicated. FP, fusion peptide; S-S, disulfide bond; HRN and HRC, heptad repeat domains at the N terminus or at the C terminus; TM, transmembrane domain; CTD, cytoplasmic domain. (B) Ribbon diagrams of the measles F model structure in prefusion conformation. The F SSPE clinical sample had a total of 6 mutations compared to sequence of the wild-type B3 strain. Residues G168G and E170G map in the HRN domain, while A440P maps close to the HRC. The residue S262G is in the region between HRN and HRC. Residues R520C and L550P are in the CTD region. One additional mutation abolished the F stop codon and resulted in a 29-amino-acid extension of the CTD (long tail). The SSPE residues are indicated in magenta. Additionally, three substitutions (L454W, T461I, and N462K) localized in the HRC domain, and previously described (6, 7) in neuropathogenic strains, are shown in green.

head domain (D530E), the latter forming part of the CD150 receptor binding site (17). In contrast, there were no changes in the H gene in related MIBE sequences.

Both SSPE and MIBE F proteins promote fusion in the absence of MeV receptors. In order to evaluate functional differences between the wild type and the SSPE virus fusion complex, we introduced the SSPE mutations found into the wild-type B3 H and F sequences, as well as the mutation that abolishes the natural stop codon at the end of the F sequence (LT). We then compared the fusion phenotype of the SSPE F to the MIBE F L454W (7). Figure 3 depicts a quantitative assay assessing the fusion properties of these MeV H/F pairs and their requirements for receptor engagement. Coexpression of WT H and F proteins resulted in similar fusion in the presence of nectin-4 and CD150 (Fig. 3). WT F does not fuse in the absence of known MeV receptors, and WT F-LT did not significantly alter the fusion phenotype compared to that of the WT, either in the presence or absence of MeV receptors (Fig. 3). In contrast, SSPE F and MIBE F L454W promote fusion in the absence of the two MeV receptors (8). The SSPE H promotes F-mediated fusion to a lesser extent than wild-type H (Fig. 3A to C and Fig. 3D to F).

The 6 mutations in SSPE F are cumulatively responsible for the fusion phenotype. To determine whether any of the 6 substitutions found in the SSPE F were solely responsible for the hyperfusogenic phenotype we observed, we compared each mutation (G168R, E170G, S262G, A440P, R520C, and L550P) individually to wild-type B3 F. In the presence of nectin-4 or CD150, all of the F proteins showed fusion similar to that of wild-type B3 F (Table 1). In the absence of MeV receptors, fusion activity was only detected in the SSPE F bearing all 6 mutations (Fig. 4).

The SSPE F requires the presence of a homotypic protein H in order to fuse, but the MIBE-related F does not. The MeV H protein has a dual function of tethering the virus to the target cell and activating the F protein. To assess the regulation of fusion

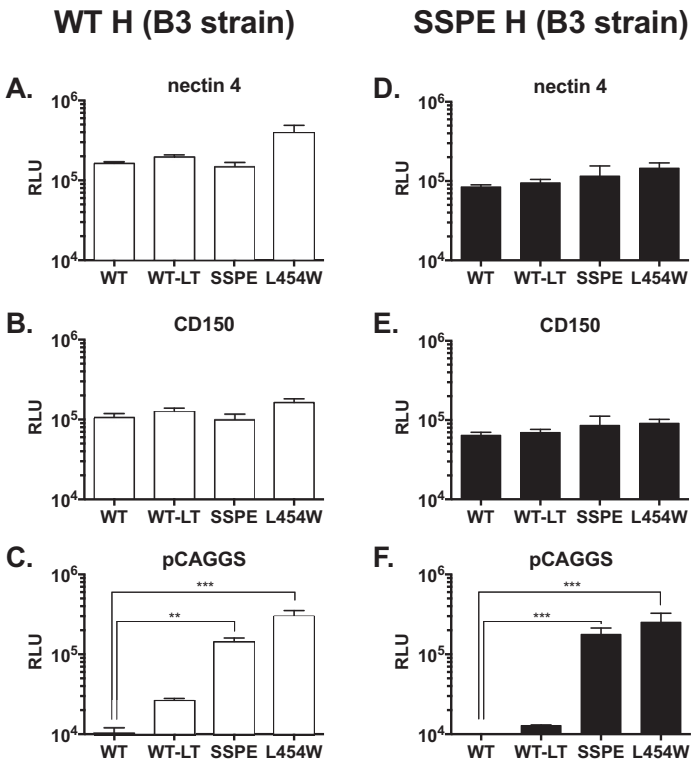

FIG 3 Functional analysis of F/H protein pairs from MeV B3 SSPE clinical sample. The cell-to-cell fusion of 293T cells coexpressing the indicated MeV B3 F protein and MeV B3 H WT (white bars) or MeV B3 H SSPE (black bars) with 293T cells transfected with MeV receptor nectin-4 (A and D), CD150 (B and E), or with an empty vector (C and F) was assessed by a β-Gal complementation assay. The values are expressed as the relative luminescence unit (RLU) averages (with SEM) of results from three independent experiments in triplicate. **, $P < 0.01$; ***, $P < 0.001$ (two-way ANOVA and Fisher's *post hoc* test). WT, wild-type F; WT-LT, wild-type F with long cytoplasmic tail; SSPE, F bearing 5 mutated amino acids (G168R, E170G, S262G, A440P, R520C, and L550P) and the ablation of the stop codon that leads to a longer cytoplasmic tail. Levels of expression of the different proteins were comparable (data not shown).

promotion by H independently from its tethering function, cells were transfected with uncleaved influenza virus hemagglutinin (HA), in addition to MeV H and F. The HA protein binds sialic acid, ubiquitously expressed on cells, but does not activate MeV F. It was used here to tether the membranes of the effector and target cells as previously done (18–20). The fusion properties of MeV H/F pairs were assessed in the quantitative fusion assay as before but without MeV receptor (nectin-4 and CD150) expression. Effector cells coexpressed influenza HA (HA_0) with MeV F (wild-type B3 F, SSPE F-LT, or MIBE F L454W) and MeV H (wild-type B3 H or SSPE H). As expected, no significant fusion was detected when wild-type F was coexpressed with MeV H (WT or SSPE), while the SSPE-LT F still fused at levels similar to those of MIBE F L454W when coexpressed with MeV H (both WT and SSPE) (Fig. 5A and B). We next tested whether, in the absence of H, the SSPE-LT F could still promote membrane fusion. Under these conditions, the SSPE-LT F did not mediate fusion (Fig. 5C). These results indicate that either SSPE-LT F can be activated independently of receptor engagement by H or it requires H engagement to an unknown MeV receptor of low affinity. Also, SSPE-LT F activation is possible only in the presence of H, with similar results obtained for the SSPE F variant without the long tail (data not shown). In contrast, the MIBE L454W F protein shows an inherent ability to mediate fusion even in the absence of H, albeit with lower fusion activity than that observed when H (WT or SSPE) is also expressed, in agreement with previous observations (8).

Both SSPE and MIBE F proteins show thermal instability. As previously shown, decreased thermal stability of F correlates with enhanced fusogenicity (8, 21) and ease

TABLE 1 Fusion activity of F proteins cotransfected with WT or SSPE patient MeV H in the presence of known MeV receptors

H/F protein	Fusion activity[a]:	
	Nectin-4	CD150
WT H		
SSPE F	1.34 ± 0.11	1.32 ± 0.14
G168R	0.97 ± 0.12	1.22 ± 0.10
E170G	0.97 ± 0.18	1.13 ± 0.15
S262G	1.06 ± 0.17	1.18 ± 0.15
A440P	0.90 ± 0.06	1.12 ± 0.09
R520C	0.92 ± 0.02	0.78 ± 0.02
L550P	0.82 ± 0.11	0.80 ± 0.15
SSPE H		
SSPE F	0.94 ± 0.03	0.98 ± 0.17
G168R	1.01 ± 0.07	0.79 ± 0.09
E170G	0.90 ± 0.05	0.83 ± 0.06
S262G	1.13 ± 0.05	0.82 ± 0.04
A440P	1.00 ± 0.15	0.84 ± 0.14
R520C	1.01 ± 0.06	0.88 ± 0.03
L550P	0.86 ± 0.13	0.73 ± 0.04

[a]Values are fold change relative to values for WT F.

of activation to a triggered conformation. The thermal stability of SSPE F and MIBE F L454W were compared at various time points by incubating cells expressing the indicated F proteins at 55°C (Fig. 6 and Table 2). Significantly more prefusion epitopes were detected after 5 min at 55°C in cells expressing SSPE F than in cells expressing MIBE F L454W, suggesting that SSPE F is more stable than L454W F. Both mutant F proteins were less stable than wild-type B3 F, which maintained 70% prefusion epitope expression after 5 min. In Table 2, the F proteins bearing single mutations are compared to the three F proteins shown in Fig. 6.

The data shown in Table 2 suggest that mutations at positions 168 and 262 reduce F stability, while the other mutations do not appear to individually affect stability. However, the SSPE substitutions in combination reduced thermal stability of the protein compared to that of wild-type F. For the hyperfusogenic MIBE F L454W, we confirmed that the single-amino-acid substitution was sufficient to decrease F stability (8).

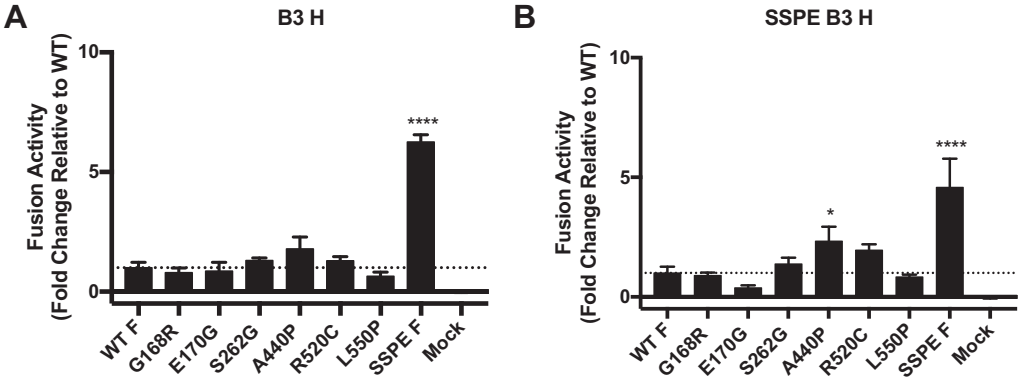

FIG 4 Multiply mutated SSPE B3 F has higher fusion activity than any individually mutated F in the absence of MeV host cell receptors. HEK-293T cells were cotransfected with the indicated F protein, α-subunit of β-galactosidase, and wild-type B3 MeV H (A) or B3 MeV SSPE H (B). Transfected cells were subsequently overlain with HEK-293T cells expressing the ω-subunit of β-galactosidase for 6 h to allow fusion. Resulting luminescence from β-galactosidase activity was quantified using TECAN Infinite M1000 Pro. Results depict a representative experiment with means and SEM from three biological replicates. Activity of mutants was compared with wild-type B3 F activity by one-way ANOVA. Fusion activities significantly different ($P < 0.05$) from that of wild-type B3 F are indicated by an asterisk(s).

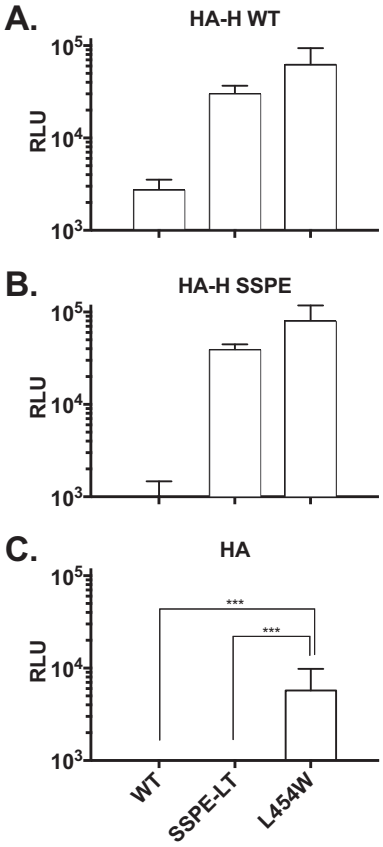

FIG 5 Regulation of fusion promotion by receptor binding protein. The cell-to-cell fusion of 293T cells coexpressing uncleaved influenza virus (HA), the indicated F proteins (*x* axis), and MeV H WT (A), MeV H SSPE (B), or the empty vector pCAGGS (C) was assessed by a β-Gal complementation assay using target cells that do not express MeV H receptor. The values are expressed as the mean RLU (with SEM) of results from three independent experiments in triplicate. ***, $P < 0.001$ (two-tailed, unpaired *t* test).

Recombinant viruses bearing CNS-adapted F proteins form syncytia in Vero cells. Since the SSPE mutations in F conferred a hyperfusogenic phenotype of cell-to-cell fusion in the absence of known MeV receptors, we assessed the properties of the mutated glycoproteins in the context of infectious recombinant MeV IC323-enhanced green fluorescent protein (EGFP) viruses. In Fig. 7, recombinant MeV expressing wild-type F, MIBE F L454W, SSPE H, or SSPE F (with the long tail) and EGFP were used to

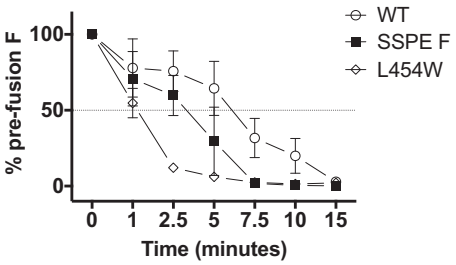

FIG 6 Thermal stability of the MeV wild-type and mutant F proteins. 293T cells expressing the indicated MeV F proteins (*x* axis) were incubated overnight at 37°C. The cells were then incubated for the indicated times at 55°C and then at 4°C with mouse MAbs recognizing the prefusion conformation of MeV F (21). The values on the *y* axis represent the percentages of conformational antibody binding and indicate the averages (with SEM) of results from four independent experiments in triplicate. WT, wild-type F; SSPE, F bearing G168R, E170G, S262G, A440P, R520C, and L550P. The L454W F (found in two MIBE clinical samples) (7) was added for comparison.

TABLE 2 Thermal stability of the B3 F mutant proteins detected by binding of a MAb specific for the prefusion conformation of F[a]

F protein	TS_{50}	Lower 95% CI	Upper 95% CI
WT	5 min 9 s	3 min 52 s	6 min 51 s
SSPE	2 min 29 s	1 min 47 s	3 min 28 s
G168R	4 min 24 s	3 min 22 s	5 min 45 s
E170G	6 min 37 s	5 min 13 s	8 min 25 s
S262G	3 min 10 s	2 min 32 s	3 min 59 s
A440P	5 min 11 s	3 min 37 s	7 min 24 s
R520C	5 min 54 s	4 min 36 s	7 min 33 s
L550P	6 min 26 s	5 min 27 s	7 min 37 s
L454W	1 min 5 s	0 min 53 s	1 min 19 s

[a]Data are reported as averages from four independent experiments and are expressed as the time (minutes) at 55°C that decreases the fraction of prefusion epitope to 50% (TS_{50}) compared to that at time zero (100%; after overnight incubation at 37°C). WT, wild-type F; SSPE, MeV F bearing G168R, E170G, S262G, A440P, R520C, and L550P.

infect Vero cells lacking known MeV receptors. Although all of the viruses were infectious, the wild-type B3 F and SSPE H recombinant viruses did not form syncytia (Fig. 7A). As previously shown, the hyperfusogenic MIBE F L454W induced syncytium formation after 24 h (8). The SSPE F recombinant virus formed less extensive syncytia and did so only after 72 h, suggesting that a less stable F allows MeV to spread from cell to cell in the absence of known MeV receptors, as observed for the MIBE F L454W mutant (8). Syncytium comparison demonstrated that MIBE F L454W mutant plaques were significantly larger than those of all other recombinant viruses 24 h postinfection (Fig. 7B). After 72 h, both MeV F L454W and MeV F SSPE mutants produced plaques significantly bigger than those of wild-type B3 F and SSPE H viruses. Thus, the accumulated mutations in SSPE F recombinant virus lead to a hyperfusogenic phenotype that is intermediate between wild-type B3 virus and the previously described MeV F L454W mutant virus.

DISCUSSION

Measles infection at a young age is the greatest risk factor for SSPE (22). The child in this report had been vertically infected with HIV and acquired measles before 6 months of age. The maternal immunity status and level of maternal antibodies is unknown. HIV-related immune compromise and the young age of this patient could have contributed to poor immune function during acute infection, allowing for extensive virus replication and dissemination to the brain (23), despite SSPE (in contrast to MIBE) not generally being associated with immune defects. While the MeV in this child was not extensively mutated genome-wide, it showed characteristic SSPE genetic changes, including hypermutation at the N-P gene border and in the M and P genes, mutations and loss of the stop codon in F, and relative preservation of the N and L genes. Hypermutations were largely U to C, indicating that nucleotide modification was taking place mainly on the antisense (+) strand. The lower mutation burden in this virus than is typically found in SSPE may relate to the shorter-than-usual incubation period of 4 years. There were even fewer mutations in the related MIBE viruses, possibly reflecting the shorter incubation associated with this disorder (7).

Mutations that were present in the ectodomain of F in both SSPE and MIBE viruses conferred a hyperfusogenic phenotype, evident in two functional assays. First, fusion activity revealed that H/F pairs from MIBE and SSPE viruses mediated membrane fusion in the absence of the recognized MeV receptors, CD150 and nectin-4 (37–40). Second, the SSPE and MIBE F proteins lose the prefusion conformation more readily than the wild-type B3 F. By both measures, MIBE F L454W showed greater fusion activity than SSPE F. In the case of SSPE F, the increased fusion activity was due to a combination of mutations. When assessed, significant fusion activity in the absence of a known receptor(s) was observed only when all 6 mutations were present (Fig. 4). To assess cell-to-cell fusion, the extent of syncytium formation was also examined (data not shown). In this qualitative assay, the only amino acid substitution derived from the SSPE

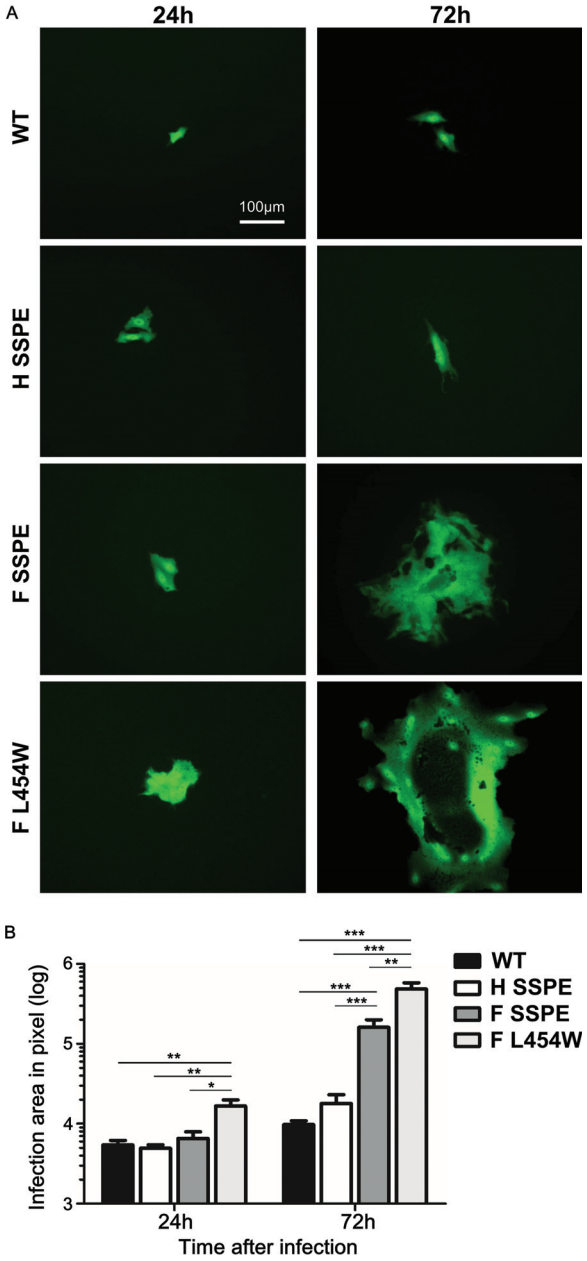

FIG 7 MeV recombinant viruses spread in the absence of known receptor. (A) Vero cells (without known MeV receptor) were infected with the indicated recombinant viruses expressing EGFP and incubated at 37°C. Infected cells were detected 24 and 72 h postinfection using an epifluorescence Nikon TS2R-FL inverted microscope. (B) Areas of infection, in pixels, were measured using ImageJ software on images randomly acquired from three separate experiments (*, $P < 0.05$; **, $P < 0.01$; ***, $P < 0.001$; each by Mann-Whitney U test, $n = 8$ at least).

F that enhanced fusion on its own was S262G. This residue is located at the interface of three protomers, a region that is involved in fusion activation. A different substitution at residue 262 (S262R) has been reported previously and also confers a hyperfusogenic phenotype (6).

A hyperfusogenic phenotype is characteristic of MeV from brain tissue (4, 6, 24). While other genetic changes, including alterations to the F protein cytoplasmic tail or a nonfunctional M protein, have also been shown to enhance fusion in an animal model (25, 26), mutations in the F ectodomain alone also induce this phenotype. Recombinant viruses bearing F proteins with hyperfusogenic ectodomain substitutions spread effi-

ciently in neurons but less so in cells expressing regular MeV receptors, possibly due to cytopathology (4, 5). In this study, Vero cells that did not express nectin-4 or CD150 were used to assess infection and spread of recombinant viruses bearing the F mutations found in MIBE and SSPE MeV. As previously shown, recombinant viruses expressing MIBE F L454W were infectious and caused large syncytium without engagement of known MeV receptors. The SSPE F recombinants were infectious as well, but cell-to-cell spread was slower than that for the MIBE recombinant, suggesting that the specific mutations in F were responsible. Thus, mutations in the ectodomain of F permit fusion without H engaging known MeV receptors; we suggest that these mutations promote infection of the brain. Our observations are supported by a recent finding by Sato et al. (4) where hyperfusogenic MeV bearing the T461I mutation in the F protein spread exclusively from cell to cell in terminally differentiated neuron cultures (4), without extracellular virus or budding. In contrast, wild-type MeV did not spread. Interestingly, however, monoclonal antibodies (MAbs) against H protein impaired the spread of hyperfusogenic viruses. Our findings support an ongoing role of H in SSPE. Indeed, although SSPE F could be activated independently of receptor engagement by H, activation was possible only when H was present. In contrast, F bearing the MIBE mutation L454W can mediate fusion in either the presence or absence of H (though at a lower level).

A notable clinical difference between MIBE and SSPE is that the former generally affects patients with defective cellular immunity. In MIBE there is little evidence of an antiviral immune response either peripherally or in the central nervous system, allowing MeV to spread in the brain more readily. In contrast, SSPE patients are generally immunocompetent, and high levels of anti-MeV antibodies are present in blood and CSF, with characteristic oligoclonal anti-MeV antibodies in the CNS. Most clones of these antibodies are directed to epitopes on the MeV N protein (the most abundant viral protein present in the brain) (27). Although only a few clones recognize other viral structural proteins, such as H and F, these antibodies would still be likely to bind to H and F proteins expressed on neurons and slow cell-to-cell spread. While the SSPE patient in our study was HIV infected, he had high levels of MeV antibodies in his CSF and his disease process ran a course typical of SSPE.

In this work, we limited our analysis to the MeV H and F proteins, and our findings are in line with evidence from our and other groups showing a direct correlation between the fusion phenotype described here (i.e., fusion in the absence of known receptor) and neuropathogenesis *in vivo* (4–6, 8, 11, 28). It remains unknown to what extent the other genetic alterations present in the SSPE viral sequence contribute to neuron invasion versus neurovirulence. To address this question, future work will assess the impact of each specific genetic change present in the SSPE MeV genome *in vitro* and *in vivo*. We propose that understanding the determinants for measles CNS infection and neurovirulence will shed light on longstanding questions about the mechanism of measles persistence and may guide antiviral approaches.

MATERIALS AND METHODS

MIBE and South African epidemic control samples. Viral sequence data from patients acutely infected during the 2009-2010 epidemic and from the brains of patients with MIBE were compared. The GenBank accession numbers of MIBE and control virus sequences are KC305651 to KC305689. The clinical details of patients have been previously described (7).

PCR of MeV genes from postmortem brains. Fresh brain tissue was collected and extracted using the manual Qiagen tissue protocol (Qiagen GmbH, Hilden, Germany). cDNA synthesis and nested PCR of the N, M, F, and H genes were performed as previously described (7). The P genes of one SSPE and two MIBE viruses were amplified using previously described primers (29). The L gene of the SSPE virus was amplified using primers from Bankamp et al. (29).

Sequencing and phylogenetic analysis. Products were sequenced using the BigDye Terminator cycle sequencing kit (Applied Biosystems, Foster City CA, USA) and PCR primers, except for the P and L, where M13 F (−20) and M13R (−26) primers were used. All six genes and intergenic regions were sequenced, except for the leader and trailer sequences. Sequences were assembled and aligned against a genotype B3 reference sequence (GenBank accession no. HM439386) using DNA Baser Sequence Assembler, v3.5.4 (Heracle BioSoft; www.DnaBaser.com). N and H genes were aligned with genotype B

sequences from GenBank using BioEdit, and a maximum likelihood tree was constructed using Mega 6.06 and the Tamura Nei model with 1,000 bootstrap resamplings (30).

Consensus epidemic sequence. A consensus sequence representing the 2009-2010 epidemic virus was determined by alignment of sequences from patients with acute measles. This was used to compare MIBE and SSPE brain virus sequences.

Structural modeling. Twenty models of the wild-type measles virus fusion glycoprotein (MeV F) were generated using the protein homology server Phyre2 (31). The model was built from the crystal structure of MeV fusion glycoprotein in its prefusion state (PDB entry 5YXW) (16).

Cell cultures. HEK-293T (human kidney epithelial) and Vero (African green monkey kidney) cells were grown in Dulbecco's modified Eagle's medium (DMEM; Gibco, Invitrogen) supplemented with 10% fetal bovine serum (FBS) and 1% antibiotics at 37°C and 5% CO_2.

Plasmids. The genes of MeV B3 and IC323 F and H proteins, and nectin-4 and CD150, were codon optimized, synthesized, and subcloned into the mammalian expression vector pCAGGS by Epoch Biolabs (Missouri City, TX).

Transient expression of viral glycoproteins. Transfections were performed in HEK-293T cells according to the protocols of the Lipofectamine 2000 manufacturer (Invitrogen). Alternatively, cells were transfected using polyethyleneimine (PEI; Polysciences, Inc.) (32). Briefly, DNA constructs, dissolved in Opti-MEM (Thermo Scientific), were mixed with PEI (1:2.5 ratio), incubated for 20 min at room temperature, and then added to the cells. After 4 h, the transfection mix was replaced with DMEM supplemented with 10% FBS and antibiotics.

***β*-Gal complementation-based fusion assay.** To quantify cell-to-cell fusion, we used a fusion assay based on alpha-omega complementation of *β*-galactosidase (*β*-Gal) that was previously described (33, 34). Briefly, 293T cells transiently transfected with the omega reporter subunit and the receptor plasmids were incubated with cells coexpressing viral glycoproteins and the alpha reporter subunit (35). Cell fusion, which leads to *β*-Gal complementation, was stopped by lysing cells, and the luminescence obtained by adding the Galacton-Star substrate (Applied Biosystems) was measured on an Infinite M1000PRO (Tecan) microplate reader.

***β*-Gal assay for cell immunity staining with F-conformation-specific MAbs.** 293T cells transiently transfected with viral glycoprotein constructs were incubated overnight at 32°C in complete medium (DMEM, 10% FBS) and processed as previously described (8). Briefly, 20 h posttransfection, cells were transferred to the temperatures and times indicated in the figures. Thereafter, cells were incubated with mouse MAbs that specifically detect MeV F in its prefusion conformation (1:1,000) for 1 h on ice. Cells were washed with phosphate-buffered saline (PBS) and then incubated for 1 h on ice with biotin-conjugated anti-mouse secondary antibody (1:500; Life Technologies). Cells were washed with PBS and then fixed for 10 min on ice with 4% paraformaldehyde (PFA). Cells were then washed twice with PBS, blocked for 20 min on ice with 3% bovine serum albumin (BSA) in PBS, washed, and then incubated for 1 h on ice with streptavidin conjugated with *β*-galactosidase (1:1,000; Life Technologies). Cells were washed with PBS, *β*-galactosidase substrate (1:50; Applied Biosystems) was added, and luminescence was measured by an Infinite M1000PRO (Tecan) microplate reader.

Cell surface expression. Cells expressing glycoproteins were incubated for 1 h with cycloheximide to synchronize protein expression and treated with 2.5 mg/ml of NHS-S-S-dPEG4-biotin (Quanta Biodesign) in PBS for 30 min at 4°C. Cells were washed with Dulbecco's PBS and lysed with DH buffer (50 mM HEPES, 100 mM NaCl, 0.005 g/ml dodecyl maltoside) containing a protease inhibitor cocktail (Sigma) and clarified by centrifugation. Samples were then incubated overnight at 4°C on a rotary wheel with streptavidin-agarose (Thermo Scientific). The next day, samples were centrifuged at 5,000 rpm for 5 min and the pellet (biotinylated proteins) washed and processed for Western blot analysis.

Recombinant virus production and analysis. MeV IC323-EGFP is a recombinant virus expressing the EGFP gene. All variant mutations, including F L454W, F SSPE, and H SSPE, were engineered in the MeV IC323-EGFP background using reverse genetics. MeV IC323 recombinant viruses were rescued in 293-3-46 cells as previously described (36). MeV recombinants were titrated by plaque assay on Vero/human SLAM cells. In the experiment to assess spread of virus, Vero cells (without known MeV receptor) were infected (multiplicity of infection of 0.03) with the indicated recombinant viruses expressing EGFP and incubated at 37°C for 2 h. The media were replaced with DMEM–10% FBS, and infected cells were incubated again for up to 72 h at 37°C. Micrographs were obtained using an epifluorescence Nikon TS2R-FL inverted microscope. Areas of infection in pixels were measured using ImageJ software on images randomly acquired from three separate experiments ($n = 8$ minimum).

Statistical analysis. Statistical analysis was performed with GraphPad Prism 5 (GraphPad Software, Inc., La Jolla, CA, USA) software. All data were expressed as the means ± standard errors of the means (SEM) from at least three independent experiments in triplicate and analyzed by the unpaired Student's *t* test or analysis of variance (ANOVA), and *post hoc* test when required, or by Mann-Whitney U test. Data were considered significant at a P value of <0.05.

Ethical approval. Ethics approval was obtained from the University of Cape Town Human Research Ethics Committee (HREC REF 163/2011).

SUPPLEMENTAL MATERIAL

Supplemental material for this article may be found at https://doi.org/10.1128/JVI.01700-18.

SUPPLEMENTAL FILE 1, PDF file, 0.1 MB.

ACKNOWLEDGMENTS

The work was supported by NIH grants NS091263 and NS105699 to M.P.; French ANR NITRODEP (ANR-13-PDOC-0010-01) to C.M.; Region Auvergne Rhone Alpes and LABEX ECOFECT (ANR-11-LABX-0048) of Lyon University, "Investissements d'Avenir" (ANR-11-IDEX-0007)/French National Research Agency (ANR), to B.H.; and Japan AMED J-PRIDE (JP18fm0208022h).

REFERENCES

1. Ntshoe GM, McAnerney JM, Archer BN, Smit SB, Harris BN, Tempia S, Mashele M, Singh B, Thomas J, Cengimbo A, Blumberg LH, Puren A, Moyes J, van den Heever J, Schoub BD, Cohen C. 2013. Measles outbreak in South Africa: epidemiology of laboratory-confirmed measles cases and assessment of intervention, 2009-2011. PLoS One 8:e55682. https://doi.org/10.1371/journal.pone.0055682.
2. Albertyn C, van der Plas H, Hardie D, Candy S, Tomoka T, Leepan EB, Heckmann JM. 2011. Silent casualties from the measles outbreak in South Africa. S Afr Med J 101:313–314. https://doi.org/10.7196/SAMJ.4616.
3. Kija E, Ndondo A, Spittal G, Hardie DR, Eley B, Wilmshurst JM. 2015. Subacute sclerosing panencephalitis in South African children following the measles outbreak between 2009 and 2011. S Afr Med J 105:713–718. https://doi.org/10.7196/SAMJnew.7788.
4. Sato Y, Watanabe S, Fukuda Y, Hashiguchi T, Yanagi Y, Ohno S. 2018. Cell-to-cell measles virus spread between human neurons is dependent on hemagglutinin and hyperfusogenic fusion protein. J Virol 92:e02166-17. https://doi.org/10.1128/JVI.02166-17.
5. Watanabe S, Ohno S, Shirogane Y, Suzuki SO, Koga R, Yanagi Y. 2015. Measles virus mutants possessing the fusion protein with enhanced fusion activity spread effectively in neuronal cells, but not in other cells, without causing strong cytopathology. J Virol 89:2710–2717. https://doi.org/10.1128/JVI.03346-14.
6. Watanabe S, Shirogane Y, Suzuki SO, Ikegame S, Koga R, Yanagi Y. 2013. Mutant fusion proteins with enhanced fusion activity promote measles virus spread in human neuronal cells and brains of suckling hamsters. J Virol 87:2648–2659. https://doi.org/10.1128/JVI.02632-12.
7. Hardie DR, Albertyn C, Heckmann JM, Smuts HE. 2013. Molecular characterisation of virus in the brains of patients with measles inclusion body encephalitis (MIBE). Virol J 10:283. https://doi.org/10.1186/1743-422X-10-283.
8. Jurgens EM, Mathieu C, Palermo LM, Hardie D, Horvat B, Moscona A, Porotto M. 2015. Measles fusion machinery is dysregulated in neuropathogenic variants. mBio 6:e02528-14. https://doi.org/10.1128/mBio.02528-14.
9. Cattaneo R, Schmid A, Eschle D, Baczko K, ter Meulen V, Billeter MA. 1988. Biased hypermutation and other genetic changes in defective measles viruses in human brain infections. Cell 55:255–265. https://doi.org/10.1016/0092-8674(88)90048-7.
10. Rima BK, Duprex WP. 2005. Molecular mechanisms of measles virus persistence. Virus Res 111:132–147. https://doi.org/10.1016/j.virusres.2005.04.005.
11. Schmid A, Spielhofer P, Cattaneo R, Baczko K, ter Meulen V, Billeter MA. 1992. Subacute sclerosing panencephalitis is typically characterized by alterations in the fusion protein cytoplasmic domain of the persisting measles virus. Virology 188:910–915. https://doi.org/10.1016/0042-6822(92)90552-Z.
12. Ayata M, Komase K, Shingai M, Matsunaga I, Katayama Y, Ogura H. 2002. Mutations affecting transcriptional termination in the p gene end of subacute sclerosing panencephalitis viruses. J Virol 76:13062–13068. https://doi.org/10.1128/JVI.76.24.13062-13068.2002.
13. Cattaneo R, Rebmann G, Schmid A, Baczko K, ter Meulen V, Billeter MA. 1987. Altered transcription of a defective measles virus genome derived from a diseased human brain. EMBO J 6:681–688. https://doi.org/10.1002/j.1460-2075.1987.tb04808.x.
14. Cattaneo R, Schmid A, Rebmann G, Baczko K, Ter Meulen V, Bellini WJ, Rozenblatt S, Billeter MA. 1986. Accumulated measles virus mutations in a case of subacute sclerosing panencephalitis: interrupted matrix protein reading frame and transcription alteration. Virology 154:97–107. https://doi.org/10.1016/0042-6822(86)90433-2.
15. Patterson JB, Cornu TI, Redwine J, Dales S, Lewicki H, Holz A, Thomas D, Billeter MA, Oldstone MB. 2001. Evidence that the hypermutated M protein of a subacute sclerosing panencephalitis measles virus actively contributes to the chronic progressive CNS disease. Virology 291:215–225. https://doi.org/10.1006/viro.2001.1182.
16. Hashiguchi T, Fukuda Y, Matsuoka R, Kuroda D, Kubota M, Shirogane Y, Watanabe S, Tsumoto K, Kohda D, Plemper RK, Yanagi Y. 2018. Structures of the prefusion form of measles virus fusion protein in complex with inhibitors. Proc Natl Acad Sci U S A 115:2496–2501. https://doi.org/10.1073/pnas.1718957115.
17. Mateo M, Navaratnarajah CK, Cattaneo R. 2014. Structural basis of efficient contagion: measles variations on a theme by parainfluenza viruses. Curr Opin Virol 5:16–23. https://doi.org/10.1016/j.coviro.2014.01.004.
18. Porotto M, Palmer SG, Palermo LM, Moscona A. 2012. Mechanism of fusion triggering by human parainfluenza virus type III: communication between viral glycoproteins during entry. J Biol Chem 287:778–793. https://doi.org/10.1074/jbc.M111.298059.
19. Porotto M, Salah ZW, Gui L, DeVito I, Jurgens EM, Lu H, Yokoyama CC, Palermo LM, Lee KK, Moscona A. 2012. Regulation of paramyxovirus fusion activation: the hemagglutinin-neuraminidase protein stabilizes the fusion protein in a pretriggered state. J Virol 86:12838–12848. https://doi.org/10.1128/JVI.01965-12.
20. Russell CJ, Jardetzky TS, Lamb RA. 2001. Membrane fusion machines of paramyxoviruses: capture of intermediates of fusion. EMBO J 20:4024–4034. https://doi.org/10.1093/emboj/20.15.4024.
21. Ader N, Brindley M, Avila M, Orvell C, Horvat B, Hiltensperger G, Schneider-Schaulies J, Vandevelde M, Zurbriggen A, Plemper RK, Plattet P. 2013. Mechanism for active membrane fusion triggering by morbillivirus attachment protein. J Virol 87:314–326. https://doi.org/10.1128/JVI.01826-12.
22. Griffin DE, Lin WH, Pan CH. 2012. Measles virus, immune control, and persistence. FEMS Microbiol Rev 36:649–662. https://doi.org/10.1111/j.1574-6976.2012.00330.x.
23. McQuaid S, Cosby SL, Koffi K, Honde M, Kirk J, Lucas SB. 1998. Distribution of measles virus in the central nervous system of HIV-seropositive children. Acta Neuropathol 96:637–642. https://doi.org/10.1007/s004010050945.
24. Ayata M, Shingai M, Ning X, Matsumoto M, Seya T, Otani S, Seto T, Ohgimoto S, Ogura H. 2007. Effect of the alterations in the fusion protein of measles virus isolated from brains of patients with subacute sclerosing panencephalitis on syncytium formation. Virus Res 130:260–268. https://doi.org/10.1016/j.virusres.2007.07.017.
25. Cathomen T, Mrkic B, Spehner D, Drillien R, Naef R, Pavlovic J, Aguzzi A, Billeter MA, Cattaneo R. 1998. A matrix-less measles virus is infectious and elicits extensive cell fusion: consequences for propagation in the brain. EMBO J 17:3899–3908. https://doi.org/10.1093/emboj/17.14.3899.
26. Cathomen T, Naim HY, Cattaneo R. 1998. Measles viruses with altered envelope protein cytoplasmic tails gain cell fusion competence. J Virol 72:1224–1234.
27. Burgoon MP, Owens GP, Carlson S, Maybach AL, Gilden DH. 2001. Antigen discovery in chronic human inflammatory central nervous system disease: panning phage-displayed antigen libraries identifies the targets of central nervous system-derived IgG in subacute sclerosing panencephalitis. J Immunol 167:6009–6014. https://doi.org/10.4049/jimmunol.167.10.6009.
28. Ayata M, Takeuchi K, Takeda M, Ohgimoto S, Kato S, Sharma LB, Tanaka M, Kuwamura M, Ishida H, Ogura H. 2010. The F gene of the Osaka-2 strain of measles virus derived from a case of subacute sclerosing panencephalitis is a major determinant of neurovirulence. J Virol 84:11189–11199. https://doi.org/10.1128/JVI.01075-10.
29. Bankamp B, Liu C, Rivailler P, Bera J, Shrivastava S, Kirkness EF, Bellini WJ, Rota PA. 2014. Wild-type measles viruses with non-standard

genome lengths. PLoS One 9:e95470. https://doi.org/10.1371/journal.pone.0095470.
30. Tamura K, Peterson D, Peterson N, Stecher G, Nei M, Kumar S. 2011. MEGA5: molecular evolutionary genetics analysis using maximum likelihood, evolutionary distance, and maximum parsimony methods. Mol Biol Evol 28:2731–2739. https://doi.org/10.1093/molbev/msr121.
31. Kelley LA, Mezulis S, Yates CM, Wass MN, Sternberg MJ. 2015. The Phyre2 web portal for protein modeling, prediction and analysis. Nat Protoc 10:845–858. https://doi.org/10.1038/nprot.2015.053.
32. Kirschner M, Monrose V, Paluch M, Techodamrongsin N, Rethwilm A, Moore JP. 2006. The production of cleaved, trimeric human immunodeficiency virus type 1 (HIV-1) envelope glycoprotein vaccine antigens and infectious pseudoviruses using linear polyethylenimine as a transfection reagent. Protein Expr Purif 48:61–68. https://doi.org/10.1016/j.pep.2006.02.017.
33. Moosmann P, Rusconi S. 1996. Alpha complementation of LacZ in mammalian cells. Nucleic Acids Res 24:1171–1172. https://doi.org/10.1093/nar/24.6.1171.
34. Porotto M, Carta P, Deng Y, Kellogg GE, Whitt M, Lu M, Mungall BA, Moscona A. 2007. Molecular determinants of antiviral potency of paramyxovirus entry inhibitors. J Virol 81:10567–10574. https://doi.org/10.1128/JVI.01181-07.
35. Porotto M, Rockx B, Yokoyama CC, Talekar A, Devito I, Palermo LM, Liu J, Cortese R, Lu M, Feldmann H, Pessi A, Moscona A. 2010. Inhibition of Nipah virus infection in vivo: targeting an early stage of paramyxovirus fusion activation during viral entry. PLoS Pathog 6:e1001168. https://doi.org/10.1371/journal.ppat.1001168.
36. Mathieu C, Huey D, Jurgens E, Welsch JC, DeVito I, Talekar A, Horvat B, Niewiesk S, Moscona A, Porotto M. 2015. Prevention of measles virus infection by intranasal delivery of fusion inhibitor peptides. J Virol 89:1143–1155. https://doi.org/10.1128/JVI.02417-14.
37. Hashiguchi T, Ose T, Kubota M, Maita N, Kamishikiryo J, Maenaka K, Yanagi Y. 2011. Structure of the measles virus hemagglutinin bound to its cellular receptor SLAM. Nat Struct Mol Biol 18:135–141. https://doi.org/10.1038/nsmb.1969.
38. Mateo M, Navaratnarajah CK, Syed S, Cattaneo R. 2013. The measles virus hemagglutinin beta-propeller head beta4-beta5 hydrophobic groove governs functional interactions with nectin-4 and CD46 but not those with the signaling lymphocytic activation molecule. J Virol 87:9208–9216. https://doi.org/10.1128/JVI.01210-13.
39. Muhlebach MD, Mateo M, Sinn PL, Prufer S, Uhlig KM, Leonard VH, Navaratnarajah CK, Frenzke M, Wong XX, Sawatsky B, Ramachandran S, McCray PB, Jr, Cichutek K, von Messling V, Lopez M, Cattaneo R. 2011. Adherens junction protein nectin-4 is the epithelial receptor for measles virus. Nature 480:530–533. https://doi.org/10.1038/nature10639.
40. Noyce RS, Bondre DG, Ha MN, Lin LT, Sisson G, Tsao MS, Richardson CD. 2011. Tumor cell marker PVRL4 (nectin 4) is an epithelial cell receptor for measles virus. PLoS Pathog 7:e1002240. https://doi.org/10.1371/journal.ppat.1002240.

4) Annexe 4 : High Pathogenicity of Nipah Virus from Pteropus lylei Fruit Bats, Cambodia

High Pathogenicity of Nipah Virus from *Pteropus lylei* Fruit Bats, Cambodia

Maria Gaudino, Noémie Aurine, Claire Dumont, Julien Fouret, Marion Ferren
Cyrille Mathieu, Olivier Reynard, Viktor E. Volchkov, Catherine Legras-Lachuer,
Marie-Claude Georges-Courbot, Branka Horvat

We conducted an in-depth characterization of the Nipah virus (NiV) isolate previously obtained from a *Pteropus lylei* bat in Cambodia in 2003 (CSUR381). We performed full-genome sequencing and phylogenetic analyses and confirmed CSUR381 is part of the NiV-Malaysia genotype. In vitro studies revealed similar cell permissiveness and replication of CSUR381 (compared with 2 other NiV isolates) in both bat and human cell lines. Sequence alignments indicated conservation of the ephrin-B2 and ephrin-B3 receptor binding sites, the glycosylation site on the G attachment protein, as well as the editing site in phosphoprotein, suggesting production of nonstructural proteins V and W, known to counteract the host innate immunity. In the hamster animal model, CSUR381 induced lethal infections. Altogether, these data suggest that the Cambodia bat-derived NiV isolate has high pathogenic potential and, thus, provide insight for further studies and better risk assessment for future NiV outbreaks in Southeast Asia.

Nipah virus (NiV) is a zoonotic paramyxovirus that was first identified as the cause of an outbreak of encephalitis in humans in Malaysia and Singapore during 1998–1999 (*1*). Although NiV infection remains rare in humans, this virus has captured the attention of the public health community and scientists because of its high case-fatality rate, ranging from 40% in Malaysia to >90% in Bangladesh and India (*2*,*3*). Its high pathogenicity, potential for interspecies transmission, and lack of validated medical countermeasures led to the classification of NiV as a Biosafety Level 4 (BSL-4) pathogen. In 2015, the World Health Organization (WHO) listed NiV as a priority pathogen because of its probability of causing severe outbreaks and subsequently placed NiV on the WHO Blueprint list of priority diseases (*4*). This designation was strengthened by the NiV outbreak in Kerala, India, where the virus had not previously been reported (*3*).

NiV is a member of the *Henipavirus* genus, together with Hendra virus, which first emerged in Brisbane, Queensland, Australia, in 1994 (*5*), and the nonpathogenic Cedar virus, which was discovered in Australia in 2009 (*6*). In addition, full-length henipa-like viral sequences were found in fruit bats in Africa (*7*) and in rats in China (Moijang virus) (*8*). As part of the Mononegavirales, NiV has a nonsegmented, negative-sense, single-stranded RNA genome. *Pteropus* fruit bats, commonly known as flying foxes, are considered the henipavirus natural reservoir; these bats, when infected with NiV, do not seem to display any apparent clinical signs of disease (*9*).

Only 2 NiV lineages are known to circulate in Asia and cause disease in humans: NiV-Malaysia and NiV-Bangladesh. In India and Bangladesh, NiV transmission from bats to humans was shown to occur through the consumption of raw date palm juice or fruits contaminated with the saliva or urine from fruit bats (*10*). In addition, as observed during the outbreaks in Malaysia in 1998 and 1999, transmission can occur via contact with infected domestic animals, such as pigs, that act as amplifying hosts of the virus (*11*). Interhuman transmission has been reported in Bangladesh and India in >50% of NiV outbreaks (*12*).

Clinical manifestations of NiV infection in humans can range from asymptomatic to acute

Author affiliations: Centre International de Recherche en Infectiologie, CIRI, INSERM U1111, CNRS, UMR5308, Univ Lyon, University Claude Bernard Lyon 1, École Normale Supérieure de Lyon, Lyon, France (M. Gaudino, N. Aurine, C. Dumont, J. Fouret, M. Ferren, C. Mathieu, O. Reynard, V.E. Volchkov, M.-C. Georges-Courbot, B. Horvat); ViroScan 3D, Trévoux, France (J. Fouret, C. Legras-Lachuer); University Claude Bernard Lyon 1, LEM, UMR5557, CNRS, INRA, VetAgro Sup, Lyon (C. Legras-Lachuer); Unité de Biologie des Infections Virales Emergentes, Institut Pasteur, INSERM P4, Jean Mérieux, Lyon (M.-C. Georges-Courbot)

DOI: https://doi.org/10.3201/eid2601.191284

respiratory syndrome, generalized vasculitis, and fatal encephalitis. Among the few survivors of NiV outbreaks, long-term neurologic problems have been reported; 20% of patients have residual neurologic sequelae (*13*), and NiV-Malaysia–infected patients experienced relapse and late-onset encephalitis (*14*).

NiV and henipa-like viruses have been detected molecularly or serologically in *Pteropus* bats in different countries of Asia (*15*) and Africa (*7*), Australia (*16*), and Brazil (*17*), and the worldwide distribution of fruit bats poses a continuous threat to another spillover with possible pandemic potential (*18*). However, since 1998, all NiV cases in humans have been identified in Malaysia, India, Bangladesh, and the Philippines (*19*). Human cases of NiV have not been reported in Cambodia or neighboring countries since the first serologic detection of NiV in Cambodia and isolation of CSUR381 in *Pteropus lylei* bats in Cambodia in 2003 (*20*,*21*). Initial phylogenetic analyses of the nucleoprotein and attachment glycoprotein of CSUR381 suggested the virus was part of the NiV-Malaysia genotype (*21*). However, a full-genome characterization and phylogenetic analysis have not been performed. In addition, the growth dynamics and virulence of this virus have not been analyzed, thus limiting more comprehensive evaluation of this virus's pathogenic potential. In this study, we performed an in-depth characterization of CSUR381, including its pathogenicity both in vitro and in vivo, ultimately to assess the outbreak risk that isolates circulating in Cambodia pose in Southeast Asia.

Materials and Methods

Viruses

In this study, we used 3 different NiV isolates: the NiV isolate CSUR381 from Cambodia (GenBank accession no. MK801755), NiV-Malaysia isolate UMMC1 (GenBank accession no. AY029767), and NiV-Bangladesh isolate SPB200401066 (GenBank accession no. AY988601). CSUR381 was isolated from *P. lylei* bat urine at the Institut Pasteur in Battambang, Cambodia, in 2003 (*21*), and the other 2 isolates were obtained from infected patients. We produced and titrated all viruses on Vero E6 cells.

Full-Genome Sequencing

We amplified and titrated the Cambodia NiV isolate on Vero cells and, after the second cell passage, extracted viral RNA from supernatant using the QIAamp Viral RNA Mini Kit (QIAGEN, https://www.qiagen.com) according to the manufacturer's instructions. We treated samples with DNase, purified and quantified RNA using the QuantiFluor RNA System (Promega, https://www.promega.com), and analyzed using the AATI High Sensitivity Genomic DNA Analysis Fragment Analyzer (Advanced Analytical Technologies Inc., https://www.agilent.com). Then, we amplified viral RNA using the Single Primer Isothermal Amplification Kit (NuGEN, https://www.nugen.com). We prepared a library using Ovation Ultra Low (NuGen), which gave us average DNA fragment sizes of 382–426 bp. We then sequenced the whole genome of CSUR381 using MiSeq Nano v2 (Illumina, https://www.illumina.com), which produced read lengths of 2 × 150 nt.

We carried out genome assembly de novo using SPAdes (http://cab.spbu.ru/software/spades) and predicted open reading frames with Prodigal (https://omictools.com/prodigal-tool). We reconstructed the missing 5′ and 3′ extremities using the 5′ RACE System for Rapid Amplification of cDNA Ends (Invitrogen, https://www.thermofisher.com) according to the manufacturer's recommendations. We performed reverse transcription with SuperScript II Reverse Transcriptase (Invitrogen) using the primer GSP1-leader (5′-GACCATTGATCCAACATC-3′) to recover the viral leader sequence and GSP-trailer (5′-AAAGTGATTGTCTACTCACT-3′) to recover the trailer sequence. After column purification, we tailed cDNA sequences with cytidine triphosphate and terminal deoxynucleotidyl transferase. Last, we amplified dC-tailed cDNA using the Abridged Anchor Primer provided in the 5′ RACE System for Rapid Amplification of cDNA Ends Kit and primers nested-GSP2-leader (5′-TACAGCTTCAATGTCTGGGTCATT-3′) to amplify the viral leader sequence, and nested-GSP2-trailer (5′-CAAGTTCAAGGACACCAAAAGT-3′) to amplify the viral trailer sequence. We sequenced PCR products using Sanger technology and submitted the complete genome sequence of CSUR381 to GenBank (accession no. MK801755).

Phylogenetic Analyses

Using the ClustalW algorithm (http://www.clustal.org), we performed multiple alignments for complete genomes and individual gene sequences. We implemented and manually checked the quality of alignments using BioEdit version 7.2.6 (*22*) and conducted genomic characterization and evolutionary analyses in MEGA version 7.0.26 (*23*). After determining the best DNA model to use for each alignment, we constructed maximum-likelihood phylogenetic trees for complete NiV genomes and all virus coding sequences. For statistical support, we used 500 bootstrap replicates for the analysis of the complete genome and 1,000 replicates for analyses of each gene.

Cell Lines and Infection

We cultured NCI-H358 (human bronchioalveolar carcinoma) and Vero E6 (African green monkey kidney) cells in Dulbecco's modified Eagle medium (DMEM) with GlutaMAX (Thermo Fisher Scientific, https://www.thermofisher.com) supplemented with 1% penicillin-streptomycin (10,000 U/mL), 1% L-glutamine, and 10% heat-inactivated (56°C for 30 minutes) fetal calf serum (FCS). We cultured human pulmonary microvascular endothelial cells (HPMECs) (*24*) in endothelial cell growth medium (Growth Medium MV 2 Kit; PromoCell, https://www.promocell.com). We incubated all these cell lines at 37°C with 5% carbon dioxide; all cell lines, including the *Pteropus* cell line described in the next paragraph, tested negative for *Mycoplasma* spp. by the MycoAlert kit (Lonza, https://www.lonza.com).

We generated a *Pteropus* flying fox cell line using a skin biopsy from the wing membrane of a female *P. giganteus* (also known as *P. medius* and flying fox) bat (*25*) of the order Yinpterochiroptera. Biopsies were collected from bats by Tiergarten Schönbrunn (Vienna, Austria) staff during regular veterinary checkups following appropriate guidelines to minimize animal stress. The biopsies were washed with sterile phosphate-buffered saline and transferred into Freezing Medium Cryo-SFM (PromoCell), and sample vials were put on dry ice for shipment to Centre International de Recherche en Infectiologie in Lyon, France. To obtain primary cell cultures, we fractionated the biopsies into petri dishes, harvested the homogenates, and incubated them at 37°C with 5% carbon dioxide in DMEM/F-12 (Gibco, https://www.thermofisher.com) supplemented with 10% fetal calf serum FCS, 1% L-glutamine (200 mM), 1,000 U/mL of penicillin, 1,000 U/mL of streptomycin, and 2.50 µg/mL amphotericin B (Gibco). We subsequently immortalized primary cells using the lentiviral vector SV40 large T-antigen produced at Genetic Analysis and Vectorology Platform (AniRA, École Normale Supérieure de Lyon, Lyon). We evaluated different clones on the basis of their morphologic stability and transfectability using jetPRIME kit (Polyplus, https://www.polyplus-transfection.com). We confirmed immortalization of clones by detecting large T-antigen inserts by reverse transcription PCR (RT-PCR). We cultured the final *Pteropus* cell line, which we designated PATGV1.12, in DMEM GlutaMAX supplemented with 10% heat-inactivated FCS. We additionally confirmed that this cell line was derived from *P. giganteus* bats by sequencing the mitochondrial region D-loop (*26*) and nuclear introns ACOX2, COPS7A, BGN, ROGD1, and STAT5A, which has been suggested to be pertinent for distinguishing among closely related bat species (*27*).

We infected cells in 12-well plates at 80% confluence with a multiplicity of infection (MOI) of 0.3. For virus replication kinetics studies, we took 4 time points postinfection into consideration: 0 h, 24 h, 48 h, and 72 h. We performed infections in BLS-4 facility Jean Mérieux (Lyon). For each time point, we collected cell lysates according to validated BSL-4 procedures. We collected supernatants and kept them at –80°C until titration by plaque assay on Vero E6 cells.

Pseudotyping of Vesicular Stomatitis Virus and Evaluation of Cell Permissiveness

We used rVSVΔG-RFP (a recombinant vesicular stomatitis virus [VSV] in which the envelope glycoprotein G gene is replaced with the red fluorescent protein gene) (*28*,*29*) to generate pseudotyped VSVs harboring different combinations of NiV envelope glycoprotein G (attachment protein) and F (fusion protein) on their surfaces. Complementing rVSVΔG-RFP–infected cells with NiV glycoproteins expressed in trans, we were able to produce stocks of pseudotyped VSVs identical in their genetic background and differing only in the nature of their surface glycoproteins. Because the infectivity of rVSVΔG-RFP pseudotypes is restricted to a single round of replication, this tool is largely used for studying viral entry for a broad range of highly pathogenic viruses (*30*).

To create the pseudotypes, we cloned the NiV glycoprotein G and F genes from RNA isolated from CSUR381, UMMC1, and SPB200401066 into 6 separate pCAGGS plasmid vectors. We transfected these 3 plasmid pairs separately into BSR-T7 cells using TransIT-LT1 Transfection Reagent (Mirus Bio, https://www.mirusbio.com). We infected cells with rVSVΔG-RFP 16 h after transfection to produce a pseudotyped VSV for each NiV isolate. We collected supernatants at 24 h postinfection and concentrated pseudotyped VSVs by ultracentrifugation (28,000 rpm for 2 h at 4°C). We titrated these viruses on Vero cells. To evaluate viral entry into different cell lines, we performed infections in 24-well plates using 80% confluent, adherent cells and a 1-h contact between virus and cells. We determined the percentage of cells infected 6 h postinfection by quantifying cells expressing RFP via flow cytometry on a BD LSRFortessa (https://www.bd.com).

RNA Extraction and Real-Time RT-PCR

At the indicated time points, we collected cells and extracted RNA using the NucleoSpin RNA Kit (Macherey-Nagel, https://www.mn-net.com) according

to the manufacturer's instructions. We assessed the yield and purity of extracted RNA using the DS-11-FX spectrophotometer (DeNovix, https://www.denovix.com). We reverse transcribed extracted RNA using the iScript Select cDNA Synthesis Kit (Bio-Rad, https://www.bio-rad.com) and performed real-time PCR using Platinum SYBR Green qPCR SuperMix-UDG (Invitrogen) on a StepOnePlus Real-Time PCR System (Applied Biosystems, https://www.thermofisher.com). As previously described (*31*), we amplified the NiV nucleoprotein gene and the *Pteropus* glyceraldehyde 3-phosphate dehydrogenase housekeeping gene using forward primer 5′-ATCATCCCTGCTTCTACT-3′ and reverse primer 3′AGGTCAGATCCACAACT-5′. We analyzed quantitative RT-PCR results using StepOne version 2.3 (Applied Biosystems).

Experimental Infection of Hamsters

We obtained 2-month-old male golden hamsters (*Mesocricetus auratus*) from Janvier Labs (https://www.janvier-labs.com). We housed hamsters in a BSL-4 containment facility (INSERM P4, Jean Mérieux, Lyon) and handled them according to the regulations for animal maintenance of France. We treated hamsters with isoflurane anesthesia before manipulations. We subcutaneously infected 2 groups of 6 hamsters with a high dose (13,500 PFU/animal) of either the NiV-Malaysia or Cambodia NiV isolate and followed hamsters daily to record their body temperature and weight. The regional ethics committee for animal experimentation (Lyon) approved these animal experiments.

Results

Full-Genome Characterization and Phylogenetic Analyses

Analysis of the assembled viral sequence of CSUR381 showed a total genome length of 18,246 nt, similar to the lengths of NiV isolates reported in Malaysia. The nucleotide composition was 27.8% T or U, 18.4% C, 33.6% A, and 20.2% G; total GC content was 38.6%. To investigate genetic relationships between CSUR381 and other henipaviruses, we constructed distance matrices for the complete genome and for each gene using the p-distance method. When we compared the sequence of CSUR381 with those of other NiVs available in GenBank, the most similar sequences (with 97.7% nucleotide identity) were from NiV-Malaysia human isolates (GenBank accession nos. NC002728.1 and AY029768.1; Table 1). We also calculated nucleotide identity and amino acid homology for each of the 6 structural genes (Table 2). Genetic pairwise comparisons with other NiV isolates showed the lowest nucleotide identity and amino acid homology for phosphoprotein (087.1/82.7%) and the highest for matrix protein (98.9/99.4%).

Using the maximum-likelihood method, we constructed phylogenetic trees on the basis of the complete genome (Figure 1, panel A) and the nucleocapsid gene (Figure 1, panel B). The general time-reversible model for the complete genome and the Kimura 2-parameter model for the nucleocapsid gene were predicted to be the best for performing those particular phylogenetic analyses. CSUR381 clustered with the monophyletic group of the NiV-Malaysia genotype

Table 1. Whole-genome pairwise nucleotide identity comparisons between Nipah virus CSUR381, Cambodia, 2003, and other available henipaviruses

Henipavirus (GenBank accession no.)	Nucleotide identity, %*
Nipah/Malaysia/2000/human (NC002728.1)	97.7
Nipah/Malaysia/2001/human (AY029768.1)	97.7
Nipah/Malaysia/1999/swine (AJ627196.1)	97.6
Nipah/Bangladesh/2004/human (AY988601.1)	91.6
Nipah/India/2007/human (FJ513078.1)	91.4
Nipah/Bangladesh/2008/human (JN808863.1)	91.4
Nipah/India/2018/human (MH396625.1)	91.3
Hendra/Australia/2008/human (JN255805.1)	70.0
Hendra/Australia/2009/bat (JN255803.1)	69.9
Hendra/Australia/2007/horse (HM044321.1)	69.9
Cedar/Australia/2009/Ptalecto (JQ001776.1)	56.7
Paramyxo/Ghana/2009/Eidolonhelvum (HQ660129.1)	52.9
Mojiang/China/2012/Rattusflavipectus (NC025352.1)	48.9

*Calculated by using the p-distance method.

Table 2. Pairwise comparison of NiV CSUR381, Cambodia, 2003, and other available NiVs, by NiV gene*

NiV (GenBank accession no.)	NiV gene, % nucleotide identity/% homology of deduced amino acid†					
	N	P	M	F	G	L
Nipah/Malaysia/2010/Pvampyrus (FN869553.1)	98.3/99.2	96.3/94.9	98.9/99.4	98.4/98.7	97.1/98.5	98.0/99.3
Nipah/Malaysia/2000/human (NC002728.1)	97.9/98.7	95.9/94.1	98.5/99.1	98.1/98.9	97.1/98.5	98.1/99.4
Nipah/Bangladesh/2004/human (AY988601.1)	93.8/98.5	87.8/84.8	93.0/99.1	93.0/98.2	88.3/95.5	91.7/98.2
Nipah/Bangladesh/2008/human (JN808863.1)	93.9/98.7	87.6/84.4	93.0/99.1	93.3/98.5	88.1/95.5	91.8/98.4
Nipah/India/2007/human (FJ513078.1)	93.5/98.5	87.4/84.3	92.9/98.9	93.1/98.4	88.0/95.3	91.9/98.4
Nipah/India/2018/human (MH396625.1)	93.3/98.5	87.1/82.7	92.6/99.1	93.0/98.5	87.2/95.3	91.7/98.5
Nipah/Thailand/2010/Plylei (KT163252.1)	93.7/98.7					
Nipah/Thailand/2010/Phypomelaneus (KT163247.1)	97.8/99.0					

*F, fusion protein; G, attachment protein; L, polymerase; M, matrix protein; N, nucleoprotein; NiV, Nipah virus; P, phosphoprotein.
†Both calculated by using the p-distance method.

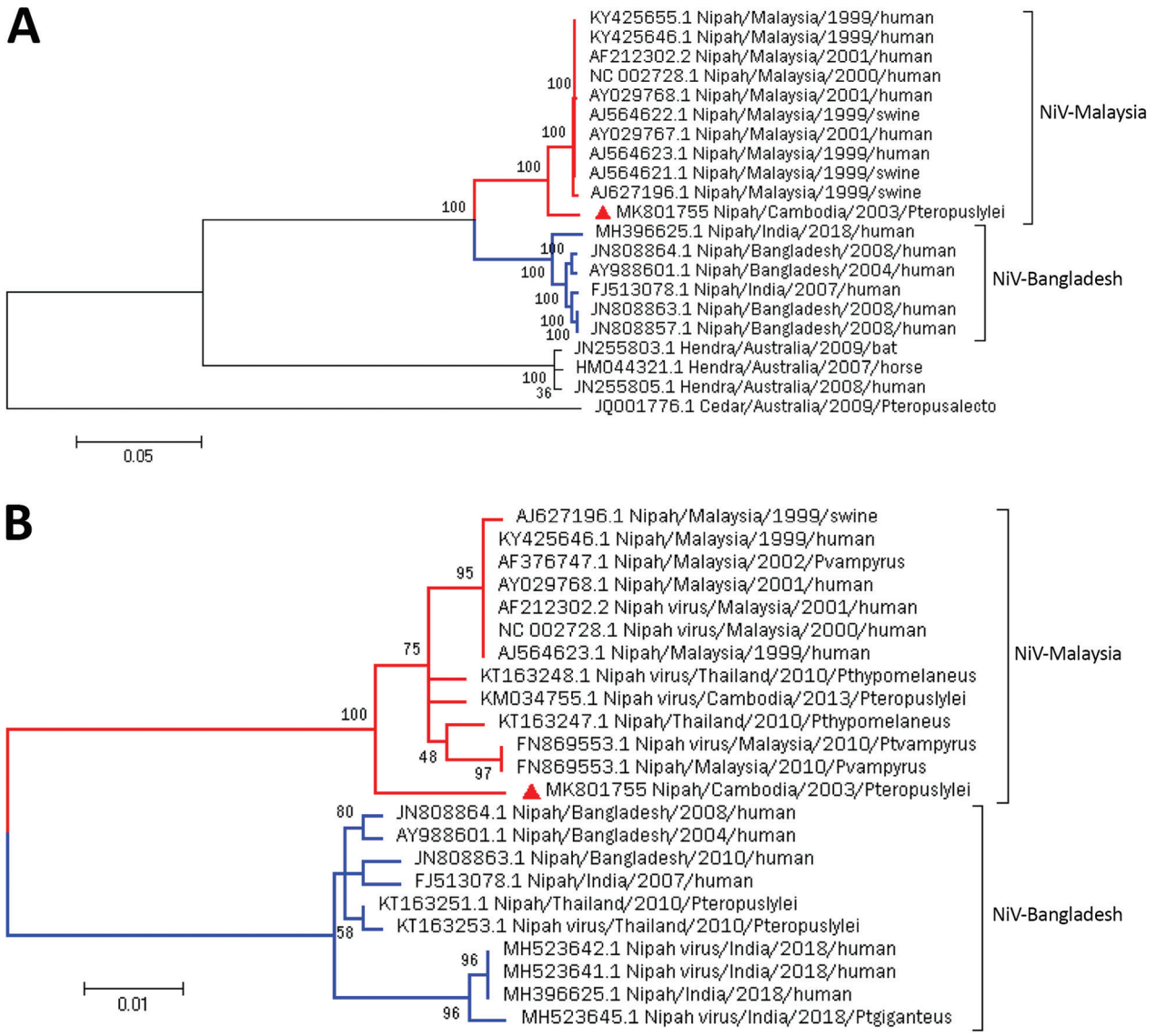

Figure 1. Maximum-likelihood phylogenetic analysis of NiV CSUR381, Cambodia, 2003 (red triangle), compared with other henipaviruses and NiVs. A) Phylogenetic tree constructed with complete genome sequences. A general time-reversible model was calculated as the best DNA model to conduct this analysis. B) Phylogenetic tree constructed by using the nucleocapsid gene. The Kimura 2-parameter model was calculated as the best DNA model to conduct this analysis. Bootstrap statistical support is marked on branch nodes. GenBank accession numbers of isolates are provided in branches, and NiV lineages of isolates are indicated. Phylogenetic trees are drawn to scale; scale bars represent branch lengths measured in the number of substitutions per site. NiV, Nipah virus.

for both the whole genome and nucleocapsid gene; bootstrap support was >98% in all cases, confirming the previous partial genomic characterization of CSUR381 (*24*). We then generated phylogenetic trees for each of the coding sequences of the 6 NiV structural proteins, which gave equivalent results (Appendix Figure 1, https://wwwnc.cdc.gov/EID/article/26/1/19-1284-App1.pdf).

Multiple alignment of the henipavirus phosphoprotein gene (Figure 2) revealed high conservation of the editing site (5′-AAAAAGGG-3′) in CSUR381, similar to other NiV and Hendra virus isolates and different from Cedar virus, a nonpathogenic virus isolated from a *P. alecto* bat in Australia (*6*). This finding suggests that CSUR381 might produce the nonstructural proteins V and W, capable of interacting with the host innate cellular immune response (*32*). Comparisons of the deduced V, W, and C amino acid homologies between CSUR381 and other known NiVs showed a variation of 88%–100% (Appendix Table).

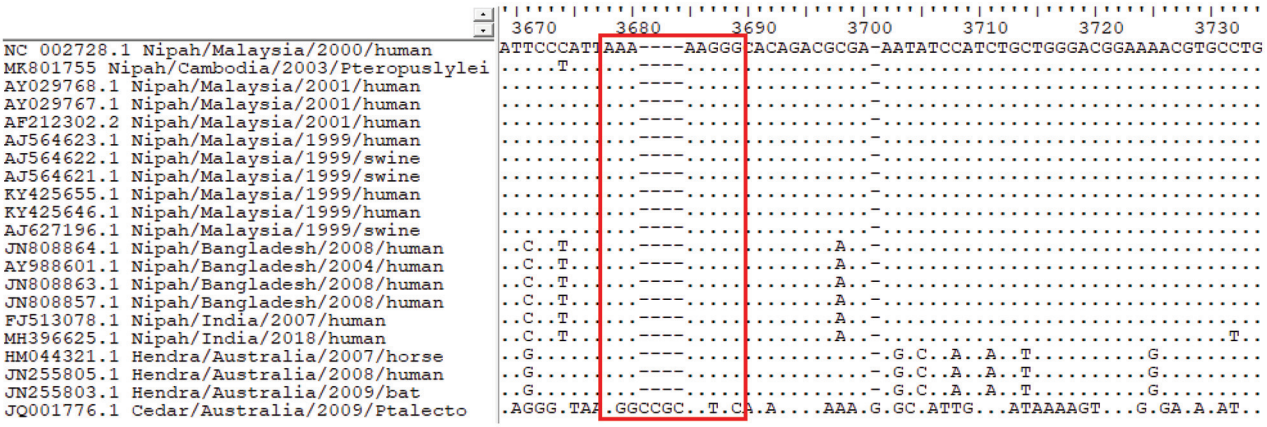

Figure 2. Multiple alignment of the phosphoprotein gene of Nipah virus CSUR381, Cambodia, 2003, and other henipavirus isolates. The highly conserved editing site (5′-AAAAAGGG-3′, red outline) is present in all Nipah and Hendra virus sequences but absent in the nonpathogenic Cedar virus sequence. GenBank accession numbers are provided for all isolates.

Evaluation of Virus Entry

We next determined the cellular permissiveness of a human endothelial cell line (HPMEC), a human respiratory epithelial cell line (NCI-H358), the newly generated *Pteropus* bat cell line (PATGV1.12), and Vero cells to CSUR381 compared with the NiV-Malaysia (UMMC1) and NiV-Bangladesh (SPB200401066) isolate using pseudotyped rVSVΔG-RFP viruses. Cell lines were infected for 1 h at an MOI of 0.3. The percentages of cells infected were analyzed by flow cytometry 6 h after infection (Figure 3), and results from HPMEC, NCI-H358, and PATGV1.12 were normalized to the findings from Vero. All tested cell lines were permissive to infection with all 3 viruses tested. Entry of NiV pseudotypes into the bat cell line PATGV1.12 and human respiratory epithelial cell line was similar. Compared with the NiV-Malaysia and NiV-Bangladesh pseudotypes, the CSUR381 pseudotyped virus showed higher but not significantly increased entry into the 3 tested cell lines (1-way analysis of variance).

We further analyzed the amino acid sequences of the F and G proteins of the 3 viruses by multiple alignment. The glycosylation site (N529/Q530/T531) (*33*) and ephrin-B2 and ephrin-B3 binding sites (*34*) in the G attachment protein were preserved (Appendix Figure 2). In addition, multiple alignments showed that the F cleavage site was preserved among all analyzed NiV isolates (Appendix Figure 3). Last, an analysis of the predicted N-terminal and C-terminal heptad-repeat regions within the F protein, which are needed for NiV fusion (*35*), showed high conservation, and compared with NiV-Malaysia and NiV-Bangladesh, only 1 aa difference (V159→I) was detected in CSUR381 (Appendix Figure 3). Altogether, the high conservation of the NiV glycoproteins and results from pseudotype virus studies suggest that CSUR381 can enter target cells at least as well as NiV-Malaysia and NiV-Bangladesh.

Replication of NiV Isolates in Different Cell Types

To further evaluate the virulence of CSUR381, we compared the replication kinetics of this virus with those of the NiV-Malaysia and NiV-Bangladesh isolates.

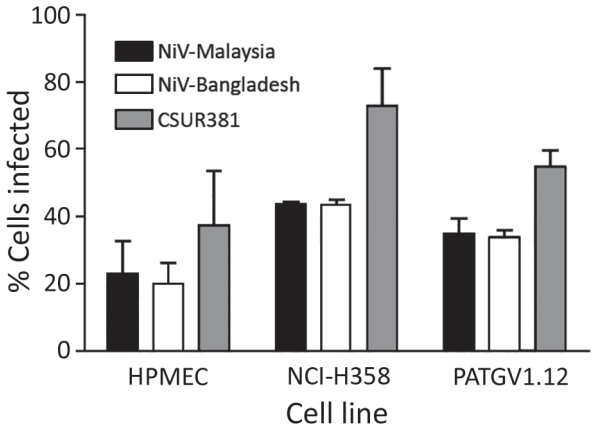

Figure 3. Evaluation of entry of VSVΔG-RFPs (vesicular stomatitis virus in which the envelope glycoprotein G gene is replaced with the red fluorescent protein gene) pseudotyped with the surface glycoproteins of NiVs CSUR381 (Cambodia 2003 isolate), UMMC1 (NiV-Malaysia isolate), and SPB200401066 (NiV-Bangladesh isolate) in different cell types. Infections of HPMEC, NCI-H358 (human bronchioalveolar cells), PATGV1.12 (bat cells), and Vero cells were performed at a multiplicity of infection of 0.3, and the percentages of infected cells were evaluated 6 hours postinfection by measuring RFP by flow cytometry and normalizing values to those from Vero cells. Histograms indicate the mean of 3 independent experiments, and error bars indicate upper half of SD. HPMEC, human pulmonary microvascular endothelial cell; NiV, Nipah virus.

We infected cell types known to be primary targets of NiV in humans, pulmonary endothelial (HPMEC) and bronchioalveolar epithelial (NCI-H358) cells, and the bat cell line PATGV1.12 at an MOI of 0.3 (Figure 4). NiV RNA synthesis was highest in HPMEC, where NiV-Bangladesh replicated the best, although a similar level of RNA and infectious virus particle production was observed for all 3 viruses (Figure 4, panel A). In accordance with virus entry studies (Figure 3), virus replication was also observed in PATGV1.12 (Figure 4, panels A and B). Differences among the 3 tested NiV isolates were observed only in NCI-H358, where NiV-Malaysia RNA synthesis was significantly increased ($p<0.001$ by 2-way analysis of variance) compared with NiV-Bangladesh, provoking remarkable cytopathic effects (Figure 4, panel C). The formation of giant multinucleated cells, a hallmark of NiV infection, were already visible at 24 hours postinfection in all cell types and further developed during the course of the infection (Figure 4, panels C–E). Vero cells showed the most visible cytopathic effects, probably because of their interferon incompetence (*36*).

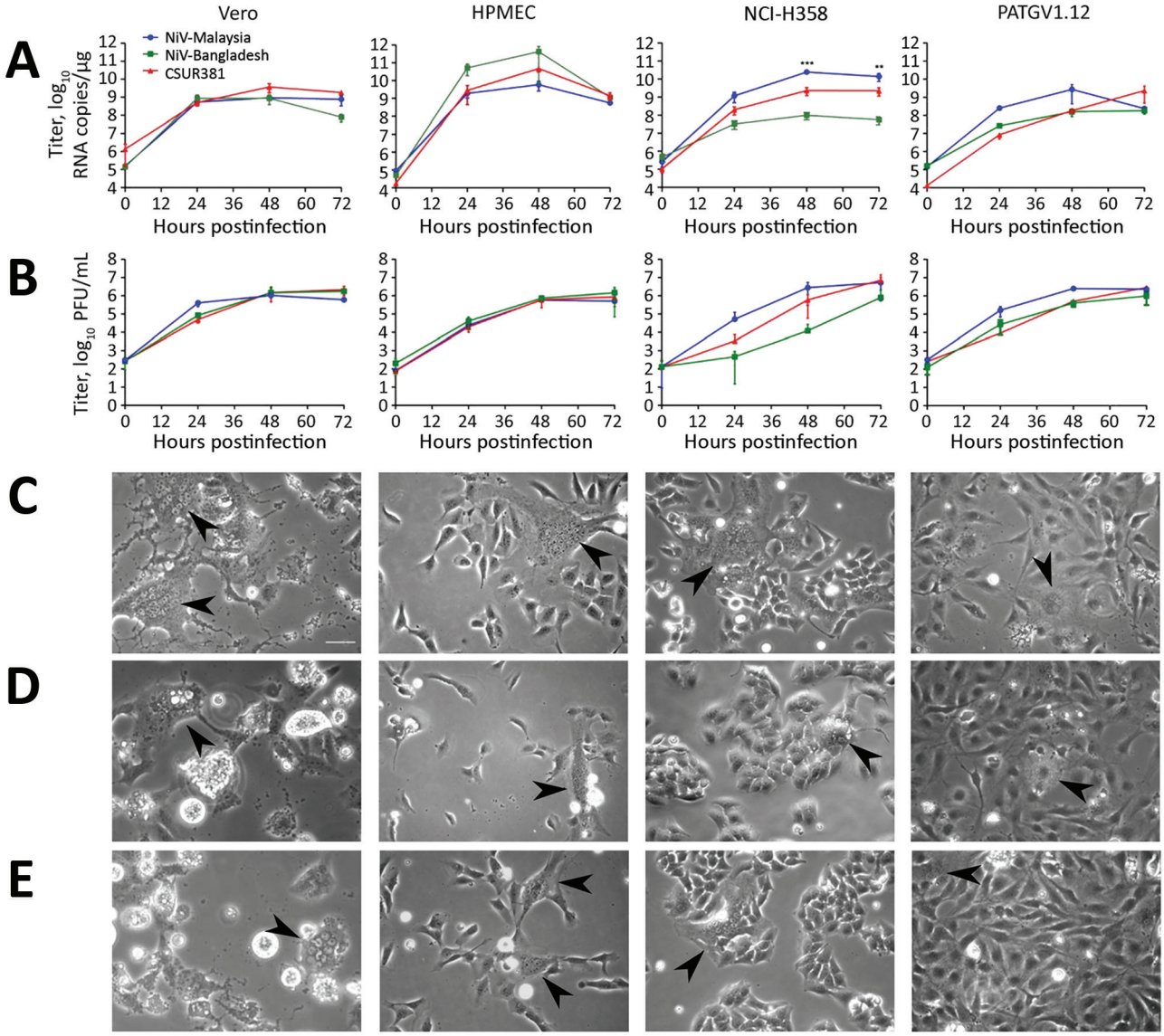

Figure 4. Replication of NiVs CSUR381 (Cambodia 2003 isolate), UMMC1 (NiV-Malaysia isolate), and SPB200401066 (NiV-Bangladesh isolate) in Vero, HPMEC, NCI-H358 (human bronchioalveolar cells), and PATGV1.12 (bat cells). A) Real-time reverse transcription PCR titer. Cells were infected at a multiplicity of infection of 0.3, and the production of the nucleocapsid gene was measured. Significance was measured by 2-way analysis of variance. B) Kinetics of infectious virus particle production in supernatant measured by Vero plaque assay. The average of 2 independent experiments is presented. C–E) Cytopathic effect of observed by light microscopy 48 h after infection with the NiV-Malaysia isolate (C), the NiV-Bangladesh isolate (D), and CSUR381 (E). Giant multinucleated cells are indicated with arrowheads. Scale bar indicates 25 µm. HPMEC, human pulmonary microvascular endothelial cell; NiV, Nipah virus. **p<0.01; ***p<0.001.

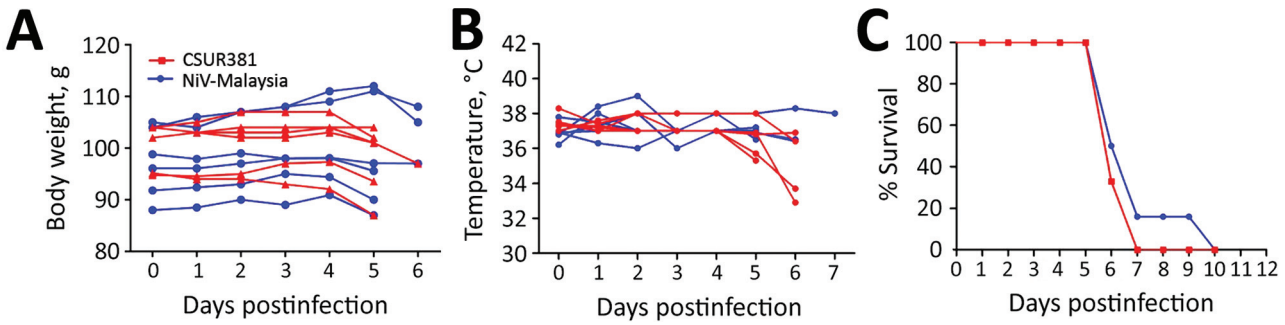

Figure 5. Pathogenicity of NiV CSUR381 (Cambodia 2003 isolate) and UMMC1 (NiV-Malaysia isolate) in golden hamsters (6 hamsters/group). A) Body weight. B) Body temperature. C) Survival. Survival between groups was not significantly different (Mantel-Cox test). NiV, Nipah virus.

Experimental Infection of Hamsters

We compared the pathogenicities of CSUR381 and the NiV-Malaysia isolate using the golden hamster animal model (*37*). We infected 6 hamsters with either CSUR381 or the NiV-Malaysia isolate and followed them for clinical signs of infection. At 6 days postinfection, the first neurologic signs (which included paralysis and trembling limbs) were observed in both groups; their presentation rapidly evolved toward breathing difficulties and prostration. Weight reductions were evident in several animals in the late stages of infection (Figure 5, panel A), and decreases in body temperature were found in a few hamsters (Figure 5, panel B). At 7 days postinfection, 100% lethality was observed in the CSUR381 group. In the Malaysia group, 1 animal survived until 10 days postinfection (Figure 5, panel C); however, the difference between the 2 groups was not significant. These results demonstrate similar lethality of the 2 analyzed NiV isolates, supporting our other data and suggesting CSUR381 has a high pathogenic potential.

Discussion

In this study, we performed a molecular and genetic characterization of CSUR381, a NiV isolated from *P. lylei* bats in Cambodia. Furthermore, we analyzed its pathogenicity compared with those of 2 other NiV isolates derived from human patients from the Malaysia and Bangladesh outbreaks. Our results highly suggest that CSUR381 is part of the NiV-Malaysia genotype. Further phylogenetic comparisons with other NiV isolates demonstrated 83%–99% amino acid homology for each of the 6 structural proteins. In addition, the editing site of the phosphoprotein gene was preserved, suggesting possible production of the nonstructural V and W proteins known to be involved in counteracting the host innate immune system and thus contributing to pathogenicity of CSUR381 (*32*).

Our virus entry studies showed highly similar results among the NiVs tested. All isolates entered *Pteropus* bat and human cell lines at similar levels; high conservation of the NiV entry receptors (ephrin-B2 and ephrin-B3) (*38*) might be responsible for the observed results. Our data also indicate that CSUR381 enters all tested cell types as well as the other 2 NiV isolates tested, suggesting that virus entry is not a limiting factor preventing CSUR381 spillover from bats to humans. In addition, all 3 tested NiV isolates infected cells and replicated in bat and human cell lines at similar levels. Results of infections with CSUR381 in hamsters additionally strengthened the notion that CSUR381 is possibly similar pathogenically to the tested NiV-Malaysia strain, which caused fatal outbreaks in Malaysia (*1*).

Although NiV has been shown to circulate in Cambodia (*20*,*21*), Thailand (*39*), and Vietnam (*40*), transmission to humans or domestic animals has not been reported in these countries. According to our results, the absence of detected outbreaks in this region cannot be attributed to lower pathogenicity of the circulating NiVs; our results suggest that other factors probably contribute. However, the NiV isolate presented in this report has been the only live NiV isolated in this region, and the existence of other NiVs with different pathogenic potentials cannot be excluded.

In Cambodia, *P. lylei* bats were found to often forage in residential areas and visit palm trees used in the region as a source of date palm sap; thus, opportunities abound for bats to interact with humans and livestock in this country (*41*). Bat colony migration toward urban sites is further enhanced by the presence of hunters in rural areas (*42*) and deforestation (causing consequent damage to roosting trees and food sources) (*43*). Contamination of palm sap, which is consumed raw by persons in the region, with bat urine, saliva, or feces was found to be a major route of NiV transmission to humans during annual outbreaks in Bangladesh (*10*).

Diverse agricultural practices in Southeast Asia could also play a role in NiV regional ecodynamics, potentially favoring easier NiV spillover in some

countries over others. High intensity pig farming was recognized as a major risk factor for outbreaks in Malaysia during 1998–1999; because of the low-scale pig production ongoing in Cambodia (*44*), the risk for NiV transmission from *Pteropus* spp. to domestic animals and humans in this country might be reduced.

Unrecognized NiV outbreaks might have occurred in Cambodia and neighboring countries; hospital-based surveillance in Bangladesh was shown to have missed nearly half of the NiV outbreaks in that country since the first reported virus emergence (*45*). Interdisciplinary approaches are certainly required to identify these outbreaks and the drivers of NiV emergence (*46*), and regular testing of patients with encephalitis in Cambodia and neighboring countries could provide additional insight. Our study contributes to the assessment of the risk for NiV outbreaks in Asia. Our findings can be used to help target adequate preventive measures, which could ultimately help reduce the risk for NiV emergence.

Acknowledgments

We thank Jean-Marc Reynes and Pasteur Institute staff for providing us with the NiV Cambodia isolate and Doris Preininger, Anton Weissenbacher, and Tiergarten Schönbrunn for *P. giganteus* bat sampling. We thank Amelia Charlotte Coggon for English proofreading of the manuscript, and we also thank François Enchéry, Kévin Dhondt, Mathieu Iampietro, Sylvain Baize, and Géraldine Gourru-Lesimple for help initiating and finalizing this work.

This work was supported by LABEX ECOFECT (ANR-11-LABX-0048) of Lyon University, within the program Investissements d'Avenir (ANR-11-IDEX-0007) operated by the French National Research Agency, ANR-18-CE11-0014-02, Aviesan Sino-French Agreement on Nipah Virus Study, and the International Division of the Institut Pasteur in Paris (Actions Concertées Inter-Pasteurienne). J.F. was supported by the doctoral fellowship CIFRE-Défense operated by the Direction Générale de l'Armement.

About the Author

Ms. Gaudino is a graduate student at the International Centre for Infectiology Research in Lyon, France. Her main research interests include the study of mechanisms of pathogenicity and epidemiology of viral zoonoses.

References

1. Chua KB, Bellini WJ, Rota PA, Harcourt BH, Tamin A, Lam SK, et al. Nipah virus: a recently emergent deadly paramyxovirus. Science. 2000;288:1432–5. https://doi.org/10.1126/science.288.5470.1432
2. Arunkumar G, Chandni R, Mourya DT, Singh SK, Sadanandan R, Sudan P, et al.; Nipah Investigators People and Health Study Group. Outbreak investigation of Nipah virus disease in Kerala, India, 2018. J Infect Dis. 2019;219:1867–78. https://doi.org/10.1093/infdis/jiy612
3. Luby SP, Gurley ES, Hossain MJ. Transmission of human infection with Nipah virus. Clin Infect Dis. 2009;49:1743–8. https://doi.org/10.1086/647951
4. Sweileh WM. Global research trends of World Health Organization's top eight emerging pathogens. Global Health. 2017;13:9. https://doi.org/10.1186/s12992-017-0233-9
5. Murray K, Selleck P, Hooper P, Hyatt A, Gould A, Gleeson L, et al. A morbillivirus that caused fatal disease in horses and humans. Science. 1995;268:94–7. https://doi.org/10.1126/science.7701348
6. Marsh GA, de Jong C, Barr JA, Tachedjian M, Smith C, Middleton D, et al. Cedar virus: a novel henipavirus isolated from Australian bats. PLoS Pathog. 2012;8:e1002836. http://dx.doi.org/10.1371/journal.ppat.1002836
7. Drexler JF, Corman VM, Müller MA, Maganga GD, Vallo P, Binger T, et al. Bats host major mammalian paramyxoviruses. Nat Commun. 2012;3:796. https://doi.org/10.1038/ncomms1796
8. Wu Z, Yang L, Yang F, Ren X, Jiang J, Dong J, et al. Novel henipa-like virus, Mojiang paramyxovirus, in rats, China, 2012. Emerg Infect Dis. 2014;20:1064–6. https://doi.org/10.3201/eid2006.131022
9. Middleton DJ, Morrissy CJ, van der Heide BM, Russell GM, Braun MA, Westbury HA, et al. Experimental Nipah virus infection in pteropid bats (*Pteropus poliocephalus*). J Comp Pathol. 2007;136:266–72. https://doi.org/10.1016/j.jcpa.2007.03.002
10. Luby SP, Rahman M, Hossain MJ, Blum LS, Husain MM, Gurley E, et al. Foodborne transmission of Nipah virus, Bangladesh. Emerg Infect Dis. 2006;12:1888–94. https://doi.org/10.3201/eid1212.060732
11. Middleton DJ, Westbury HA, Morrissy CJ, van der Heide BM, Russell GM, Braun MA, et al. Experimental Nipah virus infection in pigs and cats. J Comp Pathol. 2002;126:124–36. https://doi.org/10.1053/jcpa.2001.0532
12. Luby SP, Gurley ES, Hossain MJ. Transmission of human infection with Nipah virus. Clin Infect Dis. 2009;49:1743–8. https://doi.org/10.1086/647951
13. Sejvar JJ, Hossain J, Saha SK, Gurley ES, Banu S, Hamadani JD, et al. Long-term neurological and functional outcome in Nipah virus infection. Ann Neurol. 2007;62:235–42. https://doi.org/10.1002/ana.21178
14. Tan CT, Goh KJ, Wong KT, Sarji SA, Chua KB, Chew NK, et al. Relapsed and late-onset Nipah encephalitis. Ann Neurol. 2002;51:703–8. https://doi.org/10.1002/ana.10212
15. Enchéry F, Horvat B. Understanding the interaction between henipaviruses and their natural host, fruit bats: paving the way toward control of highly lethal infection in humans. Int Rev Immunol. 2017;36:108–21. https://doi.org/10.1080/08830185.2016.1255883
16. Halpin K, Young PL, Field HE, Mackenzie JS. Isolation of Hendra virus from pteropid bats: a natural reservoir of Hendra virus. J Gen Virol. 2000;81:1927–32. https://doi.org/10.1099/0022-1317-81-8-1927
17. de Araujo J, Lo MK, Tamin A, Ometto TL, Thomazelli LM, Nardi MS, et al. Antibodies against henipa-like viruses in Brazilian bats. Vector Borne Zoonotic Dis. 2017;17:271–4. https://doi.org/10.1089/vbz.2016.2051
18. Luby SP. The pandemic potential of Nipah virus. Antiviral Res. 2013;100:38–43. https://doi.org/10.1016/j.antiviral.2013.07.011

19. Mathieu C, Horvat B. Henipavirus pathogenesis and antiviral approaches. Expert Rev Anti Infect Ther. 2015;13:343–54. https://doi.org/10.1586/14787210.2015.1001838
20. Olson JG, Rupprecht C, Rollin PE, An US, Niezgoda M, Clemins T, et al. Antibodies to Nipah-like virus in bats (*Pteropus lylei*), Cambodia. Emerg Infect Dis. 2002;8:987–8. https://doi.org/10.3201/eid0809.010515
21. Reynes J-M, Counor D, Ong S, Faure C, Seng V, Molia S, et al. Nipah virus in Lyle's flying foxes, Cambodia. Emerg Infect Dis. 2005;11:1042–7. https://doi.org/10.3201/eid1107.041350
22. Thomas HA. BioEdit, a user friendly biological sequence alignment editor and analysis program for Windows 95/98/NT. Nucleic Acids Symp Ser. 1999;41:95–8.
23. Kumar S, Stecher G, Tamura K. MEGA7: Molecular Evolutionary Genetics Analysis version 7.0 for bigger datasets. Mol Biol Evol. 2016;33:1870–4. https://doi.org/10.1093/molbev/msw054
24. Krump-Konvalinkova V, Bittinger F, Unger RE, Peters K, Lehr HA, Kirkpatrick CJ. Generation of human pulmonary microvascular endothelial cell lines. Lab Invest. 2001;81:1717–27. https://doi.org/10.1038/labinvest.3780385
25. Mlíkovský J. Correct name for the Indian flying fox (*Pteropodidae*). Vespertilio. 2012;16:203–4.
26. Saccone C, Attimonelli M, Sbisà E. Structural elements highly preserved during the evolution of the D-loop-containing region in vertebrate mitochondrial DNA. J Mol Evol. 1987;26:205–11. https://doi.org/10.1007/BF02099853
27. Dool SE, Puechmaille SJ, Foley NM, Allegrini B, Bastian A, Mutumi GL, et al. Nuclear introns outperform mitochondrial DNA in inter-specific phylogenetic reconstruction: lessons from horseshoe bats (*Rhinolophidae*: Chiroptera). Mol Phylogenet Evol. 2016;97:196–212. https://doi.org/10.1016/j.ympev.2016.01.003
28. Reynard O, Volchkov VE. Characterization of a novel neutralizing monoclonal antibody against Ebola virus GP. J Infect Dis. 2015;212(Suppl 2):S372–8. https://doi.org/10.1093/infdis/jiv303
29. Talekar A, Pessi A, Glickman F, Sengupta U, Briese T, Whitt MA, et al. Rapid screening for entry inhibitors of highly pathogenic viruses under low-level biocontainment. PLoS One. 2012;7:e30538. https://doi.org/10.1371/journal.pone.0030538
30. Whitt MA. Generation of VSV pseudotypes using recombinant ΔG-VSV for studies on virus entry, identification of entry inhibitors, and immune responses to vaccines. J Virol Methods. 2010;169:365–74. http://dx.doi.org/10.1016/j.jviromet.2010.08.006
31. Mathieu C, Guillaume V, Sabine A, Ong KC, Wong KT, Legras-Lachuer C, et al. Lethal Nipah virus infection induces rapid overexpression of CXCL10. PLoS One. 2012;7:e32157. https://doi.org/10.1371/journal.pone.0032157
32. Satterfield BA, Cross RW, Fenton KA, Agans KN, Basler CF, Geisbert TW, et al. The immunomodulating V and W proteins of Nipah virus determine disease course. Nat Commun. 2015;6:7483. https://doi.org/10.1038/ncomms8483
33. Guillaume V, Aslan H, Ainouze M, Guerbois M, Wild TF, Buckland R, et al. Evidence of a potential receptor-binding site on the Nipah virus G protein (NiV-G): identification of globular head residues with a role in fusion promotion and their localization on an NiV-G structural model. J Virol. 2006;80:7546–54. https://doi.org/10.1128/JVI.00190-06
34. Xu K, Broder CC, Nikolov DB. Ephrin-B2 and ephrin-B3 as functional henipavirus receptors. Semin Cell Dev Biol. 2012;23:116–23. https://doi.org/10.1016/j.semcdb.2011.12.005
35. Porotto M, Rockx B, Yokoyama CC, Talekar A, Devito I, Palermo LM, et al. Inhibition of Nipah virus infection in vivo: targeting an early stage of paramyxovirus fusion activation during viral entry. PLoS Pathog. 2010;6:e1001168. https://doi.org/10.1371/journal.ppat.1001168
36. Desmyter J, Melnick JL, Rawls WE. Defectiveness of interferon production and of rubella virus interference in a line of African green monkey kidney cells (Vero). J Virol. 1968;2:955–61.
37. Wong KT, Grosjean I, Brisson C, Blanquier B, Fevre-Montange M, Bernard A, et al. A golden hamster model for human acute Nipah virus infection. Am J Pathol. 2003;163:2127–37. https://doi.org/10.1016/S0002-9440(10)63569-9
38. Bossart KN, Tachedjian M, McEachern JA, Crameri G, Zhu Z, Dimitrov DS, et al. Functional studies of host-s pecific ephrin-B ligands as henipavirus receptors. Virology. 2008;372:357–71. https://doi.org/10.1016/j.virol.2007.11.011
39. Wacharapluesadee S, Lumlertdacha B, Boongird K, Wanghongsa S, Chanhome L, Rollin P, et al. Bat Nipah virus, Thailand. Emerg Infect Dis. 2005;11:1949–51. https://doi.org/10.3201/eid1112.050613
40. Hasebe F, Thuy NTT, Inoue S, Yu F, Kaku Y, Watanabe S, et al. Serologic evidence of Nipah virus infection in bats, Vietnam. Emerg Infect Dis. 2012;18:536–7. https://doi.org/10.3201/eid1803.111121
41. Choden K, Ravon S, Epstein JH, Hoem T, Furey N, Gely M, et al. *Pteropus lylei* primarily forages in residential areas in Kandal, Cambodia. Ecol Evol. 2019;9:4181–91. https://doi.org/10.1002/ece3.5046
42. Thanapongtharm W, Linard C, Wiriyarat W, Chinsorn P, Kanchanasaka B, Xiao X, et al. Spatial characterization of colonies of the flying fox bat, a carrier of Nipah virus in Thailand. BMC Vet Res. 2015;11:81. http://dx.doi.org/10.1186/s12917-015-0390-0
43. Thanapongtharm W, Paul MC, Wiratsudakul A, Wongphruksasoong V, Kalpravidh W, Wongsathapornchai K, et al. A spatial assessment of Nipah virus transmission in Thailand pig farms using multi-criteria decision analysis. BMC Vet Res. 2019;15:73. https://doi.org/10.1186/s12917-019-1815-y
44. Huynh TTT, Aarnink AJA, Drucker A, Verstegen MWA. Pig production in Cambodia, Laos, Philippines, and Vietnam: a review. Asian J Agric Dev. 2006;3:69–90.
45. Hegde ST, Salje H, Sazzad HMS, Hossain MJ, Rahman M, Daszak P, et al. Using healthcare-seeking behaviour to estimate the number of Nipah outbreaks missed by hospital-based surveillance in Bangladesh. Int J Epidemiol. 2019;48:1219–27. https://doi.org/10.1093/ije/dyz057
46. Daszak P, Zambrana-Torrelio C, Bogich TL, Fernandez M, Epstein JH, Murray KA, et al. Interdisciplinary approaches to understanding disease emergence: the past, present, and future drivers of Nipah virus emergence. Proc Natl Acad Sci U S A. 2013;110(Suppl 1):3681–8. https://doi.org/10.1073/pnas.1201243109

Address for correspondence: Branka Horvat, CIRI, INSERM U1111, 21 Ave Tony Garnier, 69007, Lyon, France; email: branka.horvat@inserm.fr

Physiopathologie de l'infection du système nerveux central par des virus respiratoires

Les virus respiratoires aéroportés sont particulièrement préoccupants du fait de la difficulté de contrôler leur transmission. Parmi ces virus, le virus du syndrome respiratoire aigu sévère 2 (SARS-CoV-2), le virus de la rougeole (VR) et les Henipavirus Nipah (NiV) et Hendra (HeV) peuvent infecter également le système nerveux central (SNC) chez l'homme et provoquent alors souvent des encéphalites létales. Par exemple, le SARS-CoV-2, responsable de la pandémie de COVID-19, entraine un syndrome respiratoire aigu sévère et des atteintes neurologiques. De son côté, et malgré un vaccin efficace, la rougeole connaît une réémergence inquiétante et cause la mort de plus de 200 000 personnes par an. Le VR peut entraîner des encéphalites rougeoleuses à corps d'inclusion (MIBE) dans un contexte d'immunodéficience ou une panencéphalite sclérosante subaiguë (PESS) parfois des décennies après l'exposition au virus chez des patients immunocompétents. NiV et HeV sont des Paramyxovirus zoonotiques hautement pathogènes du genre Henipavirus. Malgré le faible nombre de cas humains recensés depuis leur émergence à la fin des années 1990, les NiV et HeV sont classés parmi les huit pathogènes prioritaires pour la recherche par l'Organisation Mondiale de la Santé en raison de leur fort potentiel pandémique. Certaines souches sont mortelles dans plus de 70% des cas en moyenne.

À ce jour il n'existe pas de traitement efficace commercialisé pour traiter ces infections virales chez l'homme. De plus, les étapes précoces de l'infection du SNC par ces virus restent peu documentées car la majorité des données proviennent d'analyses réalisées *post mortem*. L'objectif global de cette thèse a été d'identifier des facteurs influençant l'invasion du SNC par ces virus. Le tropisme initial, la dissémination, ainsi que l'implication des glycoprotéines virales de surface et l'évolution génétique virale ont été analysées pour le SARS-CoV-2, le VR et plusieurs souches d'Henipavirus à l'échelle organique, cellulaire et moléculaire.

Deux nouveaux modèles de cultures organotypiques de poumons et de tronc cérébral chez le hamster ont été développés et caractérisés. Ces modèles *ex vivo* sont susceptibles à l'infection par le SARS-CoV-2 et par le NiV. En revanche, un mutant hyperfusogène du VR, pourtant capable de fusionner en l'absence de récepteur connu, n'infecte que les cultures de cerveau. Ces cultures organotypiques ont permis de valider le tropisme initial du SARS-CoV-2 dans les poumons et démontré la permissivité de certains neurones dans le cerveau. Ces modèles ont également permis d'établir que l'infection par le SARS-CoV-2 induit une réponse interféron spécifique et une réponse immunitaire innée, ainsi qu'une mort cellulaire par apoptose, nécroptose et pyroptose dans ces organes. Enfin, ces cultures organotypiques ont montré leur pertinence dans la validation d'antiviraux. L'étude de VR portant des mutations dans leur protéine de fusion observées lors d'encéphalites rougeoleuses a montré l'importance du caractère hyperfusogène de ces mutants pour se disséminer dans le SNC pourtant dépourvu de récepteurs connus. Des différences dans la machinerie de fusion de trois souches pathogènes d'Henipavirus ont aussi été identifiées et analysées.

Grace aux cultures organotypiques cérébrales de hamster et de souris transgéniques plusieurs candidats antiviraux ont été testés pour bloquer la dissémination du VR sauvage et de variants neuroinvasifs, mais aussi du NiV et du SARS-CoV-2. Ces résultats donnent des perspectives nouvelles d'utilisation de ces modèles *ex vivo* pour étudier l'infection par des virus émergents et pour évaluer l'efficacité de traitements en amont de validation *in vivo*. L'étude comparative de l'infection des cultures organotypiques par ces virus respiratoires à pathogénicité variable a illustré comment la machinerie de fusion peut influencer la dissémination virale dans le cerveau.

Marion Ferren